Tetsuo Tobita
Koji Ichii
Kyohei Ueda *Editors*

Model Tests and Numerical Simulations of Liquefaction and Lateral Spreading II

LEAP-ASIA-2019

Springer

Model Tests and Numerical Simulations of Liquefaction and Lateral Spreading II

Tetsuo Tobita • Koji Ichii • Kyohei Ueda
Editors

Model Tests and Numerical Simulations of Liquefaction and Lateral Spreading II

LEAP-ASIA-2019

Springer

Editors
Tetsuo Tobita
Kansai University
Osaka, Japan

Koji Ichii
Kansai University
Osaka, Japan

Kyohei Ueda
Division of Geotechnics
Kyoto University, Disaster Prevention
Research Institute
Kyoto, Japan

ISBN 978-3-031-48820-7 ISBN 978-3-031-48821-4 (eBook)
https://doi.org/10.1007/978-3-031-48821-4

This Springer imprint is published by the registered company Springer Nature Switzerland AG
The registered company address is: Gewerbestrasse 11, 6330 Cham, Switzerland

Paper in this product is recyclable.

This book is dedicated to the memory of the late Prof. Dong-Soo Kim whose unyielding support and encouragement have enriched our souls and inspired us to pursue and continue this project.

Preface

This book presents work collected through the **L**iquefaction **E**xperiments and **A**nalysis **P**rojects in 2019 (LEAP-ASIA-2019). This LEAP follows LEAP-UCD-2017 which culminated in the publication of the LEAP-2017 proceedings as a first volume. In addition to the 2017 research targets, such as repeatability, variability, and sensitivity of lateral spreading on mildly sloping liquefiable sand, this volume includes research efforts to validate the generalized scaling law (GSL) using centrifuge testing of a prototype identical to the one employed in LEAP-UCD-2017. In LEAP-ASIA-2019, round-robin centrifuge model tests were conducted in collaboration with 10 international institutes on identical saturated sloping sand layers with a wider range of initial conditions in terms of density and amplitude of input acceleration than those of UCD-2017 series. Two tests were assigned to each institute for two purposes: (1) validation of the generalized scaling law (GSL) and (2) development of additional experimental data sets to fill the gaps in the existing experimental data sets. It was the first multi-institutional attempt to investigate the validity of the generalized scaling law for a saturated sandy sloping deposit under a wide range of initial and testing conditions. The experimental data provided a unique basis for assessing the capabilities of six different numerical simulation platforms for the numerical simulation of soil liquefaction.

Close communication through many international on-line meetings held in 2018-2019 were the key in obtaining high-quality and consistent results as they had been done in the previous exercises. Finally, results were presented in an international workshop held in March 2019 at Kansai University, Osaka, Japan. The project participants presented and discussed the results of the experiments and the numerical simulations as described in the papers in this book. Although some results have been already published in the special issue of *Soil Dynamics and Earthquake Engineering* (https://www.sciencedirect.com/journal/soil-dynamics-and-earthquake-engineering/special-issue/10NXRLS4NFM), this book contains full measures of results obtained in LEAP-ASIA-2019.

This book consists of the following three parts:

1. Overall summary of the results of the centrifuge model experiments, calibration results for the numerical element tests, and results of Type B and C analyses (Chaps. 1, 2, 3 and 4).
2. Detailed reports on the centrifuge model experiments of each institute (Chaps. 5, 6, 7, 8, 9, 10, 11, 12 and 13).
3. Detailed reports on the numerical analysis of each institute (Chaps. 14, 15, 16, 17, 18, 19 and 20).

The following is a list of major findings and issues that were identified through LEAP-ASIA-2019.

1. Since LEAP-GWU-2015 and LEAP-UCD-2017, one of the main objectives of LEAP has been to create and publish a large and high-quality database of physical models and element tests to contribute to evaluating and validating the ability of analytical tools to predict liquefaction mechanisms and consequences. Researchers have worked hard to establish and extend the laboratory test database to characterize the physical and mechanical properties of the Ottawa F-65 sand. This is being continued in LEAP-ASIA-2019. All the data produced by LEAP-ASIA-2019 are now open to public through the NHERI Cyberinfrastructure Center's DesignSafe at https://www.designsafe-ci.org/data/browser/public/designsafe.storage.published/PRJ-2438v2.
2. A series of stress-controlled undrained cyclic hollow cylinder torsional shear tests were conducted at the Disaster Prevention Research Institute, Kyoto University, for four different relative densities (D_r = 50%, 60%, 70%, and 85%) to contribute to understanding the mechanical properties of the Ottawa F-65 sand. Details of the modeling and the results of the tests conducted prior to the LEAP-ASIA-2019 workshop are reported. The database was enriched by adding new data on the physical and mechanical properties of Ottawa F-65 sand.
3. The GSL was verified for acceleration and excess pore water pressure within the range of densities and input accelerations performed in this experimental series. For displacements, deviation from the displacements converted from the conventional scaling law for centrifuge modeling increased as displacement increased. Under the present experimental conditions, the error was found to be large for displacements exceeding 250 mm in the prototype scale.
4. The trend surface relating among the lateral displacement U_{x2}, the relative density Dr_q_c (2.0 m) estimated from the penetration test, and the filtered input acceleration PGA_{eff} proposed in LEAP-UCD-2017 were updated by adding new data.
5. Stress-controlled undrained cyclic hollow cylinder torsional shear test results of Ottawa F-65 sand with 50% and 60% relative density were used to calibrate the numerical analysis model. Although liquefaction strength curves were reproduced well by the majority of participated models, some models showed difficulty in simulating stress paths and stress-strain relationships.

6. In the Type-B and Type-C numerical simulations, the time histories of response acceleration, excess pore water pressure, and lateral displacement were compared with the experimental results and were able to reproduce the trends observed in the centrifuge experiments well. In particular, the Type-C simulations reproduced the experimental results more accurately by adjusting the model parameters. Although it is very difficult to perfectly reproduce all measured responses, such as acceleration, pore pressure, and displacement, it was shown that accumulating a database of high-quality experimental results can provide valuable data for improving numerical simulations.

Through the course of the LEAP-ASIA-2019, new ideas of building models and measuring physical parameters in centrifuge modelling have been tested and reported, which may be quite useful to readers who are encountering similar problems. Also, for numerical modelers, by referring the high-quality laboratory test data and centrifuge experimental data, their models can be tested, for example, by comparing results with the trend surface developed in the series of LEAP exercises.

Osaka, Japan Tetsuo Tobita
Osaka, Japan Koji Ichii
Kyoto, Japan Kyohei Ueda

Participants in the LEAP-ASIA-2019 Workshop at Kansai University, Japan

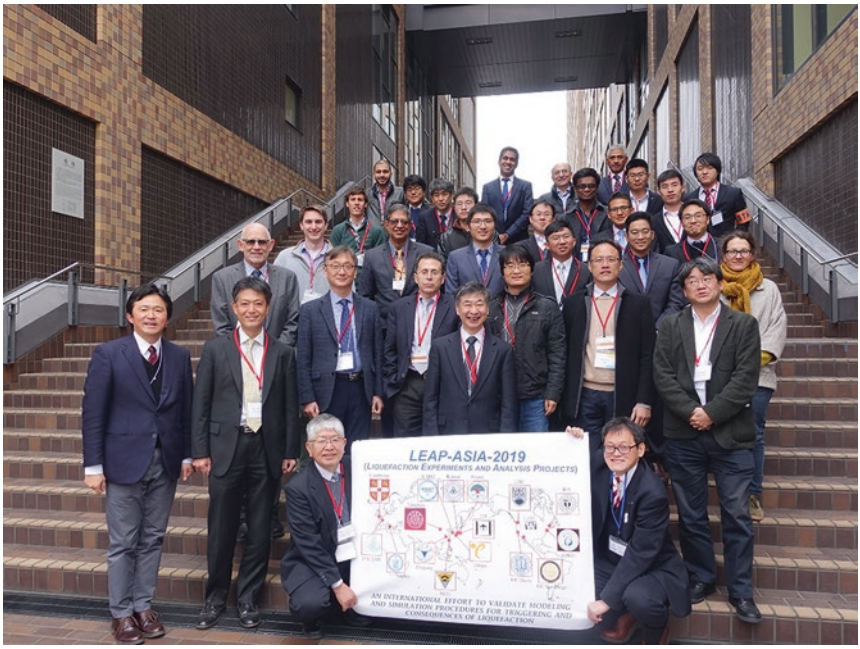

Location of Participating Institutes

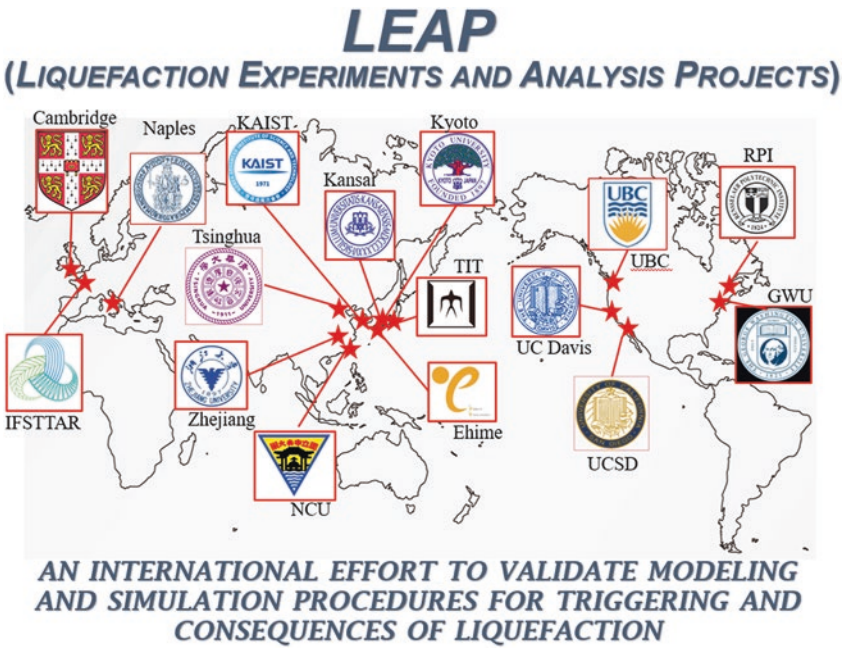

Participants List

Attendee	Affiliation
Trevor Carey	University of California, Davis
Ahmed Elgamal	University of California, San Diego
Mohamed El Ghoraiby	George Washington University
Sandra Escoffier	Univ Gustave Eiffel
Wen-Yi Hung	National Central University
Susumu Iai	DPRI (Kyoto University)/ Flip Consortium
Koji Ichii	Kansai University
Liu Kai	Zhejiang University
Kei Kashiwagi	Kansai University
Dong-Soo Kim	KAIST
Bruce Kutter	University of California, Davis
Gopal Madabhushi	University of Cambridge
Satish Manandhar	KAIST
Majid Manzari	George Washington University
Mitsu Okamura	Ehime University
Ma Qiang	Zhejiang University
Zhijian Qiu	University of California San Diego
Ruben Rodrigo Vargas Tapia	Penta-Ocean Construction Co. Ltd. (Former Kyoto University)
Anurag Sahare	DPRI (Kyoto University)
Nicholas Stone	University of California, Davis
Mahdi Taiebat	University of British Columbia
Yoshikazu Tanaka	DPRI (Kyoto University)
Tetsuo Tobita	Kansai University
Kyohei Ueda	DPRI (Kyoto University)
Ryosuke Uzuoka	DPRI (Kyoto University)
Nozomu Yoshida	Kanto Gakuin University
Mourad Zeghal	Rensselaer Polytechnic Institute
Yan-Guo Zhou	Zhejiang University

Acknowledgments

This work is [was] supported by the Future Development Funding Program of Kyoto University Research Coordination Alliance.

Contents

Contributors

Tarek Abdoun Department of Civil and Environmental Engineering, Rensselaer Polytechnic Institute, Troy, NY, USA

Pedro Arduino Department of Civil and Environmental Engineering, University of Washington, Seattle, WA, USA

Philippe Audrain Centrifuges for Geotechnics Lab., Univ. Gustave Eiffel, GERS-CG, Bouguenais, France

Andrés R. Barrero Department of Civil Engineering, University of British Columbia, Vancouver, BC, Canada

SRK Consulting Inc., Vancouver, BC, Canada

Emilio Bilotta Department of Civil, Architectural and Environmental Engineering, University of Naples Federico II, Naples, Italy

Department of Civil, Construction-Architectural and Environmental Engineering, University of L'Aquila, L'Aquila, Italy

Jad I. Boksmati Department of Engineering, Cambridge University, Cambridge, UK

Trevor J. Carey Department of Civil and Environmental Engineering, University of California, Davis, USA

Department of Civil Engineering, The University of British Columbia, Vancouver, Canada

Yun-Min Chen MOE Key Laboratory of Soft Soil and Geoenvironmental Engineering, Institute of Geotechnical Engineering, Center for Hypergravity Experiment and Interdisciplinary Research, Zhejiang University, Zhejiang, Hangzhou, P. R. China

Anna Chiaradonna Department of Civil, Architectural and Environmental Engineering, University of Naples Federico II, Naples, Italy

Mohamed A. Elbadawy Department of Civil Engineering, Zhejiang University, Hangzhou, People's Republic of China

MOE Key Laboratory of Soft Soils and Geoenvironmental Engineering, Institute of Geotechnical Engineering, Center for Hypergravity Experiment and Interdisciplinary Research, Zhejiang University, Hangzhou, P. R. China

Ahmed Elgamal Department of Structural Engineering, University of California San Diego, La Jolla, CA, USA

Sandra Escoffier Department GERS, Laboratory GC, University Gustave Eiffel, Nantes, France

Centrifuges for Geotechnics Lab., Univ. Gustave Eiffel, GERS-CG, Bouguenais, France

Gianluca Fasano Department of Civil, Architectural and Environmental Engineering, University of Naples Federico II, Naples, Italy

Alessandro Fusco Department of Engineering, Cambridge University, Cambridge, UK

Samy Garcia-Torres Department of Engineering, Cambridge University, Cambridge, UK

Stuart K. Haigh Department of Engineering, Cambridge University, Cambridge, UK

Lyu Hang Department of Civil and Environmental Engineering, Tokyo Institute of Technology, Tokyo, Japan

Jun-Xue Huang Department of Civil Engineering, National Central University, Taoyuan, Taiwan

Wen-Yi Hung Department of Civil Engineering, National Central University, Taoyuan, Taiwan

Junichi Hyodo Tokyo Electric Power Services Co., Tokyo, Japan

Susumu Iai FLIP Consortium, Kyoto, Japan

Koji Ichii Faculty of Societal Safety Science, Kansai University, Osaka, Japan

Dong-Soo Kim Department of Civil and Environmental Engineering, Korean Advanced Institute of Science and Technology, KAIST, Daejeon, Republic of Korea

Seong-Nam Kim Department of Civil and Environmental Engineering, Korean Advanced Institute of Science and Technology, KAIST, Daejeon, Republic of Korea

Evangelia Korre Department of Civil and Environmental Engineering, Rensselaer Polytechnic Institute, New York, USA

Department of Civil, Environmental and Geomatic Engineering, ETH Zürich (Former Department of Civil and Environmental Engineering, Rensselaer Polytechnic Institute, Troy, NY, USA), Zürich, Switzerland

Bruce L. Kutter Department of Civil and Environmental Engineering, University of California, Davis, CA, USA

Zheng Li Department GERS, Laboratory GC, University Gustave Eiffel, Nantes, France

Centrifuges for Geotechnics Lab., Univ. Gustave Eiffel, GERS-CG, Bouguenais, France

Kai Liu Department of Civil Engineering, Zhejiang University, Hangzhou, People's Republic of China

MOE Key Laboratory of Soft Soil and Geoenvironmental Engineering, Institute of Geotechnical Engineering, Center for Hypergravity Experiment and Interdisciplinary Research, Zhejiang University, Zhejiang, Hangzhou, P. R. China

Qiang Ma Department of Civil Engineering, Zhejiang University, Hangzhou, People's Republic of China

MOE Key Laboratory of Soft Soil and Geoenvironmental Engineering, Institute of Geotechnical Engineering, Center for Hypergravity Experiment and Interdisciplinary Research, Zhejiang University, Zhejiang, Hangzhou, P. R. China

Gopal Madabhushi Department of Engineering, Cambridge University, Cambridge, UK

Gopal S. P. Madabhushi Department of Engineering, Cambridge University, Cambridge, UK

Satish Manandhar Department of Civil and Environmental Engineering, Korean Advanced Institute of Science and Technology, KAIST, Daejeon, Republic of Korea

Majid Manzari Department of Civil and Environmental Engineering, George Washington University, Washington, DC, USA

Mitsu Okamura Department of Civil and Environmental Engineering, Ehime University, Matsuyama, Japan

Graduate School of Science and Engineering, Ehime University, Matsuyama, Japan

Andres Reyes Parra Department of Civil Engineering, University of British Columbia, Vancouver, BC, Canada

Truong-Nhat-Phuong Pham Department of Civil Engineering, National Central University, Taoyuan, Taiwan

Zhijian Qiu Department of Structural Engineering, University of California San Diego, La Jolla, CA, USA

School of Architecture and Civil Engineering, Xiamen University, Xiamen, Fujian, China

Andrés Reyes Department of Civil Engineering, University of British Columbia, Vancouver, BC, Canada

Anurag Sahare Disaster Prevention Research Institute, Kyoto University, Kyoto, Japan

Anthony Santana Department of Civil and Environmental Engineering, University of California, Davis, CA, USA

Asri Nurani Sjafruddin Department of Civil and Environmental Engineering, Ehime University, Matsuyama, Japan

Graduate School of Science and Engineering, Ehime University, Matsuyama, Japan

Nicholas S. Stone Department of Civil and Environmental Engineering, University of California, Davis, CA, USA

Mahdi Taiebat Department of Civil Engineering, University of British Columbia, Vancouver, BC, Canada

Jiro Takemura Department of Civil and Environmental Engineering, Tokyo Institute of Technology, Tokyo, Japan

Yoshikazu Tanaka Disaster Prevention Research Institute, Kyoto University, Kyoto, Japan

Tetsuo Tobita Department of Civil, Environmental and Applied Systems Engineering, Kansai University, Osaka, Japan

Samy Torres-Garcia Department of Engineering, Cambridge University, Cambridge, UK

Kyohei Ueda Disaster Prevention Research Institute, Kyoto University, Kyoto, Japan

Kazuaki Uemura Core Laboratory, Oyo Corporation, Saitama, Japan

Ryosuke Uzuoka Disaster Prevention Research Institute, Kyoto University, Kyoto, Japan

Ruben R. Vargas Disaster Prevention Research Institute, Kyoto University, Kyoto, Japan

Penta-Ocean Construction Co. Ltd. (Former Department of Civil and Earth Resources Engineering, Kyoto University, Kyoto, Japan), Tokyo, Japan

Rui Wang Department of Hydraulic Engineering, Tsinghua University, Beijing, China

Department of Hydraulic Engineering, State Key Laboratory of Hydroscience and Engineering, Tsinghua University, Beijing, China

Waka Yuyama FLIP Consortium, Kyoto, Japan

Mourad Zeghal Department of Civil and Environmental Engineering, Rensselaer Polytechnic Institute, Troy, NY, USA

Jian-Min Zhang Department of Hydraulic Engineering, Tsinghua University, Beijing, China

Department of Hydraulic Engineering, State Key Laboratory of Hydroscience and Engineering, Tsinghua University, Beijing, China

Chuang Zhou Department of Hydraulic Engineering, Tsinghua University, Beijing, China

Department of Hydraulic Engineering, State Key Laboratory of Hydroscience and Engineering, Tsinghua University, Beijing, China

Yan-Guo Zhou Department of Civil Engineering, Zhejiang University, Hangzhou, People's Republic of China

MOE Key Laboratory of Soft Soil and Geoenvironmental Engineering, Institute of Geotechnical Engineering, Center for Hypergravity Experiment and Interdisciplinary Research, Zhejiang University, Zhejiang, Hangzhou, P. R. China

Tong Zhu Department of Hydraulic Engineering, Tsinghua University, Beijing, China

Department of Hydraulic Engineering, State Key Laboratory of Hydroscience and Engineering, Tsinghua University, Beijing, China

Part I
Overview Papers

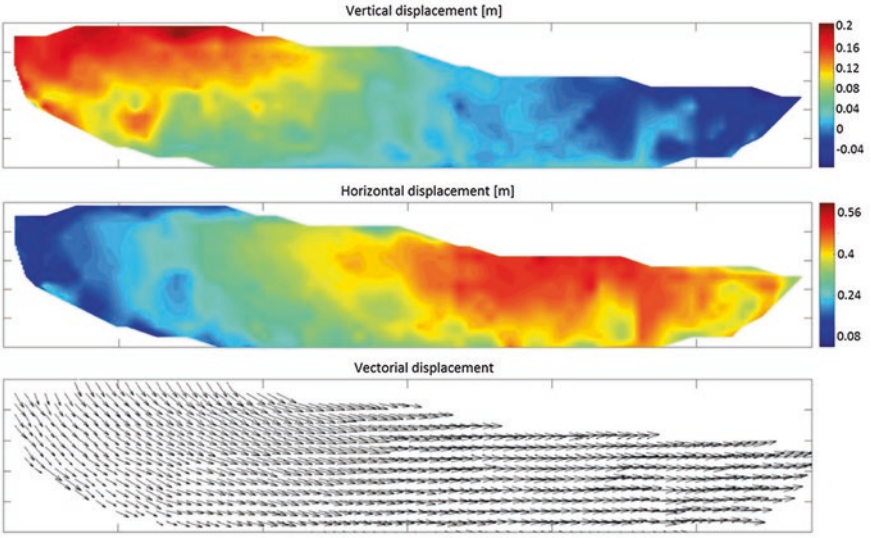

Gopal S.P. Madabhushi, Stuart K. Haigh, Jad I. Boksmati, Samy Garcia-Torres, and Alessandro Fusco

Chapter 1
LEAP-ASIA-2019: Summary of Centrifuge Experiments on Liquefaction-Induced Lateral Spreading – Application of the Generalized Scaling Law

Tetsuo Tobita, Koji Ichii, Kyohei Ueda, Ryosuke Uzuoka, Ruben R. Vargas, Mitsu Okamura, Asri Nurani Sjafruddin, Jiro Takemura, Lyu Hang, Susumu Iai, Jad Boksmati, Alessandro Fusco, Samy Torres-Garcia, Stuart Haigh, Gopal Madabhushi, Majid Manzari, Sandra Escoffier, Zheng Li, Dong Soo Kim, Satish Manandhar, Wen-Yi Hung, Jun-Xue Huang, Truong-Nhat-Phuong Pham, Mourad Zeghal, Tarek Abdoun, Evangelia Korre, Bruce L. Kutter, Trevor J. Carey, Nicholas Stone, Yan-Guo Zhou, Kai Liu, and Qiang Ma

Abstract In the framework of Liquefaction Experiments and Analysis Projects (LEAP), round-robin centrifuge model tests were conducted in collaboration with ten international institutes on identical saturated sloping sand layers with a wide range of initial conditions. Two tests, one with a model following conventional centrifuge scaling law and the other with a model following the generalized scaling law (GSL), were assigned to each institute for two purposes: (1) validation of the generalized scaling law (GSL) and (2) development of additional experimental data sets to fill the gaps in the existing experimental data sets. The GSL may be validated when the ground deformation is small (less than 250 mm in the present study). The

Part of the contents has been published in Tobita et al. (2022).

T. Tobita (✉)
Department of Civil, Environmental and Applied Systems Engineering, Kansai University, Osaka, Japan
e-mail: tobita@kansai-u.ac.jp

K. Ichii
Faculty of Societal Safety Science, Kansai University, Osaka, Japan

K. Ueda · R. Uzuoka · R. R. Vargas
Disaster Prevention Research Institute, Kyoto University, Kyoto, Japan

M. Okamura · A. N. Sjafruddin
Department of Civil and Environmental Engineering, Ehime University, Matsuyama, Japan

T. Tobita et al. (eds.), *Model Tests and Numerical Simulations of Liquefaction and Lateral Spreading II*, https://doi.org/10.1007/978-3-031-48821-4_1

trend surface was updated with the new data sets, whose trend is consistent with the previous one.

Keywords Liquefaction Experiments and Analysis Projects (LEAP-ASIA-2019) · Generalized scaling law (GSL) · Centrifuge modeling

1.1 Introduction

With major advances in computer science and technology, numerical modeling has made great strides in the field of earthquake geotechnical engineering. More than three decades ago, under the project called VELACS (Arulanandan & Scott, 1993, 1994), various institutes conducted centrifuge experiments to simulate ground response under liquefaction, and consistency with experimental results was verified for several numerical methods. At present, numerical simulation is a common practice to validate a design under static and dynamic loading conditions. To name a few, numerical models employed in practice are FLIP (Iai et al., 1992; Iai et al., 2013), LIQCA (Oka et al., 1999), PM4Sand (Boulanger & Ziotopoulou, 2015), and

J. Takemura · L. Hang
Department of Civil and Environmental Engineering, Tokyo Institute of Technology, Tokyo, Japan

S. Iai
FLIP Consortium, Kyoto, Japan

J. Boksmati · A. Fusco · S. Torres-Garcia · S. Haigh · G. Madabhushi
Department of Engineering, Cambridge University, Cambridge, UK

M. Manzari
Department of Civil and Environmental Engineering, George Washington University, Washington, DC, USA

S. Escoffier · Z. Li
Department GERS, Laboratory GC, University Gustave Eiffel, Nantes, France

D. S. Kim · S. Manandhar
Department of Civil and Environmental Engineering, Korean Advanced Institute of Science and Technology, KAIST, Republic of Korea

W.-Y. Hung · J.-X. Huang · T.-N.-P. Pham
Department of Civil Engineering, National Central University, Taoyuan, Taiwan

M. Zeghal · T. Abdoun · E. Korre
Department of Civil and Environmental Engineering, Rensselaer Polytechnic Institute, New York, USA

B. L. Kutter · T. J. Carey · N. Stone
Department of Civil and Environmental Engineering, University of California, Davis, USA

Y.-G. Zhou · K. Liu · Q. Ma
Department of Civil Engineering, Zhejiang University, Hangzhou, People's Republic of China

GEOASIA (Asaoka & Noda, 2007). Recently, particle methods, such as DEM (Cundall & Strack, 1979), SPH (Lucy, 1977; Monaghan, 1992), and MPS (Koshizuka et al., 1996), have been evolved and increasing users along with the advances in computing. However, they may not be advanced enough to be used in practice.

LEAP (Liquefaction Experiments and Analysis Projects) is an international collaboration project aiming at validating both experimental and analytical methods to study liquefaction-related phenomena (Manzari et al., 2015). So far, three exercises under the LEAP have been developed. All dealt with the dynamic response on saturated slopes. In LEAP-GWU-2015 (Manzari et al., 2018), six international institutions set up the model to be identical in density of the model ground and input motion in prototype scale and conducted centrifuge tests. The model ground consisted of a uniform sand layer of Ottawa F-65 sand, with a depth of 4 m in the middle, a length of 20 m, and a slope of 5 degrees (Fig. 1.1). As reported in Kutter et al. (2018), the strong correlation in the results prompted the development of a large-scale database for centrifuge modeling.

Then the LEAP-UCD-2017 had been initiated and produced a sufficient number of tests and obtained the mean response of a specific sloping sand deposit (Kutter et al., 2020a). In their exercise, in 9 different international centrifuge facilities, 24 centrifuge experiments were conducted with various densities of the ground and

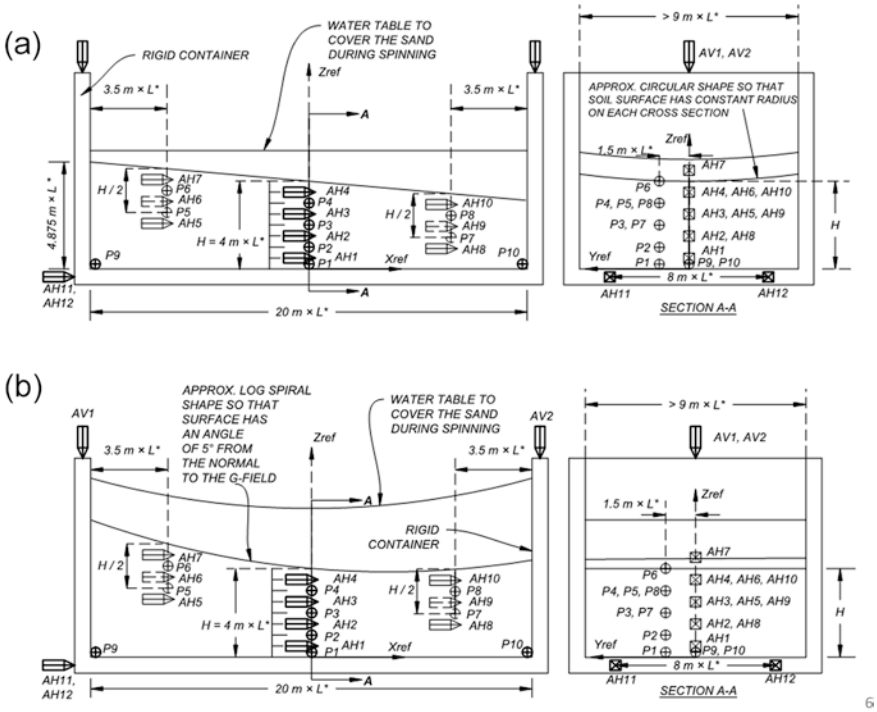

Fig. 1.1 Dimensions of the model and sensor position when shaken (**a**) parallel and (**b**) perpendicular to the centrifuge rotation axis. (After Kutter et al., 2018)

peak ground acceleration (PGA) while keeping the same geometry as in the previous exercise. As the results, clear and consistent trends were found among the density of the ground, the input PGA, and the residual surface ground displacements.

Following the successful exercises, LEAP-ASIA-2019 set two objectives: (1) to validate the "generalized scaling law" (Iai et al., 2005) and (2) to increase the amount of experimental data to supplement the existing database developed by the "LEAP-UCD-2017." Therefore, the model ground in prototype scale was intended to have the same geometries to that used in UCD-2017 (Fig. 1.1). With a new data set from 24 centrifuge tests in total (Table 1.1) from 10 international institutes, the previously observed results are expected to be confirmed and extended.

Table 1.1 Scaling factors employed in each institute

Test Type	Institute	Test ID	Achieved Centrifuge acc [1] G	Virtual 1G, μ [2]	Centrifuge, η [3]
A	**CU**	**CU2 (2017)**	40.0	1.0	40.0
	Ehime	**Ehime2 (2017)**	40.0	1.0	40.0
	IFSTTAR	**IFSTTAR_A_A1_1**	50.0	1.0	50.0
	KAIST	**KAIST_A_A1_1**	40.0	1.0	40.0
	KyU	**KyU_A_A1_1**	44.4	1.0	44.4
	KyU	**KyU_A_A2_1**	44.4	1.0	44.4
	NCU	**NCU_A_A1_1**	26.0	1.0	26.0
	RPI	**RPI_A_A1_1**	23.0	1.0	23.0
	UCD	**UCD_A_A1_1**	43.8	1.0	43.8
	UCD	**UCD_A_A2_1**	43.8	1.0	43.8
	ZJU	**ZJU_A_A1_1**	30.0	1.0	30.0
	TIT	**TIT_A_A1_1**	44.4	1.0	44.4
	TIT	**TIT_A_A2_1**	44.4	1.0	44.4
B	**CU**	**CU_A_B1_1**	71.6	0.5	80.0
	Ehime	**Ehime_A_B1_1**	20.0	2.0	20.0
	IFSTTAR	**IFSTTAR_A_B1_1**	25.0	2.0	25.0
	KAIST	**KAIST_A_B1_1**	26.7	1.5	26.7
	KyU	**KyU_A_B1_1**	22.2	2.0	22.2
	KyU	**KyU_A_B1_2**	11.1	4.0	11.1
	KyU	**KyU_A_B2_1**	22.2	2.0	22.2
	NCU	**NCU_A_B1_1**	13.0	2.0	13.0
	RPI	**RPI_A_B1_1**	46.0	0.5	46.0
	UCD	**UCD_A_B1_1**	21.9	2.0	21.9
	ZJU	**ZJU_A_B1_1**	15.0	2.0	15.0
	TIT	**TIT_A_B1_1**	22.2	2.0	22.2
	TIT	**TIT_A_B2_1**	22.2	2.0	22.2

In LEAP-ASIA-2019, as described later in detail, each institute conducted at least two tests: one applying conventional scaling laws (Model A) and the other applying GSL (Model B).

1.2 Generalized Scaling Law

With the development of computer technology, numerical analysis has come to be commonly used in the design of civil structures. Although numerical analysis can be used to analyze even hypothetically large structures, the results must be verified. Therefore, there is a growing need to verify the validity of numerical analysis through model experiments. Iai et al. (2005) applied a two-step similitude (Table 1.2) that combines a 1-*g* scaling law (Iai, 1989) and a centrifugal scaling law and found that it is possible to reproduce the behavior of a large prototype with a small centrifugal model, which was previously unfeasible. They name it the "generalized scaling law (GSL)" in dynamic centrifuge modeling.

In a physical model test, the scaling factor is given in general form by selecting the basic physical properties as independent and deriving the scaling factors for the other properties by the governing equations of the analytical system. In the GSL, the "two steps" scaling law, a centrifuge model is considered as a scaled model of a 1-*g* model test. Figure 1.2 illustrates the concept of the generalized scaling law (Fig. 1.2b), where the prototype is scaled down via the scaling law of the virtual 1-*g* model test with a scale factor of $\eta > 1$. In the GSL, as shown in column (3) in Table 1.2, the geometrical scaling factor (μ) in the 1-*g* test and the scaling factor (η) in the centrifuge test are multiplied to obtain a scaling factor for GSL $\lambda = \mu\eta$.

Now, for both CU (Cambridge University) and RPI (Rensselaer Polytechnic Institute), the geometrical scaling factor for 1-*g* model was selected to be less than

Table 1.2 List of the scaling factors in physical model testing (Iai et al., 2005)

	(1) Scaling factors for 1 g test	(2) Scaling factors for centrifuge test	(3) Generalized scaling factors
Length	μ	η	$\mu\eta$
Density	1	1	1
Time	$\mu^{0.75}$	η	$\mu^{0.75}\eta$
Frequency	$\mu^{-0.75}$	$1/\eta$	$\mu^{-0.75}/\eta$
Acceleration	1	$1/\eta$	$1/\eta$
Velocity	$\mu^{0.75}$	1	$\mu^{0.75}$
Displacement	$\mu^{1.5}$	η	$\mu^{1.5}\eta$
Stress	μ	1	μ
Strain	$\mu^{0.5}$	1	$\mu^{0.5}$
Stiffness	$\mu^{0.5}$	1	$\mu^{0.5}$
Permeability	$\mu^{0.75}$	η	$\mu^{0.75}\eta$
Pore pressure	μ	1	μ

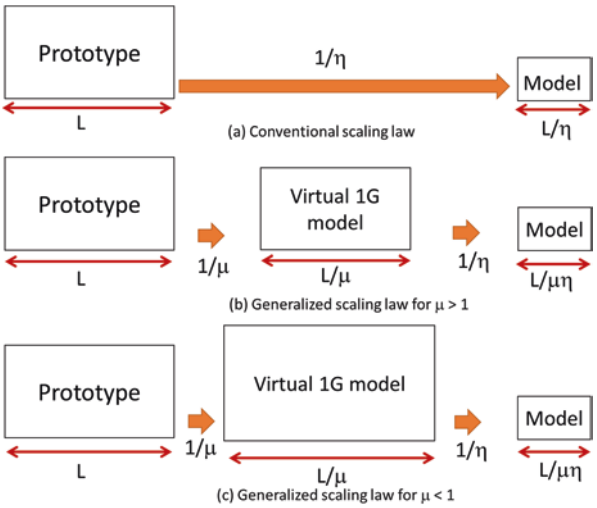

Fig. 1.2 Concept of the generalized scaling law: (**a**) conventional centrifuge scaling law (Model A) and generalized scaling law for (**b**) $\mu > 1$ and (**c**) $\mu < 1$ (Model B)

1 ($\mu < 1$), in which a size of the prototype is virtually increased as shown in Fig. 1.2c. Scaling up the 1-g model larger than the prototype and down to the centrifuge model is theoretically admissible. However, although it is theoretically feasible, its practicality is unknown. If verified, this could stretch the boundaries of centrifuge experiments.

To validate the GSL, physical parameters in prototype scale of Model A converted by the conventional centrifuge scaling law [e.g., $\mu = 1$, $\eta = 50$] are compared with those of Model B obtained by multiplying the generalized scaling factor [e.g., $\mu = 2$, $\eta = 25$].

1.3 Initial Conditions of the Model

As mentioned earlier, LEAP-ASIA-2019 required institutions to develop two minimum model tests. One is Model A, which is a model constructed using the conventional centrifuge scaling laws (Fig. 1.2a). The other, Model B, is the same prototype as Model A, but scaled by applying the GSL (Fig. 1.2b). Model A is built by the same procedures taken in LEAP-UCD-2017. Depending on the direction of excitation relative to the centrifuge rotation axis, a model was constructed, as shown in Fig. 1.1. Model B is built so that the viscosity of the pore fluid is the same as for Model A in the prototype scale, and the input PGA is adjusted when shaken. The two models are outlined below.

Model A: Same model as LEAP-UCD-2017 to fill gaps in the existing database.

Model B: A model for validation of the GSL. The same geometry as Model A with adjusted viscosity and input PGA in prototype scale.

Although the target input acceleration was a tapered sine wave of 1 Hz, it is important to note that the measured motion is contaminated with a variety of high-frequency components originating from characteristics of shaking table in each institute. Therefore, in order to standardize the PGA for each test and considering the relatively small effect of the high-frequency component on the model behavior, the concept of effective PGA "PGA_{eff}" was used in this project (as a first approximation). Equation 1.1 defines PGA_{eff} (Kutter et al., 2020b). Here, "PGA_{1Hz}" denotes the filtered 1 Hz component of PGA, while "PGA_{hf}" represents the contaminated higher-frequency components.

$$PGA_{eff} = PGA_{1Hz} + 0.5 \times PGA_{hf} \tag{1.1}$$

As an example, Fig. 1.3 depicts the filtered 1 Hz wave, filtered high-frequency wave, and a wave of the measured base acceleration of the model KyU_A_A1_1. For each test, different destructive and non-destructive motions were applied to the model; however, this paper reports the results of only the first destruction motion. Responses to other input motions can be described in the associated paper.

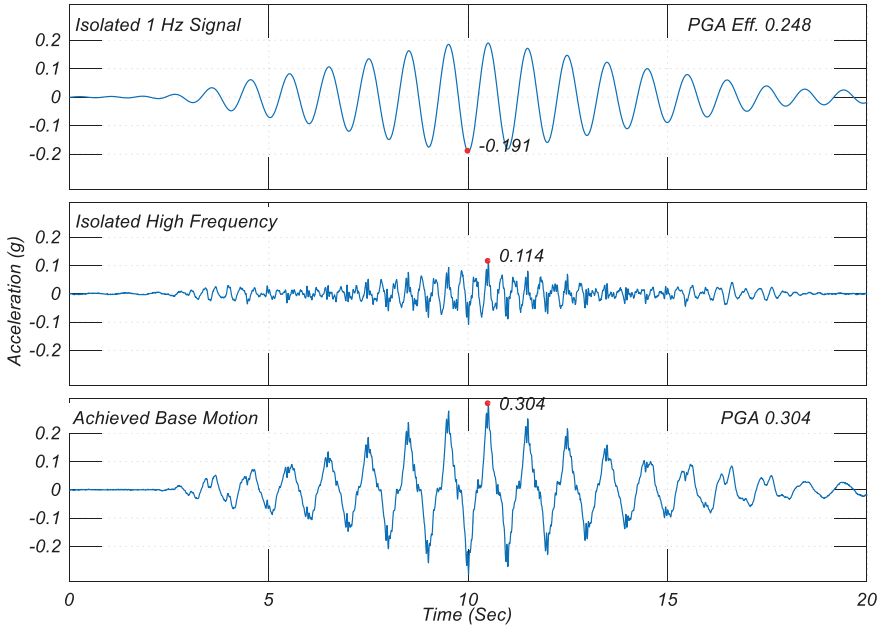

Fig. 1.3 Decomposition of the input acceleration to derive PGA_{eff}: (top) filtered 1 Hz motion, (middle) filtered higher frequency, and (bottom) recorded base motion (KyU-A1). (Tobita et al., 2022)

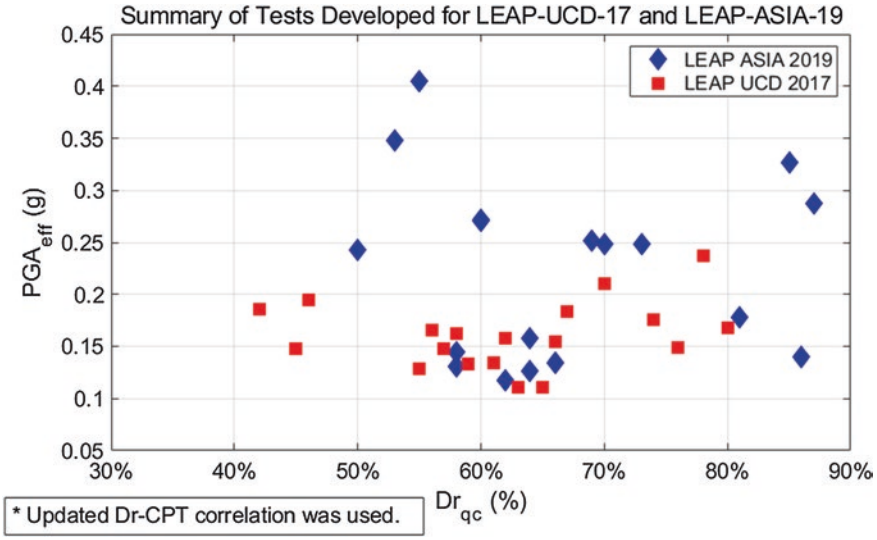

Fig. 1.4 Dr_q_c(2.0 m) and PGA_{eff} ranges covered by LEAP-UCD-2017 and LEAP-ASIA-2019. (Tobita et al., 2022)

Figure 1.4 compares the initial conditions addressed in the LEAP-UCD-2017 and LEAP-ASIA-2019 series, namely, the PGA_{eff} and relative density ranges. As mentioned earlier, one of the goals of LEAP-ASIA-2019 was to supply and add data to the database developed by the LEAP-UCD-2017 and to identify trends in Dr-PGA_{eff} combinations. In Fig. 1.4, it can be seen that the PGA_{eff} varies from 0.1 g to 0.4 g, and the relative density Dr_q_c(2.0 m) varies from 45 to 85%. Their values assigned to each laboratory can be found in Tables 1.3a and 1.3b, where Dr_q_c(2.0 m) is the relative density obtained through the correlation with tip resistance of CPT at a depth of 2 m. Note that in LEAP-UCD-2017, the CPT test results have been shown to be reliable (compared to estimates of mass and volume measurements) in estimating ground uniformity and the associated dry density, although they are indirect measurements (Vargas, 2020). Table 1.3c summarizes the surface lateral displacements for each of the tests for the first destructive motion. Detailed discussion will be made in Sect. 1.4.4.

Kutter et al. (2018) found that tip resistance at medium depth (i.e., 2.0 m) showed good correlation with the relative density of the ground. Hence, based on LEAP-UCD-2017, the parameter q_c (2.0 m) was used in the linear correlation with the dry density (Carey et al., 2020). As noted by Bolton et al. (1999) and Kutter et al. (2020b), values are influenced by container width "*w*" and CPT rod diameter (prototype scale "*Dc*"). Here, three correlations depending on the container size are derived: narrower containers (*w*/*Dc* = 20–25), deeper models (*z*/*Dc* = 11.0–14.5), and shallow models (*z*/*Dc* = 6.7–8.3). Vargas (2020) updated the correlations to include the results obtained in LEAP-ASIA-2019 and found that the power-type

Table 1.3a Summary table of density measures for each of the tests (Tobita et al., 2022)

Test type	Test ID	Dry density from mass and volume (M & V)	Dr (M & V) assuming ρ_max = 1757 ρ_min = 1491	Pen. Resist. at 2 m depth, qc2	Density qc(2 m) = a qc^b	Dr (qc) from qc2 and ρ_max = 1757 ρ_min = 1491	Container shape
		kg/m³		MPa	kg/m³		
A	**CU2 (2017)**	1606	0.47	0.95	1603	0.46	Shallow
	Ehime2 (2017)	1657	0.66	3.50	1645	0.62	Narrow
	IFSTTAR_A_A1_1	1645	0.62	1.27	1622	0.53	Shallow
	KAIST_A_A1_1	1717	0.87	5.20	1717	0.87	Shallow
	KyU_A_A1_1	1677	0.73	5.55	1667	0.70	Narrow
	KyU_A_A2_1	1628	0.56	3.61	1647	0.62	Narrow
	NCU_A_A1_1	1643	0.61	1.54	1634	0.58	Deep
	RPI_A_A1_1	1651	0.64				Deep
	UCD_A_A1_1	1713	0.86	3.98	1698	0.81	Shallow
	UCD_A_A2_1	1658	0.67	2.12	1656	0.66	Shallow
	ZJU_A_A1_1	1625	0.54	2.68	1640	0.60	Deep
	TIT_A_A1_1	1645	0.62				Narrow
	TIT_A_A2_1	1645	0.62				Narrow
B	**CU_A_B1_1**	1606	0.47	1.10	1612	0.50	Shallow
	Ehime_A_B1_1	1651	0.64	4.01	1651	0.64	Narrow
	IFSTTAR_A_B1_1	1645	0.62	1.35	1625	0.55	Shallow
	KAIST_A_B1_1	1721	0.88	3.26	1684	0.76	Shallow
	KyU_A_B1_1	1673	0.72	5.24	1664	0.69	Narrow
	KyU_A_B1_2	1669	0.71	6.86	1677	0.73	Narrow
	KyU_A_B2_1	1633	0.58	4.03	1652	0.64	Narrow
	NCU_A_B1_1	1626	0.55	2.41	1635	0.58	Deep
	RPI_A_B1_1	1644	0.62				Deep
	UCD_A_B1_1	1712	0.85	5.04	1714	0.86	Shallow
	ZJU_A_B1_1	1633	0.57	2.71	1640	0.60	Deep
	TIT_A_B1_1	1654	0.65				Narrow
	TIT_A_B2_1	1648	0.63				Narrow

Container condition: narrow containers (w/Dc = 20–25), shallow models (z/Dc = 6.7–8.3), and deep models (z/Dc = 11–14.5), where "w" is the container width and "Dc" the CPT's rod diameter in prototype scale

Table 1.3b Summary table of input motions for each of the tests for the first destructive motion (Tobita et al., 2022)

Test type	Test ID	Target PGA effective	Measured PGA (First Destructive Motion)	Measured PGA1 Hz (First Destructive Motion)	Estimated PGAhf (First Destructive Motion)	Estimated PGAeff (First Destructive Motion)	PGV	Arias Intensity, I_a
		g	*g*	*g*	*g*	*g*	m/s	m^2/s
A	**CU2 (2017)**	0.15	0.206	0.122	0.146	0.195	0.259	1.31
	Ehime2 (2017)	0.15	0.18	0.134	0.048	0.158	0.206	1.07
	IFSTTAR_A_A1_1	0.3	0.432	0.263	0.169	0.348	0.427	4.17
	KAIST_A_A1_1	0.25	0.326	0.247	0.079	0.287	0.384	3.08
	KyU_A_A1_1	0.25	0.304	0.191	0.113	0.248	0.278	1.89
	KyU_A_A2_1	0.12	0.134	0.101	0.033	0.118	0.177	0.62
	NCU_A_A1_1	0.1	0.176	0.112	0.064	0.144	0.180	0.68
	RPI_A_A1_1	0.08	0.15	0.135	0.015	0.143	0.219	0.93
	UCD_A_A1_1	0.2	0.213	0.143	0.07	0.178	0.271	0.93
	UCD_A_A2_1	0.2	0.15	0.117	0.033	0.134	0.202	0.61
	ZJU_A_A1_1	0.25	0.352	0.192	0.16	0.272	0.303	1.91
	TIT_A_A1_1	0.14	0.157	0.109	0.048	0.133	0.174	0.50
	TIT_A_A2_1	0.14	0.154	0.112	0.042	0.133	0.184	0.48

B	**CU_A_B1_1**	0.15	0.326	0.159	0.167	0.243	0.224	1.49
	Ehime_A_B1_1	0.18	0.198	0.117	0.081	0.158	1.998	81.26
	IFSTTAR_A_B1_1	0.3	0.53	0.28	0.25	0.405	0.442	4.42
	KAIST_A_B1_1	0.25	0.369	0.283	0.086	0.326	0.453	3.98
	KyU_A_B1_1	0.25	0.312	0.192	0.12	0.252	0.294	1.82
	KyU_A_B1_2	0.25	0.307	0.189	0.118	0.248	0.284	2.46
	KyU_A_B2_1	0.12	0.163	0.089	0.074	0.126	0.155	0.78
	NCU_A_B1_1	0.1	0.158	0.104	0.054	0.131	0.176	0.60
	RPI_A_B1_1	0.08	0.164	0.138	0.026	0.151	0.203	0.84
	UCD_A_B1_1	0.2	0.154	0.125	0.029	0.14	0.201	0.64
	ZJU_A_B1_1	0.25	0.333	0.209	0.124	0.271	0.363	2.41
	TIT_A_B1_1	0.14	0.145	0.099	0.046	0.122	0.168	0.57
	TIT_A_B2_1	0.14	0.158	0.111	0.047	0.135	0.174	0.62

Table 1.3c Summary table of surface lateral displacements for each of the tests for the first destructive motion (Tobita et al., 2022)

Test type	Test ID	Integrated Pos. Rel. Vel.	Peak Dynamic Rel. Disp.	Duration of liq. at P4	U_x mean All Markers	U_x σ All Markers	U_{x8} mean 8 Markers	U_{x8} σ 8 Markers	U_{x2} mean 2 Markers	U_{x2} σ 2 Markers
		m	m	s	mm	mm	mm	mm	mm	mm
A	**CU2 (2017)**	5.52	0.06	28	358.9	95.7	427.5	65.0	490.0	42.4
	Ehime2 (2017)	7.18	0.06	0	89.4	48.0	102.9	39.0	100.0	28.3
	IFSTTAR_A_A1_1	1.33	0.09		358.3	134.5	475.0	80.2	550.0	0.0
	KAIST_A_A1_1	0.51	0.04	0	30.5	13.1	34.7	9.3	33.9	0.0
	KyU_A_A1_1	0.41	0.04	8	84.4	13.2	83.6	15.0	71.0	0.0
	KyU_A_A2_1	0.03	0.00	0	14.5	5.6	11.1	2.4	11.1	3.1
	NCU_A_A1_1	0.58	0.05		150.7	31.5	162.7	21.1	181.5	27.0
	RPI_A_A1_1	0.45	0.04	16	87.7	22.2	0.0	0.0	99.6	13.6
	UCD_A_A1_1	0.25	0.03	0	19.8	11.7	24.7	8.8	30.6	7.3
	UCD_A_A2_1	0.95	0.07	8	55.6	24.4	71.8	14.2	77.5	2.6
	ZJU_A_A1_1	0.93	0.08	22	321.7	100.7	393.8	32.8	390.0	42.4
	TIT_A_A1_1	0.40	0.05	0	0.0	0.0	0.0	0.0	0.0	0.0
	TIT_A_A2_1	0.23	0.03	0	56.2	31.2	61.1	23.0	44.4	0.0

B	**CU_A_B1_1**	0.79	0.15	112	0.0	0.0			0.0	0.0
	Ehime_A_B1_1	11.75	0.43	0	36.6	39.7	56.6	42.8	56.6	0.0
	IFSTTAR_A_B1_1	1.16	0.08	130	555.9	178.1	685.0	108.5	777.8	100.0
	KAIST_A_B1_1	0.42	0.03	0	39.6	11.1	35.6	7.1	30.6	5.4
	KyU_A_B1_1	0.65	0.05	7	130.9	33.4	153.8	22.7	153.8	4.4
	KyU_A_B1_2	1.13	0.06	15	111.3	25.3	116.9	26.6	115.4	12.6
	KyU_A_B2_1	1.28	0.06	2	48.1	16.6	46.0	18.1	34.5	4.4
	NCU_A_B1_1	0.54	0.06	0	148.7	57.6	127.8	67.9	87.2	85.9
	RPI_A_B1_1	0.57	0.04	17	283.2	56.7	0.0	0.0	303.3	0.0
	UCD_A_B1_1	0.98	0.07	0	-0.7	1.6	-0.7	1.9	−2.2	2.8
	ZJU_A_B1_1	0.88	0.07	64	486.7	176.5	594.0	122.6	678.8	60.0
	TIT_A_B1_1	0.32	0.04	0	102.0	68.3	109.9	44.4	125.6	0.0
	TIT_A_B2_1	0.38	0.04	0	62.8	32.4	70.6	22.2	62.8	0.0

correlations fit well with the results achieved (see Eq. 1.2). Figure 1.5 shows the updated correlations for the three different test conditions.

In this paper, the relative density "Dr_q_c(2.0 m)" was derived by the updated correlation equation, Eq. (1.2), by setting $\rho_{d\_\max}$ = 1757 (kg/cm^3) and $\rho_{d\_\max}$ = 1492 (kg/cm^3) (Carey et al., 2020).

$$\rho_d = a\left(q_c\left(2.0m\right)\right)^b \quad \left(\mathrm{kg/cm^3}\right) \tag{1.2}$$

Figures 1.6, 1.7 and 1.8, respectively, show the initial conditions, Dr_q_c(2.0 m), PGA_{eff}, and viscosity, achieved in each institute. Figure 1.6 shows that the difference in relative density between Model A and Model B is less than 5%. From Figs. 1.6 and 1.7, it is noticed that, for CU and IFSTTAR, severe and difficult testing conditions were assigned with much low densities and high input PGA.

For the validation of the GSL, the diffusion process of excess pore pressure should also match in the prototype scale. Therefore, the pore fluid viscosity must be properly scaled. Methylcellulose solutions are common in centrifuge modeling and were also used in this study (Adamidis & Madabhushi, 2015; Stewart et al., 1998). Each institute was asked to carefully measure the viscosity of the pore fluid because it is known to be sensitive to fluid temperature. Some laboratories used cup-and-bob viscometers for the measurement, while others used capillary or oscillating viscometers. Figure 1.9 compares the achieved viscosities of the pore fluid of Model A and Model B. Both are judged to be in good agreement.

1.4 Test Results

1.4.1 Penetration Resistance

To measure the stiffness and strength of the ground, the small CPT developed for LEAP-UCD-2017 (Kutter et al., 2020a) was used in most tests. In the penetration resistance profiles shown in Figs. 1.10a and 1.10b, CPT1 is the CPT tip resistance measured before the first shaking, CPT2 was measured after the first excitation (and before the second), and CPT3, if plotted, corresponds to before the third excitation. Tip resistances of IFSTTAR, UCD, and ZJU slightly increase after shaking. In other institute, the increments are insignificant. The profiles of CU, IFSTTAR, NCU, and ZJU whose Dr_q_c(2.0 m) is less than approx. 60% show, as expected, low resistance.

CPT tip resistance increases with depth in the range of 5–15 MPa in this study. Figure 1.11 compares q_c value. The q_c values of Models A and B show good agreements at shallow depths, and the divergence becomes more pronounced with depth. Figure 1.12 shows that Model B tends to slightly overestimate the tip resistance at all depths.

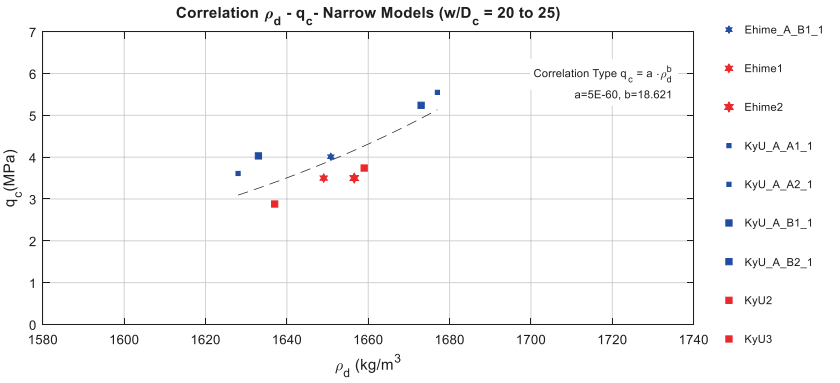

(a) Narrow Models (*w*/*Dc*=20 - 25)

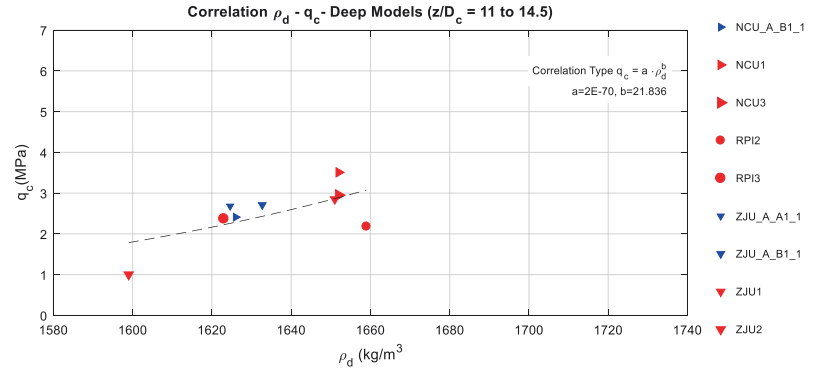

(b) Deep Models (*z*/*Dc*=11.0 - 14.5)

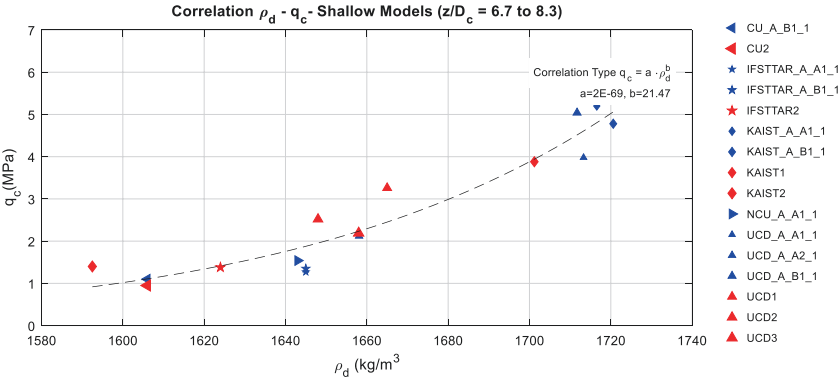

(c) Shallow Models (*z*/*Dc* = 6.7 - 8.3)

Fig. 1.5 Relationship between the dry density ρ_d and the CPT tip resistance q_c at 2.0 m with data from LEAP-UCD-2017 and LEAP-ASIA-2019: (**a**) narrow models (*w*/*Dc* = 20–25), (**b**) deep models (*z*/*Dc* = 11.0–14.5), and (**c**) shallow models (*z*/*Dc* = 6.7–8.3)

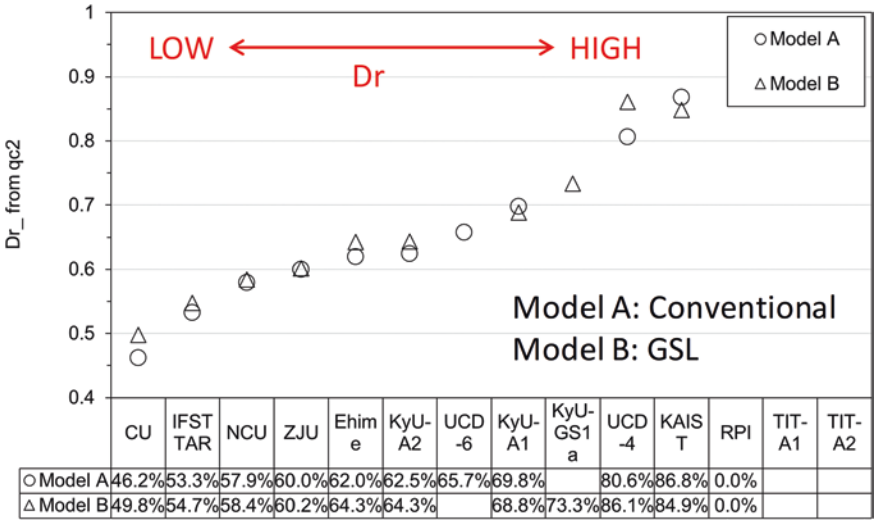

	CU	IFST TAR	NCU	ZJU	Ehime	KyU-A2	UCD-6	KyU-A1	KyU-GS1a	UCD-4	KAIST	RPI	TIT-A1	TIT-A2
○ Model A	46.2%	53.3%	57.9%	60.0%	62.0%	62.5%	65.7%	69.8%		80.6%	86.8%	0.0%		
△ Model B	49.8%	54.7%	58.4%	60.2%	64.3%	64.3%		68.8%	73.3%	86.1%	84.9%	0.0%		

Fig. 1.6 Relative density, Dr_q_c(2.0 m), computed by the updated correlation equation based on the CPT measurements. Sorted by the value of Dr_q_c(2.0 m): lower (left) to higher (right). (Tobita et al., 2022)

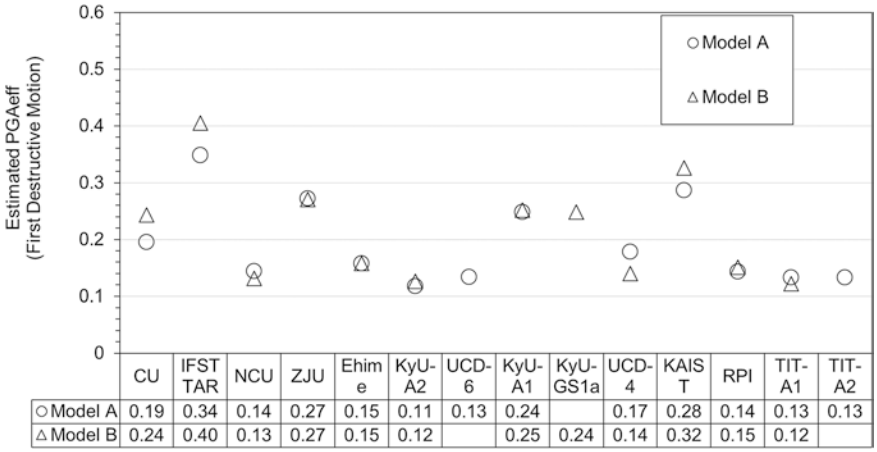

	CU	IFST TAR	NCU	ZJU	Ehime	KyU-A2	UCD-6	KyU-A1	KyU-GS1a	UCD-4	KAIST	RPI	TIT-A1	TIT-A2
○ Model A	0.19	0.34	0.14	0.27	0.15	0.11	0.13	0.24		0.17	0.28	0.14	0.13	0.13
△ Model B	0.24	0.40	0.13	0.27	0.15	0.12		0.25	0.24	0.14	0.32	0.15	0.12	

Fig. 1.7 Effective PGA_{eff} of the first destructive motion. Sorted by the order of Dr_q_c(2.0 m) (Fig. 1.6). (Tobita et al., 2022)

	CU	IFST TAR	NCU	ZJU	Ehime	KyU-A2	UCD-6	KyU-A1	KyU-GS1a	UCD-4	KAIST	RPI	TIT-A1	TIT-A2
○ Model A		62.	24.	30.		37.	43.	40.		43.	40.	23.	37.	45.
△ Model B	47.	43.	28.	25.		39.		36.	32.	36.	36.	27.	32.	

Fig. 1.8 Achieved viscosity of pore fluid. Sorted by the same order of Dr_q_c(2.0 m) (Fig. 1.6)

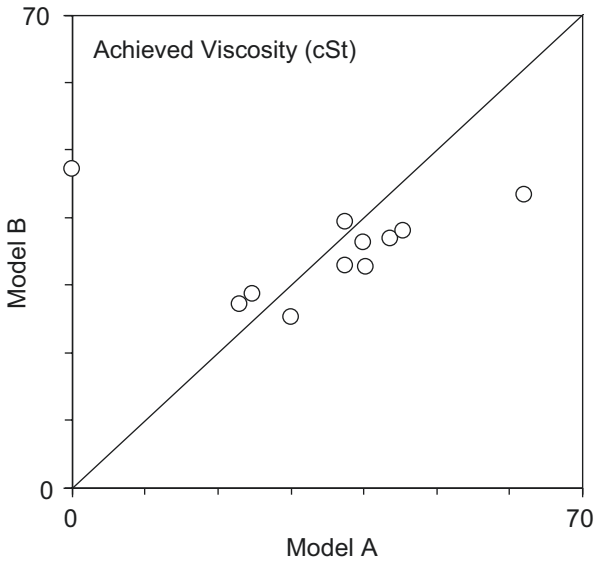

Fig. 1.9 Comparison of the achieved viscosity for Models A and B

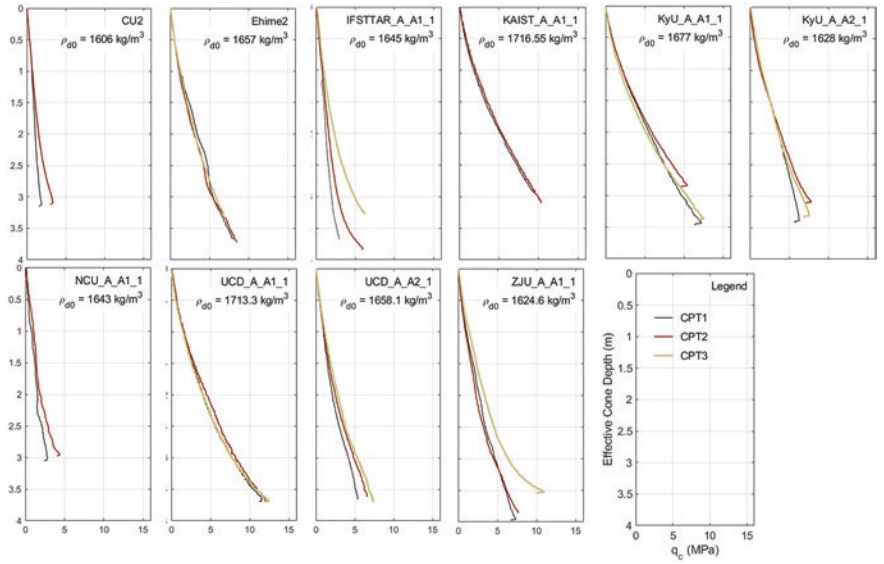

Fig. 1.10a All CPT profile for Model A. (Tobita et al., 2022)

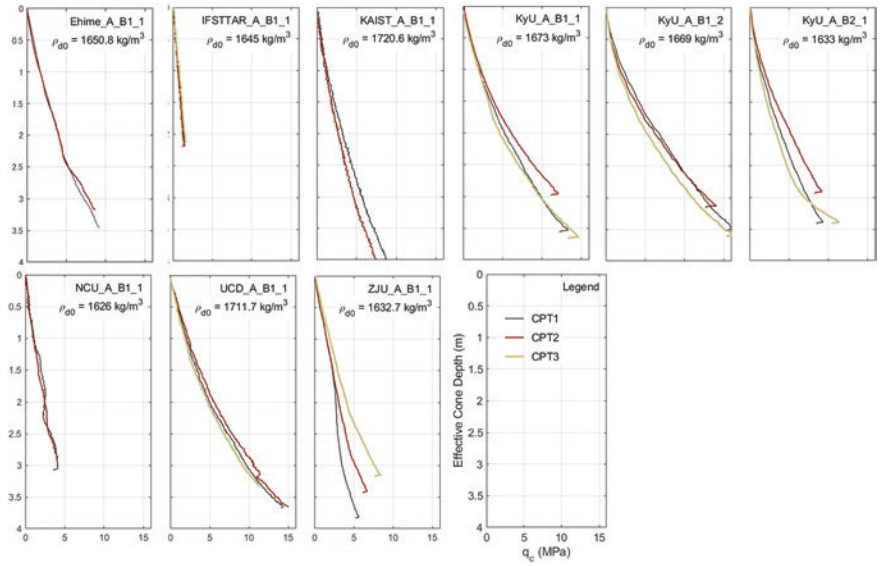

Fig. 1.10b All CPT profile for Model B. (Tobita et al., 2022)

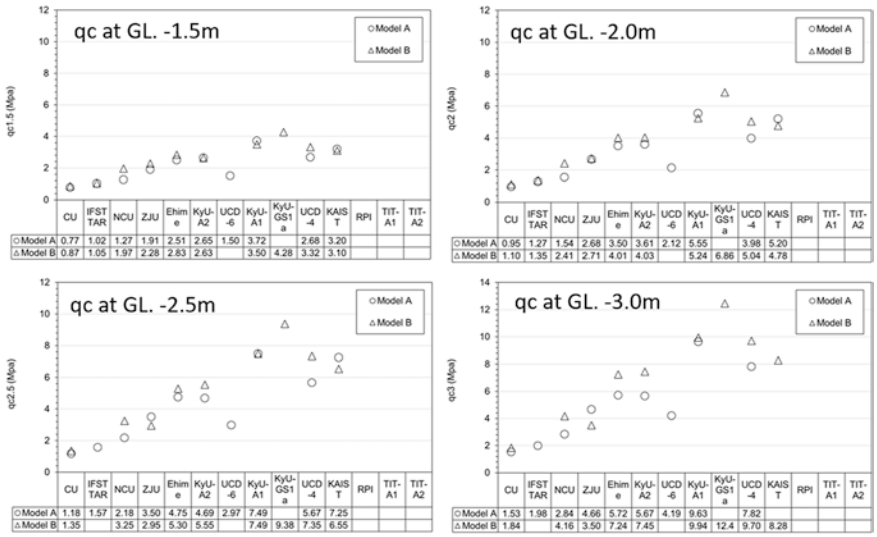

Fig. 1.11 CPT tip resistance measured at the specified depth. Sorted by the same order of Dr_q_c(2.0 m) (Fig. 1.6). (Tobita et al., 2022)

1.4.2 Response of Acceleration

Figures 1.13a (Model A) and 1.13b (Model B) plot all the acceleration time histories for the center column (AH1–AH4) and the average of the two lower time histories (AH11 and AH12). Before conducting the Model B test, calibration of the shaker was made in each institute to have the identical input motion with Model A in prototype scale. Figures 1.14a and 1.14b show better agreements on the PGA_{eff} (Fig. 1.14b) than the measured PGA (Fig. 1.14a) between Models A and B. This indicates that the identical input motions in terms of PGA_{eff} were input in both models for each institute.

Response acceleration varies with the input seismic motion and soil density. In the records at shallow depth, dilatancy spikes can be seen, which might be caused by the gradual ground movement in the downstream direction. KAIST_A_A1_1 and KAIST_A_B1_1, in which higher Dr_q_c(2.0 m) and larger PGA_{eff} were given, show good agreements between two models. Also, NCU and ZJU show good agreements.

Time histories of acceleration response of Models A and B depicted in Fig. 1.15a for higher target density and higher PGA_{eff} for KyU experiment (Tables 1.3a and 1.3b) show dilatancy spikes in common in the record shallower than 2.5 m (AH2), and their wave shapes at the same depth are quite similar. On the other hand, in time histories of acceleration response depicted in Fig. 1.15b for lower target density and lower PGA_{eff} for KyU experiment, dilatancy spikes appear only on the record of AH4 in Model B. As shown in the figure, the larger input acceleration amplitude of Model B may have caused this difference. It should be noted that due to the

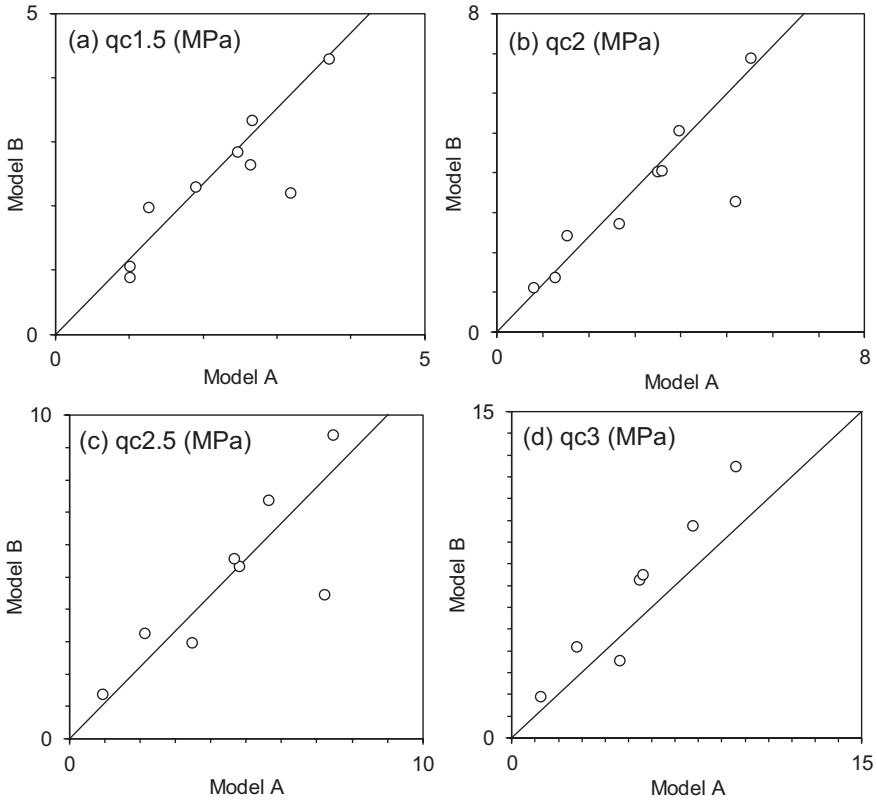

Fig. 1.12 Comparison of CPT tip resistance measured at the specified depth. (Tobita et al., 2022)

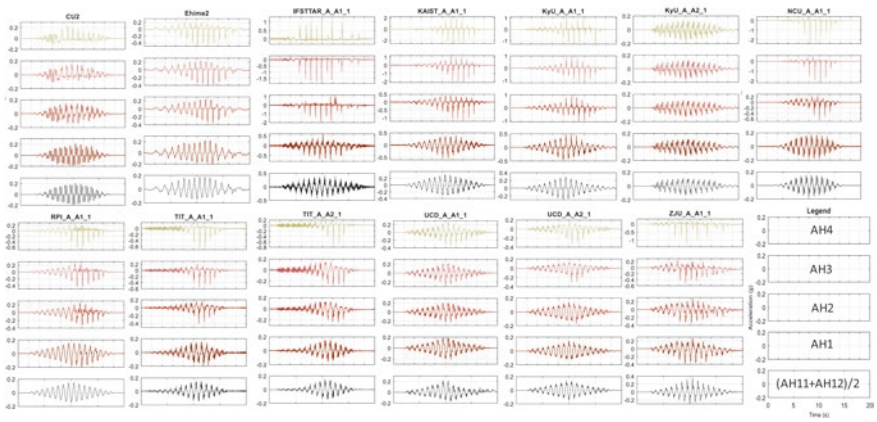

Fig. 1.13a All records of measured acceleration for Model A. (Tobita et al., 2022)

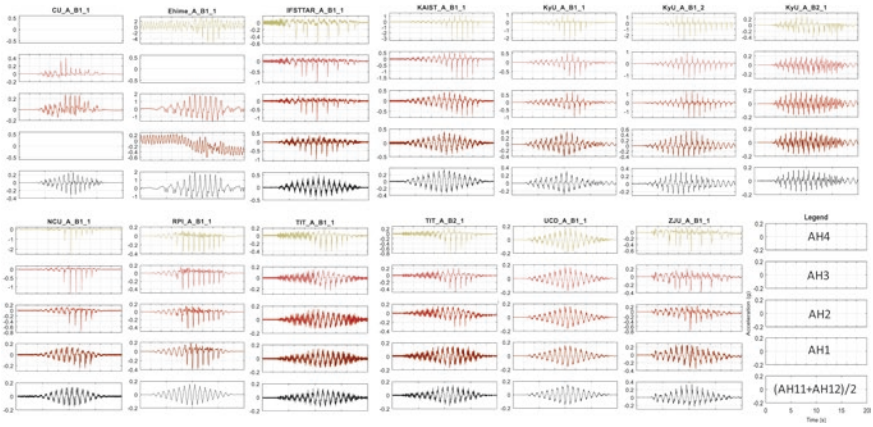

Fig. 1.13b All records of measured acceleration for Model B. (Tobita et al., 2022)

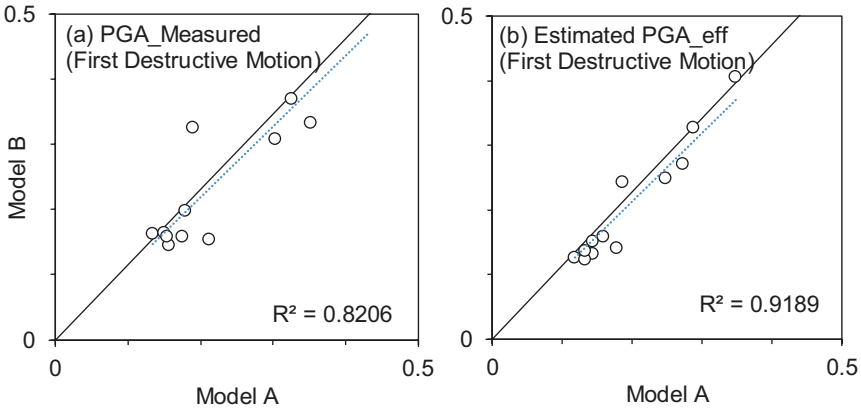

Fig. 1.14 Consistency of the input PGA for Models A and B: (**a**) measured PGA and (**b**) processed $PGA_{eff.}$ (Tobita et al., 2022)

characteristics of the shaking table, a given acceleration level may not be achieved in the designated centrifugal field.

As mentioned in Sect. 1.2, 1-*g* scaling factor employed in RPI experiment is $\mu = 0.5 < 1$, in which a virtual 1-*g* model is twice as large as a prototype. As shown in Fig. 1.16, response accelerations of Models A and B have some similarities except for the record of AH1. Response acceleration of AH1 of Model B shows dilatancy spikes which is not clearly appearing in the record of Model A.

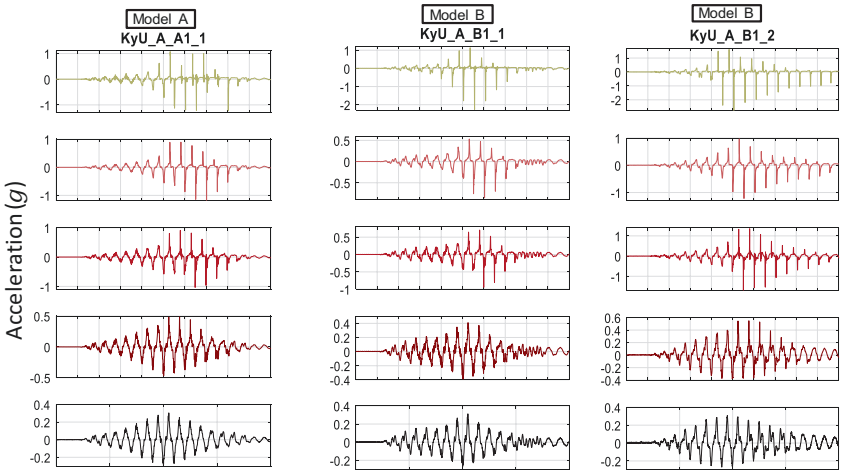

(a) Higher PGA_{eff} and Dr_q_c(2.0m) series

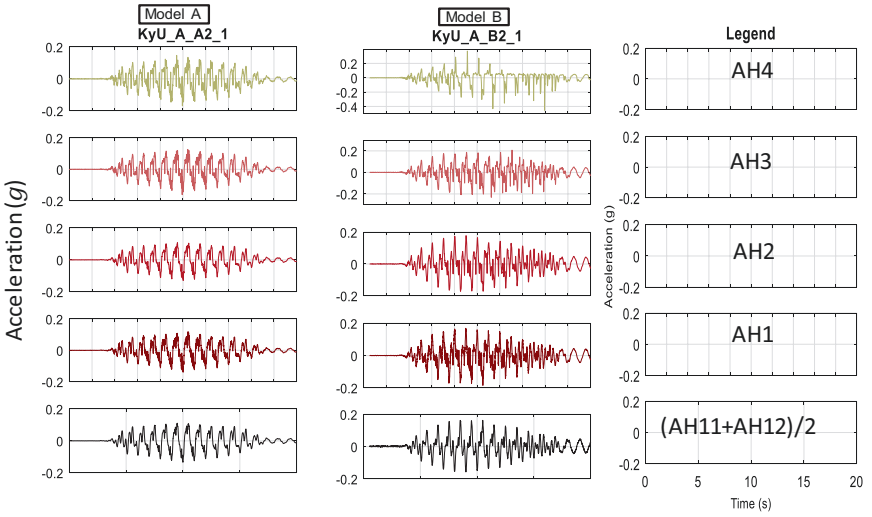

(b) Lower PGA_{eff} and Dr_q_c(2.0m) series

Fig. 1.15 Comparison of response acceleration for Models A and B for KyU experiments: (**a**) higher and (**b**) lower PGA_{eff} and Dr_q_c(2.0 m) series

1.4.3 Response of Excess Pore Water Pressure

Figure 1.17a, b plots all records of the excess pore water pressures. In each plot, the first half is representing the excess pore pressure buildup during excitation period, and the second half is those during dissipation period. Figure 1.17a shows that the

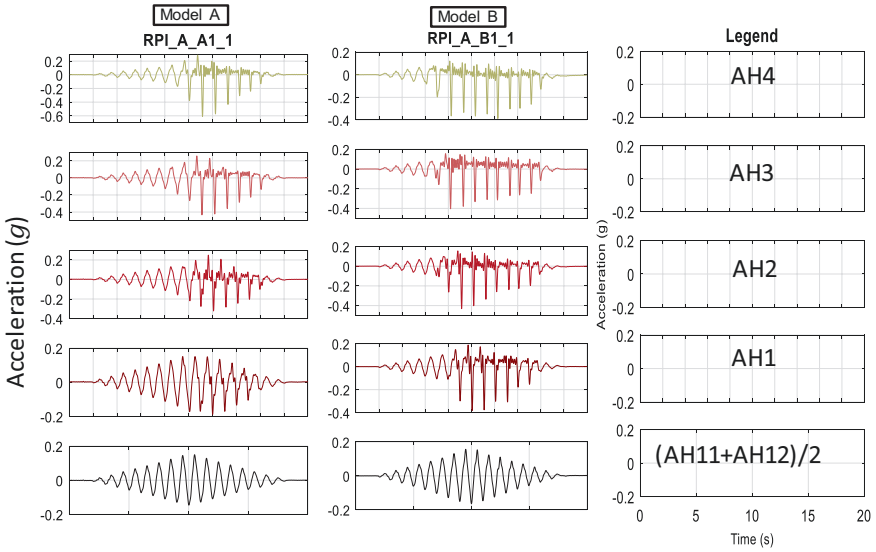

Fig. 1.16 Measured acceleration records of RPI experiment which employed the 1-g scaling factor $\mu = 0.5 < 1$ for Model B

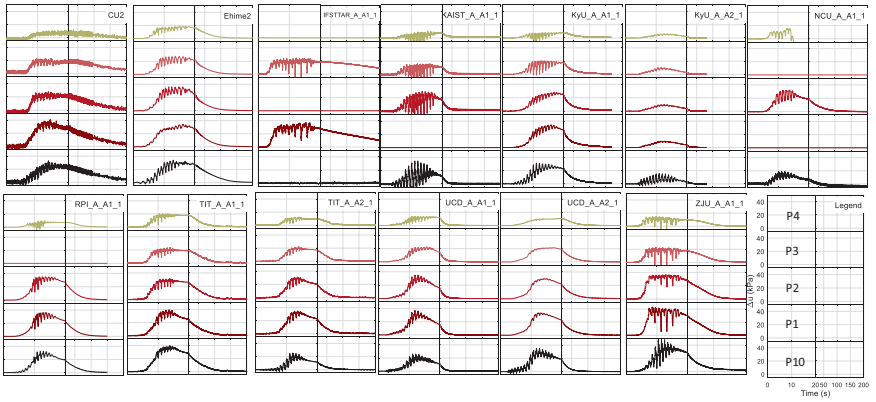

Fig. 1.17a All records of excess pore water pressure measurements for Model A. (Tobita et al., 2022)

excess pore water pressure in the downstream lower corner may not have reached the initial effective stress. Both Figs. 1.17a and 1.17b show that the records IFSTTAR_A_A1_1, KAIST_A1_1, KYU_A1_1, and ZJU_A1_1 have dilatancy spikes in the negative direction. For medium-density soils with moderate PGA_{eff}, dilatancy spikes tend to be smaller as in KyU and UCD. For loose ground, records of CU_A_B1_1 show small spikes.

Figure 1.18 shows results of KyU experiments and compares the response of excess pore water pressure. Figure 1.18a is the case with relatively higher PGA_{eff}

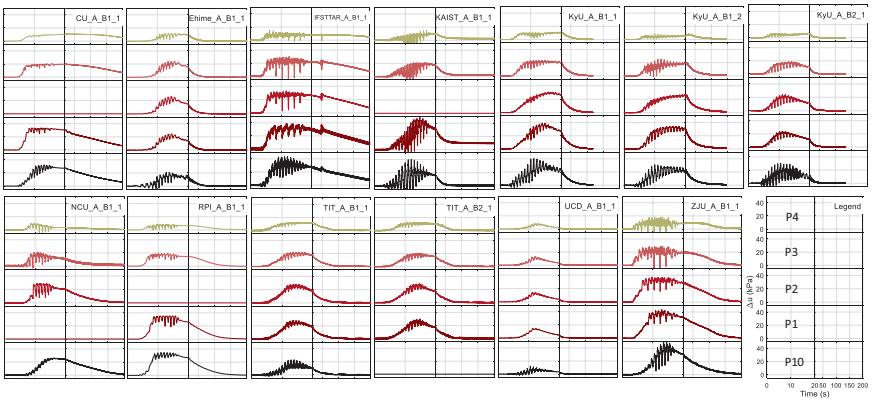

Fig. 1.17b All records of excess pore water pressure measurements for Model B. (Tobita et al., 2022)

and Dr_q_c(2.0 m) series, while Fig. 1.18b is for lower case. As in Fig. 1.18a, both in Models A and B, the curves of buildup and dissipation phase show a relatively good match. However, as shown in Fig. 1.18b, no negative spikes are seen in the buildup phase. This is, as mentioned earlier, due to the difference in the input acceleration amplitude (Fig. 1.15b).

Figure 1.19 compares results obtained by RPI experiments which employed the 1-g scaling factor $\mu = 0.5 < 1$. The responses are similar as shown in the figure. This demonstrates the applicability of the GSL even with the 1-g scaling factor less than unity.

The maximum excess pore pressure ratios of P1 to P4 are compared in Fig. 1.20. The maximum excess pore pressure is almost 1 in most of the tests, except for CU, IFSTTAR, ZJU, and KAIST, which have low density or large PGA. As for the second round of tests developed at Kyoto University, a significant difference was found in the excess pore water pressure ratio (i.e., KyU_A_A2_1 and KyU_A_B2_1), despite having similar Dr. (56% and 58%, respectively) and PGA_{eff} (0.118 and 0.126, respectively) values. At this facility, it has been found that for "small" PGA levels at a "low" gravity level, a significant increase in the high-frequency contents of the input acceleration (i.e., additional high-frequency components are induced in Model B than in Model A) was induced by the shaking table, causing significant differences in the PGA values (0.134 and 0.163, respectively), when similar PGA_{eff} values are achieved. From this, if the acceleration record is contaminated with high-frequency components of relatively large amplitudes, the definition of PGA_{eff} might need to be modified to better represent the demand; however, further research is required to clarify this point. One of the possible causes of this excessive high-frequency amplitude might be due in part to the vertical component induced by the rocking motion at large cyclic amplitude under lower centrifugal accelerations. This is a known restriction of a shaker, and in some institute, its use at low centrifugal acceleration is prohibited.

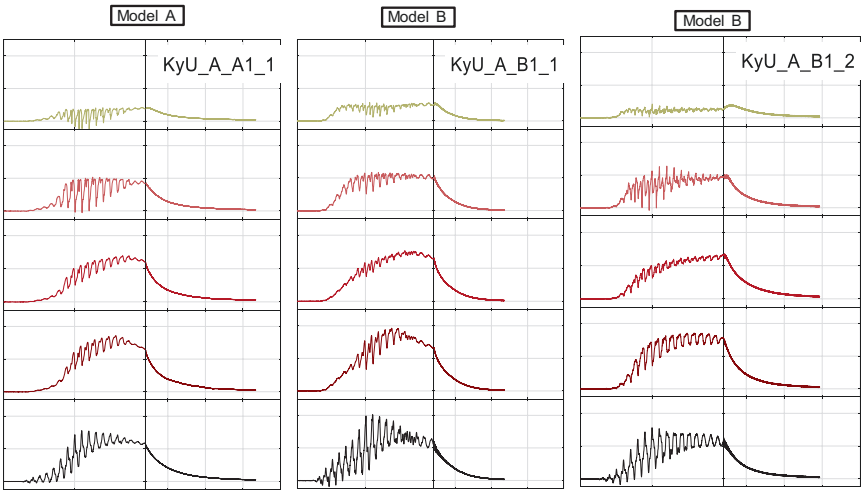

(a) Higher PGA_{eff} and Dr_q_c(2.0m) series

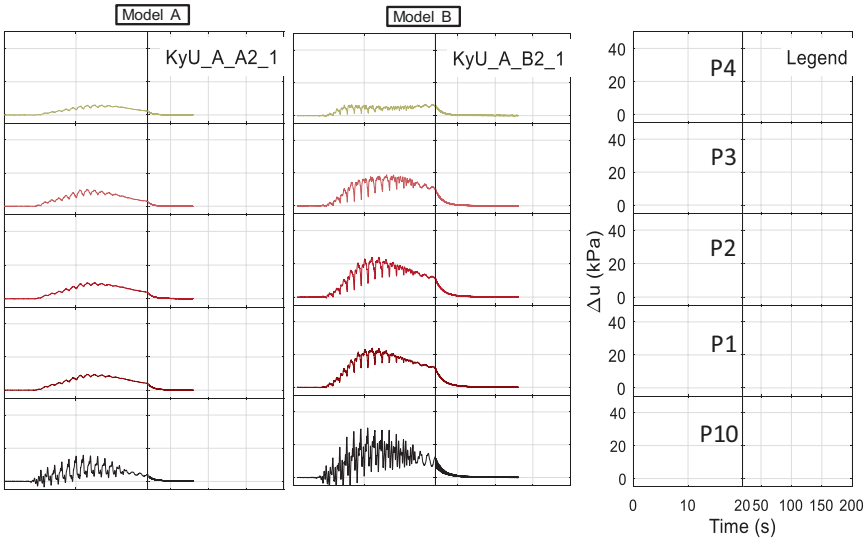

(b) lower PGA_{eff} and Dr_q_c(2.0m) series

Fig. 1.18 Comparison of excess pore water pressure responses of Models A and B in the KyU experiments: (**a**) higher and (**b**) lower PGA_{eff} and Dr_q_c(2.0 m) series

Figure 1.21 compares the max. Excess pore water pressures measured at different depths. While a consistent relationship is observed, some tests are far from a one-to-one relationship.

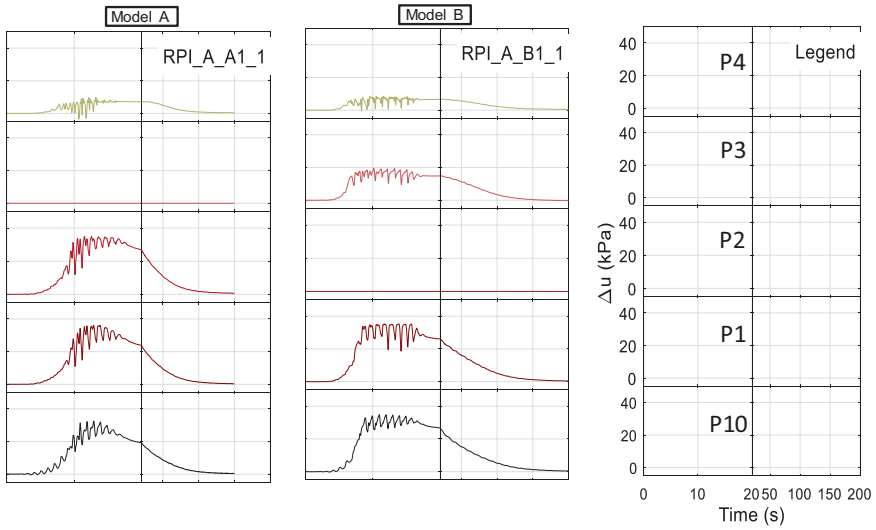

Fig. 1.19 Measured excess pore water pressure records of RPI experiment which employed the 1-g scaling factor $\mu = 0.5 < 1$ for Model B

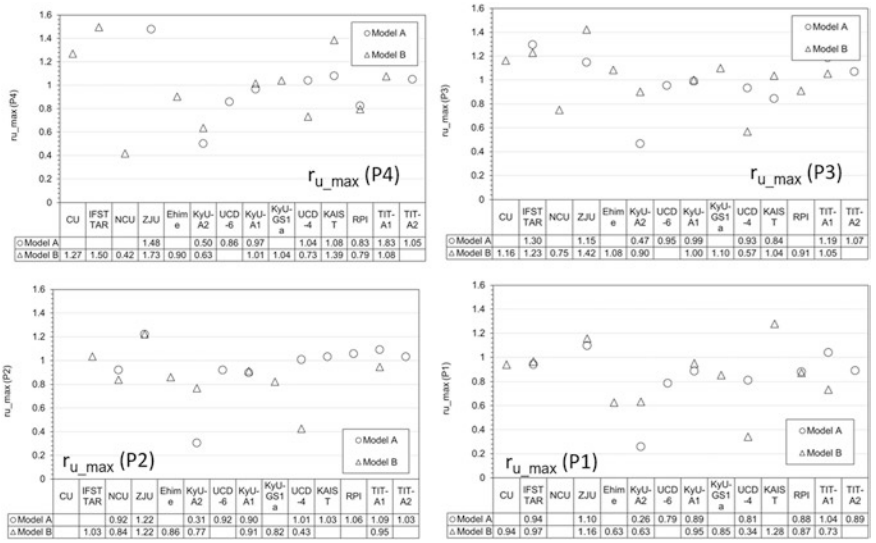

	CU	IFST TAR	NCU	ZJU	Ehime	KyU-A2	UCD-6	KyU-A1	KyU-GS1a	UCD-4	KAIST	RPI	TIT-A1	TIT-A2
○Model A				1.48		0.50	0.86	0.97		1.04	1.08	0.83	1.83	1.05
△Model B	1.27	1.50	0.42	1.73	0.90	0.63		1.01	1.04	0.73	1.39	0.79	1.08	

	CU	IFST TAR	NCU	ZJU	Ehime	KyU-A2	UCD-6	KyU-A1	KyU-GS1a	UCD-4	KAIST	RPI	TIT-A1	TIT-A2
○Model A		1.30		1.15		0.47	0.95	0.99		0.93	0.84		1.19	1.07
△Model B	1.16	1.23	0.75	1.42	1.08	0.90		1.00	1.10	0.57	1.04	0.91	1.05	

	CU	IFST TAR	NCU	ZJU	Ehime	KyU-A2	UCD-6	KyU-A1	KyU-GS1a	UCD-4	KAIST	RPI	TIT-A1	TIT-A2
○Model A			0.92	1.22		0.31	0.92	0.90		1.01	1.03	1.06	1.09	1.03
△Model B		1.03	0.84	1.22	0.86	0.77		0.91	0.82	0.43			0.95	

	CU	IFST TAR	NCU	ZJU	Ehime	KyU-A2	UCD-6	KyU-A1	KyU-GS1a	UCD-4	KAIST	RPI	TIT-A1	TIT-A2
○Model A		0.94		1.10		0.26	0.79	0.89		0.81		0.88	1.04	0.89
△Model B	0.94	0.97		1.16	0.63	0.63		0.95	0.85	0.34	1.28	0.87	0.73	

Fig. 1.20 Comparison of the excess pore water pressure ratio for Models A and B. Sorted by the same order with Dr_q_c(2.0 m) (Fig. 1.6). (Tobita et al., 2022)

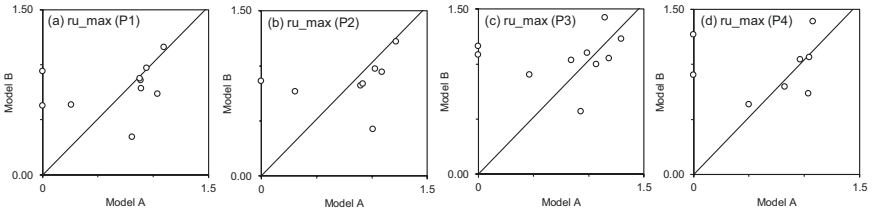

Fig. 1.21 Comparison of the maximum excess pore pressure ratios for Models A and B. (Tobita et al., 2022)

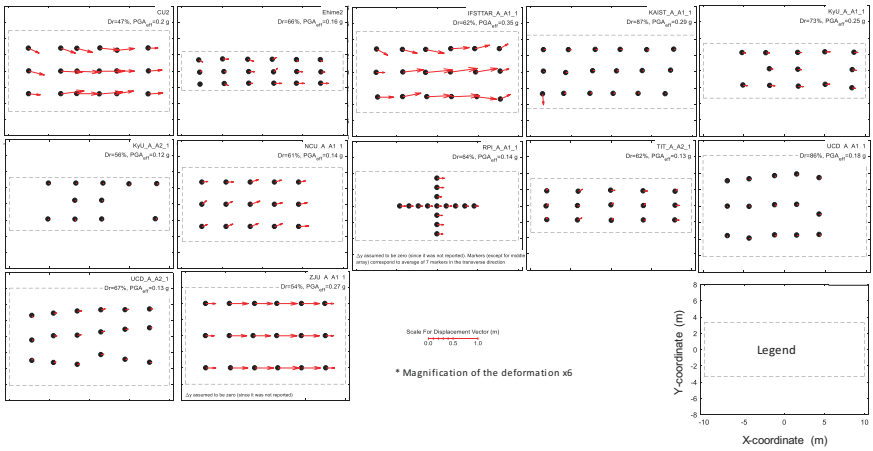

Fig. 1.22a Displacement vectors at the location of markers – after the first destructive motion for Model A. (Tobita et al., 2022)

1.4.4 Response of Ground Surface Deformation

The surface displacements of the markers after the first destructive motion are summarized in Table 1.3c, and are plotted in Figs. 1.22a and 1.22b for Models A and B, respectively, with arrows. As expected, soft ground (Dr_q_c(2.0 m) < 55%) (CU, ZJU) and large PGA_{eff} (PGA_{eff} = 0.35) (IFSTTAR) resulted in large displacements (about 300–600 mm). Figure 1.23 compares the lateral displacements averaged over all markers in Models A and B. Figure 1.24 shows the displacement in the x-, y-, and z-directions. When the displacement in the x-direction is large (more than 250 mm for Model B), a large discrepancy between the displacement of Model A and Model B is observed, indicating the limit of GSL application. Care should be taken when applying the GSL in such severe cases. Interested reader should refer to Tobita et al. (2022) for discussion on the limitation of the GSL. Displacements in y-direction show small fluctuation. This appears to be a random error that occurred during the model construction and measurement process. On settlement (negative values in the z-direction), agreements for Models A and B can be seen.

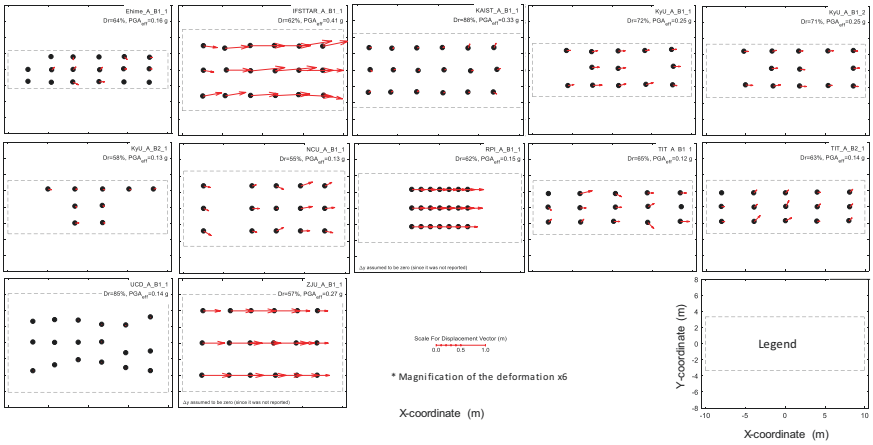

Fig. 1.22b Displacement vectors at the location of markers – after the first destructive motion for Model B. (Tobita et al., 2022)

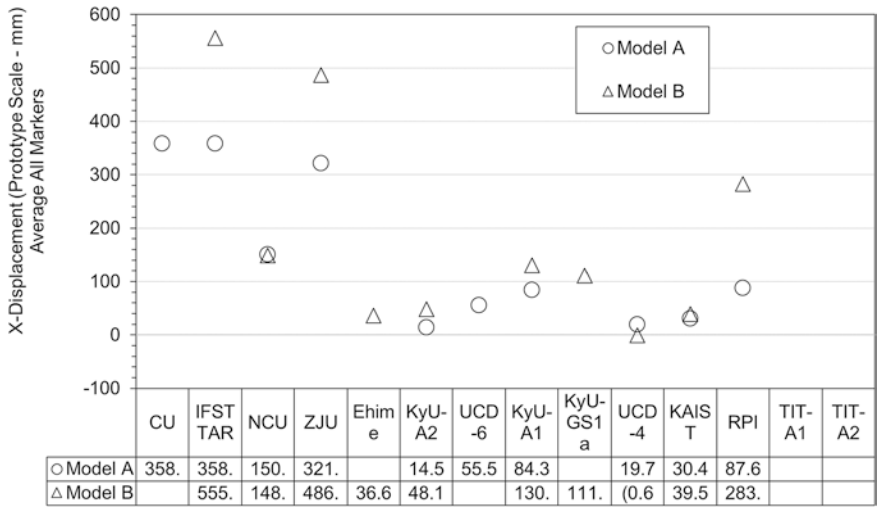

	CU	IFST TAR	NCU	ZJU	Ehime	KyU-A2	UCD-6	KyU-A1	KyU-GS1a	UCD-4	KAIST	RPI	TIT-A1	TIT-A2
○Model A	358.	358.	150.	321.		14.5	55.5	84.3		19.7	30.4	87.6		
△Model B		555.	148.	486.	36.6	48.1		130.	111.	(0.6	39.5	283.		

Fig. 1.23 Lateral displacements of Models A and B (average of all markers) after the first destructive motion. Sorted by the order of Dr_q_c(2.0 m) (Fig. 1.6). (Tobita et al., 2022)

1.5 Updated Correlation among Dr_q_c(2.0 M), PGA_{eff}, and U_x

Kutter et al. (2020b) found that in lateral spreading, residual surface displacement is primarily a function of the intensity of shaking and the relative density of the sand; indeed, based on the LEAP-UCD-2017 results, a good correlation was obtained between these three variables. The three variables for a better agreement

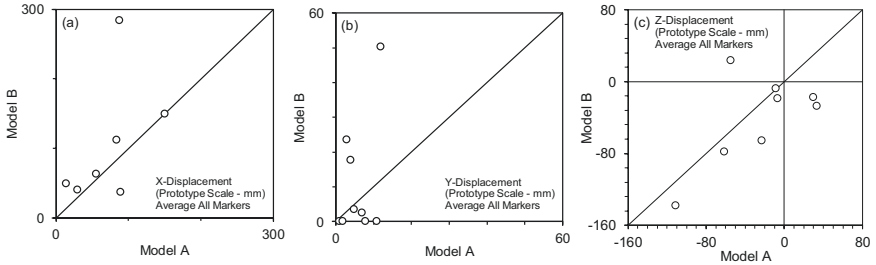

Fig. 1.24 Residual displacements for Models A and B: (**a**) x-, (**b**) y-, and (**c**) z-directions. (Tobita et al., 2022)

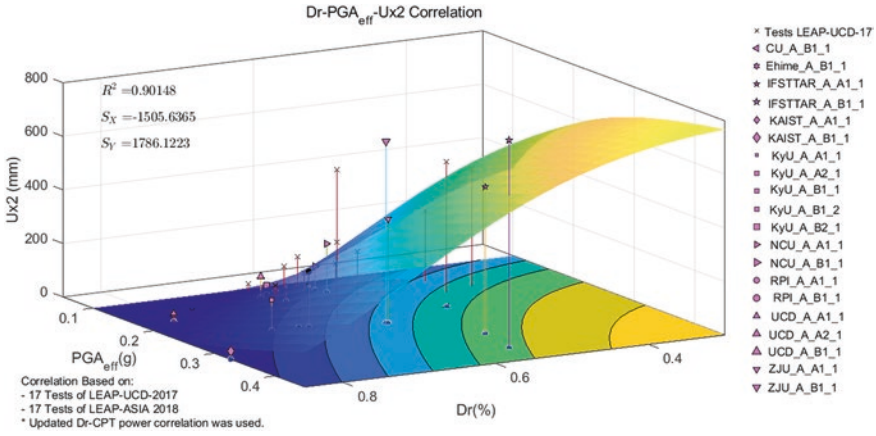

Fig. 1.25 Updated Dr_q_c(2.0 m)-PGA$_{eff}$-U$_x$ correlations based on 17 tests in LEAP-UCD-2017 and 17 tests in LEAP-ASIA-2019 (results of Model B are included). (Tobita et al., 2022)

are "U$_{x2}$" for residual displacement averaged over the two central markers, PGA$_{eff}$ for shaking intensity, and Dr_q_c(2.0 m) for density of the ground.

This correlation is based on the curve proposed by Yoshimine et al. (2006) to estimate the maximum shear strain generated and the factors of safety against liquefaction proposed by Idriss and Boulanger (2008). The equation of the regression is shown in Eq. (1.3) (Kutter et al., 2018).

$$U_{x2} = b_2 \left[b_1 - \frac{\left(D_r\_q_c\left(2.0m\right) - 0.125\right)^{n_3} + 0.05}{1.3PGA_{\text{eff}}} \right]^{n_1} \tag{1.3}$$

where b_1, b_2, n_1, and n_3 are the regression parameters.

Based on the results of LEAP-UCD-2017 and LEAP-ASIA-2019, the correlation equation is updated to incorporate and build a reliable and large-scale database for centrifuge model. Figure 1.25 shows a surface plot of Eq. (1.3) with the values for

a median response $b_1 = 1.756$, $b_2 = 100$, $n_1 = 4$, and $n_3 = 3.245$ derived from the entire LEAP-UCD-2017 and LEAP-ASIA-2019 experimental data (Vargas, 2020). In addition to some tests being out of trend (considered outliers and excluded), a significant improvement in the correlation can be observed with the R^2 value increasing from 0.75 (LEAP-UCD-2017 data only) to 0.90 (this study).

1.6 Conclusions

Following the LEAP-UCD-2017, centrifuge model tests with a wider range of input conditions were conducted at ten institutions in LEAP-ASIA-2019. In addition to the conventional centrifuge model test (Model A), a model test (Model B) was conducted to validate the generalized scaling law. This was the first multi-institutional attempt to validate a generalized scaling law for saturated sandy slope deposits under a wide range of initial conditions. A detailed discussion is expected to be provided by the associated papers from each institute. A brief overview of test results from each institute is presented here so that the reader can locate the results of interest.

The correlation between tip resistance and initial relative density of the ground at 2.0 m deep was updated by using a power-type correlation, which depends on the size of the container and the diameter of the rod. This is because the achieved value of q_c (2.0 m) was found to be strongly influenced by the distance from the boundary and the diameter of the rod.

Based on the results obtained in LEAP-UCD-2017 and LEAP-ASIA-2019, the correlation surface between Dr_q_c(2.0 m), PGA_{eff}, and U_{x2} was updated to incorporate new findings and build a reliable large-scale centrifuge model database. As a result, the correlation was greatly improved with a fit coefficient R^2 of 0.90.

One facility reported that for "small" PGA levels at a "low" gravity level, the high-frequency component of the input acceleration is significantly increased by the shaking table, resulting in large differences in PGA values even when similar PGA_{eff} values are obtained. One of the causes of this excessive high-frequency amplitude may be partially due to the vertical component, which induces oscillatory motion with a large periodic amplitude at low centrifugal acceleration of the shaking.

When the displacements in the x-direction (down slope direction) are larger, say more than 250 mm in Model B, because of low density and high PGA, significant discrepancies between Models A and B were found. This is considered to indicate the limitation of GSL, and caution should be exercised when applying GSL under such severe conditions.

Acknowledgments The experimental work on LEAP-ASIA-2019 was supported by different funds depending mainly on the location of the work. The work at Kyoto University and Kansai University was supported by JSPS KAKENHI grant number 17H00846. The work by the US PIs (Manzari, Kutter, and Zeghal) is funded by the National Science Foundation grants: CMMI 1635524, CMMI 1635307, and CMMI 1635040. The work at KAIST was part of a project titled

"Development of performance-based seismic design," funded by the Ministry of Oceans and Fisheries, Korea. The work at Zhejiang University was supported by NSF (grant nos. 51778573, 51978613, and 51988101) and the 111 Project (grant no. B18047). The work at NCU was supported by MOST: 106-2628-E-008-004-MY3. The work at Ehime University was supported by JSPS KAKENHI grant numbers 26282103 and 17H00846.

References

Adamidis, O., & Madabhushi, S. P. G. (2015). On preparation of viscous pore fluids for dynamic centrifuge modelling. *International Journal for Physical Modelling in Geomechanics*.

Arulanandan, K., & Scott, R. F. (1993 and 1994). *Verification of numerical procedures for the analysis of soil liquefaction problems, proceedings of the international conference on the verification of numerical procedures for the analysis of soil liquefaction problems, Vols. 1 and 2*. A. A. Balkema, Rotterdam.

Asaoka, A., & Noda, T. (2007). All soils all states all round geo-analysis integration, international workshop on constitutive modelling – Development, implementation, evaluation, and application, Hong Kong, China. pp. 11–27.

Bolton, M. D., Gui, M. W., Garnier, J., Corte, J. F., Bagge, G., Laue, J., & Renzi, R. (1999). Centrifuge cone penetration tests in sand. *Geotechnique, 49*(4), 543–552.

Boulanger, R. W., & Ziotopoulou, K. (2015). PM4Sand (Version 3): A sand plasticity model for earthquake engineering applications. Report No. UCD/CGM-15/01.

Carey, T. J., Stone, N., & Kutter, B. L. (2020). Chapter 2 grain size analysis and maximum and minimum dry density of Ottawa F-65 sand for LEAP-UCD-2017 *B*. In B. L. Kutter & M. T. Manzari Mourad Zeghal (Eds.), *Model tests and numerical simulations of liquefaction and lateral spreading* (pp. 31–44). Springer. https://doi.org/10.1007/978-3-030-22818-7_2

Cundall, P. A., & Strack, O. D. L. (1979). A discrete numerical model for granular assemblies. *Geotechnique, 29*(1), 47–65.

Iai, S. (1989). Similitude for shaking table tests on soil-structure-fluid model in 1g gravitational field. *Soils and Foundations, 29*(1), 105–118.

Iai, S., Matsunaga, Y., & Kameoka, T. (1992). Strain space plasticity model for cyclic mobility. *Soils and Foundations, 32*(2), 1–15.

Iai, S., Tobita, T., & Nakahara, T. (2005). Generalized scaling relations for dynamic centrifuge tests. [full review (ISI)]. *Geotechnique, 55*(5), 355–362.

Iai, S., Ueda, K., Tobita, T., & Ozutsumi, O. (2013). Finite strain formulation of a strain space multiple mechanism model for granular materials. *International Journal for Numerical and Analytical Methods in Geomechanics, 37*(9), 1189–1212.

Idriss, I. M., & Boulanger, R. W. (2008). Soil liquefaction during earthquakes. Earthquake Engineering Research Institute (EERI), Oakland, California, USA., MNO-12.

Koshizuka, S., Tamako, H., & Oka, Y. (1996). A particle method for incompressible viscous flow with fluid fragmentation. *Computational Fluid Dynamics Journal, 29*(4).

Kutter, B., Carey, T., Hashimoto, T., Zeghal, M., Abdoun, T., Kokalli, P., Madabhushi, G., Haigh, S., Hung, W.-Y., Lee, C.-J., Iai, S., Tobita, T., Zhou, Y. G., Chen, Y., & Manzari, M. T. (2018). LEAP-GWU-2015 experiment specifications, results, and comparisons. *Soil Dynamics and Earthquake Engineering, 113*, 616–628. https://doi.org/10.1016/j.soildyn.2017.05.018

Kutter, B. L., Carey, T. J., Stone, N., Bonab, M. H., Manzari, M. T., Zeghal, M., Escoffier, S., Haigh, S. K., Madabhushi, G. S. P., Hung, W.-Y., Kim, D.-S., Kim, N. R., Okamura, M., Tobita, T., Ueda, K., & Zhou, Y.-G. (2020a). LEAP-UCD-2017 V. 1.01 model specifications. In B. Kutter, M. T. Manzari, & M. Zeghal (Eds.), *Model tests and numerical simulations of liquefaction and lateral spreading* (pp. 3–29). Springer. https://doi.org/10.1007/978-3-030-22818-7_1

Kutter, B. L., Carey, T. J., Stone, N., Zheng, B. L., Gavras, A., Manzari, M. T., Zeghal, M., Abdoun, T., Korre, E., Escoffier, S., Haigh, S. K., Madabhushi, G. S. P., Madabhushi, S. S. C., Hung, W.-Y., Liao, T.-W., Kim, D.-S., Kim, S.-N., Ha, J.-G., Kim, N. R., Okamura, M., Sjafruddin, A. N., Tobita, T., Ueda, K., Vargas, R., Zhou, Y.-G., & Liu, K. (2020b). LEAP-UCD-2017 comparison of centrifuge test results. In B. Kutter, M. T. Manzari, & M. Zeghal (Eds.), *Model tests and numerical simulations of liquefaction and lateral spreading* (pp. 69–103). Springer. https://doi.org/10.1007/978-3-030-22818-7_4

Lucy, L. B. (1977). A numerical approach to the testing of the fission hypothesis. *Astronomical Journal, 82*, 1013–1024.

Manzari, M. T., Kutter, B. L., Zeghal, M., Iai, S., Tobita, T., Madabhushi, S., Haigh, S. K., Mejia, L., Gutierrez, D. A., Armstrong, R. J., Sharp, M. K., Chen, Y. M., & Zhou, Y. G. (2015). LEAP projects: Concept and challenges. In *Geotechnics for catastrophic flooding events* (pp. 109–116). CRC Press.

Manzari, T. M., Ghoraiby, M., Kutter, B. L., Zeghal, M., Abdoun, T., Arduino, P., Armstrong, R. J., Beaty, M., Carey, T., Chen, Y.-M., Ghofrani, A., Gutierrez, D., Goswami, N., Haigh, S. K., Hung, W.-Y., Iai, S., Kokkali, P., Lee, C.-J., Madabhushi, G., Mejia, L., Sharp, M., Tobita, T., Ueda, K., Zhou, Y.-G., & Ziotopoulou, K. (2018). Liquefaction experiment and analysis projects (LEAP): Summary of observations from the planning phase. Soil dynamics and earthquake engineering, LEAP2015 special volume, Ed. Manzari, Kutter and Zeghal, 113, 714–743. https://doi.org/10.1016/j.soildyn.2017.05.015.

Monaghan, J. J. (1992). Smoothed particle hydrodynamics. *Annual Review of Astronomy and Astrophysics, 30*, 543–574.

Oka, F., Yashima, A., Tateishi, Y., Taguchi, Y., & Yamashita, S. (1999). A cyclic elasto-plastic constitutive model for sand considering a plastic-strain dependence of the shear modulus. *Geotechnique, 49*(5), 661–680.

Stewart, D. P., Chen, Y.-R., & Kutter, B. L. (1998). Experience with the use of methylcellulose as a viscous pore fluid in centrifuge models. *Geotechnical Testing Journal, 21*(4), 365–369.

Tobita, T., Ueda, K., Vargas, R. R., Ichii, K., Okamura, M., Sjafruddin, A. N., Takemura, J., Hang, L., Uzuoka, R., Iai, S., Boksmati, J., Fusco, A., Torres-Garcia, S., Haigh, S., Madabhushi, G., Manzari, M., Escoffier, S., Li, Z., Kim, D. S., Manandhar, S., Hung, W.-Y., Huang, J.-X., Pham, T.-N.-P., Zeghal, M., Abdoun, T., Korre, E., Kutter, B. L., Carey, T. J., Stone, N., Zhou, Y.-G., Liu, K., & Ma, Q. (2022). LEAP-ASIA-2019: Validation of centrifuge experiments and the generalized scaling law on liquefaction-induced lateral spreading. *Soil Dynamics and Earthquake Engineering, 157*, 1–19. https://doi.org/10.1016/j.soildyn.2022.107237

Vargas, R. (2020). *Validation of numerical predictions of lateral spreading based on "hollow-cylinder torsional shear tests" and "a large centrifuge-models database"*. Master thesis submitted to Department of Civil and Earth Resources Engineering, Kyoto University.

Yoshimine, M., Nishizaki, H., Amano, K., & Hosono, Y. (2006). Flow deformation of liquefied sand under constant shear load and its application to analysis of flow slide in infinite slope. *Soil Dynamics and Earthquake Engineering, 26*, 253–264.

Chapter 2
LEAP-ASIA-2019 Simulation Exercise: Calibration of Constitutive Models and Simulations of the Element Tests

Kyohei Ueda, Yoshikazu Tanaka, Anurag Sahare, Ahmed Elgamal, Zhijian Qiu, Rui Wang, Tong Zhu, Chuang Zhou, Jian-Min Zhang, Andres Reyes Parra, Andres Barrero, Mahdi Taiebat, Waka Yuyama, Susumu Iai, Junichi Hyodo, Koji Ichii, Mohamed A. Elbadawy, Yan-Guo Zhou, Gianluca Fasano, Anna Chiaradonna, Emilio Bilotta, Pedro Arduino, Mourad Zeghal, Majid Manzari, and Tetsuo Tobita

Abstract This chapter presents a summary of the calibration exercises (i.e., element test simulations) submitted by nine numerical simulation teams that participated in the LEAP-ASIA-2019 prediction campaign. The standard sand selected for the campaign is Ottawa F-65, and researchers have developed several efforts to increase the database of laboratory tests to characterize the physical and mechanical properties of this sand (Carey TJ, Stone N, Kutter BL, Grain Size Analysis and Maximum and Minimum Dry Density of Ottawa F-65 Sand for LEAP-UCD-2017. Model tests and numerical simulations of liquefaction and lateral spreading: LEAP-UCD-2017. Springer, 2019; El Ghoraiby MA, Park H, Manzari MT. Physical and mechanical properties of Ottawa F65 sand. In: Model tests and numerical simulations of liquefaction and lateral spreading: LEAP-UCD-2017, Springer, 2019; Ueda K, Vargas RR, Uemura K, LEAP-Asia-2018: Stress-strain response of Ottawa sand in Cyclic Torsional Shear Tests, DesignSafe-CI [publisher], Dataset, https://doi.org/10.17603/DS2D40H, 2018; Vargas RR, Ueda K, Uemura K, Soil Dyn Earthq

K. Ueda (✉) · Y. Tanaka · A. Sahare
Disaster Prevention Research Institute, Kyoto University, Kyoto, Japan
e-mail: ueda.kyohei.2v@kyoto-u.ac.jp

A. Elgamal · Z. Qiu
Department of Structural Engineering, University of California San Diego, La Jolla, CA, USA

R. Wang · T. Zhu · C. Zhou · J.-M. Zhang
Department of Hydraulic Engineering, Tsinghua University, Beijing, China

A. R. Parra · A. Barrero · M. Taiebat
Department of Civil Engineering, University of British Columbia, Vancouver, BC, Canada

W. Yuyama · S. Iai
FLIP Consortium, Kyoto, Japan

T. Tobita et al. (eds.), *Model Tests and Numerical Simulations of Liquefaction and Lateral Spreading II*, https://doi.org/10.1007/978-3-031-48821-4_2

Eng 133:106111, 2020; Vargas RR, Ueda K, Uemura K, Dynamic torsional shear tests of Ottawa F-65 Sand for LEAP-ASIA-2019. Model tests and numerical simulations of liquefaction and lateral spreading: LEAP-ASIA-2019, Springer, 2023). The objective of this element test simulation exercise is to assess the performance of the constitutive models used by the simulation teams for simulating the experimental results of a series of undrained stress-controlled cyclic torsional shear tests on Ottawa F-65 sand for two different relative densities (Dr = 50% and 60%) (Ueda K, Vargas RR, Uemura K, LEAP-Asia-2018: Stress-strain response of Ottawa sand in Cyclic Torsional Shear Tests, DesignSafe-CI [publisher], Dataset, https://doi.org/10.17603/DS2D40H, 2018; Vargas RR, Ueda K, Uemura K, Soil Dyn Earthq Eng 133:106111, 2020; Vargas RR, Ueda K, Uemura K, Dynamic torsional shear tests of Ottawa F-65 sand for LEAP-ASIA-2019. Model tests and numerical simulations of liquefaction and lateral spreading: LEAP-ASIA-2019, Springer, 2023). The simulated liquefaction strength curves demonstrate that majority of the constitutive models are capable of reasonably capturing the measured liquefaction strength curves both for Dr = 50% and 60%. However, the simulated stress paths and stress-strain relationships show some differences from the corresponding laboratory tests in some cases.

J. Hyodo
Tokyo Electric Power Services, Tokyo, Japan

K. Ichii
Faculty of Societal Safety Science, Kansai University, Osaka, Japan

M. A. Elbadawy · Y.-G. Zhou
Department of Civil Engineering, Zhejiang University, Hangzhou, People's Republic of China

G. Fasano · A. Chiaradonna · E. Bilotta
Department of Civil, Architectural and Environmental Engineering, University of Naples Federico II, Naples, Italy

P. Arduino
Department of Civil and Environmental Engineering, University of Washington, Seattle, WA, USA

M. Zeghal
Department of Civil and Environmental Engineering, Rensselaer Polytechnic Institute, Troy, NY, USA

M. Manzari
Department of Civil and Environmental Engineering, George Washington University, Washington, DC, USA

T. Tobita
Department of Civil, Environmental and Applied Systems Engineering, Kansai University, Osaka, Japan

Keywords Liquefaction Experiments and Analysis Projects (LEAP-ASIA-2019) · Numerical simulation · Constitutive model · Ottawa F-65 · Liquefaction strength curve

2.1 Introduction

The LEAP-ASIA-2019 project involved nine numerical simulation teams from different academic institutions and geotechnical companies from around the world; they participated in the modeling of some of the centrifuge model experiments performed at several research institutions. The simulation exercise consisted of the calibration of constitutive model parameters, Type-B predictions, and Type-C predictions. This chapter presents an overview of the results of the first phase (i.e., model calibration) of this exercise. The main objective of this phase was to provide the numerical simulation teams with the opportunity to calibrate their constitutive models, which will be used in the Type-B simulations, using the results of cyclic shear tests performed on Ottawa F-65 sand during the LEAP-2019 project.

For the calibration phase of constitutive models, a series of hollow cylinder torsional shear tests were performed at Kyoto University (KyU) for Ottawa F-65 sand with a relative density (Dr) of 50% and 60% under an initial effective confining stress of 100 kPa. Also, direct simple shear tests were performed at George Washington University (GWU) for Dr = 71% under an initial effective vertical stress of 100 kPa and Dr = 69% under 40 kPa.

The element tests mentioned above provided new datasets that complement the monotonic and cyclic triaxial shear tests reported by Vasko (2015) and Vasko et al. (2018), monotonic and cyclic simple shear tests by Bastidas (2016) and Bastidas et al. (2017), and cyclic triaxial tests by El Ghoraiby and Manzari (2018) and El Ghoraiby et al. (2019). These tests were previously made available to the numerical simulation teams that participated in the numerical simulation of the LEAP-2017 project. The new datasets were made available to all the numerical simulation teams that participated in the LEAP-2019 project via DesignSafe, as described below.

The timeline for this calibration phase of the LEAP-2019 project was as follows:

1. All the element test data were made available on DesignSafe to the numerical simulation teams by December 5, 2018. These are as follows:
   - LEAP-2015 GWU Laboratory Tests: https://doi.org/10.17603/DS2TH7Q
   - LEAP-2017 GWU Laboratory Tests: https://doi.org/10.17603/DS2210X (cyclic triaxial shear tests for Dr = 71%, 87%, and 97% at GWU).
   - LEAP-2018 GWU Cyclic Simple Shear: https://doi.org/10.17603/DS2HX3H (cyclic direct simple shear tests for Dr = 71% and 69% at GWU).
   - LEAP-2018 KyU Cyclic Torsional Shear: https://doi.org/10.17603/DS2D40H (cyclic torsional shear tests for Dr = 50% and 60% at KyU).

2. The participating teams were requested to simulate a selected number of the provided test data and liquefaction strength curves that were obtained from cyclic direct simple shear tests and cyclic torsional shear tests. The critical tests to be simulated were the cyclic torsional shear test for Dr = 50% and 60% (under an initial effective confining stress of 100 kPa). It was required to compare the simulated stress paths and stress-strain responses to the experimental results reported by KyU. If time allowed, it was desirable to show the validity of constitutive models for the other experimental results having higher relative densities. The numerical simulation team submitted the results of their element test simulations and comparisons with those of the provided element tests in the form of a detailed report by January 11, 2019.

2.2 The Numerical Simulation Teams

Table 2.1 shows the numerical simulation teams who submitted their calibration reports and participated in the Type-B simulation exercise. The constitutive model and the analysis platform used by each numerical simulation team are also listed in the table. Mode-detailed information of each constitutive model and the numerical simulation techniques used by each simulation team are provided in separate papers (Tanaka et al., 2023; Hyodo & Ichii, 2023; Fasano et al., 2023; Qiu & Elgamal, 2023; Elbadawy & Zhou, 2023; Reyes et al., 2023; Wang et al., 2023).

2.3 Results of the Element Test Simulations

Figures 2.1, 2.2, 2.3 and 2.4 show a detailed comparison of the numerical simulations of the undrained cyclic torsional shear tests on Ottawa F-65 sand for Dr = 50% with different cyclic stress ratios (i.e., CSR = 0.19, 0.15, 0.13, and 0.10). The

Table 2.1 Numerical simulation teams

No.	Numerical simulation team	Constitutive model	Analysis platform
1	Kyoto university (two different predictors)	Cocktail glass model	FLIP ROSE
2			
3	FLIP consortium	Cocktail glass model	FLIP ROSE
4	Tokyo electric power services	Cocktail glass model	FLIP ROSE
5	University of Naples Federico II	PM4Sand model	PLAXIS
6	University of Washington	PM4Sand model	OpenSees
7	University of California, san Diego	PDMY02 model	OpenSees
8	Zhejiang university	PDMY02 model	OpenSees
9		CPSP model	
10	University of British Columbia	SANISAND model	FLAC3D
11	Tsinghua University	CycLiqCP model	OpenSees

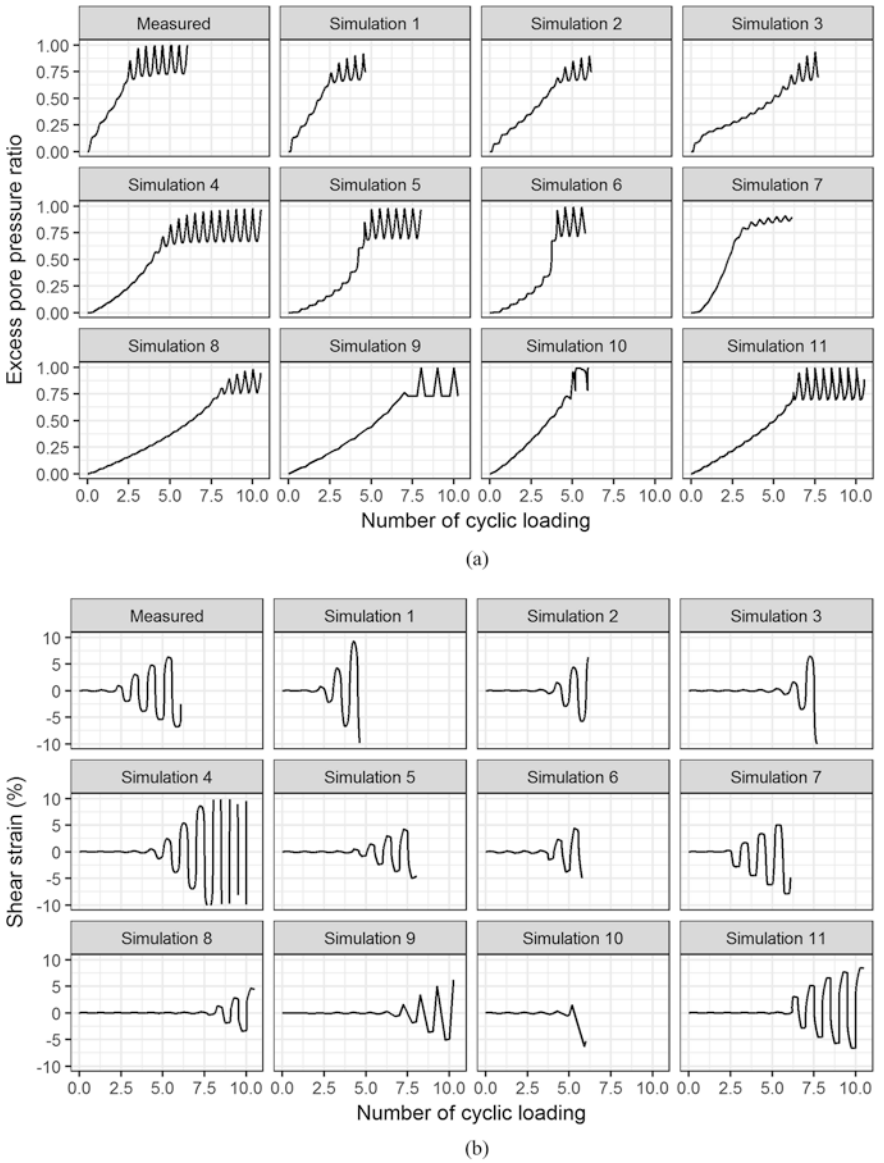

Fig. 2.1 Comparison of the numerical simulations of an undrained cyclic torsional shear test on Ottawa F-65 sand for Dr = 50%, CSR = 0.19. (**a**) Time history of excess pore pressure ratio, (**b**) Time history of shear strain, (**c**) Effective stress path, (**d**) Shear stress-shear strain relationship

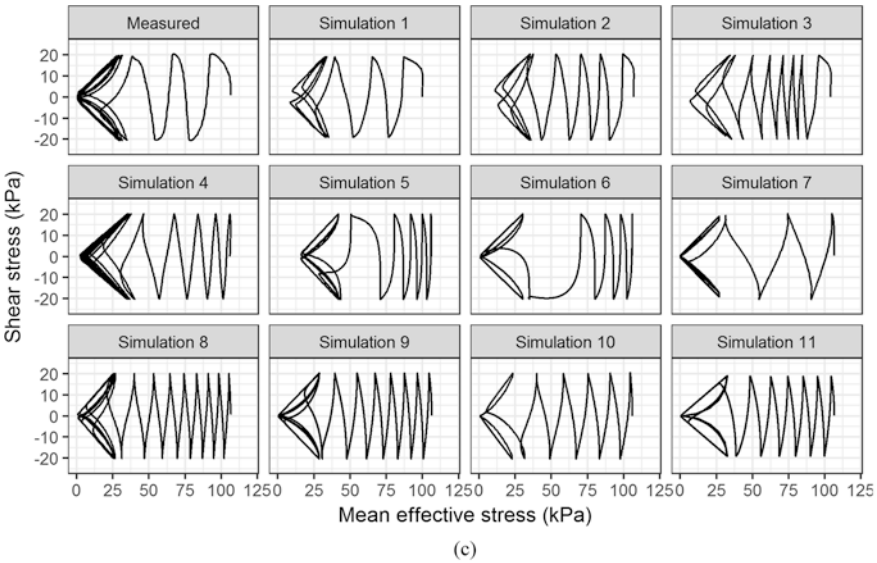

Fig. 2.1 (continued)

simulations are labeled Simulations 1 to 11. The numbers refer to the order of the simulation teams in the table presented above. The numerical simulation teams 1 and 2 belonging to the same organization used the same analysis platform with the same constitutive model, but they are distinguished because they carried out the

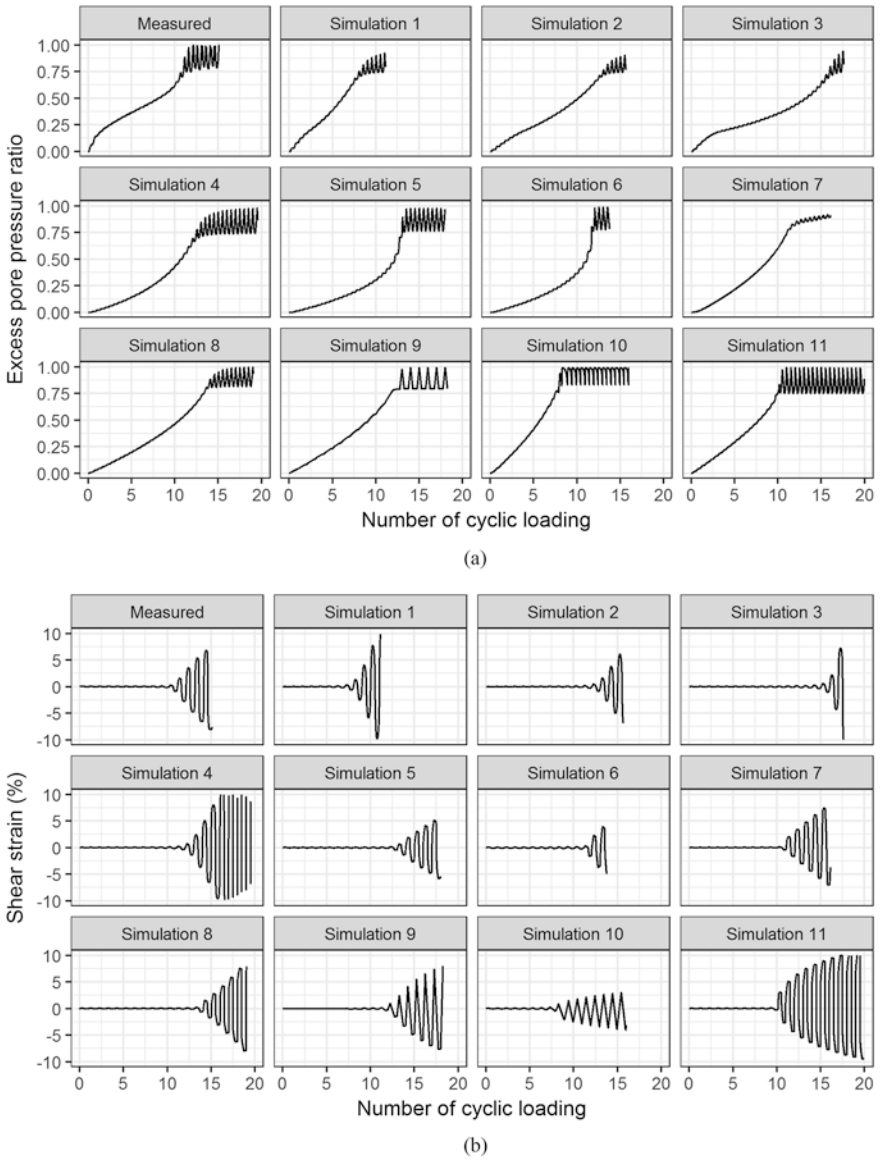

Fig. 2.2 Comparison of the numerical simulations of an undrained cyclic torsional shear test on Ottawa F-65 sand for Dr = 50%, CSR = 0.15. (**a**) Time history of excess pore pressure ratio, (**b**) Time history of shear strain, (**c**) Effective stress path, (**d**) Shear stress-shear strain relationship

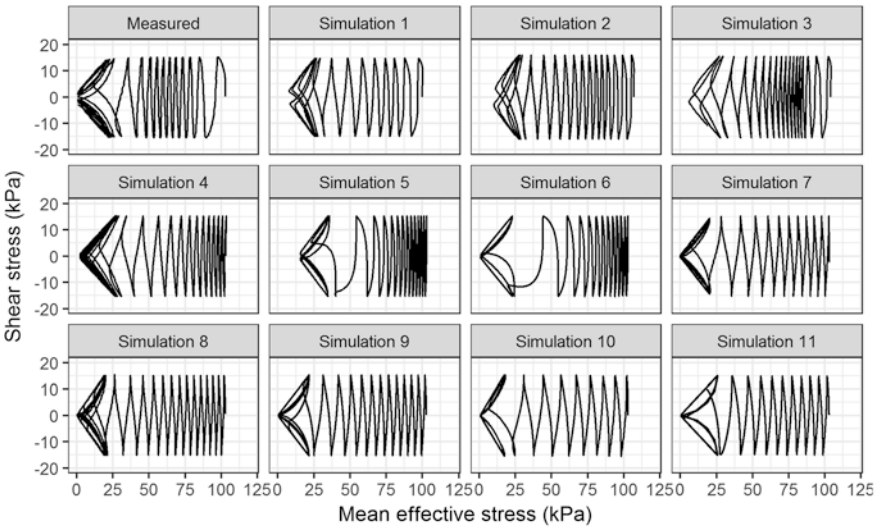

(c)

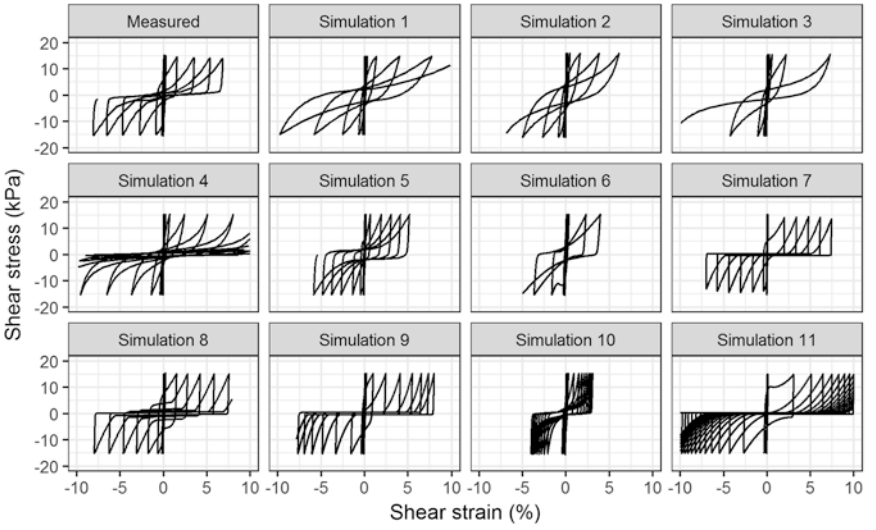

(d)

Fig. 2.2 (continued)

calibration independently. It is also noted that the same predictor performed Simulations 8 and 9, but they are distinguished because different constitutive models were used in the simulations. Figures 2.5, 2.6, 2.7, 2.8 and 2.9 show a similar comparison of the numerical simulations of the undrained cyclic torsional shear tests for Dr = 60% with different cyclic stress ratios (i.e., CSR = 0.20, 0.18, 0.15, 0.13, and 0.12). The numerical simulation team 3 did not submit simulations for Dr = 60% with CSR of 0.12.

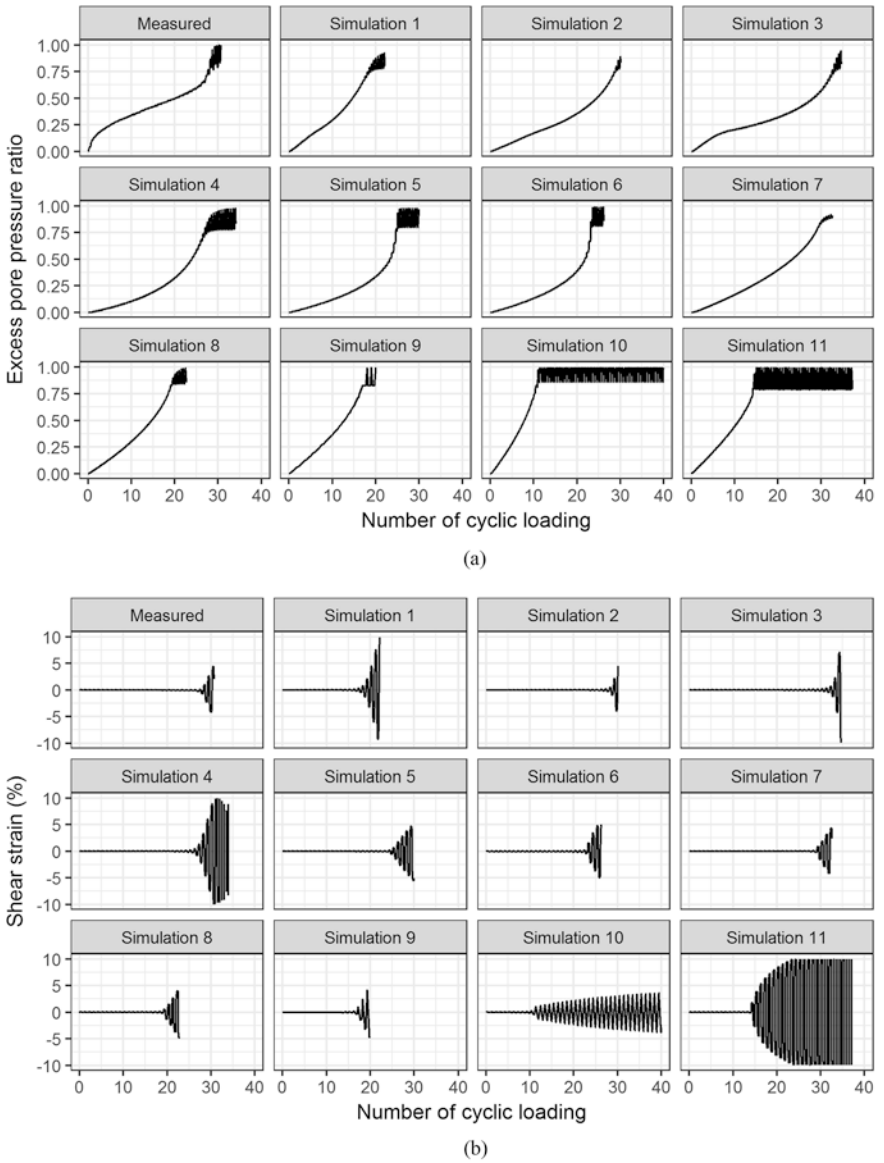

Fig. 2.3 Comparison of the numerical simulations of an undrained cyclic torsional shear test on Ottawa F-65 sand for Dr = 50%, CSR = 0.13. (**a**) Time history of excess pore pressure ratio, (**b**) Time history of shear strain, (**c**) Effective stress path, (**d**) Shear stress-shear strain relationship

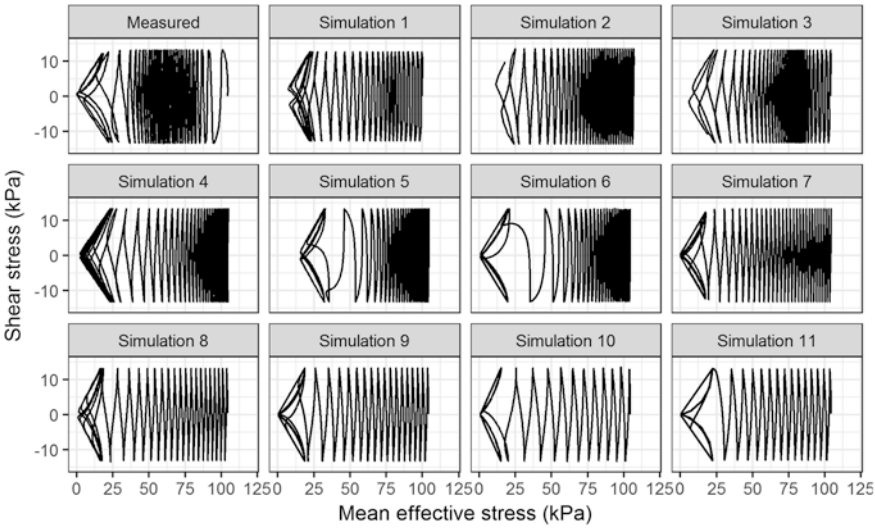

(c)

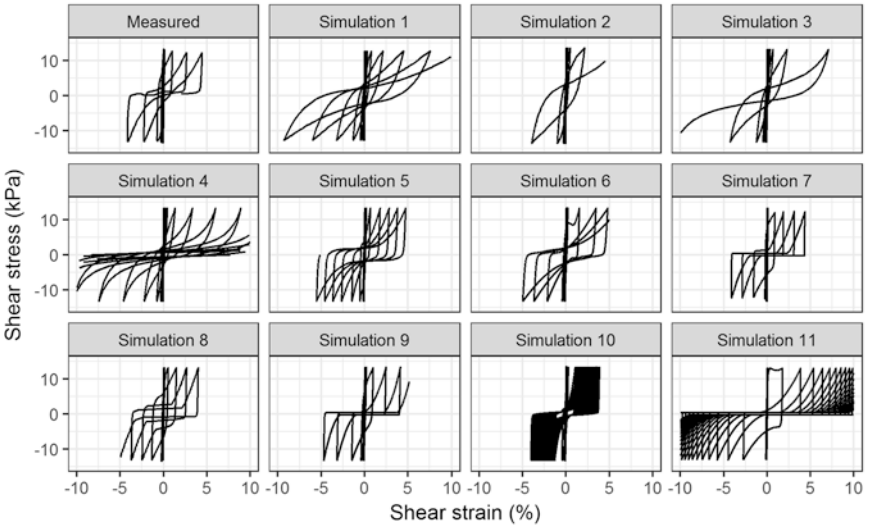

(d)

Fig. 2.3 (continued)

A review of Figs. 2.1, 2.2, 2.3, 2.4, 2.5, 2.6, 2.7, 2.8 and 2.9 indicates the following trends:

1. The majority of the constitutive models are capable of reasonably capturing the overall trends of the measured time histories of excess pore pressure ratio and shear strain, effective stress paths, and stress-strain responses both for Dr = 50% and 60%.

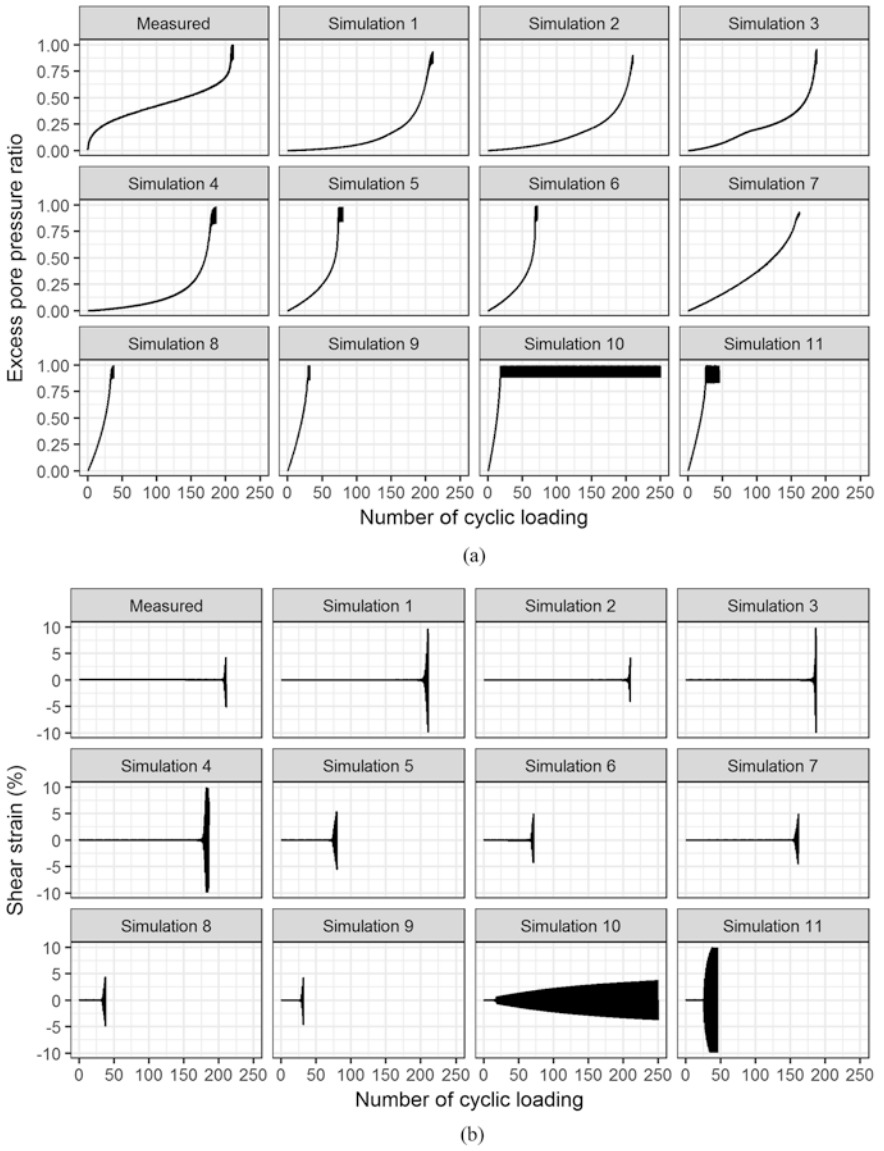

Fig. 2.4 Comparison of the numerical simulations of an undrained cyclic torsional shear test on Ottawa F-65 sand for Dr = 50%, CSR = 0.10. (**a**) Time history of excess pore pressure ratio, (**b**) Time history of shear strain, (**c**) Effective stress path, (**d**) Shear stress-shear strain relationship

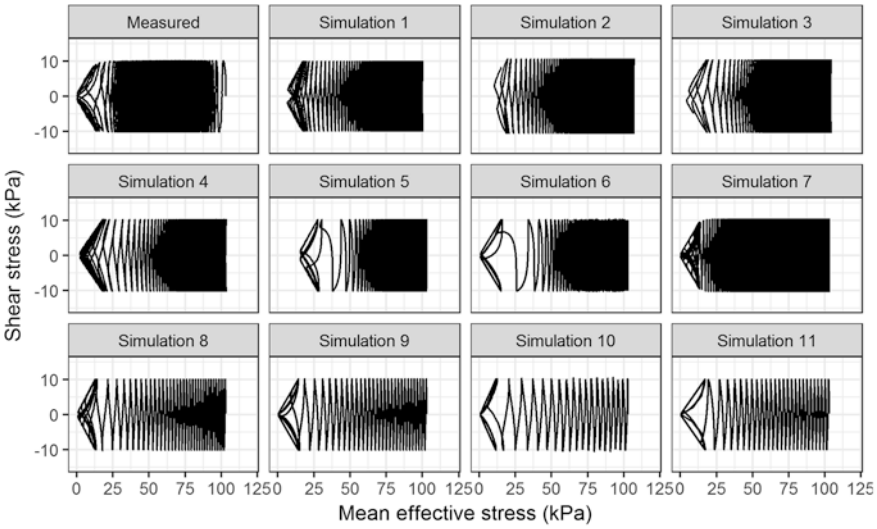

(c)

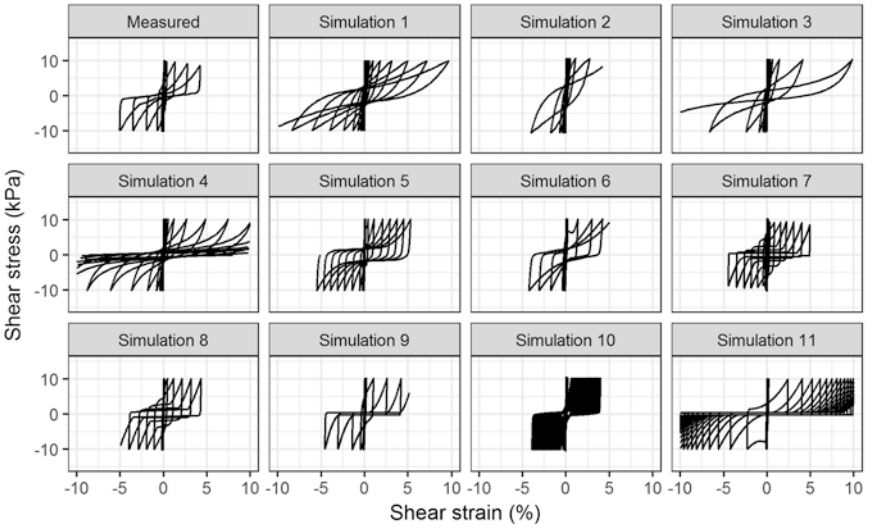

(d)

Fig. 2.4 (continued)

2. Simulations 1–4: Since the constitutive model and the analysis platform are the same, the simulated results are similar to some extent. However, different responses are observed depending on the model parameters; there are many cases where the effective stress path does not reach the origin (i.e., complete liquefaction) in Simulations 1 and 2, but it almost reaches the origin in Simulations 3 and 4.

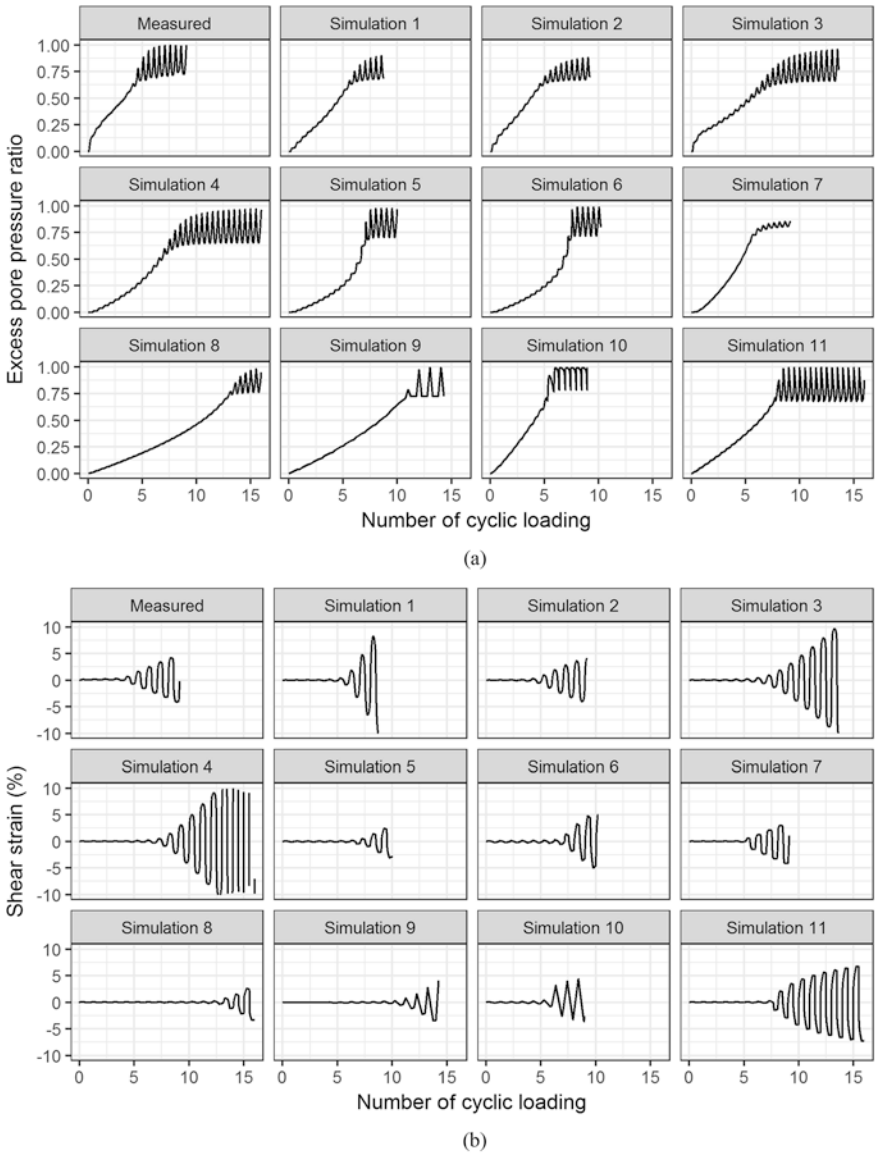

Fig. 2.5 Comparison of the numerical simulations of an undrained cyclic torsional shear test on Ottawa F-65 sand for Dr = 60%, CSR = 0.20. (**a**) Time history of excess pore pressure ratio, (**b**) Time history of shear strain, (**c**) Effective stress path, (**d**) Shear stress-shear strain relationship

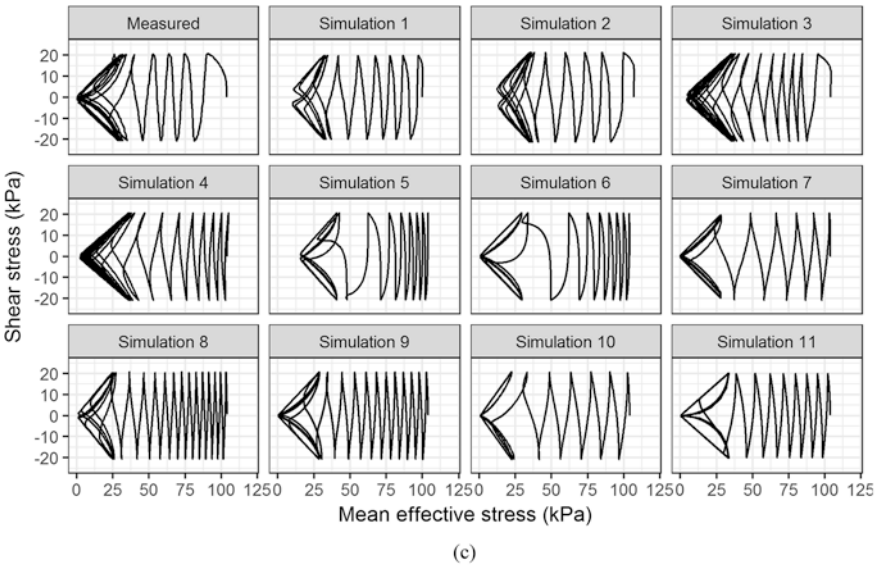

(c)

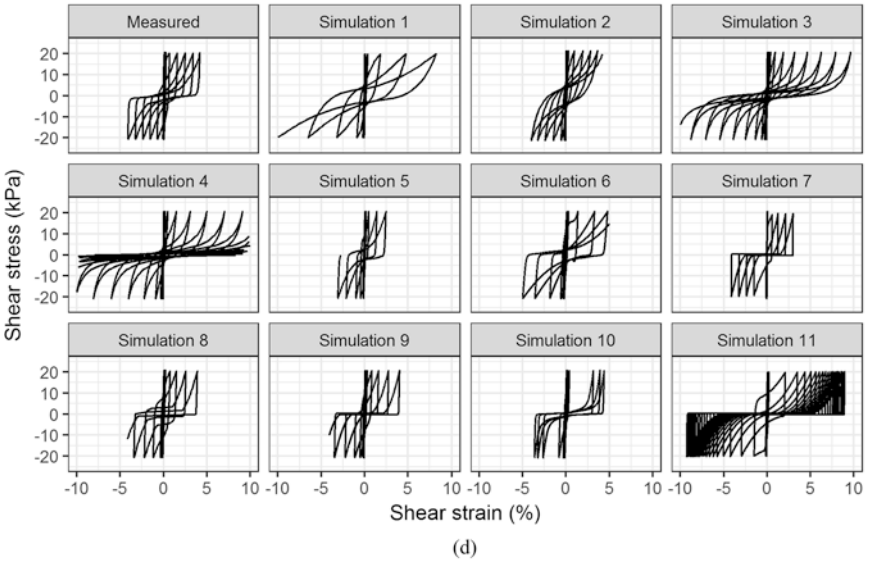

(d)

Fig. 2.5 (continued)

3. Simulations 5 and 6: Since the analysis platforms are different but the constitutive model is the same, the overall response tendency is very similar. The time history of the simulated excess pore water pressure shows that the pressure tends to rise rapidly at a certain stage, while it is relatively slow in the early stage of loading. This trend can also be seen in the simulated effective stress path.
4. Simulations 7 and 8: Although the constitutive model and the analysis platform are the same, the time history of the simulated excess pore water pressure, the effective stress path, and the associated strain development seem to be slightly

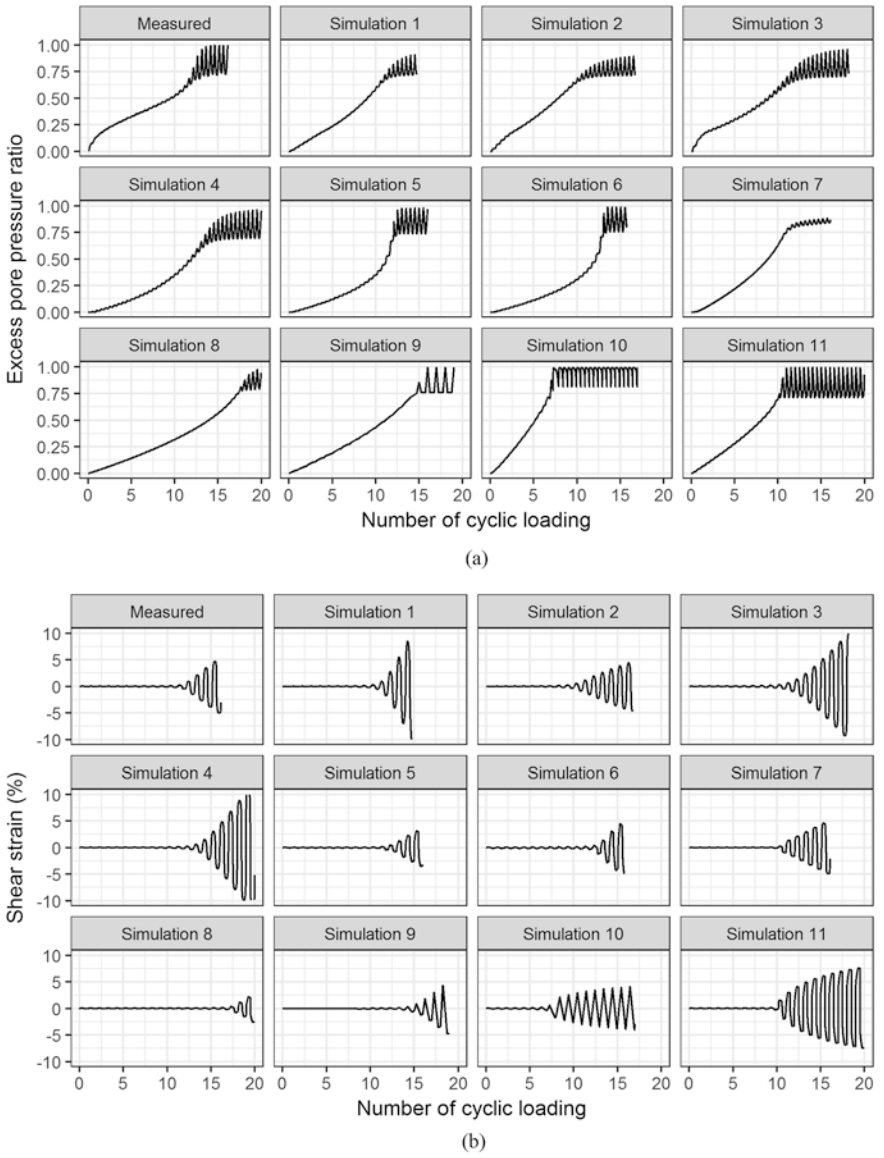

Fig. 2.6 Comparison of the numerical simulations of an undrained cyclic torsional shear test on Ottawa F-65 sand for Dr = 60%, CSR = 0.18. (**a**) Time history of excess pore pressure ratio, (**b**) Time history of shear strain, (**c**) Effective stress path, (**d**) Shear stress-shear strain relationship

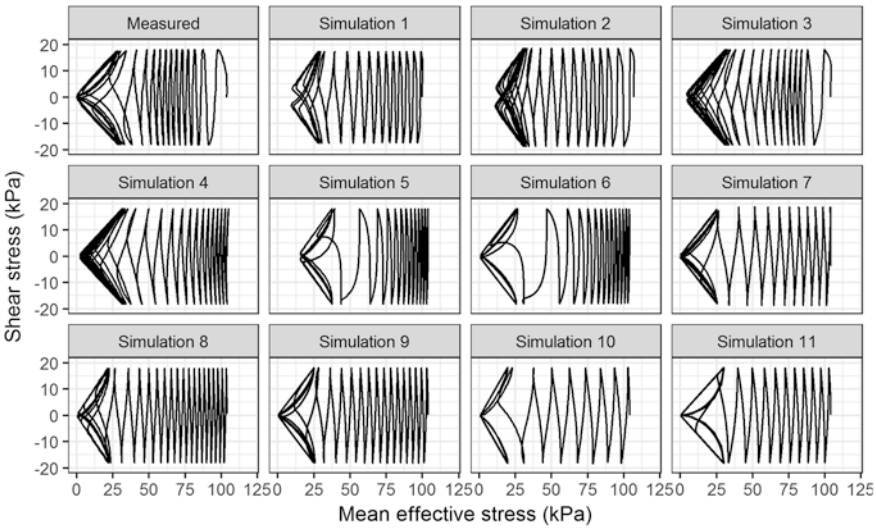

(c)

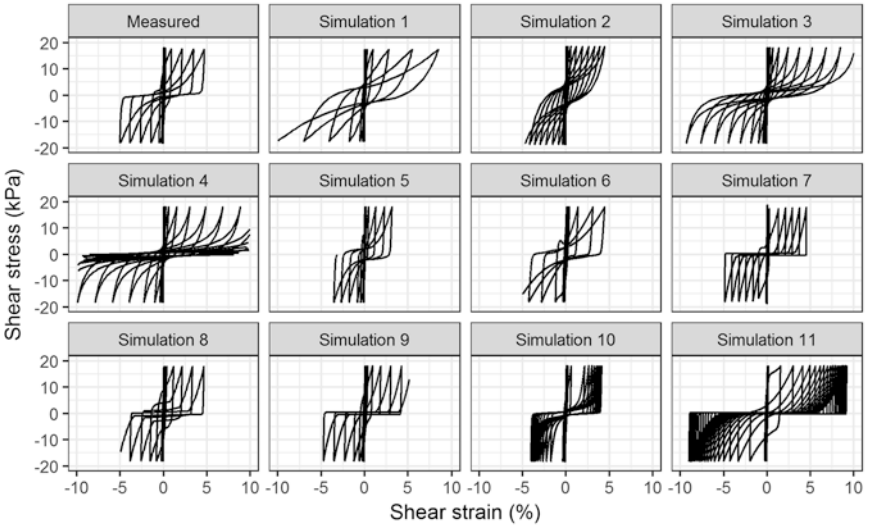

(d)

Fig. 2.6 (continued)

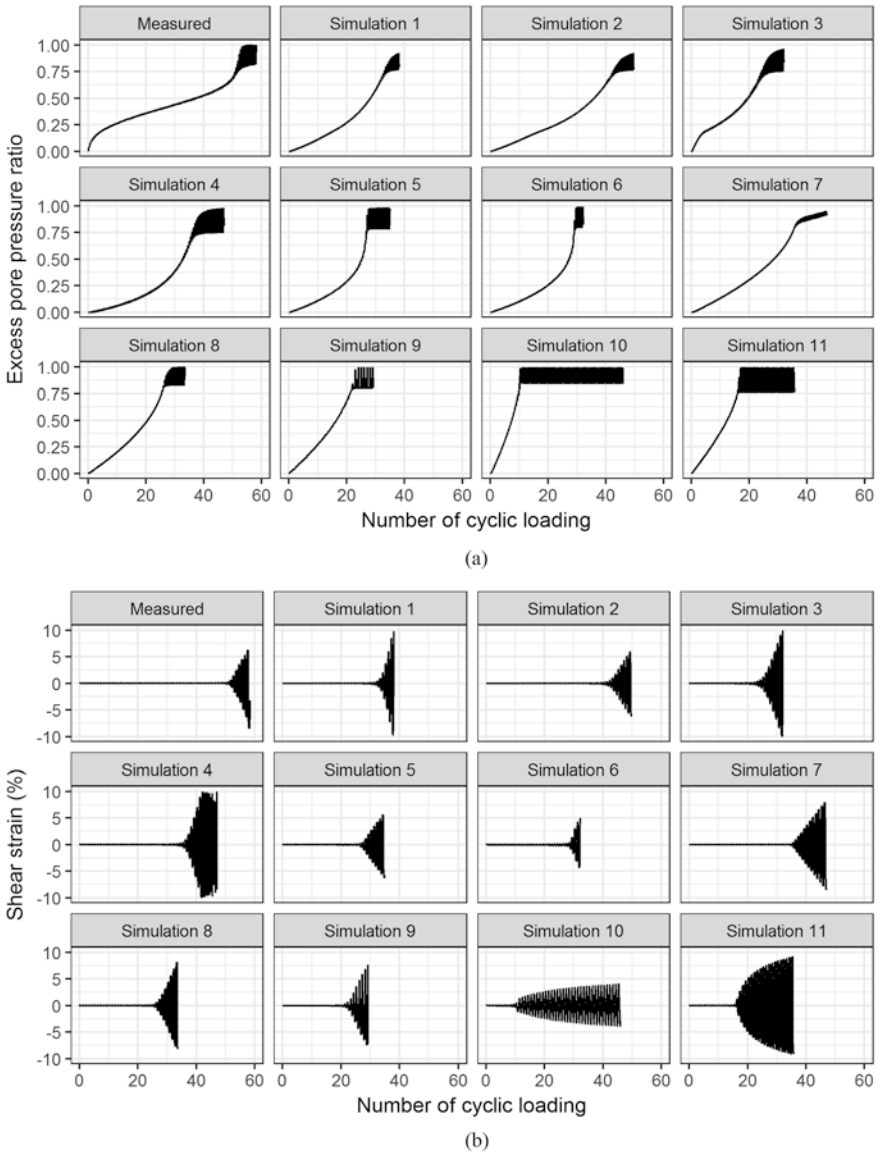

Fig. 2.7 Comparison of the numerical simulations of an undrained cyclic torsional shear test on Ottawa F-65 sand for Dr = 60%, CSR = 0.15. (**a**) Time history of excess pore pressure ratio, (**b**) Time history of shear strain, (**c**) Effective stress path, (**d**) Shear stress-shear strain relationship

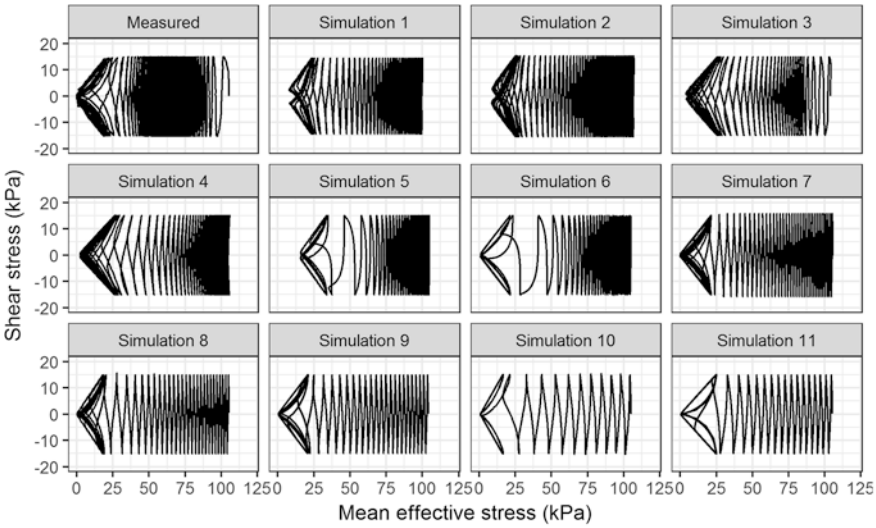

(c)

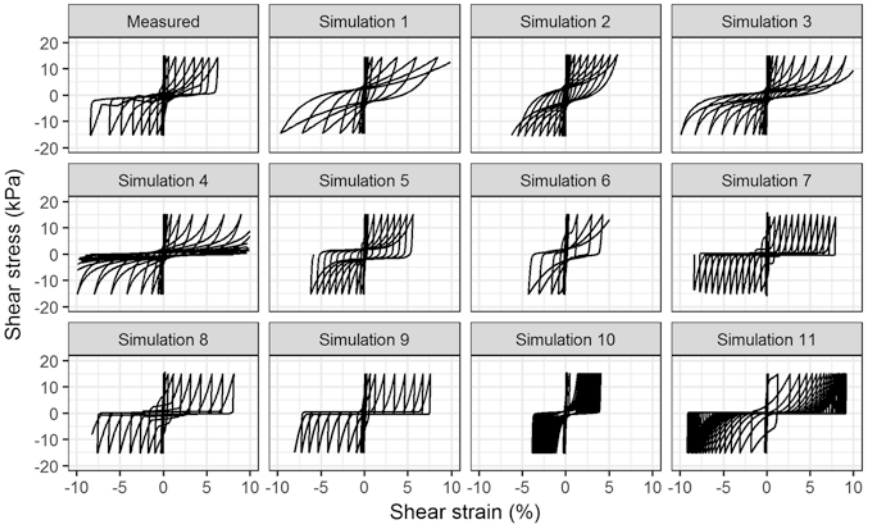

(d)

Fig. 2.7 (continued)

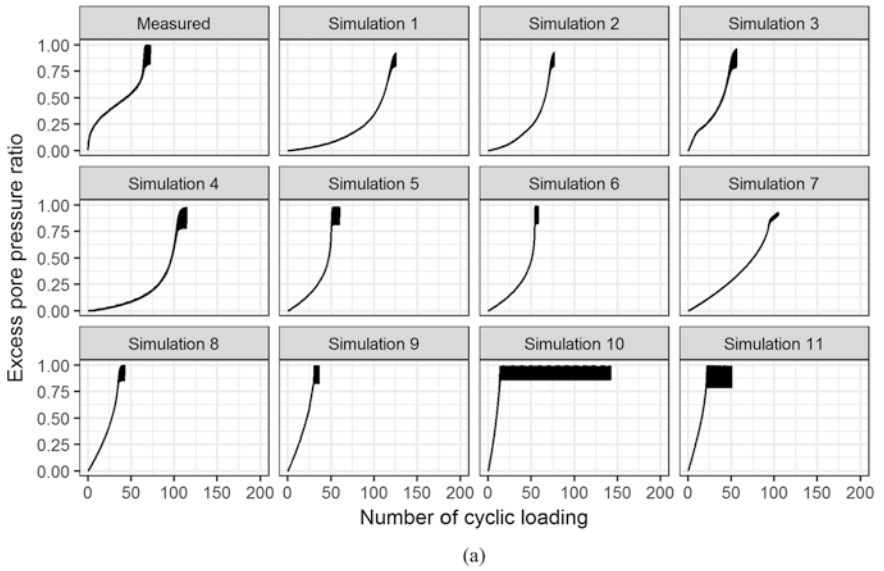

Fig. 2.8 Comparison of the numerical simulations of an undrained cyclic torsional shear test on Ottawa F-65 sand for Dr = 60%, CSR = 0.13. (**a**) Time history of excess pore pressure ratio, (**b**) Time history of shear strain, (**c**) Effective stress path, (**d**) Shear stress-shear strain relationship

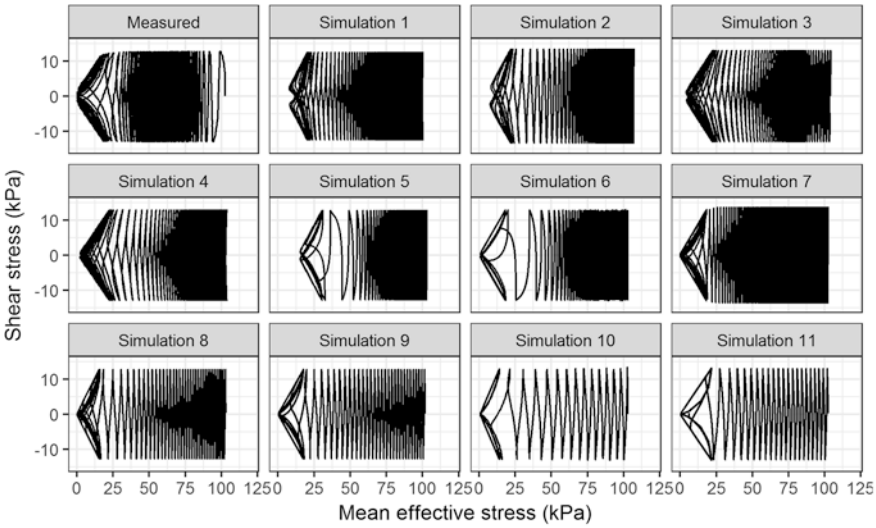

(c)

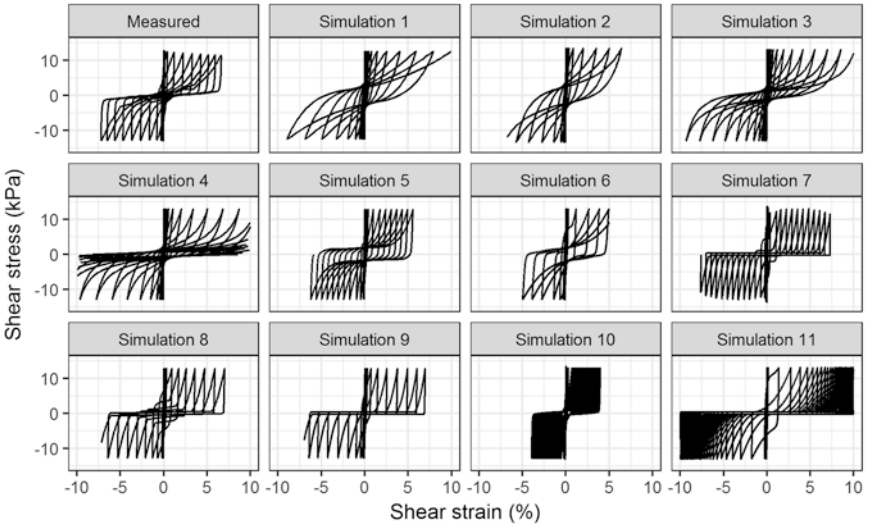

(d)

Fig. 2.8 (continued)

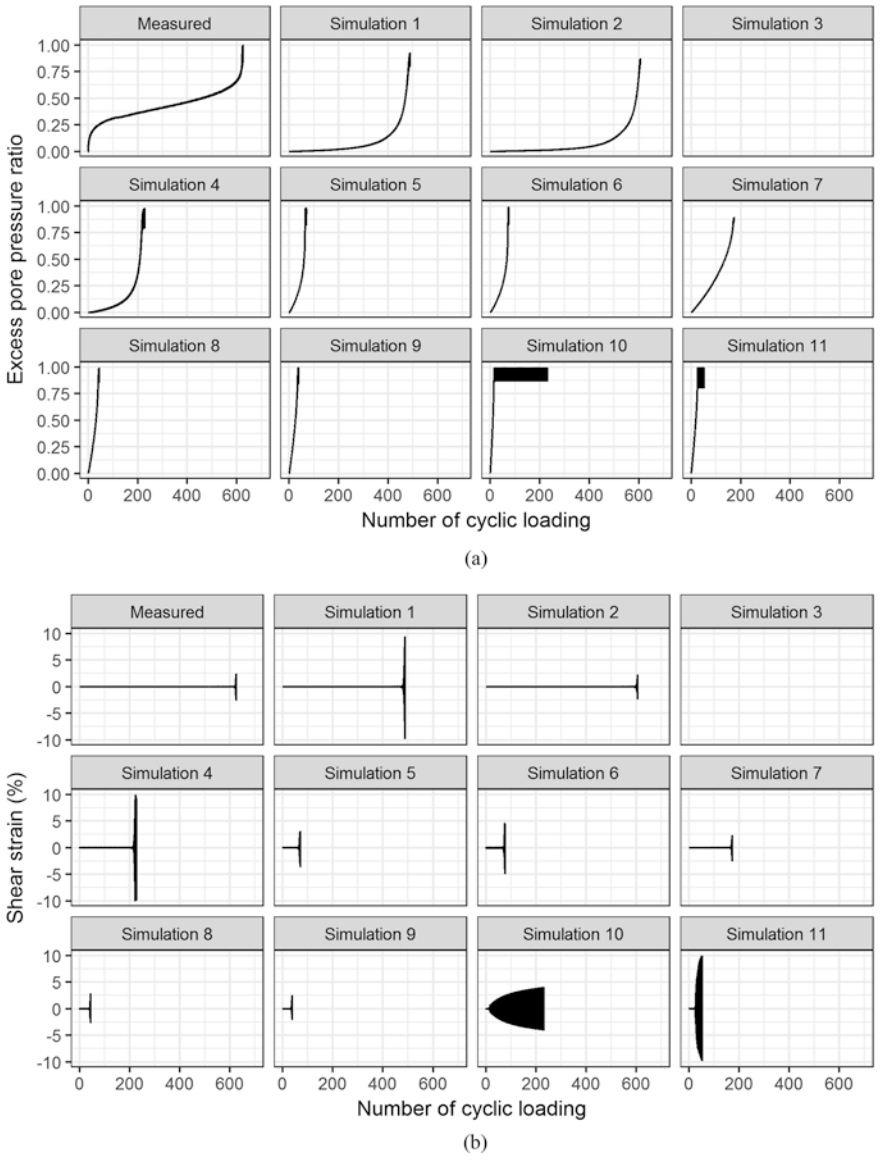

Fig. 2.9 Comparison of the numerical simulations of an undrained cyclic torsional shear test on Ottawa F-65 sand for Dr = 60%, CSR = 0.12. (**a**) Time history of excess pore pressure ratio, (**b**) Time history of shear strain, (**c**) Effective stress path, (**d**) Shear stress-shear strain relationship

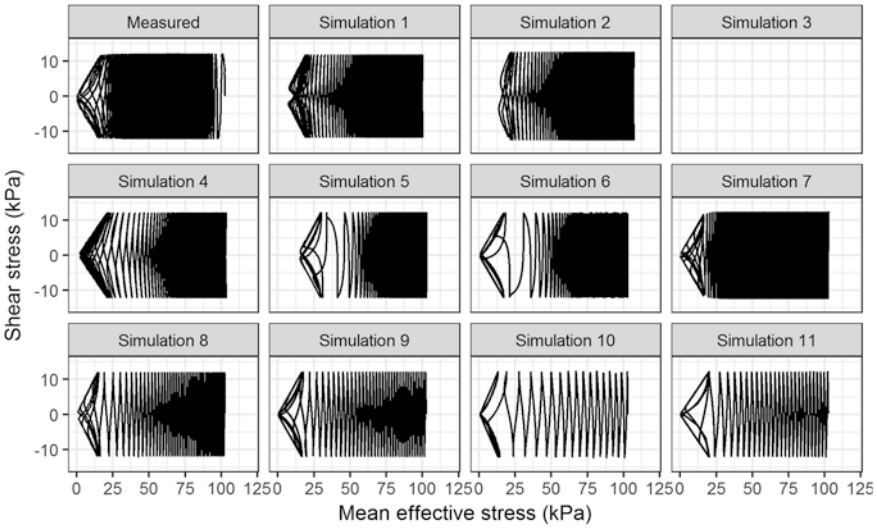

(c)

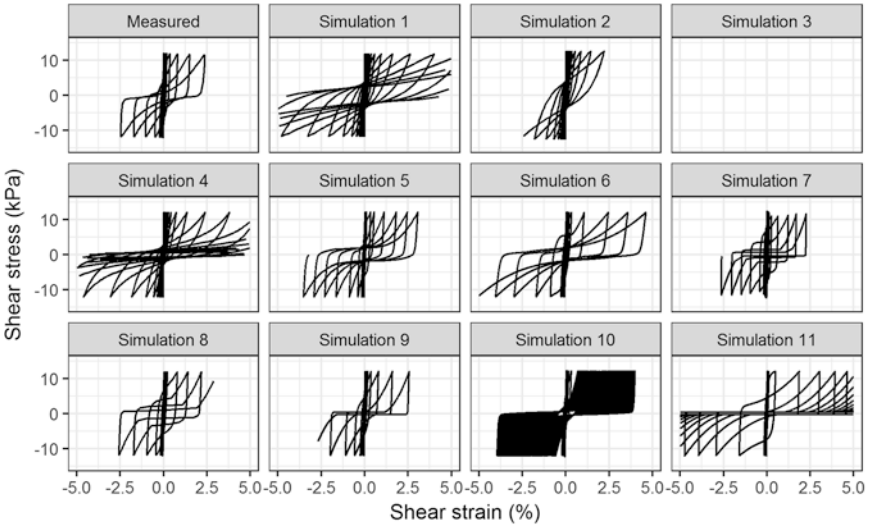

(d)

Fig. 2.9 (continued)

different. This is probably due to the difference in the values of the model parameters used.

5. Simulation 10: When the excess pore pressure ratio increases to 0.8–0.9, large shear strains are generated, which is common to other simulations. However, after that, the strain tends to extend relatively slowly; the strain development is almost linear.
6. Simulation 11: As in the other simulations, the shear strain begins to develop when the excess pore pressure ratio exceeds 0.8–0.9. However, the development is not linear and tends to converge gradually; the brittle behavior, in which the strain increases rapidly, is suppressed compared to the other simulations.

2.4 Liquefaction Resistance Curves

The simulated liquefaction resistance curves for γ_{DA} = 7.5% (i.e., the number of cycles required to reach a 7.5% double amplitude shear strain) are compared with the laboratory test results in Figs. 2.10a, b for Dr = 50% and 60%, respectively. The following trends are observed from the curves:

1. The majority of the constitutive models are capable of reasonably capturing the overall trends of the measured liquefaction resistance curves both for Dr = 50% and 60%; in particular, the liquefaction strength is accurately simulated for a cyclic stress ratio (CSR) of 0.149 and 0.174 for Dr = 50% and 60%, respectively.
2. Simulations 1–4: Since the constitutive model and the analysis platform are the same, the simulations show similar liquefaction resistance curves, although there are slight differences due to differences in the model parameters used. They can accurately simulate the experimental results even for low CSRs (i.e., a large number of cycles).
3. Simulations 5 and 6: Since the analysis platforms are different but the constitutive model is the same, the simulated liquefaction resistance curves are quite similar. The simulations are capable of reasonably simulating the experimental results, particularly in a relatively large CSR range.
4. Simulations 7 and 8: Although the constitutive model and the analysis platform are the same, the simulated liquefaction resistance curves look different; Simulation 8 shows steeper curves than the experimental curves, although both Simulations 7 and 8 can simulate the measured liquefaction strength for 20 cycles. The difference is probably due to the difference in the values of the model parameters used.
5. Simulation 10: The experimental curves are reasonably simulated over a wide range of CSRs, as in Simulations 1–4.
6. Simulations 9 and 11: The simulations show steeper curves than the experimental curves, although they can simulate the measured liquefaction strength for 10–20 cycles. It is unclear whether this is due to the characteristic of the constitutive models or the model parameters used.

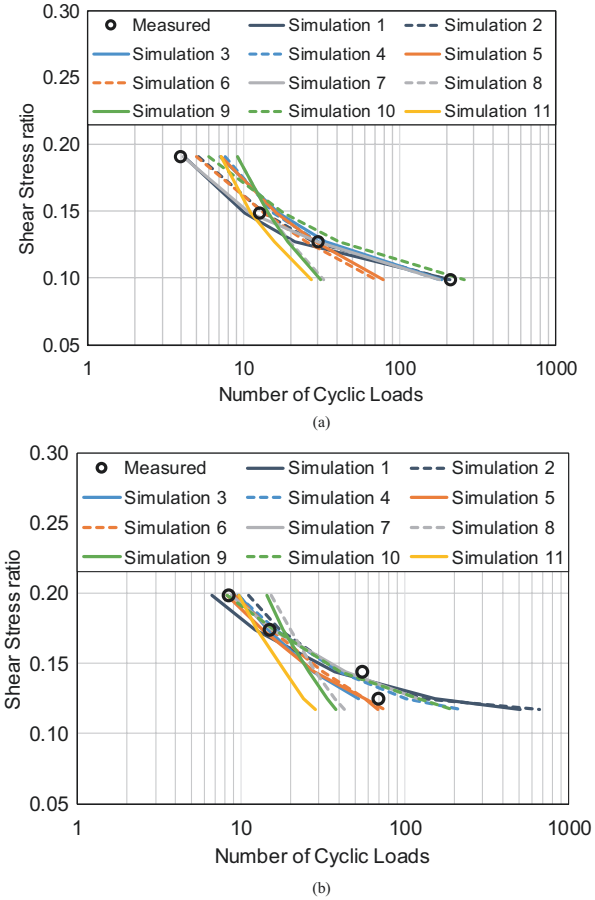

Fig. 2.10 Comparison of the simulated liquefaction strength curves by different numerical simulation teams with the experimental results reported by Ueda et al. (2018) and Vargas et al. (2020, 2023). (**a**) Dr = 50%, (**b**) Dr = 60%

2.5 Conclusions

This chapter presented a summary of the calibration exercises (i.e., element test simulations) submitted by nine numerical simulation teams that participated in the LEAP-ASIA-2019 prediction campaign. The objective of this element test simulation exercise was to assess the performance of the constitutive models used by the simulation teams for simulating the experimental results of a series of undrained stress-controlled cyclic torsional shear tests on Ottawa F-65 sand for two different relative densities (Dr = 50% and 60%). These simulations demonstrate that majority of the constitutive models are capable of reasonably capturing the measured liquefaction strength curves as well as the overall trends of the stress paths and

stress-strain responses both for Dr = 50% and 60%. However, it appeared to be still left for future work to evaluate the validity of constitutive models in consideration of the variations in the laboratory test and/or numerical simulation results.

Acknowledgments The experimental work and numerical simulations on LEAP-ASIA-2019 were supported by different funds depending mainly on the location of the work. The work by the Japan PIs (Tobita, Ichii, Okamura, Takemura, and Ueda) was supported by JSPS KAKENHI grant number JP17H00846.

References

Bastidas, A. M. P. (2016). *Ottawa F-65 sand characterization*. Ph.D. Dissertation, University of California, Davis.

Bastidas, A. M. P., Boulanger, R. W., Carey, T., & DeJong, J. (2017). Ottawa F-65 sand data from Ana Maria Parra Bastidas, https://datacenterhub.org/resources/ottawa_f_65

El Ghoraiby, M. A., & Manzari, M. (2018). LEAP-2018 - stress-strain response of Ottawa F65 sand in cyclic simple shear, DesignSafe-CI [publisher], Dataset. https://doi.org/10.17603/DS2HX3H

El Ghoraiby, M. A., Park, H., & Manzari, M. T. (2019). Physical and mechanical properties of Ottawa F65 sand. In *Model tests and numerical simulations of liquefaction and lateral spreading: LEAP-UCD-2017*. Springer.

Elbadawy, M. A., & Zhou, Y. G. (2023). Class-C simulations of LEAP-ASIA-2019 via OpenSees platform by using a pressure dependent multi yield-surface model. In *Model tests and numerical simulations of liquefaction and lateral spreading: LEAP-ASIA-2019*. Springer.

Fasano, G., Chiaradonna, A., & Bilotta, E. (2023). LEAP-ASIA-2019 centrifuge test simulation at UNINA. In *Model tests and numerical simulations of liquefaction and lateral spreading: LEAP-ASIA-2019*. Springer.

Hyodo, J., & Ichii, K. (2023). LEAP-ASIA-2019 type-B simulations through FLIP at Kyoto University. In *Model tests and numerical simulations of liquefaction and lateral spreading: LEAP-ASIA-2019*. Springer.

Qiu, Z., & Elgamal, A. (2023). LEAP-ASIA-2019 centrifuge test simulations of liquefiable sloping ground. In *Model tests and numerical simulations of liquefaction and lateral spreading: LEAP-ASIA-2019*. Springer.

Reyes, A., Barrero, A. R., & Taiebat, M. (2023). Type-C simulations of centrifuge tests from LEAP-ASIA-2019 using SANISAND-sf. In *Model tests and numerical simulations of liquefaction and lateral spreading: LEAP-ASIA-2019*. Springer.

Tanaka, Y., Sahare, A., Ueda, K., Yuyama, W., & Iai, S. (2023). LEAP-ASIA-2019 numerical simulations using a strain space multiple mechanism model for a liquefiable sloping ground. In *Model tests and numerical simulations of liquefaction and lateral spreading: LEAP-ASIA-2019*. Springer.

Ueda, K., Vargas, R. R., & Uemura, K. (2018). LEAP-Asia-2018: Stress-strain response of Ottawa sand in cyclic torsional shear tests, DesignSafe-CI [publisher], Dataset. https://doi.org/10.17603/DS2D40H

Vargas, R. R., Ueda, K., & Uemura, K. (2020). Influence of the relative density and K0 effects in the cyclic response of Ottawa F-65 sand - cyclic torsional hollow-cylinder shear tests for LEAP-ASIA-2019. *Soil Dynamics and Earthquake Engineering, 133*, 106111.

Vargas, R. R., Ueda, K., & Uemura, K. (2023). Dynamic torsional shear tests of Ottawa F-65 sand for LEAP-ASIA-2019. In *Model tests and numerical simulations of liquefaction and lateral spreading: LEAP-ASIA-2019*. Springer.

Vasko, A. (2015). *An investigation into the behavior of Ottawa sand through monotonic and cyclic shear tests*. Master's thesis, The George Washington University.

Vasko, A., El Ghoraiby, M. A., & Manzari, M. T. (2018). *Characterization of Ottawa sand*. DesignSafe. https://doi.org/10.17603/DS2TH7Q

Wang, R., Zhu, T., Zhou, C., & Zhang, J. M. (2023). LEAP-ASIA-2019 simulations at Tsinghua University. In *Model tests and numerical simulations of liquefaction and lateral spreading: LEAP-ASIA-2019*. Springer.

Chapter 3
LEAP-ASIA-2019 Simulation Exercise: Comparison of the Type-B and Type-C Numerical Simulations with Centrifuge Test Results

Kyohei Ueda, Yoshikazu Tanaka, Anurag Sahare, Ahmed Elgamal, Zhijian Qiu, Rui Wang, Tong Zhu, Chuang Zhou, Jian-Min Zhang, Andres Reyes Parra, Andres Barrero, Mahdi Taiebat, Waka Yuyama, Susumu Iai, Junichi Hyodo, Koji Ichii, Mohamed A. Elbadawy, Yan-Guo Zhou, Gianluca Fasano, Anna Chiaradonna, Emilio Bilotta, Pedro Arduino, Mourad Zeghal, Majid Manzari, and Tetsuo Tobita

Abstract This chapter presents a summary of Type-B and Type-C numerical simulations submitted by nine numerical simulation teams that participated in the LEAP-ASIA-2019 prediction campaign, with the results of a selected set of centrifuge model tests on the seismic behavior of a uniform-density, 20-m-long, and 5-degree sandy slope. Time histories of response accelerations, excess pore water pressures, and lateral displacements at the ground surface are compared to the experimental results. A majority of Type-B and Type-C numerical simulations were capable of simulating well the experimental trends observed in the centrifuge tests; in particular, Type-C simulations were found to capture the measured responses more accurately by adjusting the model parameters. Although it is quite challenging to perfectly capture all measured responses (e.g., accelerations, pore pressures, and displacements), the simulation exercises demonstrate that the numerical simulations can be further improved by accumulating high-quality experimental results as a database.

Keywords Liquefaction Experiments and Analysis Projects (LEAP-ASIA-2019) · Type-B and Type-C numerical simulations

K. Ueda (✉) · Y. Tanaka · A. Sahare
Disaster Prevention Research Institute, Kyoto University, Kyoto, Japan
e-mail: ueda.kyohei.2v@kyoto-u.ac.jp

A. Elgamal · Z. Qiu
Department of Structural Engineering, University of California San Diego, La Jolla, CA, USA

T. Tobita et al. (eds.), *Model Tests and Numerical Simulations of Liquefaction and Lateral Spreading II*, https://doi.org/10.1007/978-3-031-48821-4_3

3.1 Introduction

LEAP-ASIA-2019 project is a sequel to the LEAP-GWU-2015 project (Kutter et al., 2018; Manzari et al., 2018; Zeghal et al., 2018) and the LEAP-UCD-2017 project (Kutter et al., 2019; Manzari et al., 2019a, b) that investigated the repeatability and reproducibility of centrifuge tests, the sensitivity of the experimental results to variation of testing parameters and conditions, and the performance and validity of constitutive models and numerical modeling tools in predicting the observed response. The goals of LEAP-ASIA-2019 are to (1) validate the "generalized scaling law" for centrifuge modeling (Iai et al., 2005) on the seismic behavior of a liquefiable sloping ground and (2) fill the gaps of the LEAP-UCD-2017's data with the aim to identify trends in the experimental results (in terms of a combination of Dr and PGA) and to build an experimental database for numerical modelers.

The LEAP-ASIA-2019 project involved nine numerical simulation teams from different academic institutions and geotechnical companies from around the world; they participated in the modeling of some of the centrifuge model experiments

R. Wang · T. Zhu · C. Zhou · J.-M. Zhang
Department of Hydraulic Engineering, Tsinghua University, Beijing, China

A. R. Parra · A. Barrero · M. Taiebat
Department of Civil Engineering, University of British Columbia, Vancouver, BC, Canada

W. Yuyama · S. Iai
FLIP Consortium, Kyoto, Japan

J. Hyodo
Tokyo Electric Power Services, Tokyo, Japan

K. Ichii
Faculty of Societal Safety Science, Kansai University, Osaka, Japan

M. A. Elbadawy · Y.-G. Zhou
Department of Civil Engineering, Zhejiang University, Hangzhou, China

G. Fasano · A. Chiaradonna · E. Bilotta
Department of Civil, Architectural and Environmental Engineering, University of Naples Federico II, Naples, Italy

P. Arduino
Department of Civil and Environmental Engineering, University of Washington, Seattle, WA, USA

M. Zeghal
Department of Civil and Environmental Engineering, Rensselaer Polytechnic Institute, Troy, NY, USA

M. Manzari
Department of Civil and Environmental Engineering, George Washington University, Washington, DC, USA

T. Tobita
Department of Civil, Environmental and Applied Systems Engineering, Kansai University, Osaka, Japan

performed at several research institutions. The simulation exercise consisted of the calibration of constitutive model parameters, Type-B predictions, or Type-C simulations. In the first phase (i.e., model calibration), the numerical simulation teams were provided with a series of hollow cylinder torsional shear tests and direct simple shear tests to calibrate their constitutive models. Ueda et al. (2023) present an overview of the results of the first phase. In the second phase of the simulation exercise, the numerical simulation teams performed Type-C or Type-B simulations using their constitutive models, which were calibrated in the first phase, with or without iterative adjustment of the model parameters. This chapter presents a summary of key aspects of the second phase and their comparisons with the experimental data obtained from centrifuge model tests on the seismic behavior of a uniform-density, 20-m-long, and 5-degree sandy slope (Tobita et al., 2022, 2023).

3.2 LEAP-2019 Centrifuge Experiments

As described in the Introduction, one of the objectives of the LEAP-ASIA-2019 project is to fill the gaps in LEAP-UCD-2017's experimental data. To this end, the LEAP-ASIA-2019 centrifuge experiments were designed to study the lateral spreading of a uniform-density, 20-m-long, 4-m-deep at center, and 5-degree sloping liquefiable deposit, similar to the LEAP-GWU-2015 and LEAP-UCD-2017 projects (Kutter et al., 2018, 2019). As illustrated in Figs. 3.1 and 3.2, the sloping ground was created with Ottawa F-65 sand in a rigid container. Three arrays of accelerometers and pore pressure transducers are placed in the central section and at 3.5 m away from the left- and right-side walls. In the vertical direction, the sensors were placed 1.0 m apart. Tables 3.1 and 3.2 show the specified locations of the accelerometers and pore pressure transducers, respectively. Also, 3D printed surface markers were placed on the ground surface to measure the surface horizontal

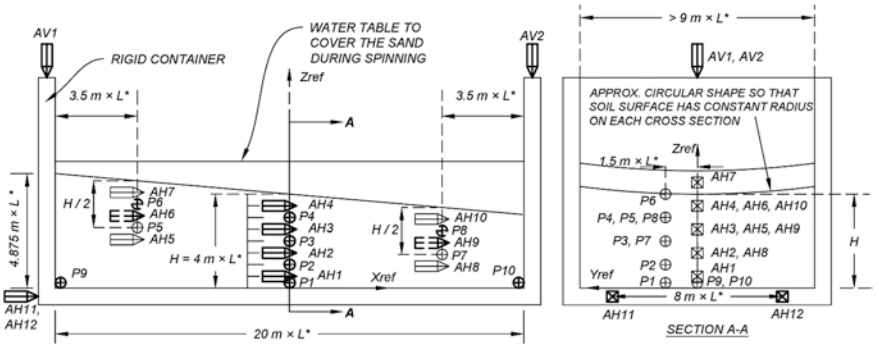

Fig. 3.1 Baseline schematic for LEAP-ASIA-2019 experiment for shaking parallel to the axis of the centrifuge (e.g., RPI, ZJU, NCU). L^* in the figure corresponds to 1/μη

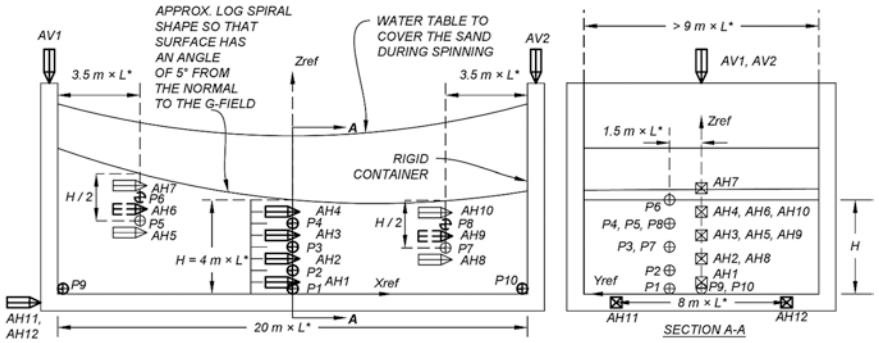

Fig. 3.2 Baseline schematic for LEAP-ASIA-2019 experiment for shaking in the circumferential direction of the centrifuge (e.g., UCD, KyU). L^* in the figure corresponds to $1/\mu\eta$

Table 3.1 Positions of the accelerometers in LEAP-ASIA-2019 experiments

Sensor	AH1	AH2	AH3	AH4	AH5	AH6	AH7	AH8	AH9	AH10
x-pos. (m)	0.0	0.0	0.0	0.0	−6.5	−6.5	−6.5	6.5	6.5	6.5
Depth (m)	3.5	2.5	1.5	0.5	2.5	1.5	0.5	2.5	1.5	0.5

Table 3.2 Positions of the pore water pressure sensors in LEAP-ASIA-2019 experiments

Sensor	P1	P2	P3	P4	P5	P6	P7	P8
x-pos. (m)	0.0	0.0	0.0	0.0	−6.5	−6.5	6.5	6.5
Depth (m)	4.0	3.0	2.0	1.0	2.0	1.0	2.0	1.0

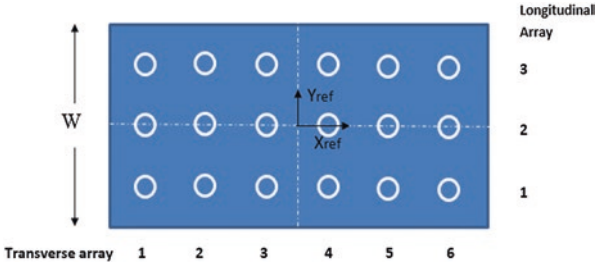

Fig. 3.3 Surface marker locations for displacement measurement (top view)

displacements under seismic loading. Figure 3.3 illustrates the surface marker locations for displacement measurement (top view).

As part of the LEAP-ASIA-2019 project, 10 institutes performed 24 centrifuge model tests in total (Tobita et al., 2022, 2023; Madabhushi et al., 2023; Stone et al., 2023; Okamura & Sjafruddin, 2023; Escoffier et al., 2023; Manandhar et al., 2023; Vargas et al., 2023; Huang & Hung, 2023; Korre et al., 2023; Ma et al., 2023). Since another aim of the LEAP-ASIA-2019 project is to validate the "generalized scaling law" for centrifuge modeling (Iai et al., 2005) as noted in Introduction, 11 model tests applied the conventional centrifuge scaling law (hereafter called "Model A"),

Table 3.3 Summary of centrifuge experiments, Model A in LEAP-ASIA-2019

Test case	Density (kg/m^3)	Dr (%)	Virtual 1G, μ	Centrif uge, η	PGAeff (g)	Avg. disp. (mm)	Shaking direction
IFSTTAR_A_A1_1	1645	62	1	50	0.348	550.00	Axial
KAIST_A_A1_1	1716.55	87	1	40	0.287	33.93	Axial
KyU_A_A1_1	1677	73	1	44.4	0.248	71.04	Tangential
KyU_A_A2_1	1628	56	1	44.4	0.118	11.10	Tangential
NCU_A_A1_1	1643	61	1	26	0.144	181.51	Axial
RPI_A_A1_1	1651	64	1	23	0.143	99.56	Axial
UCD_A_A1_1	1713.3	86	1	43.75	0.178	30.56	Tangential
UCD_A_A2_1	1658.1	67	1	43.75	0.134	77.50	Tangential
ZJU_A_A1_1	1624.6	54	1	30	0.272	390.00	Axial

Table 3.4 Summary of centrifuge experiments, Model B in LEAP-ASIA-2019

Test case	Density (kg/m^3)	Dr (%)	Virtual 1G, μ	Centrif uge, η	PGAeff (g)	Avg. disp. (mm)	Shaking direction
CU_A_B1_1	1606	47	0.5	80	-		Tangential
Ehime_A_B1_1	1650.8	64	2	20	0.158	56.57	Axial
IFSTTAR_A_B1_1	1645	62	2	25	0.405	777.82	Axial
KAIST_A_B1_1	1720.6	88	1.5	26.7	0.317	30.58	Axial
KyU_A_B1_1	1673	72	2	22.2	0.252	153.84	Tangential
KyU_A_B1_2	1669	71	4	11.1	0.248	115.44	Tangential
KyU_A_B2_1	1633	58	2	22.2	0.126	34.54	Tangential
NCU_A_B1_1	1626	55	2	13	0.131	87.18	Axial
RPI_A_B1_1	1644	62	0.5	46	0.151	303.27	Axial
UCD_A_B1_1	1711.7	85	2	21.9	0.140	-2.23	Tangential
ZJU_A_B1_1	1632.7	57	2	15	0.271	678.82	Axial

while 13 model tests did the "generalized scaling law" (hereafter called "Model B"). Tables 3.3 and 3.4 show a summary of the centrifuge experiments "Model A" and "Model B," respectively, selected for the LEAP-ASIA-2019 Type-B or Type-C simulations. The table lists the main characteristics of each experiment: the reported achieved soil density, relative density, combinations of the virtual 1G scaling factor μ and centrifuge scaling factor η, input acceleration levels (i.e., PGA_{eff} (Kutter et al., 2018, 2019)), and observed horizontal displacements (average value) at the ground surface after shaking.

3.3 Type-B/Type-C Numerical Simulations

The second phase of the simulation exercise consisted of Type-B or Type-C numerical simulations of centrifuge model tests that were conducted as part of the LEAP-ASIA-2019 centrifuge modeling campaign. Table 3.5 shows the numerical simulation teams who participated in the Type-B or Type-C simulation exercises and submitted the report on their simulation results. The constitutive model and the

Table 3.5 Numerical simulation teams

No.	Numerical simulation team	Simulation type	Constitutive model	Analysis platform
1	Kyoto university (two different predictors)	Type-B+[a]	Cocktail glass model	FLIP ROSE
2				
3	FLIP consortium	Type-B+[a]	Cocktail glass model	FLIP ROSE
4	University of Naples Federico II	Type-B	PM4Sand model	PLAXIS
5	University of Washington	Type-C	PM4Sand model	OpenSees
6	University of California, san Diego	Type-C	PDMY02 model	OpenSees
7	Zhejiang university	Type-C	PDMY02 model	OpenSees
8	University of British Columbia	Type-B+[a]	SANISAND model	FLAC3D
9	Tsinghua University	Type-B	CycLiqCP model	OpenSees

[a]The parameters for dynamic deformation characteristics and dilatancy remain the same as those determined from the element simulations for the laboratory tests, but only the hydraulic conductivity was adjusted

analysis platform used by each numerical simulation team are also listed in the table as well as the simulation type (i.e., Type-B or Type-C). It should be noted that Simulations 1–3 and Simulation 8 can be classified as between Type-B and Type-C simulations (but close to Type-B); this is because the model parameters for dynamic deformation characteristics and dilatancy remain the same as those determined from the element simulations for the laboratory tests, but only the hydraulic conductivity was adjusted. Mode-detailed information of each constitutive model and the numerical simulation techniques used by each simulation team are provided in separate papers (Tanaka et al., 2023; Hyodo & Ichii, 2023; Fasano et al., 2023; Qiu & Elgamal, 2023; Elbadawy & Zhou, 2023; Reyes et al., 2023; Wang et al., 2023).

The main steps of the second phase were as follows:

1. Results of three sets (KyU_A_A2_1, RPI_A_A1_1, and UCD_A_A2_1 in Table 3.3) of centrifuge tests, known as Model A tests in LEAP-ASIA-2019, were provided to the numerical simulation teams. Some of the tests were performed as part of the LEAP-UCD-2017 project. The numerical simulation teams were able to refer to detailed information of the experimental conditions such as the achieved base excitation and the centrifuge specimen (e.g., the density of the prepared specimen, as-built geometry, location of the sensors). For the Type-C simulations, the measured pore water pressures, accelerations (the sensor positions are shown in Tables 3.1 and 3.2), and displacements (the surface marker locations are shown in Fig. 3.3) could also be used to fine-tune the parameters of their constitutive models and the key parameters of their numerical simulation platform (damping ratio, permeability, etc.).
2. The achieved base excitations, the density of the soil specimen, and the locations of the sensors in two sets (KyU_A_B2_1 and RPI_A_B1_1 in Table 3.4) of centrifuge tests conducted as Model B tests for LEAP-ASIA-2019 were provided (including the complete set of the experimental results) to the numerical model-

ing teams. They were asked to simulate the results of these tests in terms of time histories of excess pore pressure, accelerations, and lateral displacements at selected locations. The Model B tests had the same prototype and model sizes as the corresponding Model A tests, but the centrifugal acceleration (η) was scaled in accordance with the generalized scaling law (Iai et al., 2005). Since the centrifugal accelerations in the Model B tests at a few facilities were much lower than that in the Model A tests, the model parameters might have needed to be fine-tuned to take into account the low confining stress effect on liquefaction strength. Such issues (revision of the parameters and their effects on liquefaction strength curves) should have been clearly documented in the reports submitted by the numerical simulation teams.

3. (Optional) If time allowed, the numerical simulation teams were welcome to perform Type-C simulations for the other centrifuge experiments in Tables 3.3 and 3.4 and submit the simulation results. Test cases highlighted in green were not mandatory but highly recommended.

The timeline of the second phase of the numerical simulations was as follows:

1. All the necessary data regarding Model A and Model B tests were provided to the numerical modelers on January 18, 2019.
2. The numerical simulation teams were requested to submit the results of their simulations for the required test cases (highlighted in yellow in Tables 3.3 and 3.4) by February 8, 2019.

3.4 Summary of Type-B/Type-C Simulation Results for Models A and B

As shown in Table 3.5, six simulation teams submitted the results (i.e., time histories of predicted accelerations, excess pore water pressures, and displacements at selected locations) of the Type-B numerical simulations, including the Type-B+ simulations with the adjustment of the hydraulic conductivity, for the selected LEAP-ASIA-2019 centrifuge tests. Also, three simulation teams submitted the results of the Type-C numerical simulations. Due to space limitation, only a subset of these data for mandatory test cases highlighted in yellow in Tables 3.3 and 3.4 is presented herein. In the following, selected time histories of accelerations, excess pore pressures, and lateral displacements are compared to provide representative samples of the performance of each simulation in comparison with the experimental data.

Figures 3.4, 3.5, 3.6, 3.7, 3.8, 3.9, 3.10, 3.11 and 3.12 illustrate the comparison of the numerical simulation results with the experiments for the three sets of Model A tests in Table 3.3 (i.e., KyU_A_A2_1, RPI_A_A1_1, and UCD_A_A2_1). For KyU_A_A2_1, the following observations are noted from a comparison in Figs. 3.4, 3.5 and 3.6:

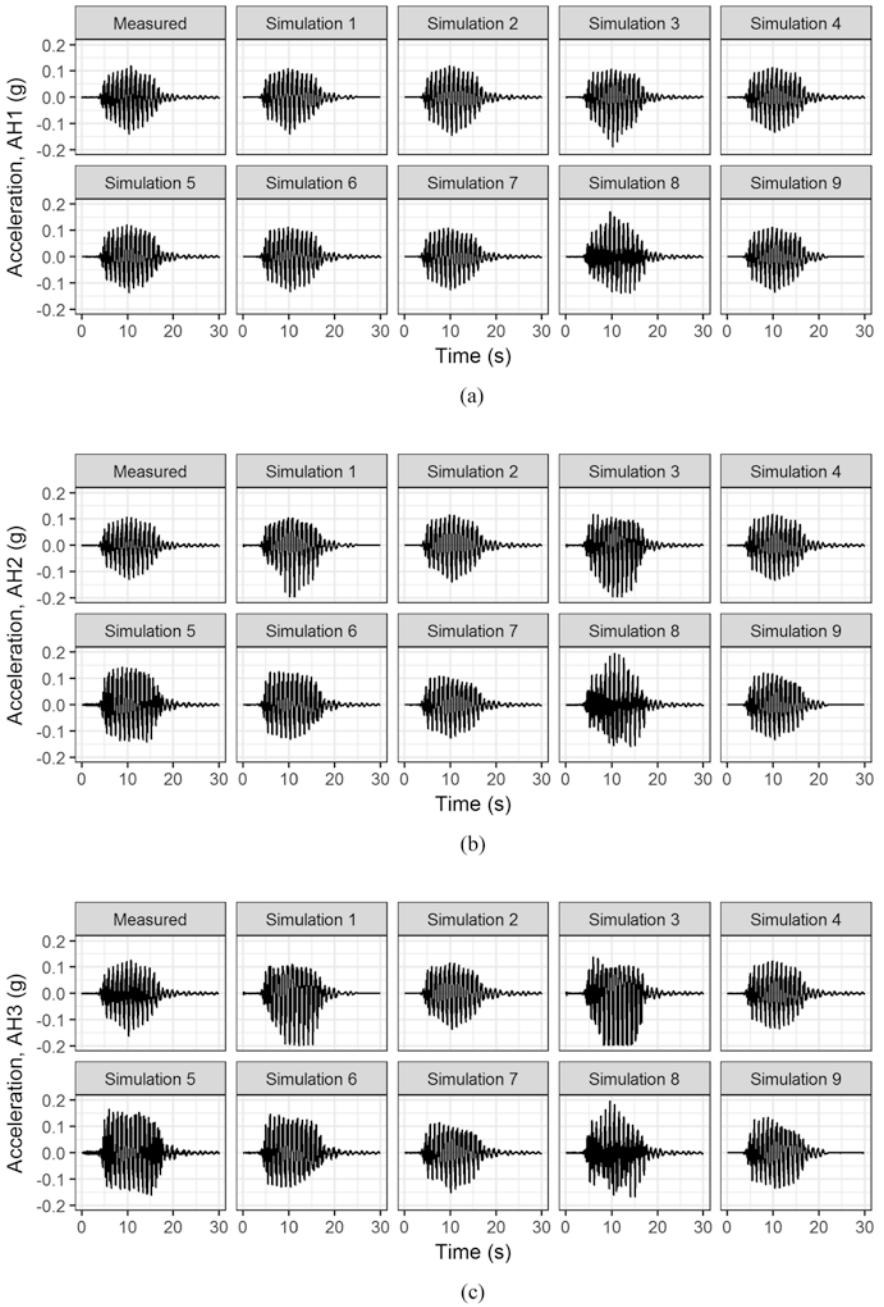

Fig. 3.4 Comparison of the measured and computed acceleration time histories for KyU_A_A2_1 test. (**a**) AH1, (**b**) AH2, (**c**) AH3, (**d**) AH4, (**e**) AH6, (**f**) AH9

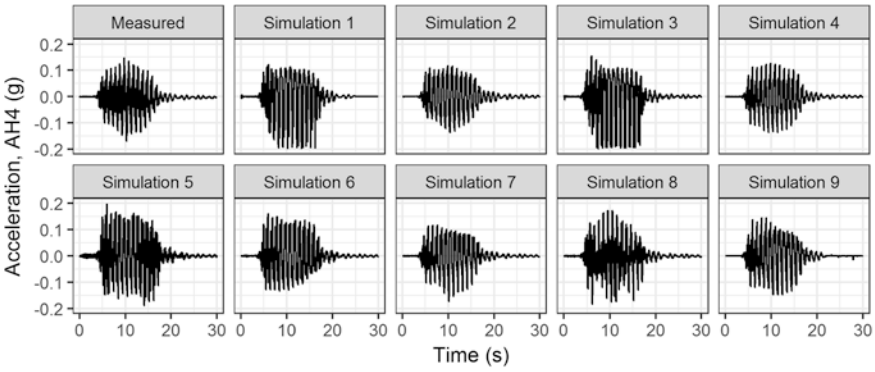

(d)

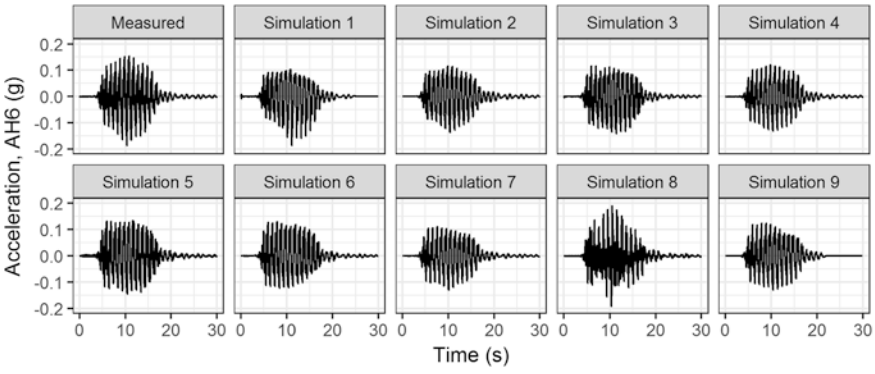

(e)

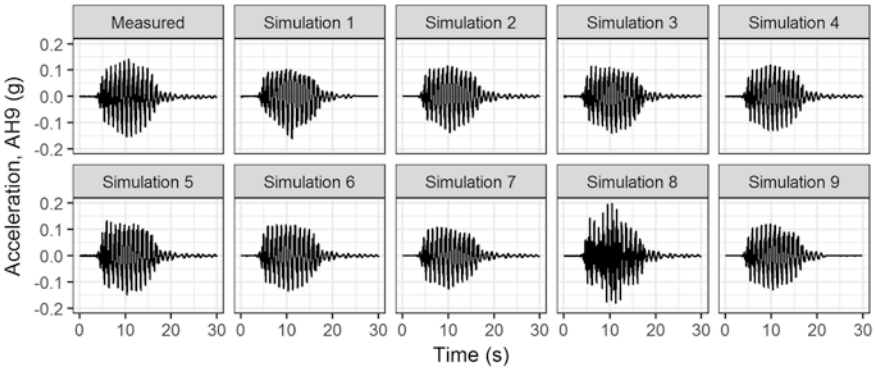

(f)

Fig. 3.4 (continued)

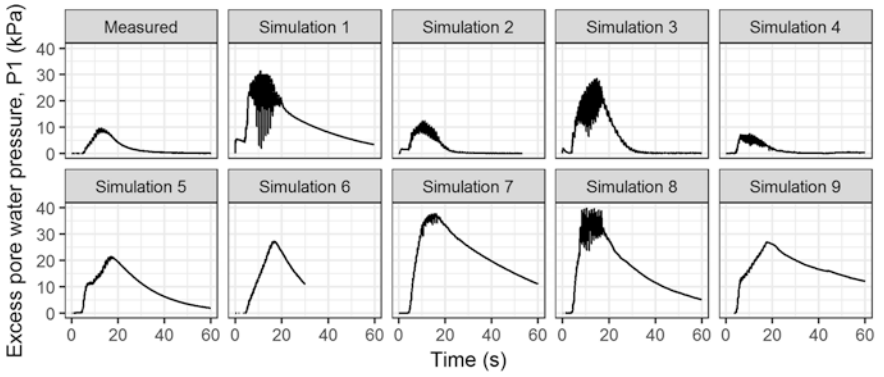

(a)

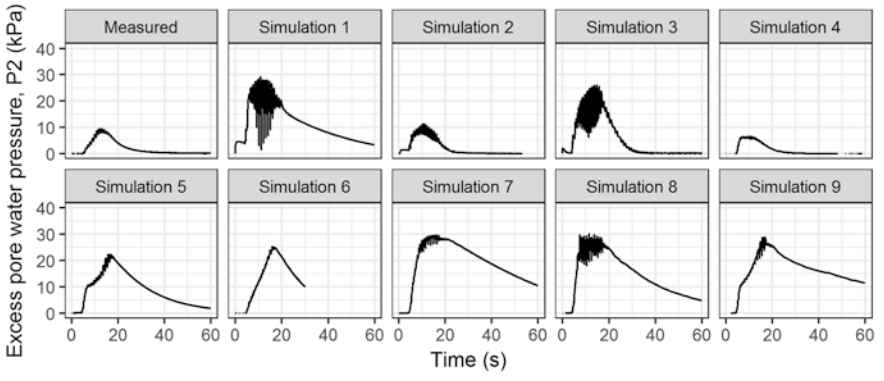

(b)

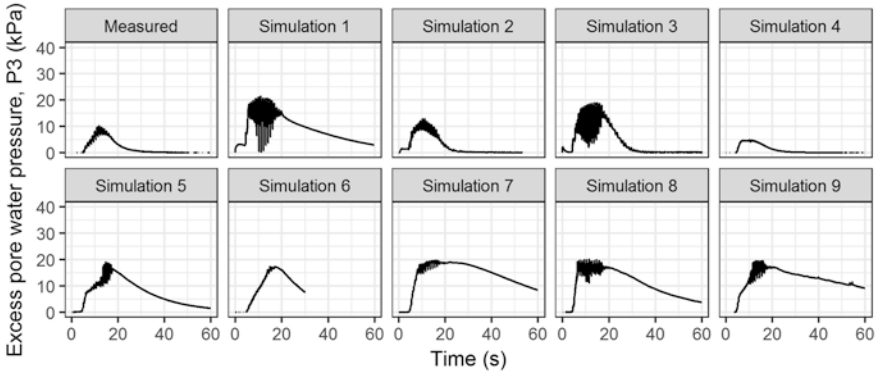

(c)

Fig. 3.5 Comparison of the measured and computed time histories of excess pore water pressures for KyU_A_A2_1 test. (**a**) P1, (**b**) P2, (**c**) P3, (**d**) P4, (**e**) P6, (**f**) P8

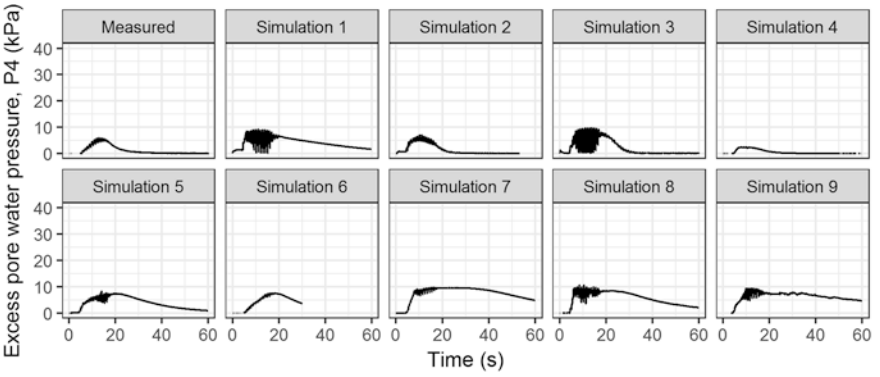

(d)

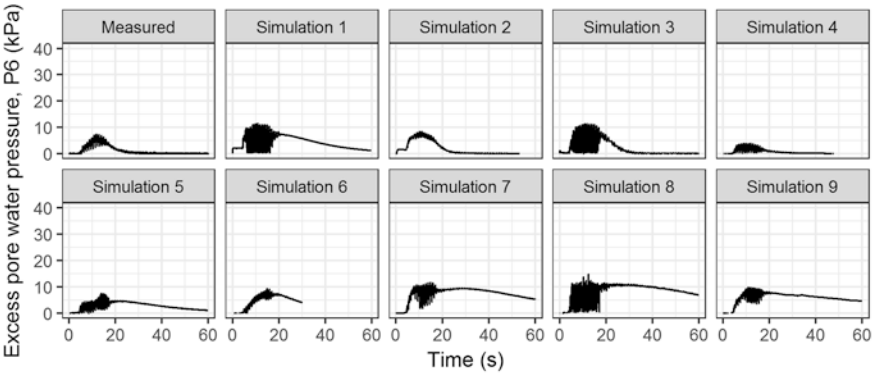

(e)

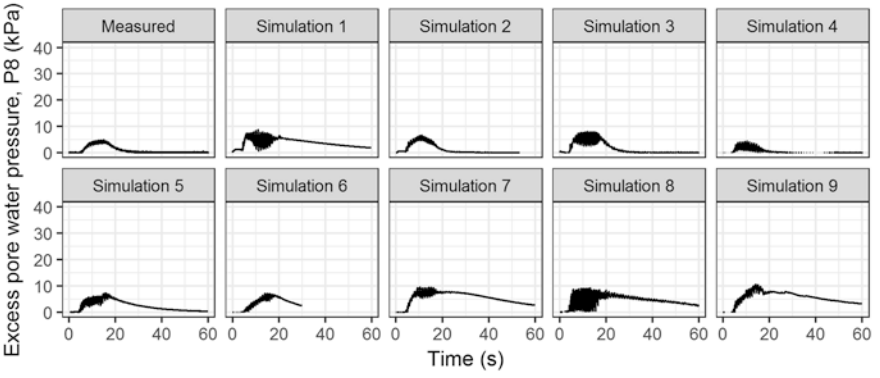

(f)

Fig. 3.5 (continued)

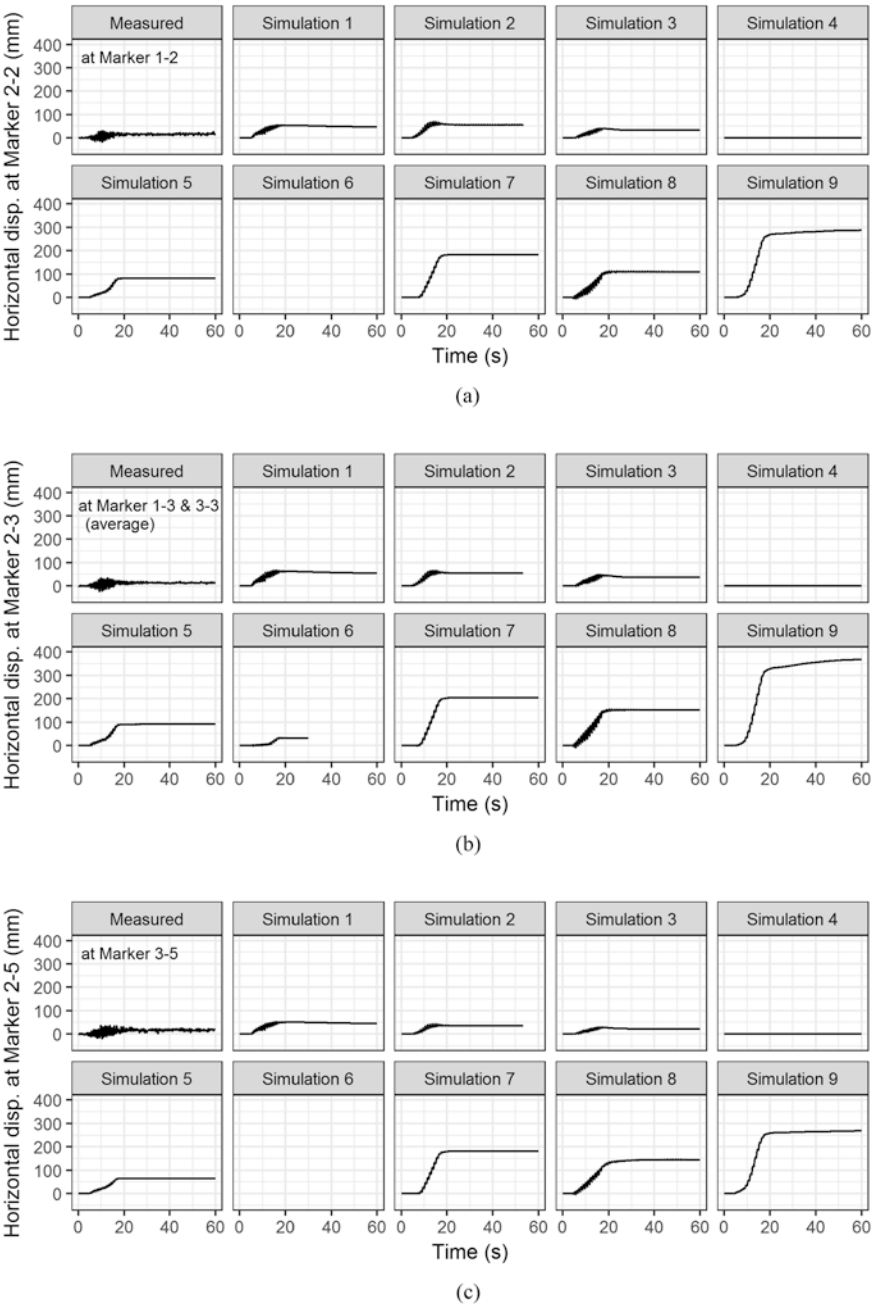

Fig. 3.6 Comparison of the measured and computed time histories of ground surface lateral displacements for KyU_A_A2_1 test. (**a**) Marker 2–2, (**b**) Marker 2–3, (**c**) Marker 2–5

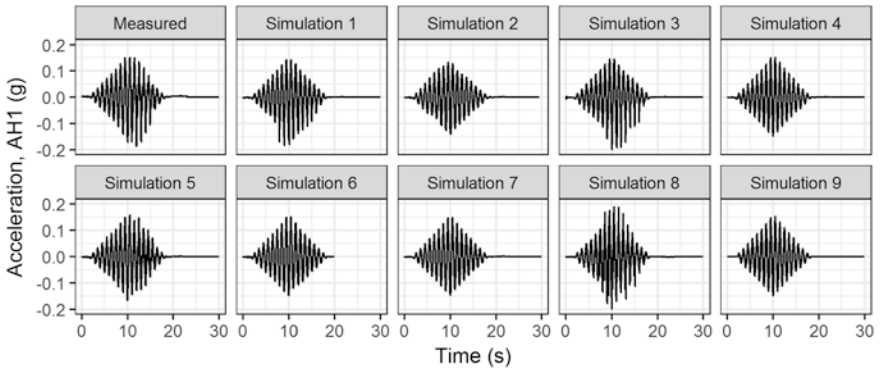

(a)

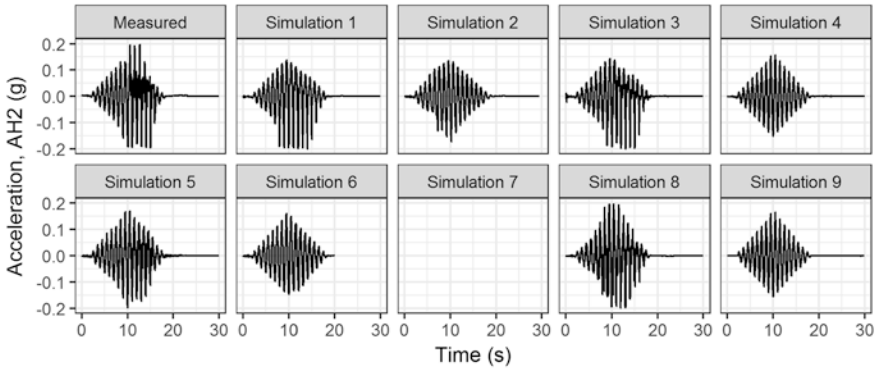

(b)

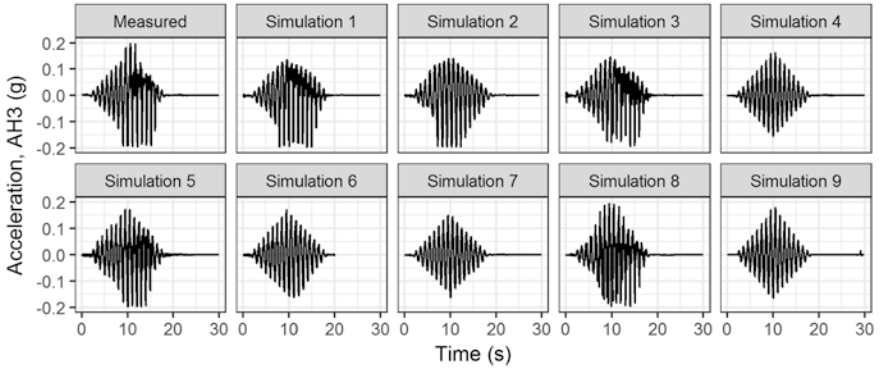

(c)

Fig. 3.7 Comparison of the measured and computed acceleration time histories for RPI_A_A1_1 test. (**a**) AH1, (**b**) AH2, (**c**) AH3, (**d**) AH4, (**e**) AH6, (**f**) AH10

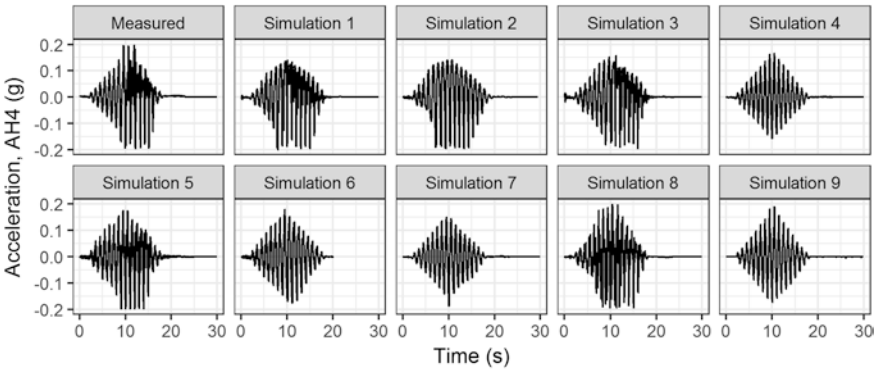

(d)

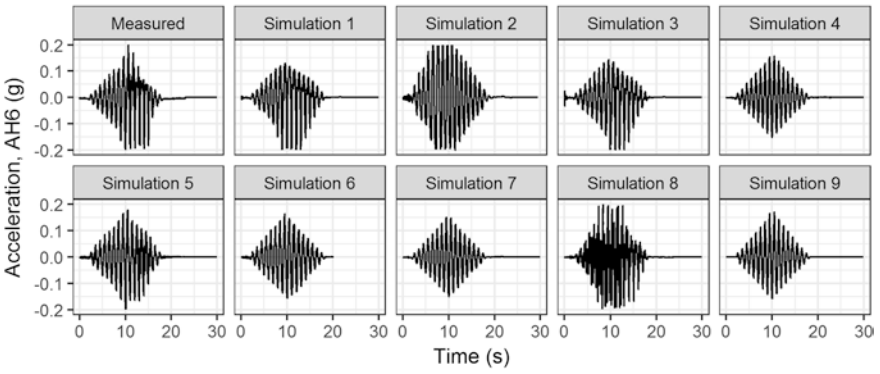

(e)

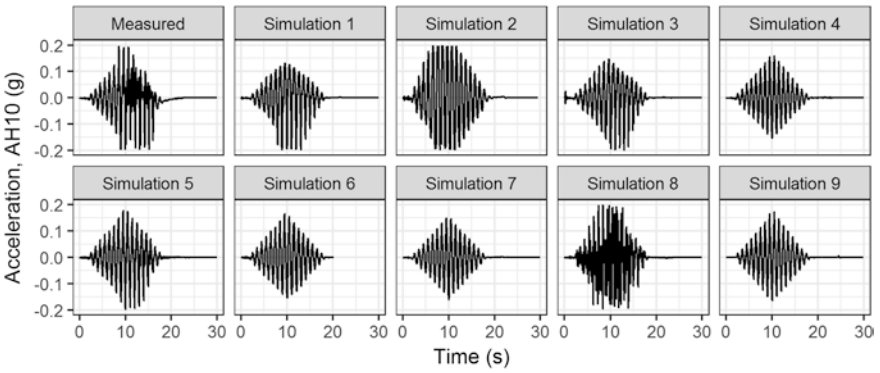

(f)

Fig. 3.7 (continued)

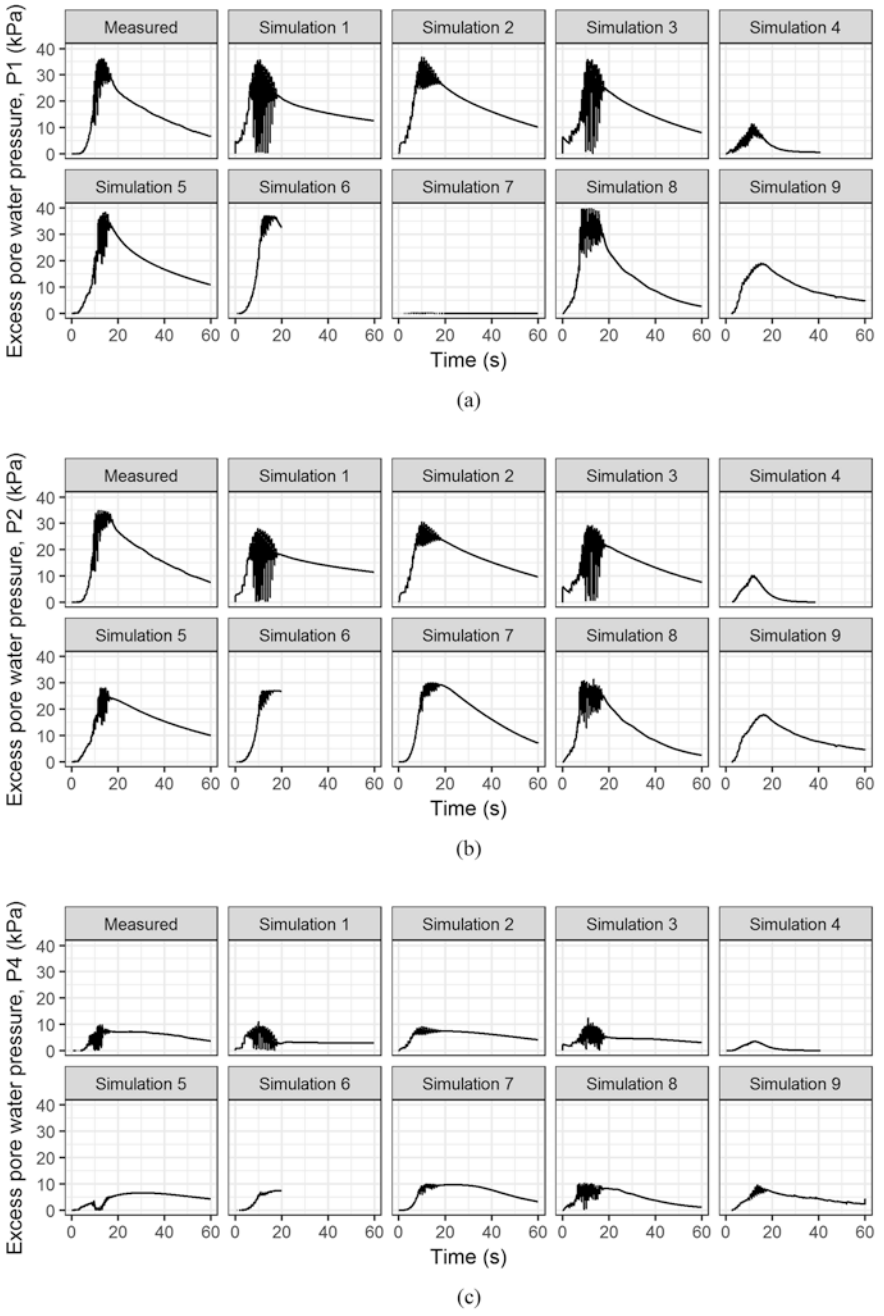

Fig. 3.8 Comparison of the measured and computed time histories of excess pore water pressures for RPI_A_A1_1 test. (**a**) P1, (**b**) P2, (**c**) P4, (**d**) P6, (**e**) P7, (**f**) P8

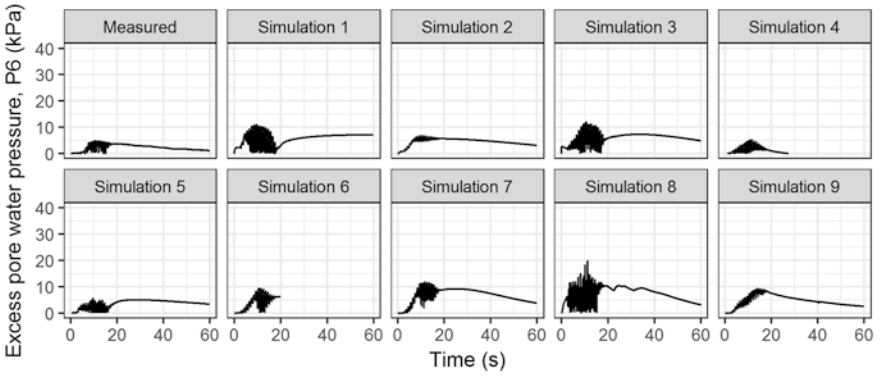

(d)

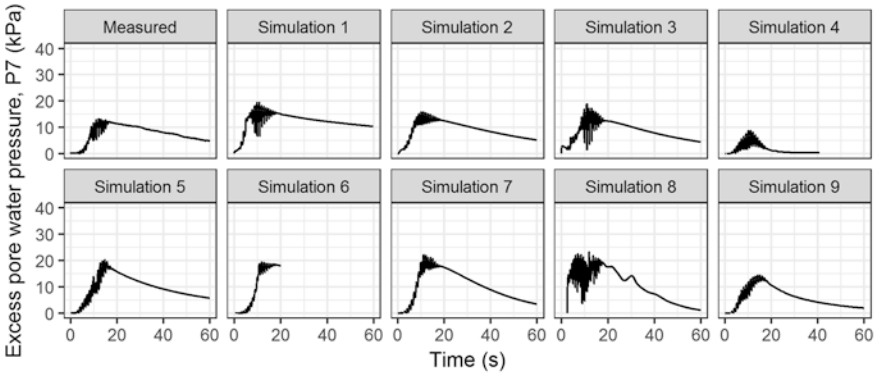

(e)

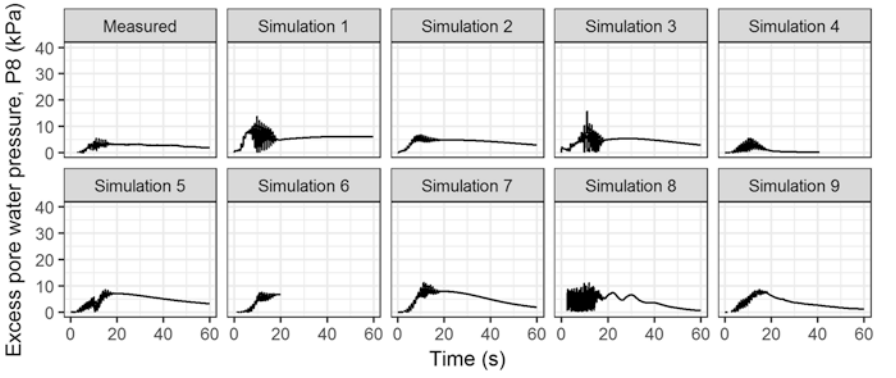

(f)

Fig. 3.8 (continued)

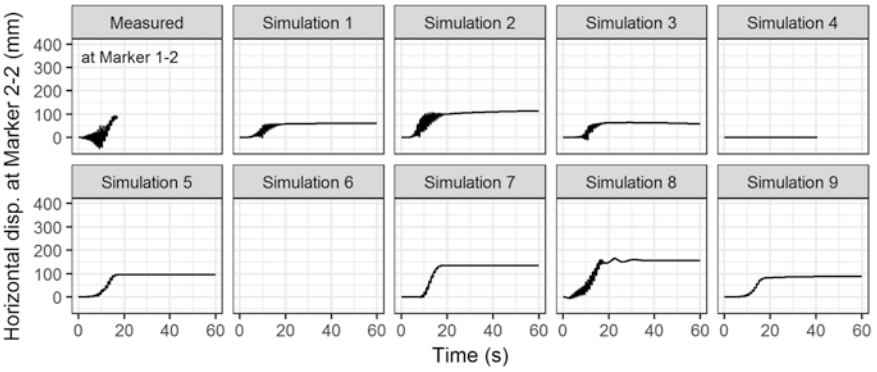

(a)

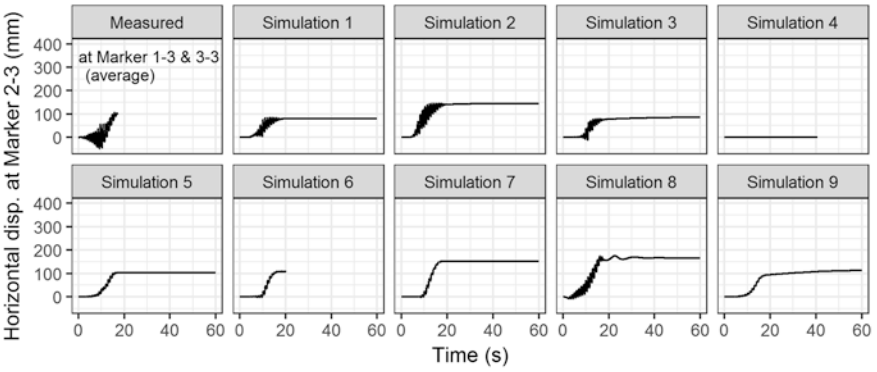

(b)

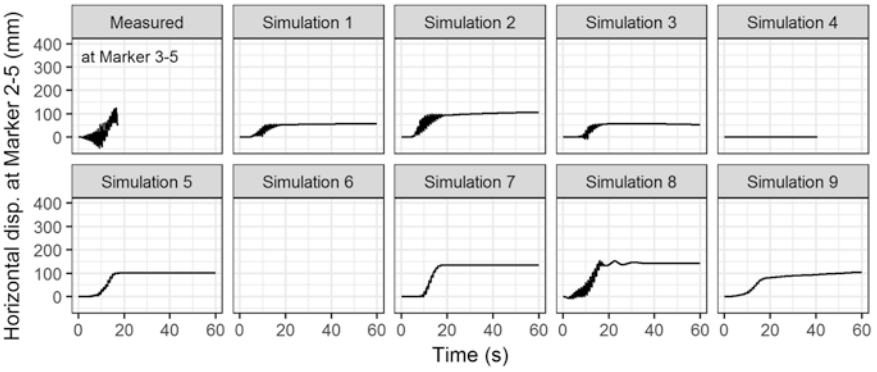

(c)

Fig. 3.9 Comparison of the measured and computed time histories of ground surface lateral displacements for RPI_A_A1_1 test. (**a**) Marker 2–2, (**b**) Marker 2–3, (**c**) Marker 2–5

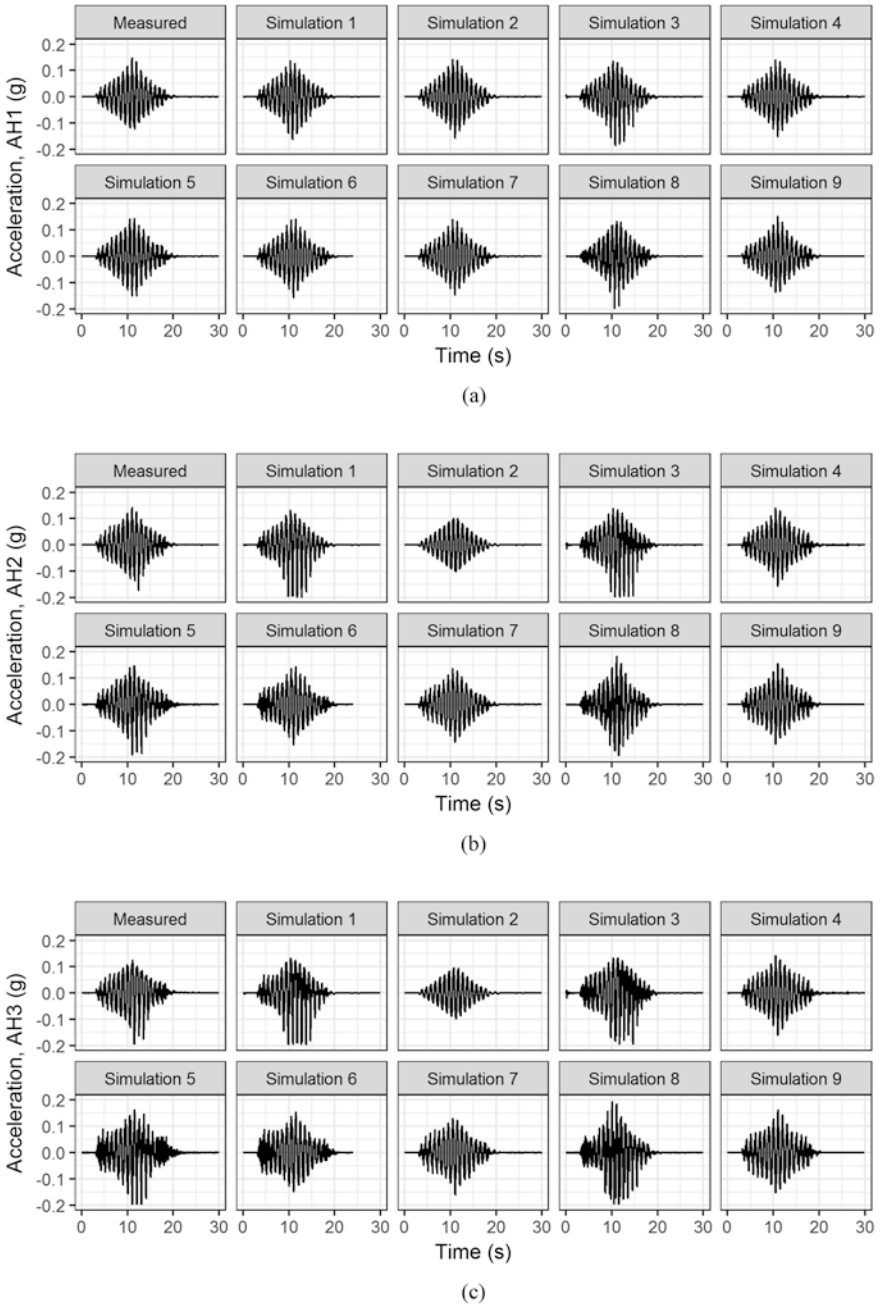

Fig. 3.10 Comparison of the measured and computed acceleration time histories for UCD_A_A2_1 test. (**a**) AH1, (**b**) AH2, (**c**) AH3, (**d**) AH4, (**e**) AH6, (**f**) AH9

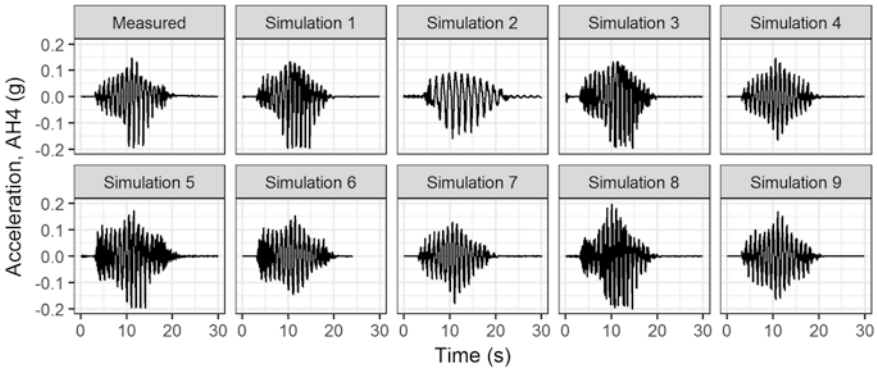

(d)

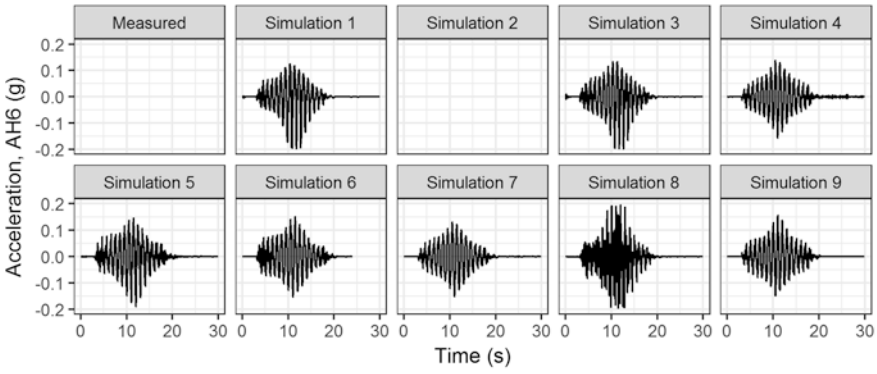

(e)

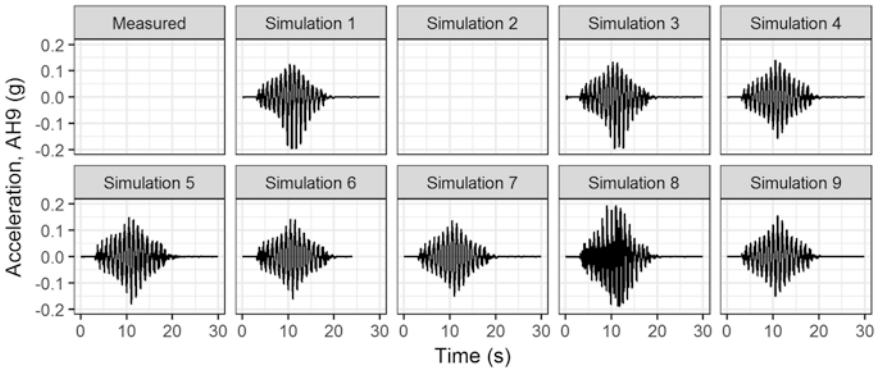

(f)

Fig. 3.10 (continued)

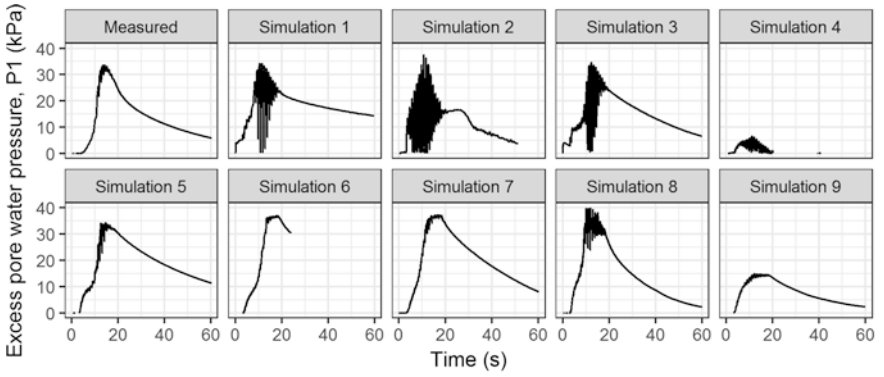

(a)

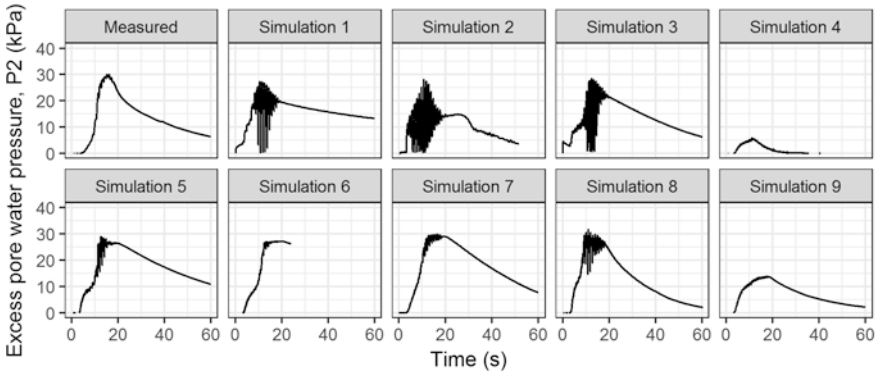

(b)

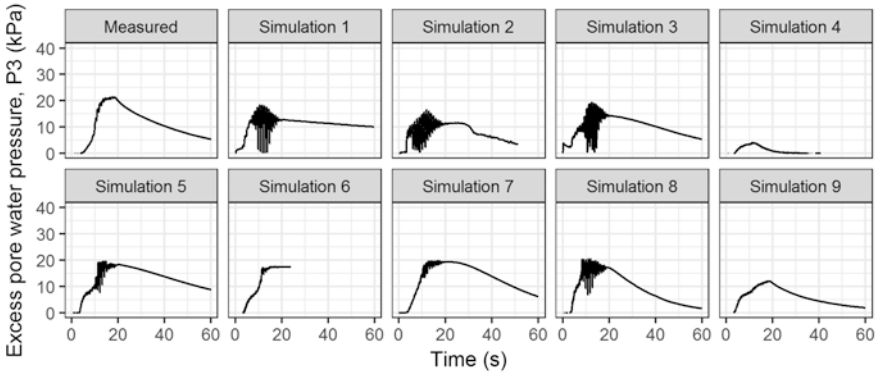

(c)

Fig. 3.11 Comparison of the measured and computed time histories of excess pore water pressures for UCD_A_A2_1 test. (**a**) P1, (**b**) P2, (**c**) P3, (**d**) P4, (**e**) P7, (**f**) P8

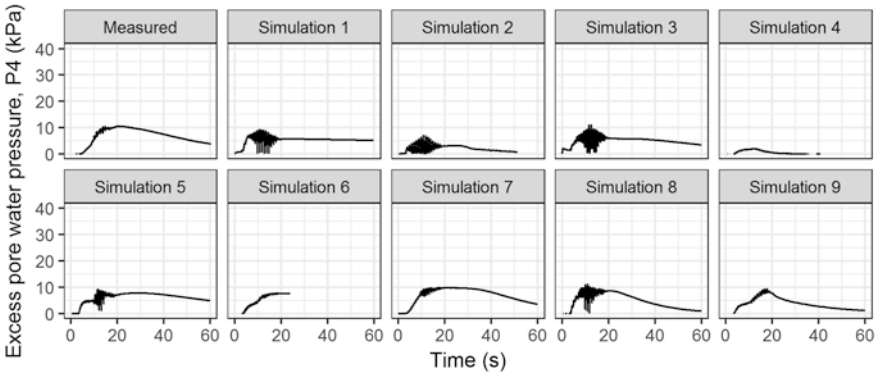

(d)

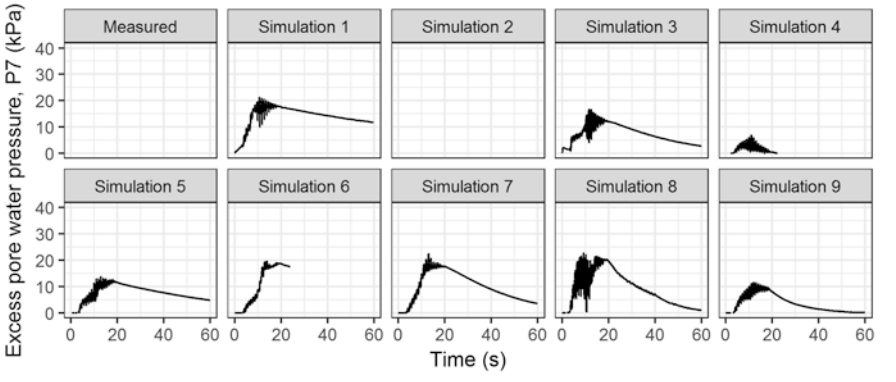

(e)

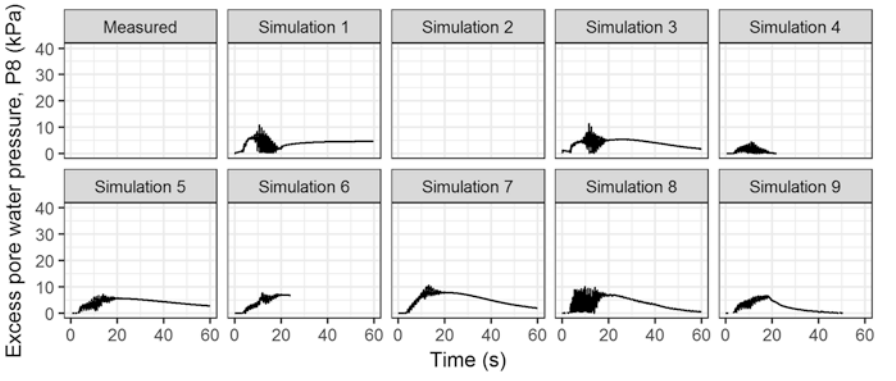

(f)

Fig. 3.11 (continued)

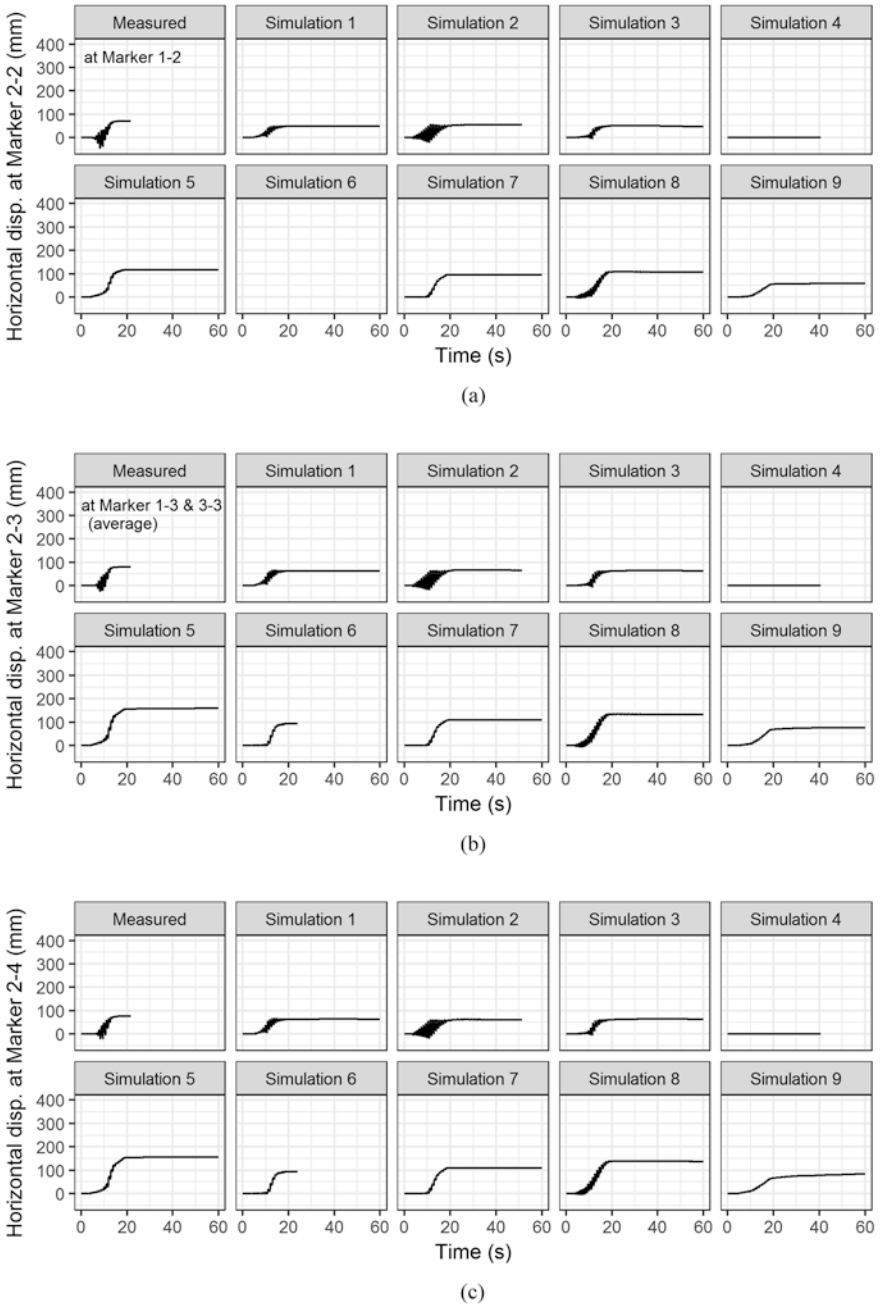

Fig. 3.12 Comparison of the measured and computed time histories of ground surface lateral displacements for UCD_A_A2_1 test. (**a**) Marker 2–2, (**b**) Marker 2–3, (**c**) Marker 2–4

- The acceleration responses at deep sensor locations (e.g., AH1) do not differ significantly among simulations. However, the amplitude and waveform shape differ to some extent among simulations near the ground surface (e.g., AH4), where soil nonlinearity associated with the excess pore pressure increase may be strong.
- In addition to the peak value of excess pore pressure, the experimental dynamic amplitudes during shaking and dissipation processes after shaking are challenging to fully capture at some sensor locations (e.g., P1 and P2), even in the Type-C simulations.
- Although the amount of the residual displacements varies among simulations to some extent, the experimental tendency of accumulating displacement associated with lateral spreading in one direction during shaking is adequately simulated in a majority of the numerical simulations.

A close examination of Figs. 3.7, 3.8 and 3.9 shows the following trend for RPI_A_A1_1:

- As in the case of KyU_A_A2_1, most of the numerical simulations can reproduce the experimental acceleration responses at deep sensor locations (e.g., AH1). However, the simulated accelerations near the ground surface (e.g., AH4) are different among simulations; Simulations 1–3, 5, and 8 are capable of capturing well the observed spike waveform due to positive dilatancy.
- Compared to the variation in the simulated excess pore pressure for KyU_A_A2_1, the simulated variation for RPI_A_A1_1 is not large; Simulations 2, 5, and 8 can reasonably simulate the observed pore pressure response, including the peak value, dynamic amplitude, and dissipation phase.
- The variation in the simulated horizontal displacements for RPI_A_A1_1 looks smaller than that for KyU_A_A2_1; the observed displacement waveform is well simulated, particularly in Simulations 1 and 3, including the residual value as well as the dynamic amplitude.

For UCD_A_A2_1, Figs. 3.10, 3.11 and 3.12 demonstrate the following trend:

- As in the previously mentioned two cases, a majority of the numerical simulations can adequately reproduce the observed acceleration responses at deep sensor locations (e.g., AH1). When it comes to the accelerations near the ground surface (e.g., AH4), most of the numerical simulations show spike waveforms due to positive dilatancy; in particular, Simulations 1–3, 5, and 8 can capture well the experimental result.
- The variation in the simulated excess pore pressure for UCD_A_A2_1 looks similar as that for RPI_A_A1_1; Simulations 1–3 have a larger dynamic amplitude, which may be caused by strong positive dilatancy, while the amplitude is small for Simulations 5–7.
- A majority of the numerical simulations can adequately capture the observed horizontal displacement waveform; the variation in the simulated residual displacements is not considerable.

Figures 3.13, 3.14, 3.15, 3.16, 3.17 and 3.18 compare the numerical simulation results with the corresponding experiments for the two sets of Model B tests in Table 3.4 (i.e., KyU_A_B2_1 and RPI_A_B1_1). As in the case of the numerical simulations for Model A tests, the variation in the simulated responses (i.e., accelerations, excess pore pressures, and horizontal displacements) exists among simulations. However, the comparison demonstrates that a majority of the numerical simulations are capable of simulating well the experimental trends; in particular, the Type-C simulations are found to capture the measured responses more accurately by adjusting the model parameters.

3.5 Comparison of Numerical Simulation Performance in Terms of Horizontal Displacement

In order to further assess the quality of numerical simulations' fit to the centrifuge test results and their performance in terms of horizontal displacement due to lateral spreading, Fig. 3.19 compares the relationship between Dr, PGA_{eff}, and horizontal displacement (i.e., residual value) in the form of a balloon plot; the balloon size represents the amount of measured and simulated horizontal displacements. In the figure, the displacement (i.e., balloon size) should be smaller as Dr increases, whereas the displacement should be larger as PGA_{eff} increases. The experimental results are generally in line with this trend, but some results do not follow this trend; this may be due to the variability of the centrifuge experiments. If such experimental variability could not be known prior to the Type-B simulations (e.g., Simulations 3, 4, and 8), it would be difficult to reproduce the observed results of such experiments accurately. On the other hand, the Type-C simulations can reproduce the experimental results, as shown in Simulations 5–7, because the model parameters are adjusted to match the experimental results. Thus, it is considered quite challenging to capture all measured responses perfectly by taking into account the experimental variability, but accumulating high-quality experimental results as a database can be essential to improve constitutive models and analytical platforms further.

3.6 Conclusions

In the LEAP-ASIA-2019 prediction campaign, nine numerical simulation teams submitted Type-B or Type-C simulations on the seismic behavior of a uniform-density, 20-m-long, and 5-degree sandy slope; this chapter presented an overview of the simulation results (i.e., time histories of response accelerations, excess pore water pressures, and lateral displacements at the ground surface) and their comparison with the results of a selected set of centrifuge model tests. The comparison demonstrated that a majority of Type-B and Type-C numerical simulations were

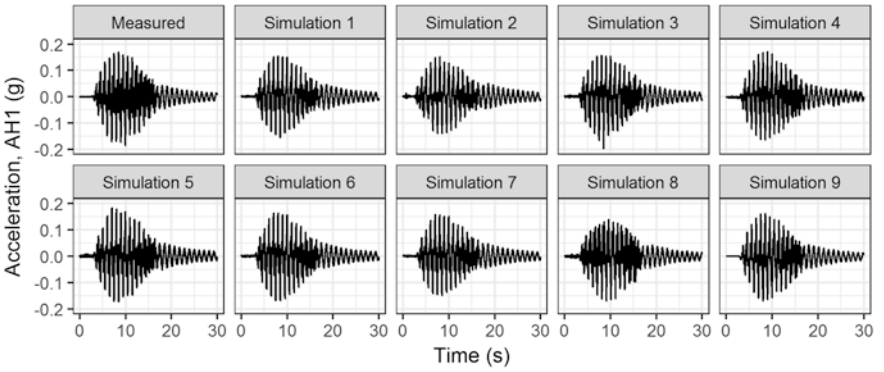

(a)

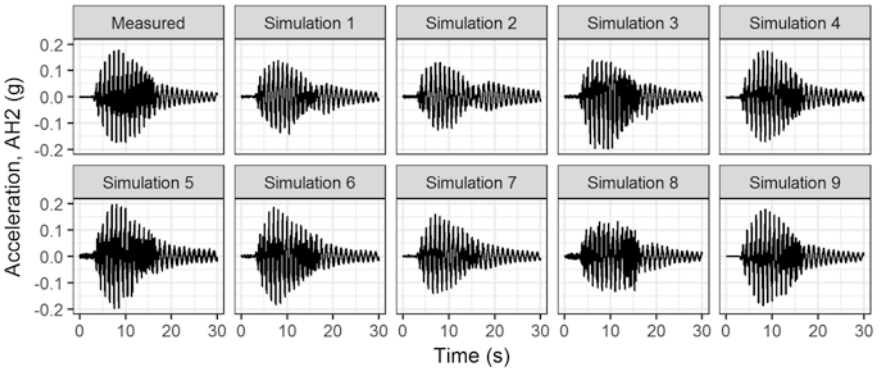

(b)

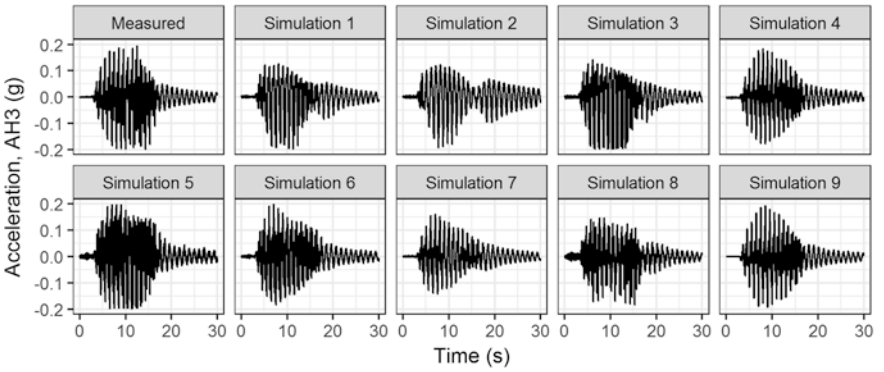

(c)

Fig. 3.13 Comparison of the measured and computed acceleration time histories for KyU_A_B2_1 test. (**a**) AH1, (**b**) AH2, (**c**) AH3, (**d**) AH4, (**e**) AH6, (**f**) AH9

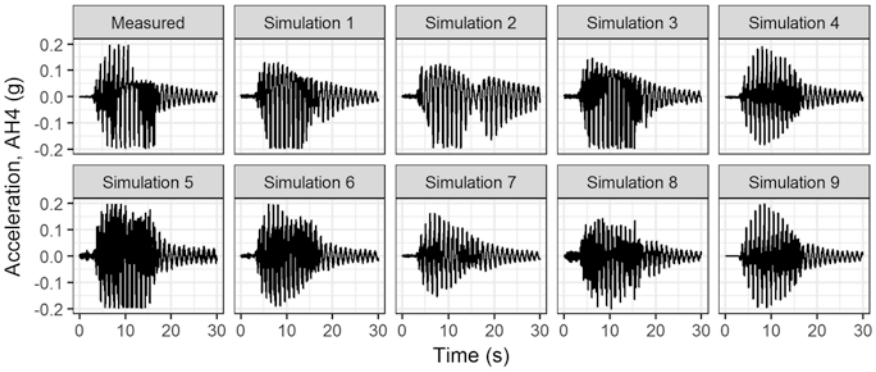

(d)

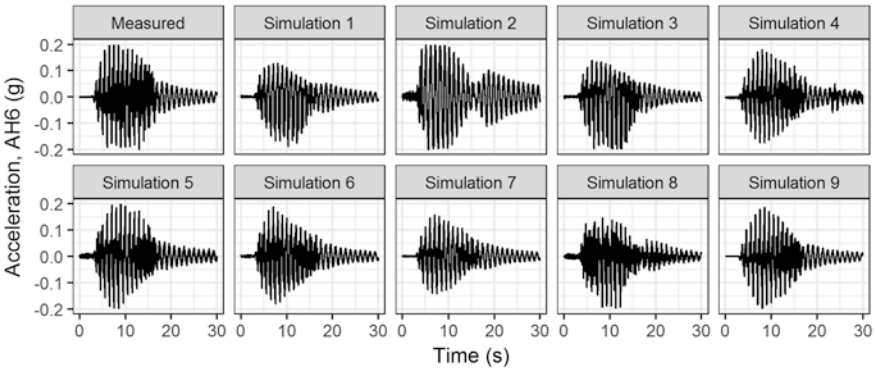

(e)

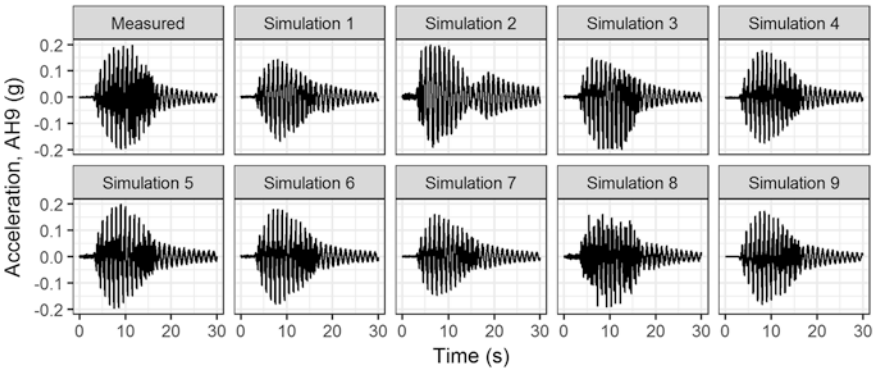

(f)

Fig. 3.13 (continued)

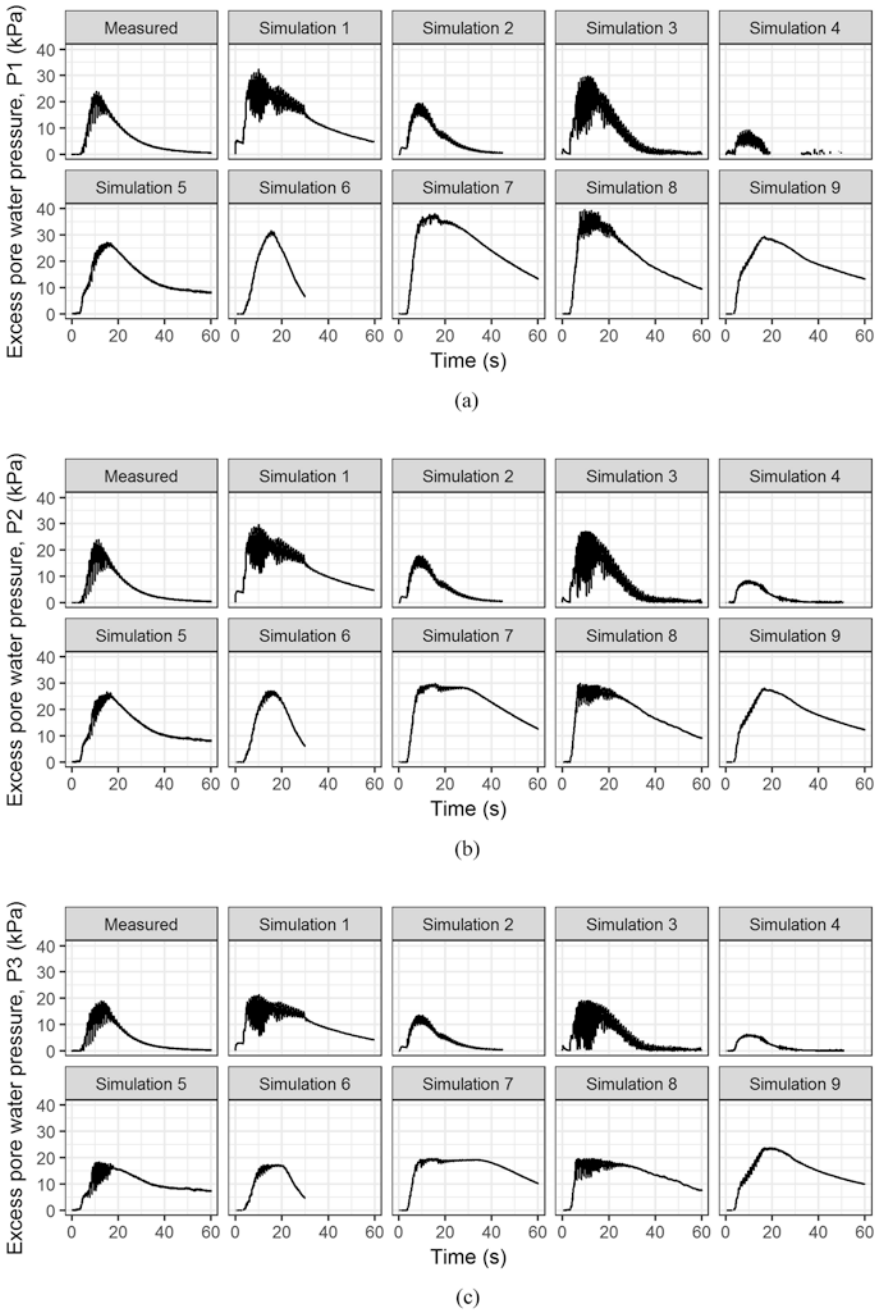

Fig. 3.14 Comparison of the measured and computed time histories of excess pore water pressures for KyU_A_B2_1 test. (**a**) P1, (**b**) P2, (**c**) P3, (**d**) P4, (**e**) P6, (**f**) P8

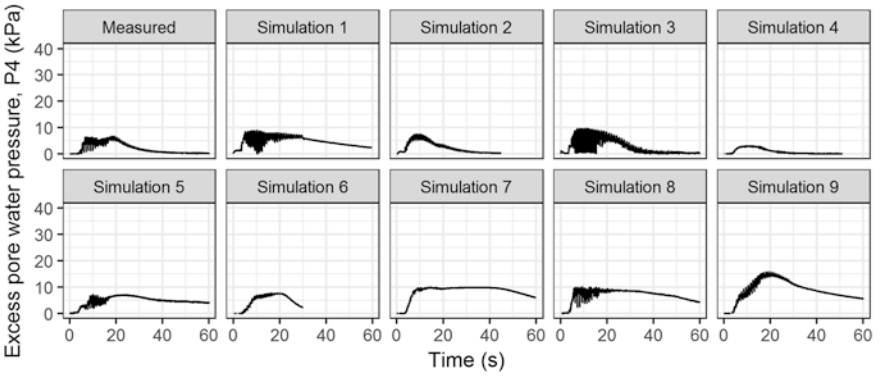

(d)

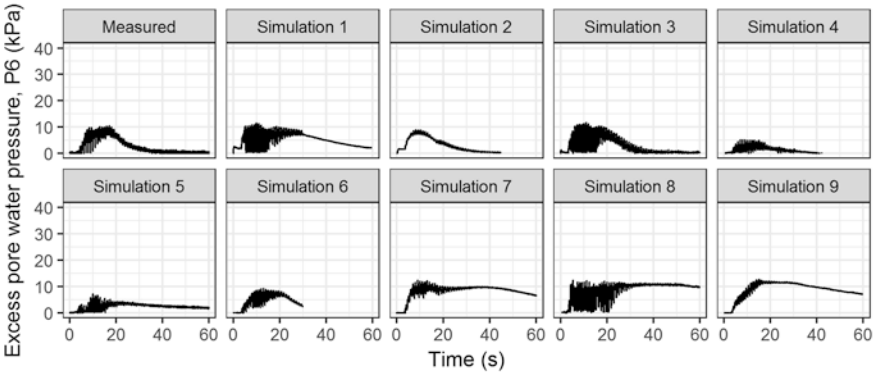

(e)

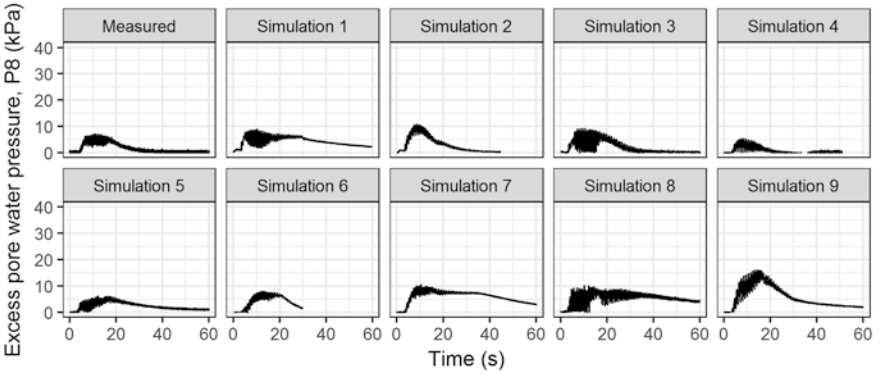

(f)

Fig. 3.14 (continued)

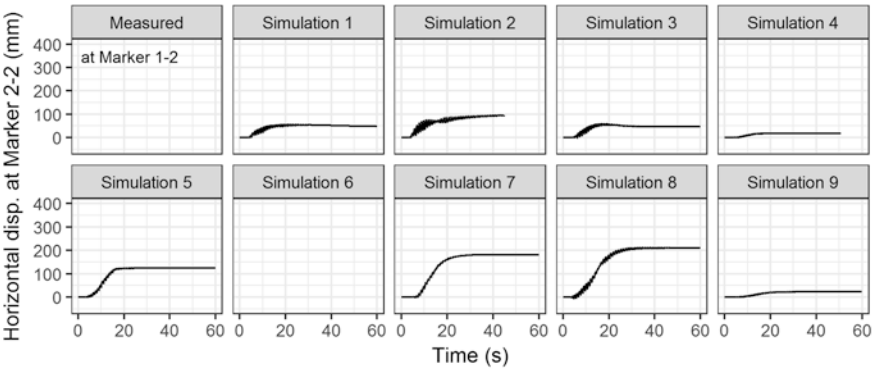

(a)

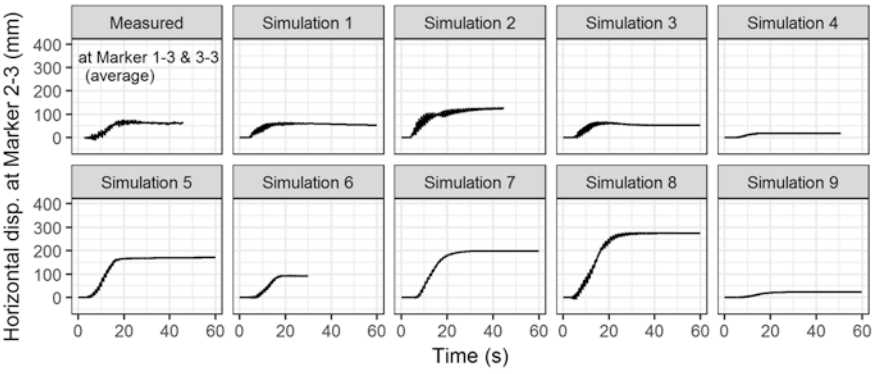

(b)

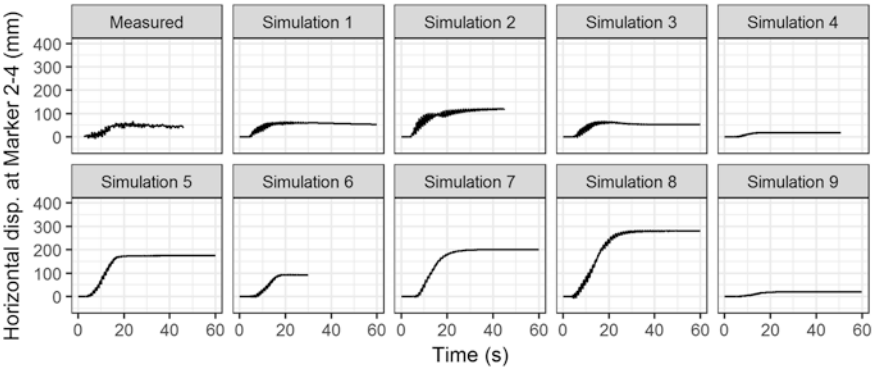

(c)

Fig. 3.15 Comparison of the measured and computed time histories of ground surface lateral displacements for KyU_A_B2_1 test. (**a**) Marker 2–2, (**b**) Marker 2–3, (**c**) Marker 2–4

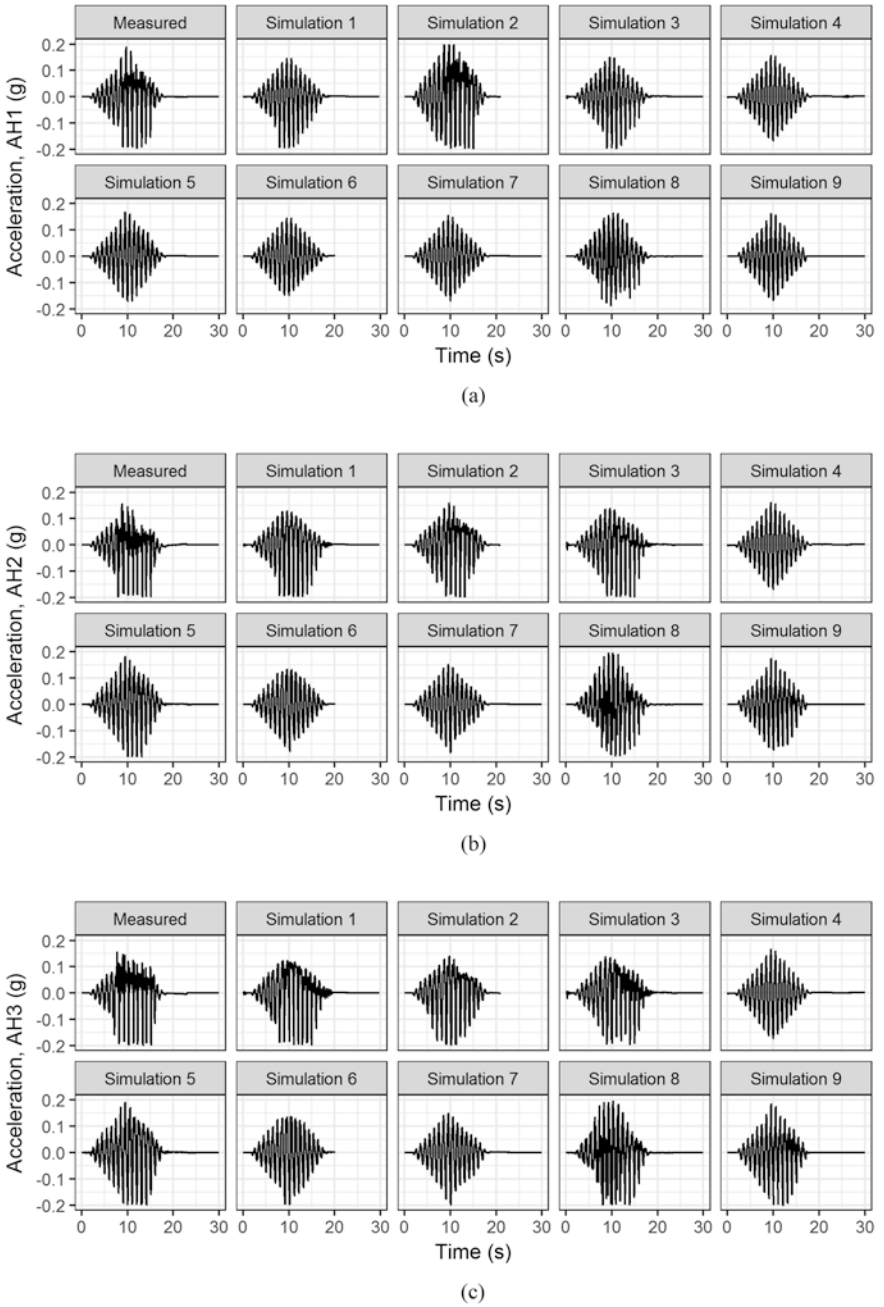

Fig. 3.16 Comparison of the measured and computed acceleration time histories for RPI_A_B1_1 test. (**a**) AH1, (**b**) AH2, (**c**) AH3, (**d**) AH4, (**e**) AH6, (**f**) AH9

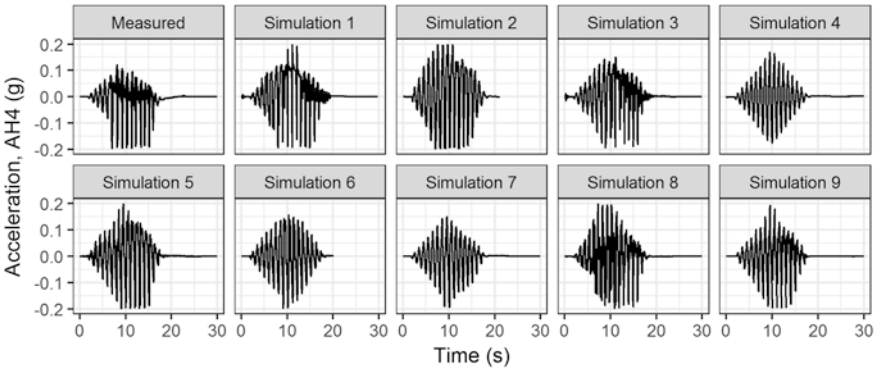

(d)

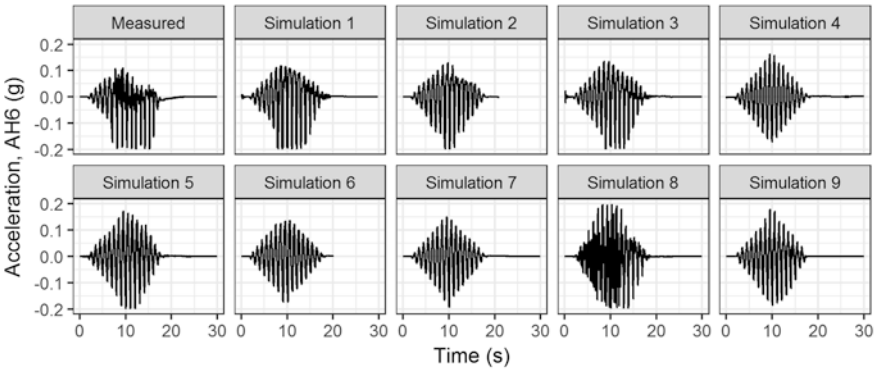

(e)

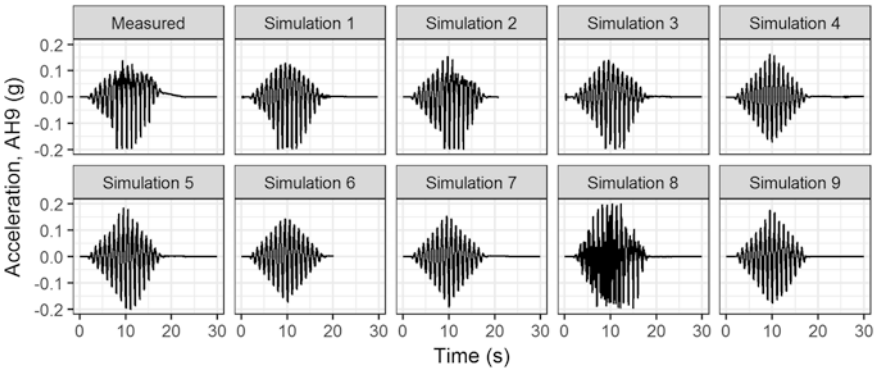

(f)

Fig. 3.16 (continued)

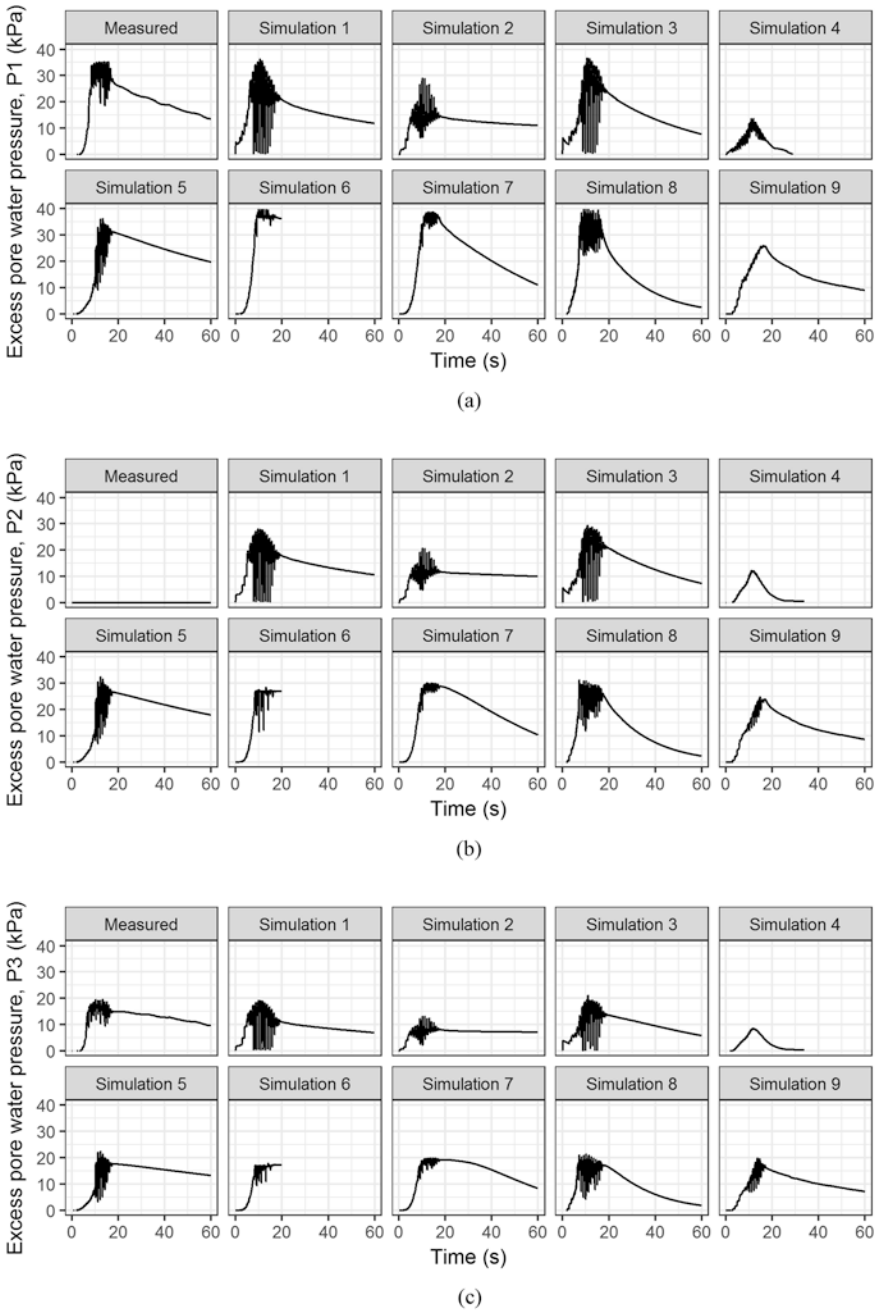

Fig. 3.17 Comparison of the measured and computed time histories of excess pore water pressures for RPI_A_B1_1 test. (**a**) P1, (**b**) P2, (**c**) P3, (**d**) P4, (**e**) P6, (**f**) P8

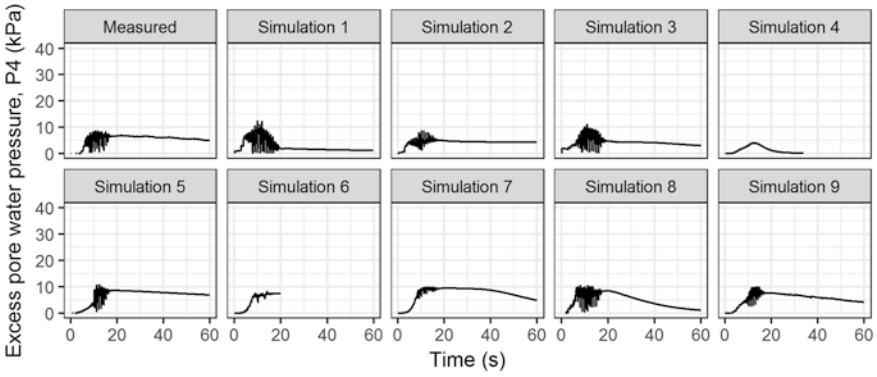

(d)

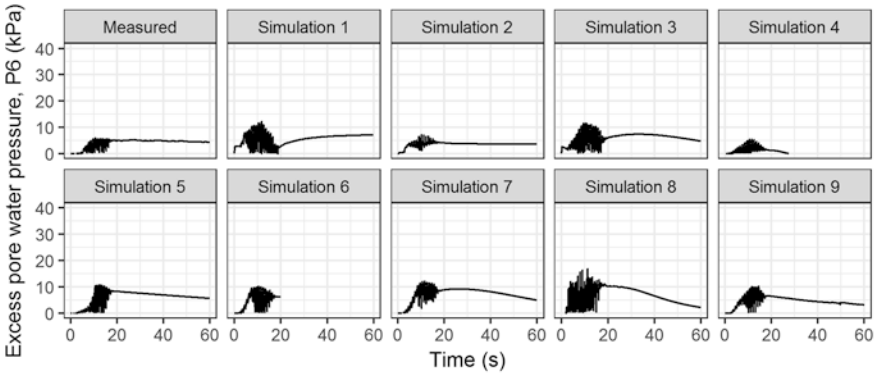

(e)

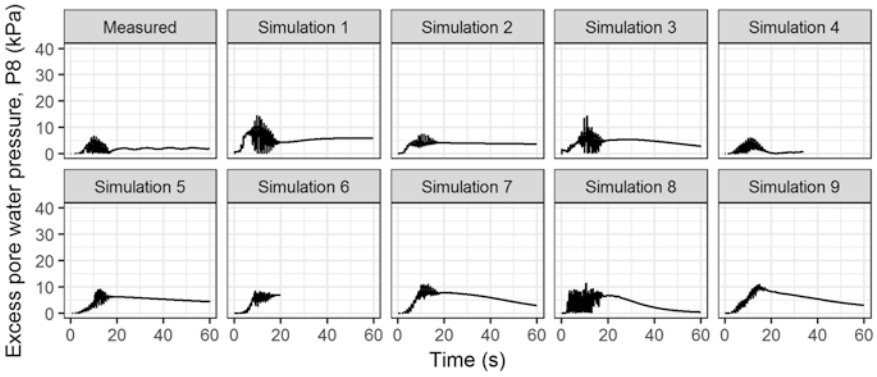

(f)

Fig. 3.17 (continued)

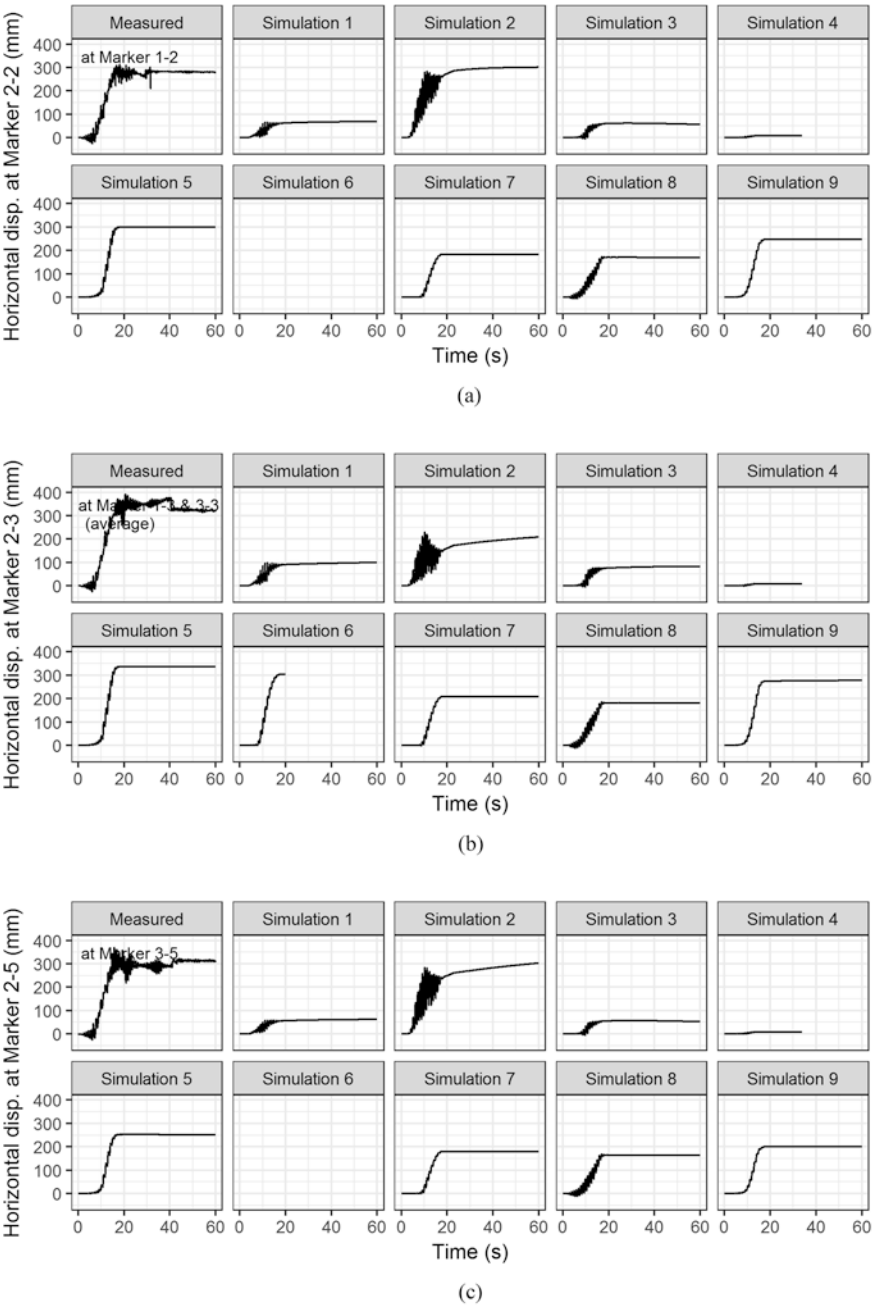

Fig. 3.18 Comparison of the measured and computed time histories of ground surface lateral displacements for RPI_A_B1_1 test. (**a**) Marker 2–2, (**b**) Marker 2–3, (**c**) Marker 2–5

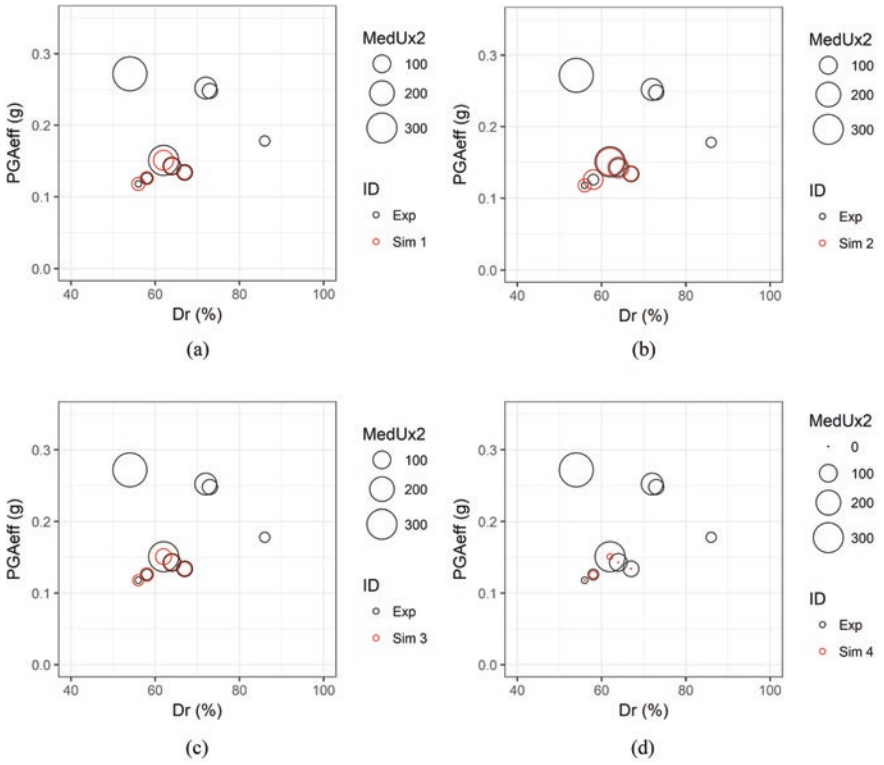

Fig. 3.19 Summary of the measured and computed lateral displacements at the center of ground surface. (**a**) Simulation 1, (**b**) Simulation 2, (**c**) Simulation 3, (**d**) Simulation 4, (**e**) Simulation 5, (**f**) Simulation 6, (**g**) Simulation 7, (**h**) Simulation 8, (**i**) Simulation 9

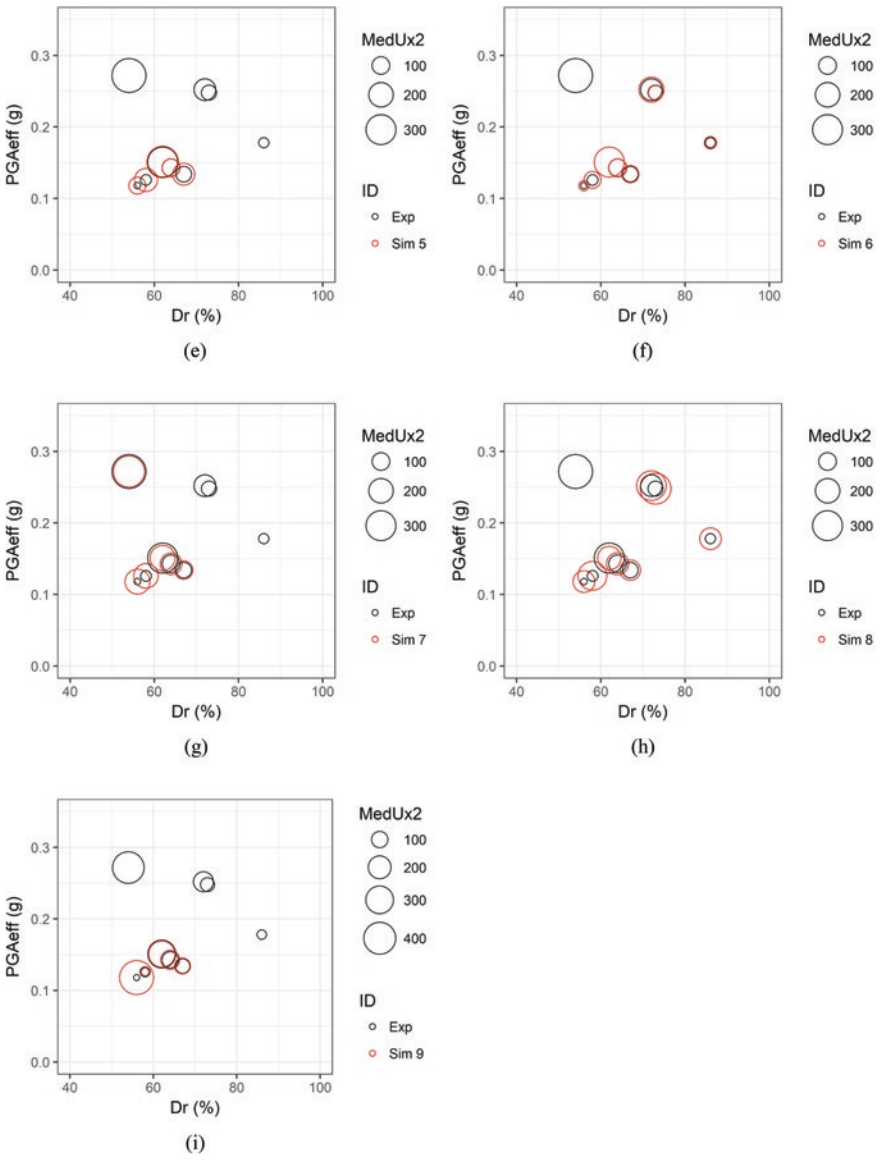

Fig. 3.19 (continued)

capable of simulating well the experimental trends observed in the centrifuge tests; in particular, Type-C simulations were found to capture the measured responses more accurately by adjusting the model parameters. Although it is quite challenging to capture all measured responses perfectly, the simulation exercises indicated that the numerical simulations could be further improved by accumulating high-quality experimental results as a database.

Acknowledgments The experimental work and numerical simulations on LEAP-ASIA-2019 were supported by different funds depending mainly on the location of the work. The work by the Japan PIs (Tobita, Ichii, Okamura, Takemura, and Ueda) was supported by JSPS KAKENHI grant number JP17H00846.

References

Elbadawy, M. A., & Zhou, Y. G. (2023). Class-C simulations of LEAP-ASIA-2019 via OpenSees platform by using a pressure dependent multi yield-surface model. In *Model tests and numerical simulations of liquefaction and lateral spreading: LEAP-ASIA-2019*. Springer.

Escoffier, S., Li, Z., & Audrain, P. (2023). LEAP-ASIA-2019 centrifuge tests at university Gustave Eiffel. In *Model tests and numerical simulations of liquefaction and lateral spreading: LEAP-ASIA-2019*. Springer.

Fasano, G., Chiaradonna, A., & Bilotta, E. (2023). LEAP-ASIA-2019 centrifuge test simulation at UNINA. In *Model tests and numerical simulations of liquefaction and lateral spreading: LEAP-ASIA-2019*. Springer.

Huang, J. X., & Hung, W. Y. (2023). LEAP-ASIA-2019 centrifuge test at NCU. In *Model tests and numerical simulations of liquefaction and lateral spreading: LEAP-ASIA-2019*. Springer.

Hyodo, J., & Ichii, K. (2023). LEAP-ASIA-2019 type-B simulations through FLIP at Kyoto University. In *Model tests and numerical simulations of liquefaction and lateral spreading: LEAP-ASIA-2019*. Springer.

Iai, S., Tobita, T., & Nakahara, T. (2005). Generalised scaling relations for dynamic centrifuge tests. *Geotechnique, 55*(5), 355–362.

Korre, E., Abdoun, T., & Zeghal, M. (2023). Experimental evaluation of lateral spreading of a liquefiable sloping deposit using centrifuge and generalized scaling law tests. In *Model tests and numerical simulations of liquefaction and lateral spreading: LEAP-ASIA-2019*. Springer.

Kutter, B. L., Carey, T. J., Hashimoto, T., Zeghal, M., Abdoun, T., Kokkali, P., Madabhushi, G., Haigh, S., d'Arezzo, F. B., Madabhushi, S., Hung, W. Y., Lee, C. J., Cheng, H. C., Iai, S., Tobita, T., Ashino, T., Ren, J., Zhou, Y. G., Chen, Y. M., Sun, Z. B., & Manzari, M. T. (2018). LEAP-GWU-2015 experiment specifications, results, and comparisons. *Soil Dynamics and Earthquake Engineering, 113*, 616–628.

Kutter, B., Carey, T., Stone, N., Zheng, B. L., Garvas, A., Manzari, M., Zeghal, M., Abdoun, T., Korre, E., Escoffier, S., Haigh, S. K., Madabhushi, G. S., Madabhushi, S. S. C., Hung, W. Y., Liao, T. W., Kim, D. S., Kim, S. N., Ha, J. G., Kim, N. R., Okamura, M., Sjafruddin, A. N., Tobita, T., Ueda, K., Vargas, R., Zhou, Y. G., & Liu, K. (2019). Chapter 4 LEAP-UCD-2017 comparison of centrifuge test results. In *Model tests and numerical simulations of liquefaction and lateral spreading, LEAP-UCD-2017* (pp. 69–103). Springer.

Ma, Q., Zhou, Y. G., Liu, K., & Chen, Y. M. (2023). Centrifuge model tests at Zhejiang University for LEAP-ASIA-2019. In *Model tests and numerical simulations of liquefaction and lateral spreading: LEAP-ASIA-2019*. Springer.

Madabhushi, G. S. P., Haigh, S. K., Boksmati, J. I., Garcia-Torres, S., & Fusco, A. (2023). LEAP-ASIA-2019 centrifuge tests at university of Cambridge. In *Model tests and numerical simulations of liquefaction and lateral spreading: LEAP-ASIA-2019*. Springer.

Manandhar, S., Kim, S. N., & Kim, D. S. (2023). LEAP-ASIA-2019 centrifuge test at KAIST. In *Model tests and numerical simulations of liquefaction and lateral spreading: LEAP-ASIA-2019*. Springer.

Manzari, M. T., Ghoraiby, M. E., Kutter, B. L., Zeghal, M., Abdoun, T., Arduino, P., Armstrong, R. J., Beaty, M., Carey, T., Chen, Y., Ghofrani, A., Gutierrez, D., Goswami, N., Haigh, S. K.,

Hung, W. Y., Iai, S., Kokkali, P., Lee, C. J., Madabhushi, G., Mejia, L., Sharp, M., Tobita, T., Ueda, K., Zhou, Y., & Ziotopoulou, K. (2018). Liquefaction experiment and analysis projects (LEAP): Summary of observations from the planning phase. *Soil Dynamics and Earthquake Engineering, 113*, 714–743.

Manzari, M., Ghoraiby, M., Zeghal, M., Kutter, B., Arduino, P., Barrero, A. R., Bilotta, E., Chen, L., Chen, R., Chiaradonna, A., Elgamal, A., Fasano, G., Fukutake, K., Fuentes, W., Ghofrani, A., Ichii, K., Kiriyama, T., Lascarro, C., Mercado, V., Montgomery, J., Ozutsumi, O., Qiu, Z., Taiebat, M., Travasarou, T., Tsiaousi, D., Ueda, K., Ugalde, J., Wada, T., Wang, R., Yang, M., Zhang, J. M., & Ziotopoulou, K. (2019a). Chapter 9 LEAP-2017 simulation exercise: Calibration of constitutive models and simulation of the element tests. In *Model tests and numerical simulations of liquefaction and lateral spreading, LEAP-UCD-2017* (pp. 165–185). Springer.

Manzari, M., Ghoraiby, M., Zeghal, M., Kutter, B., Arduino, P., Barrero, A. R., Bilotta, E., Chen, L., Chen, R., Chiaradonna, A., Elgamal, A., Fasano, G., Fukutake, K., Fuentes, W., Ghofrani, A., Haigh, S., Hung, W. Y., Ichii, K., Kim, D. S., Kiriyama, T., Lascarro, C., Madabhushi, G., Mercado, V., Montgomery, J., Okamura, M., Ozutsumi, O., Qiu, Z., Taiebat, M., Tobita, T., Travasarou, T., Tsiaousi, D., Ueda, K., Ugalde, J., Wada, T., Wang, R., Yang, M., Zhang, J. M., Zhou, Y. G., & Ziotopoulou, K. (2019b). Chapter 10 LEAP-2017: Comparison of the type-B numerical simulations with centrifuge test results. In *Model tests and numerical simulations of liquefaction and lateral spreading, LEAP-UCD-2017* (pp. 187–218). Springer.

Okamura, M., & Sjafruddin, A. N. (2023). LEAP-ASIA-2019 centrifuge test at Ehime University. In *Model tests and numerical simulations of liquefaction and lateral spreading: LEAP-ASIA-2019*. Springer.

Qiu, Z., & Elgamal, A. (2023). LEAP-ASIA-2019 centrifuge test simulations of liquefiable sloping ground. In *Model tests and numerical simulations of liquefaction and lateral spreading: LEAP-ASIA-2019*. Springer.

Reyes, A., Barrero, A. R., & Taiebat, M. (2023). Type-C simulations of centrifuge tests from LEAP-ASIA-2019 using SANISAND-sf. In *Model tests and numerical simulations of liquefaction and lateral spreading: LEAP-ASIA-2019*. Springer.

Stone, N. S., Carey, T. J., Santana, A., & Kutter, B. L. (2023). LEAP-ASIA-2019 centrifuge test at University of California, Davis. In *Model tests and numerical simulations of liquefaction and lateral spreading: LEAP-ASIA-2019*. Springer.

Tanaka, Y., Sahare, A., Ueda, K., Yuyama, W., & Iai, S. (2023). LEAP-ASIA-2019 numerical simulations using a strain space multiple mechanism model for a liquefiable sloping ground. In *Model tests and numerical simulations of liquefaction and lateral spreading: LEAP-ASIA-2019*. Springer.

Tobita, T., Ueda, K., Vargas, R. R., Ichii, K., Okamura, M., Sjafruddin, A. N., Takemura, J., Hang, L., Uzuoka, R., Iai, S., Boksmati, J., Fusco, A., Torres-Garcia, S., Haigh, S., Madabhushi, G., Manzari, M., Escoffier, S., Li, Z., Kim, D. S., Manandhar, S., Hung, W. Y., Huang, J. X., Pham, T. N. P., Zeghal, M., Abdoun, T., Korre, E., Kutter, B. L., Carey, T. J., Stone, N., Zhou, Y. G., Liu, K., & Ma, Q. (2022). LEAP-ASIA-2019: Validation of centrifuge experiments and the generalized scaling law on liquefaction-induced lateral spreading. *Soil Dynamics and Earthquake Engineering, 157*, 107237.

Tobita, T., Ichii, K., Ueda, K., Uzuoka, R., Vargas, R. R., Okamura, M., Sjafruddin, A. N., Takemura, J., Hang, L., Iai, S., Boksmati, J., Fusco, A., Torres-Garcia, S., Haigh, S., Madabhushi, G., Manzari, M., Escoffier, S., Li, Z., Kim, D. S., Manandhar, S., Hung, W. Y., Huang, J. X., Pham, T. N. P., Zeghal, M., Abdoun, T., Korre, E., Kutter, B. L., Carey, T. J., Stone, N., Zhou, Y. G., Liu, K., & Ma, Q. (2023). LEAP-ASIA-2019: Summary of centrifuge experiments on liquefaction-induced lateral spreading: Validation and applicability of the generalized scaling law. In *Model tests and numerical simulations of liquefaction and lateral spreading: LEAP-ASIA-2019*. Springer.

Ueda, K., Tanaka, Y., Sahare, A., Elgamal, A., Qiu, Z., Wang, R., Zhu, T., Zhou, C., Zhang, J. M., Parra, A. R., Barrero, A., Taiebat, M., Yuyama, W., Iai, S., Hyodo, J., Ichii, K., Elbadawy, M. A., Zhou, Y. G., Fasano, G., Chiaradonna, A., Bilotta, E., Arduino, P., Zeghal, M., Manzari, M., & Tobita, T. (2023). LEAP-ASIA-2019 simulation exercise: Calibration of constitutive models and simulations of the element tests. In *Model tests and numerical simulations of liquefaction and lateral spreading: LEAP-ASIA-2019*. Springer.

Vargas, R. R., Ueda, K., & Tobita, T. (2023). LEAP-ASIA-2019 centrifuge test at Kyoto University. In *Model tests and numerical simulations of liquefaction and lateral spreading: LEAP-ASIA-2019*. Springer.

Wang, R., Zhu, T., Zhou, C., & Zhang, J. M. (2023). LEAP-ASIA-2019 simulations at Tsinghua University. In *Model tests and numerical simulations of liquefaction and lateral spreading: LEAP-ASIA-2019*. Springer.

Zeghal, M., Goswami, N., Kutter, B. L., Manzari, M. T., Abdoun, T., Arduino, P., Armstrong, R. J., Beaty, M., Chen, Y., Ghofrani, A., Haigh, S., Hung, W. Y., Iai, S., Kokkali, P., Lee, C. J., Madabhushi, G., Tobita, T., Ueda, K., Zhou, Y., & Ziotopoulou, K. (2018). Stress-strain response of the LEAP centrifuge tests and numerical predictions. *Soil Dynamics and Earthquake Engineering, 113*, 804–818.

Chapter 4
Dynamic Torsional Shear Tests of Ottawa F-65 Sand for LEAP-ASIA-2019

Ruben R. Vargas, Kyohei Ueda, and Kazuaki Uemura

Abstract The Liquefaction Experiments and Analysis Projects (LEAP) is an international collaborative project that aims to verify, validate, and quantify the uncertainty of numerical liquefaction models. Within this project, a series of hollow cylinder cyclic torsional shear tests were performed at the Disaster Prevention Research Institute facility at Kyoto University. These tests focused on examining how the relative density affects the cyclic response of Ottawa F-65 sand. The obtained results will contribute to a dependable database for the ongoing and future verification and validation processes of liquefaction models. This paper presents the details of the model preparation and test results, as well as a brief discussion on the influence of the relative density and the tests' repeatability.

Keywords Liquefaction Experiments and Analysis Projects (LEAP-ASIA-2019) · Torsional shear test · Ottawa F-65 sand

4.1 Introduction

As stated by Tobita et al. (2023), Ottawa F-65 sand was used as the standard sand of the "LEAP-ASIA-2019" exercise. This sand is a clean, poorly graded, whole grain silica sand, containing less than 0.5% fines by mass (Carey et al., 2019).

One of the main objectives of LEAP is to generate a large and high-quality database of physical models and element tests that would contribute to assess and validate the capabilities of the analytical tools to predict the mechanism and

R. R. Vargas (✉)
Penta-Ocean Construction Co. Ltd. (Former Department of Civil and Earth Resources Engineering, Kyoto University, Kyoto, Japan), Tokyo, Japan

K. Ueda
Disaster Prevention Research Institute, Kyoto University, Kyoto, Japan

K. Uemura
Core Laboratory, Oyo Corporation, Saitama, Japan

T. Tobita et al. (eds.), *Model Tests and Numerical Simulations of Liquefaction and Lateral Spreading II*, https://doi.org/10.1007/978-3-031-48821-4_4

consequences of liquefaction. Researchers have made several efforts to establish and expand a laboratory test database to characterize the physical and mechanical properties of Ottawa F-65 sand, which has also been utilized in the LEAP-GWU-2015 and LEAP-UCD-2017 exercises (El Ghoraiby & Manzari (2018), El Ghoraiby et al., 2019; Carey et al., 2019; Parra Bastidas, 2016; Vasko, 2015).

In order to contribute to the understanding of the mechanical properties of Ottawa F-65 sand, a series of hollow cylinder dynamic torsional shear tests for four different relative densities (Dr = 50%, 60%, 70%, and 85%) were conducted in the installations of the Disaster Prevention Research Institute at Kyoto University. Although a comprehensive review of the test findings has already been published (Vargas et al., 2020), this paper focuses on the details of the model preparation and test results of the tests performed before the LEAP-ASIA-2019 workshop, which were made available to modelers for the calibration of constitutive models and simulation of element tests (Ueda et al., 2023).

4.2 Torsional Shear Apparatus

The torsional shear apparatus used in the tests presented in this paper is schematically shown in Fig. 4.1. The apparatus is capable of subjecting a hollow cylindrical sample with an inner diameter of 6 cm, outer diameter of 10 cm, and height of 10 cm to a wide range of stress paths for both monotonic and dynamic tests.

As shown in Fig. 4.1, the apparatus can apply vertical load and torque independently using pneumatic cylinders. Following the recommendation of Koseki et al. (2005), the load cell to measure vertical load and torque was placed inside the pressure cell to eliminate friction between the loading shaft and the bearing house.

To avoid non-uniform normal stresses across the sample, the same inner and outer pressures were applied at all test steps; also, since the tests were performed under isotropic conditions, no deviator stresses were applied.

Volumetric strains were measured using a low-capacity differential pressure transducer that measured changes in water volume in a burette connected to the back pressure (maintained at around 200 kPa) and the specimen. Rotational and axial deformations were measured using a potentiometer and a dial gauge, respectively. Table 4.1 summarizes the measured variables and the sensor characteristics.

4.3 Dynamic Torsional Shear Tests and Model Preparation

Prior to the LEAP-ASIA-2019 Workshop, 16 stress-controlled hollow cylinder dynamic torsional shear tests were conducted under isotropic conditions; Table 4.2 shows the characteristics of each test.

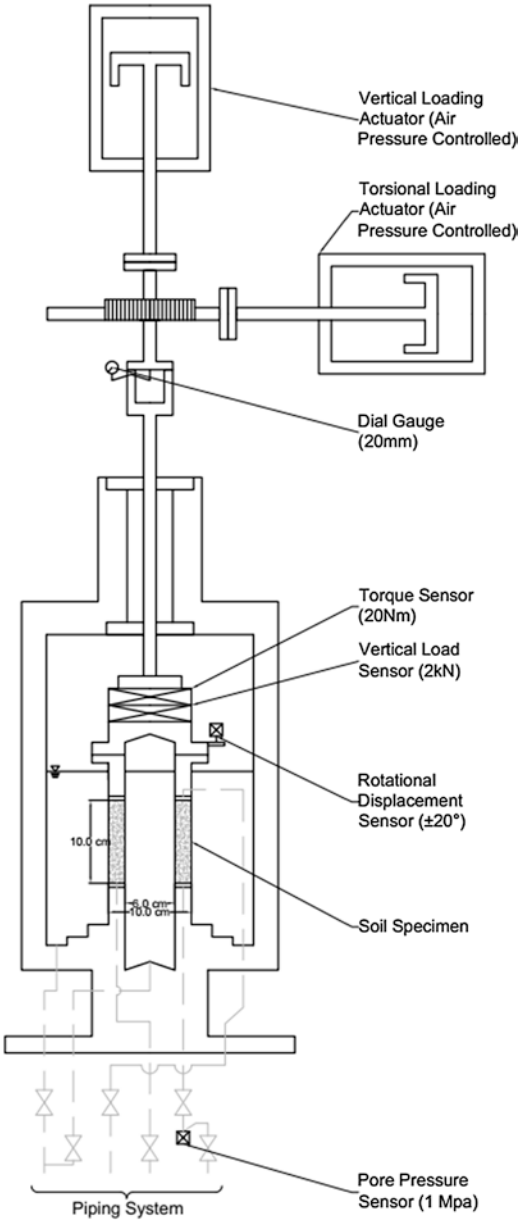

Fig. 4.1 Torsional shear apparatus at the Disaster Prevention Research Institute – Kyoto University. (Vargas et al., 2020)

The specimens were prepared taking as a reference the Japanese Standards JGS-0550-2009 (Japanese Geotechnical Society Standards, 2018a–1) and JGS-0551-2009 (Japanese Geotechnical Society Standards, 2018b–2).

Table 4.1 Sensor list

Variable	Type	Capacity	Manufacturer	Model
Torque load (M_T)	Load cell	20 N.m	Seishikou	KTU-20Ti
Vertical load (W)	Load cell	2 kN	Seishikou	KTU-20Ti
Angular deformation (θ)	Potentiometer	±20°	Midori	CP-2UTX
Volumetric deformation (ε_v)	Pressure sensor	±3200 psi	Validyne	DP15–28
Pore pressure (Δu)	Pressure sensor	1 MPa	TEAC	TP-BR
Vertical strain (ε_a)	Dial gauge	20 mm	Showa Sokki	TCL-20FA

Table 4.2 Hollow cylinder dynamic torsional shear tests developed at Kyoto University

Specimen no.	Initial Dr (%)	Dr after consolidation (%)	Effective confining stress (kPa)	Shear stress (kPa)	Shear stress ratio
Dr50_1	48.2	50.4	103.0	10.2	0.099
Dr50_2	48.5	50.5	104.5	13.3	0.127
Dr50_3	48.6	50.6	103.0	15.3	0.149
Dr50_4	50.9	53.1	106.1	20.3	0.191
Dr60_1	58.7	60.7	103.0	12.1	0.117
Dr60_2	58.4	60.4	103.0	12.8	0.125
Dr60_3	59.1	61.0	105.0	15.1	0.144
Dr60_4	59.0	60.6	104.0	18.1	0.174
Dr60_5	61.6	63.6	104.0	20.6	0.199
Dr70_1	68.7	70.2	102.9	20.5	0.199
Dr70_2	70.8	71.9	106.0	26.2	0.247
Dr70_3	73.3	73.9	106.2	26.4	0.248
Dr70_4	69.2	70.7	104.1	28.3	0.272
Dr85_1	82.3	84.0	103.1	28.3	0.274
Dr85_2	81.4	82.9	103.2	30.6	0.296
Dr85_3	83.3	84.9	106.6	41.6	0.390

4.3.1 Model Preparation: Air Pluviation and Chamber Setting

To obtain a fabric similar to the physical models (prepared for the "LEAP-ASIA-2019" exercise), the samples were prepared through the "air pluviation" technique, and, to guarantee the homogeneity of the sample and reduce the variability, the height of the pluviation tool was increased during the sample preparation, aiming to keep the dropping height constant along with the sample.

Following the air pluviation process, the top cap was placed, and negative pressure of approximately −15 kPa was applied to the model (between the membranes) to uphold the sample's shape while removing the molds and placing the cell chamber. Figure 4.2 shows the sample after the placement of the top cap and the removal of molds. To minimize variability and guarantee uniformity among the experiments, precise measurements of the specimen dimensions and sand weight were taken

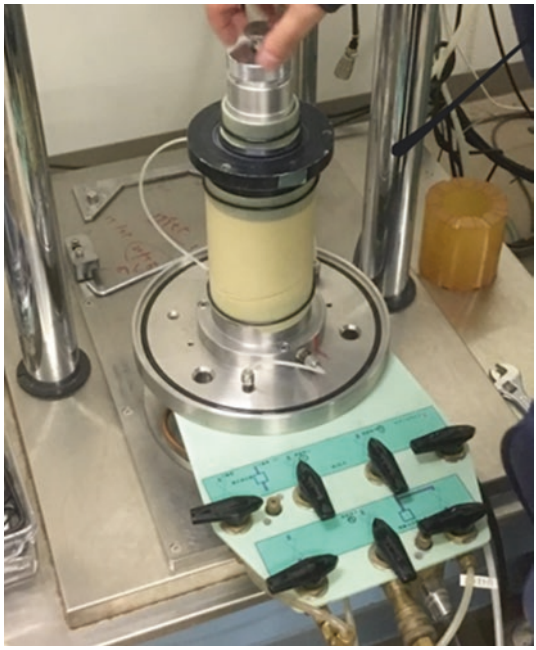

Fig. 4.2 Hollow cylinder model preparation – model after mold removal

subsequent to mold removal. It is noteworthy that even minor differences in weight or dimensions can considerably influence the estimated relative density.

After confirming the model's density, the outer chamber was carefully placed and fixed to prevent any leakage, as shown in Fig. 4.3.

4.3.2 Model Preparation: Saturation

Upon filling the outer and inner cells with water, an isotropic pre-consolidation of 20 kPa was applied to both the outer and inner cells to prevent sample deformations in subsequent steps; following this step, the vacuum pressure utilized to preserve the sample's shape was released.

The saturation process began by flowing CO_2 through the sample for around 15 min to promote the dissolution of gas bubbles trapped in the sand. Subsequently, degassed water was flowed through the sample until at least 1 liter of degassed water (roughly twice the sample's volume) had passed through.

Once the necessary quantity of water had flowed through the sample, a back pressure of 200 kPa was applied to the sample (both inner and outer chambers). The saturation level was then verified by determining the Skempton B value, which was confirmed to be above 0.95 in all experiments for an increment of 20 kPa under isotropic and undrained conditions.

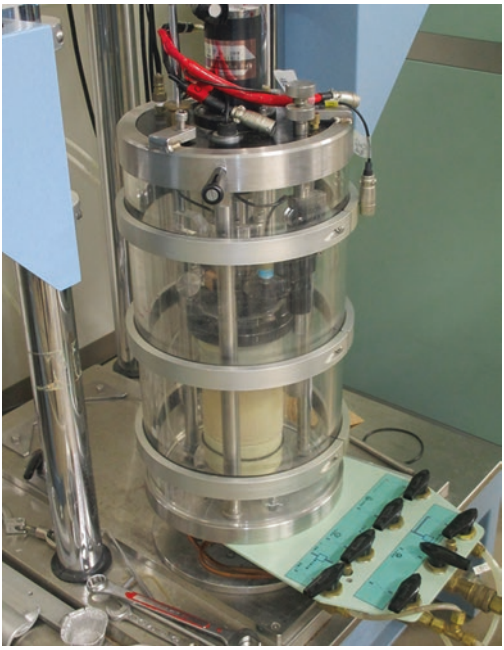

Fig. 4.3 Hollow cylinder model preparation – outer chamber setting

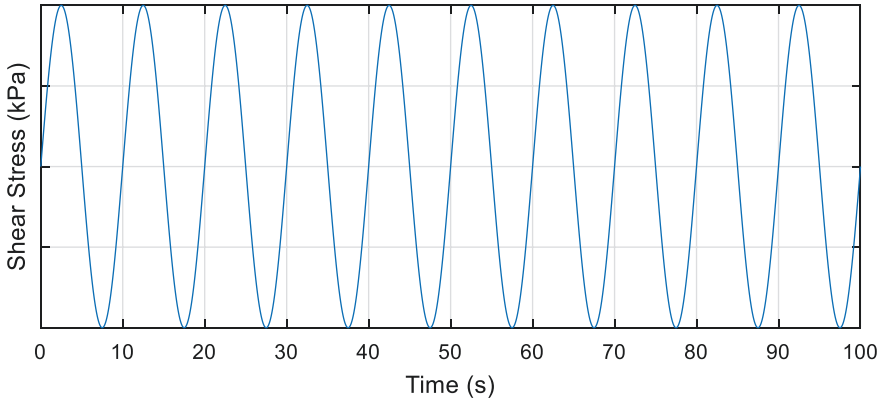

Fig. 4.4 Cyclic sinusoidal shear stress applied to the sample. (Vargas et al., 2020)

4.3.3 Model Consolidation and Testing

The specimen was isotropically consolidated to a total pressure of approximately 300 kPa (i.e., 100 kPa of effective stress) under drained conditions. Following the consolidation process, a stress-controlled cycling sinusoidal shear stress was applied to the sample in undrained conditions (Fig. 4.4 shows the applied target wave).

As specified in the Japanese Standards (Japanese Geotechnical Society Standards, 2016), the load was applied until achieving at least 7.5% of double amplitude shear strain. Additionally, since the loads were applied using a stress-controlled mechanism, reliable information could not be obtained at very large strains.

4.4 Test Results

The dynamic stress-strain characteristics of 16 hollow cylinder models were estimated using a torsional shear apparatus, as described in Sects. 4.2 and 4.3. Detailed test results (stress-strain characteristics of each model) have been included in the Appendix section.

Figure 4.5 shows the estimated liquefaction resistance curve (LRC) for $\gamma_{DA} = 7.5\%$ (i.e., the number of cycles required to reach a 7.5% DA shear strain); a clear trend and consistency among the tests is observed.

Similarly, Figs. 4.6, 4.7, and 4.8 show the LRC for $\gamma_{DA} = 3.0\%$, $\gamma_{DA} = 1.5\%$, and $r_u = 0.95$.

Additionally, as seen in Fig. 4.9, it has been found that the friction angle ϕ_f value remained constant for all relative densities ($\phi_f \approx 35°$). On the other hand, the phase transformation angle ϕ_p increased with the relative density; values of 20.2°, 22.6°, 24.0°, and 25.0° were obtained for relative densities of 50%, 60%, 70%, and 85%, respectively.

4.5 Repeatability of Test Results

To ensure the consistency of the tests, a repeatability test (Dr70_3) was performed; this repeatability test was prepared and tested under the same conditions as test Dr70_2.

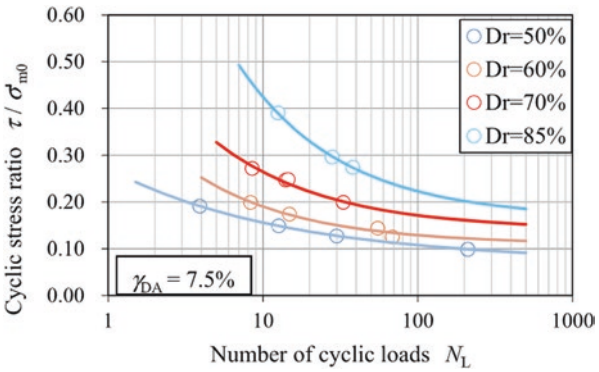

Fig. 4.5 Liquefaction resistance curve of Ottawa F-65 sand ($\gamma_{DA} = 7.5\%$). (Vargas et al., 2020)

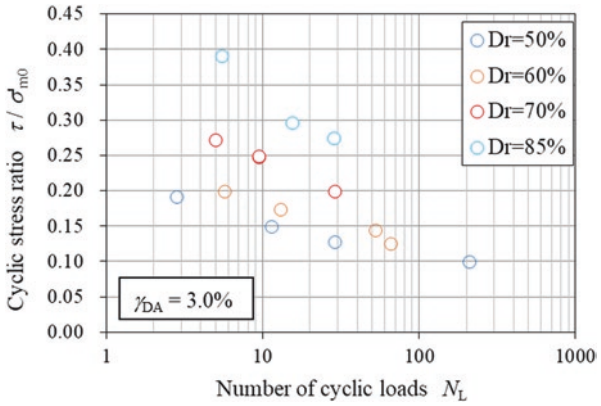

Fig. 4.6 Liquefaction resistance curve of Ottawa F-65 sand (γ_{DA} = 3.0%). (Vargas et al., 2020)

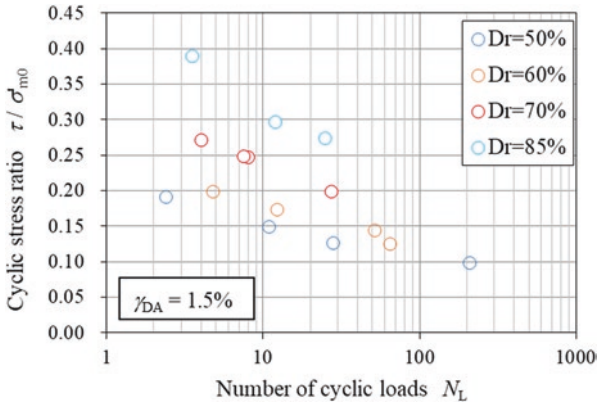

Fig. 4.7 Liquefaction resistance curve of Ottawa F-65 sand (γ_{DA} = 1.5%). (Vargas et al., 2020)

Figure 4.10 shows a comparison between the test results of Dr70_2 and Dr70_3 (repeatability test), including the development of excess pore water pressure ratio (EPWP ratio), the development of shear strain, and the corresponding stress path. The results indicate a good agreement between the tests, demonstrating that the tests are repeatable and consistent with each other.

4.6 Conclusions

This paper presents a series of hollow cylinder dynamic torsional shear tests performed to contribute to the understanding of the mechanical properties of Ottawa F-65 sand. The tests were developed at the installations of the Disaster Prevention Research Institute (DPRI) at Kyoto University, as part of the "LEAP-ASIA-2019" activities.

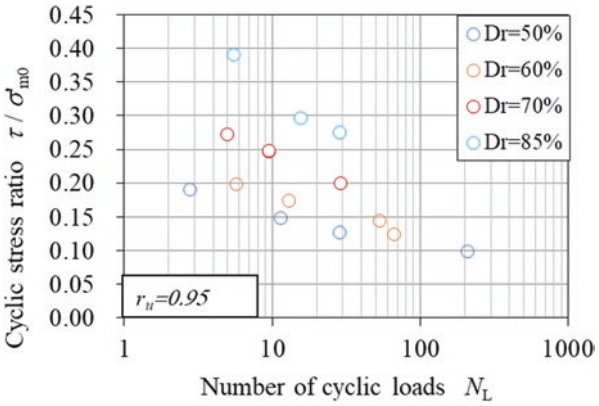

Fig. 4.8 Liquefaction resistance curve of Ottawa F-65 sand (r_u = 0.95). (Vargas et al., 2020)

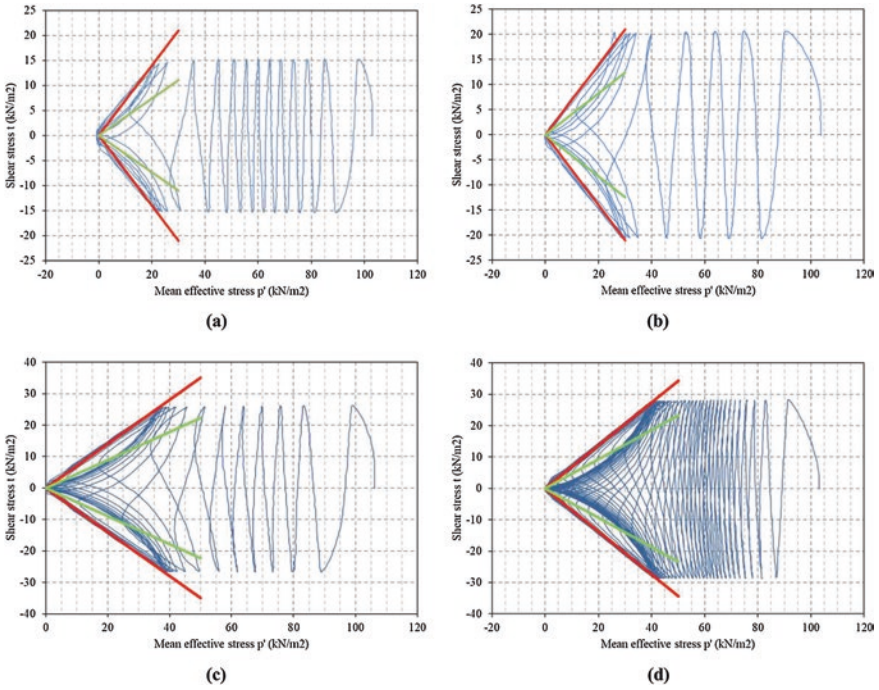

Fig. 4.9 (**a**) Stress path for Model Dr50_3. (**b**) Stress path for Model Dr60_5. (**c**) Stress path for Model Dr70_3. (**d**) Stress path for Model Dr80_2

- Based on 16 isotropically consolidated tests, the stress-strain characteristics of Ottawa F-65 sand were investigated under 4 different densities and a wide range of shear stress ratios.
- Based on the stress paths, it was shown that the friction angle ϕ_f remained constant for all relative densities ($\phi_f \approx 35°$); meanwhile, the phase transformation angle ϕ_p increased with the relative density.

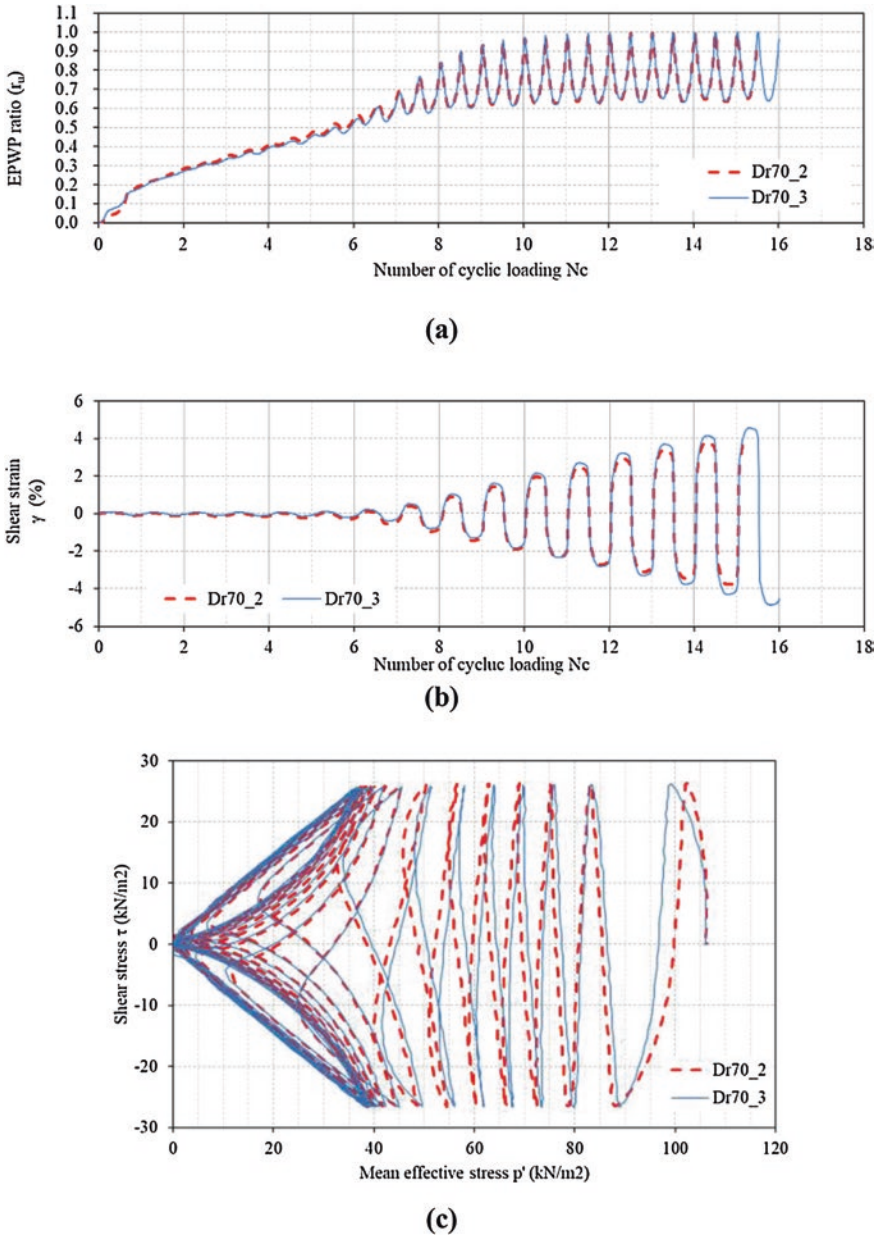

Fig. 4.10 (**a**) Development of EPWP – Models Dr70_2 and Dr70_3. (**b**) Development of shear strain – Models Dr70_2 and Dr70_3. (**c**) Stress path – Models Dr70_2 and Dr70_3. (Vargas et al., 2020)

- The good agreement in the repeatability tests shows that the tests are repeatable and consistent among each other; therefore, the provided test results are ready to be used in the calibration of constitutive models, simulation of element tests, V&V exercises/research, etc.

Appendix: Stress-Strain Characteristics of the Hollow Cylinder Dynamic Torsional Shear Tests (Figs. 4.A1, 4.A2, 4.A3, 4.A4, 4.A5, 4.A6, 4.A7, 4.A8, 4.A9, 4.A10, 4.A11, 4.A12, 4.A13, 4.A14, 4.A15 and 4.A16)

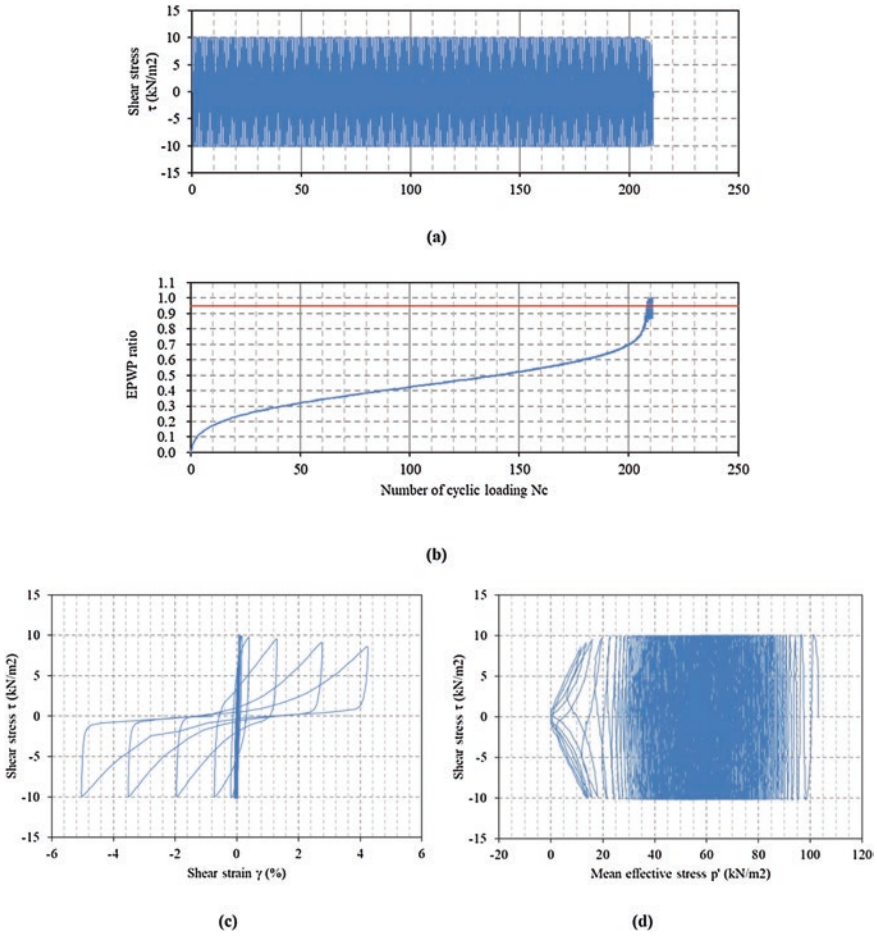

Fig. 4.A1 (**a**) Time history of shear stress – Model Dr50_1. (**b**) Time history of EPWP ratio development – Model Dr50_1. (**c**) Stress-strain curve – Model Dr50_1. (**d**) Stress path – Model Dr50_1

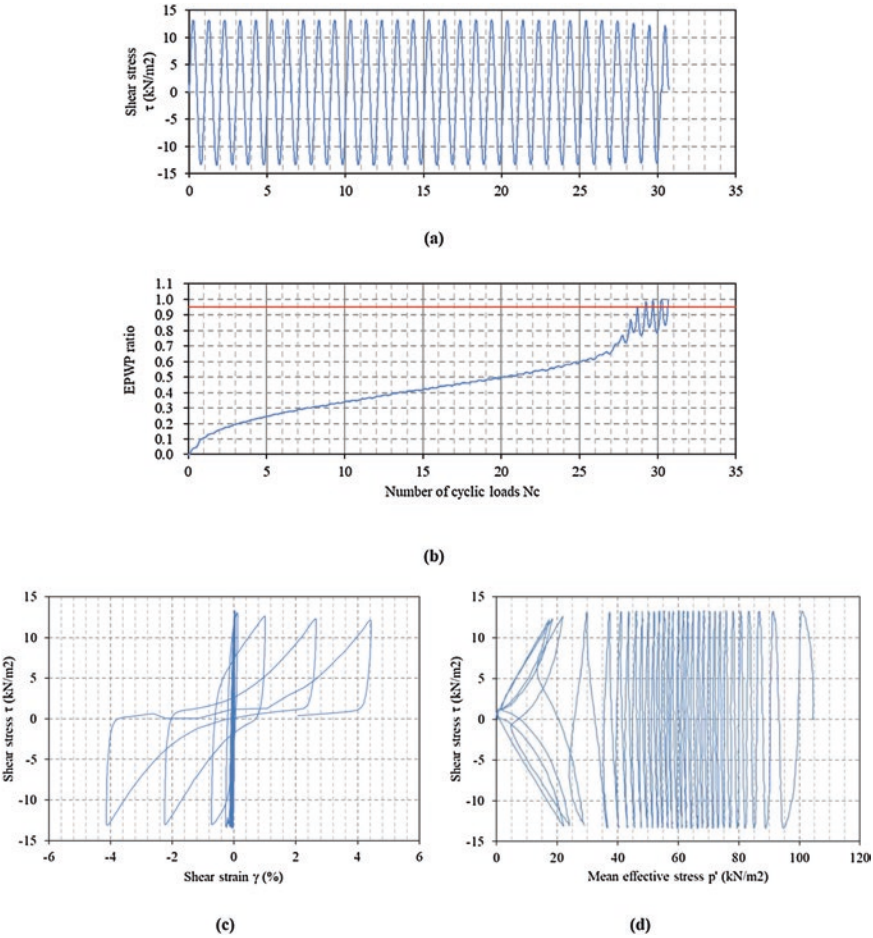

Fig. 4.A2 (**a**) Time history of shear stress – Model Dr50_2. (**b**) Time history of EPWP ratio development – Model Dr50_2. (**c**) Stress-strain curve – Model Dr50_2. (**d**) Stress path – Model Dr50_2

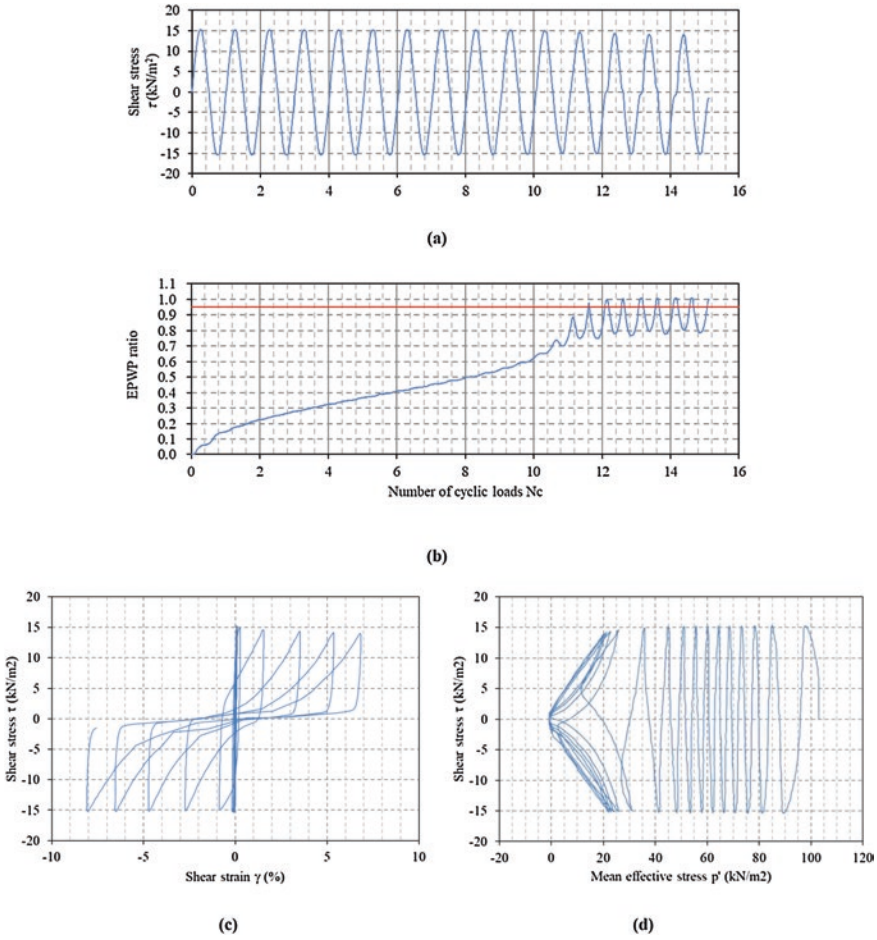

Fig. 4.A3 (**a**) Time history of shear stress – Model Dr50_3. (**b**) Time history of EPWP ratio development – Model Dr50_3. (**c**) Stress-strain curve – Model Dr50_3. (**d**) Stress path – Model Dr50_3

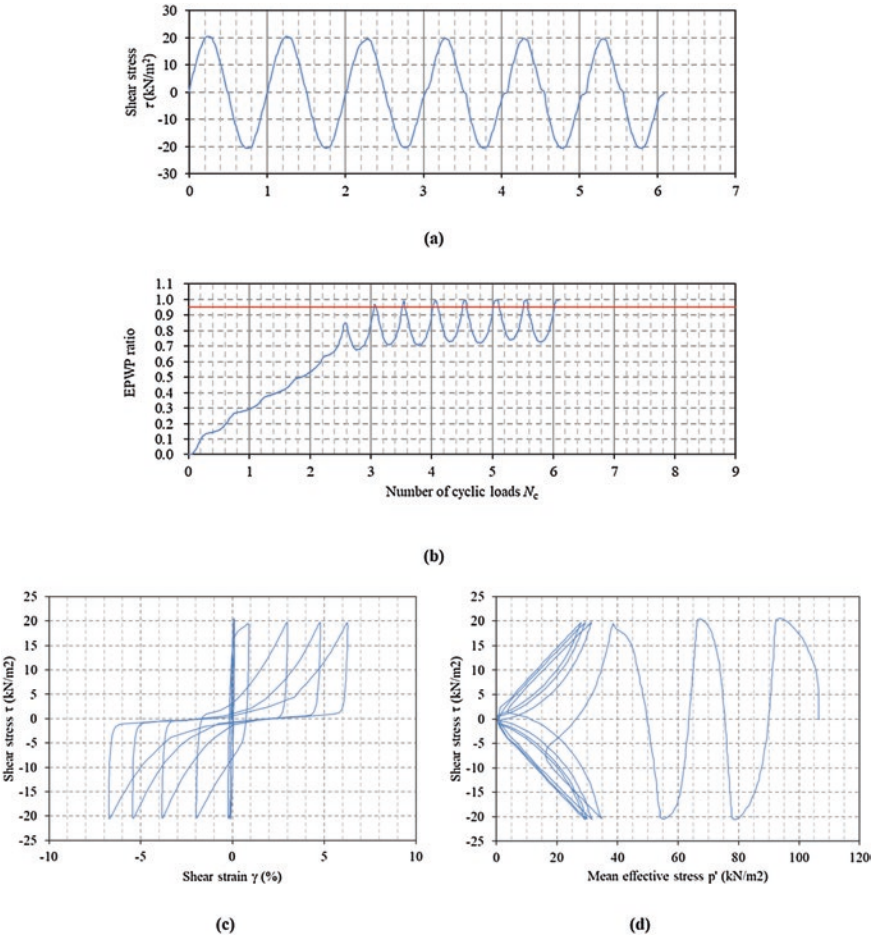

Fig. 4.A4 (**a**) Time history of shear stress – Model Dr50_4. (**b**) Time history of EPWP ratio development – Model Dr50_4. (**c**) Stress-strain curve – Model Dr50_4. (**d**) Stress path – Model Dr50_4

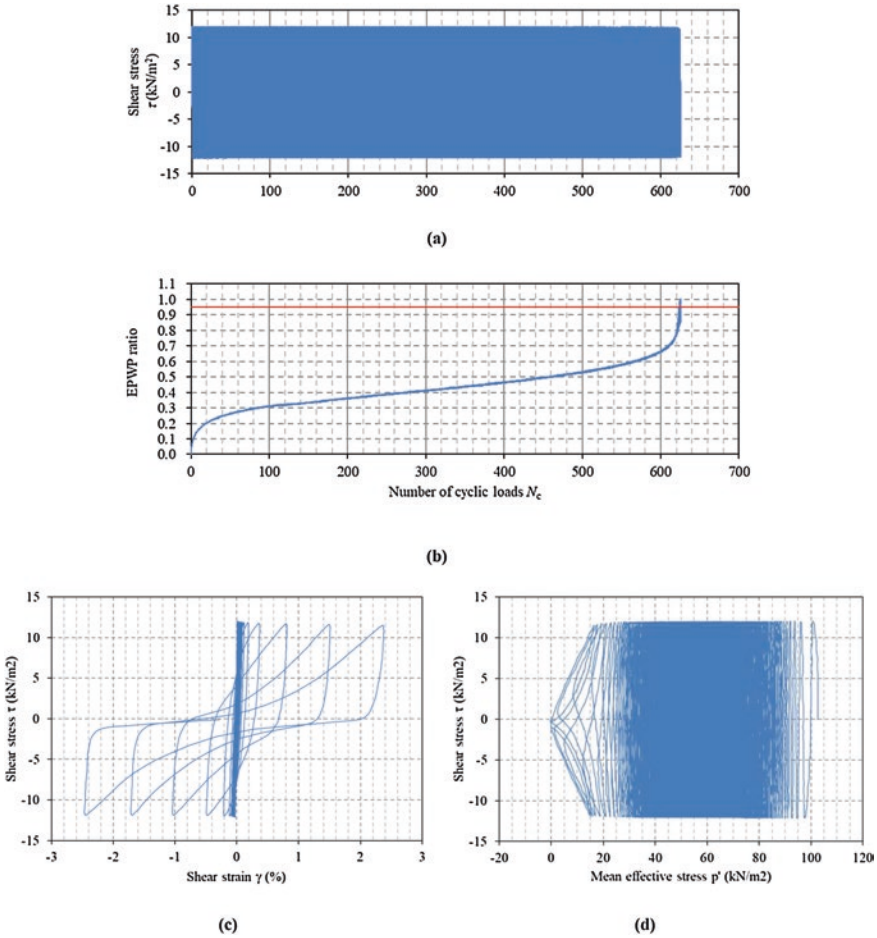

Fig. 4.A5 (**a**) Time history of shear stress – Model Dr60_1. (**b**) Time history of EPWP ratio development – Model Dr60_1. (**c**) Stress-strain curve – Model Dr60_1. (**d**) Stress path – Model Dr60_1

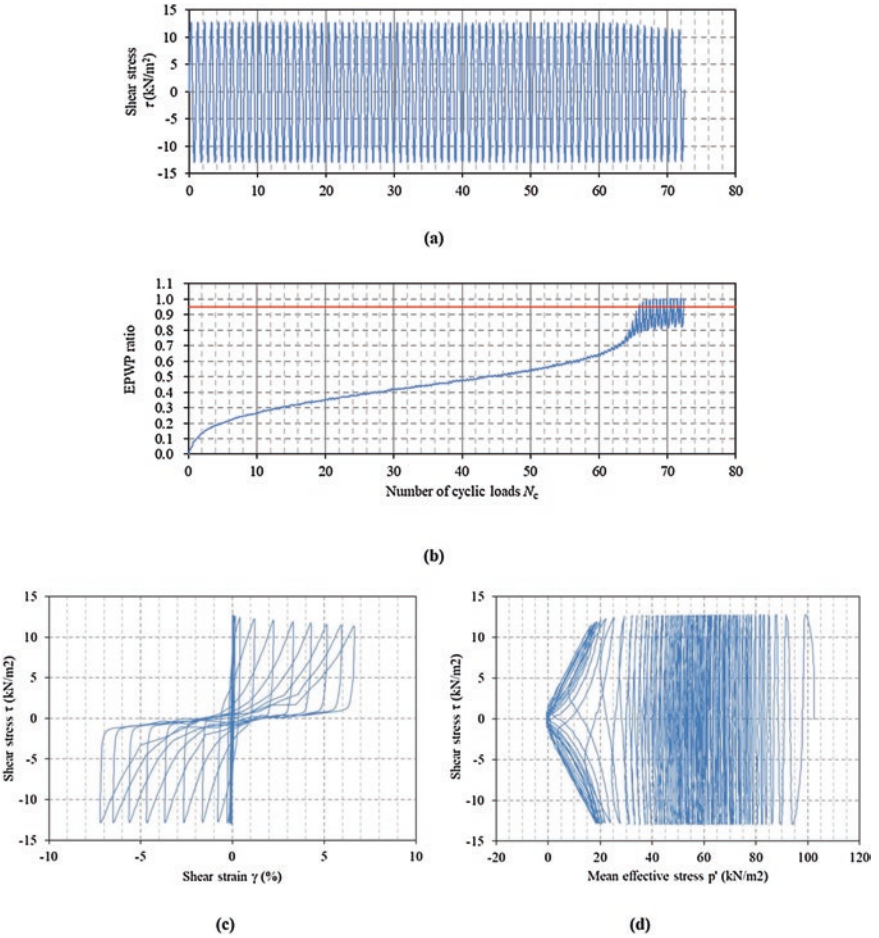

Fig. 4.A6 (**a**) Time history of shear stress – Model Dr60_2. (**b**) Time history of EPWP ratio development – Model Dr60_2. (**c**) Stress-strain curve – Model Dr60_2. (**d**) Stress path – Model Dr60_2

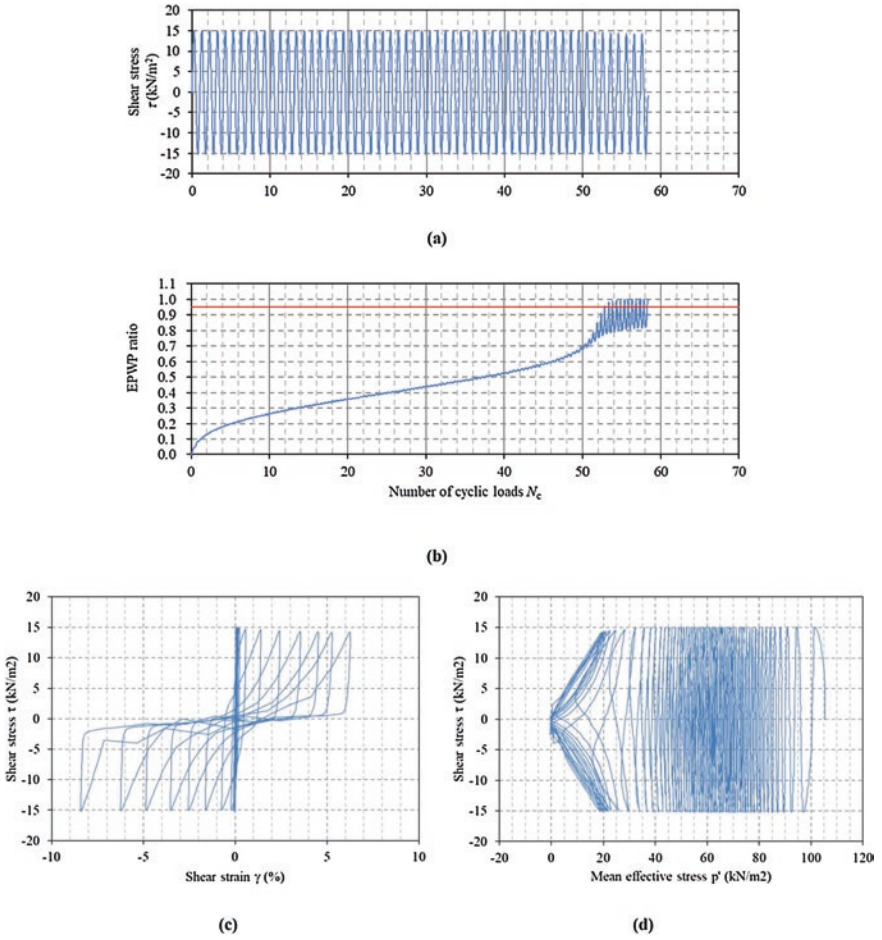

Fig. 4.A7 (**a**) Time history of shear stress – Model Dr60_3. (**b**) Time history of EPWP ratio development – Model Dr60_3. (**c**) Stress-strain curve – Model Dr60_3. (**d**) Stress path – Model Dr60_3

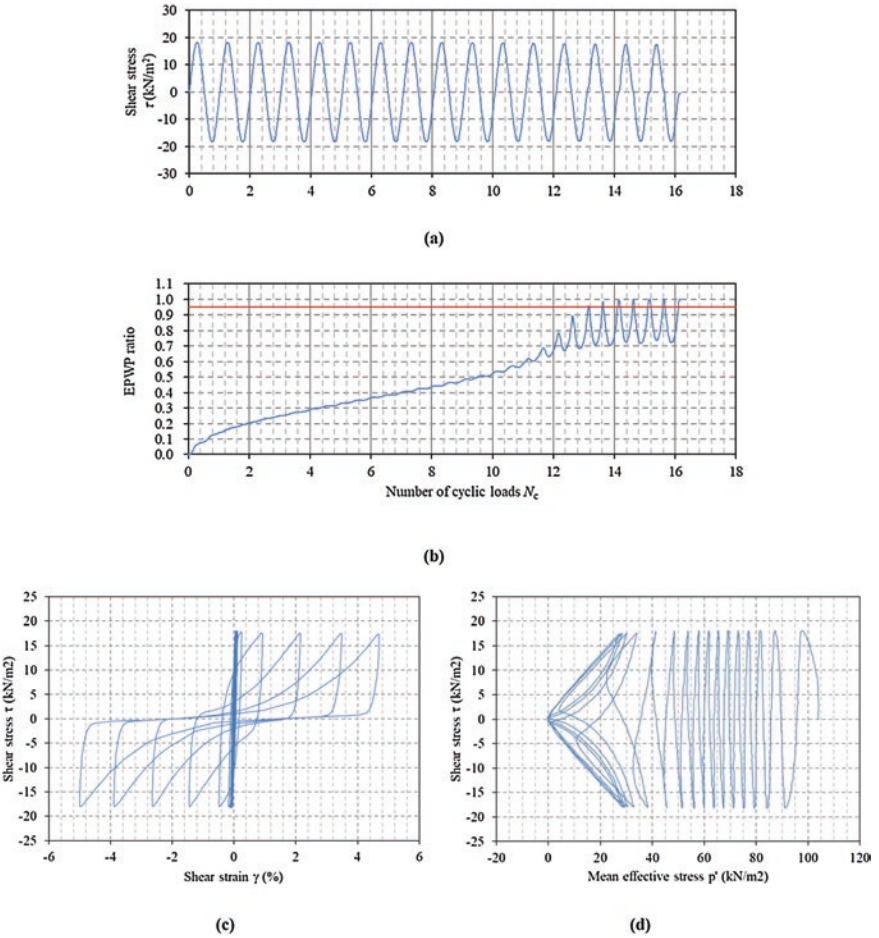

Fig. 4.A8 (**a**) Time history of shear stress – Model Dr60_4. (**b**) Time history of EPWP ratio development – Model Dr60_4. (**c**) Stress-strain curve – Model Dr60_4. (**d**) Stress path – Model Dr60_4

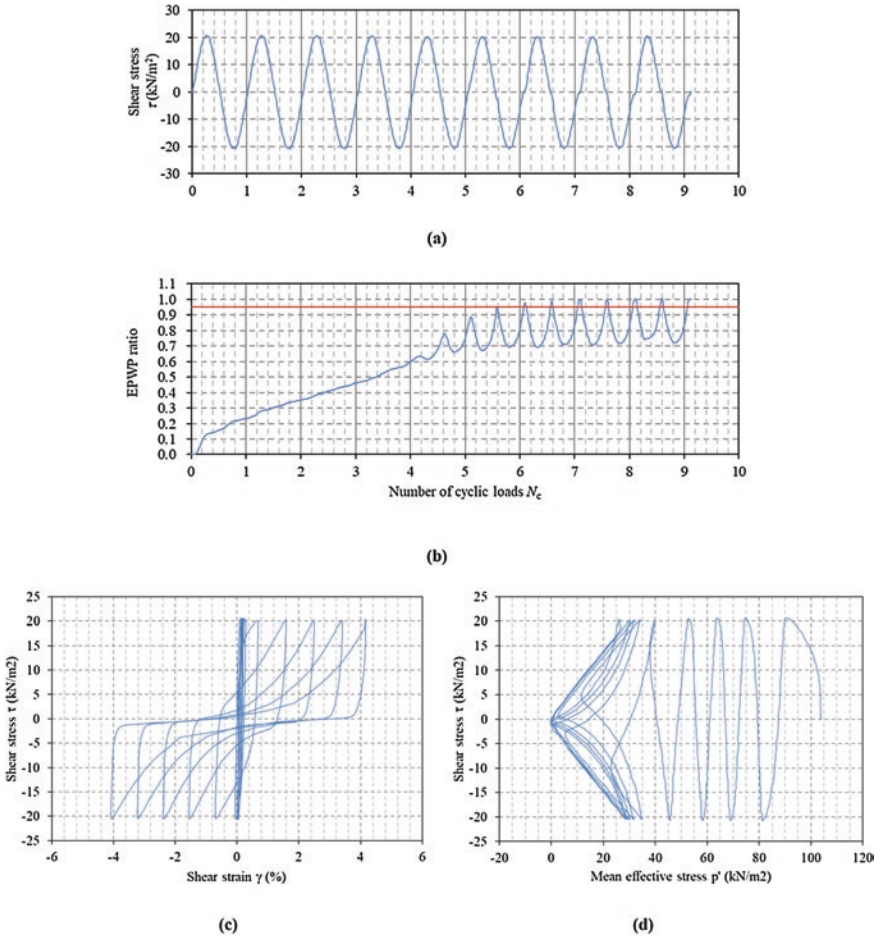

Fig. 4.A9 (**a**) Time history of shear stress – Model Dr60_5. (**b**) Time history of EPWP ratio development – Model Dr60_5. (**c**) Stress-strain curve – Model Dr60_5. (**d**) Stress path – Model Dr60_5

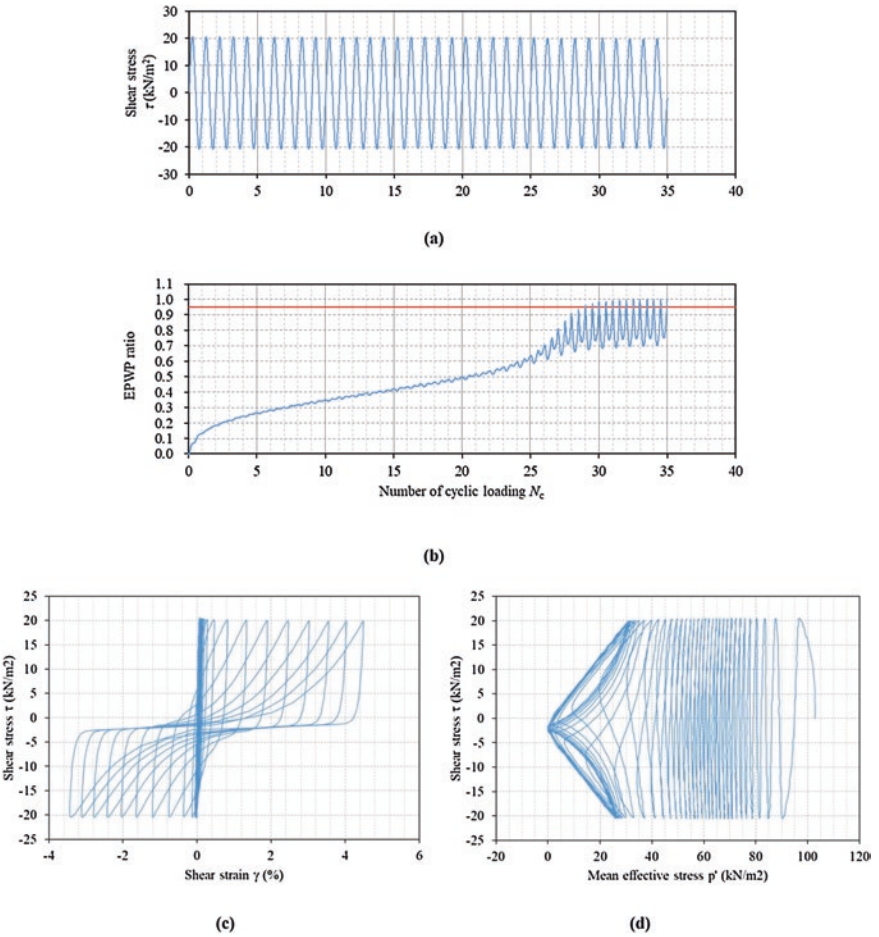

Fig. 4.A10 (**a**) Time history of shear stress – Model Dr70_1. (**b**) Time history of EPWP ratio development – Model Dr70_1. (**c**) Stress-strain curve – Model Dr70_1. (**d**) Stress path – Model Dr70_1

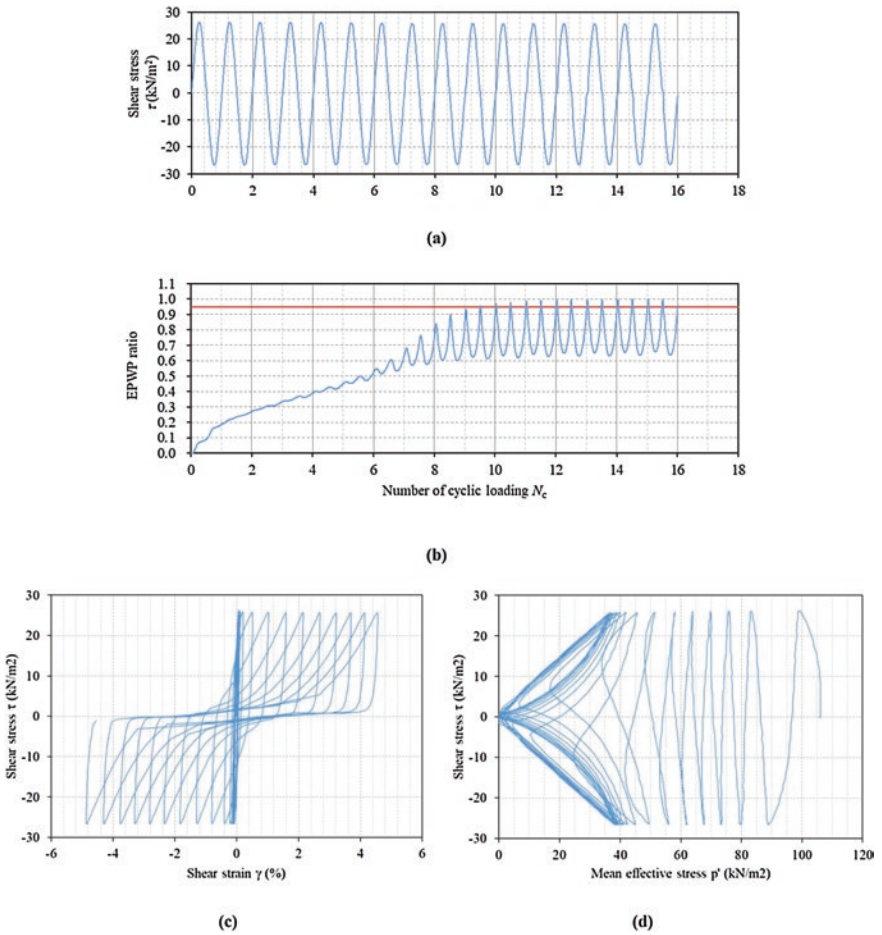

Fig. 4.A11 (**a**) Time history of shear stress – Model Dr70_2. (**b**) Time history of EPWP ratio development – Model Dr70_2. (**c**) Stress-strain curve – Model Dr70_2. (**d**) Stress path – Model Dr70_2

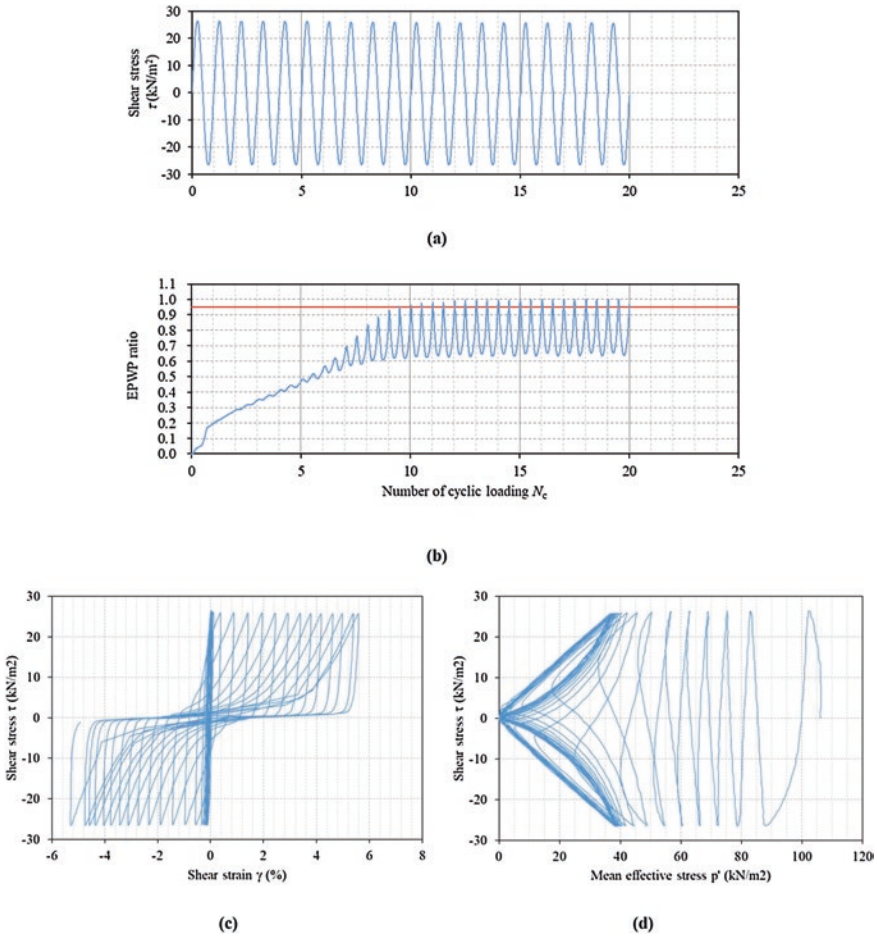

Fig. 4.A12 (**a**) Time history of shear stress – Model Dr70_3. (**b**) Time history of EPWP ratio development – Model Dr70_3. (**c**) Stress-strain curve – Model Dr70_3. (**d**) Stress path – Model Dr70_3

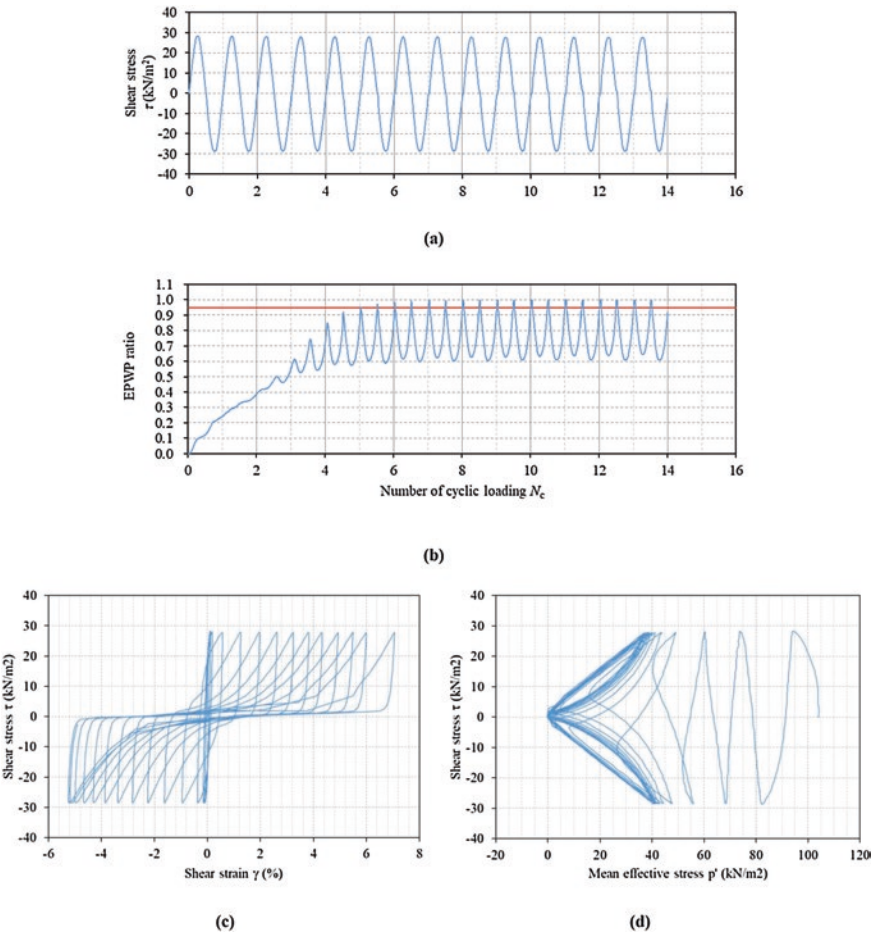

Fig. 4.A13 (**a**) Time history of shear stress – Model Dr70_4. (**b**) Time history of EPWP ratio development – Model Dr70_4. (**c**) Stress-strain curve – Model Dr70_4. (**d**) Stress path – Model Dr70_4

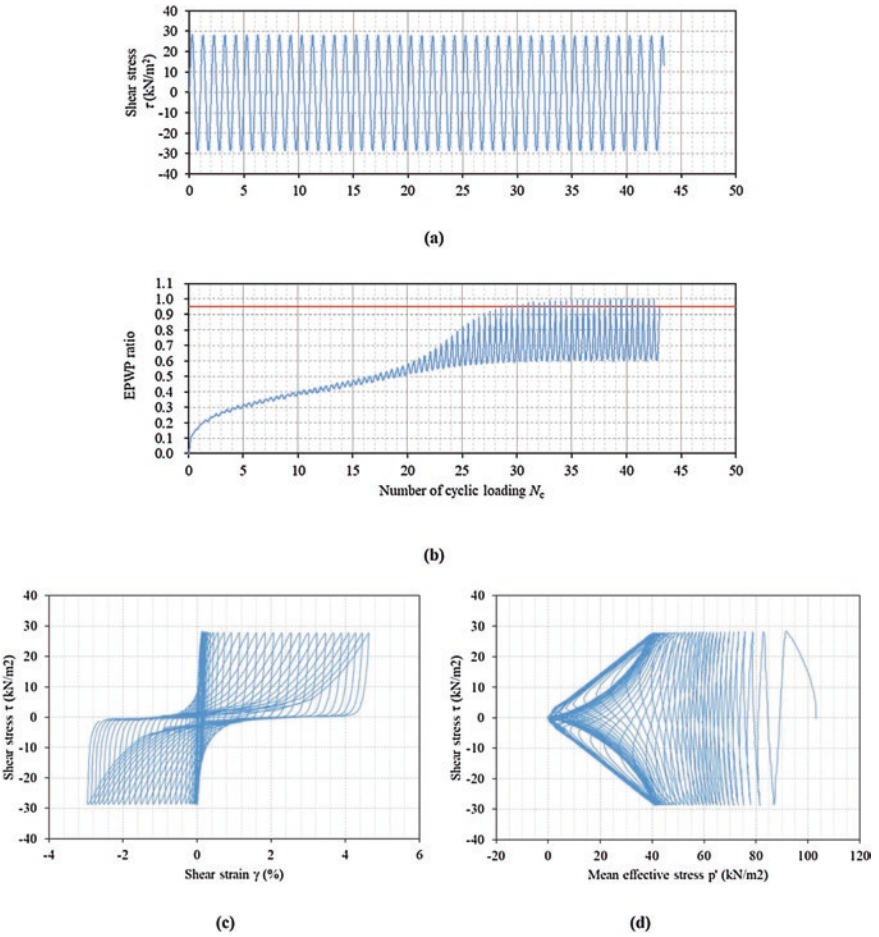

Fig. 4.A14 (**a**) Time history of shear stress – Model Dr85_1. (**b**) Time history of EPWP ratio development – Model Dr85_1. (**c**) Stress-strain curve – Model Dr85_1. (**d**) Stress path – Model Dr85_1

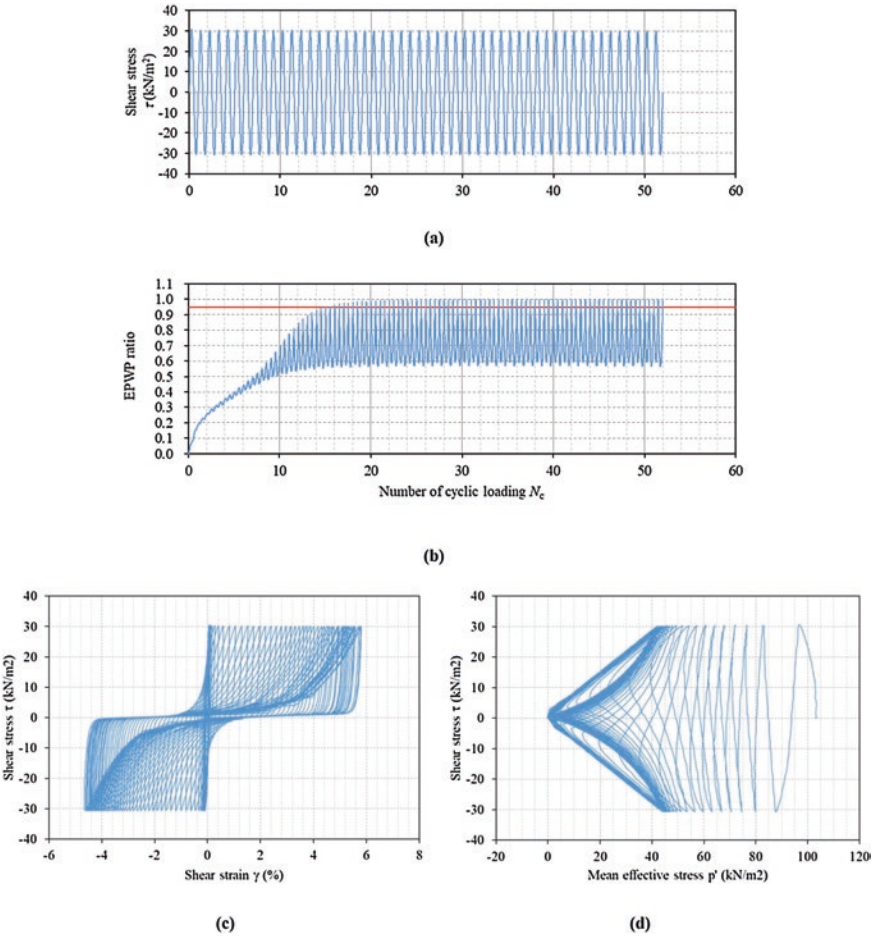

Fig. 4.A15 (**a**) Time history of shear stress – Model Dr85_2. (**b**) Time history of EPWP ratio development – Model Dr85_2. (**c**) Stress-strain curve – Model Dr85_2. (**d**) Stress path – Model Dr85_2

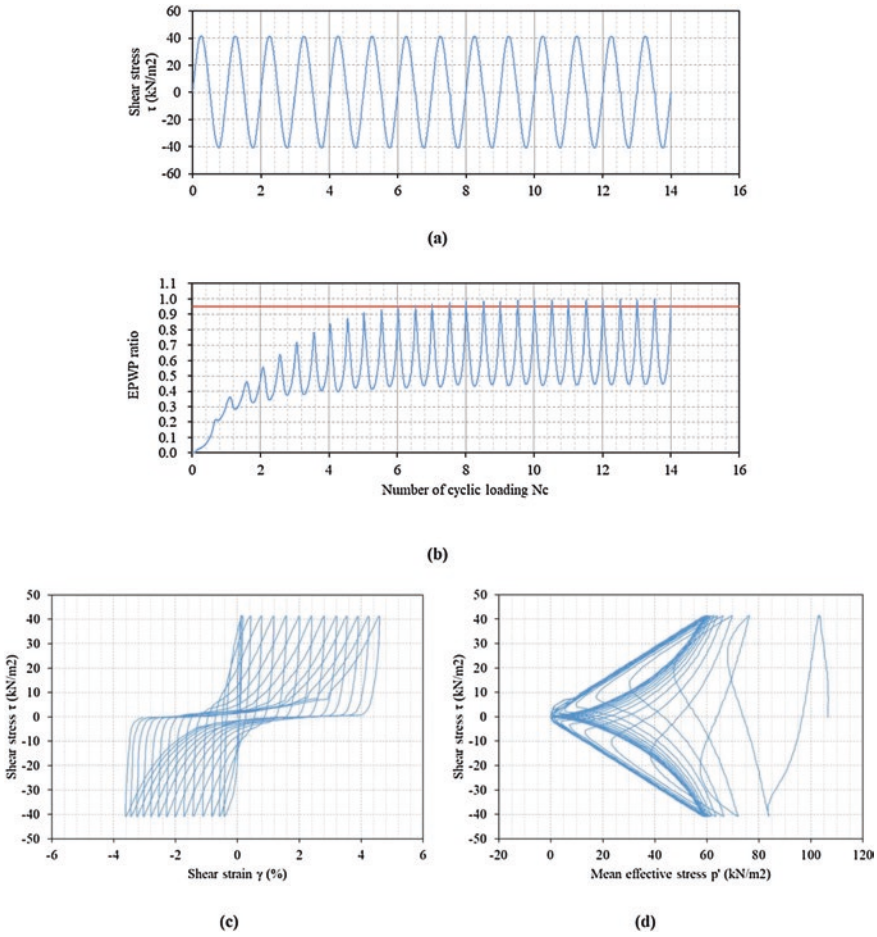

Fig. 4.A16 (**a**) Time history of shear stress – Model Dr85_3. (**b**) Time history of EPWP ratio development – Model Dr85_3. (**c**) Stress-strain curve – Model Dr85_3. (**d**) Stress path – Model Dr85_3

References

Carey, T. J., Stone, N., & Kutter, B. L. (2019). Grain size analysis and maximum and minimum dry density of Ottawa F-65 sand for LEAP-UCD-2017. Model Tests and Numerical Simulations of Liquefaction and Lateral Spreading: LEAP-UCD-2017.

El Ghoraiby, M. A., & Manzari, M. T. (2018). LEAP-2018 – Stress-strain response of Ottawa F65 sand in cyclic simple shear. *DesignSafe-CI, Dataset*, https://doi.org/10.17603/DS2HX3H

El Ghoraiby, M. A., Park, H., & Manzari, M. T. (2019). Physical and mechanical properties of Ottawa F65 sand. Model Tests and Numerical Simulations of Liquefaction and Lateral Spreading: LEAP-UCD-2017.

Japanese Geotechnical Society Standards. (2016). Method for cyclic triaxial test on soils – JGS-0541-2009 Laboratory Testing Standards of Geomaterials, Vol. 2.

Japanese Geotechnical Society Standards. (2018a). Practice for preparing hollow cylindrical specimens of soils for torsional shear test – JGS-0550-2009. Laboratory Testing Standards of Geomaterials, Vol. 3.

Japanese Geotechnical Society Standards. (2018b). Method for torsional shear test on hollow cylindrical specimens of soils – JGS-0551-2009. Laboratory Testing Standards of Geomaterials, Vol. 3.

Koseki, J., Yoshida, T., & Sato, T. (2005). Liquefaction properties of Toyoura sand in cyclic torsional shear tests under low confining stress. *Soil and Foundations, 45*(5), 103–113.

Parra Bastidas, A. M. (2016). Ottawa F-65 sand characterization. PhD Dissertation, University of California, Davis.

Tobita, T., Ichii, K., Ueda, K., Uzuoka, R., Vargas, R., Okamura, M., Sjafruddin, A. N., Takemura, J., Hang, L., Iai, S., Boksmati, J., Fusco, A., Torres-Garcia, S., Haigh S, Madabhushi G, Manzari M, Escoffier, S., Li, Z., Kim, D. S., Manandhar, S., Hung, W. Y., Huang, J. X., Pham, T. N. P., Zeghal, M., Abdoun, T., Korre, E., Kutter, B. L., Carey, T. J., Stone, N., Zhuo, Y. G., Liu, K., & Ma, Q. (2023). LEAP-ASIA-2019: Summary of centrifuge experiments on liquefaction-induced lateral spreading: Validation and applicability of the generalized scaling law.

Ueda, K., Tanaka, Y., Sahare, A., Elgamal, A., Qiu, Z., Wang, R., Zhu, T., Zhou, C., Zhang, J.M., Reyes-Parra, A., Barrero, A., Taiebat, M., Yuyama, W., Iai, S., Hyodo, J., Ichii, K., Elbadawy, M., Zhou, Y. G., Fasano, G., Chiaradonna, A., Bilotta, E., Arduino, P., Zeghal, M., Manzari, M., & Tobita, T. (2023). LEAP-ASIA-2019 simulation exercise: Calibration of constitutive models and simulations of the element tests.

Vargas, R., Ueda, K., & Uemura, K. (2020). Influence of the relative density and K0 effects in the cyclic response of Ottawa F-65 sand – Cyclic torsional hollow-cylinder shear tests for LEAP-ASIA-2019. *Soil Dynamics and Earthquake Engineering, 133*, 106111. https://doi.org/10.1016/j.soildyn.2020.106111

Vasko, A. (2015). An investigation into the behavior of Ottawa sand through monotonic and cyclic shear tests. MS thesis. George Washington University.

Part II
Centrifuge Experiment Papers

Jun-Xue Huang and Wen-Yi Hung

Chapter 5
LEAP-ASIA-2019 Centrifuge Tests at University of Cambridge

Gopal S. P. Madabhushi, Stuart K. Haigh, Jad I. Boksmati, Samy Garcia-Torres, and Alessandro Fusco

Abstract Two dynamic centrifuge tests were conducted on a 5° liquefiable slope with a slope depth of 4 m at the centre line, as part of LEAP-ASIA-2019 at the Schofield Centre, University of Cambridge. The main purpose of these tests was to investigate the suitability of the generalised scaling laws proposed by Iai et al. (Geotechnique, 55(5):355–362, 2005). The two tests were carried out at two drastically different g levels, CU Model B at 80 g and CU Model B1 at 1 g, with corresponding virtual scaling factors of 0.5 and 40, respectively. Following the principles of generalised scaling, results from both tests should be representative of the same slope profile with a slope depth of 4 m previously tested as part of LEAP-UCD-2017. CU Model B exhibited typical liquefaction behaviour with substantial reduction in acceleration transmission along the depth of the slope coupled with considerable excess pore pressure build-up during shaking. For a similar input motion, the slope in CU Model B1 at 1 g showed little deformations. Intensity of the input motion had to be increased by nearly twofolds to trigger slope movements that can be measured by PIV.

Keywords Liquefaction Experiments and Analysis Projects (LEAP-ASIA-2019) · Generalised scaling law (GSL) · Centrifuge modelling

5.1 Introduction

Numerical analysis related to geotechnical research has been widely performed during the last decades as it presents benefits in time and cost optimisation. However, reliable experimental data related to earthquake effects such as liquefaction phenomena is still required in order to validate numerical procedures. Liquefaction Experiments and Analysis Projects (LEAP) was commissioned to develop a

G. S. P. Madabhushi (✉) · S. K. Haigh · J. I. Boksmati · S. Garcia-Torres · A. Fusco
Department of Engineering, Cambridge University, Cambridge, UK
e-mail: mspg1@cam.ac.uk

T. Tobita et al. (eds.), *Model Tests and Numerical Simulations of Liquefaction and Lateral Spreading II*, https://doi.org/10.1007/978-3-031-48821-4_5

database of centrifuge data on the liquefaction of slopes from tests performed at different institutions. The LEAP-ASIA-2019 is a sub-programme of LEAP, which aims to investigate the suitability of the generalised scaling laws proposed by Iai et al. (2005) at different g levels and virtual scaling factors. In this paper, two dynamic high gravity tests were carried out on a 5° liquefiable slope subjected to a 1 Hz ramped sine wave input motion. The two tests were conducted at two drastically different g levels "η" of 80 g and 1 g, with virtual 1 g scaling factors "μ" of 0.5 and 40, respectively. Following the principles of generalised scaling laws, these two tests would represent the same slope geometry at prototype. The models have been prepared following the procedures stated in LEAP-GWU-2015 (Madabhushi et al., 2018) and LEAP-UCD-2017 (Madabhushi et al., 2019). All results presented in this paper are scaled to prototype using Iai et al. (2005) unless otherwise stated.

5.2 Experiment Setup

Two tests were performed, one at 80 g (CU Model B) and one at 1 g (CU Model B1), using the centrifuge testing facilities at the Schofield Centre, University of Cambridge. The model represents a 5-degree slope in Ottawa sand, with a length of 20 m and a central depth of 4 m at prototype scale, which was the same prototype slope profile used during LEAP-UCD-2017. The general schematic layout of the slope profile and instrumentation used in the tests is shown in Fig. 5.1.

5.2.1 Sand Pouring

Ottawa sand was poured by air pluviation using the automated spot pluviator (Madabhushi et al., 2006). The sand density was achieved by controlling the flow rate with a nozzle of 5 mm and a drop height of 810 mm. These parameters were obtained by pre-test pouring calibrations to achieve a target density of 1640 kg/m^3.

During pouring, the strong window box was placed on a scale in order to obtain the mass of sand poured after each pluviation pass. Height of poured sand was measured using a digital calliper. The readings were recorded along a grid of 20 points at specific poured layers. Figure 5.2 shows the grid pattern adopted for the sand depth measurements. Results of the sand density achieved for the different layers are presented in Fig. 5.3.

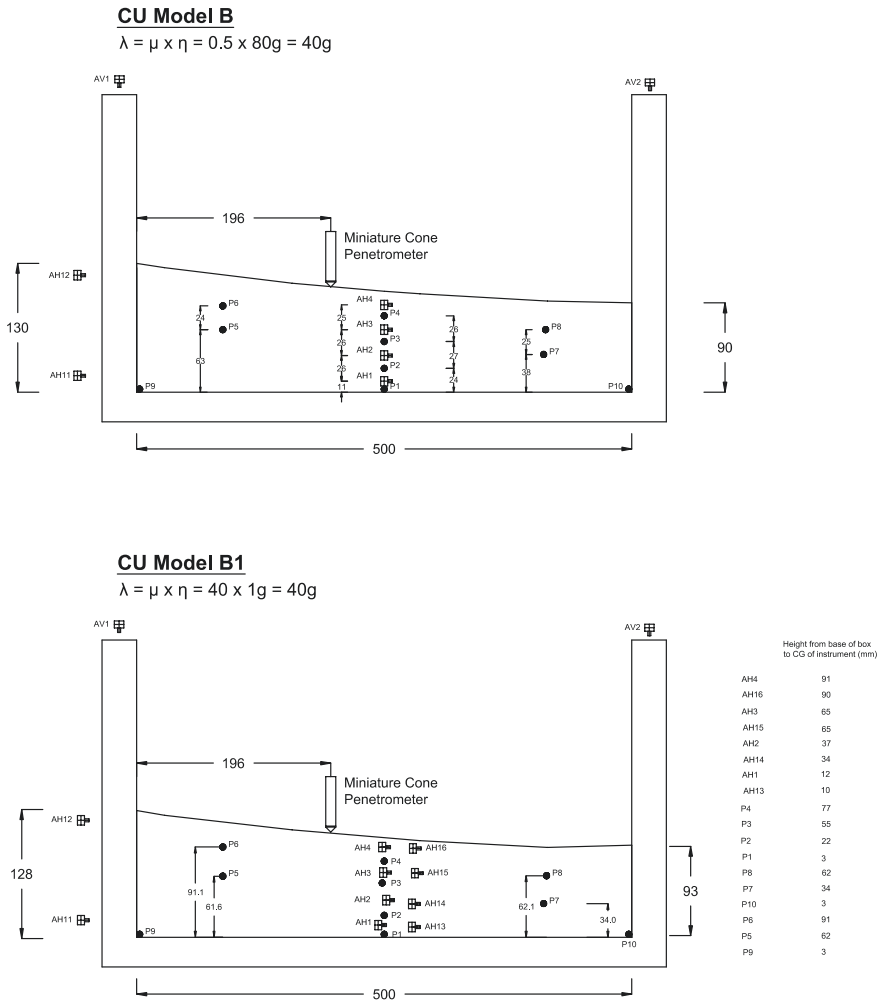

Fig. 5.1 Centrifuge model schematic showing instrument positions

5.2.2 Saturation

The saturation was conducted using the CAM-SAT system that regulates mass influx of fluid into sand models following Stringer and Madabhushi (2009). The mass rate was set to 0.4 kg/h in order to prevent sand boiling. The model was flushed with CO_2 in three cycles before the saturation stage in order to enhance the acquired vacuum. Figure 5.4 shows the saturation setup used in these two tests.

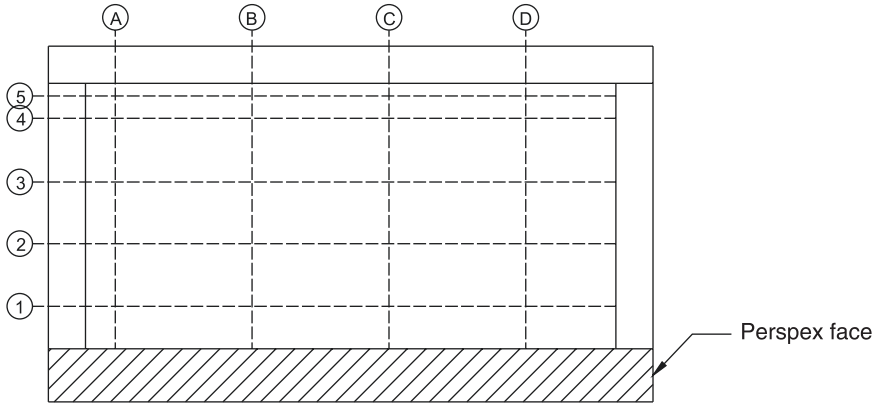

Fig. 5.2 Digital calliper grid for surface measurements

5.2.3 Viscosity Measurement

The model saturation required the use of hydroxypropyl methylcellulose (HPMC) solution in order to increase the fluid viscosity and to meet the generalised scaling laws proposed by Iai et al. (2005). Prior to initiating saturation, viscosity of the fluid was measured using a viscometer to ensure compliance with the generalised scaling factor for viscosity: 47.6 cSt for CU Model B and 15.9 cSt for CU Model B1.

5.2.4 Slope Cutting

Once saturation was complete, the flat bed of sand was cut into the required logarithmic spiral profile using cutting plate guides running along the length of the container as shown in Fig. 5.5. Before cutting, the saturated model was partially drained to lower the methylcellulose level in the sand. This procedure relies on capillary suction between individual grains to increase effective stresses in the sand to facilitate cutting (Madabhushi et al., 2018). To compensate for the 1 g gravitational component acting on the model, a 1:80 slope was also cut along the transverse direction of the container for CU Model B.

5.2.5 CPT

In both tests, an in-flight CPT was mounted on the package to obtain a soil strength profile before and after shaking. Although this device differs from the CPT used in UC Davis, previous centrifuge tests have verified the equivalence between both instruments (Carey et al., 2018; Madabhushi et al., 2019).

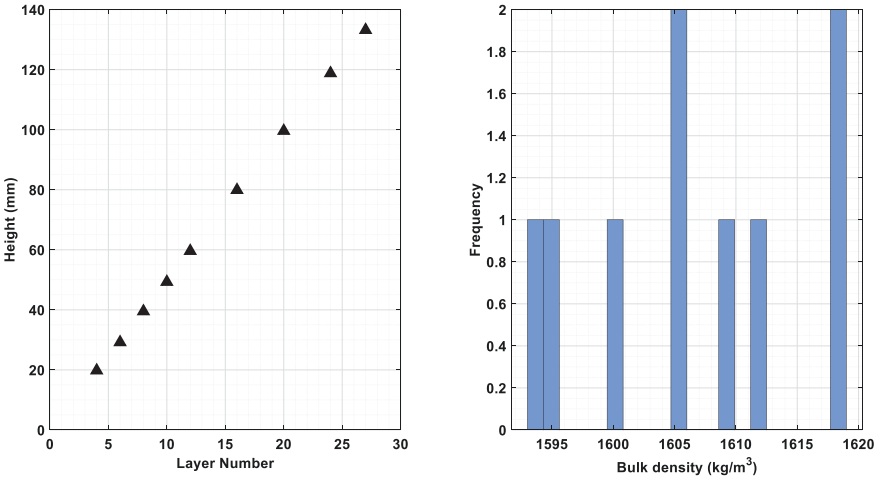

[a]

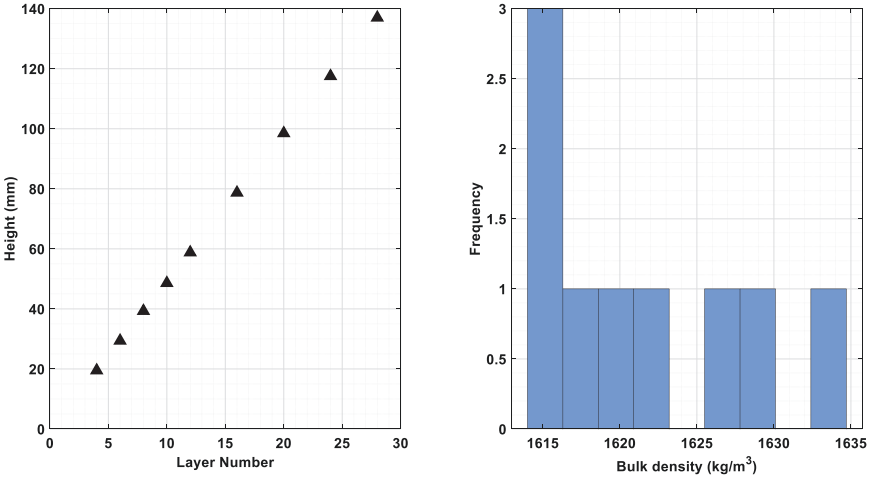

[b]

Fig. 5.3 Bulk density measurements inferred from calliper and scale measurements at each layer: (**a**) CU Model B and (**b**) CU Model B1

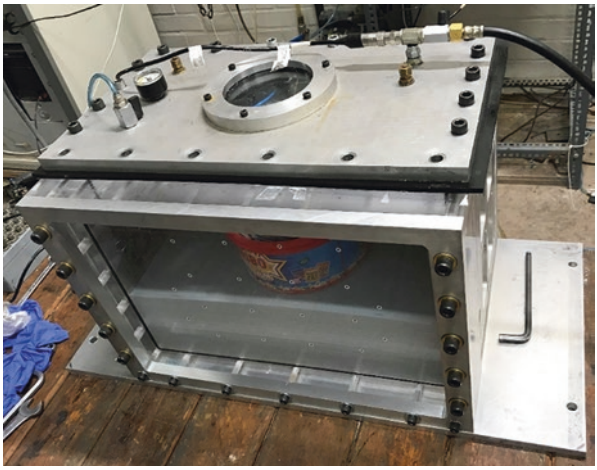

Fig. 5.4 Model saturation

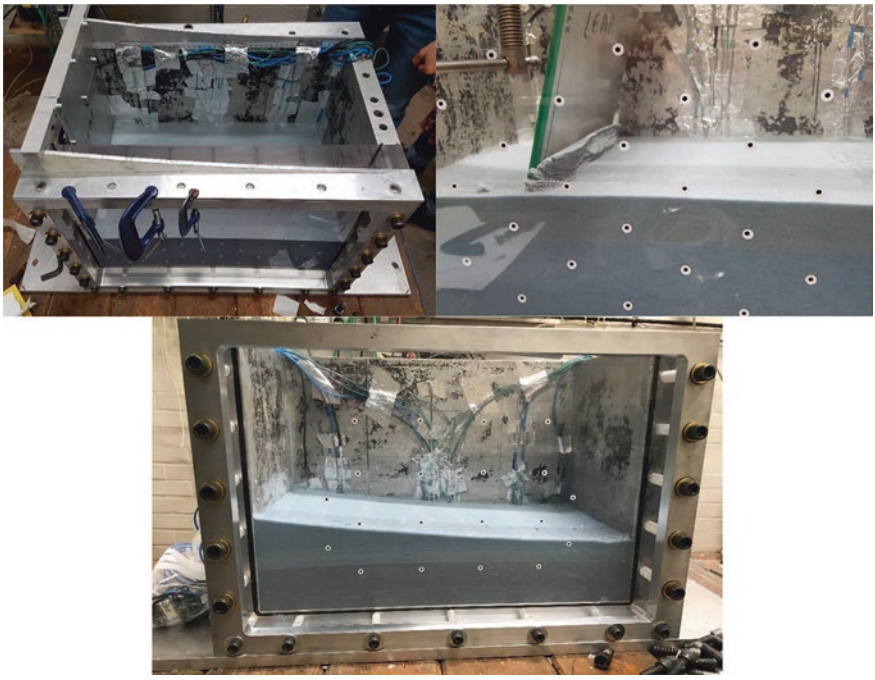

Fig. 5.5 Use of cutting guide plates to achieve the desired slope profile

Table 5.1 Generalised scaling laws for CU Model B

Quantity	Model/prototype η = 80 g (virtual/physical) μ = 0.5 (prototype/virtual)	
Length (m)	$1/\mu\eta$	$1/(0.5 \times 80) = 1/40$
Time (s)	$1/\mu^{0.75}\eta$	$1/(0.5^{0.75} \times 80) = 1/47.6$
Acceleration (g)	η	80
Frequency (Hz)	$(\mu^{0.75}\eta)$	$0.5^{0.75} \times 80 = 47.6$
Viscosity (cSt)	$\mu^{0.75}\eta$	$0.5^{0.75} \times 80 = 47.6$
Force (N)	$\mu^3\ \eta^2$	$0.5^3 \times 80^2 = 800$
Pore pressure (kPa)	μ	0.5

Table 5.2 Generalised scaling laws for CU Model B1

Quantity	Model/prototype η = 1 g (virtual/physical) μ = 40 (prototype/virtual)	
Length (m)	$1/\mu\eta$	$1/(40 \times 1) = 1/40$
Time (s)	$1/\mu^{0.75}\eta$	$1/(40.0^{0.75} \times 1) = 1/15.9$
Acceleration (g)	η	1
Frequency (Hz)	$(\mu^{0.75}\eta)$	$40^{0.75} \times 1 = 15.9$
Viscosity (cSt)	$\mu^{0.75}\eta$	$40^{0.75} \times 1 = 15.9$
Force (N)	$\mu^3\ \eta^2$	$40^3 \times 1^2 = 64{,}000$
Pore pressure (kPa)	μ	40

5.2.6 Scaling Laws

The scaling laws proposed by Iai et al. (2005) for CU Model B and CU Model B1 are summarised in Table 5.1 and Table 5.2, where η is the centrifuge scaling factor and μ is the virtual 1 g scaling factor. The generalised scaling factor λ is then the product of $\mu \times \eta$.

5.3 Results

5.3.1 Destructive Motions

The target input motion set for CU Model B and CU Model B1 was a ramped 1 Hz sine wave with a peak ground acceleration of 0.25 g. Figure 5.6 shows the recorded base accelerations for the two tests conducted. The recorded signals are decomposed into the main 1 Hz driving frequency component superimposed with higher harmonics introduced by the mechanical response of the servo-shaker. A prototype PGA of 0.29 g was recorded for CU Model B and 0.57 g for CU Model B1. Prior to firing the 0.57 g earthquake in CU Model B1, two weaker input motions were triggered. The observed slope displacements for these two motions were negligible,

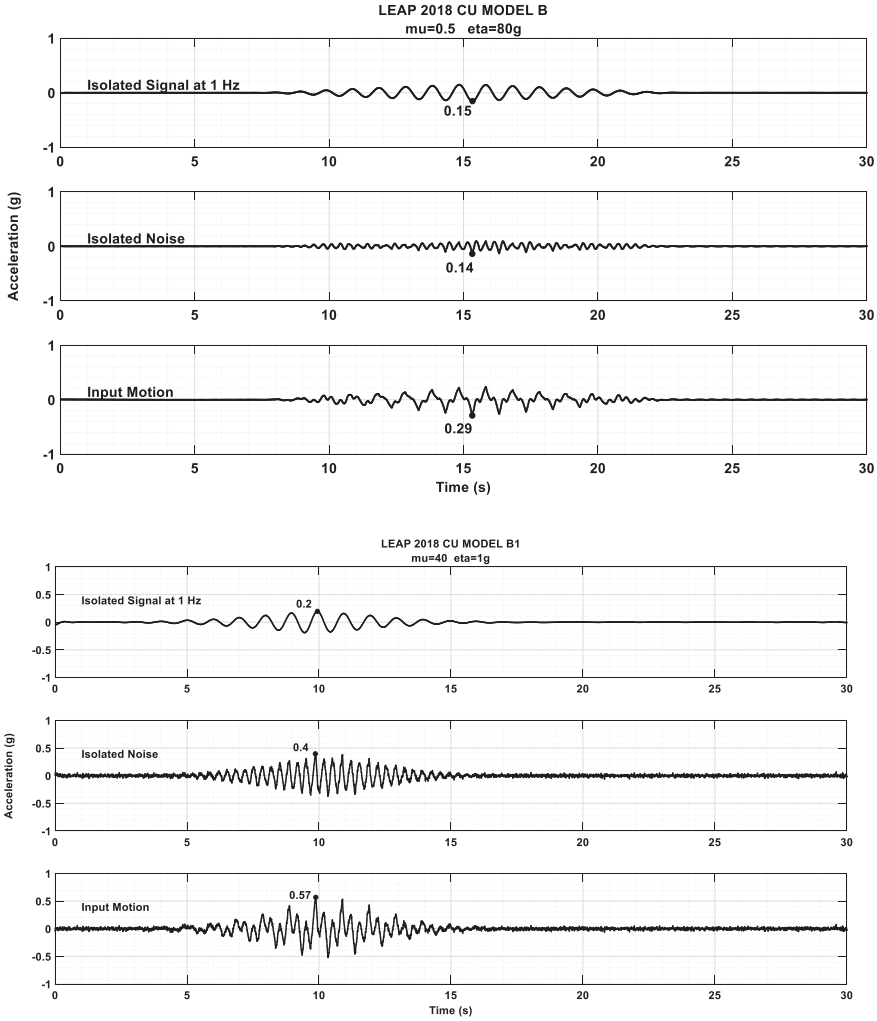

Fig. 5.6 Isolated input signal and high-frequency components of input motion

which warranted an increase in the intensity of input motion to 0.57 g to trigger measurable slope movements. Consequently, only data from the stronger ramped input motion is presented for CU Model B1.

It is worth mentioning that the intensity of the higher harmonics is more prominent in the input signal for CU Model B1 at 1 g than it is for CU Model B at 80 g. It is believed that the higher g level provides better coupling between the shaking table and driving actuator in the servo-shaker and mitigates any tendency for rocking, resulting in lower-intensity high-frequency harmonics.

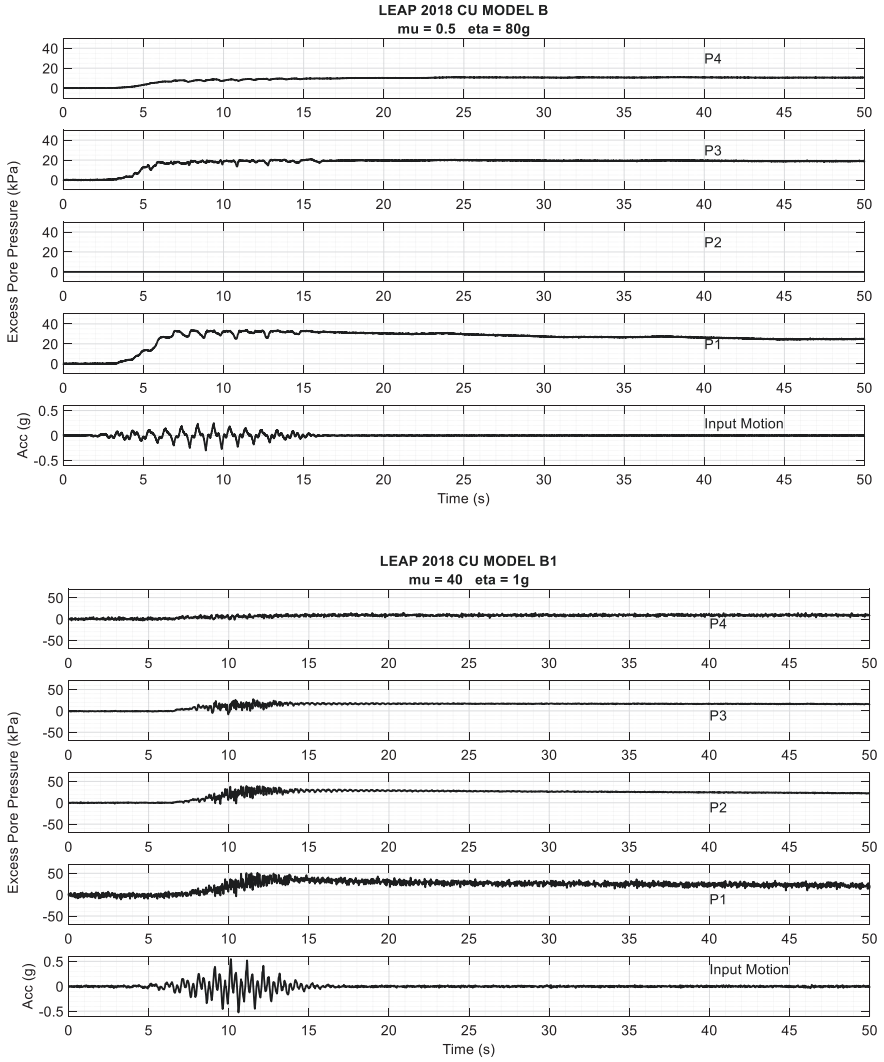

Fig. 5.7 Excess pore pressures recorded by the central PPT array

5.3.2 Excess Pore Pressure

Excess pore pressure time histories for both tests of the central arrays are presented in Figs. 5.7, 5.8 and 5.9. For CU Model B, considerable excess pore pressures were recorded after the fourth cycle of the shaking. Soil along the depth of the slope reaches complete liquefaction. In CU Model B1, after multiplying pore pressure

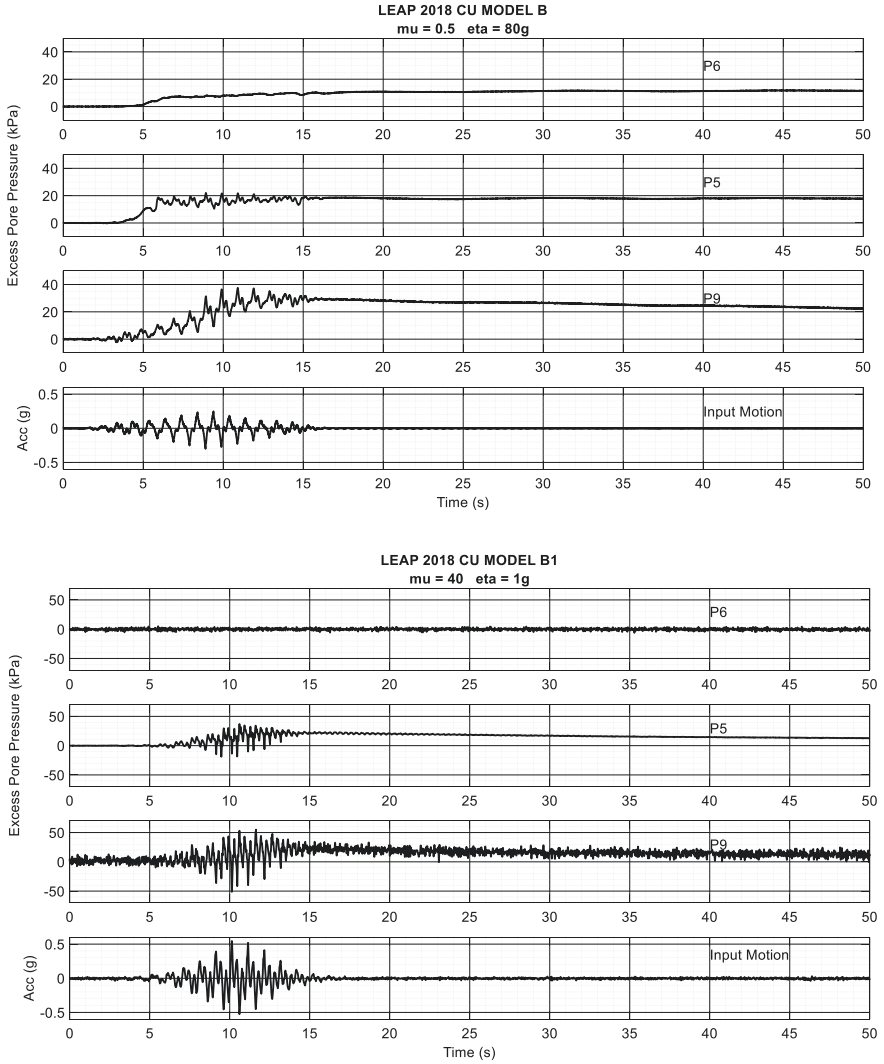

Fig. 5.8 Excess pore pressures recorded by the left PPT array

transducer results by 40 (i.e. the generalised scaling factor for pore pressure), the build-up of excess pore pressures between CU Model B and CU Model B1 is comparable. Nevertheless, the cyclic response of excess pore pressures between the two tests is different. As shown in Fig. 5.8, excess pore pressures nearer to the crest of the slope record much larger suction spikes during the earthquake at 1 g compared to the results at 80 g. During the earthquake, sand within the slope is subjected to cyclic shear stresses, which, in the case of 1 g test on CU Model B1, cause the sand

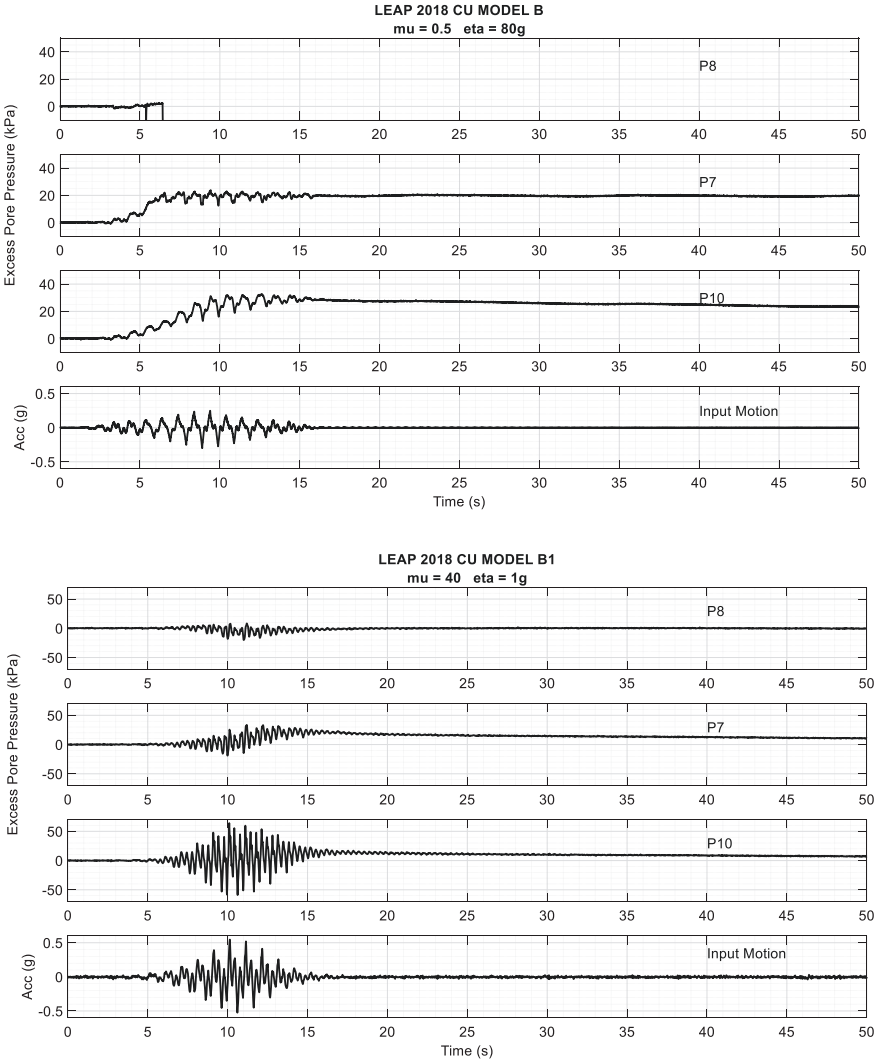

Fig. 5.9 Excess pore pressures recorded by the right PPT array

to dilate strongly owing to the low confining stresses. This results in sharp negative excess pore pressure spikes. The higher intensity of the input motion harmonics for CU Model B1 may have also contributed to this observation. However, it is felt that the scaling up of the measured excess pore pressures by a factor of "40" as prescribed by the generalised scaling laws meant that the oscillations in the excess pore pressures are amplified by a large factor.

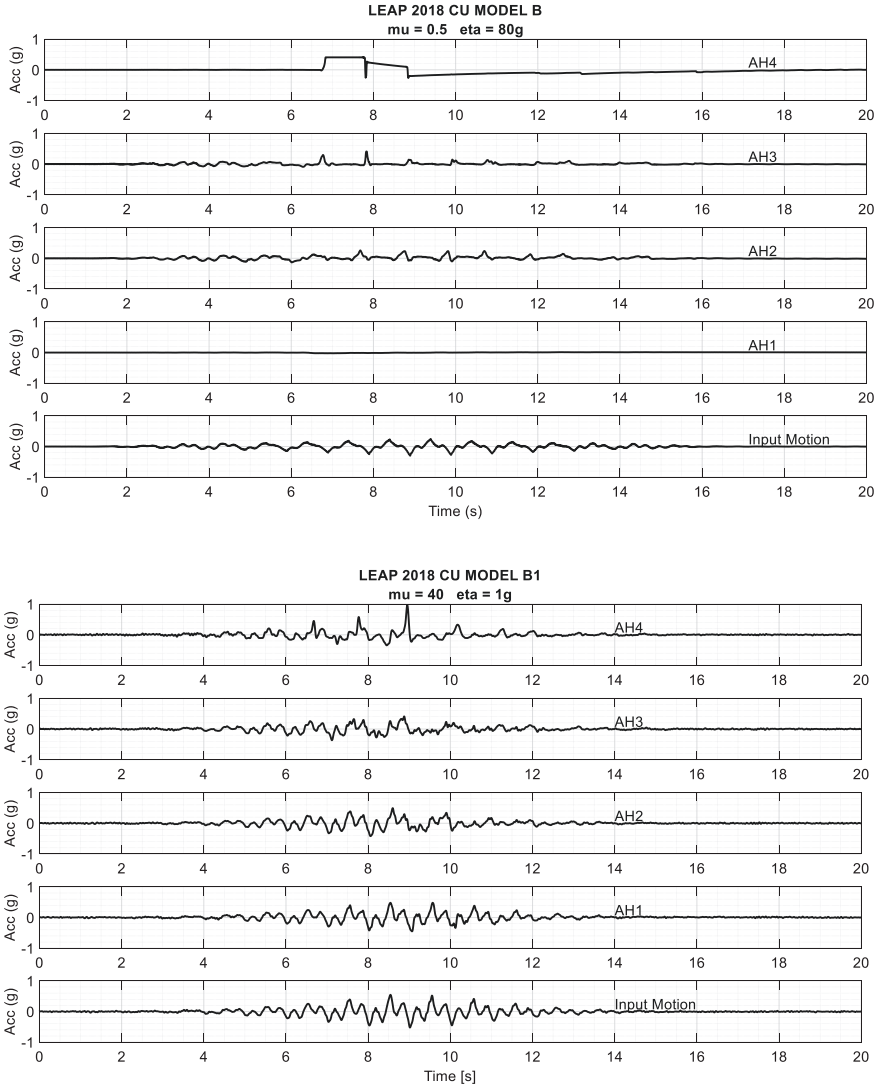

Fig. 5.10 Soil accelerations recorded by central piezo array

5.3.3 Accelerations in the Soil

Acceleration time histories of the central array of piezoelectric accelerometers together with the input motion for CU Model B and CU Model B1 are presented in Fig. 5.10. In CU Model B, significant acceleration reductions are observed along the depth of the slope particularly close to the surface. This is a typical liquefaction phenomenon resulting from the softening of sand caused by excess pore pressure

build-up and effective stress reduction. For CU Model B1, a similar reduction in accelerations is observed along the slope depth but not of the same intensity. The sand in the 1 g test continues to transmit some of the vertically propagating horizontal shear wave motion to the surface as complete liquefaction was not achieved. It is interesting to note the acceleration traces recorded from CU Model B, and the top surface of CU Model B1 shows distinctive spikes in acceleration, which can be attributed to strong dilation in the sand at low confining stresses.

5.3.4 CPT Strength Profiles

In-flight CPT testing was carried out before and after the 1 Hz ramped sine input motion for both CU Model B and CU Model B1. In Fig. 5.11, the soil depth below the slope surface is plotted on the y-axis, using the generalised scaling law for length. On the x-axis, the left-hand side plots show the cone-tip resistance in prototype scale using the generalised scaling laws. On the right-hand side plots, the x-axis is scaling using the normal centrifuge scaling laws for stress, which is unity. The effect of centrifugal acceleration on the strength and stiffness of the sand profile is very clear when comparing cone-tip resistance at model scale for CU Model B to that for CU Model B1. One would expect that if the generalised scaling laws hold well, then the two left-hand side plots should be similar. However, the peak cone-tip resistance before any shaking was applied, at a depth of 3.5 m, is approximately 2 MPa in the 80 g test and 4.6 MPa in the 1 g test. In contrast, using the normal centrifugal scaling laws, the cone-tip resistance at 3.5 m was 3.8 MPa in the 80 g test and only 0.12 MPa in the 1 g test. These latter results are consistent with the expectation that the strength of the soil will be much smaller in a 1 g test than in an 80 g test. Further, Madabhushi et al. (2019) also report a value of 1.8 MPa at a depth of 3.5 m in their 40 g centrifuge test carried out as part of the LEAP 2017 (with $\eta = 40$; $\mu = 1$ for this test). While it is acknowledged that these are extreme examples in terms of the g levels, it is clear that the generalised scaling laws are over-predicting the strength of the soil in models with smaller η and larger μ factors.

5.3.5 PIV Results

For plane strain condition problems, like the ones presented in this paper, PIV analyses can be employed to track the displacement of soil patches of a cross section of the system. Images of the cross-section view were taken using a fast digital camera placed on a gantry in front of the Perspex side of the container. Once the images were available, the displacement field of the soil was obtained employing the MATLAB-based software GeoPIV-RG (Stanier et al., 2015).

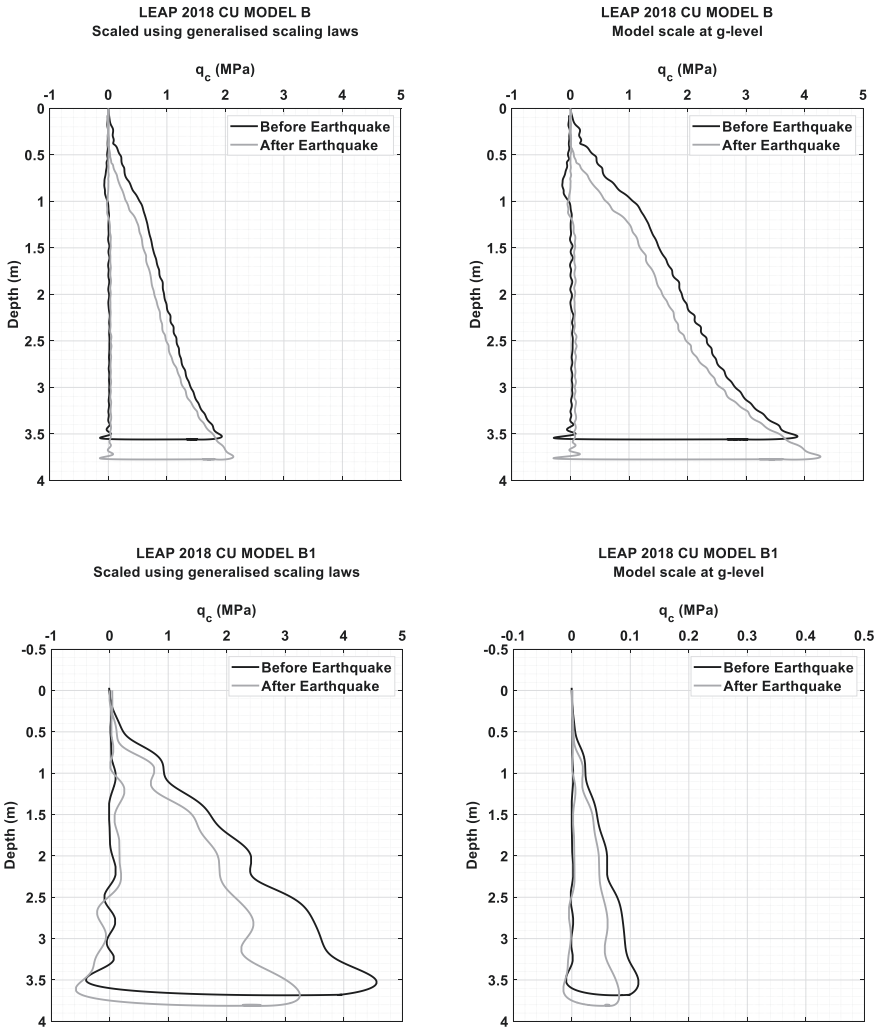

Fig. 5.11 Cone-tip penetrometer results at model scale and scaled using generalised scaling laws

Figure 5.12 shows the layout of the instruments, the portion of the slope analysed and the position of four reference points A, B, C and D for the tests CU Model B and CU Model B1, respectively. Figure 5.13 shows the horizontal and vertical displacement of the four already mentioned reference points, as well as the input motion shaking the container, for the CU Model B. Figure 5.14 shows the displacement field and displacement contours of the slope in the CU Model B. During the shaking, the slope failed following a rotational pattern, with significant vertical settlement of the crest (reference point A) and vertical upward movement of the toe of the slope (reference point C). Significant horizontal displacement was observed in the middle of the slope (reference points B and D).

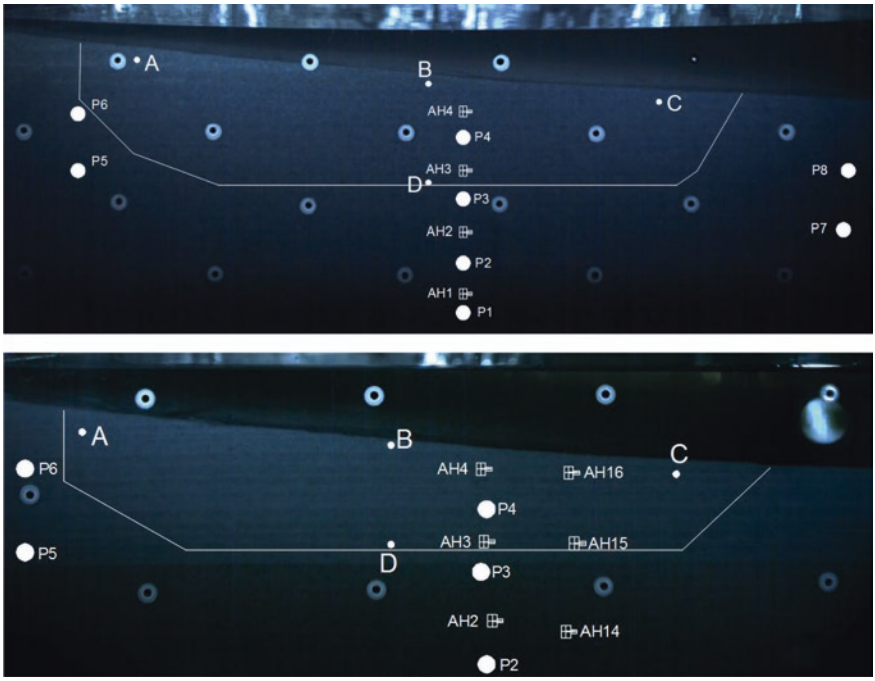

Fig. 5.12 Layout of the instruments, portion of slope analysed and position of four reference points A, B, C and D for CU Model B1 (top) and CU Model B (bottom)

Figure 5.15 shows the horizontal and vertical displacement of the four previously mentioned reference points as well as the input motion shaking the container for CU Model B1. Figure 5.16 shows displacement contours of the slope in the CU Model B1. It is observable that the magnitude of displacement for this test was very small. In addition to this, the shape of the failing mechanism seems different from the previous test, with a uniform vertical settlement of all the four reference points.

Figures 5.17 and 5.18 show a comparison between the slope before and after the earthquake, for the CU Model B and CU Model B1 (third earthquake), respectively. Again, it is observable that the magnitude of displacement for the CU Model B is significantly higher than CU Model B1, despite the larger amplitude of the input motion in the latter.

5.4 Conclusions

The methodology and results from LEAP-ASIA-2019 tests performed at Cambridge are presented in this paper. The main purpose of these tests carried out at drastically different "g" levels of 80 g and 1 g was to evaluate the validity of the generalised scaling laws. The results from the two centrifuge tests CU Model B and CU Model

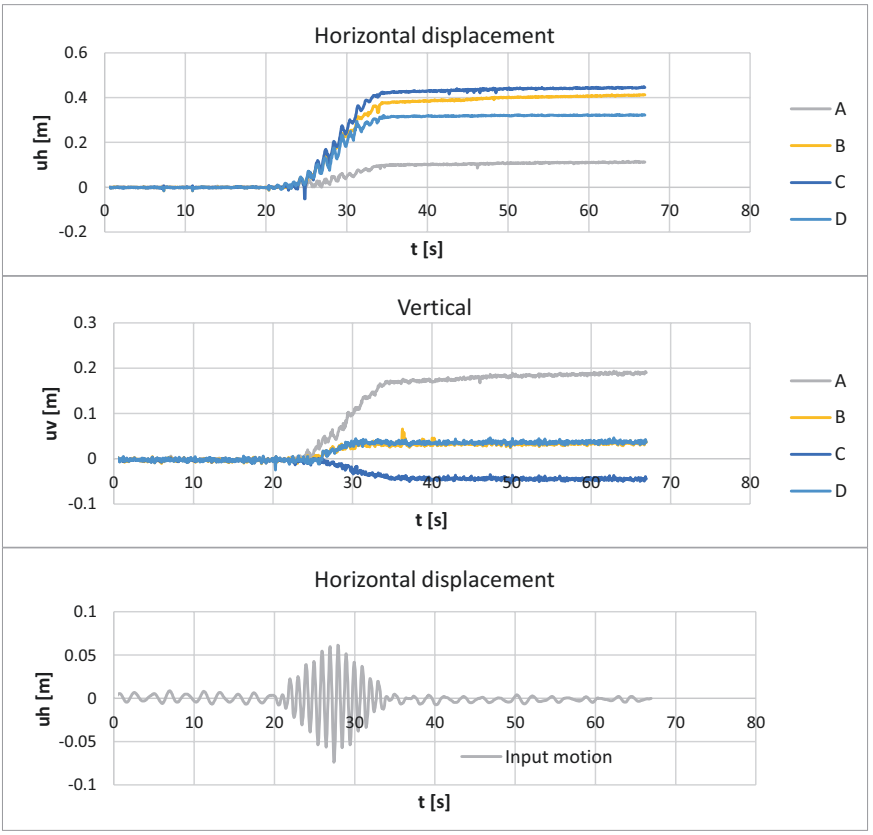

Fig. 5.13 Horizontal and vertical displacement of reference points A, B, C and D and input motion shaking the container for CU Model B

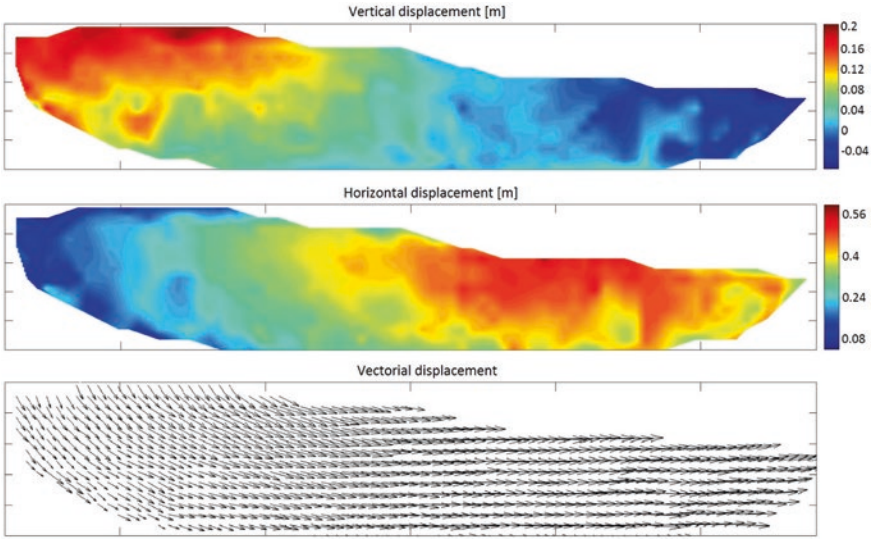

Fig. 5.14 Horizontal and vertical displacement contours at prototype scale and displacement field for CU Model B

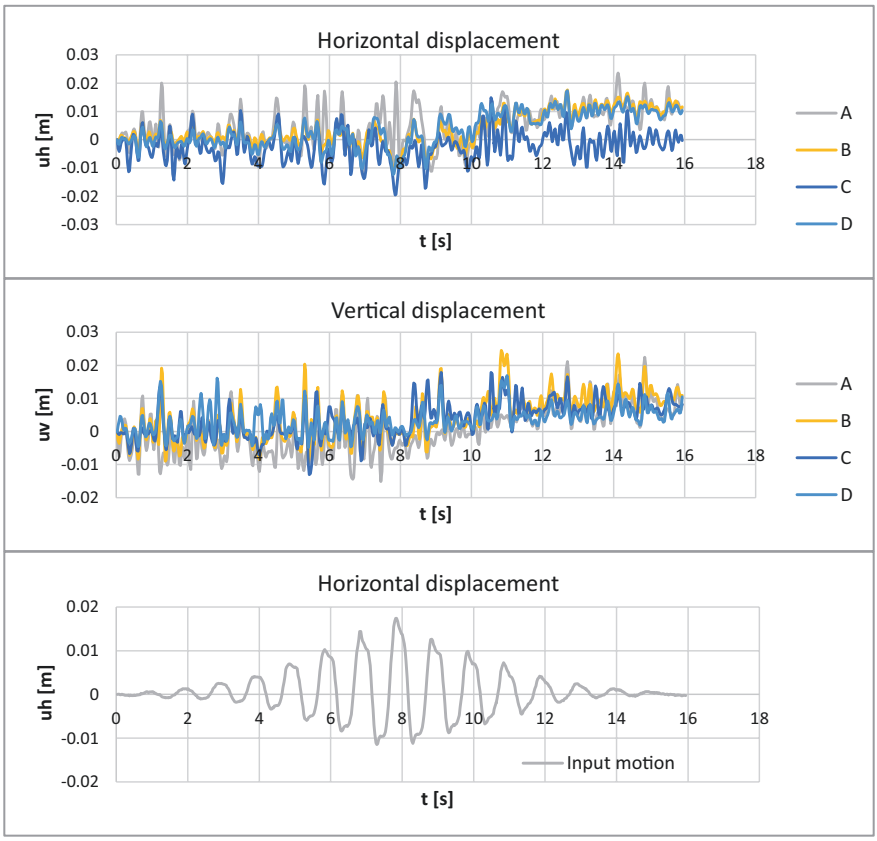

Fig. 5.15 Horizontal and vertical displacement of reference points A, B, C and D and input motion shaking the container for CU Model B1 (prototype scale)

B1 conducted at 80 g and 1 g, respectively, were quite different. This was despite scaling the model pore fluid to correct viscosities and frequency of shaking as prescribed by the generalised scaling laws.

The excess pore pressures seem to scale to similar values in both the models; however, the model tested at 1 g showed large dynamic oscillations with strong dilation-induced spikes. The accelerations in the slope showed attenuation with the build-up of excess pore pressures in the case of 80 g test, while those in the 1 g test showed large amplification due to the dilation in this model. The deformations in these centrifuge tests were obtained using PIV analyses. For the case of 80 g test, the slope deformations were as expected with large lateral movements being recorded at the mid-slope and an overall rotational motion of the slope with the top of the slope moving down and the base of the slope moving up. However, in the 1 g test, there were no observable slope movements when an equivalent base shaking was applied. In order to beget any observable movements of the slope, an earthquake that was nearly twofolds larger had to be applied to the slope.

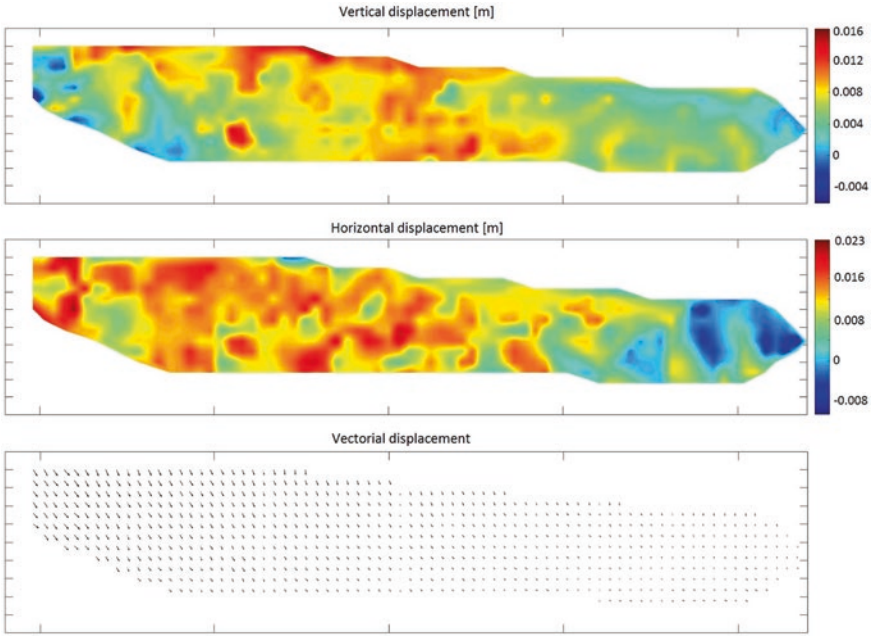

Fig. 5.16 Horizontal and vertical displacement contours at prototype scale and displacement field for CU Model B1

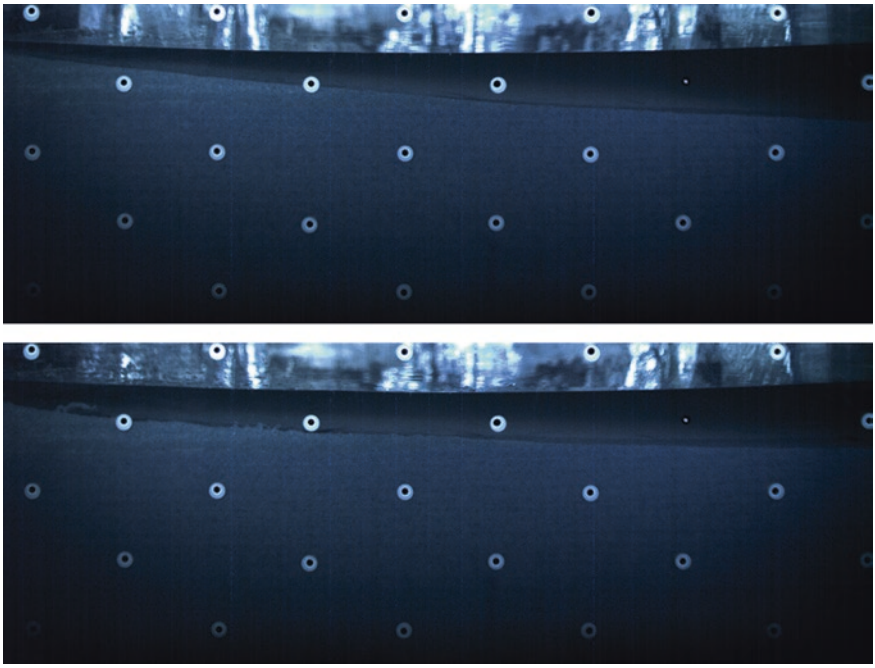

Fig. 5.17 Slope before and after the shaking for CU Model B

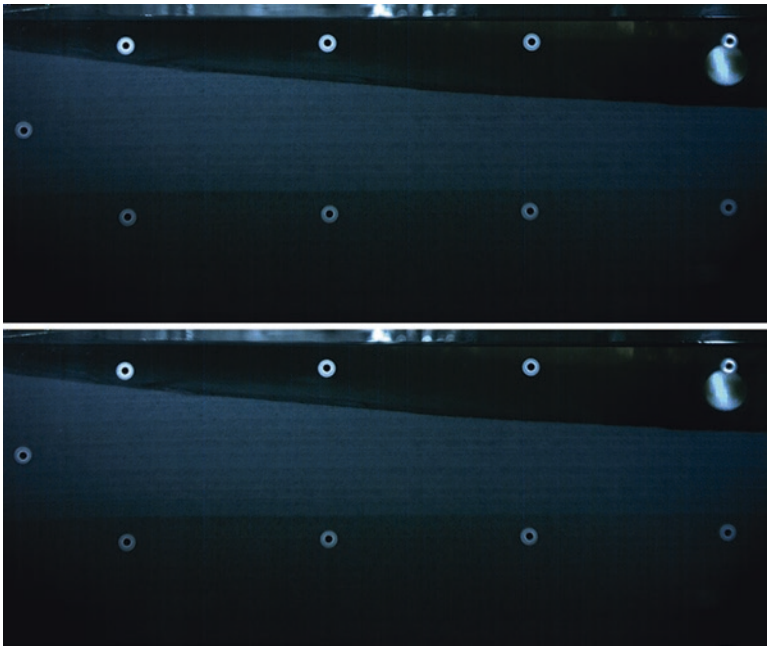

Fig. 5.18 Slope before and after the shaking for CU Model B1

In-flight cone penetration tests were conducted for the models at 80 g and 1 g before and after the ramped 1 Hz input motion. As expected, cone-tip resistance values along the depth of the slope scaled according to the centrifuge scaling law of stress (i.e. unity) showed significant discrepancies between the 80 g test and the 1 g test. This is due to the fundamentally different confining stresses in the soil body at these two different g levels. The application of the generalised scaling laws has predicted a much larger strength of the sand for the 1 g test; however, the cone-tip resistances between the 80 g test and the 40 g test conducted by previous researcher were comparable. This suggests that there is a limit on the values of virtual scaling factors μ that can be used in the generalised scaling laws.

Acknowledgments The authors would like to thank the technicians at the Schofield Centre for their assistance during the testing.

References

Carey, T., Gavras, A., Kutter, B., Haigh, S. K., Madabhushi, S. P., Okamura, M., Kim, D. S., Ueda, K., Hung, W. Y., Zhou, Y.-G., Liu, K., Chen, Y. -M, Zeghal, M., Abdoun, T., Escoffier, S., & Manzari, M. (2018). A new shared miniature cone penetrometer for centrifuge testing. In *Proceeding of the 9th international conference on Physical Modelling in Geotechnics ICPMG 2018, London, CRC Press/Balkema,* July, Vol. 1, pp. 293–298.

Iai, S., Tobita, T., & Nakahara, T. (2005). Generalised scaling relations for dynamic centrifuge tests. *Geotechnique, 55*(5), 355–362.

Madabhushi, S. P. G., Houghton, N. E., & Haigh, S. K. (2006). A new automatic sand pourer for model preparation at University of Cambridge. In *Proceedings of the 6th international conference on Physical Modelling in Geotechnics*, Taylor & Francis Group, London, UK, pp. 217–222.

Madabhushi, S. S., Haigh, S. K., & Madabhushi, G. S. (2018). LEAP-GWU-2015: Centrifuge and numerical modelling of slope liquefaction at the University of Cambridge. *Soil Dynamics and Earthquake Engineering, 113*, 671–681.

Madabhushi, S. S., Dobrisan, A., Beber, R., Haigh, S. K., & Madabhushi, G. S. (2019). LEAP-UCD-2017 Centrifuge Tests at Cambridge. In B. Kutter et al. (Eds.), *Proceeding of the Model tests and Numerical Simulations of Liquefaction and Lateral Spreading*. Springer.

Stanier, S. A., Blaber, J., Take, W. A., & White, D. J. (2015). Improved image-based deformation measurement for geotechnical applications. *Canadian Geotechnical Journal, 53*(5), 727–739.

Stringer, M. E., & Madabhushi, S. P. G. (2009). Novel computer-controlled saturation of dynamic centrifuge models using high viscosity fluids. *Geotechnical Testing Journal, 32*(6), 559–564.

Chapter 6
LEAP-ASIA-2019 Centrifuge Test at University of California, Davis

Nicholas S. Stone, Trevor J. Carey, Anthony Santana, and Bruce L. Kutter

Abstract For the LEAP-ASIA-2018 exercise, a centrifuge test was conducted in parallel at ten centrifuge facilities, including the University of California, Davis (UCD). The experiment consisted of a submerged clean sand profile oriented with a 5-degree slope subjected to 1 Hz ramped sine wave motions applied at the base of a rigid container. This paper explains several details of the experiment at UCD, including experiment results, implementation of high-speed cameras and GeoPIV software to measure slope deformation, and the presence of vertical accelerations due to the Coriolis effect and how the accelerations might affect model performance. In addition, this paper presents data and comparison for both conventional (Type A) and generalized (Type B) centrifuge scaling laws.

Keywords Liquefaction Experiments and Analysis Projects (LEAP-ASIA-2018) · Generalized scaling law (GSL) · Centrifuge modeling

6.1 Introduction

The current phase of LEAP, LEAP-ASIA-2018, involved centrifuge experiments conducted at ten different research facilities, including the University of California, Davis (UCD). The experiment, similar to LEAP-UCD-2017 and LEAP-GWU-2015, consisted of a submerged clean sand deposit sloped at 5 degrees, subjected to a 1 Hz ramped sine wave ground motion inputted at the base of the rigid model container. The experiments were performed on the 1 m radius Schaevitz centrifuge at the Center for Geotechnical Modeling at UCD. The 1 m centrifuge performs shaking in

N. S. Stone · A. Santana · B. L. Kutter
Department of Civil and Environmental Engineering, University of California, Davis, CA, USA
e-mail: Trevor.Carey@civil.ubc.ca

T. J. Carey (✉)
Department of Civil Engineering, The University of British Columbia, Vancouver, Canada

T. Tobita et al. (eds.), *Model Tests and Numerical Simulations of Liquefaction and Lateral Spreading II*, https://doi.org/10.1007/978-3-031-48821-4_6

the circumferential direction of the centrifuge. Detailed specifications by Kutter et al. (2019) were provided to facilitate replicability among the different centrifuge facilities. The goals of LEAP-ASIA-2018 were filling in the gaps and further extending/confirming the trends obtained in LEAP-UCD-2017 and evaluating the applicability of generalized scaling laws (Iai et al., 2005). Discussed in these proceedings are the model specifications, achieved input motions, sensor results, and unique aspects of three centrifuge models, referred to as UCD4, UCD5, and UCD6.

6.2 UC Davis Test Specific Information

6.2.1 Description of the Model and Instrumentation

The same container was used for the UCD experiments as during the LEAP--UCD-2017 exercise (Carey et al., 2020). The container dimensions are 457.2 mm (L) × 279.4 mm (W) × 177.8 mm (H). As in 2017, 25.4-mm-thick plastic plates were placed on each end wall of the rigid container to obtain the 457.2 mm length. The plastic plates were placed to ensure the soil would remain completely submerged at 1 g and the water would not spill out of the container during spinning. Figure 6.1 details the test geometry, sensor locations, PVC blocks, and approximate fluid level during spinning in model scale.

Modeling a flat surface under a radial g-field requires a curved surface with the same radius of curvature as the imposed g-field. A slope relative to the radial g-field is described theoretically by a log spiral. Carey et al. (2017) showed that a log spiral can be approximated by rotating a circular arc by 5 degrees. The maximum error in model depth between the log spiral surface and that of the circular arc is 2.2%. Figure 6.2 shows the procedure for vacuuming the curved surface using a wooden template and flat head vacuum attachment.

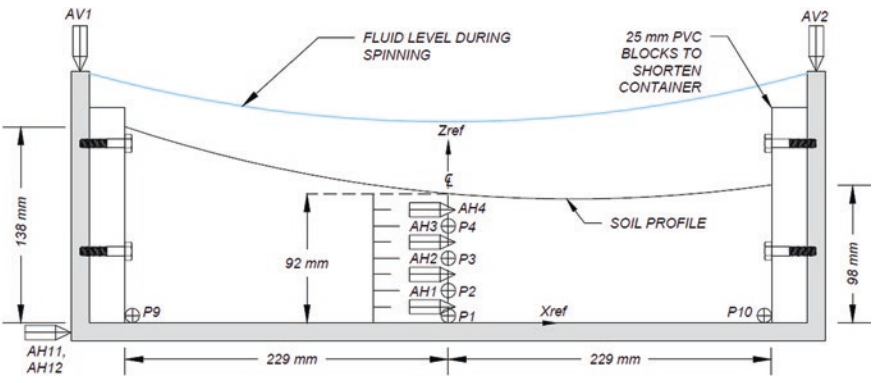

Fig. 6.1 Model geometry and sensor layout (dimensions in model scale)

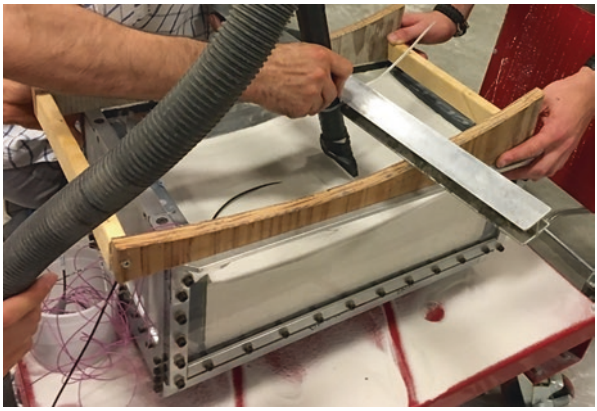

Fig. 6.2 Wooden template and vacuum tool used to approximate the log spiral surface

6.2.2 Sensors

The number of sensors placed in the model was limited by the capacity of the data acquisition system; therefore, only the required pore pressure transducers (P1, P2, P3, P4, P9, and P10) and accelerometers (AH1, AH2, AH3, AH4, AH11, AH12, AV1, and AV2) were included. Specified locations of each sensor are shown in Fig. 6.1.

6.2.3 Scaling Laws

The scaling laws for LEAP-ASIA-2018 were provided by Iai et al. (2005). In these specifications, a factor μ was defined as the virtual 1 g scaling factor, leaving η as the centrifuge scaling factor, and $\mu * \eta$ as the generalized scaling factor. Figure 6.3 provides the schematic of generalized centrifuge scaling with factors $\mu$and η. Table 6.1 provides the generalized scaling relationships for the centrifuge experiments. Two models were tested using conventional scaling laws ($\mu = 1$), while one model was tested using the generalized scaling law and a virtual scale factor of $\mu = 2$. Table 6.2 lists the scaling factors used for each experiment.

6.2.4 CPT Re-calibration

In-flight cone penetrometer (CPT) measurements were made using a device described by Carey et al. (2018b). The device uses an internal rod, protected by an outer sleeve to transmit cone tip forces to a load cell. During the final assembly of the CPT device, the internal rod was threaded into the load cell until a preload of

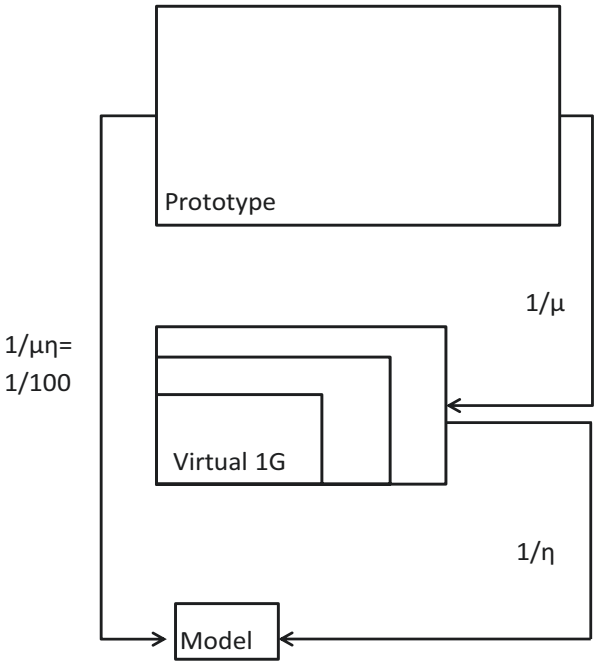

Fig. 6.3 Generalized scaling schematic

Table 6.1 Generalized scaling relationships

	(1) Scaling factors for 1 g test	(2) Scaling factors for centrifuge test	(3) Generalized scaling factors
Length	μ	η	$\mu\eta$
Density	1	1	1
Time	$\mu^{0.75}$	η	$\mu^{0.75}\eta$
Frequency	$\mu^{-0.75}$	$1/\eta$	$\mu^{-0.75}/\eta$
Acceleration	1	$1/\eta$	$1/\eta$
Velocity	$\mu^{0.75}$	1	$\mu^{0.75}$
Displacement	$\mu^{1.5}$	η	$\mu^{1.5}\eta$
Stress	μ	1	μ
Strain	$\mu^{0.5}$	1	$\mu^{0.5}$
Stiffness	$\mu^{0.5}$	1	$\mu^{0.5}$
Permeability	$\mu^{0.75}$	η	$\mu^{0.75}\eta$
Pore pressure	μ	1	μ

Table 6.2 Scaling factors used for the three UCD experiments

	Virtual 1 g scale factor, μ	Centrifuge scale factor, η
UCD4	1	43.75
UCD5	2	21.9
UCD6	1	43.75

4–9 N on the tip O-ring was achieved, using a procedure summarized by Carey et al. (2018b) and described in detail in the documents distributed with the equipment. Preloading the tip O-ring ensures the gap between the cone shoulder and sleeve is closed, and specifying the preload minimizes variable preloads. The assembled device was calibrated at the Center for Geotechnical Modeling at UCD. A calibration load cell was attached to the top of the rigid aluminum block to record the total force as the cone tip was pushed into soft plastic using a pneumatic actuator. The difference between the force measured with the CPT device load cell and calibration load cell is attributed to compression of the tip O-ring and friction between the internal bracing O-rings. Carey et al. (2018b) showed the magnitude of friction varied linearly with the cone tip force and therefore could be corrected using a calibration factor. The calibration factor was applied to the measured cone tip force, and the assembled device was checked once more to ensure the recorded force at the tip was identical to the calibration load cell. The calibration process was done prior to UCD4.

6.3 Results

6.3.1 Achieved Dry Densities

UCD performed three experiments with varying target densities. The measured dry densities were calculated by the measurement of mass and volume of the soil in the model container. A more detailed explanation of the method used to measure the volume of each model, adapted from Carey et al. (2020), is described later. Table 6.3 lists the measured dry density of each constructed model. Model construction was achieved by dry pluviation through a no. 16 sieve with three slots (Kutter et al. 2019) from a standard drop height, adjusted at each 11.4 mm lift. UCD4 and UCD5 models were pluviated through 1.2-mm-wide slots from a 660 mm drop height. UCD6 was pluviated though 10.3-mm-wide slots from a 325 mm drop height.

Table 6.3 Measured dry densities for the three UCD experiments

	Measured dry density $\left(\frac{\text{kg}}{\text{m}^3}\right)$
UCD4	1713
UCD5	1712
UCD6	1658

6.3.2 Achieved Sensor Locations

All sensors were placed in accordance with specifications for LEAP-ASIA-2018. Sensors were placed using the tools employed to measure locations throughout the model; therefore, initial sensor locations were within measurement error of their specified locations. Final locations of the sensors were measured during excavation following each experiment; these are listed in the LEAP-ASIA-2018 test template.

6.3.3 Achieved Ground Motions

The ground motion intensity parameter, $PGA_{effective}$, introduced by Kutter et al. (2019) was used to characterize the achieved input motions of each model. The measured input motions were filtered into their constituents: the 1 Hz signal and the superimposed higher frequencies. Then, PGA_{eff} is calculated as $PGA_{eff} = PGA_{1Hz} + \frac{1}{2} PGA_{HF}$. (The components of PGA_{eff} are given for the experiments in Tables 6.4a, 6.4b and 6.4c for destructive motions one, two, and three, respectively).

Table 6.4a Destructive Motion 1 PGA for the three UCD experiments

	Destructive Motion 1			
	PGA_{raw} (g)	PGA_{eff} (g)	PGA_{1Hz} (g)	PGA_{HF} (g)
UCD4	0.191	0.191	0.161	0.059
UCD5	0.154	0.150	0.131	0.038
UCD6	0.150	0.143	0.123	0.041

Table 6.4b Destructive Motion 2 PGA for the three UCD experiments

	Destructive Motion 2			
	PGA_{raw} (g)	PGA_{eff} (g)	PGA_{1Hz} (g)	PGA_{HF} (g)
UCD4	0.428	0.341	0.249	0.182
UCD5	0.341	0.299	0.241	0.117
UCD6	0.216	0.192	0.165	0.055

Table 6.4c Destructive Motion 3 PGA for the three UCD experiments

	Destructive Motion 3			
	PGA_{raw} (g)	PGA_{eff} (g)	PGA_{1Hz} (g)	PGA_{HF} (g)
UCD4	NA	NA	NA	NA
UCD5	NA	NA	NA	NA
UCD6	0.513	0.391	0.269	0.245

6.3.4 Accelerometer Readings During Destructive Motions

The acceleration time histories of the input base motions and the four central array horizontal accelerometers (AH1, AH2, AH3, and AH4) from each destructive motion are shown in Fig. 6.4. The input base motion is taken as the average of the time history recorded from AH11 and AH12. The acceleration time histories of the two vertical accelerometers (AV1 and AV2) during each destructive motion are shown in Fig. 6.5.

- UCD4
  - Destructive Motion 1: Slight amplification of the base motion occurs, especially in the top two accelerometers (AH3 and AH4). Accelerometers throughout the model remained in phase during the motion. This indicates the soil near the ground surface may have undergone some small degree of nonlinearity, but the bottom remained rigid.
  - Destructive Motion 2: Amplification of the base motion occurs in all accelerometers, with increasing amplification at shallower depths. Overall, greater amplification occurred in M2 than M1. Dilation spikes only occurred in AH4, while AH3 and AH4 both lag the base motion, indicating more severe liquefaction at shallower depths.

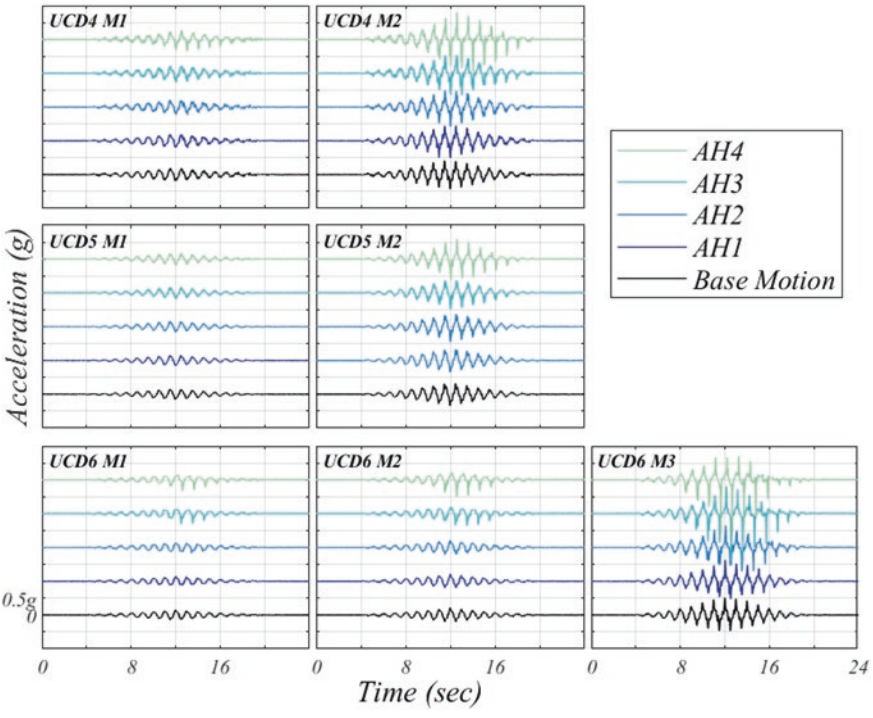

Fig. 6.4 Horizontal acceleration time histories for UCD4, UCD5, and UCD6

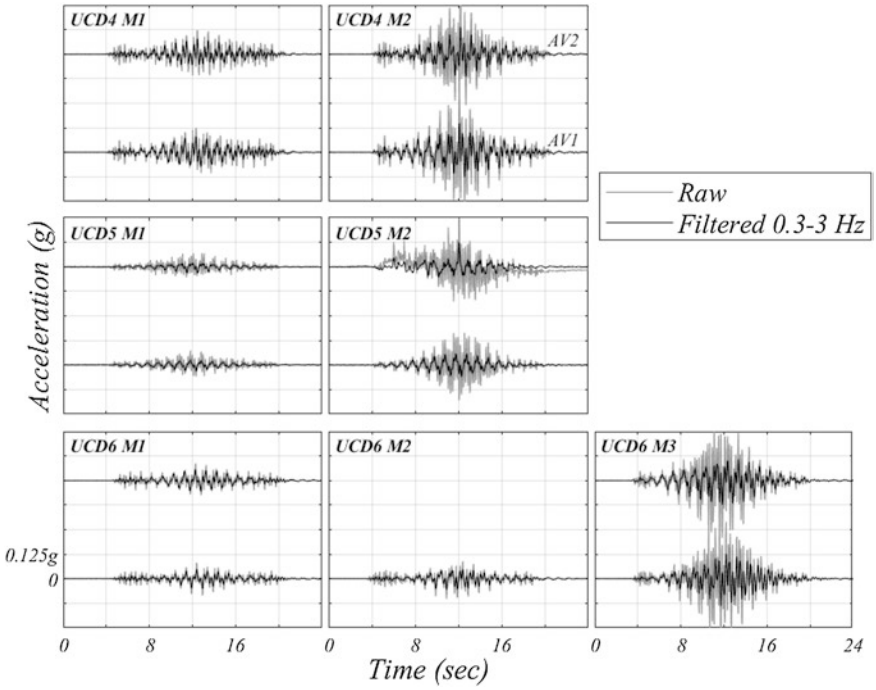

Fig. 6.5 Vertical acceleration time histories for UCD4, UCD5, and UCD6

- UCD5
  - Destructive Motion 1: No amplification or phase lag occurs at any accelerometer, indicating the model behaved as a rigid body. There is little evidence of nonlinearity or liquefaction in the acceleration time histories.
  - Destructive Motion 2: Amplification of the base motion is observed in all accelerometers, with increasing amplification at shallower depths. Similar to UCD4 M2, dilation spikes were only measured by AH4, and both AH3 and AH4 are out of phase with the base motion, indicating more severe liquefaction at shallower depths.
- UCD6
  - Destructive Motion 1: This was the smallest motion performed during the three UCD experiments. Slight amplification of the base motion occurred in AH3 and AH4 from times 12–16 s.
  - Destructive Motion 2: Amplification of the base motion occurred at AH3 and AH4. AH3 and AH4 are slightly out of phase with the base motion. This indicates liquefaction occurred at shallow depths only and at a less severe degree than other motions (e.g., UCD4 M2 and UCD5 M2). Dilation spikes during this motion are small; however, this model is less dense than UCD4 and UCD6, hence, less dilatancy is expected.

– Destructive Motion 3: Amplification of the base motion and dilation spikes occurred at each accelerometer, with increasing amplification and severity of the dilation spikes at shallower depths. AH2, AH3, and AH4 are out of phase with the base motion. This was the largest motion performed during the three UCD experiments, resulting in the most severe amplification, dilation spikes, and phase lag.

6.3.5 *Excess Pore Pressures During Destructive Motions*

The excess pore pressures recorded by pore pressure transducers in the central array (e.g., P1, P2, P3, and P4) are shown in Fig. 6.6, and the excess pore pressures as recorded at the container ends (P9 and P10) are shown in Fig. 6.7.

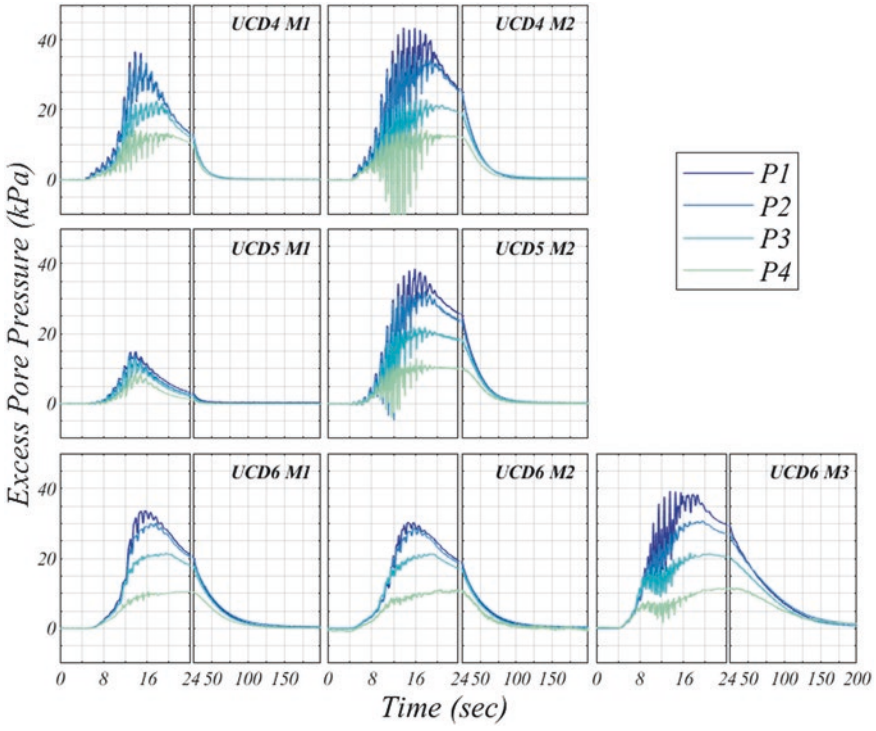

Fig. 6.6 Excess pore pressures of the central array for UCD4, UCD5, and UCD6. The initial effective stress is approximately 10, 20, 30, and 39 kPa at sensors P4, P3, P2, and P1, respectively

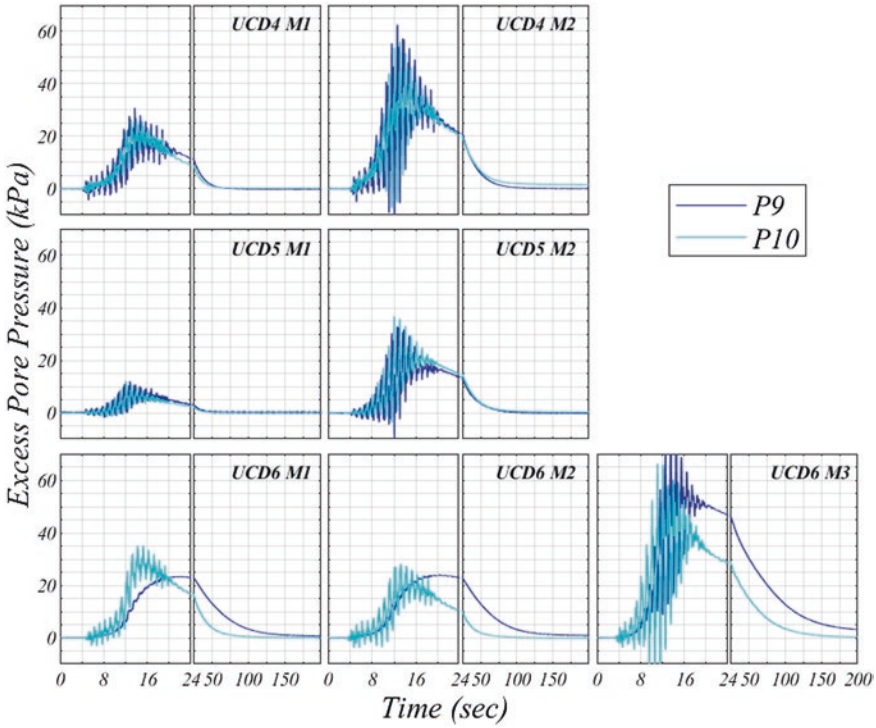

Fig. 6.7 Excess pore pressures at model ends for UCD4, UCD5, and UCD6

- UCD4
  - Destructive Motion 1: The excess pore pressure approached the initial effective stress at sensors P3 and P4, but not at P1 or P2. Zero effective stress remained after the end of the motion (at 20 s) at P4, while excess pore pressure immediately started to dissipate at P3 following the end of shaking. This implies sustained liquefaction at P4, unsustained liquefaction at P3, and no liquefaction at greater depths.
  - Destructive Motion 2: Zero effective stress was reached at sensors P2, P3, and P4. Zero effective stress sustained at P3 and P4, but not P2. This implies sustained liquefaction at P3 and P4, unsustained liquefaction at P2, and no liquefaction at the base of the container. Zero effective stress at the base of the container is difficult to reach, as no excess pore pressure is generated due to an upward hydraulic gradient.
- UCD5
  - Destructive Motion 1: Zero effective stress was not reached at any depth, indicating liquefaction did not trigger during this motion. Due to the lack of liquefaction and initially dense state, Destructive Motion 1 could likely be

considered a non-destructive event, and Destructive Motion 2 might be considered to be the first destructive motion.
  - Destructive Motion 2: Zero effective stress was reached at sensors P2, P3, and P4. Zero effective stress remained after the end of the motion at P3 and P4, but not P2. This implies sustained liquefaction at P3 and P4, unsustained liquefaction at P2, and no liquefaction at the base of the container.

- UCD6
  - Destructive Motion 1: Zero effective stress was reached at sensors P2, P3, and P4. Zero effective stress remained after the end of the motion at P4, excess pore pressure started to dissipate after shaking at P3, and excess pore pressure started to dissipate before the end of the motion at P2. This implies sustained liquefaction only at shallow depths.
  - Destructive Motion 2: Zero effective stress was reached at sensors P3 and P4. Zero effective stress remained after the end of the motion at P4, while excess pore pressure immediately started to dissipate after the motion at P3. Overall, less excess pore pressure was generated during Destructive Motion 1 than Destructive Motion 2 even though the effective PGA was greater in Destructive Motion 2. This implies the model densified during Destructive Motion 1.
  - Destructive Motion 3: Zero effective stress was reached at sensors P2, P3, and P4. Zero effective stress remained after the end of the motion at P3 and P4, but not P2. This implies sustained liquefaction at P3 and P4, unsustained liquefaction at P2, and no liquefaction at the base of the container.

6.3.6 Cone Penetration Test Results

Three cone penetration tests were performed for UCD4, while four were performed for UCD5 and UCD6 (Fig. 6.8). For each model, CPT soundings were performed prior to the first destructive motion and following each destructive motion. An additional CPT sounding was performed at the end of the UCD5 experiment for evaluation of the applicability of the generalized scaling laws to penetration resistance. This will be discussed in more detail in the following paragraphs. All soundings were performed in unique locations within the model.

- UCD4
  - Little change in tip resistance is observed between soundings, indicating the specimen did not densify significantly during shaking. This can be attributed to the model starting dense (D_R = 84%) and relatively low level of shaking.

- UCD5
  - CPT1, CPT2, and CPT3 were performed with a centrifuge scaling factor of η = 21.9 and a virtual scale factor of μ = 2. CPT4 was performed with a centrifuge scaling factor of η = 43.8 and a virtual scale factor of μ=1, as tests

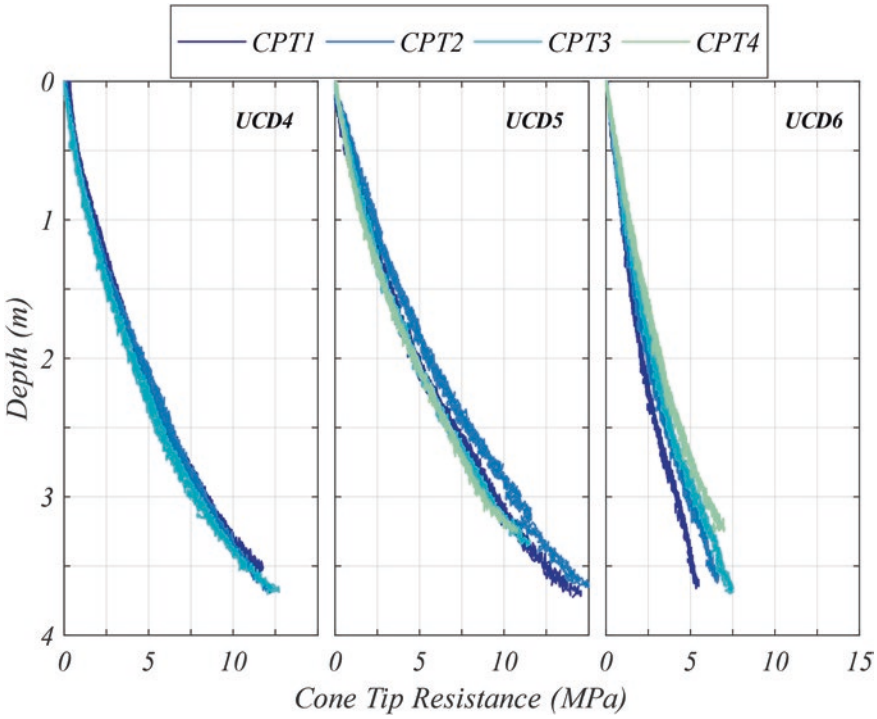

Fig. 6.8 CPT results from UCD4, UCD5, and UCD6

performed using conventional scaling laws. CPT4 was performed to assess the applicability of the generalized scaling laws to cone penetration tests. CPT4 lies on top of CPT3, indicating that generalized scaling laws appear applicable for cone penetration tests for this range of virtual scale factors.

– CPT2 showed greater tip resistance than CPT1, CPT3, or CPT4, which were almost identical. Because all other CPTs were so similar and there were no signs of liquefaction during Destructive Motion 1 in the PPT or accelerometer responses, this increase is likely attributed to spatial variability of density than densification due to shaking. As in UCD4, densification likely did not occur because the model was dense to begin with and shaking intensity was relatively low.

• UCD6.

– At 2 m depth, the cone tip resistance increased by 18% during M1, 13% during M2, and 12% during M3. At 3 m depth, the cone tip resistance increased by 16% during M1, 9% during M2, and 10% during M3. The increased tip resistance is attributed to densification, as this model began at a medium dense state (D_R = 68%).

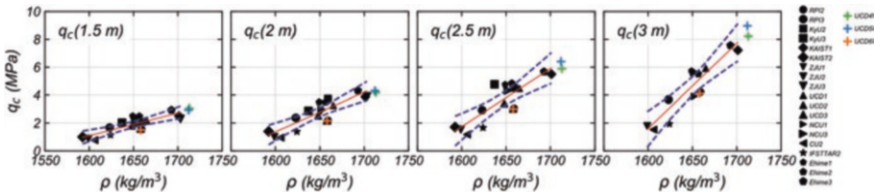

Fig. 6.9 Comparison of CPT results to correlations from LEAP-UCD-2017 (2017 data in black)

- Comparing two models of the same density, UCD6 to UCD3 (from LEAP--UCD-2017, Carey et al., 2020), UCD3 experienced approximately 5% increase in tip resistance at 2 m depth over each destructive motion, significantly less than the 18% and 13% during M1 and M2 of UCD6, respectively.
- Figure 6.9 shows the correlation between cone tip resistances prior to the first destructive motions and measured dry density from the LEAP-UCD-2017 data. The data points from the 2017 tests are shown in black, while the data points from LEAP-ASIA-2018 UCD experiments are shown in color. Overall, the correlation was able to predict the measured dry density of UCD4, UCD5, and UCD6 at various depths. The cone tip resistances used to build the correlation were taken from tests using conventional scaling laws; however, the correlation was able to predict the dry density for UCD5, which was performed using generalized scaling laws. This is a further indication that generalized scaling laws may be applicable to cone penetration tests in this sand.

6.4 Unique Aspects of UCD Experiments

6.4.1 GeoPIV Surface Survey

LEAP-GWU-2015 showed inconsistent displacement patterns attributed to variability in hand measurements of surface markers (Kutter et al., 2018); thus, a better method for displacement measurement is necessary. Prior to now, there has been little success in using conventional sensors to monitor displacement of a submerged curved slope. Displacement transducers have been used, but others (Fiegel & Kutter, 1994) have observed their measurements to be unreliable during liquefaction. During LEAP-UCD-2017, the UCD team designed and developed a new procedure for tracking lateral surface displacements of a centrifuge model using a wave suppressing window, GoPro cameras, and GeoPIV software (Carey et al., 2018a). This procedure was implemented in UCD's experiments for LEAP-UCD-2017. The bottom of the wave suppressing window is below the curved water surface to reduce the reflection of light, like a glass-bottomed boat. A 57 mm gap between the window and the side walls of the container allows for a free water surface to ensure that window confinement does not cause dynamic water pressure oscillation. Five GoPro cameras recording at 240 fps were mounted above the acrylic window (Figs. 6.10

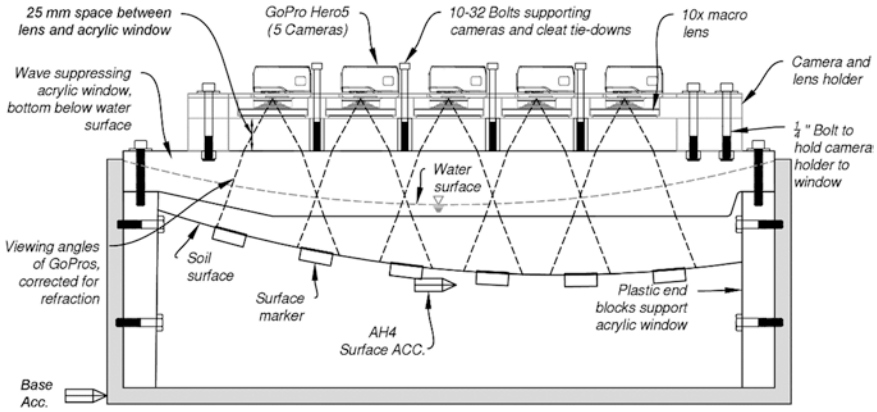

Fig. 6.10 Profile view of centrifuge container with acrylic glass window, GoPro cameras, and macro lenses

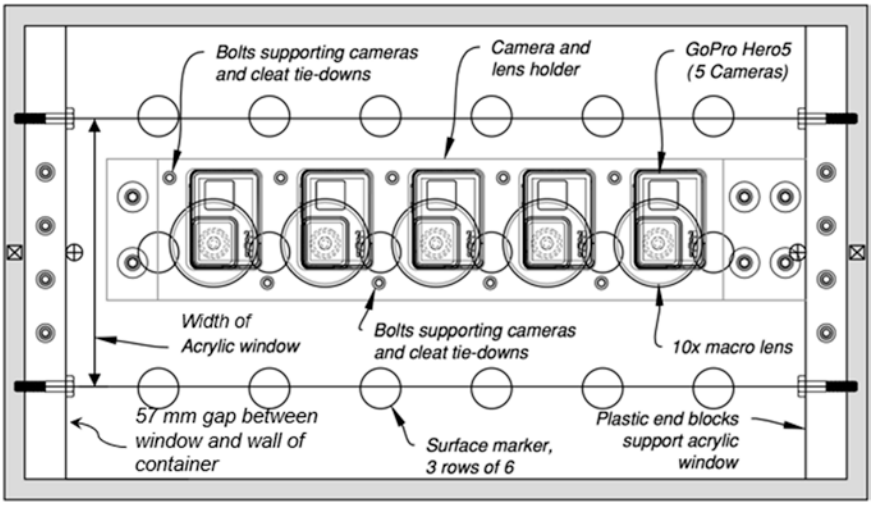

Fig. 6.11 Top view of centrifuge container with acrylic glass window, GoPro cameras, and macro lenses

and 6.11), each viewing through a 10x macro lens, allowing for a sharply focused image of the soil surface. Movement of the first and last surface markers are viewed by one camera each, while movement of the interior four surface markers (2–5) are viewed by two cameras each. Videos recorded from the five GoPro cameras were converted to a series of images using MATLAB and then processed using GeoPIV, an open-source software, which has been used extensively for geotechnical applications and centrifuge testing (Stanier et al., 2015). Displacements were converted

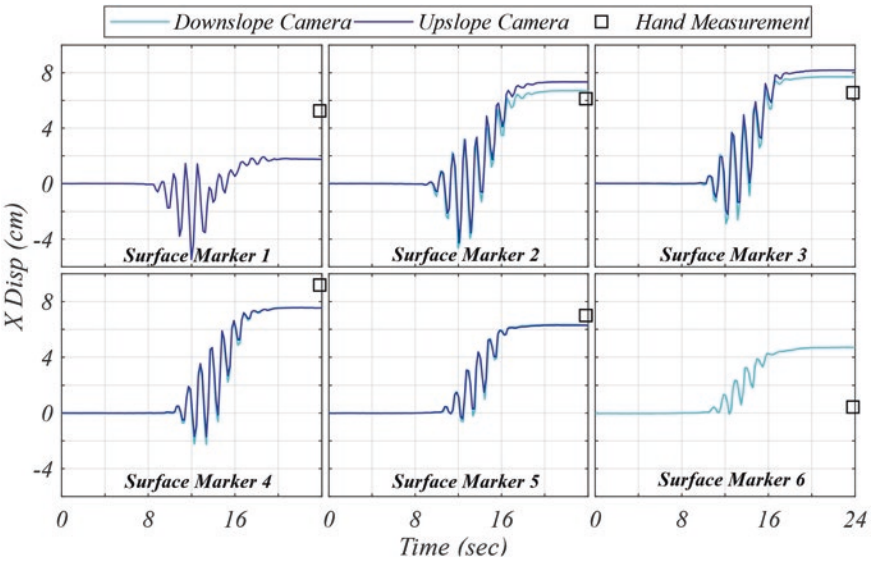

Fig. 6.12 X displacement time history (prototype scale) of six centerline surface markers during UCD6 M1

from pixels to mm using a process described in Carey et al. (2018a), with a camera-specific calibration factor. Figure 6.12 shows the displacement time histories of the six centerline surface markers from UCD6 Destructive Motion 1 found using GeoPIV and compares the final residual displacement to that measured by hand.

Another limitation in measuring surface displacements of centrifuge experiments is spatial density of measurements. The number of surface markers or displacement transducers that can fit into a model is limited, making it difficult to characterize spatial variability of displacements during liquefaction. Using the procedure developed, a grid of patches, or areas to be tracked, across each image is defined during the GeoPIV processing stage. For the UCD experiments, each image was processed using a patch size of 60 pixels square, which corresponds to approximately 10–15 mm square in model space (this varies between cameras). Figures 6.13, 6.14, and 6.15 each show x, y, and z (all dimensions in model scale) displacements from UCD4, UCD5, and UCD6, respectively. Displacements in the x and y directions were found using GeoPIV; some gaps in data are seen due to low image quality in these regions. For the centerband of patches, those within ±40 mm of the container's centerline, z displacements were interpolated using a cubic spline between the centerline surface marker measurements (measured by hand). Although not reported herein, Stone (2019) describes how principles of photogrammetry can be applied to deduce vertical displacements for regions tracked by two cameras.

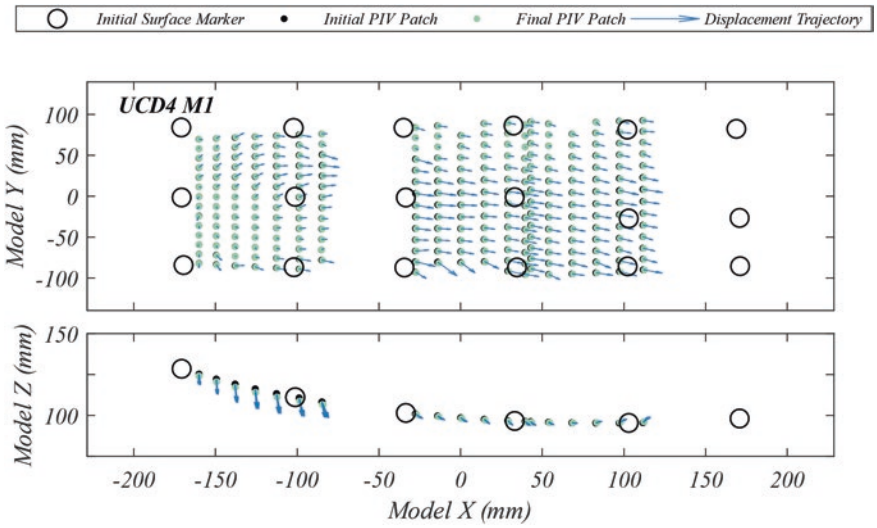

Fig. 6.13 Top and centerline profile views of model scale displacements found using GeoPIV, surface maker measurements, and cubic spline interpolation during UCD4 M1

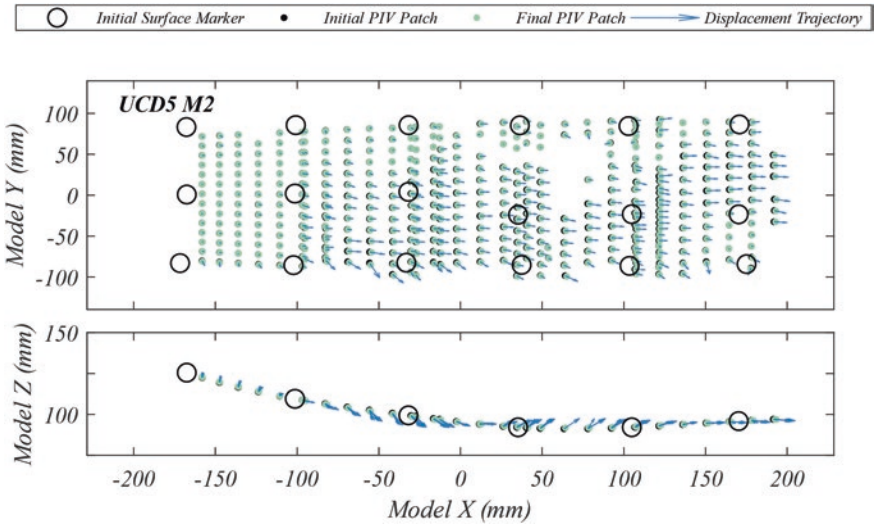

Fig. 6.14 Top view and centerline profile view of model scale displacements found using GeoPIV, surface maker measurements, and cubic spline interpolation during UCD5 M2 (almost no displacement during Destructive Motion 1)

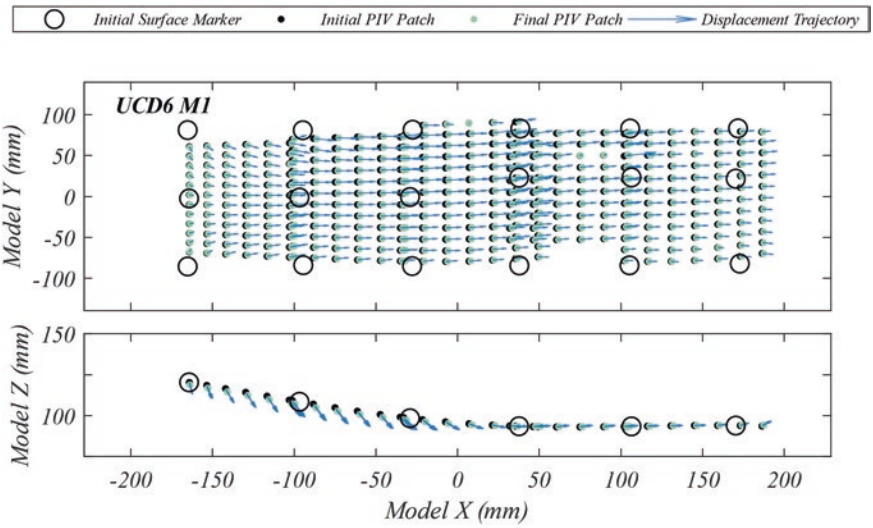

Fig. 6.15 Top view and centerline profile view of model scale displacements found using GeoPIV, surface maker measurements, and cubic spline interpolation during UCD6 M1

6.4.2 Vertical Accelerations due to the Coriolis Effect

As shown in Fig. 6.5, vertical accelerations were observed during each destructive motion. Two sources were hypothesized for their excitation: vertical rocking of the container and the Coriolis effect. Figure 6.16 shows the vertical acceleration time histories, taken as the average from accelerometers AV1 and AV2, located on opposite ends of the container. When comparing the time histories in Fig. 6.16 to those seen in Fig. 6.5, there is no longer the presence of a 3 Hz component, indicating that the 3 Hz component was due to rocking. This is corroborated in Fig. 6.5 by observing that the 3 Hz components of AV1 and AV2 are approximately 180 degrees out of phase.

The theoretical Coriolis acceleration for each destructive motion was calculated using the following vector cross product:

$$a_{\text{Coriolis}} = 2\Omega \times V_{\text{rel}} \tag{6.1}$$

where V_{rel} is found by time integration of the input base acceleration (average of AH11 and AH12) and Ω is the angular velocity of the spinning centrifuge. Figure 6.16 compares the theoretical Coriolis accelerations to the average recorded vertical accelerations. Superimposed on these time histories are the absolute cumulative normalized errors between theoretical and observed vertical accelerations. As well, the time at end of shaking is noted. During all destructive motions of UCD4 and UCD6, the vertical accelerations were under-predicted, and free vibration after the end of

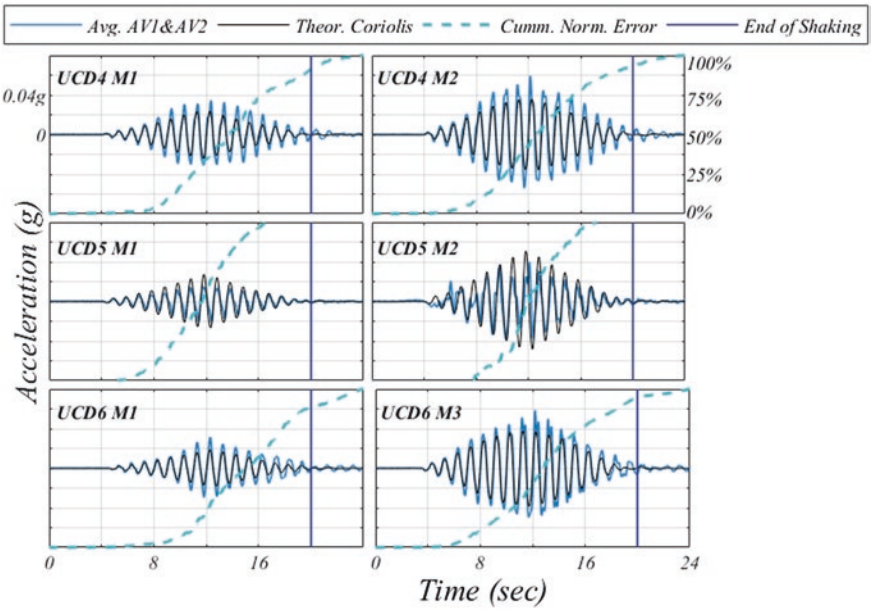

Fig. 6.16 Theoretical Coriolis acceleration versus average vertical acceleration for UCD4, UCD5, and UCD6

shaking is observed. During UCD5, the vertical accelerations were over-predicted, and no free vibration after the end of shaking is observed. This indicates that vertical vibration resonance of the shaker system was activated during UCD4 and UCD6, but not during UCD5. Using the generalized scaling laws, different shaking frequencies were used in UCD5 than in the other tests; however, all motions were intended to represent 1 Hz in prototype scale. UCD4 and UCD6 were performed with a 1 g scale factor of $\mu = 1$ and centrifuge scale factor of $\eta = 43.8$, thus requiring 43.8 Hz model scale input motion. UCD5 was performed with a 1 g scale factor of $\mu = 2$ and centrifuge scale factor of $\eta = 21.9$, thus requiring 36.8 Hz model scale input motion (see Table 6.1 for time scale factor equation). A consequence of resonance is that vertical vibrations continuing after the end of shaker excitation (time = 20 s) could result in slower pore pressure dissipation and larger displacements.

6.4.3 Reversed Slope in UCD6

The presence of vertical acceleration due to Coriolis effect may have other implications on model performance beyond the effect of additional vertical shaking cycles due to resonance. Since the Coriolis acceleration is a function of V_{rel} (found by integration of the horizontal base acceleration), it is 90 degrees out of phase with the

horizontal base acceleration, resulting in an elliptical displacement trajectory of the container during shaking. Figure 6.17(a) shows the container's horizontal and vertical displacement time histories during UCD6 M1. Horizontal displacement was found by double time integration of the filtered base acceleration (average of AH11 and AH12 processed through a 0.3–3 Hz fourth-order bandpass filter). The vertical displacement was found by double integration of the filtered vertical acceleration (average of AV1 and AV2 processed through a 0.3–3 Hz fourth-order bandpass filter). As expected, the vertical displacement is out of phase with the horizontal displacement by 90 degrees, reinforcing the conclusion that the vertical accelerations are due to the Coriolis effect. This results in a counterclockwise elliptical displacement trajectory (Fig. 6.17(b)); this is true for every UCD destructive motion.

It was hypothesized that the direction of the container trajectory, with respect to the model slope, could affect model performance. To test this hypothesis, UCD6 was built with a reversed slope, but at the same initial density (1658 kg/m^3) as UCD3. Figure 6.18 shows slope orientations of UCD3 (left) and UCD6 (right) with respect to the counterclockwise elliptical displacement trajectory of the container. The hypothesis is that the counterclockwise trajectory could inhibit downslope

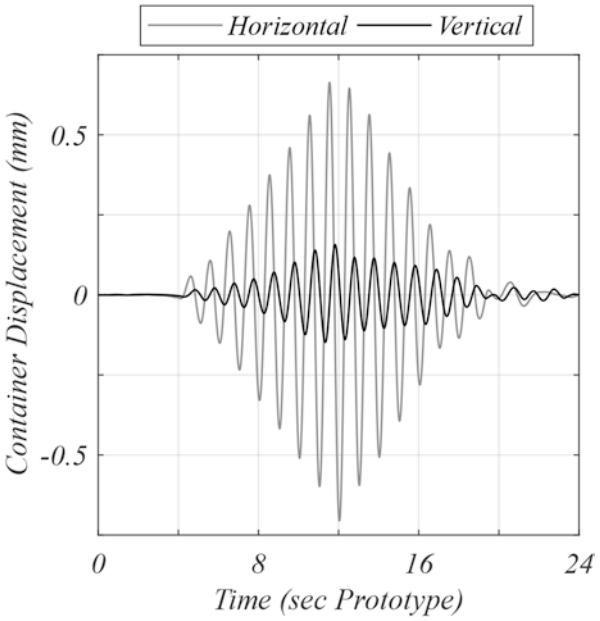

Fig. 6.17 (**a**) Horizontal and vertical displacement time histories of model container during UCD6 M1. (**b**) Vertical/horizontal container displacement during UCD6 M1

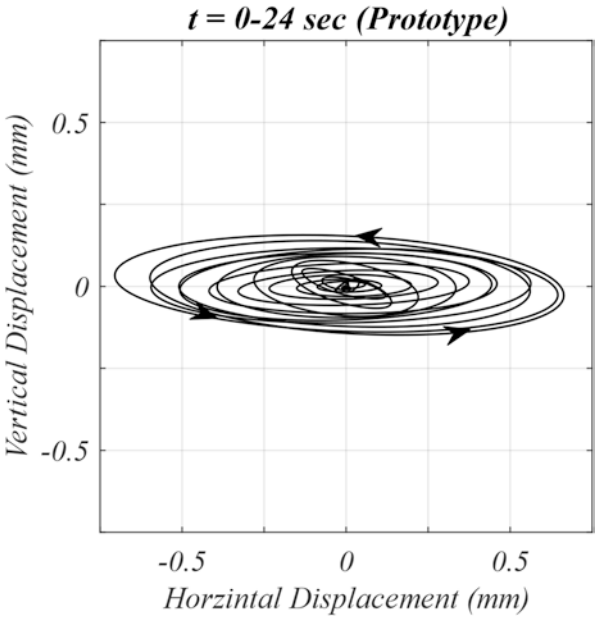

Fig. 6.17 (continued)

Fig. 6.18 Opposite slope geometry of two UCD models with respect to counterclockwise elliptical displacement trajectory

displacement for the UCD3 slope orientation and could exacerbate downslope displacement for the UCD6 slope orientation. Figure 6.19 compares hand-measured lateral and vertical surface marker displacements from UCD3 M1 and UCD6 M1.

A larger base acceleration was input during UCD3 M1 (PGA_{eff} = 0.174 g) than UCD6 M1 (PGA_{eff} = 0.137 g). This is reflected by the fact that UCD3 M1 experienced larger lateral displacements than UCD6 M1. However, Fig. 6.19 also shows that vertical displacements were slightly greater in UCD6 than UCD3, the primary component of displacement in UCD6 being vertical.

Figure 6.20 shows CPT soundings before and after M1 from both UCD3 and UCD6. It is shown that CPT1 from UCD3 and UCD6 are almost identical, as the models began with the same initial density; however, UCD6 experienced greater increase in tip resistance than UCD3, on average over the depth of the push. This may be attributed to densification during strong shaking. Although it is not

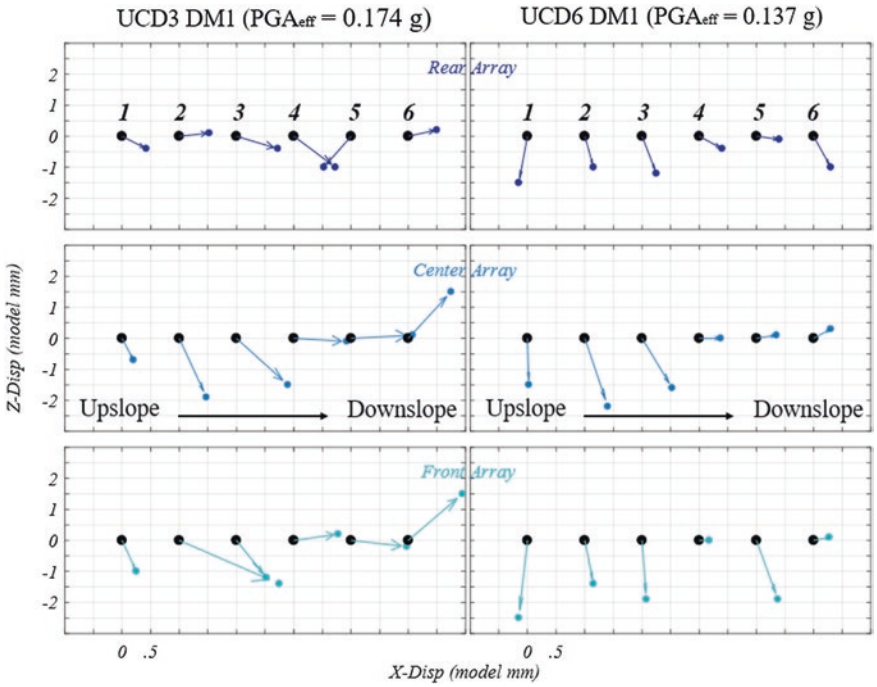

Fig. 6.19 Profile view comparison of hand-measured lateral and vertical surface marker displacements from UCD3 M1 (left) and UCD6 M1 (right). Each test is shown upslope to downslope as left to right for ease of comparison

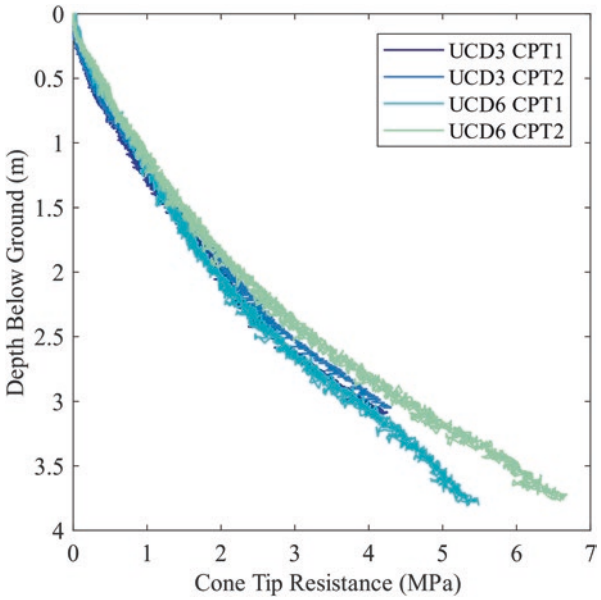

Fig. 6.20 Comparison of CPT profiles before and after M1 for UCD3 and UCD6

conclusive, as this is only one test comparison, it may be that reversing the slope in UCD6 may affect model performance, causing increased vertical settlement and densification for a smaller ground motion.

It should be noted that vertical accelerations due to the Coriolis effect will only arise if shaking occurs in the circumferential direction, and the influence of the Coriolis effect increases as the radius of the centrifuge arm decreases. Because the Coriolis acceleration is proportional to the angular velocity (Eq. 6.1), it is inversely proportional to the square root of the centrifuge radius (Eq. 6.2).

$$a_{\text{Coriolis}} = 2 * \sqrt{\frac{\mu * \eta}{r_{\text{centrifuge}}}} \times V_{\text{rel}} \tag{6.2}$$

6.5 Method for Measuring Dry Density

The procedure to measure specimen density for the LEAP-ASIA-2018 UCD experiments follows the procedure described by Carey et al. (2020). Density was calculated by mass and volume measurements at several points during model construction to check the target density was being reached consistently throughout the model depth. At each intermediate check, the surface was vacuumed flat, 15 locations were measured and then averaged, and the density was calculated using the mass of the lift.

Reported density of the model used volume and mass measurement of the final curved surface. The model height was measured at 11 locations along 3 longitudinal lines of the final curved surface, for a total of 33 measurements. Using AutoCAD, a curve was fit to the 11 points on the same longitudinal line. The area of each region was calculated, and then the model volume was taken as the average of the three cross-section areas multiplied by the 279 mm width of the container. Density was then calculated using the final mass of the model. The LEAP-ASIA-2018 test template contains supplemental documentation of density calculation for each lift during construction, including the final curved surface.

6.6 Viscous Fluid Preparation and Saturation

6.6.1 Viscous Fluid Preparation

Methylcellulose was used for each UCD experiment to scale pore fluid viscosity in accordance with the generalized scaling law, $\text{visc} = \text{visc}_{\text{water}} * \mu^{0.75} * \eta$. Prior to centrifuge testing, several batches of viscous solution were mixed to determine the correct proportion of Dow, F50 Food Grade hydroxypropyl methylcellulose power

and water, by mass, to achieve the desired viscosity. The ratio of mass of methylcellulose to mass of water for Type A ($\mu = 1,\ \eta = 43.75$) and Type B ($\mu = 2,\ \eta = 21.89$) tests were approximately 2.2% and 1.8%, respectively.

The methylcellulose was prepared in accordance with the chemical supplier recommendation for hot mixed solution. The procedure was as follows:

1. Warm roughly 1/4 of the required deionized water to 90 °C. Add methylcellulose with a mass that is equal to 8.8% of mass of the deionized water.
2. Mix solution for 45 min.
3. Dilute the mixture with the same mass of water from step 1 at room temperature. Mix for additional 10 min. Following mixing, the solution should be at roughly double concentration.
4. Cool overnight.
5. Using an approximately 200 g sample of the stock solution, 208 g of room temperature deionized water was added and mixed. Viscosity of the solution was checked using a Cannon instrument size 2 Ubbelohde viscometer.
6. Step 5 was repeated if necessary, adjusting the amount of deionized water added, to determine the correct ratio of deionized water and stock until the desired viscosity is obtained.
7. Lastly, the entire batch of methylcellulose was mixed with the correct ratio of water and stock found in step 6.

6.6.2 Saturation

The same saturation procedure, as presented in Carey et al. (2020), was followed for each of the UCD models. Initially, the dry model and container were placed in a vacuum chamber. 97 kPa of vacuum was applied, and then the vacuum was shut off, and the chamber was flooded with CO_2, until the vacuum was reduced to 1–2 kPa. The CO_2 flow was then shut off, and 97 kPa vacuum was reapplied. This cycle was repeated two more times. Following the third evacuation, the residual concentration of nitrogen and oxygen gas in the chamber should be $\left(\frac{101.4 - 97}{101.4}\right)^3 = 0.008\%$ of its initial concentration. The methylcellulose solution was de-aired and dripped onto a sponge located on the top surface of the sand. A pool of de-aired methylcellulose solution was maintained in the lowest edge of the container. As the wetting front progressed toward the top of the model, the size of the pool was allowed to grow. The top corner of the slope was the last portion of the model to saturate in order to avoid entrapping residual gas within the model. 97 kPa vacuum was maintained throughout the infiltration of methylcellulose. Once the model was completely saturated and the surface submerged, the vacuum was slowly released.

The degree of saturation was then checked using the method described in the specification (Kutter et al. 2019), modified from Okamura and Inoue (2012). The vacuum chamber was opened, and a tethered float, delineated with a 1 cm grid, was

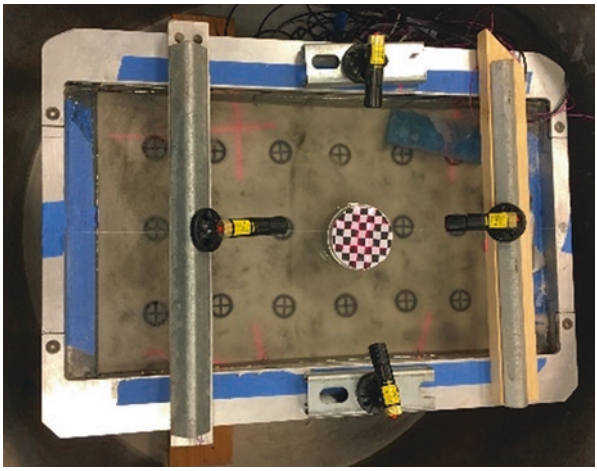

Fig. 6.21 Lasers positioned so lines make cross-hair at float on surface of methylcellulose

placed on the methylcellulose surface. Laser pointers were positioned on the container walls pointing downward at the floating grid with a 5-degree angle. The laser pointer and float configuration are shown in Fig. 6.21. The transparent cover was placed back over the vacuum chamber, and the locations of the lines from the lasers on the float were noted. A 10 kPa vacuum was applied, and the locations of the laser lines were recorded again. Changes in the location of the laser lines are presumed to be caused by volume change of trapped gas in the model. Using Boyle's law, the volume of air and degree of saturation can be estimated. No movement of the laser lines was observed for each of the experiments, so the degree of saturation was estimated to be better than 99.99%. The corresponding CO_2 gas content is 0.01% of the viscous fluid volume, which could easily dissolve in the viscous fluid during spinning.

6.7 Conclusions

This paper describes the three experiments performed on the 1 m centrifuge at the University of California, Davis as part of the LEAP-ASIA-2018 exercise. Two experiments were performed using conventional centrifuge scaling laws, and one experiment was performed using generalized scaling laws. The model performance and results for multiple destructive ground motions were presented. Two unique aspects of the tests performed were also discussed: using GeoPIV to measure surface displacements and the implications of the Coriolis effect on model performance. Additionally, methods for measuring dry density, mixing viscous fluid, and model saturation are explained.

Destructive Motion 1 in UCD5 did not cause liquefaction, which is evident by the low excess pore pressures and nearly rigid acceleration response. For this

reason, Destructive Motion 2 in UCD5 may be better suited for comparisons. Liquefaction was observed for all other motions. A third, very large, destructive motion was performed in UCD6 to cover a broad range of ground motion intensities. Little to no change in cone tip resistance was observed in UCD4 or UCD5, due to their high initial densities and relatively low level of shaking; however, cone tip resistance increased during each destructive motion in UCD6, due to its initially medium dense state. A fourth CPT was performed at the end of UCD5, to compare soundings under conventional and generalized scaling; the results coincided nicely.

GeoPIV was used to survey surface displacements during each experiment. Its use allowed for time histories of displacement and greater spatial resolution of measurements. Displacement patterns were consistent with other sensors in their indication of liquefaction severity. Final displacements, as measured by GeoPIV, also matched surface marker hand measurements reasonably well.

The cause of non-specified vertical accelerations during each destructive motion was attributed to the Coriolis effect. Additional cycles of vertical shaking were measured in UCD4 and UCD6, attributed to resonance in the shaker system being activated by the input acceleration frequency. Time integrating container mounted horizontal and vertical accelerometers showed the container displacement trajectories followed a counterclockwise elliptical trajectory for every motion. Comparing surface marker and CPT data from two models of the same initial density (UCD3 and UCD6) showed that slope orientation with respect to this orientation may affect model performance.

Acknowledgments These experiments were supported by NSF CMMI grant number 1635307. The authors would also like to thank the staff at the Center for Geotechnical Modeling (CGM) for their assistance and technical insight throughout this series of tests.

References

Carey, T. J., Hashimoto, T., Cimin, D., & Kutter, B. L. (2017). LEAP-GWU-2015 centrifuge test at UC Davis. *Soil Dynamics and Earthquake Engineering*. https://doi.org/10.1016/j.soildyn.2017.01.030

Carey T. J., Stone, N., Kutter, B. L, & Hajialilue-Bonab, M. (2018a). A new procedure for tracking displacements of submerged sloping ground in centrifuge testing. In *Proceedings of the 9th International Conference on Physical Modelling in Geotechnics 2018 (ICPMG 2018)* London, United Kingdom.

Carey T. J., Kutter, B. L., Haigh, S. K., Madabhushi, S. P. G., Okamura, M., Kim, D. S., Ueda, K., Hung, W. Y., Zhou, Y. G., Liu, K., Chen, Y. M., Zeghal, M., Abdoun T., Esco_er, S., & Manzari, M. (2018b). A new shared miniature cone penetrometer for centrifuge testing. In *Proceedings of the 9th International Conference on Physical Modelling in Geotechnics 2018 (ICPMG 2018)* London, United Kingdom.

Carey T. J., Stone N., Bonab M. H., & Kutter B. L. (2020). LEAP-UCD-2017 centrifuge test at University of California, Davis. (In press).

Fiegel, G. L., & Kutter, B. L. (1994). Liquefaction Mechanism for Layered Soils. *Journal of Geotechnical Engineering, 120*, 737–755. https://doi.org/10.1061/(asce)0733-9410(1994)120:4(737)

Iai, S., Tobita, T., & Nakahara, T. (2005). Generalized scaling relations for dynamic centrifuge tests. *Geotechnique, 55*(5), 355–362.

Kutter, B., Carey, T., Hashimoto, T., Zeghal, M., Abdoun, T., Kokalli, P., Madabhushi, G., Haigh, S., Hung, W.-Y., Lee, C.-J., Iai, S., Tobita, T., Zhou, Y. G., Chen, Y., & Manzari, M. T. (2018). LEAP-GWU-2015 experiment specifications, results, and comparisons. *Soil Dynamics and Earthquake Engineering, 113*, 616–628. https://doi.org/10.1016/j.soildyn.2017.05.018

Kutter, B. L., Carey, T. J., Stone, N., Bonab, M. H., Manzari, M. T., Zeghal, M., Escoffier, S., Haigh, S. K., Madabhushi, G. S. P., Hung, W.-Y., Kim, D.-S., Kim, N. R., Okamura, M., Tobita, T., Ueda, K., & Zhou, Y.-G. (2019). LEAP-UCD-2017 V. 1.01 Model Specifications. In Model Tests and Numerical Simulations of Liquefaction and Lateral Spreading (pp. 3–29). Springer International Publishing. https://doi.org/10.1007/978-3-030-22818-7_1

Okamura, M., & Inoue, T. (2012). Preparation of fully saturated models for liquefaction study. *International Journal of Physical Modelling in Geotechnics, 12*, 39–46. https://doi.org/10.1680/ijpmg.2012.12.1.39

Stanier, S. A., Blaber, J., Take, W. A., & White, D. J. (2015). Improved image-based deformation measurement for geotechnical applications. *Canadian Geotechnical Journal, 53*(5), 727–739.

Stone N. S. (2019). MSc thesis, Department of Civil and Environmental Engineering, University of California, Davis (In preparation).

Chapter 7
LEAP-ASIA-2019 Centrifuge Test at Ehime University

Mitsu Okamura and Asri Nurani Sjafruddin

Abstract Three centrifuge tests were conducted at Ehime University for the LEAP-ASIA-2019 exercise. The experiment consisted of a submerged clean sand, with a target relative density of 65%, with a 5-degree slope in a rigid container. Models were prepared along with the specifications, and each model was subjected to a ramped sine wave base motion. Models were designed so that they simulated the same prototype at different scaling factors to verify the validity of the generalized scaling law. This paper provides an overview of the models and some details of the effects of the scaling factor on the pore pressure responses and deformation of the models.

Keywords Liquefaction Experiments and Analysis Projects (LEAP-ASIA-2019) · Generalized scaling law (GSL) · Centrifuge modeling

7.1 Introduction

This paper presents three centrifuge tests conducted at Ehime University (EU) in the LEAP-ASIA-2019 project. Two of them, models EU-1 and EU-2, were the same as those of tests in LEAP-UCD-2017, and one test, model EU-GS1, was newly conducted in the present project. Models were designed so that they simulated the same prototype at different scaling factors to verify the validity of the generalized scaling law (Iai et al., 2005). Model configuration, preparation techniques, and sand used are in accordance with "LEAP-UCD-2017 Version 1.01 Model Specifications" (Kutter et al., 2018) otherwise mentioned.

M. Okamura (✉) · A. N. Sjafruddin
Graduate School of Science and Engineering, Ehime University, Matsuyama, Japan
e-mail: okamura@cee.ehime-u.ac.jp

T. Tobita et al. (eds.), *Model Tests and Numerical Simulations of Liquefaction and Lateral Spreading II*, https://doi.org/10.1007/978-3-031-48821-4_7

7.2 Centrifuge Model

7.2.1 Model Description

A rigid model container was used with internal dimensions of 50 cm long, 12 cm wide, and 23 cm deep. Three models were prepared at a target relative density of 65%, saturated with viscous fluid and tested at either 40 g or 20 g. Figure 7.1 shows a side view of the models. All the corresponding prototype dimensions are the same as those specified with an exception that the prototype width was approximately half of that specified.

The prototype being simulated in this study is a fully submerged medium dense Ottawa sand slope with a slope angle of 5%. This prototype was modeled in two ways; one was a well-established centrifuge modeling technique where a model geometrically reduced by a factor of 40 was tested at 40 g centrifugal acceleration. The sand in the model was the same as the prototype but saturated with a fluid which was 40 times more viscous than water to closely simulate the prototype sand permeability. The other was the generalized scaling law. Iai et al. (2005) proposed a scaling law by combining the centrifuge scaling law with a scaling law for 1 g dynamic model tests. The scaling factors for the centrifuge test $\eta = 20$ and 1 g test $\mu = 2$ were selected in this study to represent the same prototype. The model was prepared with the same sand but saturated with a fluid with different viscosity, subjected to 20 g centrifugal acceleration and shaken with similar base input motion with different acceleration amplitude and frequency. Scaling factors for tests in this study are summarized in Table 7.1.

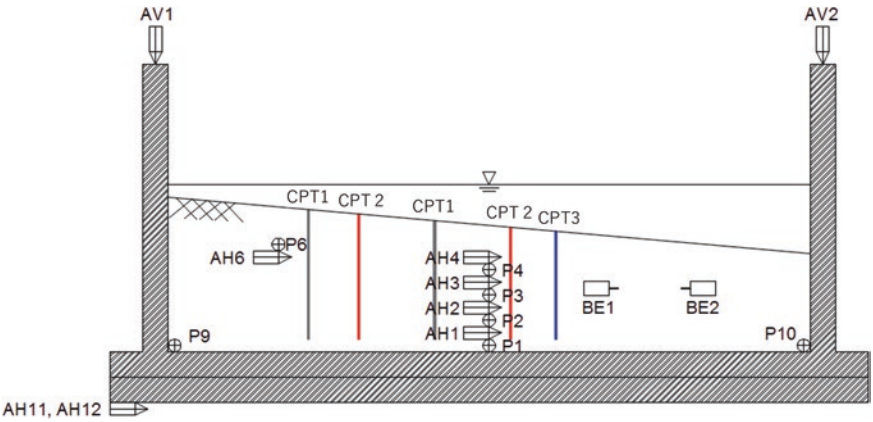

Fig. 7.1 Schematic of models

Table 7.1 Summary of scaling factors

	Scaling factors (prototype/model)	
Centrifuge: η	40	20
1 g: μ	1	2
Length	40	40
Density	1	1
Time	40	33.6
Shaking acceleration	0.025	0.05
Shaking frequency	0.025	0.0297
Stress	1	2
Strain	1	1.41
Displacement	40	56.6
Permeability	1	1

7.2.2 Sand

Ottawa F-65 sand (Bastidas et al., 2017) was used in all the experiments, which was shipped out from UC Davis on March 2017. Sieve tests on the sand confirmed that grain size distributions of the sand used in EU were consistent with those shown in the specifications.

7.2.3 Placement of Sand

Dry sand stored in an air-conditioned room, where humidity was kept low, was pluviated into the container through a screen with an opening size of 1.0 mm, rather than 1.2 mm specified in the specification, because openings of the standard sieve in JIS (Japanese Industrial Standards) are slightly different from ASTM.

An arrangement of the screen masked off was used to achieve the target relative density. 12 mm slots spaced at 25 mm were used for preparing the sand bed with a relative density of 65%. After the pluviation of the sand, the surface of the model was leveled using a vacuum device, and the height of the model surface was measured to calculate dry density. The procedure of the measuring height was the same as that specified. The surface was sloped using the vacuum device to 5 degrees, and 18 surface markers were set (Fig. 7.2). The depth of the sand on the centerline was 10 cm for all models tested in this study.

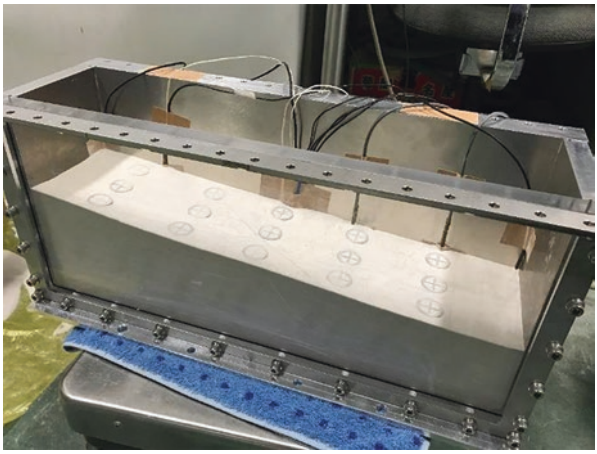

Fig. 7.2 Model before saturation

Table 7.2 Model properties and test conditions

Test code	Target Dr. (%)	Scaling factor		Peak prototype acceleration (g)	Fluid viscosity (cSt)	Before Motion #1	
		η	μ			Relative density Dr. (%)	Degree of saturation, Sr (%)
EU-1	64	40	1	0.169	44	64	99.3
EU-2	67	40	1	0.178	40	67	99.4
EU-GS1	64	20	2	0.188	33	64	99.5

7.2.4 Saturation

The model container was moved into a vacuum chamber, and the air in the chamber was replaced by CO_2. This was achieved by introducing vacuum pressure of −95 kPa and flooding CO_2 gas. De-aired viscous fluid was dripped into the lower end of the model slope while keeping the vacuum of −95 kPa constant in the chamber and a fluid supply tank (Okamura & Inoue, 2012). The viscous fluid was a mixture of water and hydroxypropyl methylcellulose (type 60SH-50) termed Metolose from Shin-Etsu Chemical Company (Shin-Etsu Chemical Co., Ltd., 1997). This Metolose solution was prepared by dissolving 1.8% or 1.5% Metolose by weight in water, so as to achieve a viscosity of 40 or 33.6 times that of water (40 cSt or 33.6 cSt kinematic viscosity), respectively. The viscosity of the fluid in each model was measured at room temperature before and after the tests with a rotational viscometer and presented in Table 7.2.

On completion of the saturation process, the vacuum in the chamber was released, and the model was rested in the atmospheric pressure for a few hours. A small change in the pressure of approximately 10 kPa was applied to the chamber at a constant rate approximately 5 kPa/min, and water level was measured with a LED

displacement transducer with the resolution of 10 μm. The degree of saturation of the models was measured with the method developed by Okamura & Inoue (2012) and summarized in Table 7.2. The degree of saturation was in a range between 99.3% and 99.5%. In the centrifuge, hydrostatic pressure of the model was enhanced, and most of the remaining air and CO_2 bubbles in soil pore are considered to have dissolved (Kutter, 2013), which increased further the degree of saturation.

7.2.5 Test Procedure

Three tests were conducted in this study. Models EU-1 and EU-2 were tests at 40 g, while the model EU-GS1 was tested at 20 g and applied the generalized scaling law to further scale up to the prototype. Shaking tests and CPT were carried out at 40 g or 20 g as schematically illustrated in Fig. 7.3. The centrifuge was spun up and down to mount and unmount the CPT device. Locations of the surface markers were measured with a ruler, and the relative density of the model was estimated from the average settlement.

Cone penetration tests were performed before and after the destructive ground motion with a CPT device designed and fabricated at UCD. Two penetration tests were conducted at a time at intervals of 5 cm (12.5 times the cone diameter). The rate of cone penetration was 0.6 mm/s in model scale, which was slower than that specified.

Two destructive shaking tests, Motion #1, were conducted with the tapered sine wave of a maximum prototype acceleration amplitude of 0.15 g. In the second destructive shaking tests, the same motion as the first one was imparted again to evaluate the evolution of the behavior of the model due to the previous shaking event.

All the data was recorded at a sampling rate of 2000 per second during shaking and after shaking for approximately 20 s until the generated pore pressure completely dissipated. In the subsequent section in this paper, all the test results are in prototype scale otherwise mentioned. Note that data were not applied any numerical filtering.

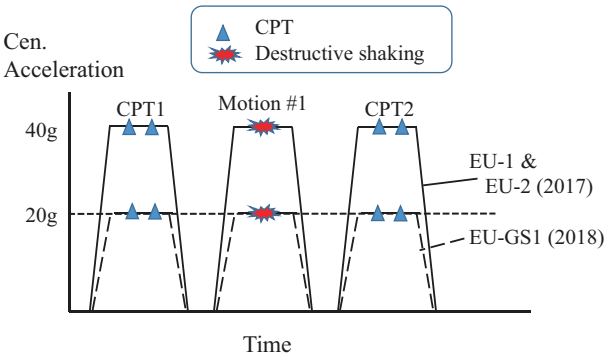

Fig. 7.3 Centrifuge test sequence

7.3 Results

7.3.1 Input Acceleration

Input base accelerations measured at the base of the container are shown in Fig. 7.4. In order to duplicate the specified tapered sine wave by the mechanical shaker, rotation rate of camshaft changed with time accordingly. The shaking initiated at the time t = 0, and the rotation rate increased linearly with time until t = 10 s and decreased thereafter. Therefore, the acceleration frequency was very close to 1.0 Hz for t = 9–13 s and between 0.7 and 0.9 Hz for t = 5–9 s and t = 13–15 s.

7.3.2 CPT

CPT was conducted at two locations indicated as "CPT1" in Fig. 7.1 before shaking. Vertical profiles of cone tip resistances before shaking are indicated in Fig. 7.5. The tip resistances for EU-GS1 at two locations are almost the same and very similar to that of EU-1, confirming the model uniformity and reproducibility.

7.3.3 Excess Pore Pressure Response

Figure 7.6 shows excess pore pressure ratios (EPPRs) measured on the centerline of the models EU-1 and EU-GS1. EPPRs of EU-1 reached unity except for p1, indicating that the soils in EU-1 liquefied from the surface to the depth close to the bottom. While for EU-GS1, EPPR increased in a quite similarly manner at the beginning of shaking event, however, the maximum value of EPPRs was slightly lower than those in EU-1 and short to the liquefaction condition (EPPR = 1) followed by initiation of pore pressure dissipation during shaking.

Figure 7.7 compares long-term excess pore pressure (EPP) responses for EU-1 and EU-GS1. Duration for liquefaction condition lasted after shaking and the time

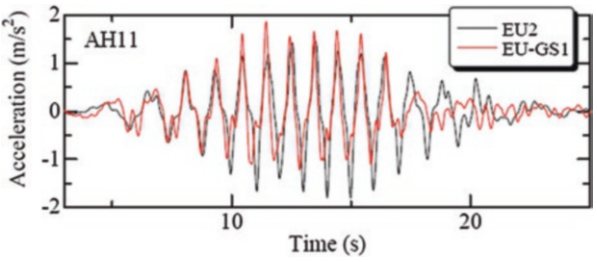

Fig. 7.4 Input accelerations of Motion #1 for EU-1 and EU-GS1

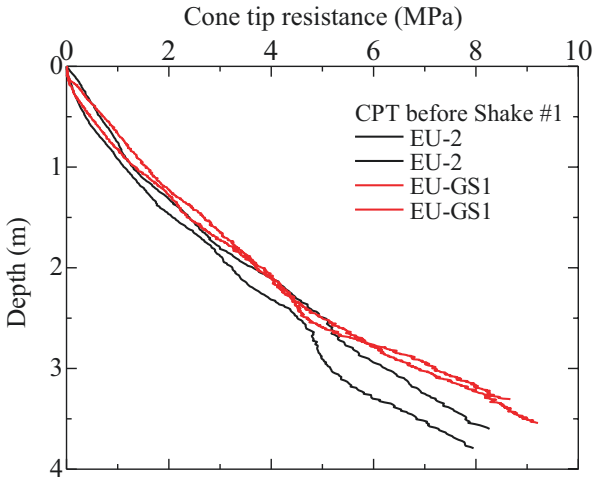

Fig. 7.5 Cone tip resistance before shaking for EU-2 and EU-GS1

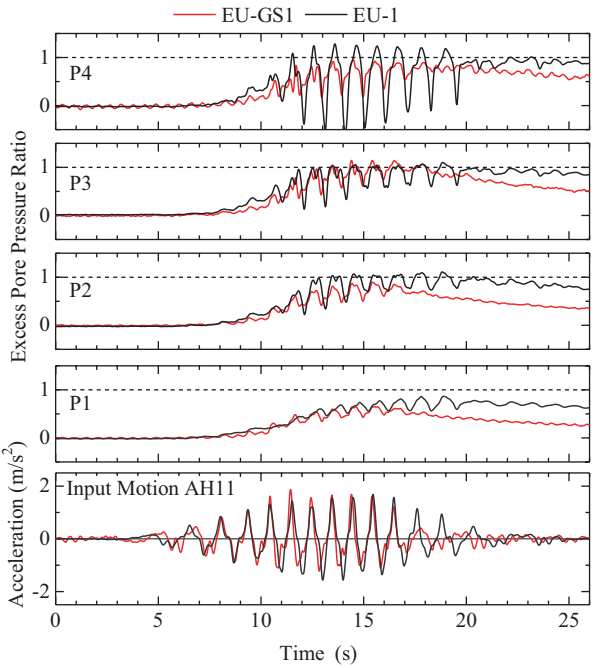

Fig. 7.6 Time histories of excess pore pressure ratio

for pore pressure dissipation were much longer for EU-1 than EU-GS1. A possible reason for the difference in pore pressure responses is permeability of the soil. The sand in EU-GS1 was saturated with the viscous fluid of 33.6 cSt, and the

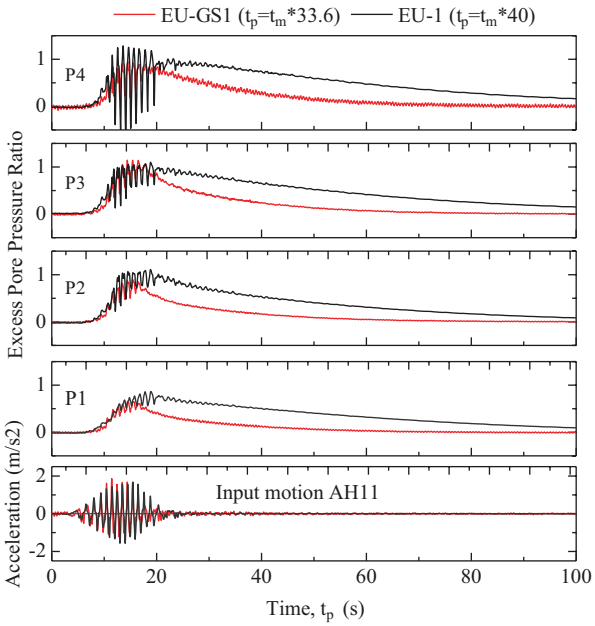

Fig. 7.7 Long-term comparison in excess pore pressures

corresponding permeability was 1.7 (=33.6/20) times lower than the prototype sand. Therefore, the permeability of the sands does not explain the difference in EPPR response between EU-1 and EU-GS1. The other reason may be the difference in stress level. The self-weigh stress in model EU-GS1 is half of that in EU-1 and the sand behaved more dilative.

7.3.4 Deformation of the Model

Figure 7.8a shows locations of surface markers in model scale before and after the shaking. For EU-2, the upmost and the downmost markers near the side walls of the rigid container stayed almost in the same location due to the side wall confinement. Except for those locations, the surface subsided in the upstream side and heaved in the downstream side. Horizontal displacement was in the range from 0 to 3 mm, while for EU-GS1, both vertical and horizontal displacements of the surface markers were half or less as compared with EU-2. Figure 7.8b indicates prototype horizontal displacement. Horizontal displacement for the EU-2 was on the order of half of EU-2. This may be due to the fact that the extent of liquefaction of sand in EU-GS1 was limited.

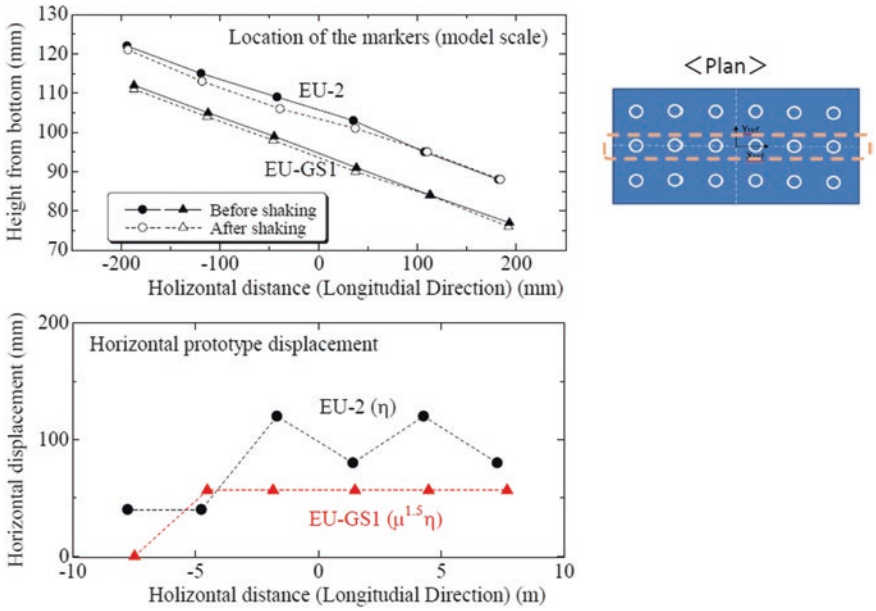

Fig. 7.8 Vertical and horizontal displacement of surface markers

7.4 Conclusion

This paper describes three centrifuge tests conducted at Ehime University for LEAP-2017 and LEAP-ASIA-2019. The tested models were fully saturated uniform sand slope with a relative density of 65%. All the models were subjected to the same simulated prototype base motion consisted with ramped sine wave.

Although the soil profiles including the relative density and cone tip resistance were quite similar for all the models, excess pore pressure was slightly lower and dissipated swiftly after shaking for model EU-GS1 (conducted at 20 g) as compared with the other two tests, EU-1 and EU-2 (performed at 40 g). Deformation of the sand for EU-GS1 was also smaller than EU-1 and EU-2. These differences may be due to the different pressure level, which resulted in more dilative behavior for EU-GS1 conducted at lower centrifugal acceleration of 20 g.

Acknowledgments The experimental work was supported by JSPS KAKENHI grant numbers 26282103 (PI: Prof. S. Iai) and 17H00846 (PI: Prof. T. Tobita). The authors would like to thank a technical staff, R. Tamaoka, and graduate student, T. Inoue, for their assistance to perform centrifuge tests.

References

Bastidas, A. M. P., Boulanger, R. W., Carey, T. C., & DeJong, J. (2017). Ottawa F-65 sand data from Ana Maria Parra Bastidas. https://datacenterhub.org/resources/ottawa_f_65

Iai, S., Tobita, T., & Nakahara, T. (2005). Generalized scaling relations for dynamic centrifuge tests. *Geotechnique, 55*(5), 355–362.

Kutter, B. L. (2013). Effects of capillary number, bond number, and gas solubility on water saturation of sand specimens. *Canadian Geotechnical Journal., 50*(2), 133–144.

Kutter, B. L., Carey, T. J., Stone, N., Bonab, M. H., Manzari, M., Zeghal, M., Escoffier, S., Haigh, S., Madabhushi, G., Hung, W. Y., Kim, D. S., Kim, N. R., Okamura, M., Tobita, T., Ueda, K., & Zhou, Y. G. (2018). LEAP-UCD-2017 V. 1.01 model specifications. In *Proc LEAP-UCD-2017 workshop – Lateral spreading in a rigid box*.

Okamura, M., & Inoue, T. (2012). Preparation of fully saturated model for liquefaction study. *International Journal of Physical Modelling in Geotechnics, 12*(1), 39–46.

Shin-etsu Chemical Co., Ltd. (1997). *Metolose brochure*. Cellulose Department.

Chapter 8
LEAP-ASIA-2019 Centrifuge Tests at University Gustave Eiffel

Sandra Escoffier, Zheng Li, and Philippe Audrain

Abstract In the framework of the LEAP-ASIA-2019 exercise, two dynamic centrifuge tests on a gentle slope of saturated Ottawa F-65 sand have been performed at the centrifuge of University Gustave Eiffel. These tests were conducted in parallel with other tests performed in nine other centrifuge centers. In addition to the objectives of the LEAP-UCD-2017 (comparison of the experimental results, e.g., effect of the experimental procedure or of test parameters on the results, and providing of a database for numerical modeling), the new objective was to evaluate, through the tested configuration, the generalized scaling approach described by Iai et al. (Géotechnique 55(5):355–362, 2005). In this framework, all the centrifuge teams have performed two types of tests. Considering the same prototype geometry, the first test was performed following the classical approach used in centrifuge modeling, and the second test was performed considering the generalized scaling law (GSL). Following the test matrix and test specifications of LEAP-ASIA-2019, University Gustave Eiffel has performed two model tests (test A2 renamed UGE-1/50-62 and test A3 renamed UGE-2/25-62). The two tests have been performed on a slope sand with the same relative density (62%) considering a target motion PGA_{eff} = 0.3 g (1 Hz ramped sine at the prototype scale).

In this paper, the test setup and the deviations from the specifications such as the experimental setup improvement that have followed the LEAP-UCD-2017 tests are presented in detail. The results obtained from the two tests are then provided at the prototype scale for comparison. The obtained input base motions are first presented followed by the characterization of the soil through CPT profiles. The responses of the saturated sand slopes for both tests are then detailed through the analysis of the pore pressure buildup, the accelerations in the soil, and the displacements measured through surface markers and embedded sensors. Some preliminary results of the global scaling approach are then discussed.

Keywords Liquefaction Experiments and Analysis Projects (LEAP-ASIA-2019) · Generalized scaling law (GSL) · Centrifuge modeling

S. Escoffier (✉) · Z. Li · P. Audrain
Centrifuges for Geotechnics Lab., Univ. Gustave Eiffel, GERS-CG, Bouguenais, France
e-mail: sandra.escoffier@univ-eiffel.fr

T. Tobita et al. (eds.), *Model Tests and Numerical Simulations of Liquefaction and Lateral Spreading II*, https://doi.org/10.1007/978-3-031-48821-4_8

8.1 Introduction

Actual researches in numerical modeling on liquefaction phenomena such as advanced numerical technics based on multiscale approach in large deformation (Callari et al., 2010) highlight the need of experimental database for the calibration and the validation processes. In an effort to improve the quality and reliability of the experimental data, a first series of cross tests was performed in the framework of the LEAP-GWU-2015. The analysis of the results, presented in Kutter et al. (2018), highlights that the control of the initial conditions and of the ground motion are key points for cross testing.

Following this first step, one of the objectives of the LEAP-UCD-2017 research program was to provide high-quality laboratory and centrifuge test data. A total of nine centrifuge teams were involved in this experimental research work. Following the model specification document, each team has performed a series of dynamic tests on a gentle slope of saturated Ottawa F-65 sand. The objective of the specifications was to minimize the discrepancies between the experimental procedures followed in each centrifuge team in order to evaluate the quality of liquefaction centrifuge tests and the effects of procedure deviations on the obtained results through cross testing. In addition to this repeatability step, additional tests with different densities and base shaking amplitudes were performed. The objective was to highlight the sensitivity of the response to the soil density and base shaking level. Analysis of the results enabled to conclude that the use of standardized centrifuge CPT is more reliable for soil characterization than the density obtained from weight and dimension measurements (Kutter et al., 2018).

For the next step of the LEAP program, LEAP-ASIA-2019, the new results will be included in the previous database, and they will be compared to the tendencies observed from the previous stages. In addition, the new objective of this LEAP exercise is to provide data to analyze the effectiveness of the generalized scaling law (GSL), described by Iai et al. (2005), for the tested configuration (i.e., gentle submerged slope of sand subjected to a ramped sine loading). In this framework, each of the ten centrifuge teams has performed centrifuge tests at two different centrifuge levels. The first test was performed considering the classical approach used in centrifuge modeling with a scaling factor for centrifuge test of η_1, and the second test was performed considering the generalized scaling law approach with a scaling factor for $1g$ test of μ_2 and a scaling factor for centrifuge test of η_2. For both tests, the prototype was the same and the scaling factors were verified $\eta_1 = \eta_2 \times \mu_2$.

In the following, the name of the tests performed highlights the test conditions. The UGE-1/50-62 test refers to a test performed at $50g$ considering a virtual test with a scaling factor of 1, and the UGE-2/25-62 test refers to a test performed at $25g$ considering a virtual test with a scaling factor of 2. In both cases, 62 refers to the relative density (61.6%).

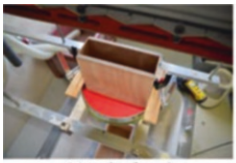

(a) tank of sand

(b) automatic back and forth device

(c) 3 density boxes

Fig. 8.1 Pluviation setup and density boxes

8.2 Test Specifications and Generalized Scaling Laws

8.2.1 Target Density

Following the LEAP-UCD-2017, it was asked to University Gustave Eiffel to perform centrifuge tests on medium dense Ottawa F-65 sand with a target density of 1654 kg.m^{-3}. Consequently, a new calibration of the pluviation system has been made. The same pluviation setup was used as in the previous LEAP exercise (Fig. 8.1). Due to the French standard, the selected sieve had an opening of 1.25 mm. This sieve was attached to an automatic hopper that enables back and forth horizontal movements along the whole length of the container (in the *X*-direction), and a sand tank placed above the sieve enables to maintain a constant flow during the pluviation process. To obtain the request density, two slots with an opening width of 25 mm and an axe-to-axe distance of 50 mm were selected. The falling height was fixed at 500 mm, and the length of the opening was sufficient to cover the whole width of the container (in the *Y*-direction) avoiding problems of overlapping for the pluviation process. A density of 1644 kg.m^{-3} was obtained (the average value obtained during the calibration process from three measurements of box density, Fig. 8.1c). Considering the average values of the maximum (1757 kg.m^{-3}) and minimum (1490 kg/m^3) densities recently provided by Carey et al. (2020), it corresponds to a relative density of 61.6%.

8.2.2 Generalyzed Scaling Laws

Due to the capacity in frequency and acceleration of University Gustave Eiffel shaker, it was asked to perform a first test at 50*g* centrifuge and a second test at 25*g* centrifuge, considering, respectively, a scaling factor for the virtual 1*g* model of 1 and 2. Due to the generalyzed scaling laws, these two configurations should enable to obtain the response of the same prototype. Table 8.1 summarizes the generalized scaling factors for the tests performed at University Gustave Eiffel.

Table 8.1 Generalyzed scaling factors for the two tests performed at University Gustave Eiffel centrifuge

	Scaling factors for 1g test	Scaling factors for centrifuge test	Generalized scaling factors		
			Theoretical expression	UGE-1/50-62 scaling factor ($\mu = 1, \eta = 50$)	UGE-2/25-62 scaling factor ($\mu = 2, \eta = 25$)
Length	μ	η	$\mu\eta$	50	50
Density	1	1	1	1	1
Time	$\mu^{0.75}$	η	$\mu^{0.75}\eta$	50	42
Frequency	$\mu^{0.75}$	$1/\eta$	$\mu^{0.75}/\eta$	0.02	0.024
Acceleration	1	$1/\eta$	$1/\eta$	0.02	0.02
Velocity	$\mu^{0.75}$	1	$\mu^{0.75}$	1	1.68
Displacement	$\mu^{1.5}$	η	$\mu^{1.5}\eta$	50	70.7
Stress	M	1	μ	1	2
Strain	$\mu^{0.5}$	1	$\mu^{0.5}$	1	1.4
Stiffness	$\mu^{0.5}$	1	$\mu^{0.5}$	1	1.4
Permeability	$\mu^{0.75}$	η	$\mu^{0.75}\eta$	50	42
Pore pressure	μ	1	M	1	2

8.3 Test Configuration and Procedure

8.3.1 Sensor Layout and Container Modifications

In the case of the tests performed at University Gustave Eiffel, the inner dimensions of the rigid container are 400 mm (L) × 200 mm (W) × 200 mm (H) (Fig. 8.2a). Due to the shaker properties, this container is rigidly fixed with 12 screws inside an ESB container where each corner is blocked with a vertical bar. As for the tests performed in the framework of LEAP-UCD-2017, additional sand was put in place between the outer and inner container to reduce the presence of harmonics due to resonance phenomena of the assembly that were observed during the preliminary tests (Fig. 8.2b).

A cross view and a top view of the sensor layout are presented in Figs. 8.3 and 8.4 in the case of the UGE-1/50-62 test (target coordinates). The target coordinates for the UGE-2/25-62 test are the same.

A total of 10 accelerometers, 6 pore pressure sensors, and 18 surface markers were used. The same markers as for the LEAP-UCD-2017 were used. The diameter of the surface markers was two times smaller than the recommended design (improved design with an external diameter of 13 mm). The locations of the markers in the X- and Y-directions were performed with a steel rule with a precision of 1 mm, and the Z location was performed with a laser sensor. The precision of the Z position is smaller than 0.5 mm as requested in the specifications. The surface markers have been put in place before the saturation process, and their locations have been measured at 1g before the first spin up of the centrifuge and after each base shaking (Motion #1 and Motion #2) once the centrifuge was spun down.

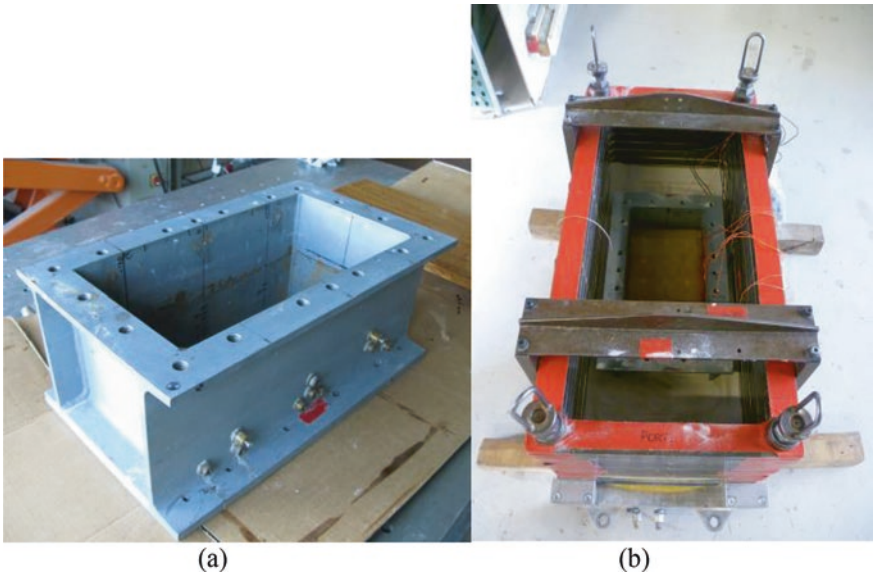

Fig. 8.2 Rigid steel box especially built for the LEAP project at University Gustave Eiffel and placement of the rigid box inside the blocked ESB container

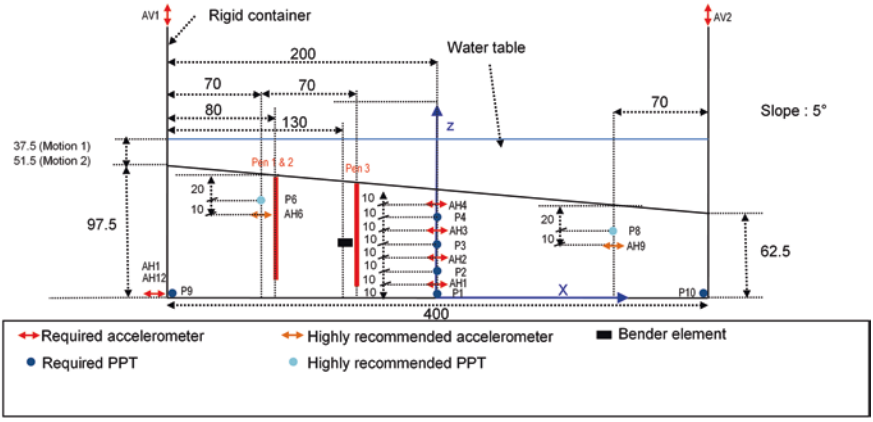

Fig. 8.3 Cross view of the instrumentation layout of the UGE-1/50-62 test (target coordinates at the model scale in mm)

The shear velocity of the soil was characterized with a pair of bender element that was put in place during the pluviation. The bender elements are of the same type as that described by Brandenberg et al. (2006). Measurements have been made before the first event and after each motion. The analysis of the results is currently underway.

In addition, in both containers, three CPTs were made. In each test, the first, second, and third CPT characterized, respectively, the initial state of the soil and the

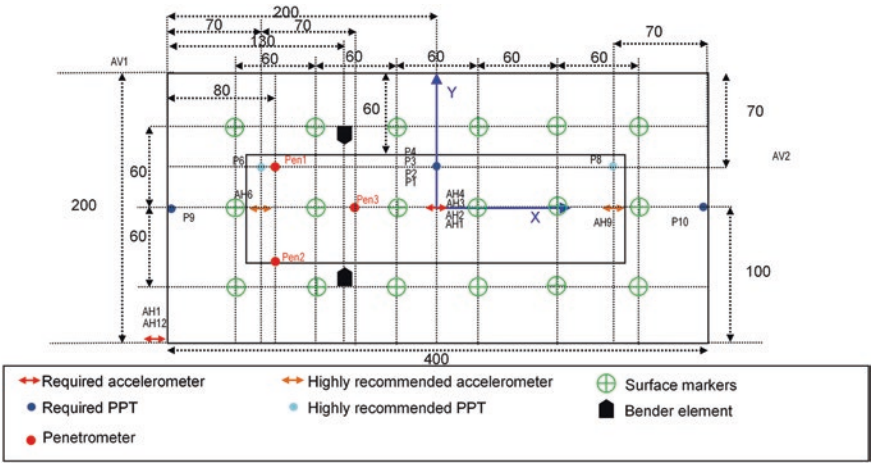

Fig. 8.4 Top view of the instrumentation layout of the UGE-1/50-62 test (target coordinates at the model scale in mm)

state of the soil after Motion #1 and Motion #2. The CPT used was the one developed at UC Davis (Carey et al., 2018), which has an external diameter of 6 mm. Previously to the centrifuge tests, the CPT was calibrated. The calibration curve highlights a hysteresis (Fig. 8.5) and a new calibration will be done. However, all the data presented for the CPTs take into consideration this initial calibration.

In the case of University Gustave Eiffel 1D shaker, the direction of the solicitation is parallel to the axis of the centrifuge (Chazelas et al., 2008). From the specifications, the radius between the surface of the soil in a transvers cross section and the center of rotation of the centrifuge should be constant. Consequently, the surface should have a circular shape in the direction perpendicular to the base shaking. However, the distance between the axis of rotation of the centrifuge and the center of the soil surface is 5.063 m. Considering that the inner dimension of the container's width is 0.2 m, the difference in height between the midpoint and the corresponding point at the lateral sides should be 1 mm. As this value is in the range of precision of the leveling of the surface, the soil surface was not curved in the *Y*-direction.

8.3.2 Viscous Fluid

In order to verify the scaling law and avoid scaling conflict between the velocity of deformation and the diffusion phenomena, viscous fluid has been used. This viscous fluid is a mixture of tap water, HPMC (Culminal MHPC 50), and biocide that is added in order to avoid the decrease of the viscosity with time (©Kathon biocide).

For the first test, the viscous fluid was obtained by mixing 28 g/l of HPMC powder with 120 ml of biocide (2% of concentration) and 880 ml of tap water based on

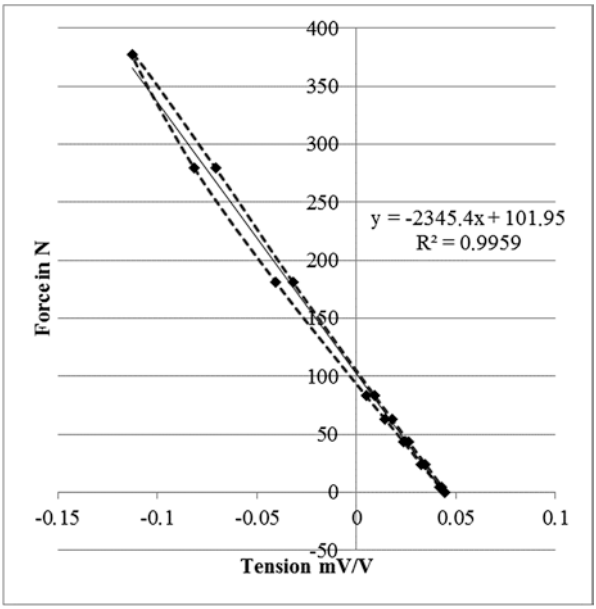

Fig. 8.5 Calibration of the UC Davis CPT

a series of viscosity measurements and the temperature of the centrifuge room. After 5 days, the viscosity was measured between 64 and 60 cSt for a temperature of 19 °C (measurements at other temperature haven't been performed due to a problem with the thermostatic bath). At the beginning of the UGE-1/50-62 test, the temperature of the centrifuge room was about 18.5 °C. However, due to the small dimensions of the container compared with that of the ESB box usually used, it was decided to introduce after Motion #1 a temperature sensor in the soil. This sensor was introduced at one corner of the box located at the top of the slope ($X = -200$ mm, $Y = 100$). Due to the length of the sensitive part of the sensor, the value is representative of a full-thickness temperature evaluation of the soil/fluid mixture. After the stabilization, the temperature was measured at 26.7 °C. Unfortunately, no viscosity test was performed on the fluid at this temperature during the day of the centrifuge test. After the centrifuge test, viscosity measurements were made but on a fluid taken directly above the soil surface. The viscosity measured was very high between 97 cSt at 19 °C and 73.07 cSt at 26 °C. Among the reasons that can explain such a large difference between the viscosity before and after the test, there is the evaporation. However, the viscosity measurements are sensitive to the presence of impurities. As the fluid was taken above the soil surface, it could have contained impurities. Consequently, these values should be considered with caution.

Therefore, for the second test, UGE-2/25-62, a temperature sensor was introduced at the same location to monitor the temperature before each base shaking. In addition, this measurement, in parallel with viscosity measurement, will be done

during the next step of the LEAP program to increase the relevance of the viscosity value during the base shaking.

8.3.3 Saturation Process

Compared to the LEAP-UCD-2017 tests performed by University Gustave Eiffel, the saturation system was improved for the LEAP-ASIA-2019 tests. Figure 8.6 presents the new experimental setup for saturation at 1g. The soil container, the viscous fluid tank, and the pump that enables the transfer of the viscous fluid from the tank to the container are all placed in the same vacuum chamber. The lid is a thick plate of Plexiglas that enables to have a top view of all the soil surface during all the saturation process. Once the container, the viscous fluid, and the fluid pump are in place inside the vacuum chamber, a powerful vacuum pump enables to obtain an absolute pressure of 90 mbar in less than 30 minutes. Once this requested absolute pressure is obtained, the vacuum chamber is filled with CO_2 up to the atmospheric pressure. Following the saturation process described by Kutter (2013), the absolute pressure is once again decreased up to 90 mbar, and a CO_2 flow is once again introduced into the vacuum chamber until the pressure returns to the value of the atmospheric pressure. After a new decrease of the absolute pressure up to 90 mbar, the saturation process starts. As indicated in the LEAP-UCD-2017 specifications, the saturation is made from the surface (at the slope tip), and the fluid pump enables to control the fluid flow all along the process.

At the end of the saturation process, an attempt to evaluate the degree of saturation was made following the method proposed by Okamura and Inoue (2012). However, the measurement did not enable the determination of the degree of saturation due to the sensor noise and, possibly, to the selected target and its fixation.

As previously indicated, the vertical motion of the surface markers was measured using a laser sensor. The use of a laser sensor implies that the source of the laser must be immersed. Due to the minimum distance required between the laser source and the marker, the water level should be at least 35 mm above the top of the

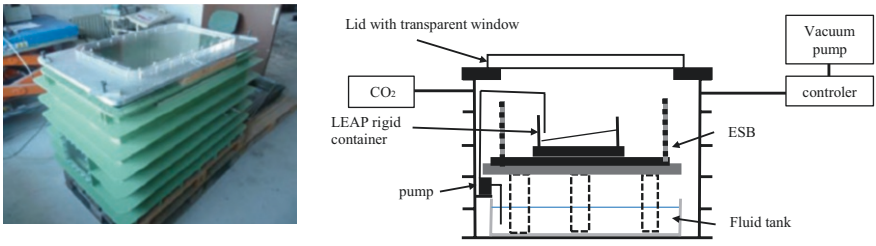

Fig. 8.6 Saturation setup at 1g

slope (Fig. 8.3). At the end of the saturation process, the fluid level was about 1 cm above the top of the slope, and additional viscous fluid was added carefully just before the beginning of the test.

8.3.4 Wave Breaker System

As previously mentioned, due to the use of a laser sensor to record the vertical displacement of the surface markers, a minimum value for the height of the water table above the soil surface was necessary. In the previous LEAP-UCD-2017 exercise (Escoffier & Audrain, 2020), an analysis of the pore water pressure variations measured at the bottom of each extremity of the container (P9 and P10, Fig. 8.2) combined with an analysis of the pore pressure variation measured by the sensors located at 1 m depth near the extremities (P6 and P8, Fig. 8.2) was made. Due to the amplitudes of the pore pressure measured by these four sensors and a phase opposition, it was concluded that one part of the pore pressure fluctuations recorded by these sensors could be due to wave creation. This analysis suggested that a wave reduction system should be built for future tests to avoid non-negligible effect of waves near the extremities of the rigid container.

As a first attempt, a simplified wave breaker was built. Its lower base was in contact with the fluid surface when the container was at rest. The width of the wave breaker was lower than the width of the container. It was assumed that if the wave breaker covers the entire fluid surface, it can create unwanted fluid pressure during the base shaking even if it has not been calculated. Consequently, the width of the wave breaker was 10 cm.

8.4 Achieved Ground Motions

8.4.1 Horizontal Component

Figure 8.7 gives the time representation of the achieved motions for the two motions of each test. The data represents the average value obtained from sensors AH11 and AH12. It should be noticed that in the case of the UGE-2/25-62 test, the time at which the maximum value of the 1 Hz component is reached coincides with the time at which the PGA of the raw acceleration is reached. This is not the case for the UGE-1/50-62 test. In this case, the PGA, which is supposed to correspond to the maximum value of the 1 Hz component, has been selected in the time interval $[t_0 + 0.1\ \text{s}, t_0 + 0.1\ \text{s}]$, where t_0 is the time at which the maximum value of the 1 Hz component is reached. Considering the effective peak ground accelerations, the values measured in the UGE-2/25-62 are 16–25% higher than that determined in the

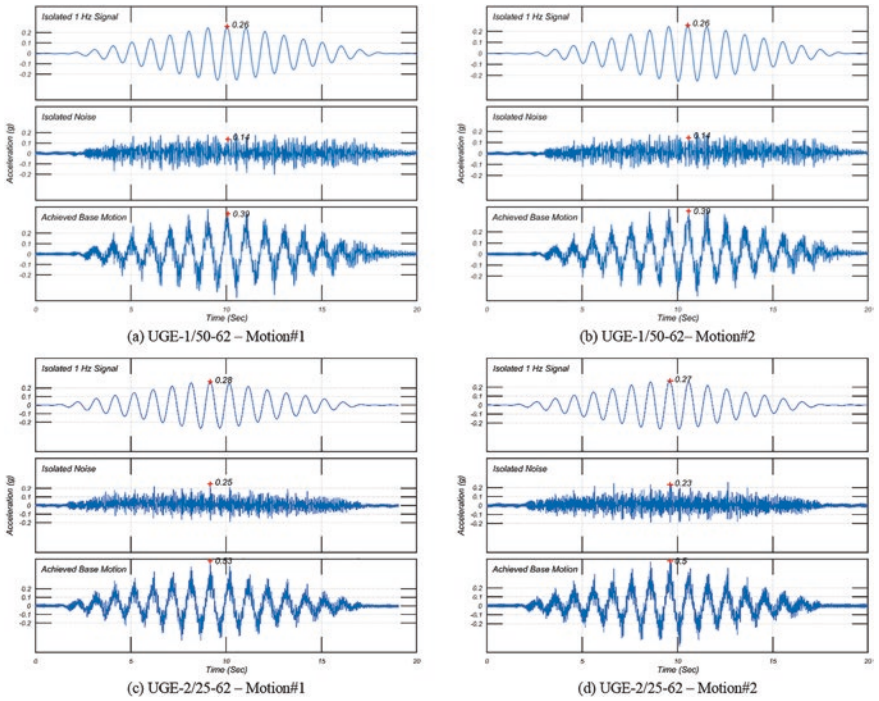

Fig. 8.7 Achieved base motions for the two tests performed at University Gustave Eiffel (prototype scale)

case of the UGE-1/50-62 test. This difference is essentially due to the level of the noise recorded during the UGE-2/25-62 that is 64–79% higher than that recorded in the UGE-1/50-62 (Table 8.2). Figure 8.8 illustrates the frequency content of the base shaking (average value of the sensors AH11 and AH12). The first five most important frequency components are illustrated by red dots, and the corresponding frequencies are indicated. At the prototype scale, the frequencies of the harmonics are somewhat different between both tests. However, if the values at the model scale for the two first harmonics are considered, they are almost the same for both tests: 380 and 449 Hz for the UGE-1/50-62 test against, respectively, 373 and 458 Hz for the UGE-2/25-62 test. One hypothesis can be that these frequencies correspond to resonance frequencies of the system assembly that are excited in both tests, and due to the generalized scaling law, it induces different frequencies at the prototype scale. However, this hypothesis should be confirmed in the future.

If the characterization of the base shaking is based on Arias intensity, the difference between both tests is less important than if the effective PGA is considered. In the case of Motion #1 and Motion #2, the Arias intensities calculated for the UGE-2/25-62 test are, respectively, 13.6 and 8.8% higher than that calculated for the UGE-1/50-62 test.

Table 8.2 Characteristics of the achieved base motions (prototype scale)

Test	Event	PGA_{eff} (g)	1 Hz component (g)	Other components (g)	Three first main noise frequencies (Hz)	I_a (m/s)
UGE-1/50-62	Motion #1	0.33	0.26	0.14	7.59/8.98/9.63	3.95
	Motion #2	0.33	0.26	0.14	7.6/8.99/9.67	4.19
UGE-2/25-62	Motion #1	0.41	0.28	0.25	8.95/11/14.99	4.49
	Motion #2	0.385	0.27	0.23	8.97/10.97/14.98	4.56

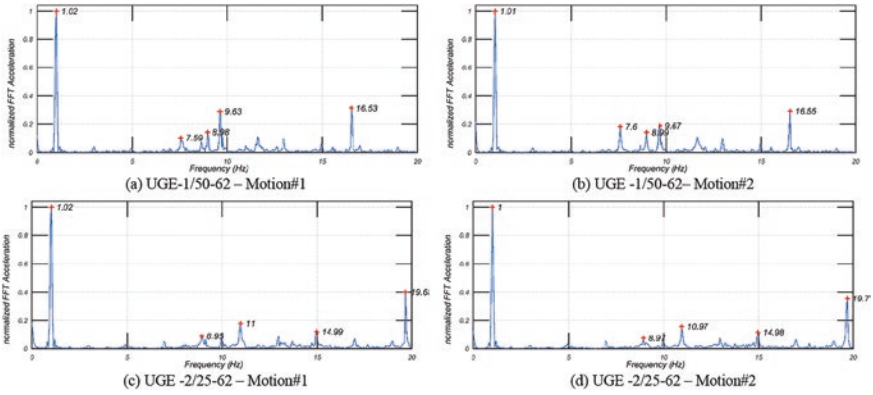

Fig. 8.8 Frequency content of the achieved base motions for the two tests performed at University Gustave Eiffel (prototype scale)

8.4.2 Vertical Component

The time representation of the vertical components measured at the top of each extremity of the container (AV1 and AV2, Fig. 8.3) is given in Fig. 8.9. Following the analysis of the vertical components made by Kutter et al. (2018), a pass band filter [0.3–3 Hz] has been applied to the raw data for analysis. A FIR filter (finite impulse response filter windowed with a Chebyshev window) was used. Considering all the tests, the maximum vertical filtered acceleration remains lower than 0.015 g. However, the vertical behavior is not constant. In the UGE-1/50-62 test for Motion #2, there is a phase opposition that indicates a rotation of the container. In the same test for Motion #1, the vertical accelerations are not the same at both extremities, but they are in phase. For the second test, UGE-2/25-62, the vertical accelerations are somewhat the same and in phase for Motion #1, whereas they are different and present a phase difference for Motion #2.

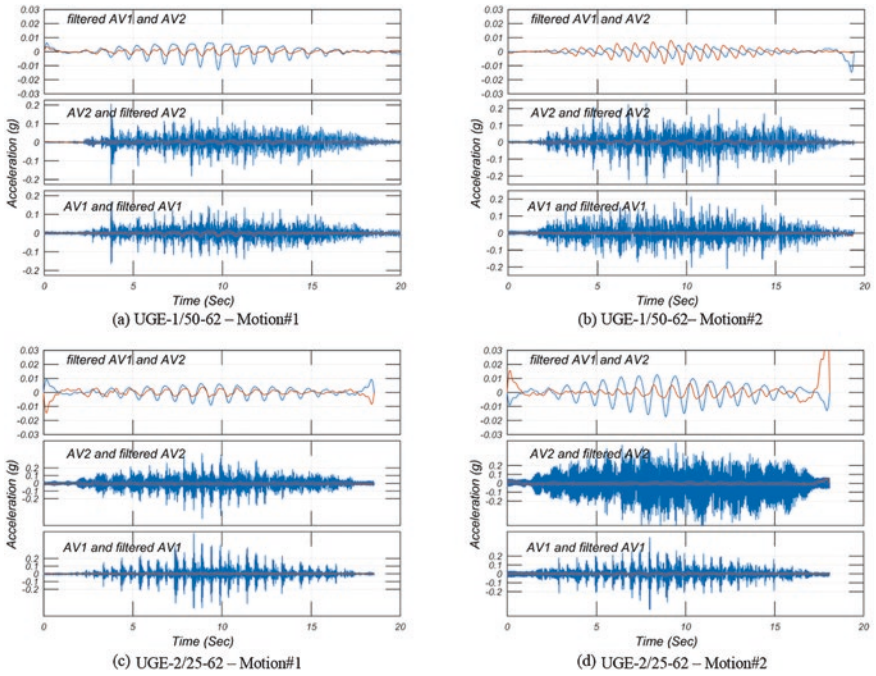

Fig. 8.9 Time representation of the vertical raw and filtered accelerations at both extremities of the rigid container (prototype scale)

8.5 Results

In this part, all the data are presented at the prototype scale using the generalized scaling laws presented in Table 8.1.

8.5.1 CPT Results

The CPT profiles are presented in Fig. 8.10 for each test. In the case of the UGE-2/25-62 test, the depth of investigation was lower than for the other test, and the recorded data were noisy. No noticeable evolution is recorded between the CPTs performed at the initial state and after both motions in the case of the UGE-2/25-62 test (Fig. 8.10b). The $q_c(z)$ profile is almost the same as the $q_c(z)$ profile that was obtained for the initial state of the soil column in the UGE-1/50-62 test. For this last test, successive base shakings induced a modification of the q_c profile: the profile increases with successive shaking indicating a densification of the soil. This result is in accordance with the liquefaction phenomena. It can be noticed that the peak

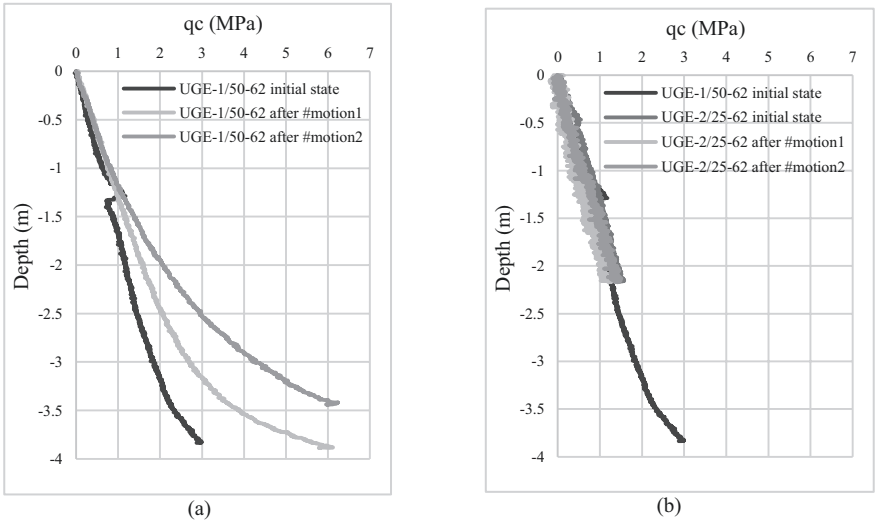

Fig. 8.10 CPT results for both University Gustave Eiffel test at the prototype scale (**a**) UGE-1/50-62 test and (**b**) UGE-2:25-62 test and initial CPT profile of UGE61/50-62

that appeared in the case of the q_c profile for the initial state of the UGE-1/50-62 test is supposed to be due to the presence of a cable of a pore pressure sensor.

8.5.2 Pore Pressure Response

Figure 8.11 shows the pore water pressure response of the central array of pore pressure sensors. Considering the positioning of the sensors during the pluviation process, the initial vertical effective stresses for the P1 and P3 sensors in the case of the UGE-1/50-62 test were, respectively, 38.9 and 18.2 kPa. In the case of the UGE-2/25-62 test, the initial vertical effective stresses for P1 to P4 were, respectively, 38.9, 30.3, 23.7, and 9.1 kPa. These limits are indicated in black dotted horizontal lines in Fig. 8.11.

During the first base shaking, the evolution of the pore pressure observed for P1 and P3 is comparable in both tests. The pore pressure buildup is a little noisier in the case of the UGE-2/25-62 test. The pore pressure buildup reached the initial effective stress at 2 m depth. At 4 m depth, the pore pressure buildup is somewhat lower than the initial vertical effective stress, and the value of $r_u = 1$ is only reached on a very limited time (this value is only reached for few pore pressure peaks in the case of UGE-2/25-62, and the maximum value of r_u reached for UGE-1/50-62 is 0.96).

In the case of UGE-2/25-62, the pore pressure buildup recorded at 3 and 1 m depth indicates liquefaction ($r_u = 1$) for both levels.

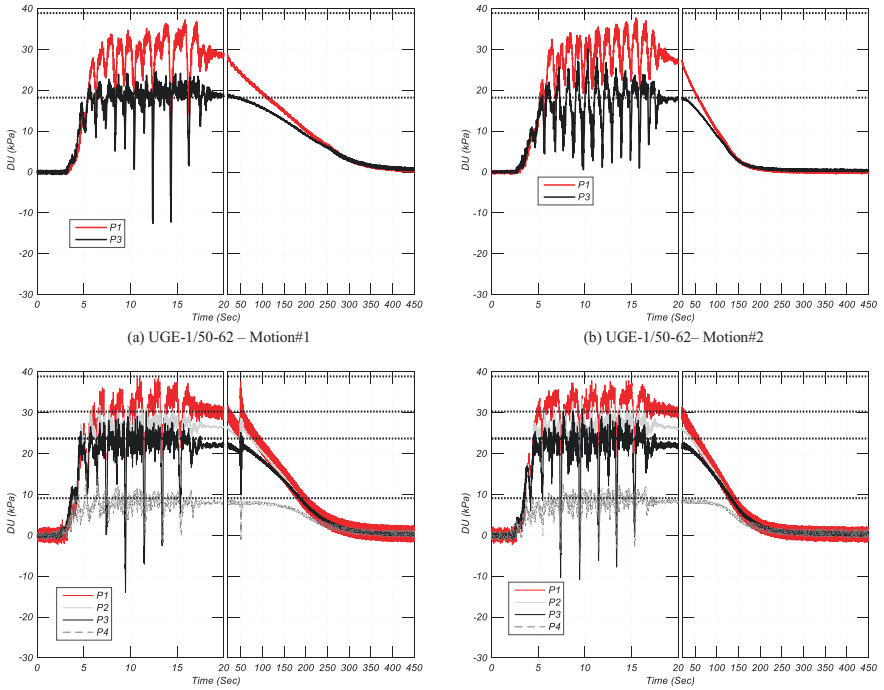

(a) UGE-1/50-62 – Motion#1

(b) UGE-1/50-62– Motion#2

(c) UGE-2/25-62 – Motion#1

(d) UGE-2/25-62 – Motion#2

Fig. 8.11 Pore pressure buildup during and after the base shaking

In addition, for both tests, some spikes appear during Motion #1, more specifically at 2 and 3 m depth, indicating a deliquefaction phenomenon (cyclic mobility-dilatancy phenomena).

In the case of Motion #2, the time histories of the pore pressure buildup were somewhat different between the two tests. No noticeable evolution appeared between the first and the second motion applied on UGE-2/25-62. On the contrary, the pore pressure buildup for the second motion applied on UGE-1/50-62 presents greater cyclic variation of pore pressure with less noticeable pore pressure spikes.

Concerning the pore pressure decay after the base shaking, it is somewhat difficult to compare both tests in the case of the first motion; as for the UGE-2/25-62 test, an aftershock took place and induced new pore pressure buildup. However, in the case of Motion #2, the pore pressure decays are somewhat the same in both tests. As previously mentioned, in the case of the UGE-1/50-62, the value of 73.07 cSt measured after the test on a sample of fluid drawn in the fluid layer above the soil surface should be considered with caution. The obtained results on the pore pressure decay after the second motion tend to confirm that this measured viscosity is not reliable.

As mentioned for the previous tests performed in the framework of the LEAP-UCD-2017, regarding the amplitude and the phase of the pore pressure measured by pore pressure sensors P10, P9, P8, and P6 (Fig. 8.2) and their initial depth, it was supposed that one part of the pore pressure fluctuations recorded by these four sensors was due to the waves created during the base shaking. These previous results

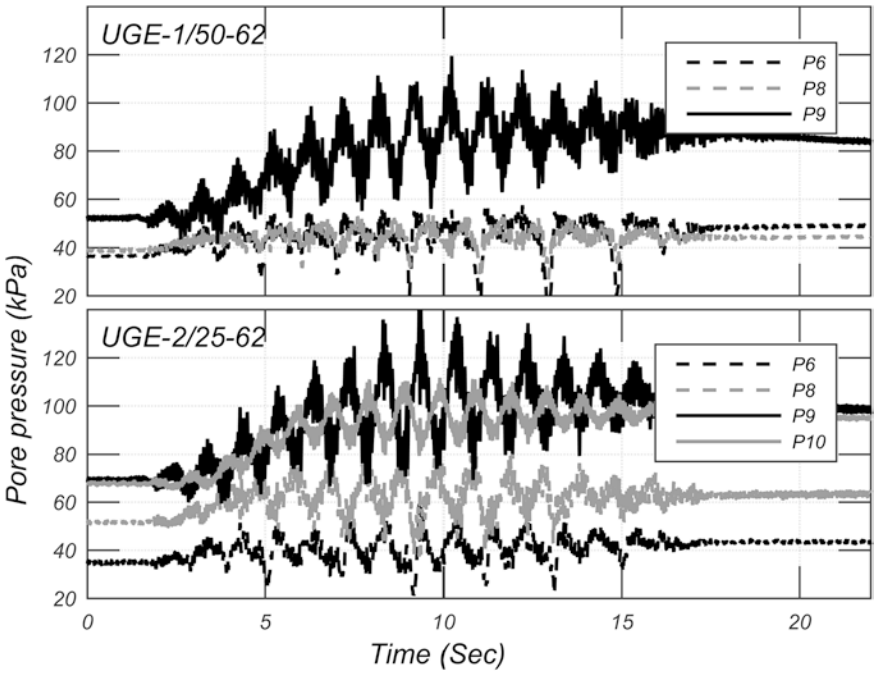

Fig. 8.12 Motion #1 pore pressure buildup during and after the base shaking – wave breaker effect

suggested the use of a wave breaker system to avoid non-negligible effects of waves near the extremities of a rigid container (the pore pressure measurement located in the center of the container was less influenced by the waves). Consequently, a wave breaker was built for the LEAP-ASIA-2019 exercise. Figure 8.12 illustrates the pore pressure evolution measured by the sensors P10, P9, P8, and P6 during Motion #1 of the UGE-1/50-62 and UGE-1/25-62 tests. For the first test, the wave breaker was not in place contrary to the second test. Without wave breaker, the three pore pressure measurements P9, P8, and P6 (P10 was out of order) are in phase. The maximum theoretical values of pore pressure calculated from the sensor locations and the viscous fluid level at rest were compared to the maximum value reached during the test. The maximum measured values reached by P9, P8, and P6 were 119, 62, and 68 kPa against 116, 50, and 49 kPa from the theoretical values. In the case of the test UGE-2/25-62, during the which one a wave breaker was used, the sensors P9 and P10, and P6 and P8, were respectively in phase opposition. The maximum pore pressure values recorded by sensors P10, P9, P8, and P6 were, respectively, 112, 143, 87, and 59 kPa. As for the test without wave breaker, they were larger than the theoretical one (respectively, 100, 111, 65, and 50 kPa).

The comparison of these two results highlights a difference in behavior between the two tests: if the measured pore pressures remain higher than the theoretical ones in both tests, the phase difference between the pore pressure measurements is not the same. Results from the UGE-2/25-62 test seem to indicate the presence of wave, and, on the contrary, there is no clear evidence of waves in the UGE-1/50-62 test.

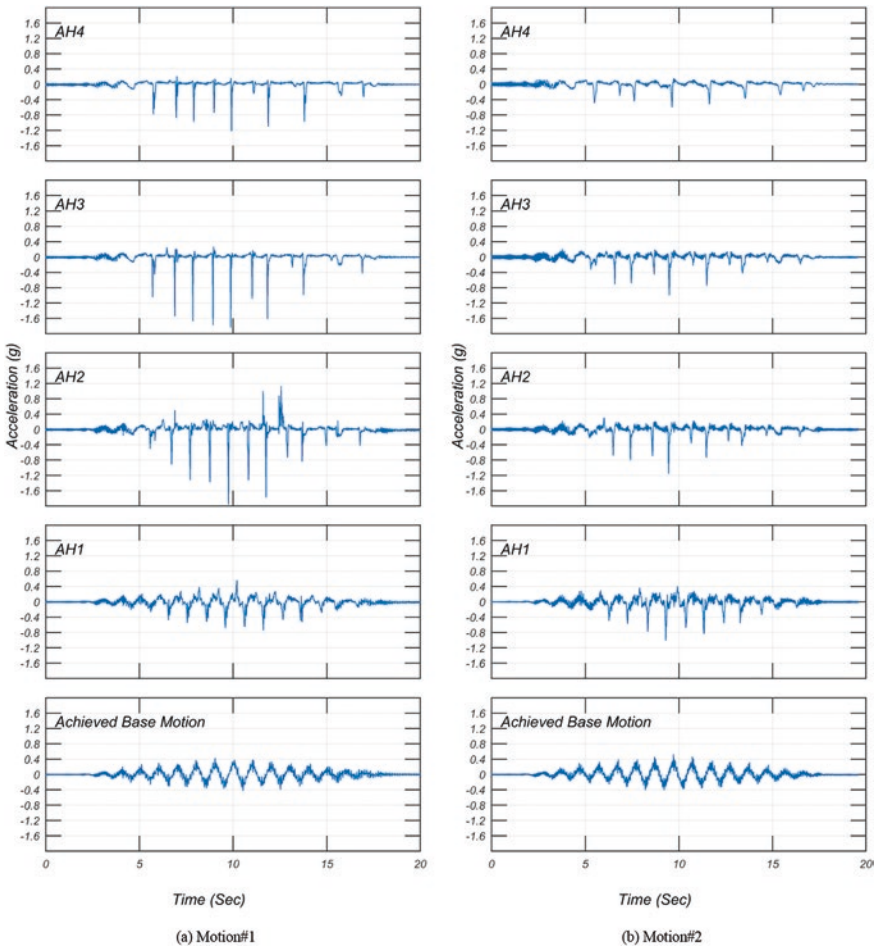

Fig. 8.13 UGE-1/50-62: time history of the acceleration measured by the central array of accelerometers

This difference can be induced by the differences between the two tests due to the use of the GSL and/or the wave breaker. However, there is a clear evidence that the wave breaker should be improved.

8.5.3 Acceleration Response

The time histories of the accelerations measured by accelerometers AH1 to AH4 are presented in Figs. 8.13 and 8.14 for, respectively, the UGE-1/50-62 and UGE-2/25-62 tests. The global behavior observed in both tests is comparable.

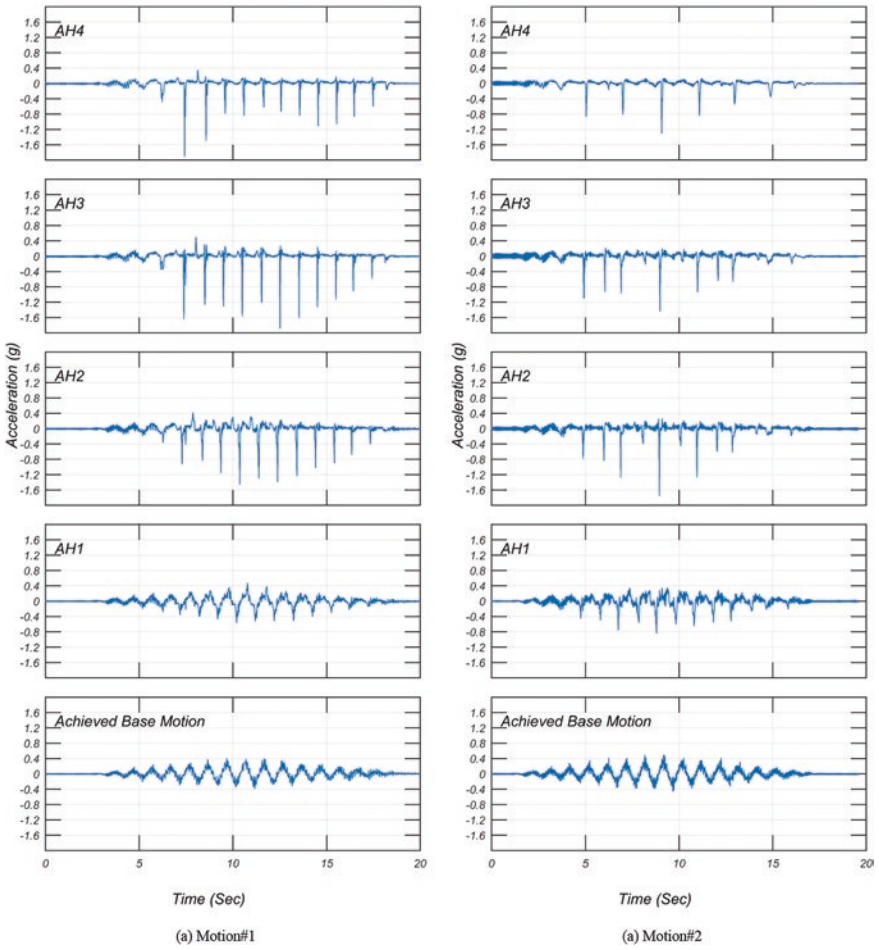

Fig. 8.14 UGE-2/25-62: time history of the acceleration measured by the central array of accelerometers

At the beginning of Motion #1, the time acceleration at 3.5 m depth (AH1) still followed the trace of the base input motion. However, after four cyclic loadings, small spikes started to appear, and even if cyclic variations of acceleration were still noticeable, they deviated from the base shaking. At 2.5 m depth (AH2) and above (AH3 and AH4), the initiation of liquefaction was observed. It is characterized by sharp spikes of acceleration that are evidence of shock waves induced by deliquefaction phenomena (Kutter & Wilson, 1999). Considering the beginning of the loading, the liquefaction occurred first near the surface, and then the phenomenon was spreading in depth. However, there was small phase lag between 0.5 and 2.5 m depth.

As previously mentioned, except in the case of the second motion in the UGE-50/1-62 test, where time history of the pore pressure presented greater cyclic

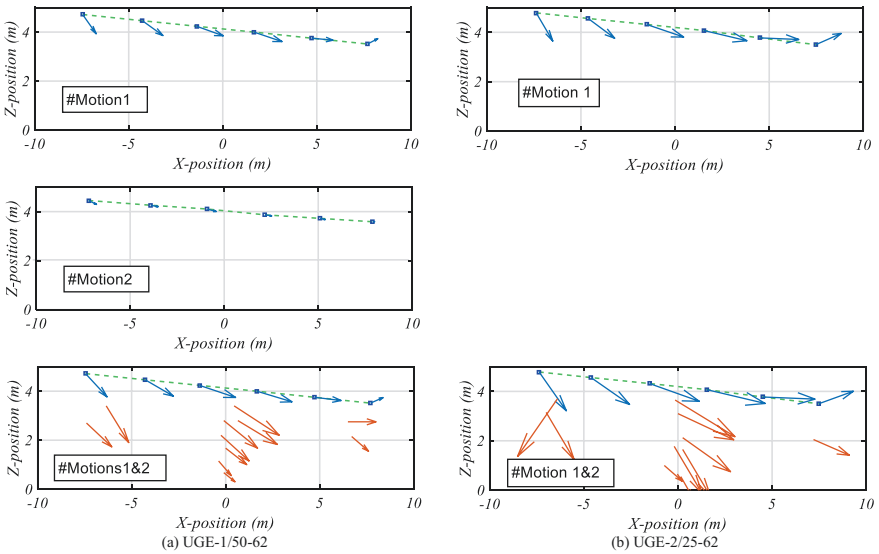

Fig. 8.15 Surface markers (blue arrows) and embedded sensor displacement (red arrows) induced by Motion #1, Motion #2, and Motions #1 and #2, for both centrifuge tests performed at University Gustave Eiffel

variation with less noticeable pore pressure spikes, the time histories of the pore pressure buildup in the other cases were similar.

There was no noticeable effect of Motion #1 on the time histories of the pore pressure observed during Motion #2. The observed time histories of the acceleration are in accordance with these results: in the case of Motion #2, the UGE-1/50-62 test presents smaller acceleration spikes than for the other cases.

8.5.4 Surface Marker Responses

Cross views of the residual displacements of the surface markers induced by Motion #1 and Motion #2 are presented in Fig. 8.15. For Motion #1, the initial positions of the surface markers correspond to the first position measurements before the first spin up of the centrifuge. For Motion #2, only the results for the direct approach are provided, and the initial positions were obtained considering the residual displacement induced by Motion #1. In order to enhance the displacements and compare the results of both tests, the length of the displacement vectors was magnified by 3.

In the case of the surface displacements induced by Motion #1, the directions of the displacements are somewhat the same in both tests (Table 8.3). However, larger displacements are observed when GSL are concerned (UGE-2/25-62). If the average values of the displacement obtained from the surface markers with the same X location are considered, the residual displacements observed when GSL is

Table 8.3 Average[a] displacement amplitude and orientation calculated from the measured displacements of the surface markers – Motion #1

Motion #1	Amplitude (m)			Orientation (°)		
Marker number	UGE-1/50-62[a]	UGE-2/25-62[a]	Relative difference in %[b]	UGE-1/50-62[a]	UGE-2/25-62[a]	Relative difference[b]
1	0.358	0.483	35	−47.5	−52.4	10
2	0.419	0.542	29	−28.9	−29.6	2
3	0.493	0.682	38	−15.4	−14.5	−6
4	0.517	0.778	50	−14.6	−10.23	−30
5	0.384	0.696	81	−4.1	−1.8	−56
6	0.198	0.473	139	22	18.7	−15

[a]The values correspond to the average value of the displacement amplitude and inclination calculated from the three markers located at the same X position. The inclination is relative to the horizontal plane

[b]The relative difference is calculated considering the UGE-1/50-62 test as a reference

concerned are 29–139% higher than that obtained in the UGE-1/50-62 test (Table 8.3).

In order to highlight the effect of the previous base shaking on the surface displacement, the displacements associated with the second base shaking are represented in the case of the UGE-1/50-62 test. The observed displacements are largely lower than that induced by the first event. This decrease can be due to the densification of the soil induced by the liquefaction that took place during Motion #1. This analysis is more complex in the case of the UGE-2/25-62 test due to scaling conflict between the displacement and the length. Consequently, only the total displacement induced by the combined effect of both motions is represented for both tests. In this case, the total displacements of the embedded sensors are also represented by red arrows in Fig. 8.15. The difference between the displacement amplitudes and their orientations between the two tests are comparable to that observed for the first motion (Table 8.4). In the case of UGE-2/25-62, based on GSL, the displacements were 38–168% higher than in the other test with larger difference at the bottom of the slope. The difference in the direction varies between 6% and −67% indicating that, at the top of the slope, the residual displacement of the soil is more downward and, near the bottom of the slope, more upward when GSL is considered (UGE-2/25-62).

8.6 Conclusions

This paper summarized the experimental setup, the followed experimental procedure, and some results of the two centrifuge tests performed at University Gustave Eiffel in the framework of the LEAP-ASIA-2019 series of tests.

Two centrifuge tests were performed by University Gustave Eiffel. The tests were done on a medium dense Ottawa F-65 sand. The first test was performed at 50*g*

Table 8.4 Average displacement amplitude and orientation calculated from the measured displacements of the surface marker cumulative effect of Motions #1 and #2

Motions #1 and #2	Amplitude (m)			Orientation (°)		
Marker number	UGE-1/50-62	UGE-2/25-62	Relative difference in %*	UGE-1/50-62	UGE-2/25-62	Relative difference*
1	0.498	0.714	43	−39.7	−47.4	19
2	0.547	0.774	41	−24	−28.0	17
3	0.662	0.916	38	−14.4	−15.2	6
4	0.642	1.054	64	−13.0	−10.2	−22
5	0.477	0.932	95	−5.4	−1.8	−67
6	0.237	0.636	168	18.6	15.4	−17

centrifuge and the second test at 25*g*. Considering the GSL approach, tests were scaled to represent the same prototype.

The main deviation from the specifications was the viscosity of the fluid for the UGE-1/50-62 test for which the viscosity is assumed higher than the requested one, despite no precise determination is available. However, based on the comparison of the pore pressure dissipation after the second base shaking in both tests, doubts might be raised on the validity of viscosity measurements that has been performed after the test.

Compared to the previous tests performed in the framework of LEAP-UCD-2017 exercise, an improved system of saturation was used, which enabled a better control of the fluid flow and less leakage due to its configuration.

The 1 Hz horizontal component of the base shaking at the base of the container was similar between the tests. The noise was somewhat higher in the case of the UGE-2/25-62 test inducing a PGA_{eff} 15–25% higher than for the UGE-1/50-62 test. This difference decreases to 13.6% up to 8.8% if the Arias intensity is considered.

The vertical motions at the top of the container weren't the same between the different motions and between the tests. Difference between the tests can be due to the difference of frequency for the base shaking that can induce different response of the experimental assembly. However, the difference of response between the motions of the same test is not actually explained.

Considering the results obtained, the characterization of the soil column through CPT measurement highlights a difference between the two tests: in the case of the GSL, no noticeable evolution of the CPT profile was recorded, while the CPT profile increases with the successive motion for the test that is not based on GSL. However, the noisy response obtained for the second test can be relevant of the problem with the experimental setup in this case. For the next LEAP exercise, a new calibration of the CPT will be made, and more caution will be taken for the CPTs.

The global scaling approach seems to give good results if the acceleration and the pore pressure buildup are considered. However, due to a problem with the fluid viscosity, these tests cannot be considered as relevant for the analysis of the global scaling approach when it concerns the pore pressure dissipation after the base shaking.

On the contrary, when the displacements are considered, large discrepancies appear especially in terms of amplitude and, to a lesser extent, in terms of orientation of the displacement.

Acknowledgments This experiment has been made in the framework of the LEAP-ASIA-2019 series of experiments. The authors would like to thank all the participating centrifuge teams that share their knowledge.

References

Brandenberg, S. J., Choi, S., Kutter, B. L., Wilson, D. W., & Santamarina, J. C. (2006). A bender element system for measuring shear wave velocities in centrifuge models. *Proceedings, 6th international conference on physical modeling in geotechnics*, p 165–170. https://nees.org/data/get/NEES-2006-0149/Documentation/References/Brandenberg_2006.pdf

Callari, C., Armero, F., & Abati, A. (2010). Strong discontinuities in partially saturated poroplastic solids. *Computer Methods in Applied Mechanics and Engineering, 199*, 1513–1535.

Carey, T., Gavras, A., Kutter, B., Haigs, S. K., Madabushi, S. P. G., Okamura, M., Kim, D. S., Ueda, K., Hung, W. Y., Zhou, Y. G., Liu, K., Zeghal, M., Abdoun, T., Escoffier, S., & Manzari, M. (2018). A new shared miniature cone penetrometer for centrifuge testing. In A. MCNamara, S. Divall, R. Goodey, N. Taylor, S. Stallebrass, & J. Panchal (Eds.), *ICPMG 2018* (Vol. 1, pp. 293–298).

Carey, T., Stone, N., & Kutter, B. L. (2020). Grain size analysis and maximum and minimum dry density testing of OTTAWA F-65 Sand for LEAP-UCD-2017. In B. L. Kutter, M. T. Manzari, & M. Zeghal (Eds.), *Model tests and numerical simulation of liquefaction and lateral spreading LEAP-UCD-2017* (pp. 31–44). Springer, ISBN 978-3-030-22817-0.

Chazelas, J.-L., Escoffier, S., Garnier, J., Thorel, L., & Rault, G. (2008). Original technologies for proven performances for the new LCPC earthquake simulator. *Bulletin of Earthquake Engineering, 6*(4), 723–728.

Escoffier, S., & Audrain, P. (2020). LEAP-UCD_2017 centrifuge test at University Gustave Eiffel. LEAP-UCD-2017. *Reproducibility and sensitivity of centrifuge tests and comparisons to simulations of lateral spreading*, to be published, pp. XXX.

Iai, S., Tobita, T., & Nakahara, T. (2005). Generalised scaling relations for dynamic centrifuge tests. *Géotechnique, 55*(5), 355–362.

Kutter, B. L. (2013). Effects of capillary number, bond number, and gas solubility on water saturation of and specimens. *Canadian Geotechnical Journal, 50*(2), 133–144.

Kutter, B. L., & Wilson, D. W. (1999). De-liquefaction shock waves. *Proceedings, 7th US-Japan workshop on earthquake resistant design of lifeline facilities and countermeasures against soil liquefaction, MCEER-99-0019*, pp. 295–310.

Kutter, B. L., Carey, T. J., Hashimoto, T., Zeghal, M., Adboun, T., Kokkali, P., Madabhushi, G., Haigh, S., Burali d'Arezzo, F., Madabhushi, S., Hung, W. Y., Lee, C. J., Chegn, H. C., Iai, S., Tobita, T., Zhou, Y. G., Chen, Y., Sun, Z. B., & Manzari, M. T. (2018). Leap-GWU-2015 experiment specifications, results, and comparisons. *Soil Dynamics and Earthquake Engineering, 113*, 616–628.

Okamura, M., & Inoue, T. (2012). Preparation of fully saturated model for liquefaction study. *International Journal of Physical Modelling in Geotechnics, 12*(1), 39–46.

Chapter 9
LEAP-ASIA-2019 Centrifuge Test at KAIST

Satish Manandhar, Seong-Nam Kim, and Dong-Soo Kim

Abstract Since Niigata and Alaska earthquakes in 1964, the dangers of liquefaction are well established, and research into liquefaction has been actively performed. In this context, Liquefaction Experiments and Analysis Projects (LEAP) was launched to provide high-quality experimental data on soil liquefaction using laboratory testing and centrifuge modeling and then validating numerical models to improve predictions. The purpose of LEAP-ASIA-2019, which is one of the LEAP programs, was to fill the gaps and further extend/establish/confirm the trends obtained in the previous LEAP-UCD-2017 program. Further, the validity of the generalized scaling law was also tested for liquefaction simulation using different 1-g and centrifuge scaling factors. During LEAP-ASIA-2019, KAIST performed two model tests (Model A and Model B) with the same target relative density (D_r = 85%) and input motion intensity of 0.3g. Models A and B were identical in construction but were tested under different centrifugal accelerations to verify the generalized scaling factors. This paper describes the experimental procedure in detail and the responses of dense model grounds to strong base shaking in terms of ground accelerations, excess pore pressure, surface displacements, stress-strain behavior, and CPT profiles. Further, discussion on the generalized scaling law and the effect of shaking history on the model behavior are also presented.

Keywords Liquefaction Experiments and Analysis Projects (LEAP-ASIA-2019) · Generalized scaling law (GSL) · Centrifuge modeling

9.1 Introduction

Liquefaction is a phenomenon in which the strength and stiffness of saturated soil are reduced because of the reduction in effective confining stress during earthquakes. Damage and ground failure due to liquefaction remain a major concern to

S. Manandhar · S.-N. Kim (✉) · D.-S. Kim
Department of Civil and Environmental Engineering, Korean Advanced Institute of Science and Technology, KAIST, Daejeon, Republic of Korea
e-mail: seong8nam@kaist.ac.kr

T. Tobita et al. (eds.), *Model Tests and Numerical Simulations of Liquefaction and Lateral Spreading II*, https://doi.org/10.1007/978-3-031-48821-4_9

geotechnical engineers. Various methods such as field investigation and laboratory tests have been conducted to evaluate the triggering phenomenon and consequences of liquefaction. Simultaneously, studies involving numerical simulations have produced different insights into liquefaction.

Numerical modeling is a cost-effective way to evaluate the consequences of liquefaction on built structures. However, the constitutive models and numerical analysis techniques that simulate complex liquefaction phenomena must be validated using well-defined experimental results (Ueda & Iai, 2018). Under such a demand, a collaborative study between numerical modelers and centrifuge experimenters was conducted 20 years ago, termed VELACS (Arulanandan & Scott, 1993). Similar to VELACS, Liquefaction Experiments and Analysis Projects (LEAP) is an ongoing collaborative project, which aims to reduce the inconsistency in experimental results and thus provide high-quality experimental data for validation of numerical models.

LEAP-GWU-2015 was one of the first validation efforts within the ongoing LEAP program, where six institutions conducted centrifuge tests on liquefaction of a sloping ground in a rigid box (Kutter et al., 2018). The 2015 exercise demonstrated the feasibility of an approach for a next-generation validation database and showed that variations in initial conditions and ground motions led to differences in results between institutions for the same model.

After LEAP-GWU-2015, 9 facilities participated in LEAP-UCD-2017 and performed 24 centrifuge tests to simulate the liquefaction of a submerged sloping sand deposit. The purpose of LEAP-UCD-2017 was to characterize the trend and sensitivity of the model response according to the relative density of the model ground and input motion intensity. The correlations between lateral displacement, relative density based on CPT cone tip resistance, and effective PGA were better than the correlations between lateral displacement, relative density based on volume and mass measurements, and PGA (Kutter et al., 2019). In addition, the accelerations and pore water pressure records at different depths were compared between different institutions.

In line with the LEAP program, LEAP-ASIA-2019 was undertaken to validate the generalized scaling law (Iai et al., 2005) using modeling of model technique and to obtain additional results, which could be used to fill the gaps and further extend/establish/confirm the trends obtained in the LEAP-UCD-2017. The generalized scaling law is needed to overcome size restrictions while testing large prototypes by combining the 1-g scaling law with the centrifuge scaling law (Garnier et al., 2007). The same nine institutions who participated in the LEAP-UCD-2017 also participated in the LEAP-ASIA-2019 round-robin centrifuge tests.

KAIST developed a geotechnical centrifuge facility with a centrifuge of 5 m radius and 240*g*-ton capacity in 2009 and participated in LEAP-UCD-2017 (Kim et al., 2020) and LEAP-ASIA-2019. Following the specifications of LEAP-ASIA-2019, KAIST performed two centrifuge model tests (Model A and Model B) with the same soil relative density (D_r = 85%) and target input motion intensity of 0.3*g*. Models A and B are identical with LEAP-UCD-2017 in construction, but the

viscosity of pore fluid and the centrifugal accelerations were scaled based on the generalized scaling law for Model B. This paper provides details of the centrifuge model tests conducted at KAIST for LEAP-ASIA-2019, including facility and equipment, test procedure, and results.

9.2 Generalized Scaling Law and Overview of Experimental Condition

Centrifuge model testing can be beneficial to test small-scaled models at higher g-levels, so that the stress distribution is similar with the prototype condition. However, for large prototype structures, the scaled model could still be large enough for testing due to centrifuge limitations, such as the size of the model container and scaling effects on materials. To resolve the demand for large-scale prototype testing and restrictions on centrifuge modeling, Iai et al. (2005) proposed the generalized scaling law by combining the scaling law for centrifuge testing and one for 1-g dynamic model testing. This is called the "generalized scaling law" in dynamic centrifuge modeling.

The main concept of the generalized scaling law is to scale the prototype twice resulting in much larger overall scaling factor, which would result in a reasonable sized centrifuge model suitable for testing. First, the prototype is scaled down via a similitude for 1-g shaking table tests to a virtual 1-g model. The virtual 1-g model is subsequently scaled down by applying a similitude for centrifuge tests to the actual physical model. Figure 9.1 visualizes the concept of the generalized scaling law using virtual 1-g models. In this way, the geometric scaling factors applied in 1-g tests (μ) can be multiplied with those for centrifuge tests (η) resulting in much larger overall scaling factor $\lambda = \mu\eta$. The generalized scaling factors are given in Table 9.1 along with scale factors for centrifuge and 1-g tests.

The generalized scaling law can be validated using modeling of model technique. Two centrifuge models (Models A and B) made with the same overall scaling factors ($\lambda = 40$) but different 1-g scale factor ($\mu = 1$ for Model A and $\mu = 1.5$ for Model B) and centrifuge scaling factor ($\eta = 40$ for Model A and $\eta = 26.7$ for Model B) can be compared with each other. These scaling factors were the ones implemented in KAIST centrifuge experiments. Model A represents conventional centrifuge scaling factors, while Model B represents the generalized scaling factors. Different scaling factors were assigned to different institutions in LEAP-ASIA-2019 for verifying the generalized scaling law. The scale factors for different physical parameters for KAIST Models A and B are given in Table 9.1.

Figure 9.2 shows the relative densities of the ground model and the intensity of the input base motions for the various tests during the LEAP-UCD-2017 program. The red circle zone is the experimental condition of LEAP-ASIA-2019, and the red star is the experimental condition for KAIST. One of the purposes in LEAP-ASIA-2019 was to evaluate the occurrence of liquefaction under the application of

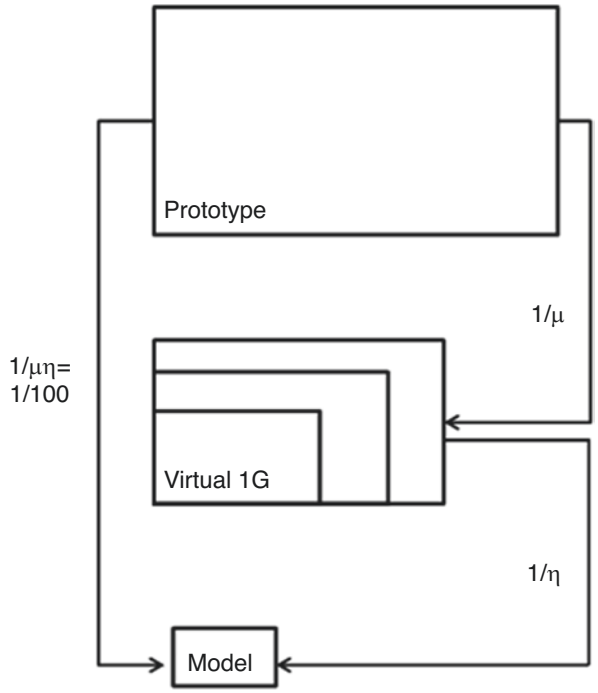

Fig. 9.1 Principle of the generalized scaling law. (Tobita & Iai, 2011)

Table 9.1 Scaling factors for KAIST Models A and B based on conventional centrifuge scaling factors and generalized scaling factors for various physical parameters

	(1) Scaling factors for 1-g test	(2) Conventional centrifuge scaling factors	(3) Generalized scaling factors	Model A Conventional centrifuge scaling factors ($\mu = 1$, $\eta = 40$)	Model B Generalized scaling factors ($\mu = 1.5$, $\eta = 26.7$)
Length	μ	η	$\mu\eta$	40.000	40.000
Density	1	1	1	1.000	1.000
Time	$\mu^{0.75}$	η	$\mu^{0.75}\eta$	40.000	36.189
Frequency	$\mu^{-0.75}$	$1/\eta$	$\mu^{-0.75}/\eta$	0.025	0.028
Acceleration	1	$1/\eta$	$1/\eta$	0.025	0.037
Velocity	$\mu^{0.75}$	1	$\mu^{0.75}$	1.000	1.355
Displacement	$\mu^{1.5}$	η	$\mu^{1.5}\eta$	40.000	49.051
Stress	μ	1	μ	1.000	1.500
Strain	$\mu^{0.5}$	1	$\mu^{0.5}$	1.000	1.225
Stiffness	$\mu^{0.5}$	1	$\mu^{0.5}$	1.000	1.225
Permeability	$\mu^{0.75}$	η	$\mu^{0.75}\eta$	40.000	36.189
Pore pressure	μ	1	μ	1.000	1.500
Tip resistance	μ	1	μ	1.000	1.500

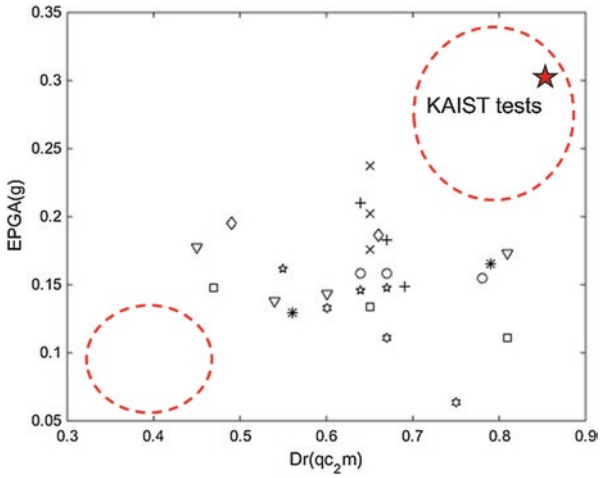

Fig. 9.2 Effective peak ground acceleration (EPGA) versus relative density (D_r) from cone tip resistance at 2 m depth (q_{c2}) for various test models in LEAP-UCD-2017 experiments. The red circles represent the experimental conditions for LEAP-ASIA-2019. Red star is the experimental condition for KAIST tests

strong base shaking on dense model grounds and weak base shaking on loose model grounds. The target experimental condition at KAIST is to evaluate liquefaction behavior by applying strong base motion of 0.3*g* intensity to the ground model of 85% relative density. The other purpose of LEAP-ASIA-2019 is to validate the applicability of the generalized scaling law in liquefaction simulation by comparing the results of Model A and Model B.

9.3 Centrifuge Model Construction

9.3.1 Centrifuge Facility at KAIST

KAIST has a geotechnical centrifuge facility housing an automatic balancing beam centrifuge with a platform radius of 5 m and maximum capacity of 240*g*-tons (Kim et al., 2013a). Target input motions were applied using an earthquake simulator that uses a dynamic self-balancing technique to eliminate a large portion of the undesired reaction forces and vibrations transmitted to the main body (Kim et al., 2013b). The geotechnical centrifuge along with the shaking table used in KAIST centrifuge tests is shown in Fig. 9.3. The centrifuge tests in KAIST were conducted at a centrifugal acceleration of 40*g* for Model A and 26.67*g* for Model B. From now on, all measurements are in prototype scale, unless explicitly stated.

Fig. 9.3 Geotechnical centrifuge facility at KAIST: (**a**) centrifuge main body and (**b**) earthquake simulator

9.3.2 Soil Material and Density

Ottawa F-65 sand was used as the standard sand for LEAP-ASIA-2019. The grain size characteristics and property of the soil are as follows: $Gs = 2.665$, $D_{10} = 0.13$ mm, $D_{30} = 0.17$ mm, $D_{50} = 0.20$ mm, and $D_{60} = 0.21$ mm (El Ghoraiby et al., 2020). Based on the specifications for LEAP-ASIA-2019, the minimum and maximum densities of sand were determined as ρ_{dmax}=1757 kg/m^3 and ρ_{dmin}=1490.5 kg/m^3, respectively. The target soil density for Models A and B in KAIST was specified as 1711 kg/m^3, equivalent to 85% relative density.

The sand model was constructed by dry pluviation through a sieve with an opening size of approximately 1.20 mm; the sieve was partially blocked to limit the flow. The density of the soil model was determined by the size of the opening slot and the drop height, for which calibration tests were done. Figure 9.4 shows the geometry of the opening slots and the calibration test results for soil density and pluviation drop heights, along with the required drop height for constructing the dense soil models.

The measured dry unit weights of the model grounds constructed in a rigid box were 1716.55 kg/m^3 and 1720.6 kg/m^3 for Models A and B, respectively, based on mass and volume measurements. After the sand was pluviated to the target height, a 5° inclined guide was installed on the top of the model box. A manufactured scraper was connected directly to the inclined guide and was used to scrap the soil surface carefully. The soil generated by the scraping was removed carefully by using a vacuum cleaner so that the resulting ground was not disturbed, and a 5° sloped model ground was achieved.

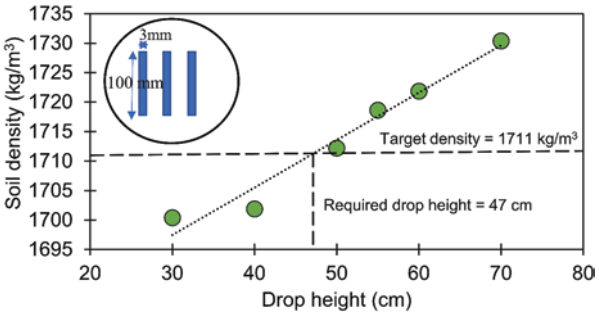

Fig. 9.4 Density versus drop height relationship for the sieve design and the required drop height to achieve model of target density

9.3.3 Viscous Fluid

The viscous fluid was a mixture of water and methylcellulose, and the target viscosity was set to 40 cSt for Model A as dictated by the centrifuge scaling law and 36.1 cSt for Model B based on the generalized scaling law. Temperature and concentration are the influencing factors of fluid viscosity; thus, calibration tests are needed before making the viscous fluid. The viscosity was measured using a Brookfield-type automatic viscometer. The automatic viscometer relates frictional resistance to viscosity by rotating a spindle inside the fluid as shown in Fig. 9.5. In addition, a temperature sensor measures the fluid temperature at the current viscosity.

The results of the calibration tests are shown in Fig. 9.6. For a given concentration, the viscosity increases with a decrease in temperature, while for a given temperature, the viscosity increases with an increase in concentration of methylcellulose. Based on the calibration results, the concentrations of methylcellulose were 2.08% (case #4) and 2.0% (case #3) at 18 °C for 40 cSt and 36.1 cSt target viscosities, respectively. Upon preparing the viscous fluid, the achieved viscosities of the fluid used in Models A and B were 41.3 cSt and 36.2 cSt, respectively, which is close to the target viscosities.

9.3.4 Model Description and Instrumentations

The model construction is identical with LEAP-UCD-2017, which consists of a 5° sloping sand ground model in a rigid box. The rigid box has an internal dimension of 570 mm × 225 mm × 450 mm (length × width × depth) in the model scale with a front transparent window. The model ground constructed through dry pluviation is described in Fig. 9.7, with the following dimensions in the prototype scale: 22.8 m × 4 m × 9 m (length × depth at midpoint × width). The length of the slope (22.8 m) was about 15% greater than the specified length (20 m). In the KAIST centrifuge facility, the 5° inclination along the length of the model was not curved

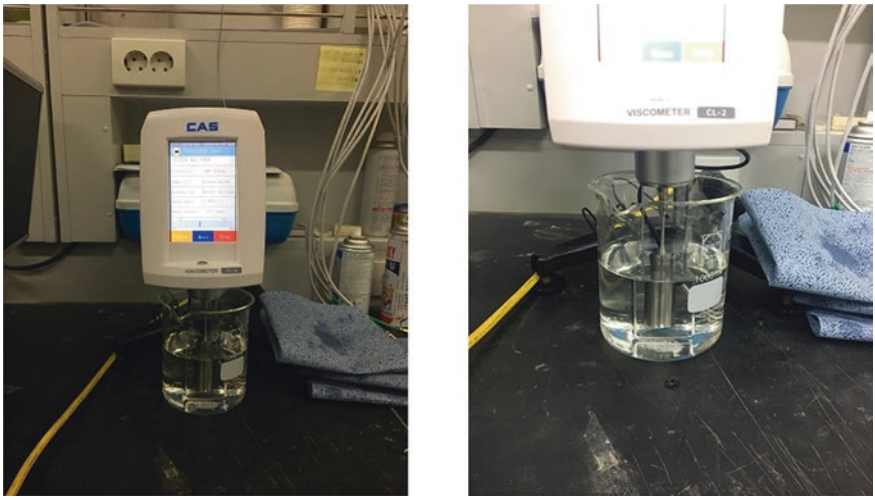

Fig. 9.5 Brookfield-type automatic viscometer used in calibration tests of viscous fluid

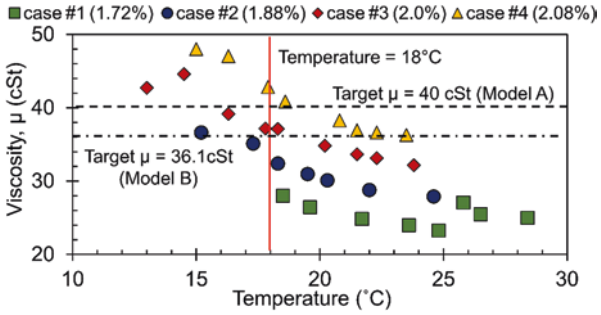

Fig. 9.6 Calibration tests for viscosity according to temperature and concentration using automatic viscometer

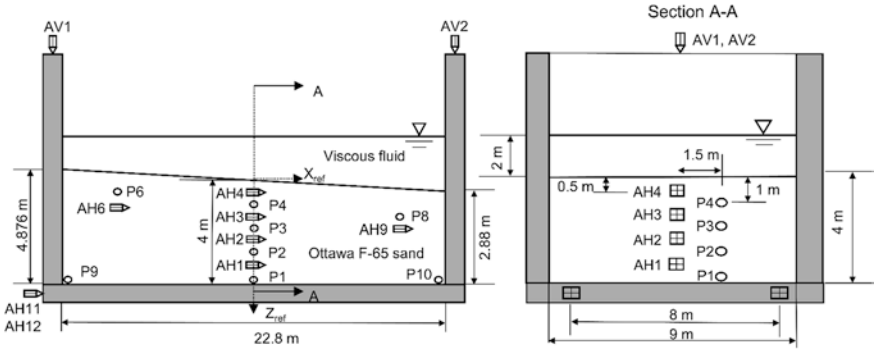

Fig. 9.7 Schematic of KAIST centrifuge test model and instrumentation

Table 9.2 Detailed information of instrumentations used in KAIST experiments

Instrument	Type	Name	Description
Accelerometer	353B17	AH1–AH4, AH6, AH9	Soil horizontal acceleration
		AH11–AH12	Box horizontal acceleration
		AV1–AV2	Box vertical acceleration
Pore pressure transducer	PDCR 81	P1–P4, P6, P8	Pore water pressure in soil
	EPB-PW-3.5BS-V5/L5M	P9–P10	Pore water pressure at the bottom boundary

because the shaking plane was perpendicular to the plane of rotation of the centrifuge, and the centrifuge arm was big enough to mitigate the effect of ground curvature.

The responses of the soil model during shaking were monitored using eight accelerometers along the direction of shaking (AH1–AH4 in the center soil, AH6 and AH9 in the soil close to container boundary, and AH11–AH12 on the rigid container), two vertical accelerometers (AV1 and AV2), and eight pore pressure transducers (P1–P4 in the center of soil model, P6 and P8 in the soil close to side boundary, and P9–P10 at the bottom boundary). The instrument layout is shown in Fig. 9.7. Table 9.2 lists the details of the instrumentation used.

The required 18 surface markers were installed on the ground uniformly with a spacing of 2 m × 2 m. The markers, with a diameter of 26 mm (model scale), were manufactured using PVC material and were designed to be anchored to the soil surface and provide a minimal restriction to pore pressure drainage. A high-speed camera was mounted on the centrifuge arm to measure the plan view lateral displacements of the surface markers during shaking. The high-speed camera at KAIST is a Phantom v5.1 HI-G, which can record videos at 1200 frames per second at a resolution of 1024 × 1024 pixels. The self-balanced system of the shaking table and the hinges connecting the basket to the centrifuge arm isolate the camera from vibrations.

9.3.5 Saturation System at KAIST

Figure 9.8 shows the schematic of the saturation system at KAIST. Before saturating, the box was confirmed to be completely sealed from external air. The procedure for the saturation process is as follows: vacuum pressure (−95 kPa) was applied and then a low-pressure CO_2 (15 kPa) was flooded in the box repeatedly. This process was performed five times. In addition, a strong vacuum pressure was also applied to eliminate the trapped air in the viscous fluid container. While maintaining the same vacuum pressure in the rigid box and viscous fluid container, the viscous fluid was slowly dripped into the ground model. The dripping point was in the downslope direction, and to minimize the impact of falling fluid on the soil surface, a sponge

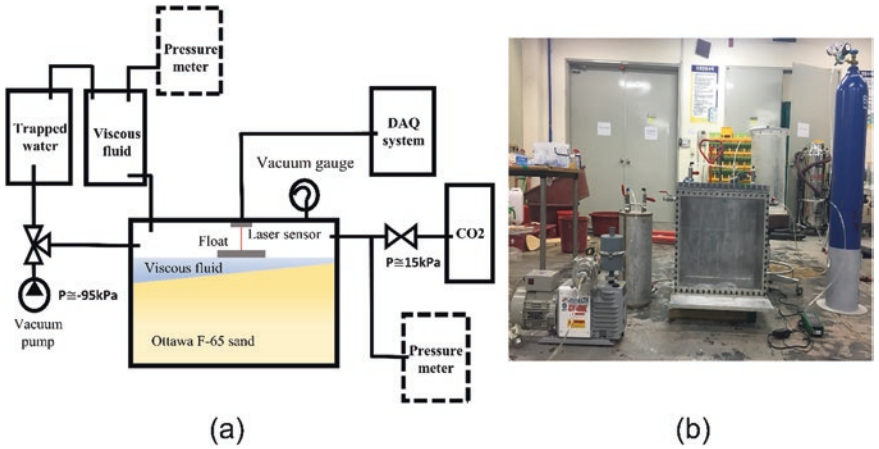

Fig. 9.8 Saturation system used in KAIST. (**a**) Schematic of saturation system. (**b**) Actual saturation system

Table 9.3 Summary of model parameters for Model A and Model B

Parameters	Model A (Conventional scaling law)	Model B (Generalized scaling law)
Density via mass and vol. measurements (kg/m^3)	1716.5	1720.6
Relative density (%)	87	88
Viscosity (cSt)	41.3	36.2
Degree of saturation (%)	99.93	99.94

was installed at the point of impact. After the fluid depth was 5 cm (in model scale) higher than the soil surface, Okamura's method was used to measure the degree of saturation (Okamura & Inoue, 2012). The degree of saturation measured was 99.93% and 99.94% for Models A and B, respectively, indicating full saturation. Table 9.3 shows the summary of model parameters for Models A and B.

9.3.6 Sequence of the Centrifuge Test

Table 9.4 summarizes the typical sequence of the centrifuge tests. In each of the centrifuge tests, four seismic excitations were applied: two low-intensity non-destructive motions and two high-intensity destructive motions. The frequency wavelets covering a wide range were used as a non-destructive motion for ground identification before and after liquefaction. A tapered sine wave with a frequency of 1 Hz was used as the destructive wave. In the KAIST centrifuge tests, the target effective PGA was specified as 0.3g for both the first (Motion #2) and the second

Table 9.4 Major events in centrifuge test sequence for Models A and B

Event	*g*-level (Model A/B)	Event description
Event #1 (CPT)	40*g*/26.7*g*	CPT (before motion #2)
Event #2 (seismic excitations)	40*g*/26.7*g*	Motion #1 and motion #2 (target: 0.3*g*)
Event #3(CPT)	40*g*/26.7*g*	CPT (after motion #2)
Event #4 (seismic excitations)	40*g*/26.7*g*	Motion #3 (target: 0.3*g*) and motion #4

(Motion #3) destructive motions. By applying the destructive motions of the same intensity, the pre- and post-liquefaction behavior can be compared.

Cone penetration tests were also conducted before and after the first destructive motion (Motion #2) to evaluate the soil condition. All facilities participating in LEAP used the same cone design with a cone tip diameter of 6 mm (Carey et al., 2020). The penetration velocity was slow at 2.5 and 3.74 mm/s (model scale) for Models A and B, respectively, and the penetration depth was more than 75 mm (model scale). The CPTs were conducted at locations selected to avoid the sensors installed in the ground model and the markers on the ground surface. As it was necessary to install guide rack and loading actuator above the model box for the CPT, the centrifuge was stopped and restarted to remove the CPT system during seismic excitations. When the centrifuge stopped, the positions of the surface markers were also investigated.

Residual pore pressures (RPPA) were also recorded before and after every major event and change in centrifuge g-level. Recording of RPPA was done while the centrifuge speed was stable and excess pore pressures were 99.9% dissipated.

9.4 Test Results

9.4.1 Achieved Input Motions

The earthquake simulators of most facilities generate various amounts of high-frequency components, which were superimposed on the smooth ramped sine wave motion. Therefore, effective PGA (PGA_{eff}) concept was introduced to compare the results among the facilities that generated different amounts of high-frequency content in the input motion. The PGA_{eff} can be calculated by Eq. 9.1.

$$PGA_{eff} = PGA_{1Hz} + 0.5 \times PGA_{hf} \tag{9.1}$$

where PGA_{1Hz} is the PGA of the isolated 1 Hz input signal and PGA_{hf} is the peak acceleration of the high-frequency components of the input motion (Kutter et al., 2018).

Figure 9.9 shows the main destructive motions (Motions #2 and #3) applied to each model along with the isolated high-frequency noise and the 1 Hz component. A notched band-pass filter with corner frequencies of 0.8 Hz and 1.2 Hz was used

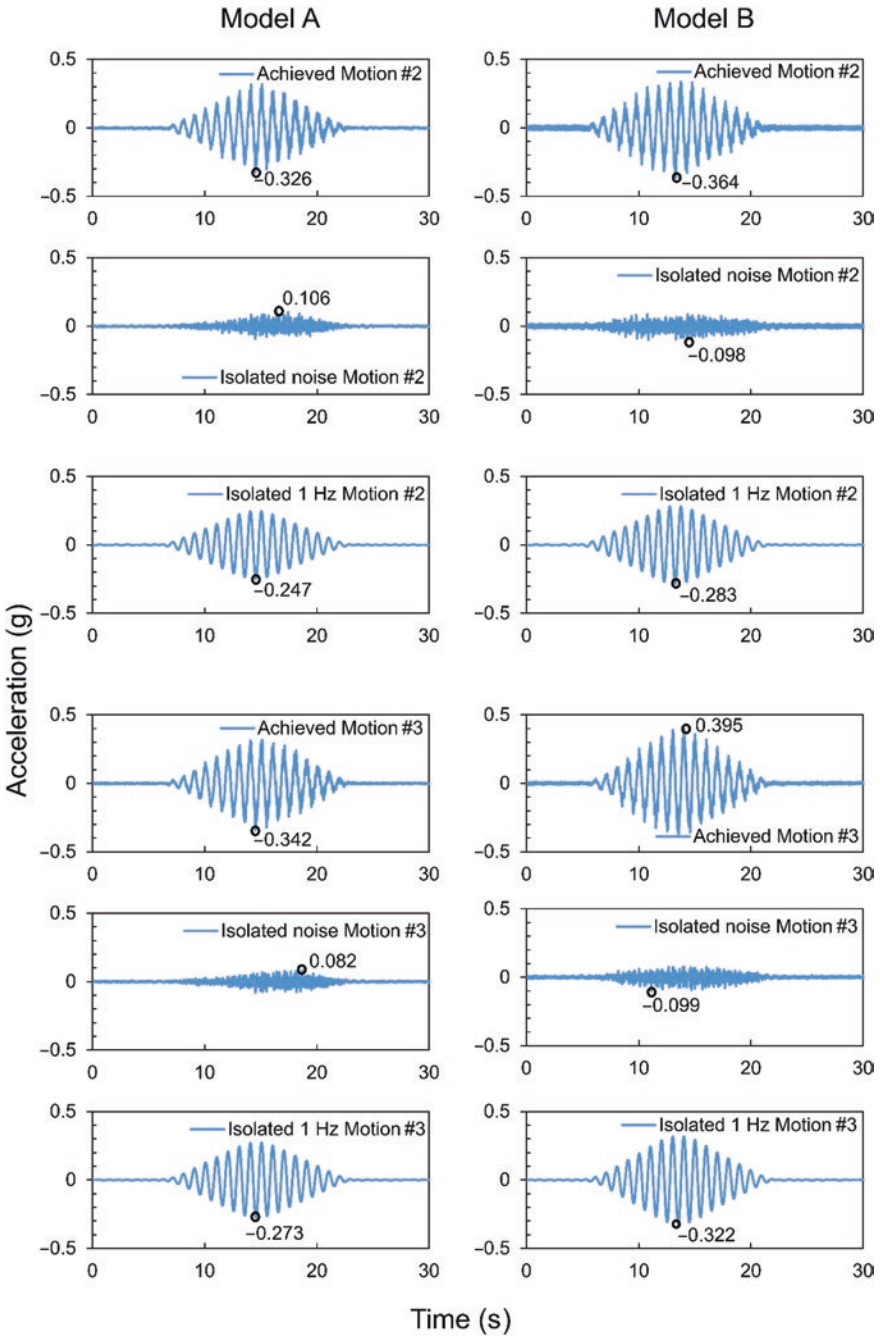

Fig. 9.9 Time series of the achieved base motion, isolated noise, and isolated 1 Hz signal of Motions #2 and #3 along with peak values in Models A and B

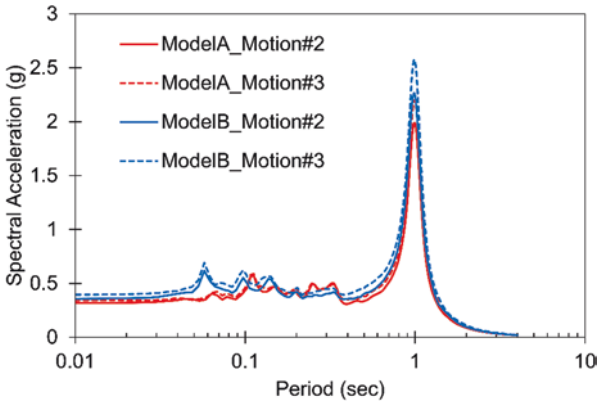

Fig. 9.10 Response spectra of the achieved base motions (Motions #2 and #3) for Models A and B (5% damping)

to obtain these results. Corresponding peak values in each plot are also shown. The achieved base motion is the raw motion recorded by AH11 and AH12 accelerometers attached to the base of the model box; the achieved base motion shown here is the average of AH11 and AH12.

The acceleration response spectra of the achieved base motions as presented in Fig. 9.10 show that the input motions contain some high-frequency components. However, compared to the achieved base motions of other facilities participating in LEAP-UCD-2017 and LEAP-ASIA-2019, the high-frequency components are smaller, and input motions similar to the target were achieved for KAIST model tests.

Table 9.5 lists the details of all the applied motions. Motions #1 and #4 are non-destructive motions with weak intensity for system identification. The PGA_{eff} of the input motions applied in these tests were slightly higher than the target PGA_{eff} (i.e., 0.3*g*) for Motions #2 and #3 of Model A and Motion #2 of Model B. However, for Motion #3 of Model B, the difference between target and achieved PGA_{eff} is large. Although the intensity of the destructive motions applied to each model is somewhat larger than the target intensity, it is reasonable for evaluating the liquefaction behavior of dense models during strong shaking, because it aligns with the objective of LEAP-ASIA-2019.

Upon comparing the PGA_{eff} for Models A and B, the destructive input motions (Motions #2 and #3) for Model B were slightly larger than that for Model A. The difference between PGA_{eff} of Models A and B was bigger in the case of Motion #3 than Motion #2. Nevertheless, the achieved base motions can be considered similar for Models A and B.

Table 9.5 Details of various motions applied to Models A and B

		Target PGA_{eff} (g)	PGA_{raw}[a] (g)	PGA_{eff} (g)	PGA_{hf} (g)	PGA_{1Hz} (g)
Model A ($\mu = 1, \eta = 40$)	Motion #1	0.015	0.052	0.044	0.021	0.033
	Motion #2	0.30	0.326	0.300	0.106	0.247
	Motion #3	0.30	0.342	0.314	0.082	0.273
	Motion #4	0.015	0.05	0.054	0.028	0.030
Model B ($\mu = 1.5, \eta = 26.7$)	Motion #1	0.015	0.088	0.074	0.046	0.051
	Motion #2	0.30	0.364	0.332	0.098	0.283
	Motion #3	0.30	0.395	0.371	0.099	0.322
	Motion #4	0.015	0.077	0.066	0.039	0.046

[a]Peak horizontal acceleration recorded at the container base

9.4.2 *Cone Penetration Test Results*

The depth of penetration and the cone tip resistance (q_c) were converted to the prototype scale using the scaling factors for Models A and B as shown in Table 9.1. The length scale factors were used for scaling the penetration depths.

Figure 9.11a, b represents the q_c with penetration depth at the model and the prototype scales for Models A and B before Motion #2. In the model scale, although Models A and B are similar in construction, the q_c profiles are very different; the q_c profile is larger for Model A than for Model B. This is due to larger confining pressure in Model A than in Model B because of the differences in the centrifugal acceleration; Model A was tested at 40g, while Model B was tested at 26.7g. In the prototype scale, the difference in q_c profiles between Models A and B is reduced. At shallow depths (<1 m), the q_c profiles of both models are similar, but at deeper depths, Model A shows relatively larger q_c than Model B. This implies that the generalized scaling law may not be applicable at deeper depths because of the effect of larger confining pressure.

Another possible reason for the difference between q_c profiles between Models A and B is due to higher CPT penetration rate used for Model B than specified. The penetration rate of CPT should be scaled depending on the pore fluid viscosity (μ^*) based on Eq. 9.2 (Kutter et al., 2020a).

$$V_{cpt} = (100\,\text{mm/s})/\mu^* \tag{9.2}$$

where μ^* is the pore fluid viscosity and V_{cpt} is the penetration velocity of the cone. For Model A (μ^* = 41.2 cSt), V_{cpt} should be 2.42 mm/s, and 2.5 mm/s was adopted. For Model B (μ^* = 36.2 cSt), V_{cpt} should be 2.76 mm/s, but 3.72 mm/s was adopted by mistake. A higher penetration rate could result in partial drainage conditions around the cone tip, which contrasts with the fully drained conditions generally assumed for CPT in sand. As a result, the q_c values for Model B could be smaller as reduced drainage causes excess pore pressure to increase around the cone tip (Kim et al., 2008). Comparison of the q_c profiles of dense models from other institutions

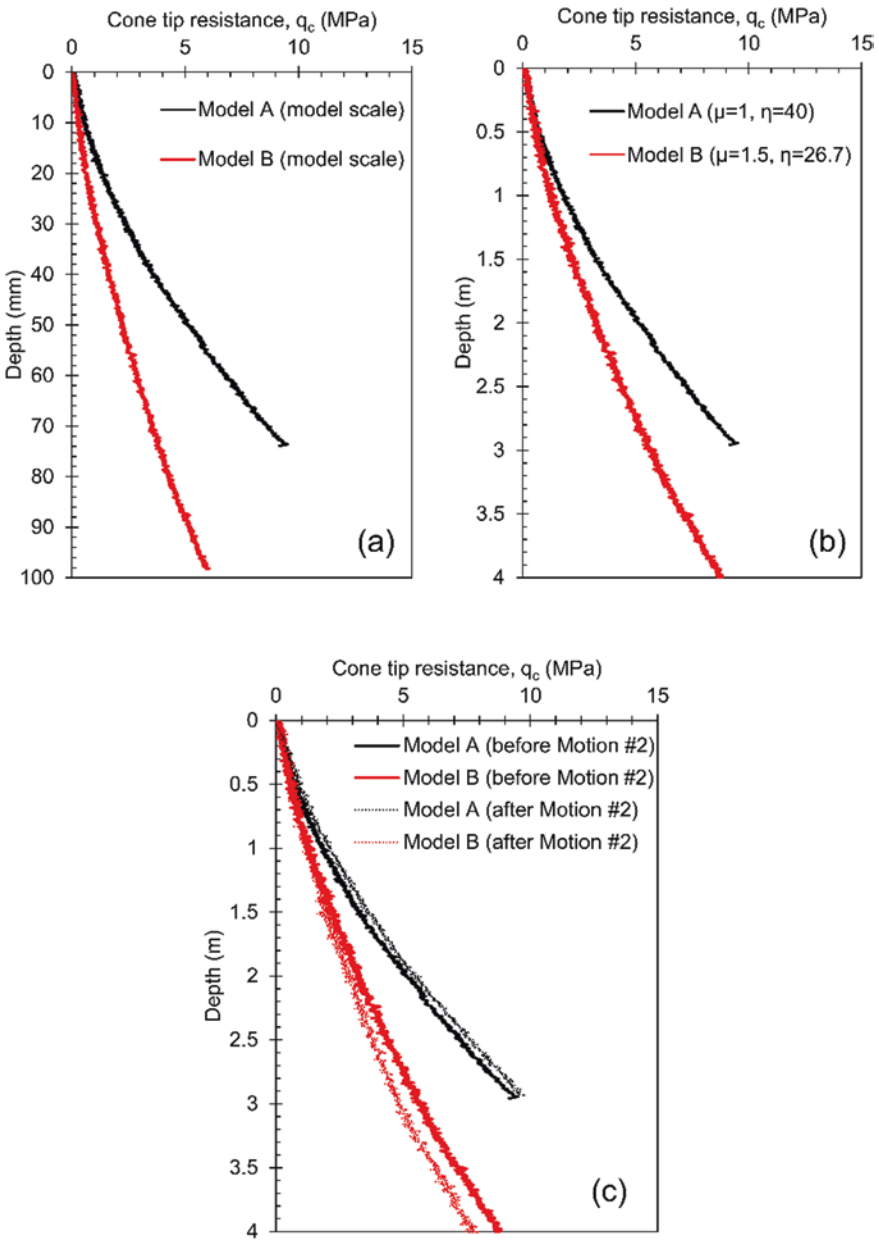

Fig. 9.11 Cone tip resistance (q_c) and penetration depth from CPT: (**a**) q_c versus depth for Models A and B before Motion #2 (model scale), (**b**) q_c versus depth for Models A and B before Motion #2 (prototype scale), and (**c**) q_c versus depth for Models A and B before and after Motion #2

under the same 1-g and centrifuge scaling factors should be performed to investigate the effect of higher penetration rate.

Figure 9.11c presents the q_c value with depth before and after Motion #2 for each model at the prototype scale. The q_c values were slightly larger after Motion #2 for Model A, while for Model B, it was almost the same at shallow depths (<1.5 m) with slight reduction at deeper depths. In the case of Model A, the increase in q_c could be due to soil densification because of particle rearrangement or liquefaction-induced reconsolidation. For Model B, the time for dissipation of excess pore pressure is longer due to smaller elastic stiffness under lower centrifugal acceleration (Tobita & Iai, 2011). Also, the time for consolidation of Model B is shorter because it has to reach centrifugal acceleration of 26.7g as opposed to 40g for Model A. Therefore, Model B may not have fully consolidated following Motion #2 resulting in smaller q_c values at the deeper depths.

9.4.3 Comparison of Acceleration Response

The acceleration response of Models A and B was converted to the prototype scale using scaling factors shown in Table 9.1. Figure 9.12 shows the response of the four accelerometers installed at the center of the model ground together with the response spectra and the ratio of response spectra (RRS) during Motion #2. The RRS is calculated based on Eq. (9.3). As seen in Table 9.5, the PGA_{eff} for Model B was slightly larger than for Model A. dilation spikes, which are caused by the de-liquefaction shock waves (Kutter & Wilson, 1999), are observed more clearly in the sensors installed near the surface (AH4 and AH3), which indicates that the soil may have liquefied. The dilation spikes are unsymmetrical due to the sloping ground model; the spikes are triggered extensively in the direction of static shear stress (downslope direction). The response spectra for both the models are similar except at the short-period range; Model A showed slightly larger high-frequency acceleration spikes than Model B. This is clearer in Fig. 9.12c, where the RRS is larger for Model A than for Model B at the short-period range. An interesting observation is that the spectral acceleration at the period of 1 s is almost the same at all depths and no amplification occurred for the main frequency component of the base motion.

$$\text{RRS} \quad \frac{\text{Response spectra of soil motions AH1 AH4}}{\text{Response spectrum of the base motion}} \tag{9.3}$$

Figure 9.13 shows the acceleration time history, the response spectra, and the RRS at different depths in Models A and B during Motion #3. In Model A, the amplitude of the dilation spikes was relatively smaller compared to Motion #2, and the dilation spikes were observed only at shallow depths (AH4 and AH3). This can be attributed to soil densification after Motion #2 as seen from the CPT results (Fig. 9.11c). Consequently, the spectral acceleration and the RRS at the short-period

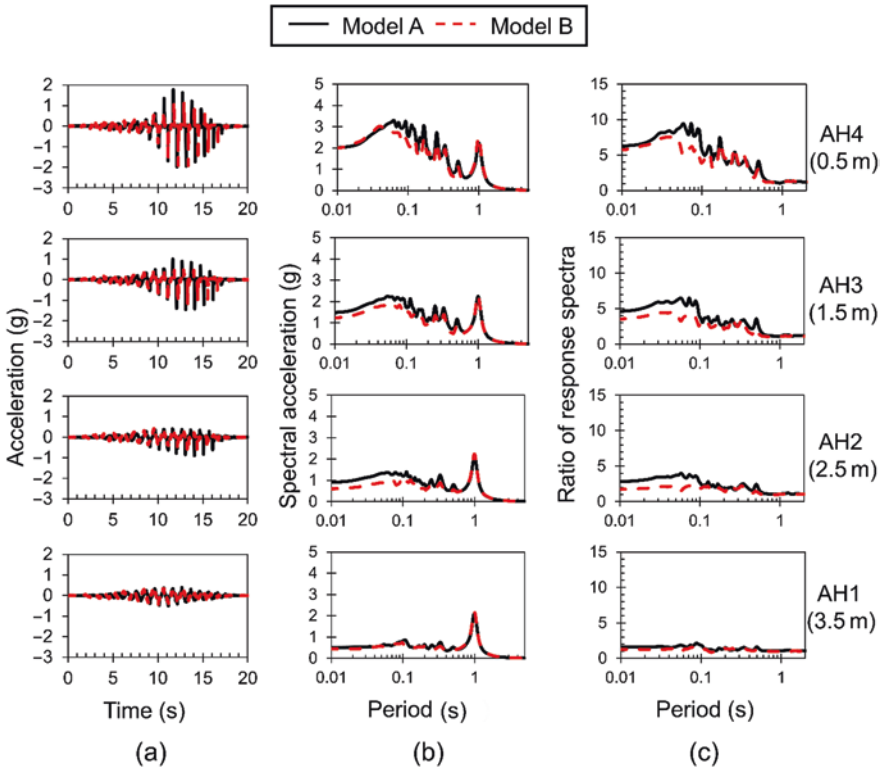

Fig. 9.12 Acceleration response at different depths for Models A and B during Motion #2: (**a**) acceleration time history, (**b**) response spectra, and (**c**) ratio of response spectra

range in Model A were smaller for Motion #3 (Fig. 9.13b, c) than for Motion #2 (Fig. 9.12b, c).

In Model B, the amplitude of dilation spikes was larger for Motion #3 than for Motion #2. This could be due to larger PGA_{eff} of Motion #3 (0.371*g*) than of Motion #2 (0.314*g*). Also, there was some evidence of loosening in Model B after Motion #2 based on the CPT result (Fig. 9.11c). So, it is reasonable to expect a larger extent of liquefaction during Motion #3, which resulted in bigger dilation spikes. Hence, the spectral acceleration and the RRS at the short-period range were larger during Motion #3 than Motion #2 for Model B.

Overall, the acceleration response of Models A and B is largely similar during Motion #2, while the acceleration response of Model B was larger than that of Model A during Motion #3.

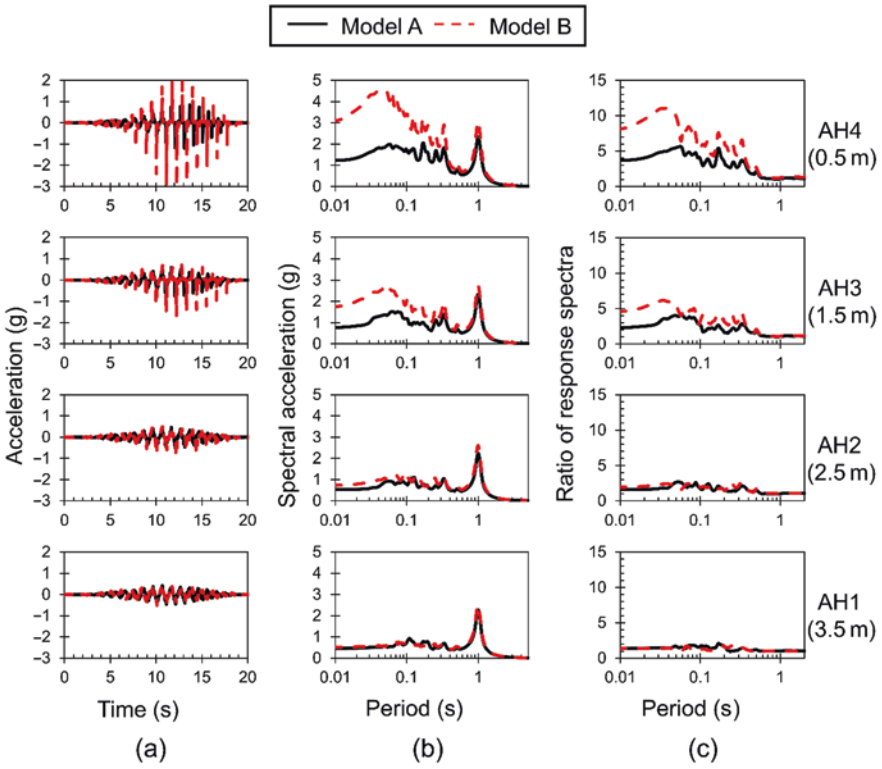

Fig. 9.13 Acceleration response at different depths for Models A and B during Motion #3: (**a**) acceleration time history, (**b**) response spectra, and (**c**) ratio of response spectra

9.4.4 Excess Pore Pressure Response

The excess pore pressure response during destructive motions in Models A and B was converted to the prototype scale based on scaling factors in Table 9.1. The excess pore water pressure recorded using pore pressure transducers placed at various depths during Motion #2 and Motion #3 is shown in Fig. 9.14. The response of pore pressure transducer P1 installed at 4 m depth in Model A and transducer P2 located at 3 m depth in Model B were not obtained due to malfunctioning of the sensors. The initial vertical effective stresses were approximately 40 kPa, 30 kPa, 20 kPa, and 10 kPa at P1, P2, P3, and P4, respectively. Negatively directed spikes in pore pressure were observed due to soil dilatancy during the destructive motions. On the other hand, the dissipation time of the excess pore pressure was longer in Model B than in Model A. In other words, the experiment, which was performed at lower centrifugal acceleration, required longer dissipation time for the excess pore pressure. These can be attributed to three possibilities: (1) the effect of time duration for consolidation before shaking, (2) small value of shear modulus due to low

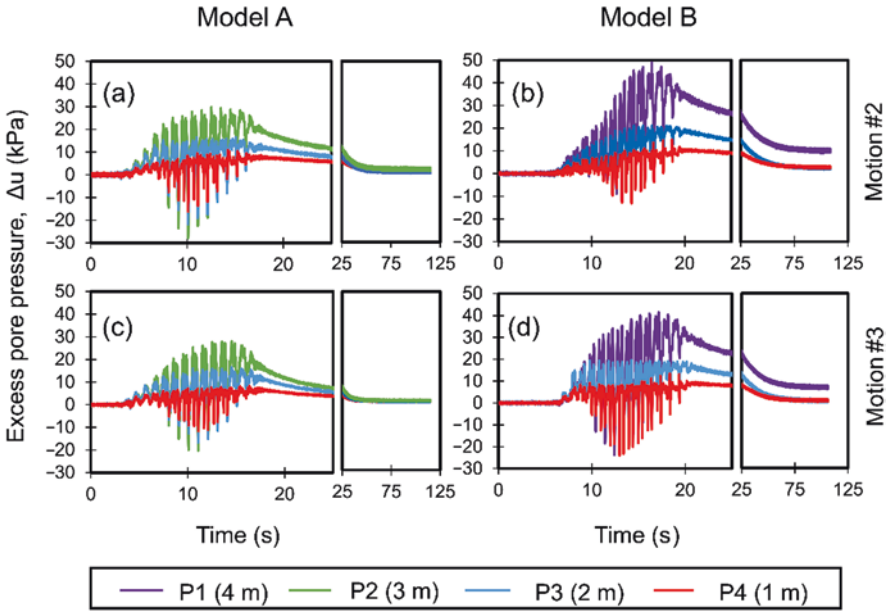

Fig. 9.14 Excess pore pressure response (Δu) at different depths: (**a**) Δu during Motion #2 in Model A, (**b**) Δu during Motion #2 in Model B, (**c**) Δu during Motion #3 in Model A, and (**d**) Δu during Motion #3 in Model B

effective confining stress under low centrifugal acceleration, and (3) possible changes in permeability of the model ground during shaking due to adsorption of the methylcellulose on sand particles (Tobita & Iai, 2011).

Figure 9.15 shows the time history of pore pressure ratio (r_u) for each model in order to compare the liquefaction occurrence in Models A and B. The r_u at a given depth was calculated by dividing the recorded excess pore pressure by the initial vertical effective stress at that depth. The r_u value equal to 1 is generally considered as an evidence of initial liquefaction. During Motion #2, the r_u value was close to 1 only at the depth of 1 m (P4) in Model A, while at other depths (P3 and P2), the r_u value was less than 1. For Model B during Motion #2, the r_u value reached 1.0 at all depths (P4, P3, and P1). The r_u value close to 1 at P1 is unlikely due to liquefaction as the dilation spikes were absent in acceleration (AH1) response. This large positive excess pore pressure could be because of an increase in total stress momentarily due to the effect of vertical accelerations, the local dynamic compressive stress around the sensor, and the effect of wire stiffness (Kutter et al., 2020b).

During Motion #3, the r_u value was less than 1 at all the measured depths for Model A, even though PGA_{eff} for Motion #3 was slightly bigger. This can be attributed to soil densification after Motion #2, which led to an increase in liquefaction resistance. For Model B, however, the r_u value reached 1.0 at shallow depths (P4 and P3), and larger dilation spikes were observed than during Motion #2. This could be because of larger PGA_{eff} for Motion #3 and soil softening following Motion #2. At

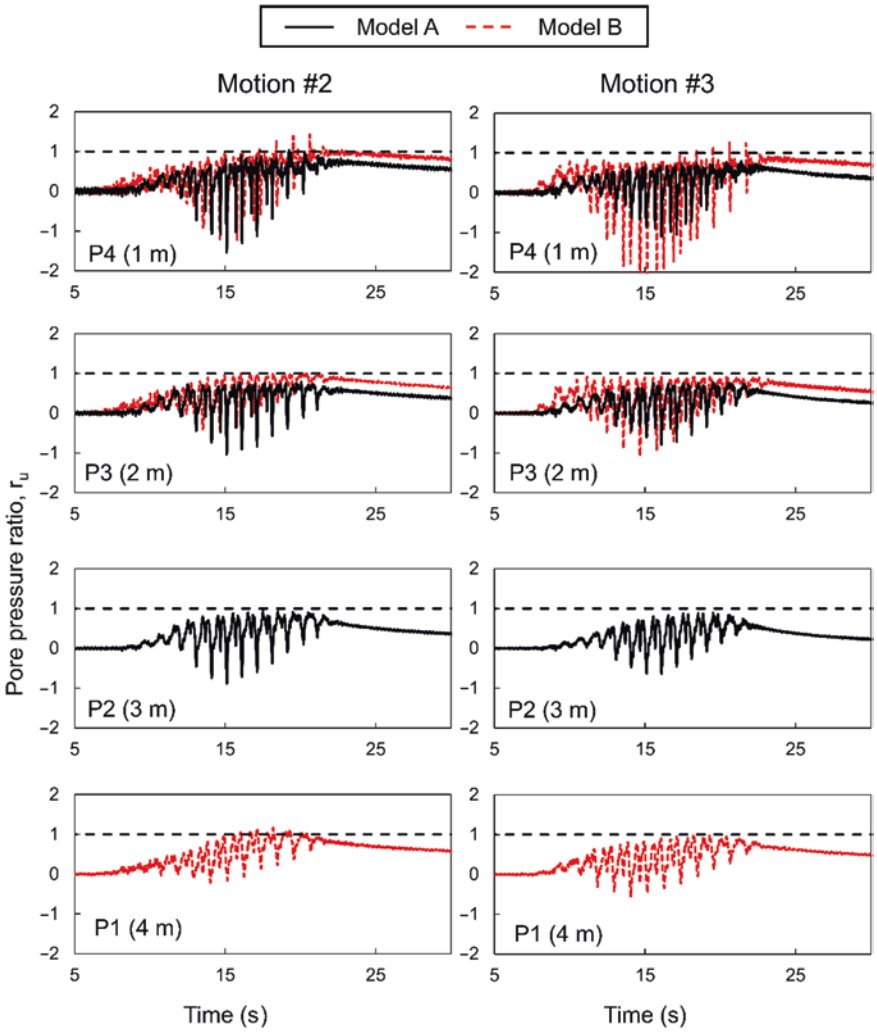

Fig. 9.15 Pore pressure ratio (r_u) for Models A and B during Motion #2 and Motion #3 at different depths

a depth of 4 m (P1), although r_u value reached 1.0, liquefaction is unlikely for reasons previously mentioned.

Even though r_u close to 1 was observed at shallow depths in both Models A and B during Motion #2 and Motion #3, it is unlikely that full liquefaction occurred at these depths. Dense soils can generate high r_u values under severe cyclic loading but still have limited shear potential due to their strong dilation tendency upon continuous shear deformation (Wu et al., 2004). Also, the excess pore pressure dissipated right after the end of shaking, indicating that the extent of liquefaction was fairly limited. This will be clearer upon observing the displacement response of the

sloping ground in Sect. 9.4.6. Hence, it would be reasonable to state that both Models A and B were partially liquefied during Motions #2 and #3.

9.4.5 Stress-Strain Response and Effective Stress Path

The stress and strain quantities were converted to the prototype scale based on the corresponding scaling factors for Models A and B (Table 9.1). Figure 9.16 shows the stress-strain curves for Models A and B during Motion #2 and Motion #3 at three different depths. Shear stress time history was calculated at midway point between two accelerometers based on the acceleration response using the equations given in Zeghal et al. (2018). Strain time history was calculated at the midway point between two accelerometers based on the displacement response obtained by the double integration of the acceleration response. During Motion #2, both Models A and B showed similar stress-strain behavior at all the depths. The shear strain was less than 1% with the maximum strain occurring near the surface. During Motion #3, however, the shear strain for Model A is reduced at all the depths as compared with Motion #2. On the other hand, the shear strain for Model B increased at all depths during Motion #3, with strain at the depth of 1 m exceeding 1%. The difference in stress-strain responses during Motion #3 can be attributed to soil densification following Motion #2 for Model A and large amplitude in Motion #3 for Model B. Additionally, stress spikes are observed in both the upslope and downslope directions at all the depths for both models. This could be due to dilative response at shallow depths and a combination of dilative response and soil-container interaction at larger depths (Zeghal et al., 2018).

Figure 9.17 shows the effective stress paths at the depths of 1 and 2 m for Models A and B during Motion #2 and Motion #3. The shear stress (τ) and the vertical effective stress (σ_v') were normalized by the initial vertical effective consolidation stress (σ_{vc}'). The normalized vertical effective stress (σ_v'/σ_{vc}') reached zero during Motion #2 at 1 m depth in Model A, while it was non-zero in all other cases. This indicates that liquefaction occurred at 1 m depth in Model A during Motion #2, which corroborates with the pore pressure ratio response in Fig. 9.15. In Model B, the σ_v'/σ_{vc}' ratio reached zero in all cases, except at the depth of 2 m during Motion #3. On the other hand, the σ_v'/σ_{vc}' ratio exceeded 1.0 in all the cases and reached almost 3.0 at 1 m depth during Motion #3 in Model B. This is due to the large negative pore pressure spikes caused by the strong dilative soil response during shaking. As a result, the effective confining stress was much larger during shaking than before shaking. Therefore, the extent of liquefaction was limited even though the σ_v'/σ_{vc}' ratio became zero momentarily during shaking.

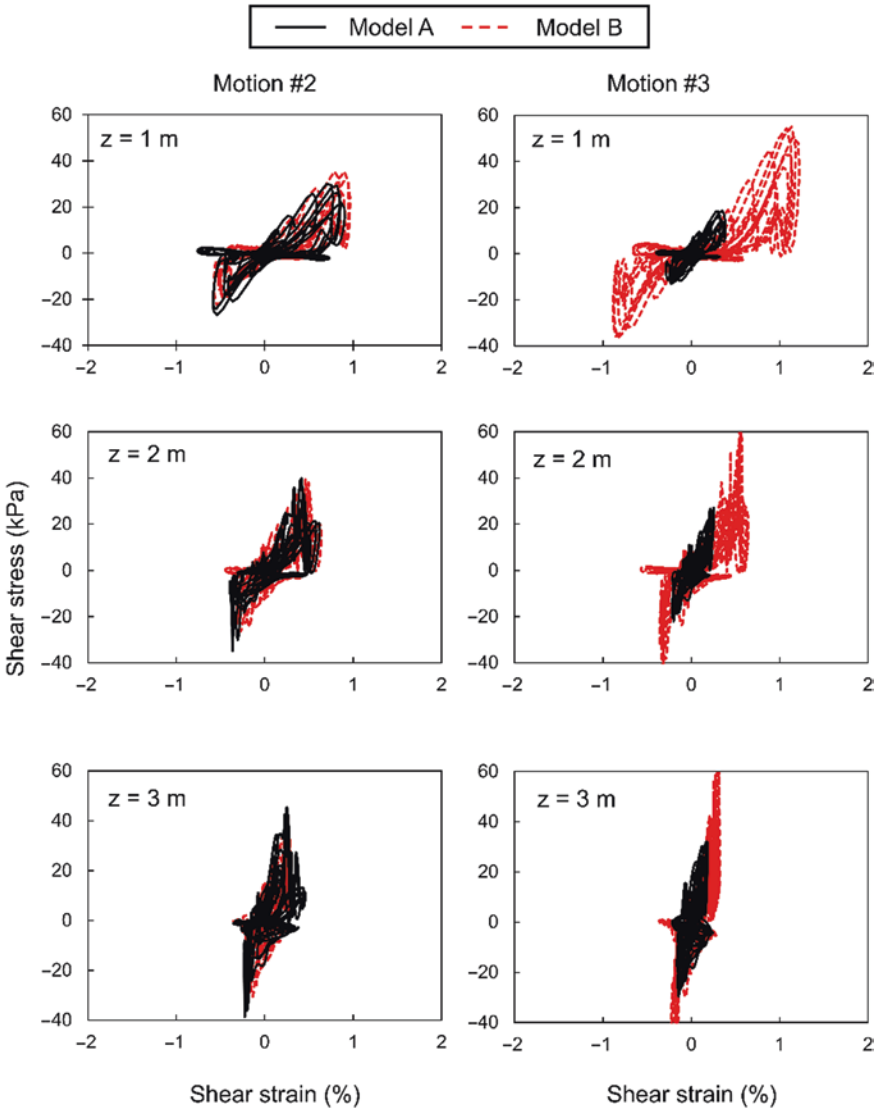

Fig. 9.16 Stress-strain response of Models A and B during Motion #2 and Motion #3 at three different depths

9.4.6 Displacement Response

The prototype displacements for Models A and B are based on scaling factors in Table 9.1. Figure 9.18 shows the schematic of the 18 surface markers and the coordinate system used. The markers were arranged in three longitudinal arrays and six transverse arrays. The coordinates (x, y, and z) of the markers were measured before

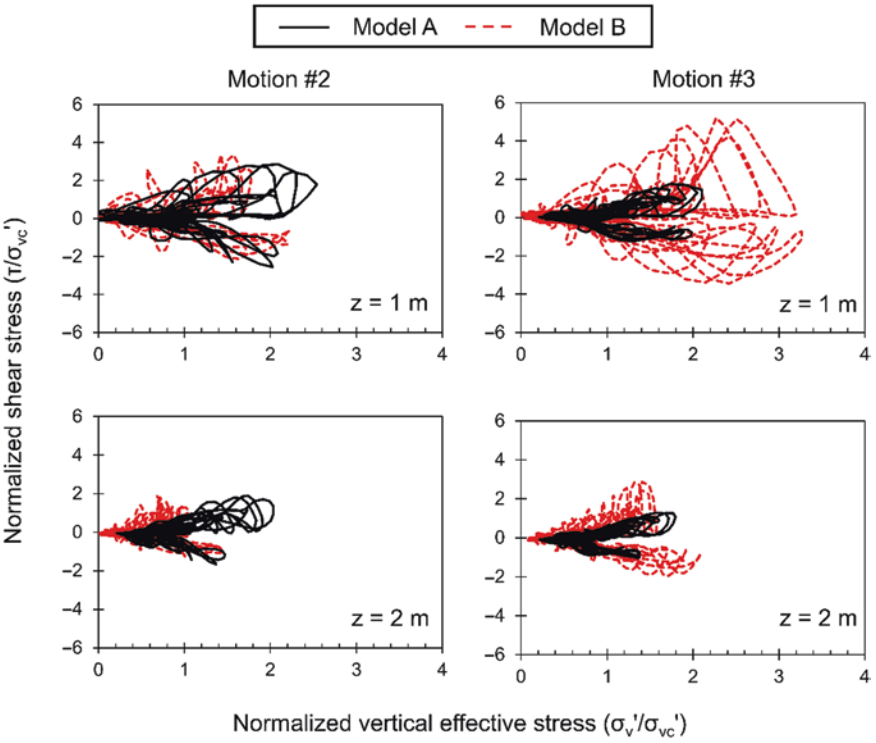

Fig. 9.17 Effective stress paths of Models A and B during Motion #2 and Motion #3

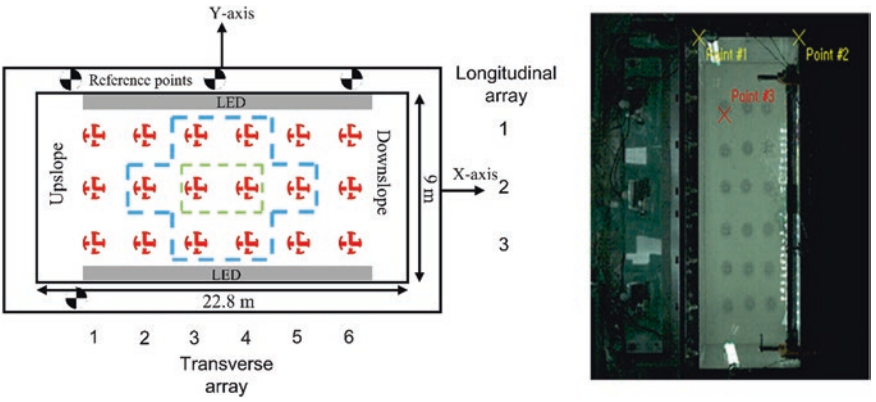

Fig. 9.18 Schematic of the surface markers and coordinate system (18 total markers; 8 markers are included in the blue dotted zone, and 2 central markers are in the green dotted zone). Points #1 and #2 represent the reference points, and Point #3 is the tracking point used in the TEMA software

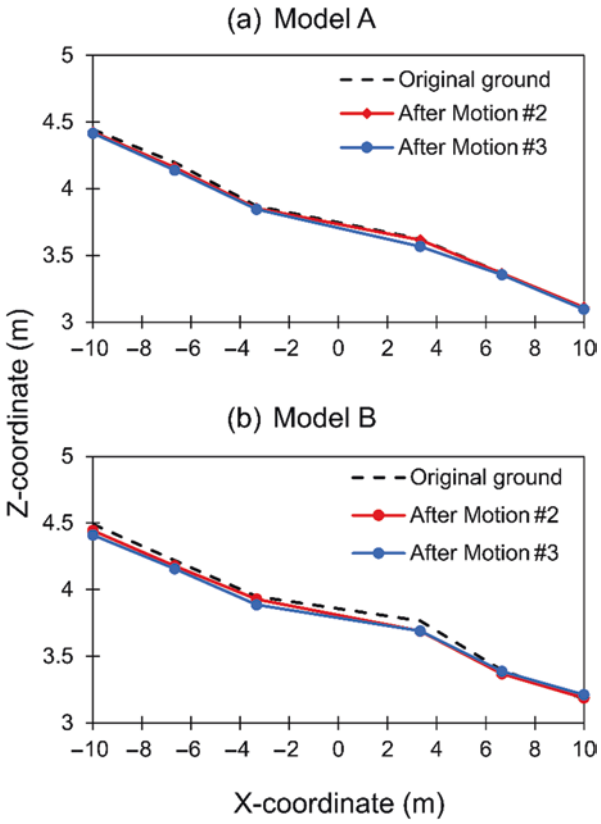

Fig. 9.19 Measured vertical settlements along the longitudinal axis of the model after Motion #2 and Motion #3 with the original ground profile: (**a**) Model A and (**b**) Model B

Motion #2 (initial position), after Motion #2, and after Motion #3 at 1-g condition. The x-coordinate is in the direction of the shaking, y-coordinate is perpendicular to the shaking direction, and z-coordinate is along the depth of the model. Additionally, horizontal displacements of the markers were recorded during shaking motion using a high-speed camera and tracked using a motion-tracking program, TEMA.

Figure 9.19 shows the variation of vertical displacement of the ground profile along the longitudinal axis after each destructive motion. The vertical displacement is the average displacement of the three markers in each transverse array. Both Models A and B showed minimal settlements with little change in the original ground profile after Motion #2 and Motion #3. The measurement of the central markers (dotted green zone) can be taken as representative as they are less affected by the container boundary. After Motion #2, the average vertical settlements of the two central markers in Models A and B were 26 and 32 mm at the prototype scale, respectively. After Motion #3, the average settlements were about 16 mm and 27 mm for Models A and B, respectively. The settlements were comparatively less

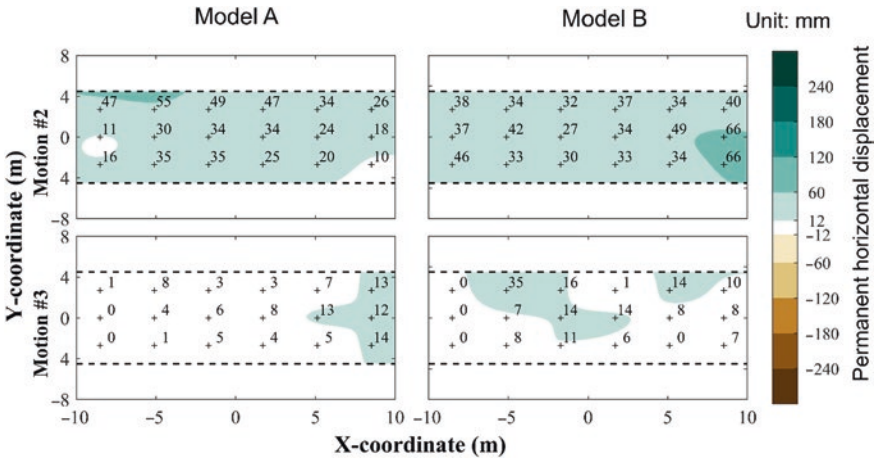

Fig. 9.20 Contour plots of permanent horizontal displacements (in mm) from tracked marker positions obtained using high-speed camera recording in Model A and Model B during Motion #2 and Motion #3

after Motion #3 than Motion #2 in both the models, and Model B had larger settlements than Model A.

Figure 9.20 shows the comparison of permanent horizontal displacement contours for Models A and B following Motion #2 and Motion #3 in the prototype scale. The values above the markers represent the permanent horizontal displacements in mm calculated based on the time history of tracked marker position during shaking (Fig. 9.21). The contour was created by interpolation between the permanent displacements of the markers. In both the models, the 18 markers moved in the downslope direction following Motion #2, and the average permanent horizontal displacements of the two central markers were 34 and 30.5 mm for Model A and Model B, respectively. Although the permanent displacements in Models A and B were almost same, the transient displacements were much larger in Model B than in Model A. There were oscillations in displacement after the end of motion due to water waves, so the average of displacement values after the end of motion was used to calculate the permanent displacement. In the case of Motion #3, the permanent horizontal displacements in both the models were largely reduced.

9.5 Discussion and Conclusions

As a part of LEAP-ASIA-2019, two centrifuge model tests were performed at KAIST to evaluate liquefaction behavior of gently sloping dense grounds (target D_r = 85%) under strong base shaking (target PGA_{eff} = 0.3g). The two models, Models A and B, represented the same prototype model but were tested under different centrifugal accelerations to evaluate the generalized scaling law for

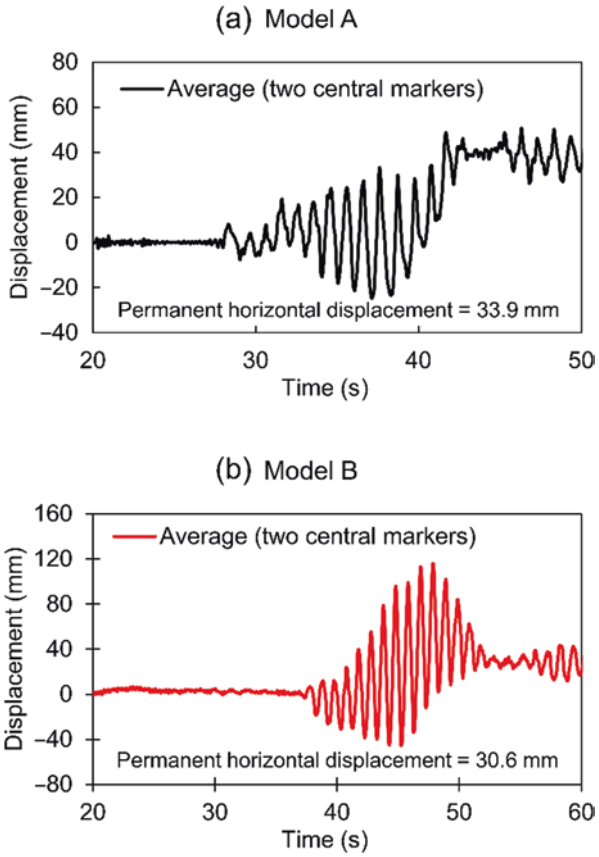

Fig. 9.21 Horizontal displacement (*x*-direction) time histories of two central markers during Motion #2 for Models A and B

simulating liquefaction phenomena in centrifuge tests. Based on the test results, the following can be inferred:

1. Although the same prototype model was simulated using Models A and B, the CPT profiles of the models were similar only at shallow depths (<1 m), while Model A was stiffer than Model B at deeper depths. This shows the effect of larger confining pressure in Model A (40-g centrifugal acceleration) than in Model B (26.7-g centrifugal acceleration), and thus, the generalized scaling law may not be applicable for deeper depths. Another possible reason could be that the generalized scaling law is valid for stress paths up to the peak deviator stress. However, the stress path during CPT testing goes well beyond the peak deviator stress and into the failure zone. Iai et al. (2005) state that we need to use looser material as compared with the prototype when stress path exceeds the peak deviator stress. This can also explain the dissimilarity of CPT results between Models A and B.

2. Upon comparing the CPT results before and after Motion #2, Model A showed ground densification, which is similar to the response of dense model tested at 40-g centrifugal acceleration in LEAP-UCD-2017 at KAIST. However, Model B showed similar q_c values at shallow depths (<1.5 m) but loosening at deeper depths.
3. Spikes due to dilatant soil behavior were observed in acceleration records at shallow depths (0.5 and 1.5 m) in both Models A and B. The acceleration response of Models A and B was similar during Motion #2, while it differed during Motion #3. This is because of ground disturbance following Motion #2 as well as the large intensity in Motion #3 in Model B.
4. Based on pore pressure ratio (r_u), it can be inferred that liquefaction did occur to some extent in dense grounds at shallow depths (1 and 2 m) in both Models A and B. This is in contrast with the response of dense model in LEAP-UCD-2017 at KAIST, where liquefaction did not occur when PGA_{eff} of 0.15g was applied. This implies that under sufficiently strong shaking, dense soil deposits can also liquefy but the extent of liquefaction will be limited. Furthermore, the dissipation time of excess pore pressures was longer in Model B than in Model A due to the effect of low confining stress in Model B.
5. Although there was evidence of liquefaction at shallow depths based on r_u values, significant shear strains were not observed (limited to 1% shear strain) because the soil was initially dense-of-critical (below the critical state line in e-p′ plot). Liquefaction of dense-of-critical sand during cyclic loading results in limited strains because the sand exhibits dilative behavior under subsequent monotonic loading (Idriss & Boulanger, 2008).
6. The stress-strain curves were qualitatively similar for Models A and B during Motion #2, while they were different during Motion #3. This indicates that the generalized scaling law may not be applicable to study stress-strain response of soil after it is disturbed by strong shaking. However, the large shaking intensity of Motion #3 in Model B also caused the observed differences. From the effective stress path, it was observed that the vertical effective stress increased well beyond the initial consolidation stress due to dilatancy causing temporary stiffening of the soil during shaking.
7. The vertical ground settlement profiles were almost the same for Models A and B. Also, there is little difference between settlements after Motion #2 and after Motion #3. Both Models A and B have similar permanent horizontal displacements in the direction of shaking. However, the transient displacements were larger in Model B than in Model A. On the other hand, the permanent horizontal displacements were significantly reduced during Motion #3 as compared to Motion #2 in both the models.

Overall, the response of Models A and B was similar in terms of acceleration, pore pressure response, stress-strain behavior, and ground displacements, except for the CPT profiles. Hence, the generalized scaling law is largely applicable for centrifuge testing of dense model grounds under strong shaking. The large PGA_{eff} of Motion #3 and the effect of soil disturbance following Motion #2 caused the observed differences in response between Models A and B during Motion #3. Thus,

in future tests, it is necessary to control shaking intensity of input motion to validate the applicability of the generalized scaling law following a destructive first motion. Further, the scaling factors used for the cone tip resistance and penetration depth should be explored more to validate the generalized scaling law for CPT.

Acknowledgments This research was part of the project titled "Development of performance-based seismic design," funded by the Ministry of Oceans and Fisheries, Korea. The authors also gratefully acknowledge the KREONET service provided by the Korea Institute of Science and Technology Information.

References

Arulanandan, K., & Scott, R. F. (Eds.). (1993). *Verification of numerical procedures for the analysis of soil liquefaction problems*. A.A. Balkema.

Carey, T. J., Gavras, A., & Kutter, B. L. (2020). Comparison of LEAP-UCD-2017 CPT results. In B. L. Kutter, M. T. Manzari, & M. Zeghal (Eds.), *Model tests and numerical simulations of liquefaction and lateral spreading* (pp. 117–129). Springer. https://doi.org/10.1007/978-3-030-22818-7_6

El Ghoraiby, M., Park, H., & Manzari, M. T. (2020). Physical and mechanical properties of Ottawa F65 sand. In B. L. Kutter, M. T. Manzari, & M. Zeghal (Eds.), *Model tests and numerical simulations of liquefaction and lateral spreading* (pp. 45–67). Springer. https://doi.org/10.1007/978-3-030-22818-7_3

Garnier, J., Gaudin, C., Springman, S. M., Culligan, P. J., Goodings, D., Konig, D., et al. (2007). Catalogue of scaling laws and similitude questions in geotechnical centrifuge modelling. *International Journal of Physical Modelling in Geotechnics, 7*(3), 1–23. https://doi.org/10.1680/ijpmg.2007.070301

Iai, S., Tobita, T., & Nakahara, T. (2005). Generalized scaling relations for dynamic centrifuge tests. *Geotechnique, 55*(5), 355–362. https://doi.org/10.1680/geot.2005.55.5.355

Idriss, I. M., & Boulanger, R. W. (2008). *Soil liquefaction during earthquakes*. Earthquake Engineering Research Institute. MNO-12.

Kim, K., Prezzi, M., Salgado, R., & Lee, W. (2008). Effect of penetration rate on cone penetration resistance in saturated clayey soils. *Journal of Geotechnical and Geoenvironmental Engineering, 134*(8), 1142–1153. https://doi.org/10.1061/(ASCE)1090-0241(2008)134:8(1142)

Kim, D.-S., Kim, N.-R., Choo, Y.-W., & Cho, G.-C. (2013a). A newly developed state-of-the-art geotechnical centrifuge in Korea. *KSCE Journal of Civil Engineering, 17*(1), 77–84. https://doi.org/10.1007/s12205-013-1350-5

Kim, D.-S., Lee, S.-H., Choo, Y.-W., & Perdriat, J. (2013b). Self-balanced earthquake simulator on centrifuge and dynamic performance verification. *KSCE Journal of Civil Engineering, 17*(4), 651–661. https://doi.org/10.1007/s12205-013-1591-3

Kim, S.-N., Ha, J.-G., Lee, M.-G., & Kim, D.-S. (2020). LEAP-UCD-2017 centrifuge test at KAIST. In B. L. Kutter, M. T. Manzari, & M. Zeghal (Eds.), *Model tests and numerical simulations of liquefaction and lateral spreading* (pp. 315–339). Springer. https://doi.org/10.1007/978-3-030-22818-7_16

Kutter, B. L., & Wilson, D. W. (1999). *De-liquefaction shock waves* (pp. 295–310). Proceedings of the seventh US–Japan workshop on earthquake resistant design of lifeline facilities and countermeasures against soil liquefaction.

Kutter, B. L., Carey, T., Hashimoto, T., Zeghal, M., Abdoun, T., Kokalli, P., Madabhushi, G., Haigh, S., Hung, W.-Y., Lee, C.-J., Iai, S., Tobita, T., Zhou, Y. G., Chen, Y., Manzari, M. T., et al.

(2018). LEAP-GWU-2015 experiment specifications, results, and comparisons. *Soil Dynamics and Earthquake Engineering, 113*, 616–628. https://doi.org/10.1016/j.soildyn.2017.05.018

Kutter, B. L., Carey, T. J., Zheng, B. L., Gavras, A., Stone, N., Zeghal, M., et al. (2019). Twenty-four centrifuge tests to quantify sensitivity of lateral spreading to Dr and PGA. In *Geotechnical earthquake engineering and soil dynamics V* (pp. 383–393). https://doi.org/10.1061/9780784481486.040

Kutter, B. L., Carey, T. J., Stone, N., Bonab, M. H., Manzari, M. T., Zeghal, M., et al. (2020a). LEAP-UCD-2017 V. 1.01 model specifications. In B. L. Kutter, M. T. Manzari, & M. Zeghal (Eds.), *Model tests and numerical simulations of liquefaction and lateral spreading* (pp. 3–29). Springer. https://doi.org/10.1007/978-3-030-22818-7_1

Kutter, B. L., Carey, T. J., Stone, N., Zheng, B. L., Gavras, A., Manzari, M. T., et al. (2020b). LEAP-UCD-2017 comparison of centrifuge test results. In B. L. Kutter, M. T. Manzari, & M. Zeghal (Eds.), *Model tests and numerical simulations of liquefaction and lateral spreading* (pp. 69–103). Springer. https://doi.org/10.1007/978-3-030-22818-7_4

Okamura, M., & Inoue, T. (2012). Preparation of fully saturated models for liquefaction study. *International Journal of Physical Modelling in Geotechnics, 12*(1), 39–46.

Tobita, T., & Iai, S. (2011). *Application of the generalized scaling law to liquefiable model ground*. Annuals of Disaster Prevention Research Institute, Kyoto University.

Ueda, K., & Iai, S. (2018). Numerical predictions for centrifuge model tests of a liquefiable sloping ground using a strain space multiple mechanism model based on the finite strain theory. *Soil Dynamics and Earthquake Engineering, 113*, 771–792. https://doi.org/10.1016/j.soildyn.2016.11.015

Wu J., Kammerer A.M., Riemer M.F., Seed R.B., Pestana J.M. (2004) *Laboratory study of liquefaction triggering criteria*. 13th world conference on earthquake engineering. Vancouver, BC, Canada, Paper No. 2580.

Zeghal, M., Goswami, N., Kutter, B. L., Manzari, M. T., Abdoun, T., Arduino, P., et al. (2018). Stress-strain response of the LEAP-2015 centrifuge tests and numerical predictions. *Soil Dynamics and Earthquake Engineering, 11*, 804–818. https://doi.org/10.1016/j.soildyn.2017.10.014

Chapter 10
LEAP-ASIA-2019 Centrifuge Test at Kyoto University

Ruben R. Vargas, Kyohei Ueda, and Tetsuo Tobita

Abstract The Liquefaction Experiments and Analysis Projects (LEAP) is an international collaborative project that aims to verify, validate, and quantify the uncertainty of numerical liquefaction models. "LEAP-ASIA-2019" is one of the LEAP's exercises, whose main objectives are to validate the "generalized scaling law" for lateral spreading and to fill the gaps of experiments to complete the dataset obtained as part of the "LEAP-UCD-2017." Within this project, a total of five models were developed at the geotechnical centrifuge of Kyoto University to simulate the dynamic behavior of a submerged, uniform-density, 20-m-long, 4-m-deep, and 5° sloping deposit of Ottawa F-65 sand. This paper presents the key features of the model preparation and testing process while also examining the applicability of the "generalized scaling law" for centrifuge modeling.

Keywords Liquefaction Experiments and Analysis Projects (LEAP-ASIA-2019) · Generalized scaling law (GSL) · Centrifuge modeling

10.1 Introduction

Due to its catastrophic consequences, soil liquefaction has been a matter of great concern to the engineering community; therefore, intensive research and development efforts have been dedicated to understand the phenomena and prevent future losses and damages. The development of liquefaction constitutive and numerical models in the last decades promoted an increase in its use for research and

R. R. Vargas (✉)
Penta-Ocean Construction Co. Ltd., (Former Department of Civil and Earth Resources Engineering, Kyoto University, Kyoto, Japan), Tokyo, Japan

K. Ueda
Disaster Prevention Research Institute, Kyoto University, Kyoto, Japan

T. Tobita
Department of Civil, Environmental and Applied Systems Engineering, Kansai University, Osaka, Japan

T. Tobita et al. (eds.), *Model Tests and Numerical Simulations of Liquefaction and Lateral Spreading II*, https://doi.org/10.1007/978-3-031-48821-4_10

engineering practice purposes. However, as stated by Kutter et al. (2018b), there is still no practical generally accepted process for validation of capabilities of the numerical implementations; therefore, V&V exercises are required to enhance its reliability.

In this sense, LEAP (Liquefaction Experiments and Analysis Projects) was established as an international joint project that pursues the verification, validation, and uncertainty quantification of numerical liquefaction models, based on high-quality experimental data (e.g., centrifuge model tests). In the LEAP framework, three main exercises ("LEAP-GWU-2015," "LEAP-UCD-2017," and "LEAP-ASIA-2019") were developed to investigate the dynamic behavior of a uniform, 4-m-deep, 5-degree slope sandy ground.

As part of the "LEAP-GWU-2015" exercise, the same 4-m-deep, 5° slope sandy ground model was repeated by six centrifuge facilities; Kutter et al. (2018a) found that despite variability, the experimental results were consistent with each other, lending credence to the approach for a next-generation validation database. In the subsequent "LEAP-UCD-2017" exercise, 9 centrifuge facilities developed 24 centrifuge models with the same geometry as the previous exercise, but with different combinations of relative density (D_r) and peak ground acceleration (PGA). Kutter et al. (2020b) found consistent results and clear trends among the experiments in this exercise.

Building on the consistency of these exercises, Tobita et al. (2023) conceived "LEAP-ASIA-2019" to use the same model geometry as the previous tests, with two main objectives: validating the "generalized scaling law" for centrifuge modeling (Iai et al., 2005) by developing two models (Model A and Model B) representing the same prototype model using conventional scaling laws and the generalized scaling laws, respectively, and filling gaps in the data from the "LEAP-UCD-2017" exercise in terms of combinations of D_r and PGA to extend, establish, and confirm observed trends.

As part of "LEAP-ASIA-2019" exercise, five centrifuge tests were developed in the 2.50 m radius and 24*g*-ton centrifuge of the Disaster Prevention Research Institute (DPRI) at Kyoto University; although a comprehensive review of the test findings has already been published (Vargas et al., 2021), this paper focuses on the details of the model preparation and presents the test results.

10.2 Test Specifications and Model Preparation

10.2.1 Description of the Model and Scaling Laws

As described by Tobita et al. (2023), a uniform-density, 20-m-long, 4-m-deep at center, and 5° sloping deposit inside a rigid container was specified for "LEAP-ASIA-2019"; since the model specifications established for "LEAP-UCD-2017" are applicable for this exercise, the models were built following the specifications established by Kutter et al. (2020a).

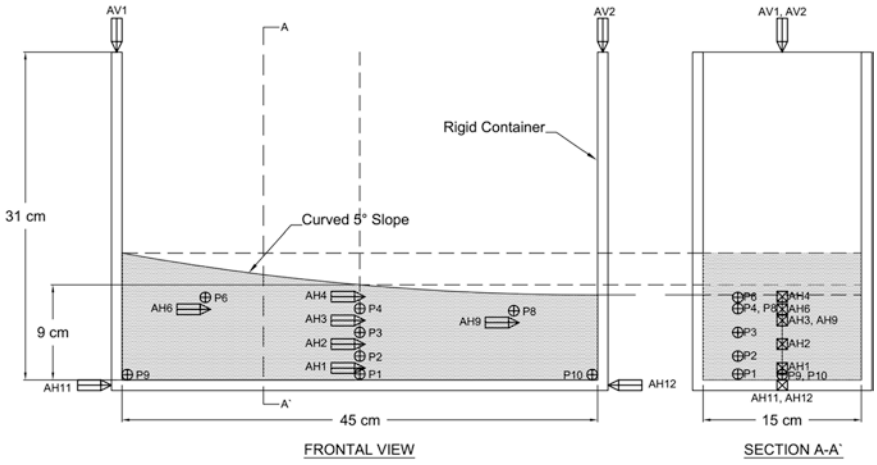

Fig. 10.1 Dimensions and instrumentation of the models. (Vargas et al., 2021)

The dimensions of the rigid box used in the tests are presented in Fig. 10.1. The instrumentation consisted of two horizontal (AH11 and AH12) and two vertical (AV1 and AV2) accelerometers placed outside the box to record the input motions. In addition, six horizontal accelerometers (AH1, AH2, AH3, AH4, AH6, and AH9) and eight pore pressure transducers (P1, P2, P3, P4, P6, P8, P9, and P10) were placed inside the ground to capture the soil response in the central array and the effects of the rigid boundaries.

The standard sand selected for the "LEAP-ASIA-2019" is Ottawa F-65, a clean, poorly graded, silica sand, with less than 0.5% fines by mass (Carey et al., 2020). In order to guarantee that all facilities use the same material, UC Davis delivered the sand to all the facilities prior to the tests.

As mentioned in the previous section, one of the goals of this exercise was the validation of the "generalized scaling law" for centrifuge modeling (Iai et al., 2005); this scaling law involves a two-stage scaling process in which physical model parameters are first scaled to a "virtual 1 g" field using the conventional centrifuge scaling factor, η, and then further scaled to the "prototype" field using scaling factors for 1g tests, μ. The scaling relationships are presented in Table 10.1.

For this exercise, five models were developed in the geotechnical centrifuge of the Disaster Prevention Research Institute at Kyoto University; Table 10.2 shows the scaling factors used for each model.

As seen in Table 10.2, all models have the same dimensions in prototype scale (i.e., the same "generalized scaling factor"); however, different scaling factors were used. In order to study the validity of the generalized scaling law, and for comparative purposes, two groups of models were generated, aiming to achieve a similar relative density (D_r) and effective peak ground acceleration "PGA_{eff}" (Kutter et al., 2020b) in each of them.

Table 10.1 Generalized scaling relationships

	(1) Scaling factors for 1g test	(2) Scaling factors for centrifuge test	(3) Generalized scaling factors
Length	μ	η	$\mu\eta$
Density	1	1	1
Time	$\mu^{0.75}$	η	$\mu^{0.75}\eta$
Frequency	$\mu^{-0.75}$	$1/\eta$	$\mu^{-0.75}/\eta$
Acceleration	1	$1/\eta$	$1/\eta$
Velocity	$\mu^{0.75}$	1	$\mu^{0.75}$
Displacement	$\mu^{1.5}$	η	$\mu^{1.5}\eta$
Stress	μ	1	μ
Strain	$\mu^{0.5}$	1	$\mu^{0.5}$
Stiffness	$\mu^{0.5}$	1	$\mu^{0.5}$
Permeability	$\mu^{0.75}$	η	$\mu^{0.75}\eta$
Pore pressure	μ	1	μ

Iai et al. (2005)

Table 10.2 Tests developed at Kyoto University and its scaling factors

Group	Model	Scale factor for 1g test (μ)	Scaling factors for centrifuge test (η)	Generalized scaling factor
1	KyU_A_A1_1	1	44.4	44.4
	KyU_A_B1_1	2	22.2	44.4
	KyU_A_B1_2	4	11.1	44.4
2	KyU_A_A2_1	1	44.4	44.4
	KyU_A_B2_1	2	22.2	44.4

10.2.2 Model Preparation

As specified, the air pluviation method was used for sand placement; the constant air pluviation height was defined following a calibration process (definition of a height-density relationship), prior to each experiment. It was found that the height-density relationship was slightly different for each experiment; although it seems that the difference could be attributable to environmental conditions (such as humidity, temperature, etc.), further research would be required for confirmation.

Density measurements were conducted at three different stages during sand placement for each model; less than 5% (in terms of relative density) of difference between layers was found. Table 10.3 shows the target and achieved dry densities, and these densities were obtained through mass and volume estimations.

Since the centrifuge facility at Kyoto University is equipped with a shaking table in the circumferential direction, to reduce the effects of variations in the radial

Table 10.3 Target and achieved dry densities for the five models

Model	Target density (kg/m^3)	Achieved density (kg/m^3)	Achieved D_r
KyU_A_A1_1	1682	1677	73.3%
KyU_A_B1_1	1682	1673	71.9%
KyU_A_B1_2	1682	1669	70.5%
KyU_A_A2_1	1628	1628	55.7%
KyU_A_B2_1	1628	1633	57.5%

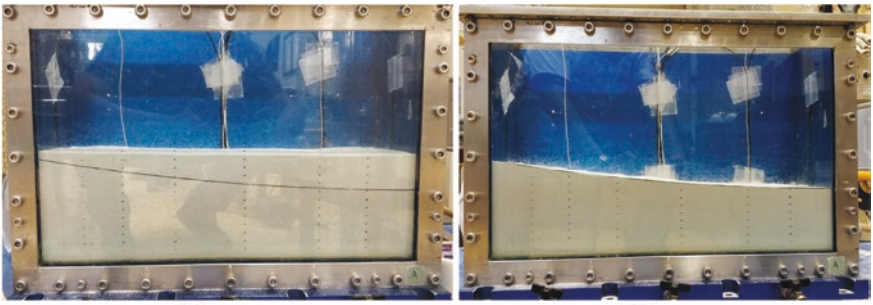

Fig. 10.2 Model KyU_A_A1_1. (**a**) Before curving the surface. (**b**) After curving the surface. (Vargas et al., 2021)

gravity field, the surface was curved according to the geometry of the facility (i.e., a circumference with 2.50 m radius), so all points in the surface would have the same slope relative to the gravity field and may represent ground with a constant, 5° slope angle in the prototype scale (Tobita et al., 2018). The procedure for curving the surface was described by Vargas et al. (2020). Figure 10.2 shows Model KyU_A_A1_1, before and after curving the surface.

10.2.3 Saturation Process

After curving the surface, the rigid container containing the model was placed in a vacuum chamber. Initially, vacuum pressure of around −0.1 MPa was applied to facilitate the dissolution of gas bubbles, and CO_2 was gradually flooded until reaching atmospheric pressure values. Vacuum pressure was then reapplied and maintained until the end of the saturation process.

Following the vacuum application, the sample was saturated from the top, using a de-aired solution of de-ionized water and methylcellulose (SM-100, Shin-Etsu Chemical Co., Ltd.); the mixing rate was iteratively adjusted to achieve the target viscosity determined by the scaling laws.

Since the viscosity experiences significant variations along with changes in temperature, the amount of methylcellulose was properly adjusted to achieve the

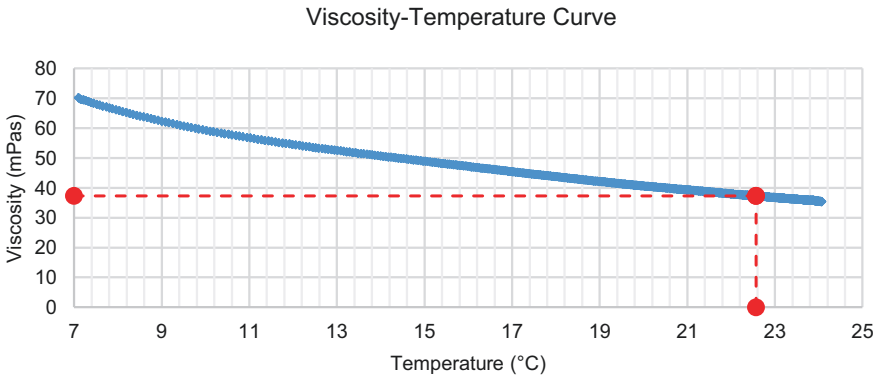

Fig. 10.3 Viscosity-temperature curve – Model KyU_A_B2_1

required viscosity at temperatures closer to the ones expected in the test. Figure 10.3 shows the viscosity-temperature curve for Model KyU_A_B2_1, measured using a "tuning fork vibration viscometer" (Izumo, 2006).

After depositing the viscous mixture, the applied vacuum was gradually removed until achieving the atmospheric pressure.

The degree of saturation of the model was estimated using Okamura's method (Okamura & Inoue, 2012), which relates the degree of saturation with small variations of the water surface caused by pressure changes. In specific, a piece of polystyrene was placed floating over the model's "water" surface (methylcellulose solution), and "small" amounts of vacuum (−0.02 ~ −0.03 MPa) were induced in the vacuum chamber. The vacuum-induced variations in the "water" surface height were measured using laser sensors, assuming that the variations of the floating polystyrene's height correspond to variations of the "water" surface.

After confirming that the saturation of the model was higher than 99%, the model was transported by means of a crane from the vacuum chamber to a scale, to confirm the actual weight prior to testing. Figure 10.4 shows the model after the saturation process.

10.2.4 Model Testing

The testing procedure included a shake sequence of three "destructive" input motions, and each motion consists of a ramped sinusoidal 1 Hz wave (as seen in Fig. 10.5).

Due to the presence of high-frequency vibrations in the achieved motions, and taking into account that higher-frequency components have some but relatively small effect on the behavior of the model, this project (as a first approximation) used the effective PGA (Kutter et al., 2020b).

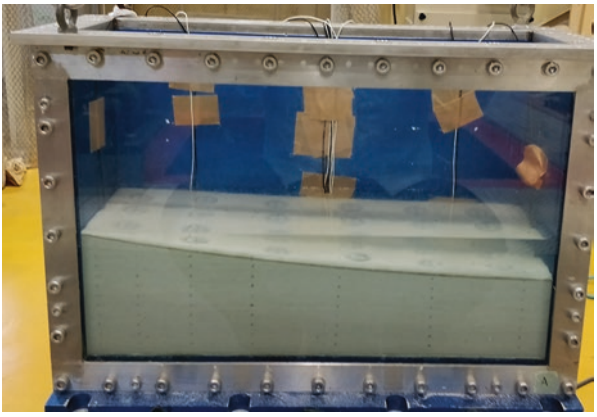

Fig. 10.4 Model after saturation

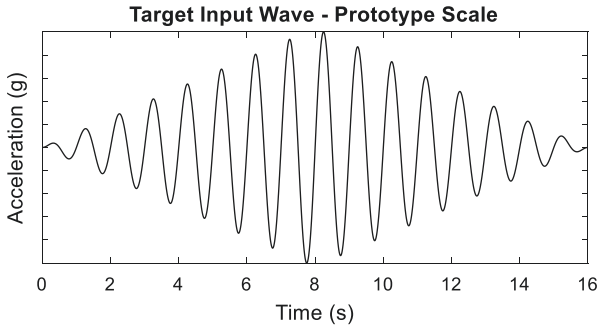

Fig. 10.5 Specified ramped sine wave. (Vargas et al., 2021)

$$\mathrm{PGA}_{\mathrm{effective}} = \mathrm{PGA}_{\mathrm{1Hz}} + 0.5^{*}\,\mathrm{PGA}_{\mathrm{hf}}$$

where "$\mathrm{PGA}_{\mathrm{1Hz}}$" represents the PGA of the 1 Hz component of the achieved motion and "$\mathrm{PGA}_{\mathrm{hf}}$" represents the higher-frequency components of the ground motion.

10.2.5 Cone Penetration Tests (CPTs) and Measurement of Surface Displacement

As a parameter to better estimate the density and ground uniformity, cone penetration tests (CPTs) were performed in each experiment; for each experiment, three CPTs were developed, one before each destructive motion, with a new 6 mm

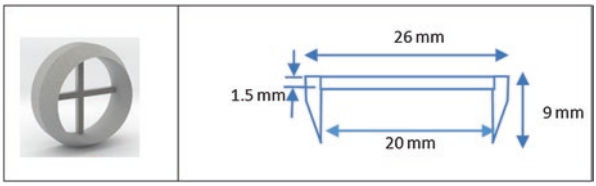

Fig. 10.6 Geometry of surface markers

mini-CPT (Carey et al., 2018); this method, although providing an indirect measurement (i.e., tip resistance "q_c"), has proven to be reliable in the estimation of the uniformity of the ground and its associated dry density (Kutter et al., 2020b). Due to the characteristics of the CPT apparatus, it was not possible to induce shaking while the apparatus was mounted; consequently, each time the CPT was performed, the centrifuge had to (1) be stopped to assemble the CPT, (2) increase the required g-level to perform the test, (3) stop again the facility to disassemble the CPT, and (4) increase the g-level for the shaking process.

Regarding the measurements of the displacements of the ground surface, the centrifuge was equipped with a high-speed camera (Nac Image Technology, Inc.; MEMRECAM fx RX-6G), which allowed the estimation (by means of image analysis) of the time history values of the relative displacement of the 3-D printed surface markers placed on the ground surface (see Fig. 10.6).

10.3 Test Results (Prototype Scale)

10.3.1 Achieved Input Motions

To estimate the $PGA_{effective}$, the PGA_{1Hz} values were calculated using a notched band-pass filter with corner frequencies between 0.9 and 1.1 times the predominant frequency. Table 10.4 shows the estimated values of PGA, PGA_{1Hz}, and PGA_{eff} of the first destructive motion.

As shown in Table 10.4, the achieved PGA_{eff} values were consistently maintained within each group's tests (i.e., 0.25*g* for Group 1 and 0.12*g* for Group 2). To achieve this, the shaking table was calibrated before each test.

Figures 10.7 and 10.8 show a comparison between the target motion and the achieved input Motion 1 for each model.

Table 10.4 Target and estimated PGA_{eff} values – prototype scale

Model	Motion	Target value	Achieved value			
		PGA_{eff}	PGA	PGA_{1Hz}	PGA_{hf}	PGA_{eff}
KyU_A_A1_1	1	0.25	0.304	0.191	0.113	0.248
KyU_A_B1_1	1	0.25	0.312	0.192	0.12	0.252
KyU_A_B1_2	1	0.25	0.307	0.189	0.118	0.248
KyU_A_A2_1	1	0.12	0.134	0.101	0.033	0.118
KyU_A_B2_1	1	0.12	0.163	0.089	0.074	0.126

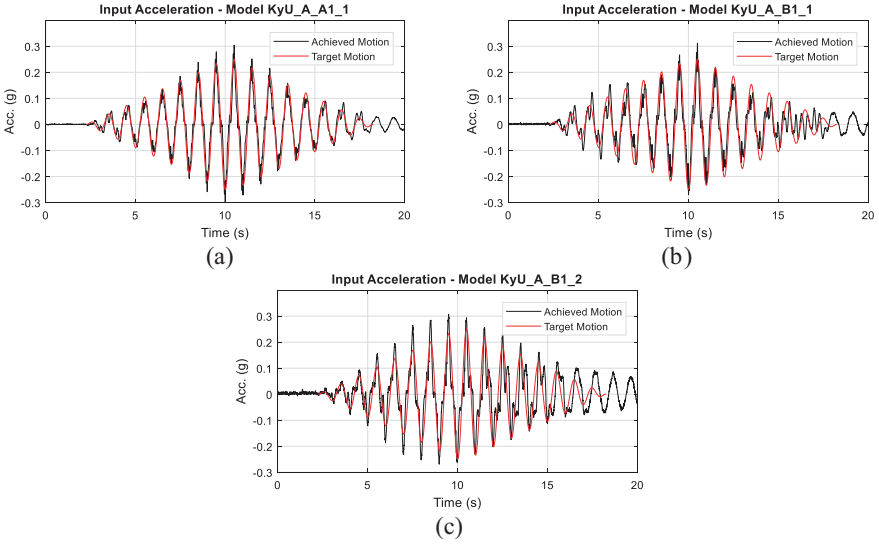

Fig. 10.7 Comparison among achieved and target input motions for Group 1 models

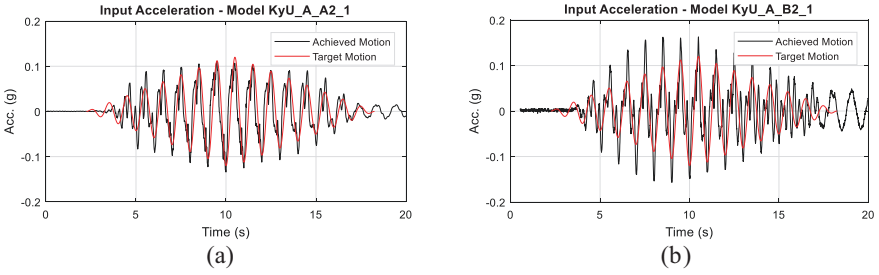

Fig. 10.8 Comparison among achieved and target input motions for Group 2 models

10.3.2 Excess Pore Water

Nine excess pore water pressure transducers (EPWPT) were installed inside the ground to estimate the excess pore water pressure (Δu). The Δu values of the first destructive motion for all sensors and the excess pore water pressure ratio (r_u) for the sensors located in the central array are shown in Figs. 10.9 and 10.10, respectively.

Figure 10.9 shows that small variations in Δu values (and thus in r_u max values) were observed among the models in Group 1. These variations were found to be associated with the achieved PGA values ($PGA_{KyU\_A\_A1\_1} < PGA_{KyU\_A\_B1\_2} < PGA_{KyU\_A\_B1\_1}$). Despite the differences and variations, the models in Group 1 exhibited similar excess pore water pressure behavior even when different scaling laws (i.e., conventional scaling laws and generalized scaling laws) are used to represent the same prototype scale.

Regarding Group 2 models, as seen in Fig. 10.10, important differences among models were found; nevertheless, as with Group 1 models, this difference was found to be correlated with the achieved PGA values. It is worth noting that, for "small" PGA levels at a "low" gravity level, a significant increase in the high-frequency components of the input acceleration (expressed as a percentage of the PGA value) was observed. This resulted in significant differences in the PGA value, even though

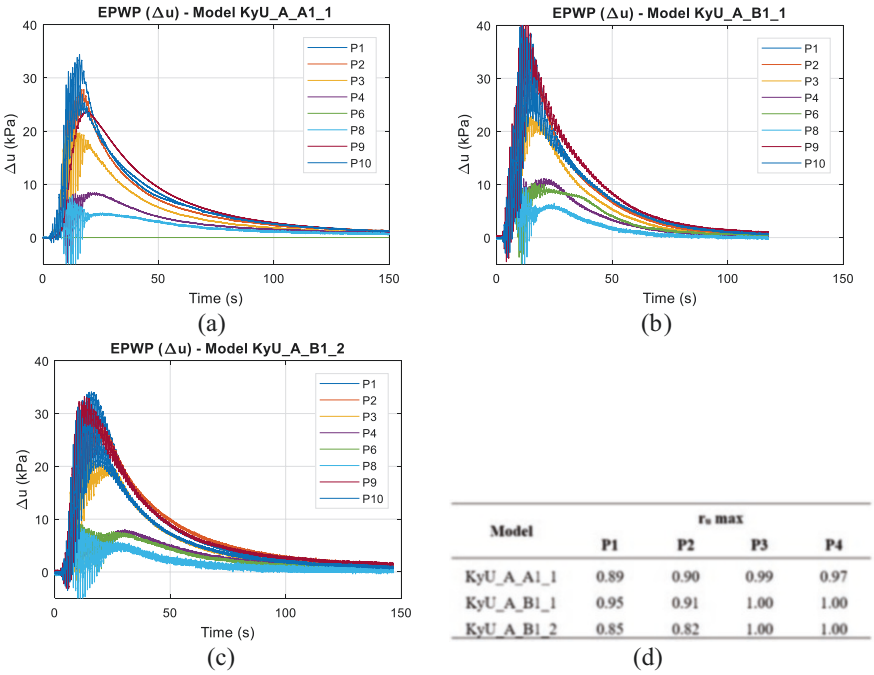

Model	r_u max			
	P1	P2	P3	P4
KyU_A_A1_1	0.89	0.90	0.99	0.97
KyU_A_B1_1	0.95	0.91	1.00	1.00
KyU_A_B1_2	0.85	0.82	1.00	1.00

Fig. 10.9 (**a**) Excess pore water pressure – Model KyU_A_A1_1. (**b**) Excess pore water pressure – Model KyU_A_B1_1. (**c**) Excess pore water pressure – Model KyU_A_B1_2. (**d**) r_u max for sensors located in the central array – Group 1. (Vargas et al., 2021)

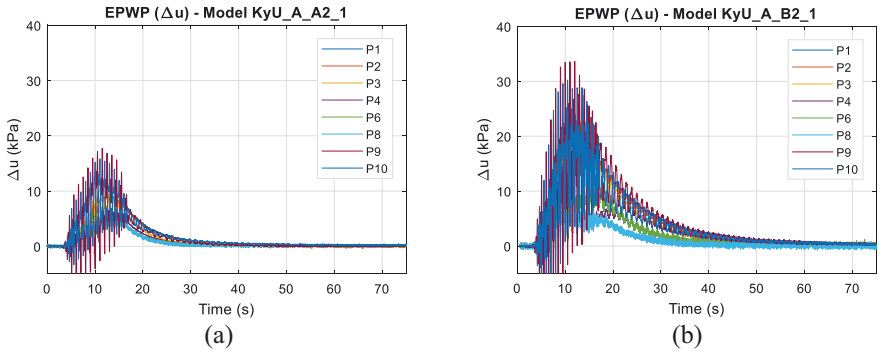

Model	r_u max			
	P1	P2	P3	P4
KyU_A_A2_1	0.26	0.31	0.47	0.50
KyU_A_B2_1	0.63	0.77	0.90	0.90

(c)

Fig. 10.10 (**a**) Excess pore water pressure – Model KyU_A_A2_1. (**b**) Excess pore water pressure – Model KyU_A_B2_1. (**c**) r_u max for sensors located in the central array – Group 2. (Vargas et al., 2021)

the PGA_{eff} values were intended to be kept almost constant. Thus, for "large" values of high-frequency content, PGA_{eff} (as previously defined) may not be an appropriate parameter to represent the demand, and further research is needed to clarify this point.

10.3.3 Ground Motion Accelerations

Figures 10.11 and 10.12 show the response time histories for all accelerometers located inside the deposit for the first destructive motion. As shown in these figures, no significant amplification or distortion of the motion is recorded prior to the development of significant EPWP. However, after significant EPWP development, the motion considerably changed, developing sharp spikes, which are typical characteristics of the dilative behavior of liquefied sand. It is noteworthy that the distortion in the acceleration starts in the shallow zones of the deposit and becomes more pronounced as the r_u value increases more rapidly in these regions.

Figure 10.11 shows that all Group 1 models exhibited similar response acceleration behaviors, both before and after the distortion caused by significant EPWP development. Although some slight differences may be noticeable, as in the case of EPWP values (Sect. 10.3.2), these were found to be correlated with the achieved PGA values. Therefore, it can be concluded that Group 1 models, including those using either conventional scaling laws (KyU_A_A1_1) or generalized scaling laws (KyU_A_B1_1 and KyU_A_B1_2), show comparable behaviors in terms of ground response acceleration.

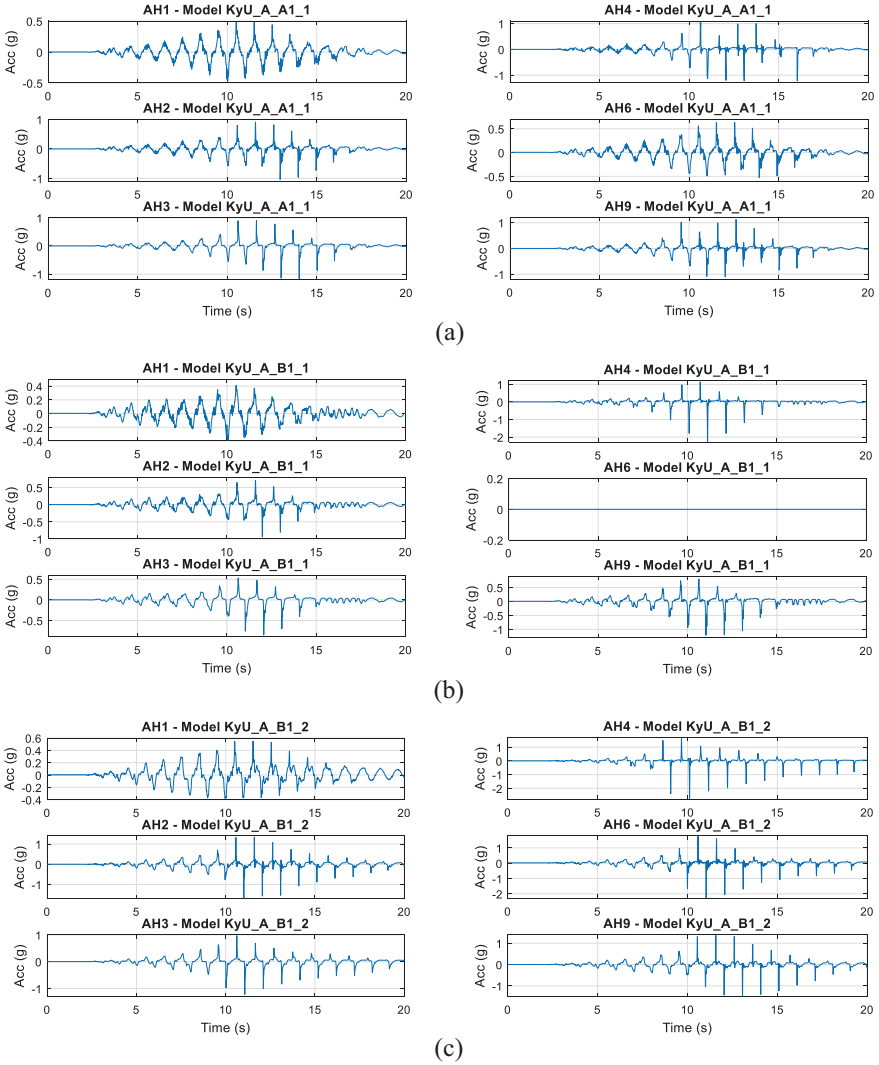

Fig. 10.11 (**a**) Ground motion accelerations for Model KyU_A_A1_1. (**b**) Ground motion accelerations for Model KyU_A_B1_1. (**c**) Ground motion accelerations for Model KyU_A_B1_2. (Vargas et al., 2021)

Regarding Group 2 models, Fig. 10.12 shows that only sensor AH4 exhibited significant distortions in the ground response acceleration, which is consistent with the EPWP values reported in Fig. 10.10. Despite the differences in PGA values, the ground response acceleration behavior appears to be reasonably similar between the two Group 2 models (KyU_A_A2_1 and KyU_A_B2_1).

Also, it is worth noting that, as mentioned in the previous section, Model KyU_A_B2_1 exhibited a significant increase in high-frequency components for

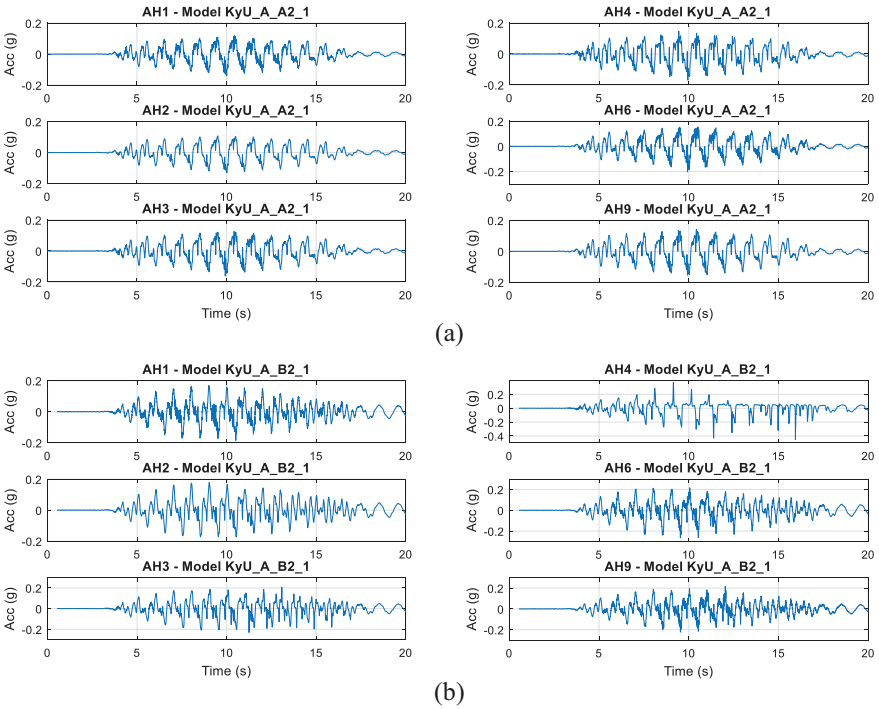

Fig. 10.12 (**a**) Ground motion accelerations for Model KyU_A_A2_1. (**b**) Ground motion accelerations for Model KyU_A_B2_1. (Vargas et al., 2021)

"small" PGA levels at a "low" gravity level; and, in addition to the increment of the high-frequency components, additional cycles of vibration (from t = 18.5 s) were recorded.

10.3.4 Cone Penetration Tests

As specified, in-flight cone penetration tests "CPTs" (Carey et al., 2018) were carried out prior to each destructive motion. Specifically, CPT1, CPT2, and CPT3 were conducted before Motions 1, 2, and 3, respectively.

Kutter et al. (2020b) found that the tip resistance at the mid-depth (i.e., at 2.0 m) is well correlated with the initial relative density of the ground, so this parameter ($qc_{2.0}$ at CPT1) can be used for comparisons among the tests.

Figures 10.13 and 10.14 show the CPT results for Group 1 and Group 2 models, respectively. The uniformity of the ground was confirmed by the absence of abrupt changes in any of the profiles. Regarding the $qc_{2.0}$ value at CPT1, a good agreement was found for tests with $\mu \leq 2$, suggesting that further experiments are needed to determine the suitability of the generalized scaling laws for $\mu > 2$.

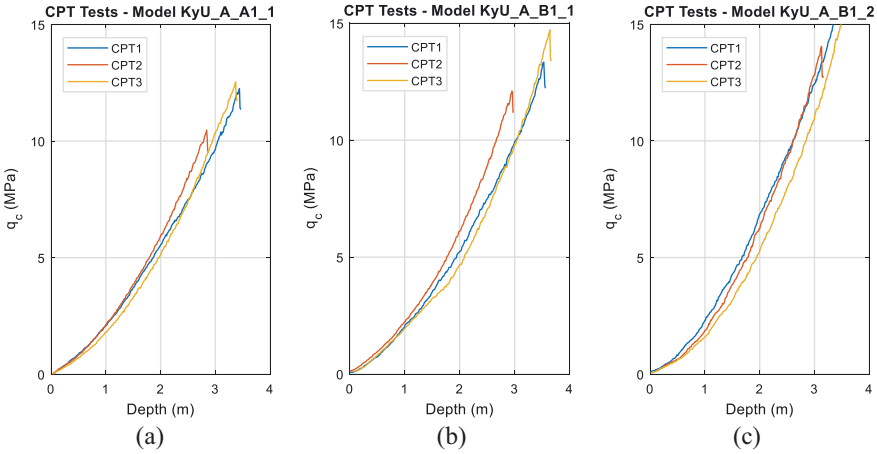

Fig. 10.13 (**a**) CPT for Model KyU_A_A1_1. (**b**) CPT for Model KyU_A_B1_1. (**c**) CPT for Model KyU_A_B1_2. (Vargas et al., 2021)

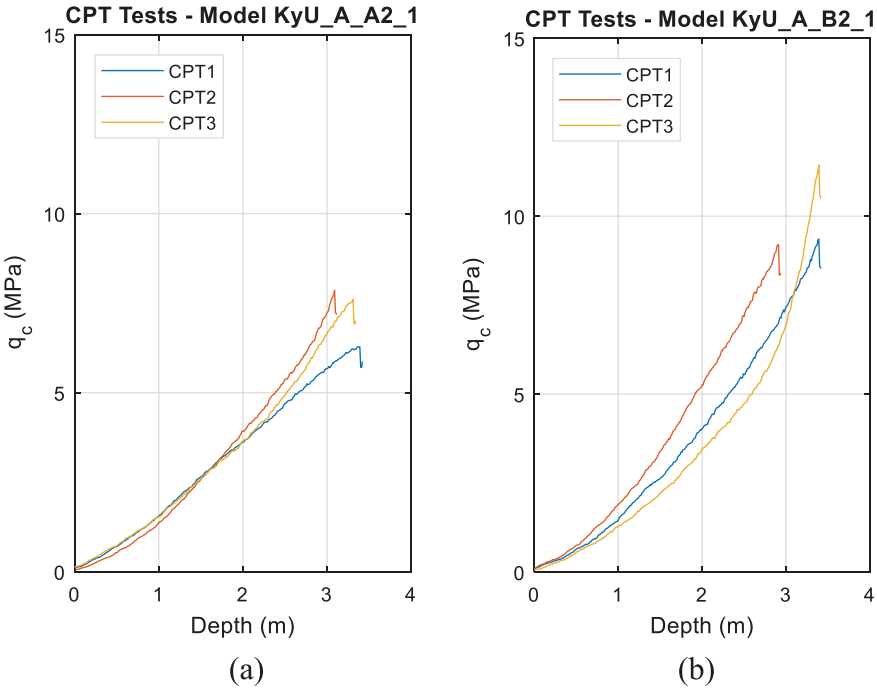

Fig. 10.14 (**a**) CPT for Model KyU_A_A2_1. (**b**) CPT for Model KyU_A_B2_1. (Vargas et al., 2021)

As for the re-liquefaction process, despite that the global relative density of the model increased after each liquefaction process, no clear trend of increase nor decrease was observed in the qc value recorded before and after each process (i.e., comparison between CPT1–CPT2 and CPT2–CPT3); so, for subsequent processes of liquefaction, additional parameters (such as strain history, induced anisotropy, changes in fabric, etc.) need to be taken into account for the determination of the relative density.

10.3.5 Surface Displacements

As part of the previous exercise (LEAP-UCD-2017), Kutter et al. (2020b) stated that the use of high-speed cameras for measuring lateral displacements of ground surface during lateral spreading proved to be particularly valuable. In this regard, as discussed in Sect. 10.2.4, a high-speed camera was installed in the centrifuge to capture the behavior of the ground surface during and after the motion. An image analysis procedure was employed using the commercial software DIPP-Motion V to obtain the surface displacement based on the recorded images. It is worth noting that the deformation of some markers could not be tracked due to light reflection issues.

Figure 10.15 shows that the displacements of Group 1 models follow a similar trend to that found in the EPWP and the ground response acceleration

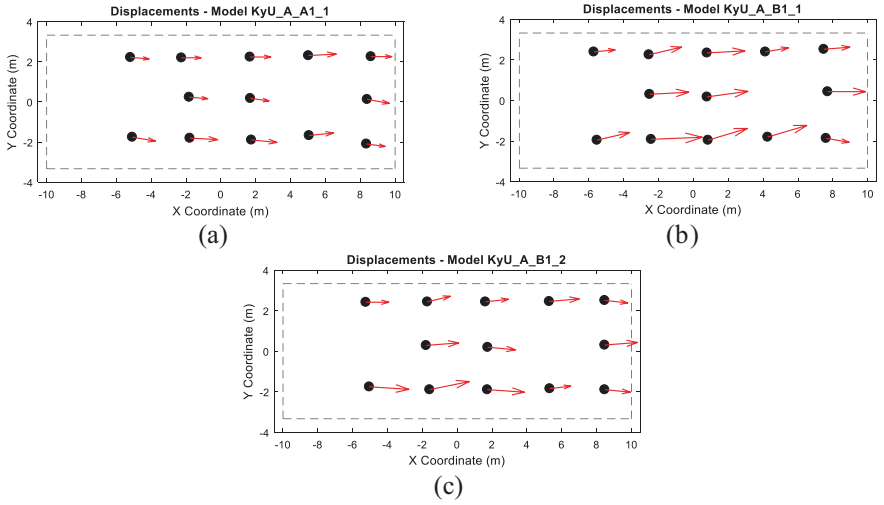

Fig. 10.15 (**a**) Surface ground displacements – Model KyU_A_A1_1. (**b**) Surface ground displacements – Model KyU_A_B1_1. (**c**) Surface ground displacements – Model KyU_A_B1_2 (magnification of deformation – 15 times). (Vargas et al., 2021)

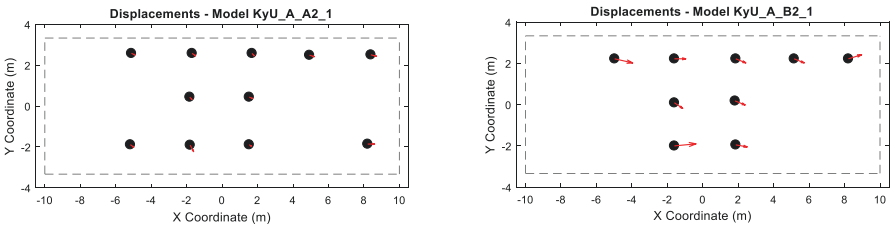

Fig. 10.16 (**a**) Surface ground displacements – Model KyU_A_A2_1. (**b**) Surface ground displacements – Model KyU_A_B2_1 (magnification of deformation – 15 times)

measurements; the small differences among the tests can be correlated with the achieved PGA values.

In contrast, Fig. 10.16 shows significant differences between the measured displacements of the Group 2 models. As described in Sect. 10.3.3, the differences can be explained by the fact that significant differences in the input motion (an increase in high-frequency components and additional vibration cycles) are recorded, resulting in an increased seismic demand in Model KyU_A_B2_1.

10.4 Conclusions

LEAP (Liquefaction Experiments and Analysis Projects) is a joint exercise that pursues the verification, validation, and uncertainty quantification of numerical liquefaction models. "LEAP-ASIA-2019" is one of the LEAP's exercises, whose main objectives are to validate the "generalized scaling law" for lateral spreading and to fill the gaps of experiments to complete the dataset obtained as part of the "LEAP-UCD-2017."

This paper presents the centrifuge tests developed in the geotechnical centrifuge of the Disaster Prevention Research Institute (DPRI) at Kyoto University, for "LEAP-ASIA-2019."

- Five models were tested under different centrifugal accelerations, keeping the same geometry in prototype scale (by changing the scaling laws); for comparison purposes, tests were divided into two groups. For Group 1 ($D_r \approx 75\%$ and $PGA_{eff} \approx 0.25g$), three models were developed at $44.4g$, $22.2g$, and $11.1g$; as for Group 2 ($D_r \approx 55\%$ and $PGA_{eff} \approx 0.12g$), two models were developed at $44.4g$ and $22.2g$.
- Image analysis was used to estimate the ground displacements as a result of each experiment; the final displacements were estimated by image analysis.
- The applicability of the generalized scaling law (for $\mu \leq 4$) was confirmed for generation of EPWP, ground motion response acceleration, and surface ground displacement.

- As for the CPTs, the applicability of the generalized scaling law was confirmed for $\mu \leq 2$ values.
- It has been found that for "large" values of high-frequency contents, the PGA_{eff} (as defined in the LEAP-UCD-2017 exercise) does not seem to be a suitable parameter to represent the seismic demand.
- As for the re-liquefaction process, no clear trend of increase nor decrease was observed in the q_c value recorded before and after each process; so, for the estimation of the relative density in grounds with prior history of liquefaction events, additional parameters need to be taken into account.

References

Carey, T., Gavras, A., Kutter, B., Haigh, S. K., Madabhushi, S. P. G., Okamura, M., Kim, D. S., Ueda, K., Hung, W. Y., Zhou, Y. G., Liu, K., Chen, Y. M., Zeghal, M., Abdoun, T., Escoffier, S., & Manzari, M. (2018). A new shared miniature cone penetrometer for centrifuge testing. In *In 9th international conference on physical modelling in Geotechnics, ICPMG 2018* (pp. 293–298). CRC Press/Balkema.

Carey, T. J., Stone, N., & Kutter, B. L. (2020). Grain size analysis and maximum and minimum dry density testing of Ottawa F-65 sand for LEAP-UCD-2017. In *Model tests and numerical simulations of liquefaction and lateral spreading: LEAP-UCD-2017* (pp. 31–44). Springer.

Iai, S., Tobita, T., & Nakahara, T. (2005). Generalised scaling relations for dynamic centrifuge tests. *Geotechnique, 55*(5), 355–362.

Izumo, N. (2006). Physical quantity measured by a vibration viscometer. *Proceedings of the 23rd sensing forum, Tsukuba*, pp. 149–152.

Kutter, B. L., Carey, T. J., Hashimoto, T., Zeghal, M., Abdoun, T., Kokkali, P., Madabhushi, G., Haigh, S. K., Burali d'Arezzo, F., Madabhushi, S., Hung, W. Y., Lee, C. J., Cheng, H. C., Iai, S., Tobita, T., Ashino, T., Ren, J., Zhou, Y. G., Chen, Y. M., Sun, Z. B., & Manzari, M. T. (2018a). LEAP-GWU-2015 experiment specifications, results, and comparisons. *Soil Dynamics and Earthquake Engineering, 113*, 616–628.

Kutter, B. L., Carey, T. J., Zheng, B. L., Gavras, A., Stone, N., Zeghal, M., Abdoun, T., Korre, E., Manzari, M., Madabhushi, G. S. P., Haigh, S., Madabhushi, S. S. C., Okamura, M., Sjafuddin, A. N., Escoffier, S., Kim, D. S., Kim, S. N., Ha, J. G., Tobita, T., Yatsugi, H., Ueda, K., Vargas, R. R., Hung, W. Y., Liao, T. W., Zhou, Y. G., & Liu, K. (2018b). Twenty-four centrifuge tests to quantify sensitivity of lateral spreading to Dr and PGA. In *Geotechnical earthquake engineering and soil dynamics V: Slope stability and landslides, laboratory testing, and in situ testing* (pp. 383–393). American Society of Civil Engineers.

Kutter, B. L., Carey, T. J., Stone, N., Bonab, M. H., Manzari, M. T., Zeghal, M., Escoffier, S., Haigh, S., Madabhushi, G., Hung, W., Kim, D., Kim, N., Okamura, M., Tobita, T., Ueda, K., & Zhou, Y. G. (2020a). LEAP-UCD-2017 v. 1.01 model specifications. In *Model tests and numerical simulations of liquefaction and lateral spreading: LEAP-UCD-2017* (pp. 3–29). Springer.

Kutter, B. L., Carey, T. J., Stone, N., Zheng, B. L., Gavras, A., Manzari, M. T., Zeghal, M., Abdoun, T., Korre, E., Escoffier, S., Haigh, S., Madabhushi, G., Madabhushi, S., Hung, W., Liao, T., Kim, D. S., Kim, S. N., Ha, J. G., Kim, N. R., Okamura, M., Sjafuddin, A. N., Tobita, T., Ueda, K., Vargas, R., Zhou, Y. G., & Liu, K. (2020b). LEAP-UCD-2017 comparison of centrifuge test results. In *Model tests and numerical simulations of liquefaction and lateral spreading: LEAP-UCD-2017* (pp. 69–103). Springer.

Okamura, M., & Inoue, T. (2012). Preparation of fully saturated models for liquefaction study. *International Journal of Physical Modelling in Geotechnics, 12*(1), 39–46.

Tobita, T., Ashino, T., Ren, J., & Iai, S. (2018). Kyoto University LEAP-GWU-2015 tests and the importance of curving the ground surface in centrifuge modelling. *Soil Dynamics and Earthquake Engineering, 113*, 650–662.

Tobita, T., Ichii, K., Ueda, K., Uzuoka, R., Vargas, R., Okamura, M., Sjafruddin, A. N., Takemura, J., Hang, L., Iai, S., Boksmati, J., Fusco, A., Torres-Garcia, S., Haigh, S., Madabhushi, G., Manzari, M., Escoffier, S., Li, Z., Kim, D. S., Manandhar, S., Hung, W. Y., Huang, J. X., Pham, T. N. P., Zeghal, M., Abdoun, T., Korre, E., Kutter, B. L., Carey, T. J., Stone, N., Zhuo, Y. G., Liu, K., & Ma, Q. (2023). LEAP-ASIA-2019: Summary of centrifuge experiments on liquefaction-induced lateral spreading: Validation and applicability of the generalized scaling law. In *Model tests and numerical simulations of liquefaction and lateral spreading 2: LEAP-ASIA-2019*. Springer.

Vargas, R. R., Tobita, T., Ueda, K., & Yatsugi, H. (2020). LEAP-UCD-2017 centrifuge test at Kyoto University. In *Model tests and numerical simulations of liquefaction and lateral spreading: LEAP-UCD-2017* (pp. 341–360). Springer.

Vargas, R. R., Ueda, K., & Tobita, T. (2021). Centrifuge modeling of the dynamic response of a sloping ground–LEAP-UCD-2017 and LEAP-ASIA-2019 tests at Kyoto University. *Soil Dynamics and Earthquake Engineering, 140*, 106472.

Chapter 11
LEAP-ASIA-2019 Centrifuge Test at NCU

Jun-Xue Huang and Wen-Yi Hung

Abstract Two centrifuge tests are performed at NCU under centrifugal acceleration field of 26*g* and 13*g* to validate the generalized scaling law for LEAP-ASIA-2019. The model arrangement and test process follow the specification of LEAP-UCD-2017. Both models are subjected one destructive motion which is 0.18*g*, 1 Hz, 16 cycles, tapered sine wave. Test results indicate the model adopted generalized scaling law with virtual 1*g* modeling factor of 2 can generally simulated the same prototype of the model only adopted centrifuge scaling law. The acceleration response, pore water pressure behavior, and cone tip resistance of both models are in good agreement with each other.

Keywords Liquefaction Experiments and Analysis Project (LEAP-ASIA-2019) · Generalized scaling law (GSL) · Centrifuge modelling

11.1 Introduction

Liquefaction Experiments and Analysis Projects (LEAP) is a series of collaborative research projects, and LEAP aims to produce reliable experimental data for assessment, calibration, and validation of constitutive models and numerical modeling techniques (Kutter et al., 2020a). In LEAP-UCD-2017, 9 different centrifuge facilities conducted 24 separate model tests to obtain the meaningful assessment of the sensitivity and variability of the tests (Kutter et al., 2020b).

For LEAP-ASIA-2019, NCU conducted two centrifuge modeling tests to validate the generalized scaling law. The acceleration response, excess pore water pressure behavior, displacement behavior, and cone tip resistance of model A and model B are compared and discussed in this paper. In addition, the shear velocity and predominate frequency of soil deposit determined by pre-shaking technique and the deposit profile movement tracked by spaghettis are presented.

J.-X. Huang (✉) · W.-Y. Hung
Department of Civil Engineering, National Central University, Taoyuan, Taiwan

T. Tobita et al. (eds.), *Model Tests and Numerical Simulations of Liquefaction and Lateral Spreading II*, https://doi.org/10.1007/978-3-031-48821-4_11

11.2 Test Equipment and Material

NCU geotechnical centrifuge has nominal radius of 3 m. The one-dimensional shaker was equipped on the basket of centrifuge. The maximum payload of shaker is 400 kg under maximum centrifugal acceleration field of 80*g*. The shaker can provide a motion with frequency range from 0 to 250 Hz. The container used for LEAP-ASIA-2019 is a rigid box composed by aluminum alloy plates with inner dimensions of 767 mm (L) × 355 mm (W) × 400 (H). The detail information could refer to Hung et al. (2022).

Ottawa sand F65 shipped from UC Davis is used to make the dry sand bed for LEAP-ASIA-2019. The value recommended by Carey et al. (2020) of minimum dry density and maximum dry density is 1490.5 kg/m^3 and 1757.0 kg/m^3, respectively. Ottawa sand F65 is classified as poorly graded sand in Unified Soil Classification System. The detail information regarding to the physical and mechanical properties of Ottawa sand F65 were presented by Carey et al. (2020) and El Ghoraiby et al. (2020).

11.3 Description of the Experiments

Two tests for LEAP-ASIA-2019 were conducted at National Central University (NCU) and the testing conditions are listed at Table 11.1. The dimensions of model are 767 mm (L) × 355 mm (W) × 153.8 mm (H) with 1643 kg/m^3 (model A) and 1626 kg/m^3 (model B) of dry unit weight by using Ottawa F-65 sand. A 5-degree slope and curvature ground surface are the same as the models of LEAP-UCD-2017. The centrifuge modeling factor, η, are 26 and 13; and the virtual 1*g* modeling scaling factor, μ, are 1 and 2 for model A and B, respectively. Therefore, models A and B were carried out under 26*g* and 13*g* acceleration field. Based on the generalized scaling law provided by Iai et al. (2005), the scaling factors of physical quantities adopted in NCU tests are listed in Table 11.2.

During spinning, total 3 shaking events were applied including 1 destructive and 2 nondestructive motions. The destructive 16-cycle tapered sine wave was 1 Hz frequency and target effective peak base acceleration (PBA_{eff}) of about 0.1*g*. Before and after destructive motion, two nondestructive motions with 3 Hz frequency and 0.04*g* amplitude of 1-cycle sine wave were input to detect the shear velocity and predominant frequency of soil strata. The characteristics of shaking events are listed

Table 11.1 Conditions of models

Test no.	Scaling factor		Achieved density (kg/m^3)	PBA (g)	PBA_{eff} (g)	PBA_{1Hz} (g)
	Centrifuge, η	Virtual 1*g*, μ				
Model A	26	1	1643	0.180	0.141	0.108
Model B	13	2	1628	0.164	0.126	0.096

Table 11.2 Scaling factors adopted for NCU models

Physical quantity	Generalized scaling factor	Model A	Model B
Length	$\mu\eta$	26	26
Density	1	1	1
Time	$\mu^{0.75}\eta$	26	21.8
Frequency	$\mu^{-0.75}/\eta$	1/26	1/21.8
Acceleration	$1/\eta$	1/26	1/13
Velocity	$\mu^{0.75}$	1	1.68
Displacement	$\mu^{1.5}\eta$	26	36.8
Stress	μ	1	2
Strain	$\mu^{0.5}$	1	1.41
Stiffness	$\mu^{0.5}$	1	1.41
Permeability	$\mu^{0.75}\eta$	26	21.8
Pore pressure	μ	1	2

Table 11.3 Characteristics of three shaking events

Event no.	Frequency (Hz)	PBA (model A / model B)	Cycle	Type
s1	3	0.036*g*/0.045*g*	1	Pre-shaking (nondestructive) Rectangular sine wave
s2	1	0.180*g*/0.164*g*	16	Main shaking (destructive) Tapered sine wave
s3	3	0.035*g*/0.046*g*	1	Pre-shaking (nondestructive) Rectangular sine wave

in Table 11.3. The achieved PBA_{eff} of destructive motions are 0.141*g* and 0.126*g* for models A and B, respectively.

The models were prepared and following the test procedure of LEAP-UCD-2017, the test flow chart is shown in Fig. 11.1 (Kutter et al., 2020a). The sand bed was made by air-pluviation method with a constant drop height of 500 mm and flow rate of 2.5 kg/min. The accelerometers and pore pressure transducers were installed at a specific location during pluviating. The 5° slope and curved surface were formed by using a vacuum and a specific curved acrylic scraper after air-pluviation completed. Eighteen PVC surface markers were then placed and 12 sticks of spaghetti were penetrated vertically into soil strata at the certain locations. The side view and top view of model A and model B before test are shown in Figs. 11.2 and 11.3, respectively.

Pure CO_2 was filled from the bottom of the container for 1.5 h with air flow rate of 0.25 kg/cm^2 to replace the air in the container before saturation. The methylcellulose solution with specific viscosity was dropped on the sponge putting on the slope surface to saturate model with a flow rate of 1 kg/h under stable vacuum pressure. The degree of saturation was measured by Okamura method and it should be higher than 99.5%. Then the location and elevation of markers were measured by using digital vernier caliper.

NCU centrifuge was spinning from 1*g* to certain g-level (26*g* for model A and 13*g* for model B), and the tests were carried out by the sequence described below;

Fig. 11.1 The procedure of LEAP tests at National Central University. (**a**) Top view of dry model; (**b**) Curved surface; (**c**) Side view of dry model; (**d**) Side view of saturated model; (**e**) Top view of saturated model

(1) the first shaking event, a nondestructive motion, was inputted; (2) the first CPT test was implemented; (3) second shaking event, a destructive motion, was input; (4) the second CPT test was implemented; (5) the third shaking event, a nondestructive motion, was input. After testing, the centrifuge was stopped to measure the final location and elevation of makers and cut the soil profile to observe deformation behavior of spaghetti and the position of pore pressure transducers at the middle array. The soil profiles of model A and model B after test are shown in Figs. 11.4 and 11.5, respectively. In addition, the detail information regarding to air-pluviation, saturation, and in-flight cone penetration test were presented by Hung and Liao (2020).

Finally, the achieved PBA_{eff} of destructive motions are 0.112 and 0.104*g* in model A and B, respectively.

11.4 Comparison Between Model A and Model B

The positions of sensors and the direction of positive acceleration are shown in Fig. 11.6. The positive acceleration is toward upslope direction, conversely, the negative acceleration is toward downslope direction. This is the definition of the

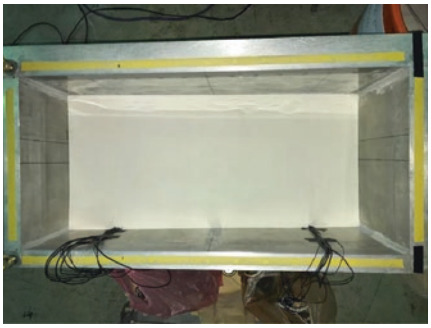

(a) Top view of dry model

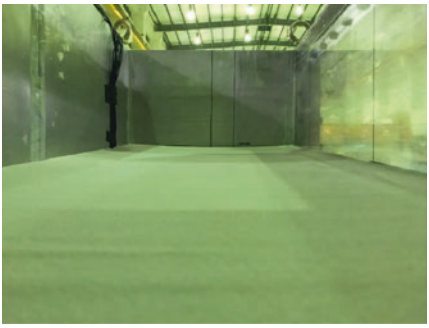

(b) Curved surface

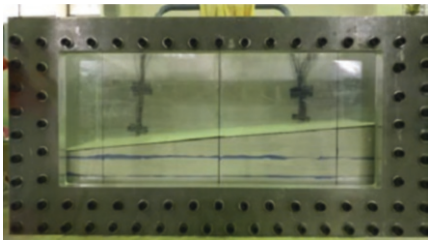

(c) Side view of dry model

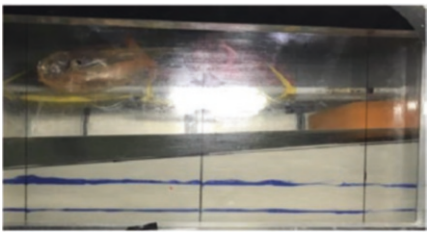

(d) Side view of saturated model

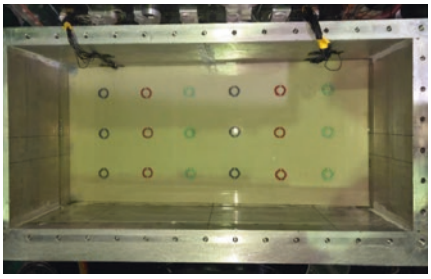

(e) Top view of saturated model

Fig. 11.2 Model A photos before test. (**a**) Side view; (**b**) Side view before profile cutting; (**c**) Profile cutting for spaghettis; (**d**) Profile cutting for middle array pore pressure transducers

direction of results in this paper, and all of the results in this paper are presented in prototype scale.

11.4.1 Acceleration Response

Figure 11.7 is the acceleration time histories of destructive motion 1 in model A and model B. The acceleration is expressed in prototype scale by taking scaling factor of 1/26 ($\eta = 26$) in model A and 1/13 ($\eta = 13$) in model B. The time histories indicate that the acceleration response of both models is very consistent; however, there is a slightly different of spike signal amplitude obtained by the accelerometers at the surface layer.

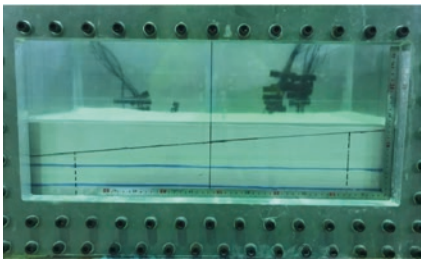

(a) Side view of dry model

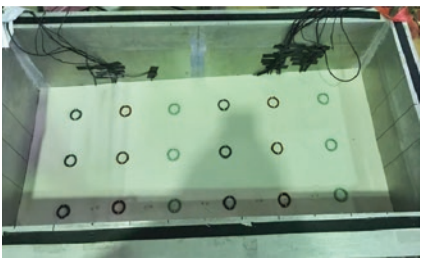

(b) Top view of dry model

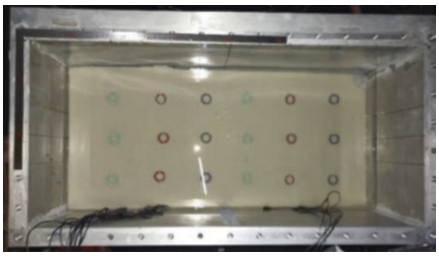

(c) Top view of saturated model

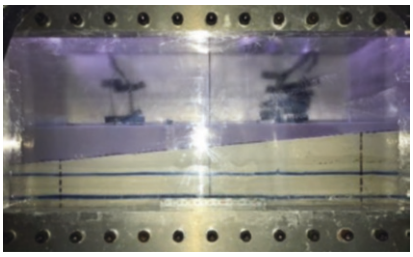

(d) Side view of saturated model

Fig. 11.3 Model B profile before test. (**a**) Side view before profile cutting; (**b**) Profile cutting for spaghetti; (**c**) Profile cutting for middle array pore pressure transducers

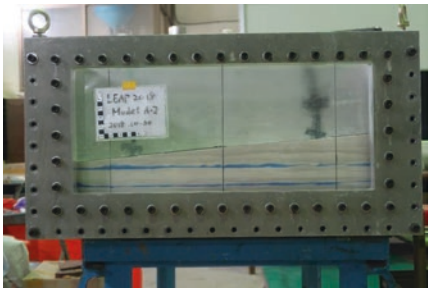

(a) Side view

(b) Side view before profile cutting

(c) Profile cutting for spaghettis

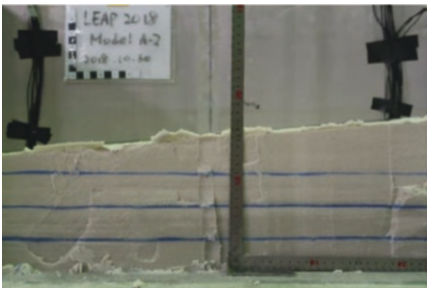

(d) Profile cutting for middle array pore pressure transducers

Fig. 11.4 Model A photos after test. (**a**) Side view of dry model; (**b**) Top view of dry model; (**c**) Top view of saturated model; (**d**) Side view of saturated model

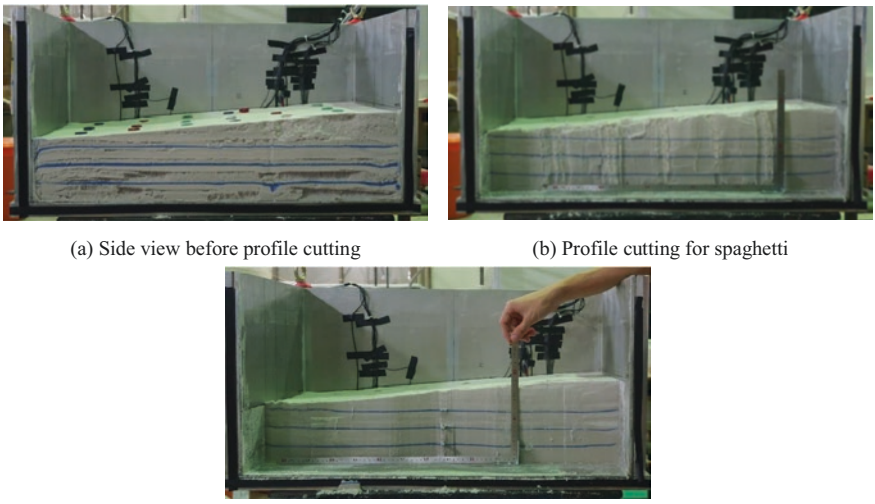

(a) Side view before profile cutting

(b) Profile cutting for spaghetti

(c) Profile cutting for middle array pore pressure transducers

Fig. 11.5 Model B photos after test

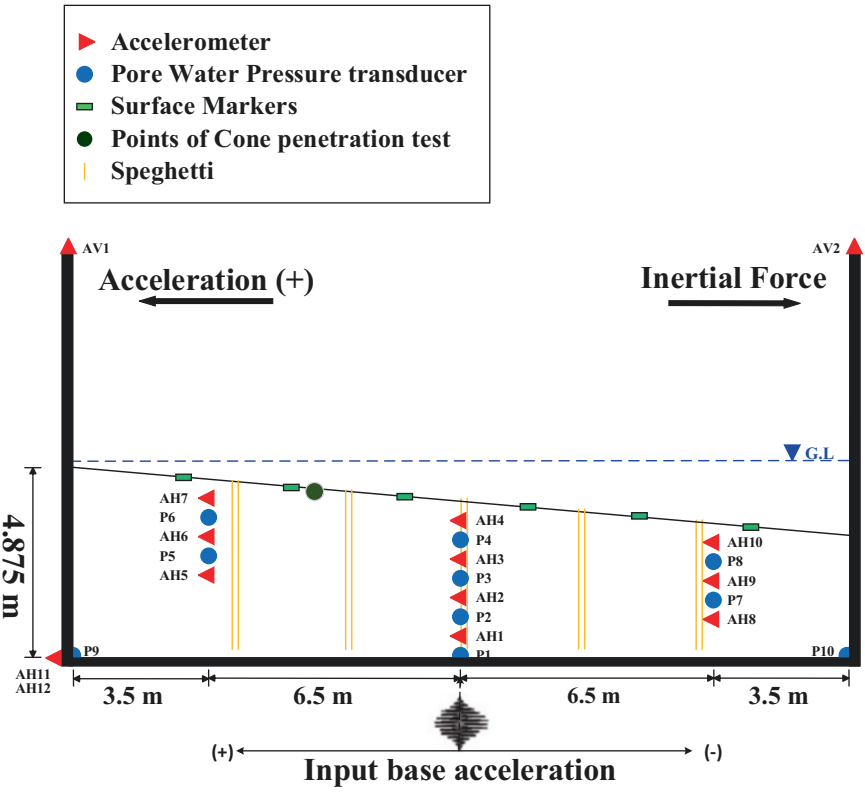

Fig. 11.6 Model arrangement and direction definition of NCU models

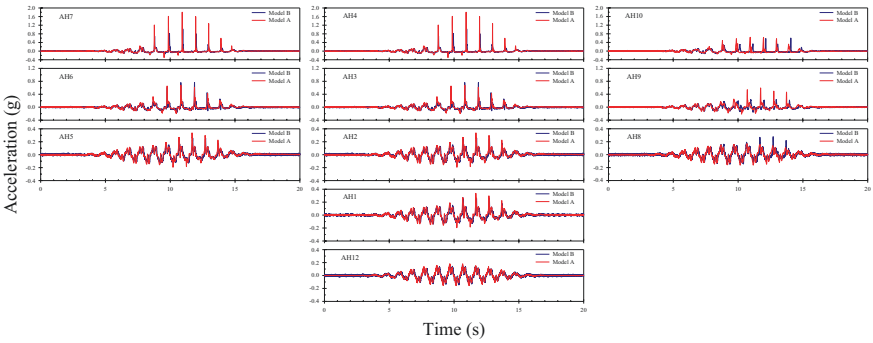

Fig. 11.7 Acceleration time histories of main shaking (s2)

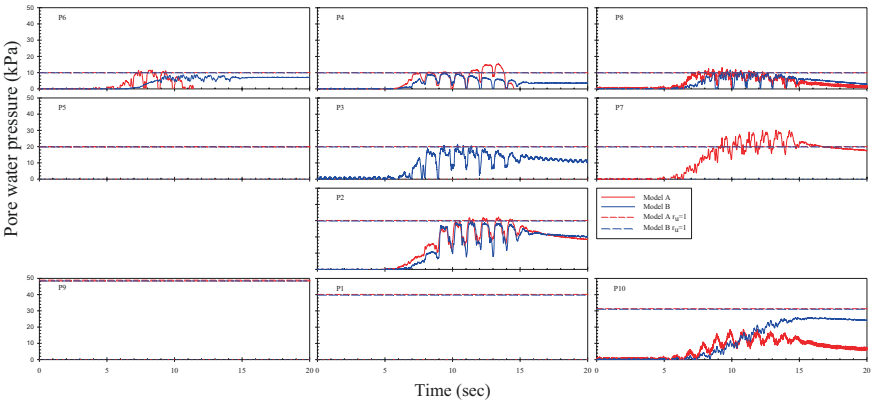

Fig. 11.8 Excess pore water pressure time histories (20 s) of main shaking (s2)

11.4.2 EPWP Behavior

Figure 11.8 shows the excess pore water pressure exceeding behavior during destructive motion 1 in model A and model B. The EPWP is expressed in prototype scale by taking scaling factor of 1 ($\mu = 1$) in model A and 2 ($\mu = 2$) in model B. The result shows that both of the magnitude and exceeding behavior are very consistent at P2, P4 and P8. Figure 11.9 shows the EPWP dissipation behavior. We could observe that the dissipation time is slightly different at P2 due to the effect of viscosity of saturation fluid.

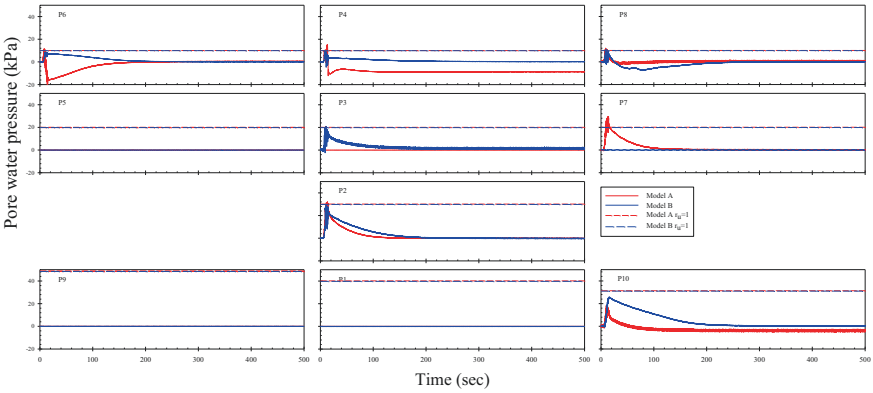

Fig. 11.9 Excess pore water pressure time histories (500 s) of main shaking (s2)

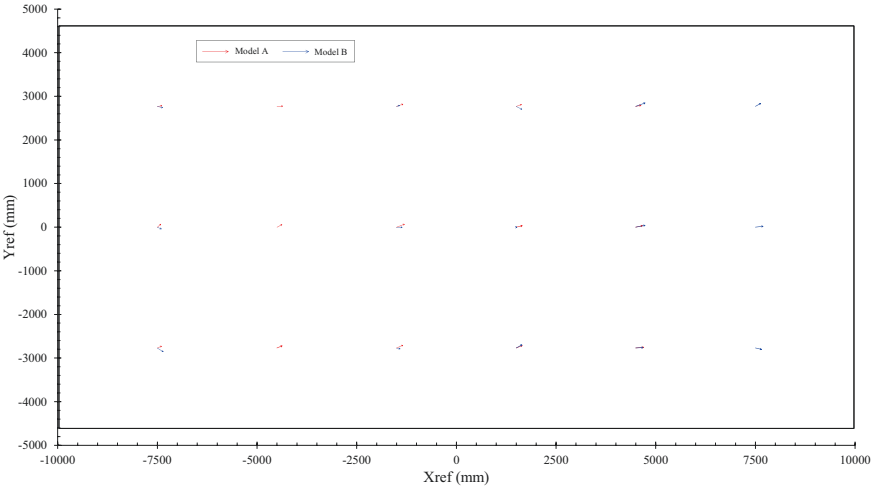

Fig. 11.10 Displacement of surface markers

11.4.3 Surface Displacement

The surface displacement and settlement are expressed in prototype scale by taking scaling factor of 26 ($\mu^{1.5}\eta = 1^{1.5} \times 26$) in model A and 36.77 ($\mu^{1.5}\eta = 2^{1.5} \times 13$) in model B. Figure 11.10 shows the displacement vector of each marker. The maximum displacement happens at middle slope in model A but at downslope in model B. There is lower consistency of surface displacement behavior, both of magnitude and direction, between each model. Figures 11.11 and 11.12 show the settlement of markers. The maximum settlement happens at number 1 marker location (upslope), and maximum upheave induced by accumulation of upslope soil happens at number 6 maker location (downslope) in both models. However, the magnitude and the trend at middle slope are not consistent between each model.

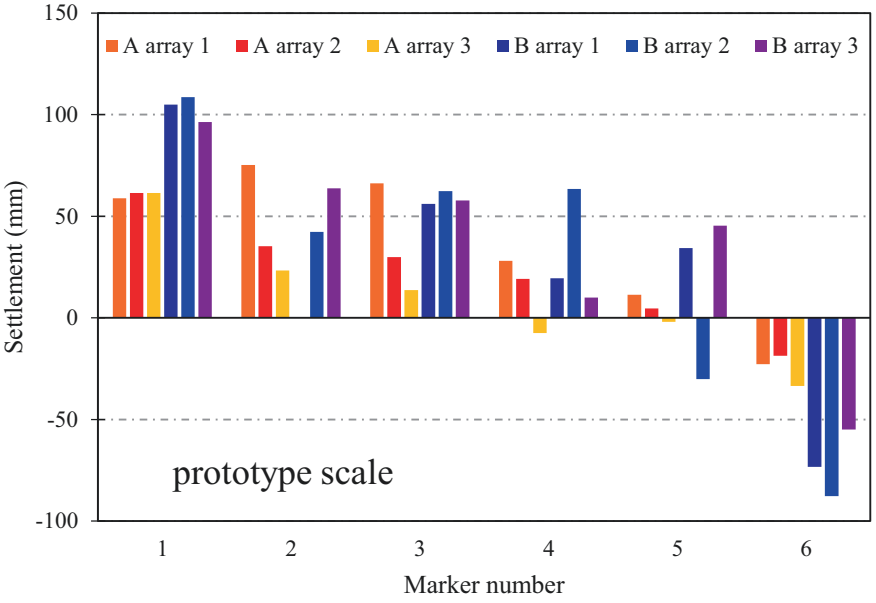

Fig. 11.11 Settlement of all markers

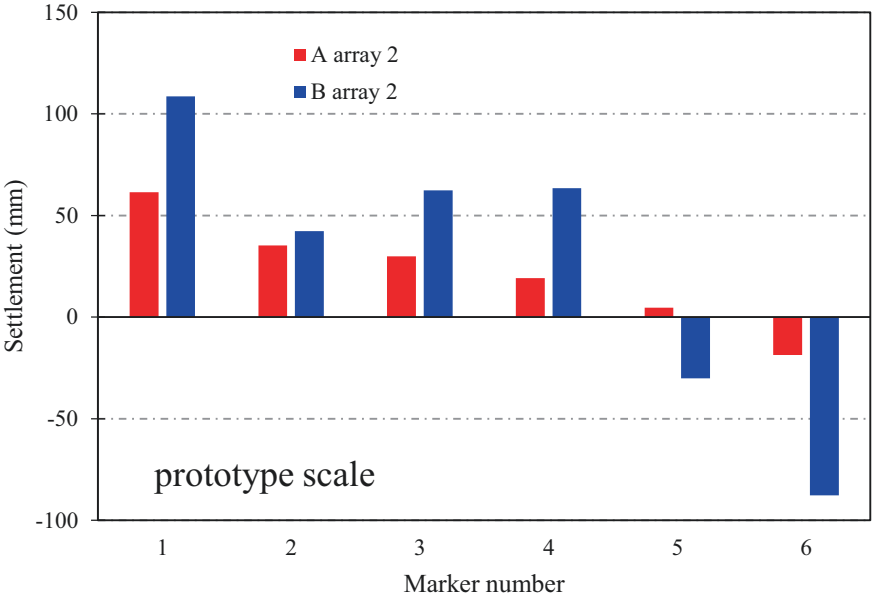

Fig. 11.12 Settlement of array 2 markers

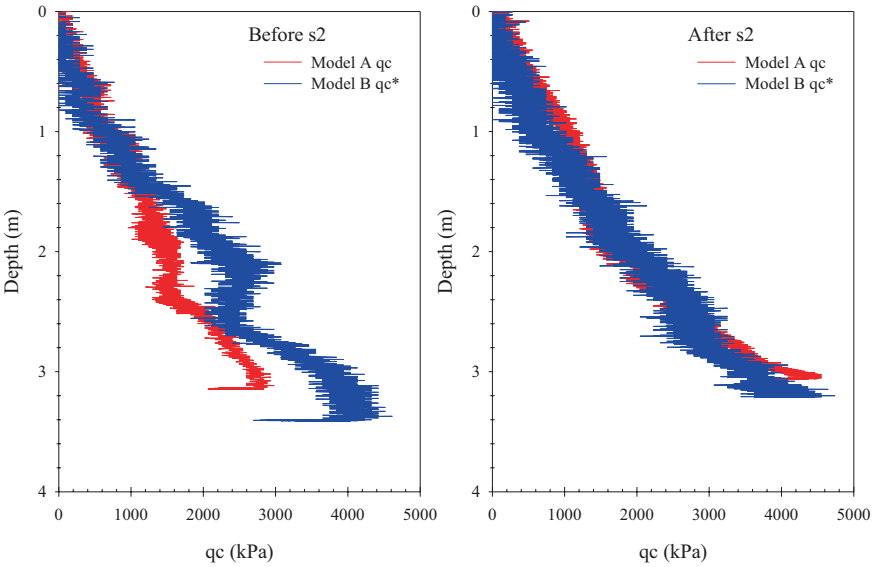

Fig. 11.13 Cone tip resistance (q_c) distribution along the depth

11.4.4 Cone Tip Resistance

The distribution of q_c along the depth is plotted at Fig. 11.13. The q_c is expressed in prototype scale by taking scaling factor of 1 ($\mu = 1$) in model A and 2 ($\mu = 2$) in model B. The value after destructive motion 1 is very consistent between model A and model B. Before destructive motion 1, the value is very consistent at depth 0–1.5 m, but the value is different at depth over 1.5 m. The difference of q_c may be influenced by the speed of penetration. The speed of penetration is not constant because the penetration force applied to CPT is applied by manually adjusting air pressure to cylinder.

11.4.5 Discussion on GSL

In general, the prototype of model B which the 1g virtual scaling factor (μ) is 2 can modeling the prototype of model A. The results of acceleration response, excess pore water pressure behavior, and cone tip resistance between model A and model B are in good agreement with each other. However, the results of acceleration response and surface displacement behavior indicate the consistency of surface soil behavior is low. Therefore, more experiments are needed to validate GSL.

11.4.6 LEAP-UCD-2017 vs. LEAP-ASIA-2019

Figures 11.14 and 11.15 are the acceleration and EPWP time histories of NCU models in LEAP-UCD-2017 (Hung & Liao, 2020). The density of models and the PBA of input motions are different with NCU models in LEAP-ASIA-2019. The density of models is 1651, 1653, and 1653 kg/cm^3 corresponding to NCU 1, NCU 2, and NCU 3 in LEAP-USD-2017. The achieved PBA of motion is 0.265, 0.221, and 0.185g corresponding to NCU 1-m1, NCU 2-m1, and NCU 3-m3. Although density and PBA of models in LEAP-UCD-2017 are denser and larger than models in LEAP-ASIA-2019, the trend of results in both projects is similar.

11.5 Pre-shaking Analysis and Spaghetti Deformation

11.5.1 Shear Velocity

Pre-shaking technique provided by Lee et al. (2012) is used to detect the shear velocity and predominant frequency of soil strata by inputting a non-destructive motion. In both model A and model B, a 3 Hz, PBA = 0.04g, 1 cycle sine wave non-destructive motion was input before and after test. The amplitude and duration of motion are small and short enough so that it would only exceed little or even no excess pore water pressure. Figures 11.16 and 11.17 show the acceleration time histories of both model in s1 and s3.

$$v_s = \frac{L}{\Delta t} \tag{11.1}$$

where v_s = shear velocity (m/s), L = distance (m), Δt = time difference (s).

Shear velocity of soil strata is determined by Formula (11.1). The arrival time of wave is got from each accelerometer time history; afterward, the difference arrival time between each accelerometer can be determined. Moreover, the distance between each accelerometer is given. The shear velocity of soil strata is finally figured out. The results are shown in Fig. 11.18. The average shear velocity is averaged out the shear velocity of 3 arrays. In model A case, the average shear velocity is 367 and 520 m/s before and after destructive motion (s2), respectively. In model B case, the average shear velocity is 296 and 340 m/s before and after destructive motion (s2), respectively. The shear velocity of soil strata is related to the density of soil strata. Denser soil has larger shear velocity, and the density of model A is larger than the density of model B. In addition, the density of soil strata after destructive motion (s2) is supposed to be larger than the density of soil strata before destructive motion (s2). Therefore, the results are reasonable.

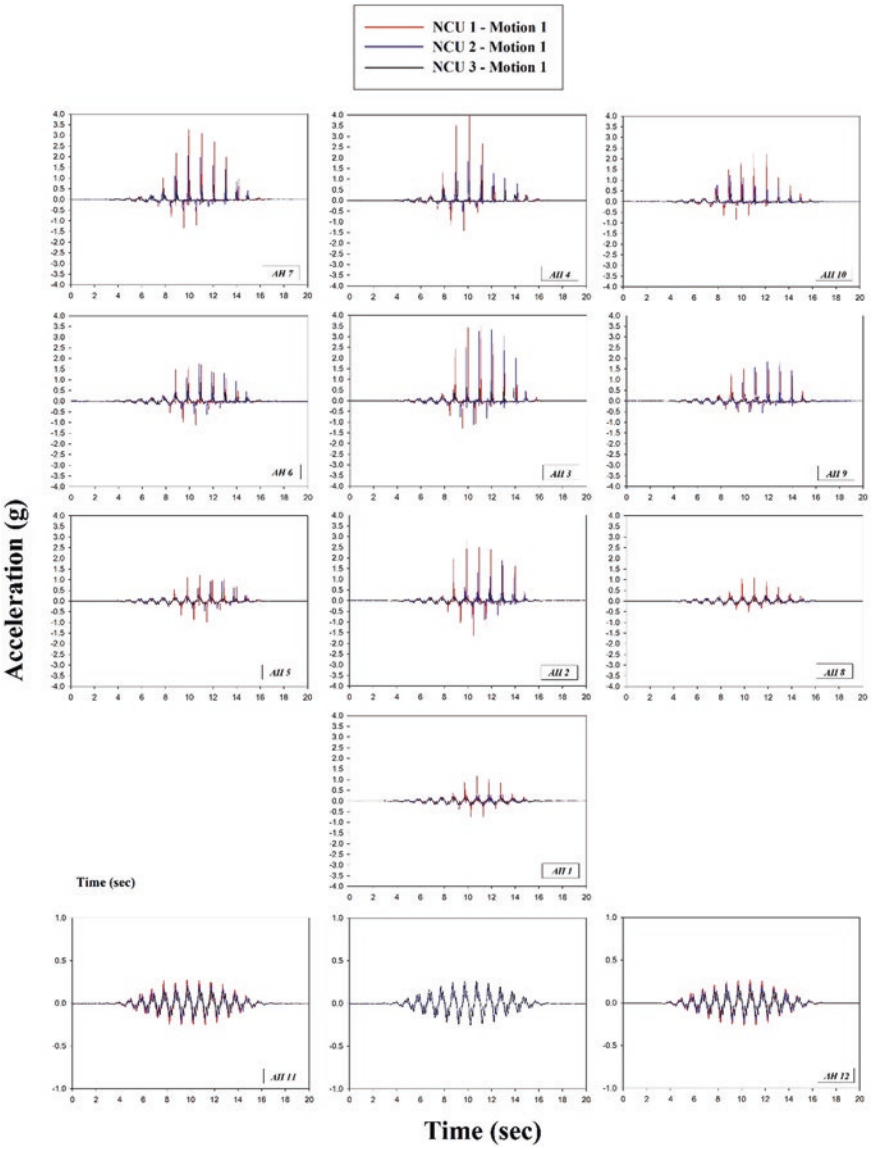

Fig. 11.14 The time histories of acceleration for NCU1-m1, NCU2-m1 and NCU3-m1 in LEAP-UCD-2017

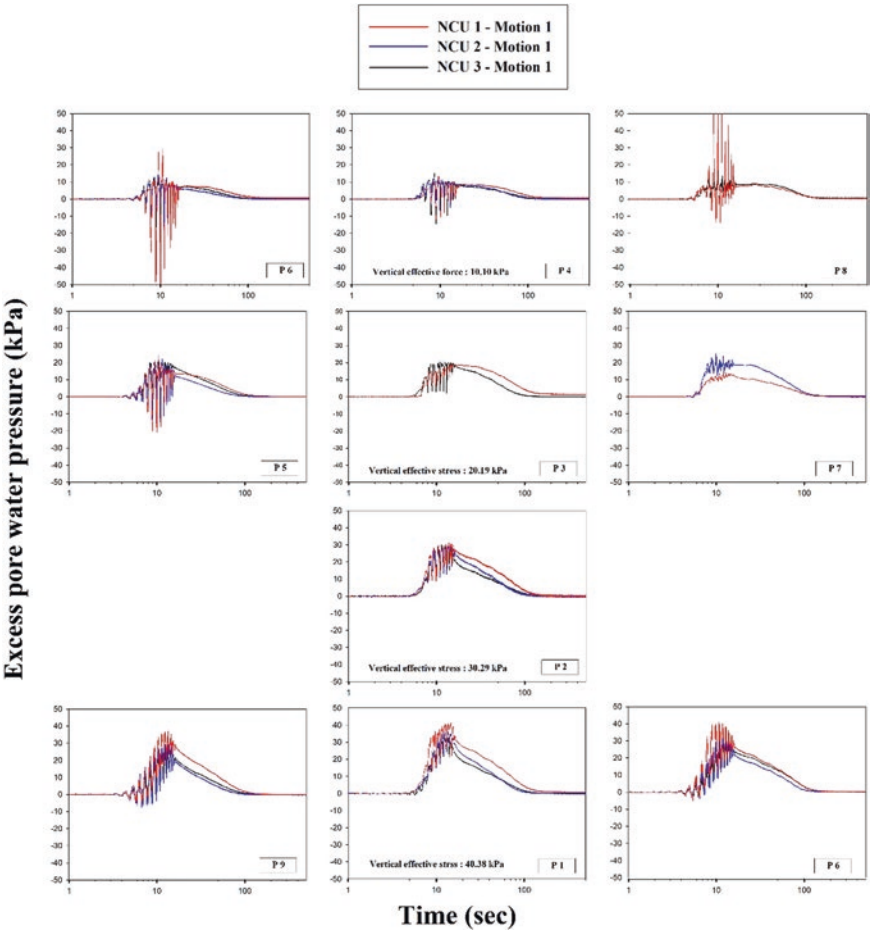

Fig. 11.15 The time histories of pore water pressure for NCU1-m1, NCU2-m1, and NCU3-m1 in LEAP-UCD-2017

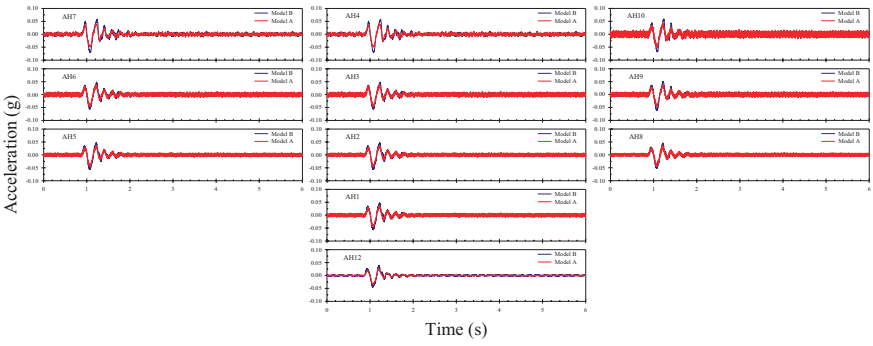

Fig. 11.16 Acceleration time histories of s1 (pre-shaking before main shaking)

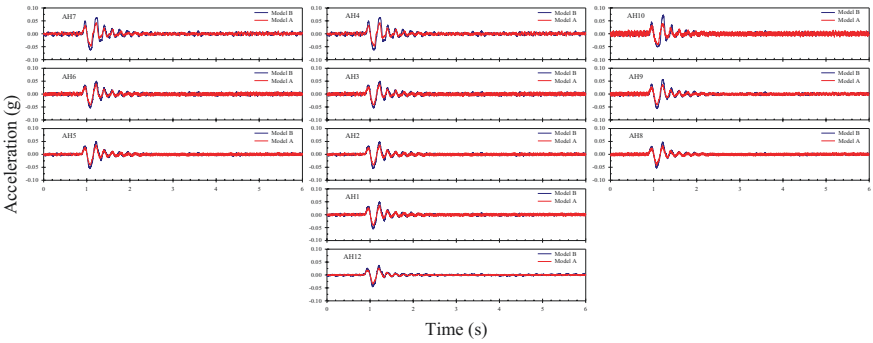

Fig. 11.17 Acceleration time histories of s3 (pre-shaking after main shaking)

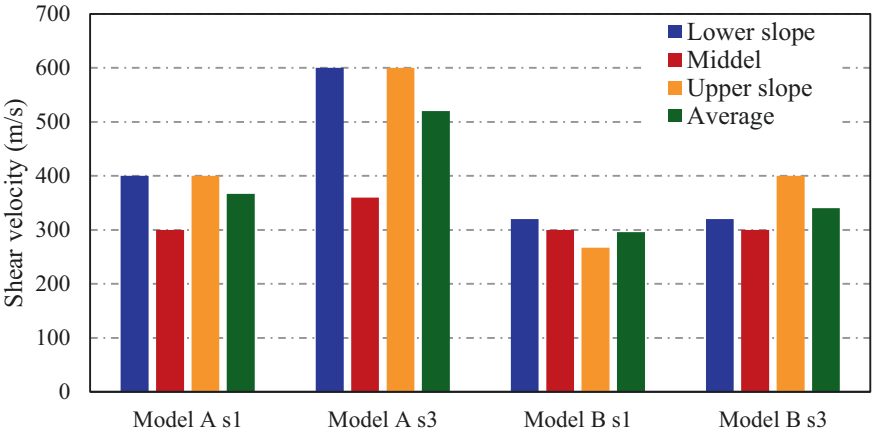

Fig. 11.18 Shear velocity of soil strata before and after main shaking

11.5.2 Predominant Frequency

Transform the free vibration signal of pre-shaking acceleration time histories to frequency domain from time domain via fast Fourier transform. Figure 11.19 shows the Fourier spectra of acceleration time histories in s1 and s3. From Fourier spectra, the predominant frequency of soil strata in model A is 5.25 Hz and in model B is 5.5 Hz. In addition, the frequency of free vibration can be estimated from acceleration time histories. The estimated frequency of free vibration is approximately at the range of 5–6 Hz.

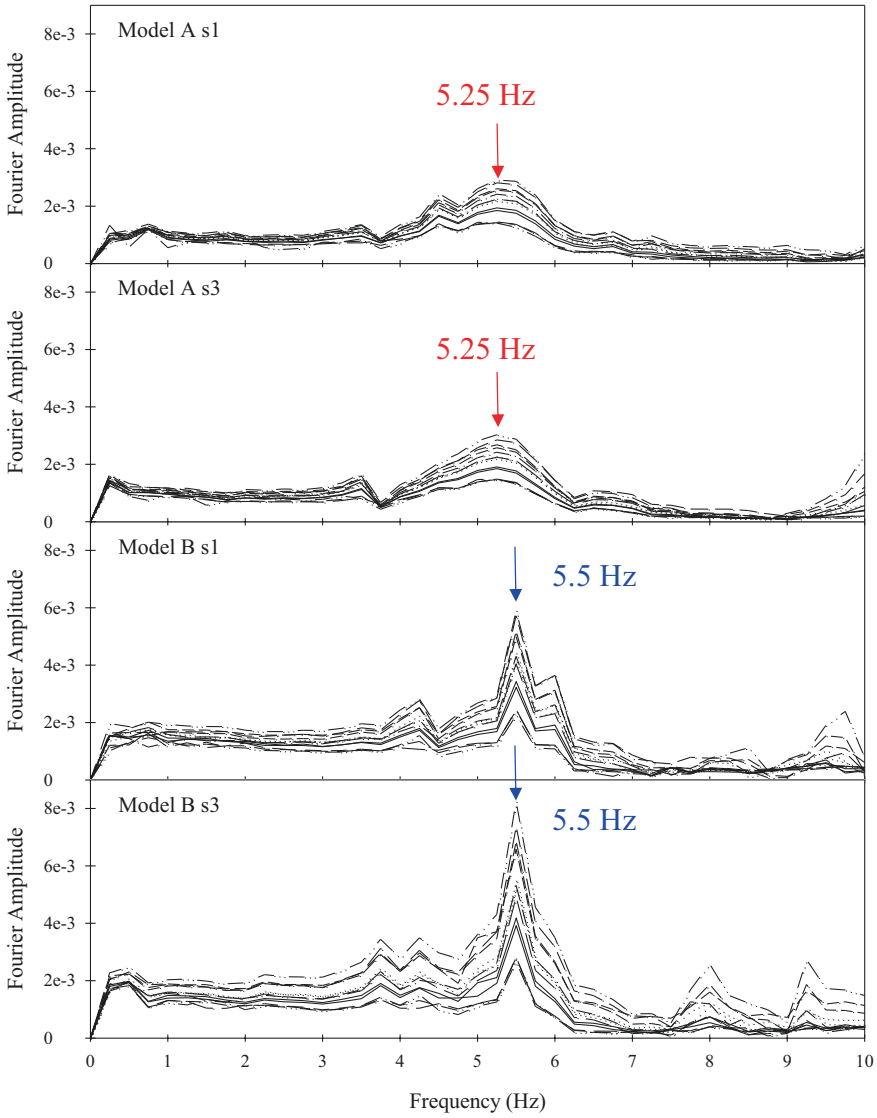

Fig. 11.19 Fourier spectra of acceleration time histories in s1 and s3

11.5.3 Spaghetti Deformation

The spaghettis were penetrated into soil strata during model preparation. The spaghettis were supposed to deform with the soil strata; therefore, the deformation behavior of soil strata can be estimated by the displacement of spaghetti. The soil strata profile is got by cutting model after test. The horizontal displacement of spaghetti along the depth (Fig. 11.20) is determined via image digitalized tool from the

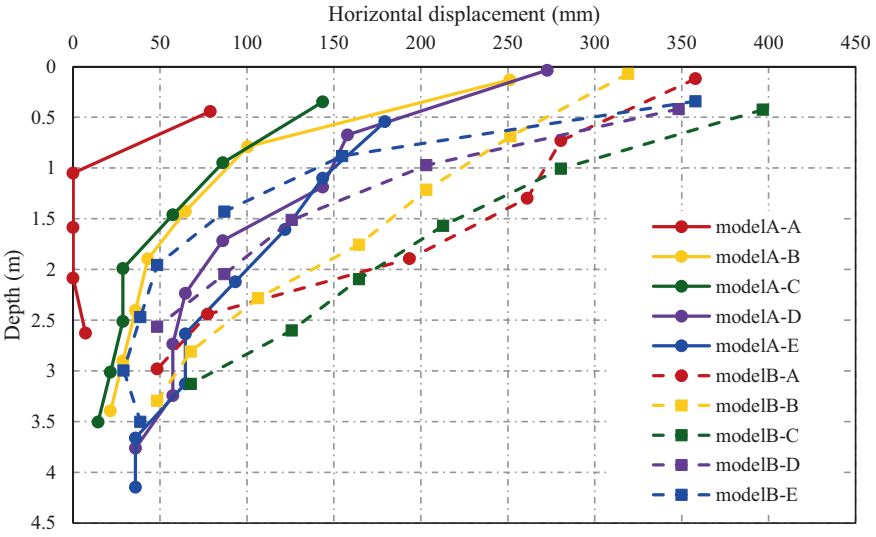

Fig. 11.20 Displacement of spaghetti along the depth after test

soil profile. The result indicates the horizontal displacement of soil decrease with increasing depth in both models, but the displacement in model B is larger than in model A. It shows the generalized scaling factor for displacement may overestimate the among of displacement.

11.6 Conclusions

Two centrifuge modeling tests were conducted to validate the generalized scaling law. Both models are 5°-inclined slope of 4-m-deep-saturated sandy ground model subjected a destructive motion with PBA 0.18 and 0.16g, respectively. Model A adopts centrifuge scaling law with centrifuge scaling factor (η) of 26. Model B adopts generalized scaling law with centrifuge scaling factor (η) of 13 and virtual 1g modeling factor (μ) of 2. The results of acceleration response, excess pore water pressure, and cone tip resistance show the generalized scaling law can simulate the same prototype simulated by centrifuge scaling law well. However, the results of surface displacement and ground displacement show the generalized scaling factor for displacement may overestimate the among of displacement.

Acknowledgement The authors would like to express our gratitude for the financial support from the Ministry of Science and Technology, Taiwan (R.O.C.) (MOST 106-2628-E-008-004 -MY3) and the technical support from the Experimental Center of Civil Engineering, National Central University. These supports made this study and further research possible and efficient.

References

Carey, T. J., Stone, N., & Kutter, B. L. (2020). Grain size analysis and maximum and minimum dry density testing of Ottawa F-65 sand for LEAP-UCD-2017. In *Model tests and numerical simulations of liquefaction and lateral spreading: LEAP-UCD-2017* (pp. 31–44). Springer.

El Ghoraiby, M., Park, H., & Manzari, M. T. (2020). Physical and mechanical properties of Ottawa F65 sand. In *Model tests and numerical simulations of liquefaction and lateral spreading: LEAP-UCD-2017* (pp. 45–67). Springer.

Hung, W. Y., & Liao, T. W. (2020). LEAP-UCD-2017 centrifuge tests at NCU. In *Model tests and numerical simulations of liquefaction and lateral spreading: LEAP-UCD-2017* (pp. 361–384). Springer.

Hung, W.-Y., Huang, J.-X., Lin-Mao, H., & Nguyen, T.-A. (2022). LEAP-UCD-2017 and additional tests at NCU. *Soil Dynamics and Earthquake Engineering, 156*. https://doi.org/10.1016/j.soildyn.2022.107206

Iai, S., Tobita, T., & Nakahara, T. (2005). Generalised scaling relations for dynamic centrifuge tests. *Geotechnique, 55*(5), 355–362.

Kutter, B. L., Carey, T. J., Stone, N., Bonab, M. H., Manzari, M. T., Zeghal, M., Escoffier, S., Haigh, S., Madabhushi, G., Hung, W., Kim, D., Kim, N., Okamura, M., Tobita, T., Ueda, K., & Zhou, Y. G. (2020a). LEAP-UCD-2017 v. 1.01 model specifications. In *Model tests and numerical simulations of liquefaction and lateral spreading: LEAP-UCD-2017* (pp. 3–29). Springer.

Kutter, B. L., Carey, T. J., Stone, N., Zheng, B. L., Gavras, A., Manzari, M. T., Zeghal, M., Abdoun, T., Korre, E., Escoffier, S., Haigh, S., Madabhushi, G., Madabhushi, S., Hung, W., Liao, T., Kim, D. S., Kim, S. N., Ha, J. G., Kim, N. R., Okamura, M., Sjafuddin, A. N., Tobita, T., Ueda, K., Vargas, R., Zhou, Y. G., & Liu, K. (2020b). LEAP-UCD-2017 comparison of centrifuge test results. In *Model tests and numerical simulations of liquefaction and lateral spreading: LEAP-UCD-2017* (pp. 69–103). Springer.

Lee, C. J., Wang, C. R., Wei, Y. C., & Hung, W. Y. (2012). Evolution of the shear wave velocity during shaking modeled in centrifuge shaking table tests. *Bulletin of Earthquake Engineering, 10*, 401–420.

Chapter 12
Experimental Evaluation of Lateral Spreading of a Liquefiable Sloping Deposit Using Centrifuge and Generalized Scaling Law Tests at RPI

Evangelia Korre, Tarek Abdoun, and Mourad Zeghal

Abstract Two centrifuge model tests of a liquefiable sloping deposit subjected to a tapered acceleration input motion were conducted at Rensselaer Polytechnic Institute as part of the Liquefaction Experiments and Analysis Projects (LEAP). The models were built at a consistent relative density D_r = 65%, observing the same methodology of model preparation, but reflected different scaling laws. Model A was designed observing the conventional similitude laws for centrifuge testing, whereas Model B was designed based on the principles of the generalized scaling laws. Albeit the response of the two models was comparable prior to liquefaction, Model B showed a higher propensity for liquefaction and exhibited higher surficial lateral displacements.

Keywords Liquefaction Experiments and Analysis Project (LEAP-ASIA-2019) · Generalized scaling law (GSL) · Centrifuge modelling · RPI

12.1 Introduction

Geotechnical centrifuge modeling is a well-established and a validated methodology of reduced-scale testing of geo-systems under static or dynamic conditions (Schofield, 1981; Steedman, 1991). The conventional scaling laws of centrifuge testing (Garnier et al., 2007) are based on equivalent stress conditions between homologous (geometrically analogous) points in the model and the prototype,

E. Korre (✉)
Department of Civil, Environmental and Geomatic Engineering, ETH Zürich (Former Department of Civil and Environmental Engineering, Rensselaer Polytechnic Institute, Troy, NY, USA), Zürich, Switzerland
e-mail: evkorre@ethz.ch

T. Abdoun · M. Zeghal
Department of Civil and Environmental Engineering, Rensselaer Polytechnic Institute, Troy, NY, USA

T. Tobita et al. (eds.), *Model Tests and Numerical Simulations of Liquefaction and Lateral Spreading II*, https://doi.org/10.1007/978-3-031-48821-4_12

rendering the geotechnical centrifuge a reliable means of testing. Despite its efficacy, conventional scaling introduces some restrictions in the design of the experimental set up. The selection of the model scaling factor, λ, depends on the available platform size in the centrifuge facility. Additional limitations may stem from the capacity of the shaking table actuators and possibly the capacity (i.e., highest g-ton level) of the centrifuge. These parameters often determine the geometrical dimensions of the model. A frequent trade-off in centrifuge physical modelling is the size of the prototype versus the size of the model. Large prototypes usually require significantly high values of the scaling factor λ, leading to rather small models. Such experimental schemes may prove problematic, due, for example, to inaccuracy in modeling the boundary conditions in small size models. An additional source of uncertainty is the possible interaction between sensors, as a result of the limited space in small models to properly install the instrumentation.

Over the past decades, performance-based design has led to an increased demand for testing larger models (Tobita & Iai, 2011). Large scale models using shaking tables in 1-g conditions have been used to test large soil systems (Tokimatsu et al., 2007; Van Den Einde et al., 2004). In 1-g testing, specific similitude laws, different from the ones for centrifuge testing, are applied. However, challenges remain for unconventionally large geo-systems. The dependence of soil behavior on overburden effective stress, combined with additional accommodations often needed to minimize the effect of the container boundaries on the model, would lead to extremely large soil system being utilized for the model, hence rendering 1-g shake table testing an unrealistic choice (Tobita & Iai, 2011).

In order to overcome these restrictions for large geotechnical prototypes, Iai et al. (2005) introduced an innovative scaling method referred to as "two-stage" scaling. This methodology employs the similitude laws for centrifuge testing and 1-g testing simultaneously, prescribing the scaling in the following two district steps:

1. The prototype is scaled down by a factor of μ under $1g$ condition. The yielded geometry corresponds to a virtual model, which is to be further scaled down as described in step 2.
2. The virtual model is scaled down by a factor of η, observing the centrifuge scaling laws.

The second scaling leads to the adopted geometry of the physical model, to be tested on the centrifuge. The comparative advantage of the generalized scaling is that unconventionally large prototypes can be tested on the centrifuge, by avoiding very large scaling factors and thus very small geometries. Instead, the unusually large scaling factors are partitioned in two parts: μ and η, corresponding to the 1-g and centrifuge scaling.

As part of the experimental campaign for the Liquefaction Experiments and Analysis Project (Manzari et al., 2014, 2018), a set of centrifuge experiments of a saturated 5° sloping deposit were undertaken in LEAP-2017. The same experimental set up was utilized for the LEAP-Asia2019, and aimed at investigating the response of the same sloping deposit observing the principles of generalized scaling laws.

This article presents and compares two centrifuge model tests (A and B) conducted at Rensselaer Polytechnic Institute (RPI) according to the two scaling methodologies. Model A was tested using the traditional centrifuge similitude laws, and Model B was tested using the laws of generalized scaling. The focus in this article is on the lateral surficial displacements and deformation. Full documentation of these two tests can be found in Korre et al. (2020a, 2021). All dimensions henceforth are presented in prototype units.

12.2 Scaling Methodology

The tested Models A and B simulated a 5° mildly sloping deposit, pluviated dry using Ottawa F-65 sand, manufactured by U. S. Silica. Both models reflected the same prototype and had the same dimensions, but they were built observing different scaling principles and they were tested at different centrifugal gravitational fields. Model A, observing the traditional scaling laws for centrifuge testing, was scaled by a factor of $\lambda = 23$ and tested under a $23g$ gravitational field (Fig. 12.1).

Model B was scaled following the methodology of generalized scaling (Iai et al., 2005):

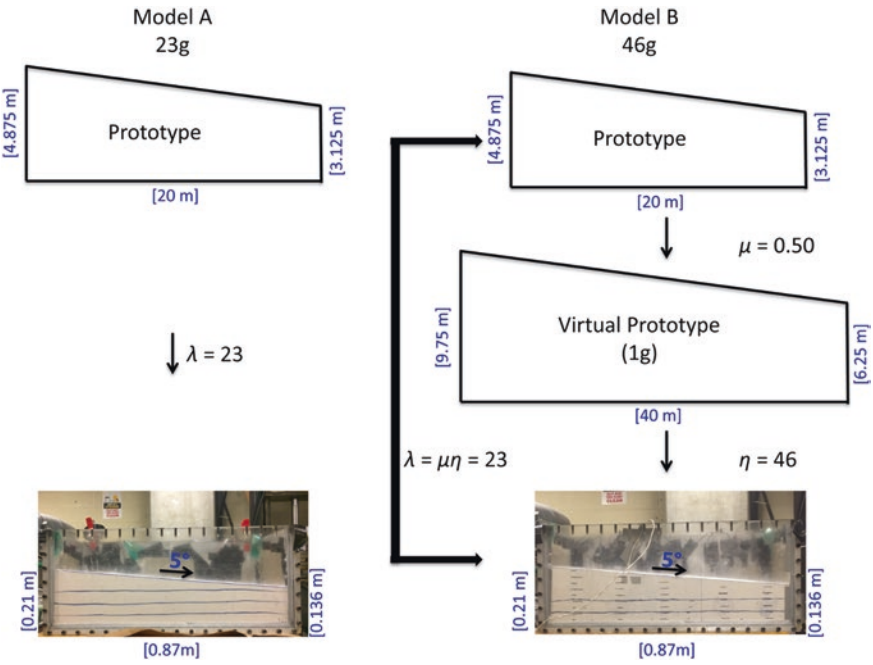

Fig. 12.1 Concept of centrifuge scaling adopted for Model A and generalized scaling for Model B

1. The prototype was scaled to a theoretical prototype based on the similitude laws for 1g testing, using a scaling factor of:

$$\mu = 0.50 \tag{12.1}$$

   Thus, the virtual model is twice as large as the prototype. This unconventional approach was adopted in order to avoid performing the centrifuge experiment at a low gravitational acceleration when using a μ larger than one. Such a case would lead to erroneous results associated with the centrifuge capabilities at Rensselaer.
2. The theoretical prototype was scaled down to the centrifuge model dimensions using a scaling factor of:

$$\eta = 46.0 \tag{12.2}$$

   Model B was therefore tested under a 46g level.
3. From steps 1 and 2, the global or "partitioned" factor (Iai et al., 2005) for Model B is:

$$\lambda = \mu\eta \tag{12.3}$$

   This factor dictates the scaling factors for Model B as presented in Table 12.1.

Figure 12.1 presents the concept of the two applied scaling methods and the g-level employed in Model A and Model B. Observe that both models reflected the same prototype and had the same dimensions.

12.3 Model Construction

Both models were prepared in a rigid container with a plexiglass window as shown in Fig. 12.1, observing the same experimental procedure. Dry air pluviation of Ottawa F-65 sand was used and performed at a constant drop-height and velocity to achieve relatively uniform relative density with depth. In both models the achieved mass density was found to be approximately 1.65g/cm^3, corresponding to $D_r = 65\%$, based on the maximum and minimum mass densities reported in Carey et al. (2020). Observing the methodology described in Korre et al. (2020b), Models A and B were saturated on the centrifuge beam with methylcellulose solution of 23cP and 27cP viscosity respectively (Table 12.1).

The employed instrumentation in Model A and Model B is shown schematically in Fig. 12.2. Three rows of accelerometers and pore pressure transducers were embedded in specified depths in the two models, along the longitudinal axis of symmetry of the model (Korre et al., 2021). The as-built coordinates of the utilized sensors, with reference to the intersection of the axes of symmetry of the container base

Table 12.1 Generalized scaling laws as adopted by Tobita and Iai (2011) and scaling factors of Model B

Parameter	Equation 1*g* scaling	Scaling factor 1*g* test	Equation centrifuge scaling	Scaling factor centrifuge test	Equation partitioned scaling factor $\lambda = \mu\eta$	Partitioned scaling factor $\lambda = \mu\eta$
Length	μ	0.500	η	46.000	$\mu\eta$	23.000
Density	1.000	1.000	1.000	1.000	1.000	1.000
Time	$\mu^{0.75}$	0.595	η	46.000	$\mu^{0.75}\eta$	27.352
Frequency	$\mu^{-0.75}$	1.682	$1/\eta$	0.022	$\mu^{-0.75}/\eta$	0.037
Acceleration	1.000	1.000	$1/\eta$	0.022	$1/\eta$	0.022
Velocity	$\mu^{0.75}$	0.595	1.000	1.000	$\mu^{0.75}$	0.595
Displacement	$\mu^{1.5}$	0.354	η	46.000	$\mu^{1.5}\eta$	16.263
Stress	μ	0.500	*1.000*	1.000	μ	0.500
Strain	$\mu^{0.5}$	0.707	*1.000*	1.000	$\mu^{0.5}$	0.707
Permeability	$\mu^{0.75}$	0.595	η	46.000	$\mu^{0.75}\eta$	27.352
Pore pressure	μ	0.500	*1.000*	1.000	μ	0.500

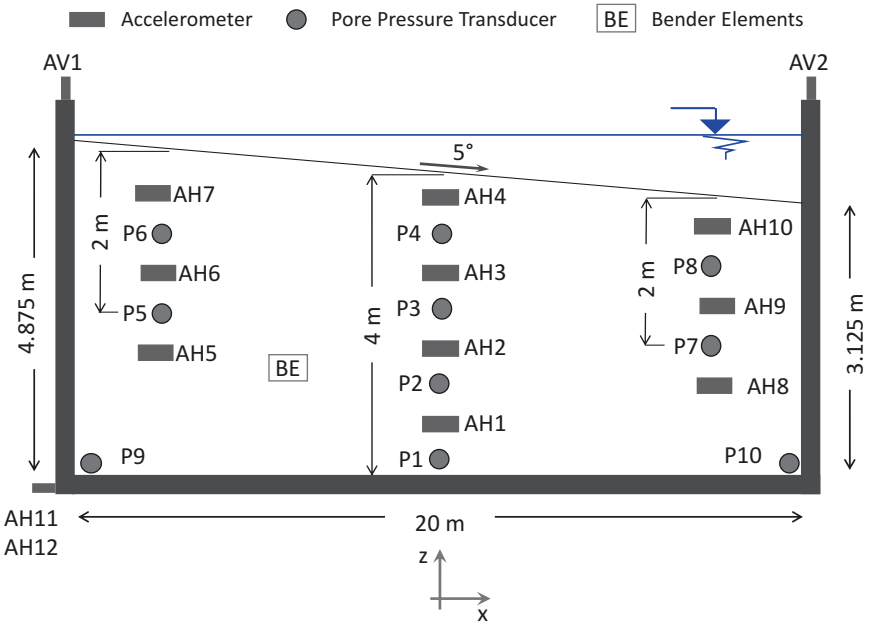

Fig. 12.2 Instrumentation scheme for Model A and Model B

Table 12.2 Location of accelerometers and pore water pressure transducers for Model B

	Coordinates during model construction			Coordinates during model dissection		
Sensor	x: m	y: m	z*: m	x: m	y: m	z*: m
(a) Accelerometers						
AH1	0.29	−0.69	0.58	0.29	−1.04	0.57
AH2	0.17	−1.15	1.50	−0.06	−0.81	1.48
AH3	−0.06	−1.15	2.46	0.40	−1.27	2.42
AH4	−0.63	1.73	3.43	0.01	1.96	3.36
AH5	−6.61	−0.58	2.51	−6.61	−0.58	2.44
AH6	−6.15	1.15	3.34	−5.92	1.04	3.13
AH7	−5.92	0.23	3.98	−5.58	0.23	3.70
AH8	6.73	−1.15	1.50	6.73	−1.15	1.53
AH9	6.73	−0.12	2.55	6.96	−0.69	2.62
AH10	6.04	0.58	3.06	6.50	0.12	3.16
AH11	10.06	−4.26	Bottom of the container	N/A	N/A	N/A
AH12	10.06	4.26		N/A	N/A	N/A
AV1	−10.06	0	Top of the container	N/A	N/A	N/A
AV2	10.06	0		N/A	N/A	N/A
(b) Pore water pressure transducers						
P1	−0.52	−0.12	0.23	−0.29	−0.23	0.23
P2	−0.52	−0.12	1.01	−0.86	−0.58	0.97
P3	0.06	−0.46	2.05	0.01	−0.69	1.98
P4	0.75	−0.46	3.04	1.44	−0.58	2.96
P5	−5.92	0.23	3.04	−5.23	0.00	2.83
P6	−4.31	0.00	3.93	−3.51	0.12	3.59
P7	6.50	1.04	2.02	6.84	0.69	2.05
P8	6.73	−0.69	3.20	7.88	−0.92	3.26
P9	−8.06	−0.69	0.28	−8.02	−0.81	0.25
P10	6.80	0.69	0.18	6.84	0.69	0.23

z* is sensors' elevation in prototype scale measured from the bottom of the container

(Kutter et al., 2020), are presented in Tables 12.2 and 12.3 showing repeatability in the majority of the achieved sensors' locations within a range of approximately 10%.

A Phantom v5.1 HI-G high-speed camera manufactured by Vision Research with a capacity to record up to 1200 frames per second at a resolution of 1024 × 1024 pixels (Kokkali et al., 2018) has been utilized in the LEAP experiments performed at the RPI geotechnical centrifuge facilities, to monitor the surficial soil response in terms of permanent lateral displacements and associated lateral spreading (Korre et al., 2020a, b, 2021; Kokkali et al., 2018; Abdoun et al., 2018).

To this end cable tie heads were cut and driven into the soil surface in a grid of 1.15 m × 1.15 m as shown in Fig. 12.3. As shown in Table 12.4, the as-built target locations on the slope surface were highly repeatable for Models A and B. To ensure

Table 12.3 Location of accelerometers and pore water pressure transducers for Model A

	Coordinates during model construction			Coordinates during model dissection		
Sensor	x: m	y: m	z*: m	x: m	y: m	z*: m
(a) Accelerometers						
AH1	0.29	−1.15	0.58	0.75	−1.27	0.58
AH2	0.17	−1.15	1.5	0.06	−1.04	1.47
AH3	−0.06	−1.15	2.53	−0.4	−1.04	2.51
AH4	−0.63	1.73	3.45	−0.4	1.73	3.43
AH5	−6.61	−0.58	2.48	−6.73	−0.58	2.44
AH6	−6.15	1.04	3.4	−6.5	1.04	3.38
AH7	−5.46	0.35	4.14	−5.58	0.58	4.12
AH8	6.73	−1.15	1.5	6.84	−1.38	1.52
AH9	6.73	−0.35	2.48	6.84	−0.35	2.53
AH10	6.73	−0.92	3.15	6.84	−1.27	3.22
AH11	10.06	−4.26	Bottom of the container	N/A	N/A	N/A
AH12	10.06	4.26		N/A	N/A	N/A
AV1	−10.06	0	Top of the container	N/A	N/A	N/A
AV2	10.06	0		N/A	N/A	N/A
(b) Pore water pressure transducers						
P1	−0.52	−0.30	0.23	−0.06	−0.81	0.23
P2	−0.52	−0.35	1.01	−1.21	−0.35	1.01
P3	0.06	−0.46	2.00	−0.17	−0.58	1.95
P4	0.75	−0.35	2.99	1.09	−0.46	2.92
P5	−7.83	1.27	2.99	−7.76	1.27	2.92
P6	−6.38	0.12	4.00	−6.38	0.00	3.88
P7	6.50	0.78	2.02	6.61	0.58	2.04
P8	6.73	0.85	2.99	6.73	0.69	3.04
P9	−8.06	−0.81	0.28	−8.11	−0.92	0.26
P10	6.80	−0.05	0.23	6.84	−0.35	0.21

z* is sensors' elevation in prototype scale measured from the bottom of the container

clear view of the targets while on flight, the camera's focus was adjusted at the center of the sloping surface. In this way only the targets within the dashed frame shown in Fig. 12.3 were visible during tracking.

12.4 Dynamic Response

Models A and B were subjected to a sinusoidal input acceleration with ramp-up and ramp-down phases and a peak amplitude of 0.15*g* as shown in Fig. 12.4. The applied input motion was highly repeatable between the two models and compared with high fidelity to the theoretical target. Figure 12.4 shows also the recorded vertical acceleration response of the rigid container, which had minimal amplitude compared to the horizontal one.

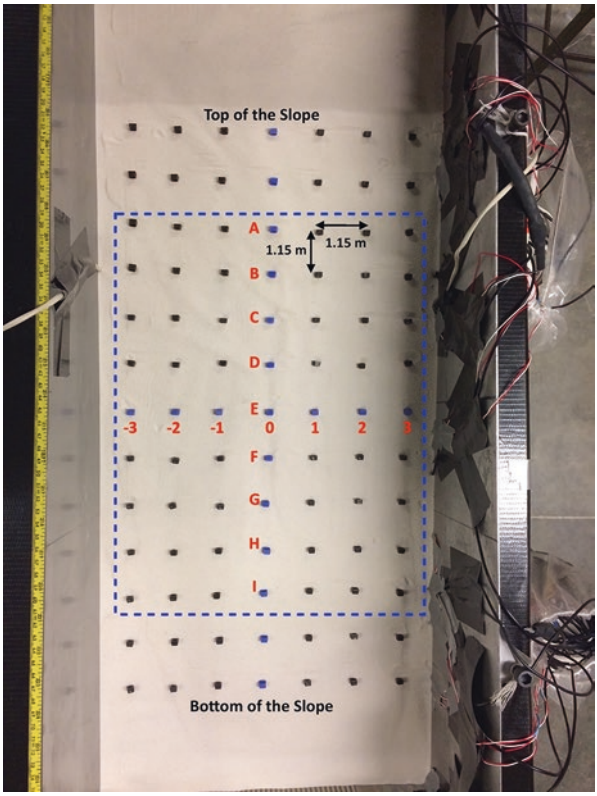

Fig. 12.3 Grid of the targets for high-speed tracking. The dashed frame marks the tracked region on the slope surface in the high-speed recording. (Korre et al., 2021)

Table 12.4 Coordinates of soil surface targets along the central array, as measured before the shaking for Model B and after the shaking for Models A and B

	Before the shaking: Models A and B		After the shaking: Model B		After the shaking: Model A	
Target	x: m	z*: m	x: m	z*: m	x: m	z*: m
	−6.38	4.81	−5.58	4.38	−6.38	4.62
	−5.23	4.69	−4.43	4.37	−5.23	4.49
A	−4.08	4.60	−3.16	4.27	−4.08	4.42
B	−3.05	4.51	−2.13	4.20	−2.93	4.32
C	−2.01	4.39	−1.09	4.15	−1.67	4.23
D	−0.86	4.32	0.17	4.06	−0.52	4.14
E	0.29	4.21	1.21	4.00	0.63	4.07
F	1.44	4.12	2.36	4.03	1.78	3.96
G	2.59	4.00	3.62	3.96	2.93	3.89
H	3.85	3.91	4.77	3.91	4.08	3.84
I	4.89	3.80	5.81	3.80	5.23	3.77
	6.04	3.66	6.84	3.70	6.38	3.63
	7.30	3.54	7.88	3.63	7.53	3.54

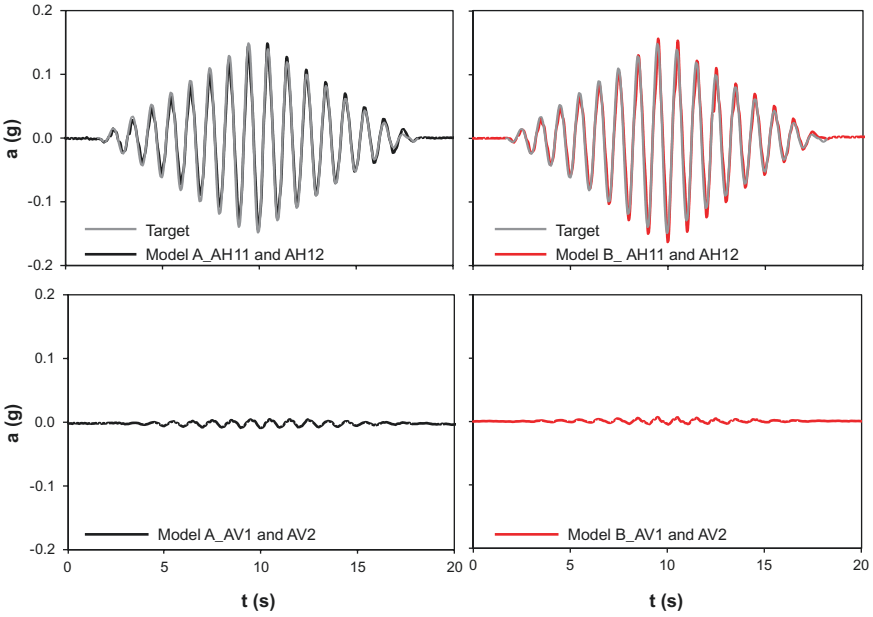

Fig. 12.4 Comparison of the target and applied input motion and associated vertical response of the rigid container

12.4.1 Accelerations

The acceleration response of Models A and B is presented in Fig. 12.5, for the central and side arrays. In the central array, the conditions resembled the ones of a shear beam (Zeghal et al., 2018), whereas in the side arrays the results may have been affected somewhat from the proximity to the side boundaries.

Along the central array (Fig. 12.5), the acceleration response of Models A and B showed reasonable agreement until approximately $t = 7$ s. Subsequently, Model B liquefied, as shown by the de-amplification in the upslope acceleration amplitude (corresponding to positive acceleration values) and the strong dilative peaks in the downslope direction (corresponding to negative acceleration values). In Model A these characteristics appeared approximately 4 s later (at about $t = 11$ s).

Similarly, along the upslope and downslope arrays (Fig. 12.5), accelerations compared satisfactorily until $t \approx 7$ s for Models A and B. Thereafter, liquefaction was triggered for Model B as revealed by the strong dilation peaks and de-amplification of the positive acceleration values. About 4 s later, similar behavior was also observed for Model A. In general, Model B seemed to exhibit milder dilative response compared to Model A. The locations sustaining the highest dilation peaks were as expected in the upslope array for both models. However, particularly in locations AH7 and AH6 at a depth $z \leq 1.00$ m (Fig. 12.5), Model B exhibited significantly lower dilation than Model A.

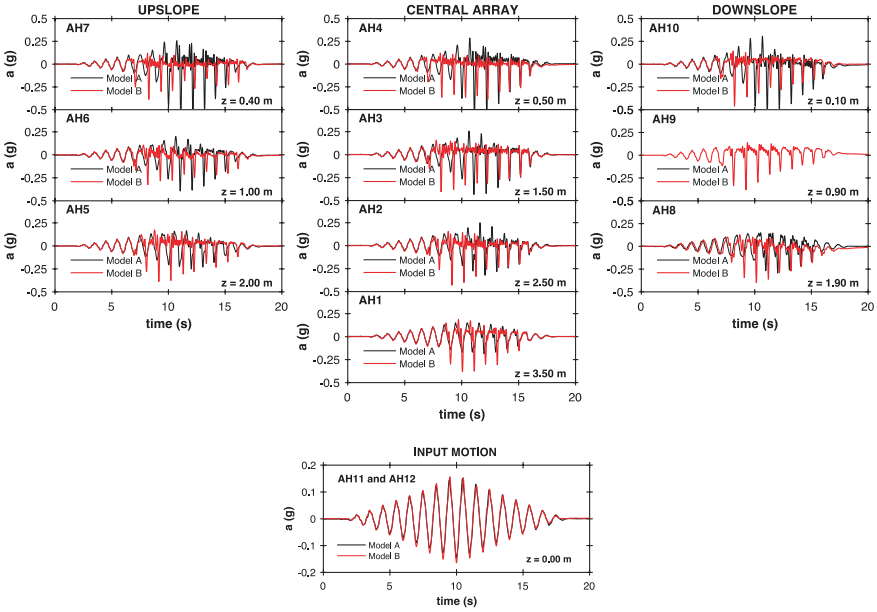

Fig. 12.5 Acceleration response and recorded input motion (average of AH11 and AH12) for Model A and Model B

12.4.2 Pore Water Pressure (PWP)

Figure 12.6 illustrates the pore water pressure build up during the input motion and dissipation, in Models A and B, along the central, upslope, and downslope arrays. The excess pore water pressure ratio, R_u, is determined as the ratio of the excess PWP to the initial effective stress in each corresponding location. Sensors P3, P9 malfunctioned for Model A and sensors P2, P5 for Model B.

The R_u response (Fig. 12.6) corroborated the acceleration results along the central array, revealing overall earlier liquefaction conditions ($R_u = 1.0$) for Model B compared to Model A (the onset of liquefaction for Model B was approximately at $t = 7$ s for Model B and at $t = 11$ s for Model A). Overall, both models developed comparable time histories of excess pore water pressure (EPWP) buildup, but slightly different rates of EPWP buildup and dissipation.

Higher rate and amplitude of EPWP generation and earlier liquefaction in Model B compared to Model A was also observed along the upslope and downslope arrays (Fig. 12.6). Overall Model B exhibited higher susceptibility to EPWP generation than Model A. This trend was consistently evident at all instrumented locations in Model B, even though both models were built with comparable relative densities (Korre et al., 2021). Soil sample tests have revealed reduction in the cyclic resistance to liquefaction as a result of increased confinement (Vaid et al., 2011). The higher confinement in Model B is presumed to be a contributing factor to the observed difference in behavior; however, more research is needed to fully assess the reasons.

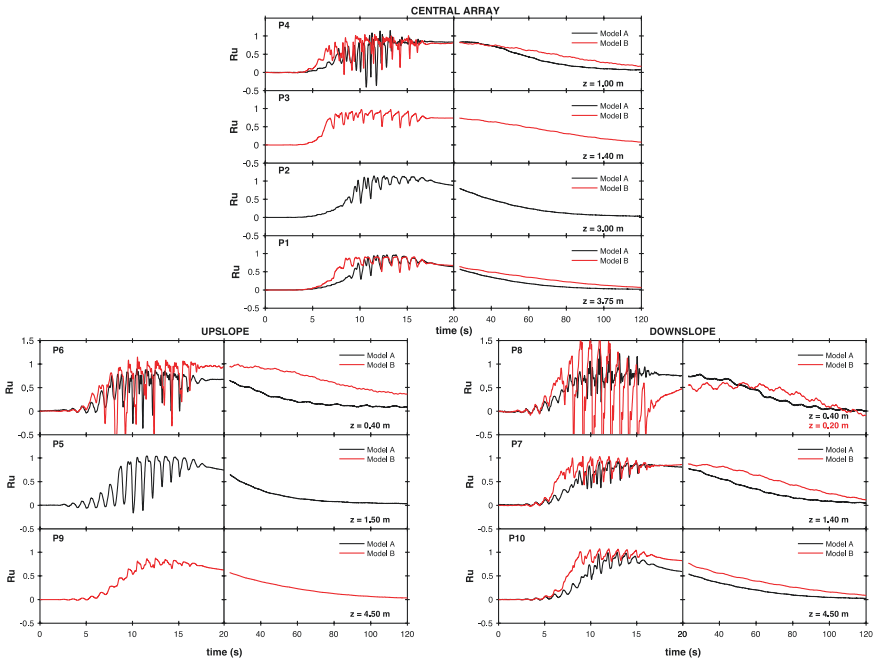

Fig. 12.6 Excess pore water pressure ratio (R_u) response for Model A and Model B

12.5 Lateral Surficial Displacements

The surficial lateral displacements were evaluated by means of image analysis of the high-speed camera recordings. The recordings were processed with the image analysis software TEMA Automotive Lite 3.5-016 by Image Systems. The geometrical relation between engineering length units in the model and pixels in the recording was facilitated by providing in the software the length between two stationary points on the model, thus introducing the geometrical scale in the recording. Based on color contrast between a tracked point and its surrounding points, the software compared in every time increment the relative location of each tracked point and the absolute displacement time history was in this way evaluated. Through differentiation of the displacement, the software produced also the velocity and acceleration response of the tracked points.

The image analysis methodology was validated against the experimental data, by comparing for Model B the acceleration response of the rigid container as recorded by accelerometers AH11-AH12 and the acceleration response of AH4 and the target E0, which was installed closest to that sensor (Fig. 12.7). Even though the accelerometers AH11-AH12 were mounted at the base of the rigid container, whereas the tracked points were at the top of the container, the comparison in Fig. 12.7a revealed good agreement between the two measuring methodologies, reaffirming in this way the high rigidity of the container. Figure 12.7b also showed satisfactory comparison

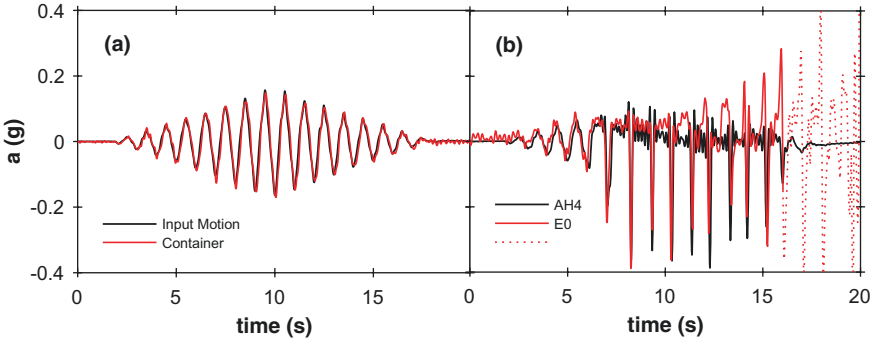

Fig. 12.7 (**a**) Comparison of the input motion as recorded on the shaking table and as determined from tracking of the container; (**b**) comparison of the acceleration time histories as determined from tracking of target E0 and as recorded by AH4

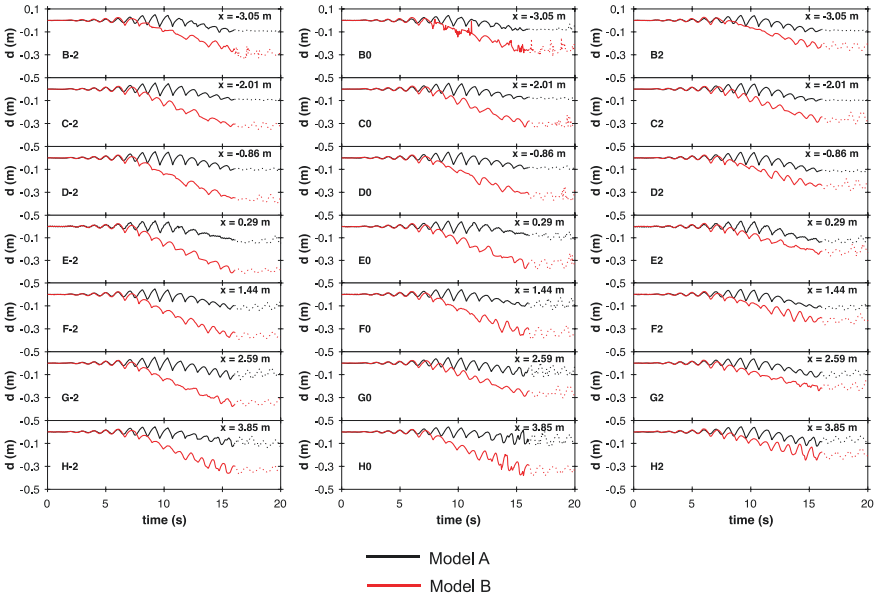

Fig. 12.8 Surficial lateral displacements for Model A and B along the slope as determined from tracking the targets in the high-speed video

between the embedded sensor and the target adjacent to it, revealing the capabilities of image analysis to capture accurately the soil response, including, for instance, the details of the dilative phase of the soil response. Tracking of the targets after the end of the input motion ($t \approx 16s$) was visually compromised, due to light reflections on the free-standing water waves. That part of the response is illustrated with dashed line (Figs. 12.7b, 12.8, and 12.12). The validation of the image analysis for Model A is presented in Korre et al. (2020a).

12.5.1 Response Along the Central Region of the Slope

The response along the arrays labelled −1 and 1 in Fig. 12.3 was practically identical to the one along the central array 0. Therefore, the presented results focus on the response along the arrays −2 and 2, as it provides a clearer view of the lateral displacement progression across the slope. The results from tracking arrays −2, 0, and 2 along the slope are presented in Fig. 12.8. Array −2 was located closer to the plexiglass window boundary of the container, whereas array 2 was located closer to the aluminum side wall (Fig. 12.3). Arrays −2 and 2 were placed approximately 8.50 cm in model scale (2 m in prototype scale) away from the side walls of the rigid container.

Before the onset of liquefaction in Model B ($t < 7$ s), the response was in good agreement with Model A (Fig. 12.8). Consistently with the acceleration and EPWP response (Figs. 12.5 and 12.6), after the onset of liquefaction in Model B (approximately at t ≈7 s), the rate of lateral displacement accumulation became larger in Model B and the associated lateral spreading led to almost three times higher lateral residual surficial displacements (Korre et al., 2021).

12.5.2 Boundary Effects

The permanent lateral surficial displacement response was affected by the container side walls as well as the container boundary at the bottom of the slope, as illustrated in Figs. 12.9, 12.10, 12.11 and 12.12. Figure 12.9 presents an overhead view of the target grid in Model A and Model B after the end of shaking. The dashed lines show schematically the distribution of residual lateral displacements across the slope, for each one of the tracked rows. The observed trend shows decreased lateral displacements in arrays 2, 3 (close to the aluminum container side) compared to the central arrays −1, 0, and 1. In contrast, the lateral displacements near the plexiglass side (array −3) were larger than along the central arrays. The two models exhibited the same trend, which was however more pronounced in Model B.

Figure 12.10 compares the distribution of ultimate lateral displacement along the slope for arrays −2, 0, and 2 of models A and B. Both models revealed similar lateral displacement trends with values increasing from the top of the slope towards the middle zone and then decreasing values closer to the container boundary at the bottom of the slope. This trend was more pronounced for the side arrays −2 and 2. The ultimate displacements for these arrays were compared to those of central array 0, as shown in Fig. 12.11. This figure illustrates the distribution of the ratio of the ultimate displacement along arrays −2 and 2 to the ultimate displacement in the central array, or $\frac{(d_{-2})_{ult}}{(d_0)_{ult}}$ and $\frac{(d_2)_{ult}}{(d_0)_{ult}}$, respectively. Model A exhibited relatively small differences in the residual lateral displacement of the side arrays −2 and 2 compared to the ultimate displacement in the central array. Nevertheless, the array

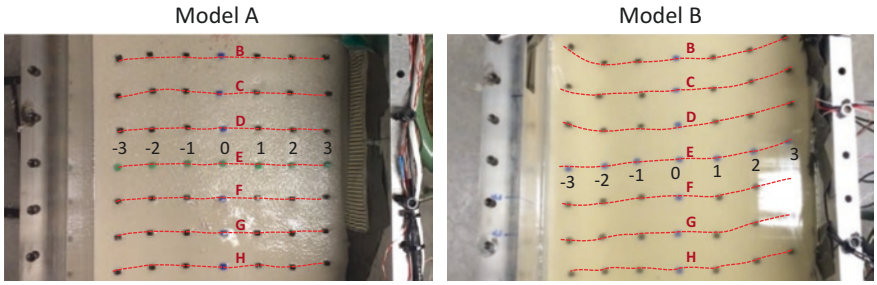

Fig. 12.9 Overhead view of Model A and Model B showing schematically the shape of the lateral displacement profiles across the slope

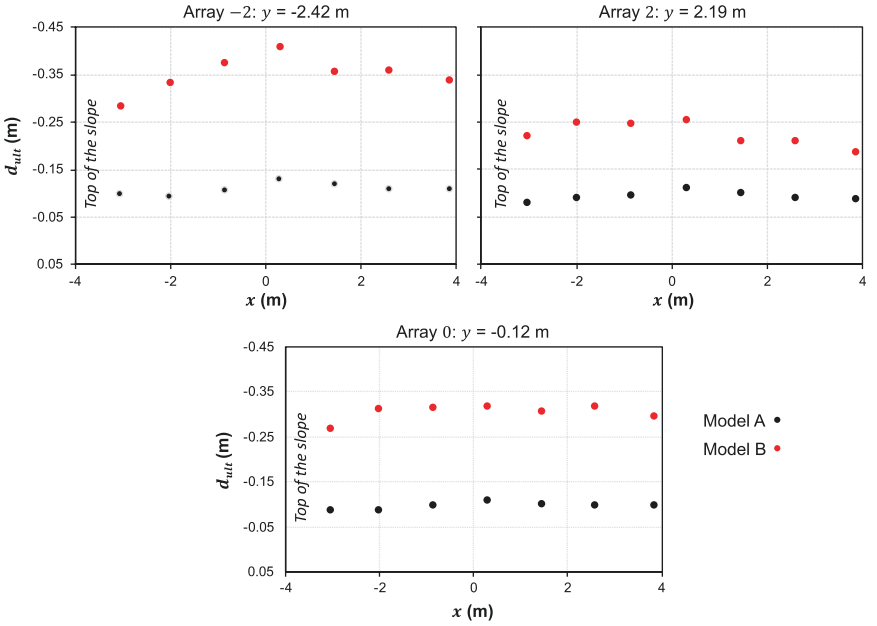

Fig. 12.10 Comparison of the ultimate lateral displacement distribution along the arrays **−2**, **0**, and **2**

closer to the plexiglass window (−2), for this model, exhibited at the end of shaking residual lateral displacements on average about 1.12 times higher than those of the central array (Figs. 12.8 and 12.11). On the other hand, array 2 of Model A (which is closer to the aluminum side), revealed mostly lower ultimate surficial displacements compared to the central array, leading to a value about 0.94 times the ultimate value in the central array.

The observed trend in Model B is quite similar to that of Model A. The array closer to the plexiglass window (−2) exhibited ultimate lateral displacements about 1.16 times the corresponding displacements of the central array (Figs. 12.8 and

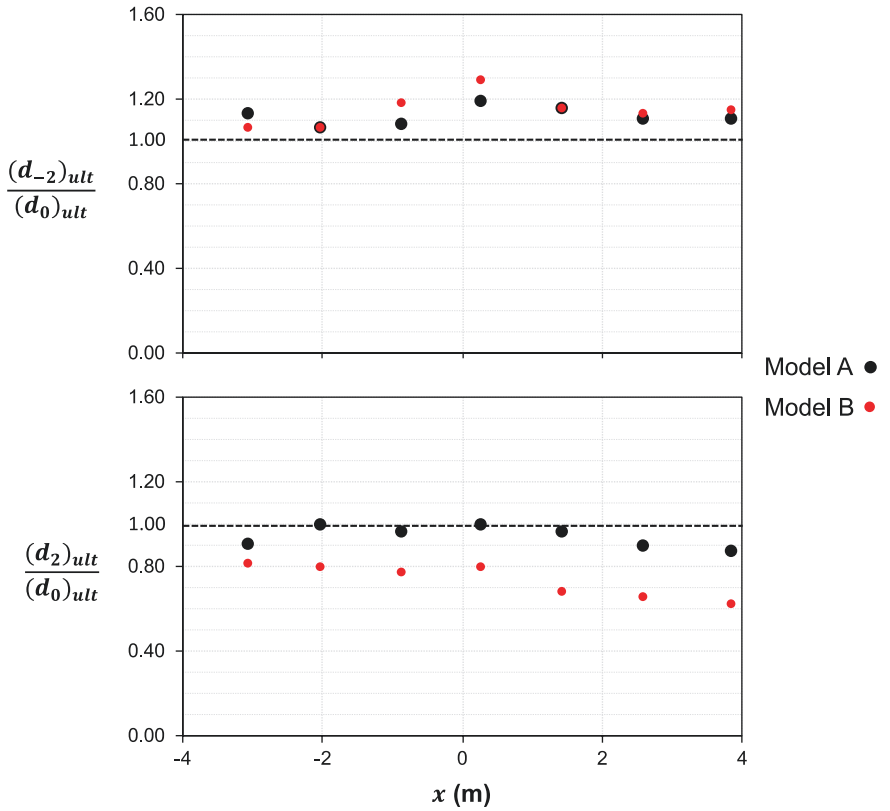

Fig. 12.11 Distribution along the slope of the ratio of the ultimate displacement in arrays **−2**, **2** to the ultimate displacement in the central array

12.11). Also, Model B exhibited lower ultimate lateral displacements in the aluminum side, compared to its central array. However, this effect was significantly more pronounced in Model B, which accumulated residual surficial lateral displacements about 0.75 times the ones in the central array (Figs. 12.8 and 12.11).

To further investigate the effects of the side container boundaries on the lateral displacement response, Fig. 12.12 presents the lateral spreading time histories across the slope for the central row *E*. Arrays −3 and 3 were located approximately 3.5 cm in model scale (0.81 m in prototype scale) away from the side container walls.

In Model A the residual lateral displacement across the slope showed small variability, and the anticipated boundary effects seemed to have minimal influence on the response. In Model B however, the influence of the boundaries was more pronounced, as shown in the response of the arrays −3 and 3, leading approximately to three times smaller lateral displacement compared to the central array 0 (Fig. 12.12). Observe that in Model B, the response in arrays −2, − 1, 1, and 2 exhibited ultimate displacement similar to the one in array 0 (Fig. 12.12), with minimal boundary effects. As discussed also previously, in both models the targets closer to the plexiglass window (−3, −2)

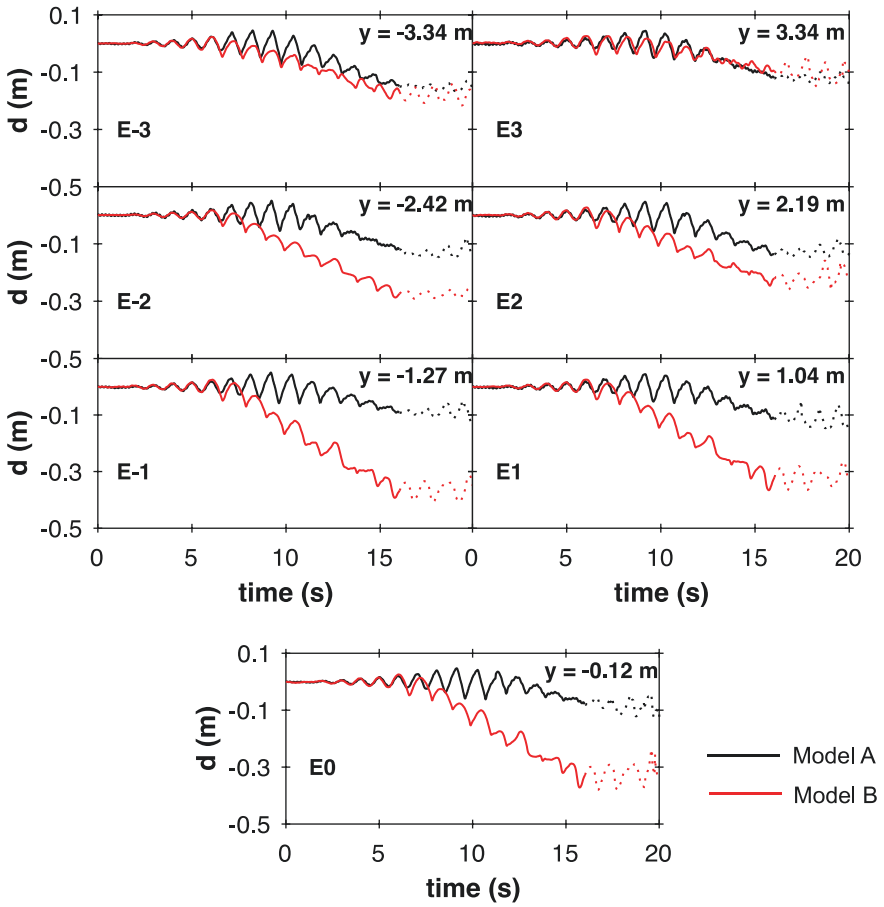

Fig. 12.12 Surficial lateral displacements for Model A and B across the slope, as determined from tracking the central row of targets

exhibited larger ultimate lateral displacement compared to the ones closer to the aluminum boundary (3, 2) as shown in Figs. 12.8, 12.9, 12.11 and 12.12.

The reduced ultimate displacement values close to the aluminum side boundary of the container may be attributed to the surface of that boundary being rougher than the plexiglass. Moreover, the secured cables on the aluminum side wall may have introduced additional friction with the neighboring soil, thus restricting the lateral displacements in arrays 2, 3

The reason behind the more pronounced boundary effects in Model B may stem from minor variations in the built Models A and B. Nonetheless, such uncertainties did not affect the results sufficiently away from the aluminum boundary, in arrays 0 and - 2, where the trend is consistent with the one observed in Model A.

12.6 Conclusions

Two centrifuge models (A and B) were tested at Rensselaer Polytechnic Institute as part of the experimental campaign for the LEAP-Asia2019. The models reflected the same prototype and soil conditions were constructed observing the same experimental methodology, but were prepared observing different scaling laws. Model A was designed observing the conventional similitude laws for geotechnical centrifuge testing, whereas Model B observed the generalized scaling laws.

The models were subjected to the same ramped sinusoidal acceleration ground motion, which was repeated in both tests with high fidelity to the theoretical target. Overall, the responses of Model A and Model B were in good agreement, before the onset of liquefaction. Model B exhibited consistently in all instrumented locations conditions of $R_u \approx 1.0$ at $t \approx 7$ s, approximately 4 s earlier than Model A. This observation was reaffirmed by the acceleration response. In terms of permanent lateral surficial displacements, Model B sustained about three times higher residual surficial displacements compared to Model A. The rates of accumulation of lateral displacements were consistent prior to liquefaction for Models A and B. Lateral surficial deformations in Model B accumulated at a higher rate than Model A after the onset of liquefaction.

Boundary effects led to reduced ultimate surficial lateral displacements in the proximity to the rigid container at the bottom of the slope. Moreover, the aluminum and plexiglass sides of the used model container appeared to have affected the surficial displacement response, in both model tests. Overall, the boundary effects were more pronounced in Model B. Nevertheless, away from the boundaries, both models revealed consistent trends of lateral surficial displacements.

References

Abdoun, T., Kokkali, P., & Zeghal, M. (2018). Physical modeling of soil liquefaction: Repeatability of centrifuge experimentation at RPI. *Geotechnical Testing Journal, 41*(1), 141–163.

Carey, T. J., Stone, N., & Kutter, B. L. (2020). Grain size analysis and maximum and minimum dry density testing of Ottawa F-65 sand for LEAP-UCD-2017. In *Model tests and numerical simulations of liquefaction and lateral spreading: LEAP-UCD-2017* (pp. 31–44). Springer.

Garnier, J., Gaudin, C., Springman, S. M., Culligan, P. J., Goodings, D., Konig, D., et al. (2007). Catalogue of scaling laws and similitude questions in geotechnical centrifuge modelling. *International Journal of Physical Modelling in Geotechnics, 7*(3), 01–23.

Iai, S., Tobita, T., & Nakahara, T. (2005). Generalised scaling relations for dynamic centrifuge tests. *Geotechnique, 55*(5), 355–362.

Kokkali, P., Abdoun, T., & Zeghal, M. (2018). Physical modeling of soil liquefaction: Overview of LEAP production test 1 at Rensselaer Polytechnic Institute. *Soil Dynamics and Earthquake Engineering, 113*, 629–649.

Korre, E., Abdoun, T., & Zeghal, M. (2020a). Verification of the repeatability of soil liquefaction centrifuge testing at Rensselaer. In *Model tests and numerical simulations of liquefaction and lateral spreading: LEAP-UCD-2017* (pp. 385–400). Springer.

Korre, E., Abdoun, T., & Zeghal, M. (2020b). Liquefaction of a sloping deposit: LEAP-2017 centrifuge tests at Rensselaer Polytechnic Institute. *Soil Dynamics and Earthquake Engineering, 134*, 106152.

Korre, E., Abdoun, T., Zeghal, M., & Kokkali, P. (2021). Verification of generalized scaling laws: Two centrifuge tests of a liquefiable sloping deposit. *Soil Dynamics and Earthquake Engineering, 141*, 106480.

Kutter, B. L., Carey, T. J., Stone, N., Bonab, M. H., Manzari, M. T., Zeghal, M., et al. (2020). LEAP-UCD-2017 v. 1.01 model specifications. In *Model tests and numerical simulations of liquefaction and lateral spreading: LEAP-UCD-2017* (pp. 3–29). Springer.

Manzari, M. T., Kutter, B. L., Zeghal, M., Iai, S., Tobita, T., Madabhushi, S. P. G., et al. (2014). LEAP projects: Concept and challenges. In *Geotechnics for catastrophic flooding events* (pp. 109–116). CRC Press.

Manzari, M. T., El Ghoraiby, M., Kutter, B. L., Zeghal, M., Abdoun, T., Arduino, P., et al. (2018). Liquefaction experiment and analysis projects (LEAP): Summary of observations from the planning phase. *Soil Dynamics and Earthquake Engineering, 113*, 714–743.

Schofield, A. N. (1981). Dynamic and earthquake geotechnical centrifuge modelling. In *International conference on recent advances in geotechnical engineering and soil dynamics* (pp. 1081–1100).

Steedman, R. S. (1991). Centrifuge modeling for dynamic geotechnical studies. In *Proceedings of the 2nd international conference on recent advances in geotechnical earthquake engineering and soil dynamics* (pp. 2401–2417).

Tobita, T., & Iai, S. (2011). *Application of the generalized scaling law to liquefiable model ground* (pp. 225–236). Annuals of Disaster Prevention Research Institute, Kyoto University, No. 54 B.

Tokimatsu, K., Suzuki, H., Tabata, K., & Sato, M. (2007). Three-dimensional shaking table tests on soil-pile-structure models using E-defense facility. In *4th international conference on earthquake engineering, June* (pp. 25–28).

Vaid, Y. P., Stedman, J. D., & Sivathayalan, S. (2011). Confining stress and static shear effects in cyclic liquefaction. *Canadian Geotechnical Journal, 38*(3), 580–591.

Van Den Einde, L., Restrepo, J., Conte, J. P., Luco, E., Seible, F., Filiatrault, A., et al. (2004, August). Development of the George E. Brown Jr. network for earthquake engineering simulation (NEES) large high performance outdoor shake table at the University of California, San Diego. In *Proceedings of the 13th world conference on earthquake engineering* (pp. 1–6).

Zeghal, M., Goswami, N., Kutter, B. L., Manzari, M. T., Abdoun, T., Arduino, P., et al. (2018). Stress-strain response of the LEAP-2015 centrifuge tests and numerical predictions. *Soil Dynamics and Earthquake Engineering, 113*, 804–818.

Chapter 13
Centrifuge Model Tests at Zhejiang University for LEAP-ASIA-2019

Qiang Ma, Yan-Guo Zhou, Kai Liu, and Yun-Min Chen

Abstract Two centrifuge models with the same target relative density (D_r = 65%) were conducted in different centrifugal acceleration (30 *g* for Model-A and 15 *g* for Model-B) at Zhejiang University (ZJU) to validate generalized scaling law in the program of LEAP-ASIA-2019. The same model used in LEAP-UCD-2017 was repeated, representing a 5-degree slope consisting of saturated Ottawa F-65 sand. This chapter describes test facilities, instrumentations layout, and test procedures. Uncertainty analysis is also carried out in input parameters (e.g., achieved peak ground acceleration, achieved density and the degree of saturation). The test results of acceleration, excess pore water pressures, and displacement etc. were compared at prototype scale to check the validity of the generalized scaling law (GSL). The preliminary experiment results of Zhejiang University show that the Type II generalized scaling law is applicable to the acceleration response while has a weak applicability to the displacement response.

Keywords Liquefaction Experiments and Analysis Projects (LEAP-ASIA-2019) · Generalized Scaling Law (GSL) · Centrifuge modelling

13.1 Introduction

LEAP (Liquefaction Experiments and Analysis Projects) is an international effort, which aims to provide a set of high quality laboratory and centrifuge test data to assess the capabilities of the advanced constitutive and numerical models developed in recent years for liquefaction problems (e.g., Kutter et al., 2014; Manzari et al., 2014). The results of LEAP-KU-2013 and 2014 showed some inconsistency between different centrifuge tests due to the differences of laminar containers,

Q. Ma · Y.-G. Zhou (✉) · K. Liu · Y.-M. Chen
MOE Key Laboratory of Soft Soil and Geoenvironmental Engineering, Institute of Geotechnical Engineering, Center for Hypergravity Experiment and Interdisciplinary Research, Zhejiang University, Zhejiang, Hangzhou, P. R. China
e-mail: qzking@zju.edu.cn

T. Tobita et al. (eds.), *Model Tests and Numerical Simulations of Liquefaction and Lateral Spreading II*, https://doi.org/10.1007/978-3-031-48821-4_13

which caused challenges for numerical simulations (Tobita et al., 2014). Therefore, rigid boxes were adopted since in LEAP-GWU-2015 to avoid the numerical modeling complexities associated with the special boundary conditions created by different types of laminar containers. In the summary of LEAP-GWU-2015, Kutter et al. (2018) suggested that more rigorous site investigation should be used to determine the density and saturation of the soils (such as in-fight CPT testing, bender elements testing etc.). New methods such as high-speed cameras with PIV analysis are also recommended to trace dynamic surface lateral displacement. Thus, better practical experimental technology and measuring techniques were adopted in LEAP-UCD-2017, including in-flight CPT testing for estimating soil density, high-speed camera for tracing marker displacement as well as in-flight shear-wave velocity for detecting initial state of the model (Zhou et al., 2018).

LEAP-ASIA-2019 was organized based on two objectives: one is to validate the Type II generalized scaling law, the other one is to fill the gaps and further update the CPT tip resistance-density correlation obtained in the LEAP-UCD-2017 (Carey et al., 2018a, b). Ten centrifuge teams have performed at least two types of tests, the first one is conducted considering the traditional centrifuge scaling law and the second one is the same geometry as the first one but executed considering the generalized scaling law.

In LEAP-ASIA-2019, two centrifuge models were conducted at Zhejiang University to check the validity of the generalized scaling law. Large geotechnical centrifuge ZJU-400, uniaxial hydraulic shaker, and advanced in-flight bender element (BE) system, other unique techniques, including a two-dimensional in-flight miniature CPT system, bending disk system (BD) and high-speed cameras were also used in this study. Zhejiang University rigorously followed the specifications and procedures and gained reliable results. The achieved density of two models is close to the target density of D_r =65%, and the achieved degree of saturation $S_r > 99.5\%$. The input motion was well controlled and matched the target values. This chapter first describes test facilities, model preparations, and test procedures. Then uncertainty analysis is carried out in input parameters, such as achieved peak ground acceleration (PGA) and achieved density. Some preliminary experimental results are discussed in prototype scale as well, which contribute to further researchers to understand the experimental benchmark data of Zhejiang University in LEAP-ASIA-2019.

13.2 Test Facilities and Specifications

13.2.1 Test Facilities

LEAP-ASIA-2019 tests of Zhejiang University were performed by using the ZJU-400 centrifuge with in-flight uniaxial shaker and bender elements /bending disks testing system, which was detailed introduced in Zhou et al. (2018), Liu et al. (2020).

The same rigid model container was used as LEAP-UCD-2017, which had the inner dimension of 770 mm long, 400 mm wide, and 500 mm deep. The container was then shortened to 666 mm in length to match the prototype specification of 20 m in length. The supporting blocks are 52 mm thick aluminum plate, which was braced at six locations and bolted to the end walls of the container, demonstrated in Fig. 13.1. The blocks were well sealed to prevent drainage along the aluminum container interfaces.

A two-dimensional miniature CPT system used in LEAP-UCD-2017 was applied to evaluate the uniformity and density of the soil models before and after each destructive motion. The size of cone tip was 6 mm in diameter with apex angle of 60°.

13.2.2 Model Geometry and Instrumentations Layout

Two models conducted in LEAP-ASIA-2019 had the same geometry as LEAP-UCD-2017, representing a 5-degree, 4 m deep at midpoint, 20 m long sand slope deposit of Ottawa F-65 sand at prototype scale. The soil surface normal to slope direction was not curved according to the radius of the centrifuge because the shaking direction is parallel to the axis of the centrifuge, and the centrifuge radius (4.5 m) is larger enough to mitigate the effect of ground curve.

Figure 13.1 illustrated the instrumentations locations in the model. Four horizontal accelerometers (AH1-AH4) and four pore pressure transducers were located at the midpoint along the shaking direction to minimize the boundary effects from the rigid walls. Two additional accelerometers (AH11 and AH12) were attached on the bottom of container to record the achieved base motion. Two vertical accelerometers were installed at the top of the container to monitor vertical and rocking accelerations. Another four horizontal accelerometers and two pore pressure transducers (AH6, AH7, AH9 and AH10; P6, P8-P10) were included at equivalent depths as sensors in the central array and were intended to help in understanding the effect of the container boundaries on the model response. Three pairs of bender elements, at the depth of 1 m, 2 m, and 3 m respectively, were placed to measure vertically polarized and horizontal travelling SV shear-wave velocity. A pare of bending disks were also installed to measure P-wave velocity after model saturation.

Eighteen (3 rows × 6 columns) specified surface markers were placed at the surface of the soil to trace the deformation during soil liquefaction. The specified surface markers were red shown in Fig. 13.2, which made by a 10 mm length, 25 mm in diameter PVC tube with an aluminum cross bar fixed in center. The black surface markers made of zip ties were also employed and all the surface markers were installed in a 50 mm × 50 mm grid (model scale). Twelve colored (blue) sand columns were used to curve lateral spreading profile by excavation after the final spin down.

Five high-speed cameras (GoPro cameras) were installed on the camera frame to record the lateral displacement of surface markers on different regions of the model during spinning. The model is photographed in Fig. 13.2.

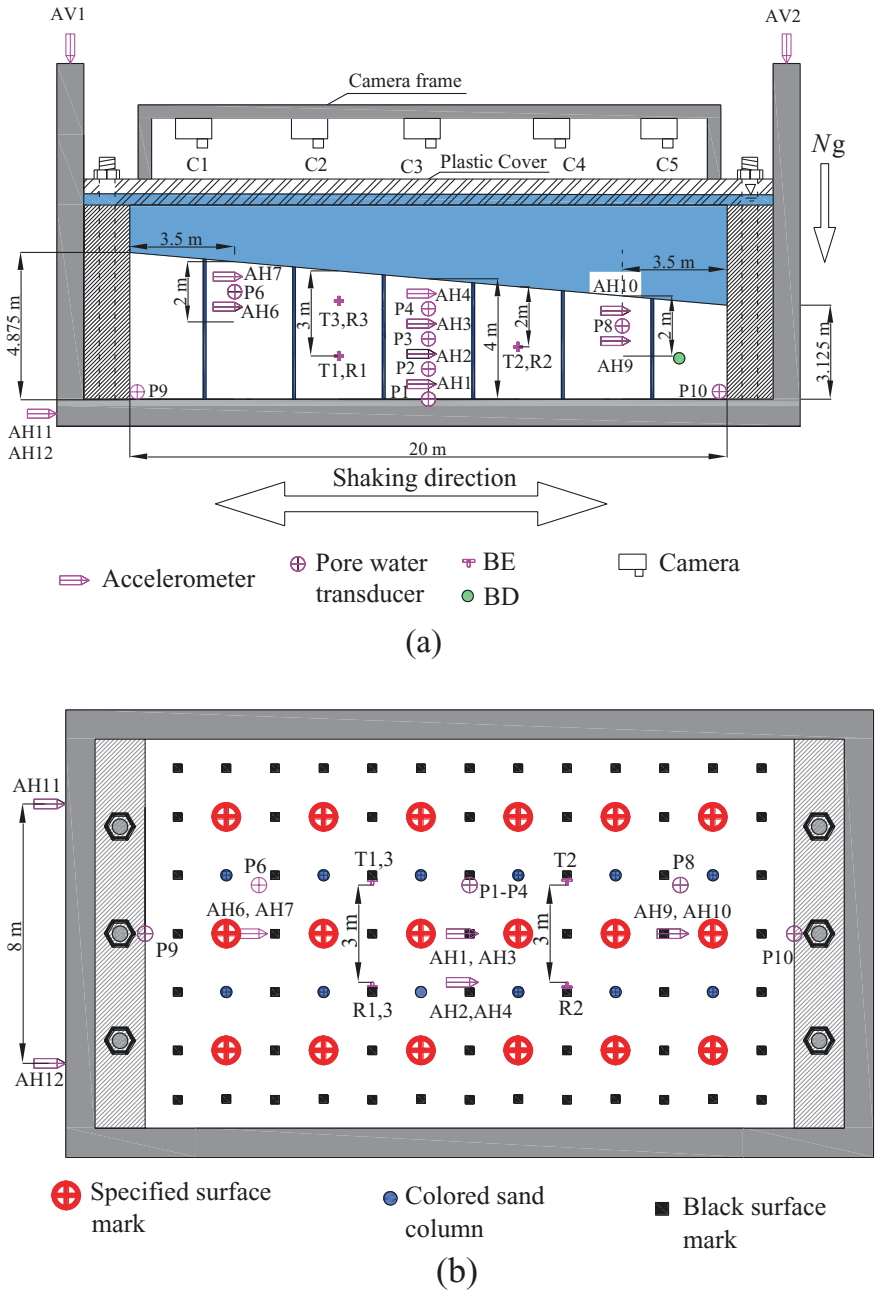

Fig. 13.1 Model geometry and instrumentations layout (prototype scale): (**a**) side view; (**b**) top view

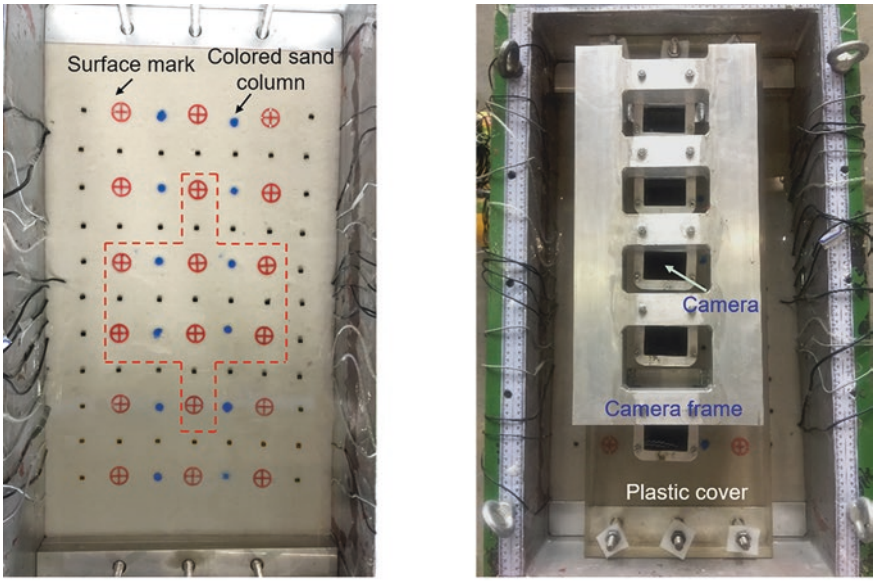

Fig. 13.2 Photograph of finished model: (**a**) surface markers and colored sand columns; (**b**) high-speed cameras

13.3 Model Preparation

13.3.1 Test Material

The same Ottawa F-65 sand was used as the LEAP-UCD-2017, the grain size distribution curve, physical properties and additional material properties of Ottawa F-65 sand, including triaxial, simple shear, and permeability test data, could be found in Carey et al. (2017).

13.3.2 Scaling Law

One of the objectives of LEAP-ASIA-2019 is the verification of the generalized scaling law. The Type II generalized scaling law (GSL) was applied in the experiment consequently, which contains two stages. In the stage I of generalized scaling law, the prototype is scaled down into a virtual model using a 1 g filed scaling law proposed by Iai (1989) with a scaling factor μ. In the stage II of generalized scaling law, the virtual model is scaled down into the physical model applying the conventional centrifuge scaling law with a scaling factor η. By this means, the overall

Table 13.1 Generalized scaling factors implemented in ZJU experiment

	Scaling factors (prototype/model)		
	GSL	Model-A	Model-B
1 g	μ	1	2
Centrifuge	η	30	15
Length	$\mu\,\eta$	30	30
Time	$\mu^{0.75}\,\eta$	30	25.2
Density	1	1	1
Frequency	$\mu^{-0.75}\,\eta^{-1}$	1/30	1/25.2
Acceleration	$1/\eta$	1/30	1/15
Displacement	$\mu^{1.5}\,\eta$	30	42.4
Stress	μ	1	2
Strain	$\mu^{0.5}$	1	1.4
Permeability	$\mu^{0.75}\,\eta$	30	25.2
Pore pressure	μ	1	2

geometric scaling factor of GSL is $\lambda = \mu\eta$, which is much larger than that of conventional centrifuge scaling law ($\lambda = \eta$). More detailed description of GSL could reference Iai et al. (2005).

In the program of LEAP-ASIA-2019, two models were designed with the same overall scaling factor (λ = 30) using the Iai's Type II scaling law, called Model-A (30 *g*), Model-B (15 *g*) respectively. Model-A was regarded as a virtual prototype and Models-B was supposed to model the prototype. The generalized scaling factors used in this study were listed in Table 13.1.

13.3.3 Model Preparation and Saturation

Air pluviation method was adopted to ensure a high level of uniformity when preparing the models. The calibration was implemented before pluviating the model. The target density is ρ_d = 1654 kg/m^3. The achieved densities were calculated by the measurements of soil mass and volume and the best estimated final achieved density was detailed in Table 13.2. Though the achieved density was slight loose than the target, the density of two models was nearly identical.

The viscous fluid used to saturation was silicone oil with density of 0.95 g/cm^3 (25 °C). The target viscosity is 30 times of viscosity of water (30 cSt) for Model-A, 25.2 cSt for Model-B according to the generalized scaling law listed in Table 13.1, which aims to overcome the conflict between dynamic and consolidation time scaling factors (Dewoolkar et al., 1999). Temperature-fluid viscosity calibration curves were obtained before saturation by using a MCR302 rotational rheometer (manufacturer: Anton Paar), which was shown in Fig. 13.3. The viscosity decreases with an increase of temperature. Owing to the spin of centrifuge, the temperature of

Table 13.2 Achieved density for each model

Model	Mass of sand g	Volume after saturation cm^3	Average density ρ_d kg/m^3
Model-A	59,098	36,376.8	1625 ± 11
Model-B	60,103	36,812.4	1633 ± 11

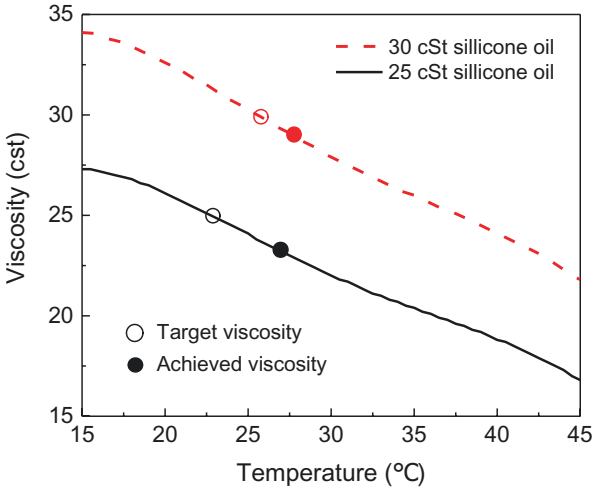

Fig. 13.3 Temperature-fluid viscosity curve of silicone oil

silicone oil commonly increases by 2–3 °C, which has a very limited influence on the viscosity of silicone oil.

When saturation, the oil tank and model container were kept under the same vacuum level (around −95 kPa) and the oil was firstly de-aired more than 24 h. Then transport silicone oil from the reservoir to the container was driven by gravity feed. The saturation speed was controlled to prevent soil disturbance at the bottom of container. When saturation was accomplished, bending disk testing system was used to check the degree of saturation. Figure 13.4 represents the typical BD test result, the measured V_p around 1160 m/s. According to Zhou et al. (2018), the achieved the degree of saturation *Sr* is higher than 99.5%.

13.3.4 Input Motion

The input base acceleration for each model consisted a sequence of three destructive motions with the same maximum acceleration of 0.25 *g* (prototype scale). All the motions represented 1 Hz ramped sine wave with 16 cycles, shown in Fig. 13.5.

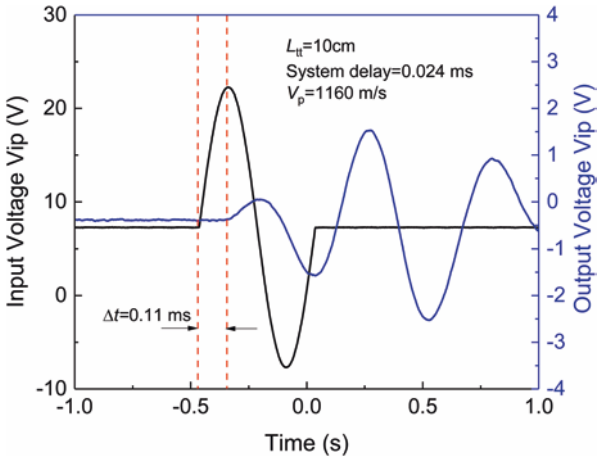

Fig. 13.4 Typical signal of BD test

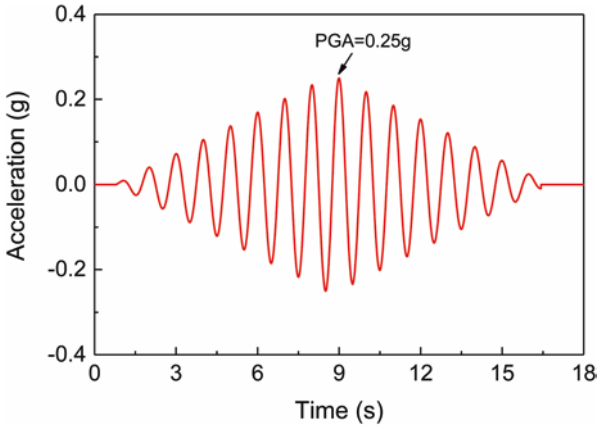

Fig. 13.5 Acceleration time history for the destructive motion

13.4 Test Procedures and Achieved Motions

13.4.1 Test Procedures

The test procedures were shown in Fig. 13.6. Before the centrifuge spin up, a careful survey of the surface markers was carried out and the temperature of silicone oil was measured. Then the centrifuge was spun up to 10 *g*, 20 *g*, and 30 *g* step by step (7.5 *g* and 15 *g* for Model-B). When the pore pressure was stable at each *g*-level, the shear wave velocity was measured by using BE testing system. After reaching the target centrifugal acceleration, the model then was subjected to a non-destructive step wave, which is used to characterize the model. The CPT test was carried out to

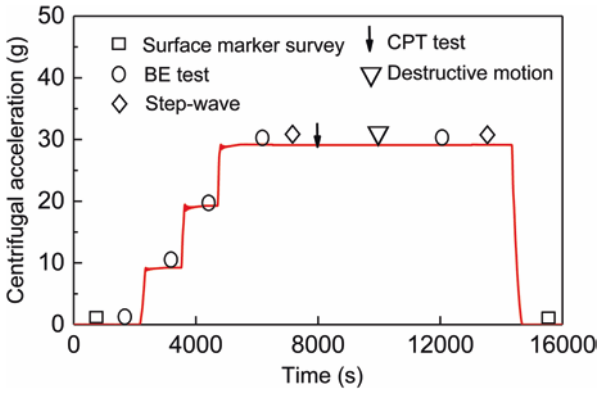

Fig. 13.6 Test procedures and shaking sequences

determine the density of the model before each destructive motion. After that, a destructive motion (shown in Fig. 13.5) was executed and then, another step-wave conducted when the excess pore pressure was fully dissipated. The centrifuge was spun down step by step and V_s was measured at each step after all the above procedures accomplished. Finally, surface markers and temperature were measured. Each model and each motion followed the same procedure except Model-B second motion missing the step-wave after destructive motion. Each model contains three cycles of abovementioned procedures.

13.4.2 In-Flight Measurement

CPT tests were conducted in 30 *g* for Model-A and 15 *g* for Model-B with the velocity of penetration 0.6 mm per second and sample rate 1 Hz. One of the key parameters controlling tip resistance is effective stress (Jamiolkowski et al., 1985), so dimensional analysis was adopted to eliminate the influence of stress caused by different centrifugal acceleration. Figure 13.7 demonstrated the normalized tip resistance (defined in Eq. (13.1)) versus normalized depth (defined in Eq. (13.2)) for two models.

$$Q = \frac{q_c}{\sqrt{\sigma_v' p_a}} \tag{13.1}$$

$$Z = \frac{z}{B} \tag{13.2}$$

where q_c and σ_v' is tip resistance and vertical effective stress, expressed in MPa, p_a is atmospheric pressure, 101 kPa; z is penetration depth, B is cone diameter, 6 mm.

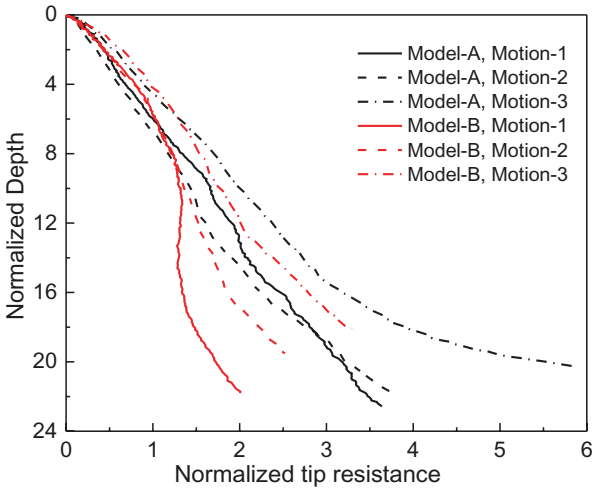

Fig. 13.7 Normalized cone tip resistance

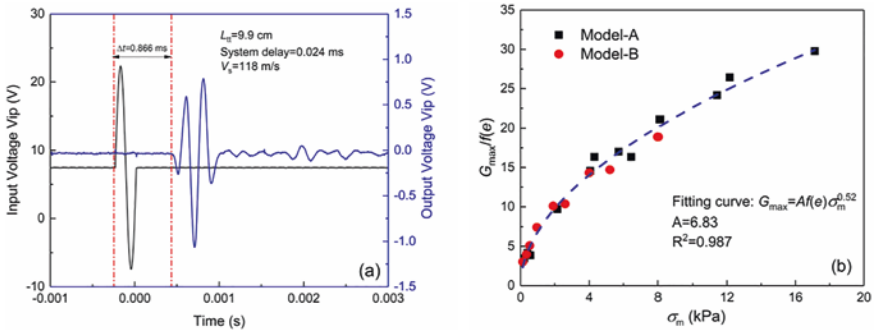

Fig. 13.8 The results of bender disks: (**a**) typical signal of BE tests; (**b**) fitted Hardin curve of Ottawa-F65 sand

The normalized resistance was nearly linearly increased, which indicated the uniformity of both two models. According to Kim et al. (2016), the slope of the curve represents the relative density of sand. The result indicated that Model-A and Model-B have a comparable density, which agreed with Table 13.2 results.

Three pairs of bender elements were used to measure the V_s of model. Figure 13.8a gives a typical signal of BE during spinning, indicating the arrival of receiver is well distinguishable to ensure the reliability of BE results. Figure 13.8b shows the fitted Hardin curve of Ottawa-F65 sand, G_{max} was calculated through Eq. (13.3):

$$G_{max} = \rho V_s^2 \tag{13.3}$$

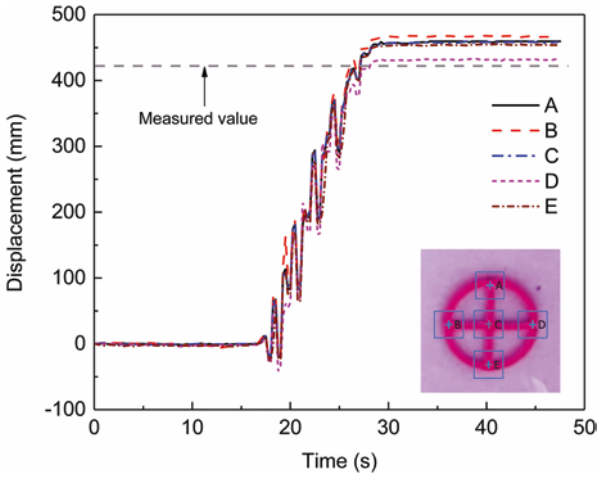

Fig. 13.9 Time history of lateral displacement obtained by PIV analysis

in which V_s is the shear wave velocity measured by BE testing in different stable g-level.

As shown in Fig. 13.1a, five high-speed GoPro cameras were installed above the slope surface to record movement of surface markers during the destructive motion. The videos were converted to displacement time history by Geo-PIV analysis procedure (e.g., White et al., 2003). Five points located at different region of the surface marker were analyzed to ensure reliable results. Figure 13.9 demonstrates typical results of dynamic displacement of one surface marker from five points, showing high consistency within five points. The residual displacement value obtained using videos agreed with that measured by hand afterwards.

13.4.3 Achieved Motions

In dynamic centrifuge testing, it is crucial to impose acceleration to models which is as close as possible to the target acceleration. Assessment of the similarities and differences between achieved input and target motions is fundamental to address the LEAP validation objectives. The concept of effective PGA was adopted to evaluate the accuracy and efficiency of the motions. The effective PGA, PGA_{eff}, is defined as below:

$$PGA_{eff} = PGA_{1Hz} + 0.5 \times PGA_{hf} \tag{13.3}$$

in which PGA_{hf} represents the peak acceleration of the high frequency component of the motion, PGA_{1Hz} denotes the peak acceleration which was isolated by use of a notched band pass filter with corner frequencies of 0.5 and 1.2 Hz. The results of all

Table 13.3 The effective PGA of Motion-1 (unit: *g*)

Model	Accelerometer	PGA_{tar}	PGA_{1Hz}	PGA_{hf}	PGA_{ach}	PGA_{eff}
Model-A	A11	0.25	0.184	0.171	0.354	0.270
	A12		0.195	0.18	0.374	0.285
Model-B	A11	0.25	0.205	0.147	0.347	0.279
	A12		0.204	0.146	0.345	0.277

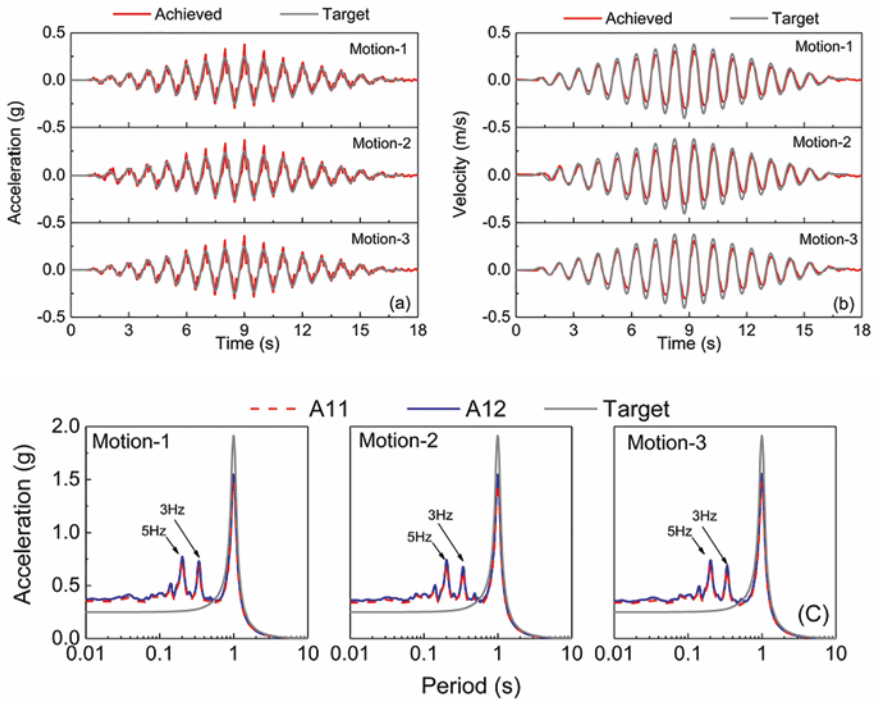

Fig. 13.10 Comparation between target and achieved motions of Model-A: (**a**) acceleration time history; (**b**) velocity time history; (**c**) acceleration response spectra

the input motions for two models are summarized in Table 13.3. It is found that PGA_{1Hz} values of AH11 are smaller than AH12 for Model-A, while almost the same between AH11 and AH12 for Model-B, indicating that there was a small angle between AH11 and motion direction in Model-A.

Figure 13.10a, b compare the achieved and target acceleration time histories and velocity histories for Model-A three motions, the velocity time series obtained by integrating acceleration. The achieved PGA usually 10–20% higher than target PGA, while the achieved PGV only about 90% of target one, which is because the achieved motion contained high frequency components. Five percent damped acceleration response spectra (ARS) for model-A three motions are shown in Fig. 13.9c, the average achieved peak spectral acceleration at T = 1 s is 1.5 *g*, lower than target

one (approximately 1.9 *g*). Figure 13.10c also indicates that the achieved motion contained some higher frequency components especially in 3 Hz and 5 Hz.

Figure 13.11 gives information about the measured vertical motions for Model-A, Motion-2. The grey lines indicate the unfiltered motions and the black lines are band-pass (0.3–3 Hz) filtered motions. Although zero vertical acceleration is expected during shaking, the hydraulic shaker produced unintended vertical component in addition to the desired horizontal accelerations. Besides, Coriolis acceleration will also contribute to the measured vertical acceleration. Little phase shift between AV1 and AV2 is observed from Fig. 13.11, revealing that the container was a negligible rocking during shaking.

13.5 Test Results

13.5.1 Acceleration Responses

Figure 13.12a shows acceleration time histories of Motion-1 in Model-A, other results in ZJU experiments are similar with the instance. The acceleration time histories show de-amplification in upslope direction and significant negative dilation spikes in downslope direction for AH1-AH4, which have been observed in LEAP-GWU-2015 and LEAP-UCD-2017 (e.g., Carey et al., 2018a, b). The spikes tend to be most exaggerated near the slope surface where the soil easily dilated. When the sharp spikes occurred, the waveform significantly changes both in frequency and

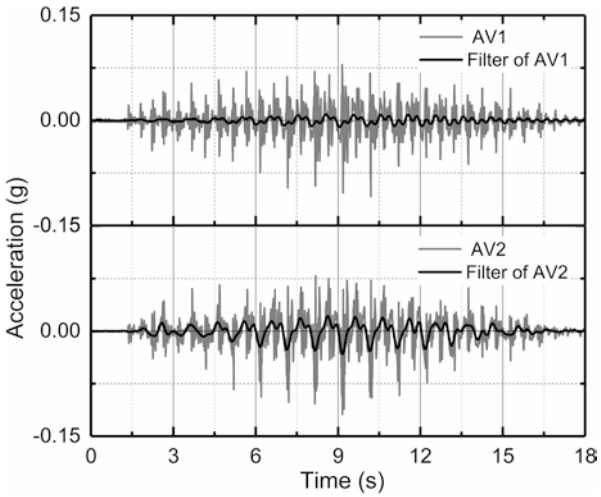

Fig. 13.11 Vertical accelerations on container ends of Model-A during Motion-2

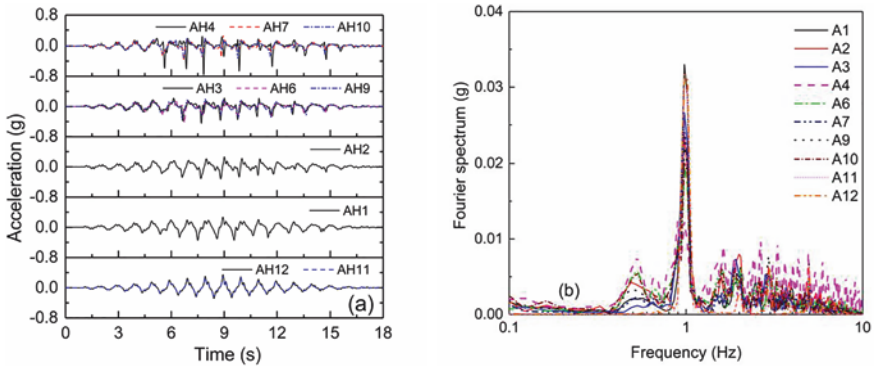

Fig. 13.12 Acceleration response of Model-A, Motion-1: (**a**) time histories; (**b**) fourier spectrums

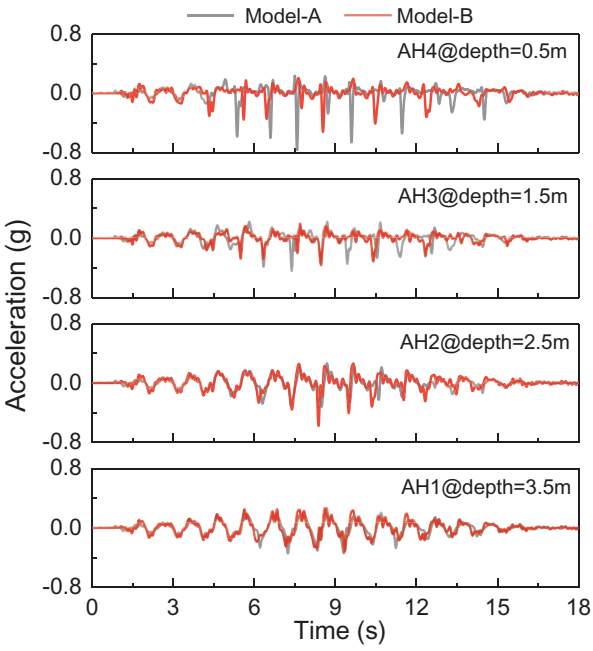

Fig. 13.13 Acceleration response between Model-A and B, Motion-1

amplitude from the base motion. Figure 13.12b demonstrates the Fourier spectrums, some higher frequency occurred owing to dilation of soil.

Figure 13.13 contrasts the central array acceleration response of two models during Motion-1. The time histories of acceleration for two models show a high consistency not only in trends but also in value, which reveals that GSL is applicable to acceleration response in the experiments.

13.5.2 Pore Pressure Response

Figure 13.14 compares the central vertical array of time histories of excess pore pressure ratio r_u ($\Delta u/\sigma_v'$) for Motion-1 in Model-A and Model-B. P1, P2, P3, and P4 were specified to be at depths of 1, 2, 3, and 4 m respectively, and the initial vertical effective stresses are approximately 10, 20, 30, and 40 kPa respectively. The process of excess pore-water pressure build-up during shaking shows a significant agreement. Severe liquefaction occurred in all three models throughout the soil layer and significant dilatancy spikes are observed over the whole depth of the slope, implying that the motion is strong enough to liquefied the slope from top to the bottom. The time required for excess pore-water dissipation, however, shows a discrepancy. Model-B need a longer duration time for pore-water dissipation in prototype scale than the others with higher centrifugal accelerations. A significant discrepancy in dissipation time also has been reported by Tobita et al. (2011) when Type II GSL is applied into saturated flat ground. They assumed that three possibilities may contribute to this phenomenon: (a) effect of duration time for consolidation before shaking; (b) effect of low effective confining stress on the scaling law; (c) possible change of permeability of the model ground due to absorption of the pore fluid on sand particles.

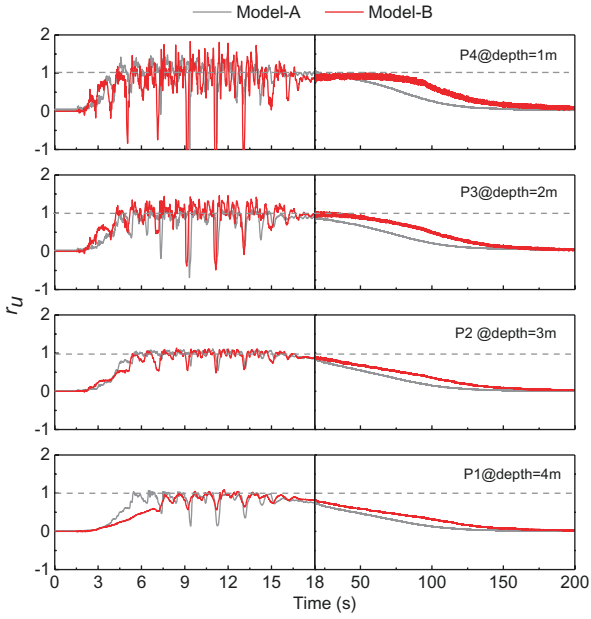

Fig. 13.14 Pore pressure time history: Motion-1

13.5.3 Displacement Response

For all experiments, similar trends are observed that the soil surface settles at the top of the slope higher than toe. A typical result (Model-A) shown in Fig. 13.15. Significant settlement at the top of the slop was occurred during the first motion while heave was observed in the toe. Then the settlement decreased with the number of motions dramatically for the destructive motions densified the soil. Noticing that Motion-3 nearly had a uniform settlements along the slope, no apparent heave at toe of the slope.

Table 13.4 lists the average horizontal displacement D_h and standard deviation of vertical displacement σ for each motion, which calculated from only red surface marker which located in red dotted line frame shown in Fig. 13.2a. Compared the average horizontal displacement of Model-A and B for each motion, some discrepancies were observed. The horizontal displacement of Model-A larger than Model-B during the Motion-2 and 3, whereas significantly smaller in Motion-1. Based on the results of two tests, GSL has a weak applicability to displacement response. Standard deviation of Model-B larger than Model-A indicating more scatter for the vertical displacement of Model-B. The scaling factor of displacement in the GSL is much larger for Model-B than A, any little measurement error would be amplified significantly and scattered the data. Hence, special care had to be taken in measurement of ground displacement when applied the GSL.

The lateral displacement profiles in Fig. 13.15 were obtained from excavation of colored sand columns. The profiles show that the displacement distributed over the whole depth and reached maximum at the surface. Consistent with the observation of surface spreading, the lateral displacements near the side walls were also smaller than those at the mid-slope.

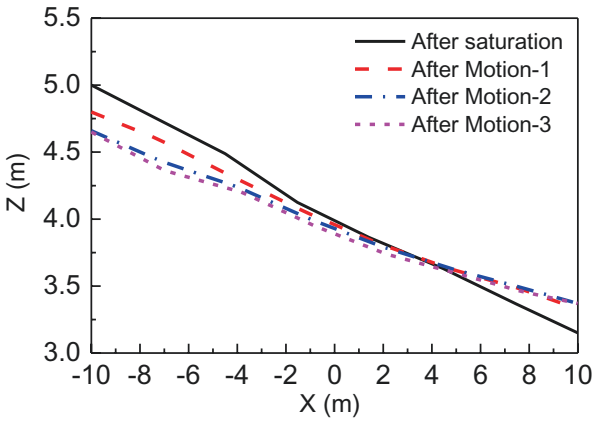

Fig. 13.15 The development of surface settlements (Model-A)

Table 13.4 Average values of lateral displacement after each motion (unit: mm)

	Motion-1		Motion-2		Motion-3	
Model	D_h	σ	D_h	σ	D_h	σ
A	393.75	30.70	187.50	30.00	110.63	37.45
B	593.97	114.73	137.89	47.43	45.08	16.56

13.6 Summary and Conclusions

Two centrifuge tests were conducted at Zhejiang University in LEAP-ASIA-2019 which were designed in the same target densities and subjected three motions under centrifugal acceleration of 30 g and 15 g respectively. Generalized scaling law was applied in the tests to verify the application of the Type II GSL. In this chapter, information on test facilities, model setup and preparation, test procedures, in-flight characterizations, and analysis of the achieved motion and preliminary tests results was presented.

The facilities adopted in LEAP-ASIA-2019 were the same as LEAP-UCD-2017. Besides the bending disk system was carried out to evaluate the degree of saturation. MCR302 rotational rheometer was used to gain temperature-fluid viscosity curve of silicone oil. The achieved viscosity of both two models was close to the target viscosity.

The achieved densities in both models were a bit loose than target one. The CPT results indicated that two models had a closed density. The achieved PGA usually 10–20% higher than target PGA, while the achieved PGV only about 90% of target one. The achieved effective PGA, PGA_{eff}, for each motion roughly matches the targets. Five percent damped ARS shows the achieved motions were smaller than the target of 1 Hz components and some high frequency components were observed in input motion. The vertical accelerations at opposite ends of container were small, indicating a negligible rocking effect during shaking.

Typical results were exampled to explain the response of two models. Liquefaction was occurred in the whole slope. Both of two models had similar acceleration response and pore water response. Spikes due to dilatancy were observed in acceleration time history, which are consistent with drops in excess pore pressure. The dissipation time of pore-water pressure shown a discrepancy two models. Lateral and vertical displacements for each motion were surveyed via some surface markers. The tests result of displacements shown a similar trend but different in value, indicating a weak applicability to the displacement response.

The above results show a promising applicability of GSL especially in modelling larger-scale prototype. However, the scaling factor of displacement in the Type II GSL is much larger than conventional scaling law if a large μ was adopted. Any little measurement error would be amplified significantly. So, special care had to be taken in measurement of ground displacement when usage of Type II GSL.

Acknowledgement This study is supported by the National Natural Science Foundation of China (Nos. 51988101, 51978613, 52278374) and the Chinese Program of Introducing Talents of Discipline to University (the 111 Project, B18047). The authors would thank Mr. Zizhuang Yan, Mr. Jinshu Huang of Zhejiang University for their great help during the centrifuge model tests.

References

Carey, T. J., Kutter, B. L., Manzari, M. T., & Zeghal, M. (2017). *LEAP soil properties and element test data*. https://datacenterhub.org/resources/leap_soil.

Carey, T., Gavras, A., Kutter, B., Haigh, S. K., Madabhushi, S. P. G., Okamura, M., Kim, D. S., Ueda, K., Hung, W. Y., Zhou, Y. G., Liu, K., Chen, Y. M., Zeghal, M., Abdoun, T., Escoffier, S., & Manzari, M. (2018a). *A new shared miniature cone penetrometer for centrifuge testing*. In 9th international conference on physical modelling in geotechnics, ICPMG 2018 (pp. 293–298). CRC Press/Balkema.

Carey, T. J., Hashimoto, T., Cimini, D., & Kutter, B. L. (2018b). LEAP-GWU-2015 centrifuge test at UC Davis. *Soil Dynamics and Earthquake Engineering, 113*, 663–670.

Dewoolkar, M. M., Ko, H. Y., Stadler, A. T., & Astaneh, S. M. F. (1999). A substitute pore fluid for seismic centrifuge modeling. *Geotechnical Testing Journal, 22*(3).

Iai, S. (1989). Similitude for shaking table tests on soil-structure-fluid model in 1 *g* gravitational field. *Soils and Foundations, 29*(1), 105–118.

Iai, S., Tobita, T., & Nakahara, T. (2005). Generalised scaling relations for dynamic centrifuge tests. *Geotechnique, 55*(5), 355–362.

Jamiolkowski, M., Ladd, C. C., Germaine, J. T., & Lancellotta, R. (1985). *New development in field and laboratory testing of soils*. In Proceedings of the 11th ICSMFE (Vol. 1, pp. 57–153).

Kim, J. H., Choo, Y. W., Kim, D. J., & Kim, D. S. (2016). Miniature cone tip resistance on sand in a centrifuge. *Journal of Geotechnical and Geoenvironmental Engineering, 142*(3), 04015090.

Kutter, B. L., Manzari, M. T., Zeghal, M., Zhou, Y. G., & Armstrong, R. J. (2014). Proposed outline for LEAP verification and validation processes. In *Geotechnics for catastrophic flooding events* (pp. 99–108). CRC Press.

Kutter, B. L., Carey, T. J., Hashimoto, T., Zeghal, M., Abdoun, T., Kokkali, P., et al. (2018). LEAP-GWU-2015 experiment specifications, results, and comparisons. *Soil Dynamics and Earthquake Engineering, 113*, 616–628.

Liu, K., Zhou, Y. G., She, Y., Meng, D., Xia, P., Huang, J. S., et al. (2020). Specifications and results of centrifuge model test at Zhejiang University for LEAP-UCD-2017. In *Model tests and numerical simulations of liquefaction and lateral spreading: LEAP-UCD-2017* (pp. 401–419). Springer.

Manzari, M. T., Kutter, B. L., Zeghal, M., Iai, S., Tobita, T., Madabhushi, S. P. G., et al. (2014). LEAP projects: Concept and challenges. In *Geotechnics for catastrophic flooding events* (pp. 109–116). CRC Press.

Tobita, T., Iai, S., Tann, L. V., & Yaoi, Y. (2011). Application of the generalized scaling law to saturated ground. *International Journal of Physical Modelling in Geotechnics, 11*(4), 138–155.

Tobita, T., Manzari, M. T., Ozutsumi, O., Ueda, K., Uzuoka, R., & Iai, S. (2014). *Benchmark centrifuge tests and analyses of liquefaction-induced lateral spreading during earthquake*. Taylor and Francis.

White, D. J., Take, W. A., & Bolton, M. D. (2003). Soil deformation measurement using particle image velocimetry (PIV) and photogrammetry. *Geotechnique, 53*(7), 619–631.

Zhou, Y. G., Sun, Z. B., & Chen, Y. M. (2018). Zhejiang University benchmark centrifuge test for LEAP-GWU-2015 and liquefaction responses of a sloping ground. *Soil Dynamics and Earthquake Engineering, 113*, 698–713.

Part III
Numerical Simulation Papers

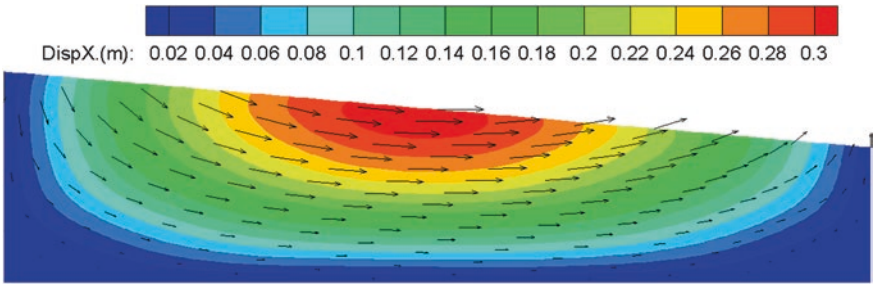

Zhijian Qiu and Ahmed Elgamal

Chapter 14
Type-C Simulations of Centrifuge Tests from LEAP-ASIA-2019 Using SANISAND-Sf

Andrés Reyes, Andrés R. Barrero, and Mahdi Taiebat

Abstract This chapter presents Type-C numerical simulations of prototype-scale centrifuge tests on gently sloped liquefiable deposits of Ottawa F65 sand for the LEAP-ASIA-2019 project. The simulations aim to assess the performance of the numerical modeling approach and a SANISAND-type constitutive model for large post-liquefaction shear deformation of sands. The constitutive model is calibrated against cyclic torsional shear tests conducted at different relative density levels and cyclic shear stress amplitudes. The laboratory-determined hydraulic conductivity of sand is doubled and kept constant during the dynamic stage of the analyses to account for the increase in permeability experienced during liquefaction. The simulations successfully capture the acceleration response and excess pore water pressure generation and dissipation of the slope deposit when soil liquefaction is observed. However, accurately modeling lateral displacements remains challenging in most cases. The results provide insights into the capabilities and limitations of the adopted Type-C numerical simulations, numerical modeling approach, and constitutive model.

Keywords Liquefaction Experiments and Analysis Project (LEAP-ASIA-2019) · Numerical modelling · SANISAND-Sf

A. Reyes · M. Taiebat (✉)
Department of Civil Engineering, University of British Columbia, Vancouver, BC, Canada
e-mail: mtaiebat@civil.ubc.ca

A. R. Barrero
Department of Civil Engineering, University of British Columbia, Vancouver, BC, Canada

SRK Consulting Inc., Vancouver, BC, Canada

T. Tobita et al. (eds.), *Model Tests and Numerical Simulations of Liquefaction and Lateral Spreading II*, https://doi.org/10.1007/978-3-031-48821-4_14

14.1 Introduction

Soil liquefaction and its consequences on infrastructure continue to be among the most challenging and important subjects of study in geotechnical earthquake engineering. In the last two decades, numerical modeling has started to play a major role in liquefaction hazard assessments, primarily through the use of relatively simple to sophisticated constitutive models, a variety of continuum mechanics-based numerical platforms, and perhaps most importantly, due to the introduction of performance-based design in engineering practice. While constitutive models allow simulating, to some extent, the key characteristics of soil stress-strain response, numerical platforms provide the means to translate such element-scale behavior into engineering demand parameters. It is then paramount to evaluate the capabilities and limitations of numerical platforms and constitutive models against reliable experimental data to properly estimate the consequences of soil liquefaction. Precisely, the LEAP (Liquefaction Experiments and Analysis Projects, Kutter et al., 2018) series of research projects is a collaborative effort with the main objective of providing high-quality laboratory and centrifuge test results to assess the performance of simulating tools and soil constitutive models and understanding their range of applicability and limitations. LEAP works upon the lessons learned in the VELACS project (Verification of Liquefaction Analysis and Centrifuges Studies, Arulanandan, 1994), and has had several installments so far. The first one was held at the University of Kyoto, followed by LEAP-GWU-2015 hosted at George Washington University, LEAP-UCD-2017 at the University of California at Davis, and LEAP-ASIA-2019 hosted at Kansai University, and LEAP-RPI-2020 hosted at the Rensselaer Polytechnic Institute in 2020.

This chapter deals with the numerical simulations conducted at the University of British Columbia (UBC) for LEAP-ASIA-2019. Phase I of this project consisted of constitutive model calibration based on the results of hollow cylinder cyclic torsional shear tests on samples of Ottawa F65 sand, which complemented the monotonic and cyclic triaxial and simple shear tests from earlier projects. For this purpose, a recently developed constitutive model for large post-liquefaction deformation (Barrero et al., 2020), based on the bounding surface plasticity model SANISAND, was used. Then, Phase II consisted of Type-C simulations of eight unidirectional shaking centrifuge tests. Each test followed almost identical specifications as in LEAP-UCD-2017 and consisted of a submerged, gently sloping ground of medium-dense sand subjected to a ramped sine base excitation. The simulations were carried out in a coupled three-dimensional (3D) finite difference numerical platform where the constitutive model was implemented and verified (Barrero, 2019). The following sections describe the simulated centrifuge tests, the constitutive model and its calibration, the numerical modeling approach, and the comparison of experimental and numerical results.

14.2 Summary of Simulated Centrifuge Experiments

14.2.1 Description of Centrifuge Tests

The results of eight unidirectional centrifuge tests (Vargas et al., 2023a; Korre et al., 2023; Stone et al., 2023) were timely shared with the UBC team. The prototype target soil deposit of the centrifuge tests was a 4 m deep, 20 m long submerged deposit of Ottawa F65 sand with a ground slope of approximately 5°. This deposit was subjected to a ramped sine wave input motion at its base; further details can be found in Tobita et al. (2023). Five of the centrifuge tests corresponded to the set labeled as Model A: "standard" centrifuge tests with a scaling factor directly related to the centrifugal acceleration η. The other three tests were labeled as Model B, in which the scaling was determined in accordance with the generalized scaling law (Iai et al., 2005), which includes a scaling factor μ for the virtual model, as well as η. The experiments made available to the UBC team were carried out in the centrifuge facilities at Kyoto University (KyU), Rensselaer Polytechnic Institute (RPI), and the University of California at Davis (UCD). The experimental test data included the time histories of acceleration at the base and within the soil deposit, the excess pore water pressures, and the displacements. Table 14.1 summarizes the relevant characteristics of the simulated centrifuge tests.

14.2.2 Base Excitations

Figure 14.1 shows the achieved or recorded base excitations in terms of acceleration time histories of centrifuge tests KyU_A1 and RPI_B1. The Fourier spectra of the recordings, also presented in Fig. 14.1, reveal the presence of low frequency (<0.1 Hz) or long-period waves in the recorded base excitations. The nature of these

Table 14.1 Summary of simulated centrifuge tests

Class	Centrifuge test	Density (kg/m^3)	D_r (%)	Void ratio[a]	Virtual μ	Centrifuge η	PGA_{eff}[b] (g)
Model A	KyU_A1	1677.0	73	0.580	1	44.4	0.248
	KyU_A2	1628.0	56	0.628	1	44.4	0.118
	RPI_A1	1651.0	64	0.605	1	23.0	0.143
	UCD_A1	1713.3	86	0.547	1	43.75	0.178
	UCD_A2	1658.1	67	0.598	1	43.75	0.134
Model B	KyU_B1	1673.0	72	0.584	2	22.2	0.252
	KyU_B2	1633.0	58	0.623	2	22.2	0.126
	RPI_B1	1644.0	62	0.612	0.5	46.0	0.151

[a]Void ratio values calculated for a specific gravity of 2.65 (El Ghoraiby et al., 2020)
[b]See Kutter et al. (2020) for the definition of PGA_{eff}

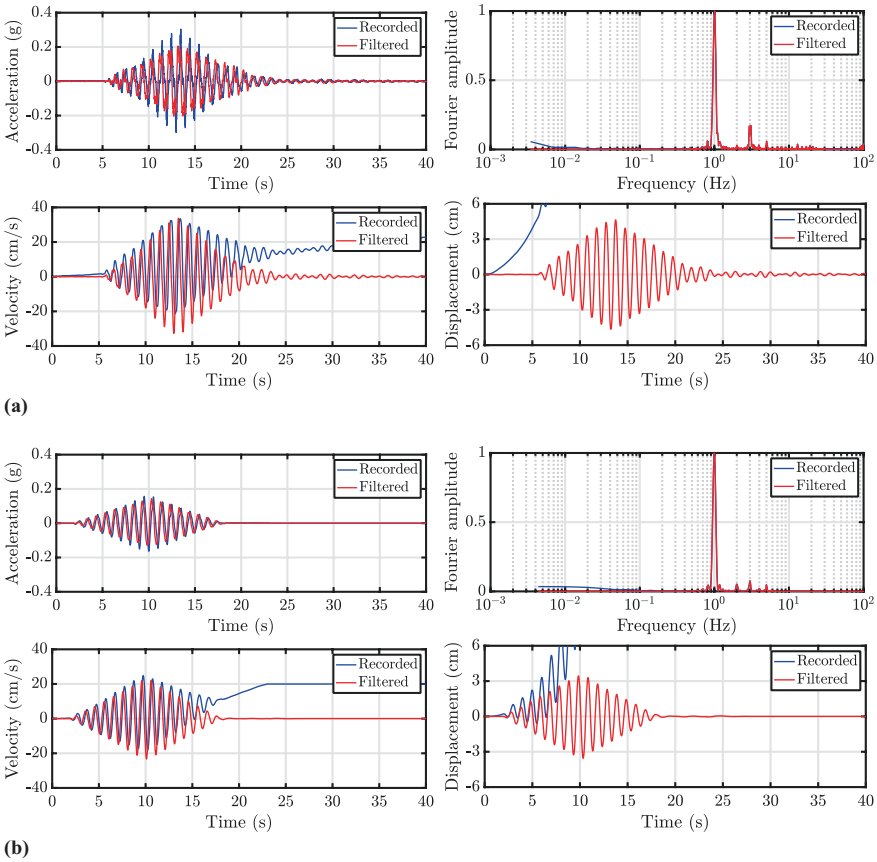

Fig. 14.1 Recorded and filtered acceleration time histories along with their respective Fourier spectra and calculated velocity and displacement records of centrifuge tests: (**a**) KyU_A1 and (**b**) RPI_B1

waves differs significantly from that of the waves with frequencies of 1–3 Hz also present in the excitations, which are consistent with the target input motion (Tobita et al., 2023). The effect of this apparent noise can be further observed in the undesired "waviness" and deviations observed in velocity and displacement time histories, obtained by integration of the acceleration records, also depicted in Fig. 14.1. Similar observations on the recorded base excitations were identified for all of the other centrifuge tests. The nature of these noises is unclear, but they were found to have negative consequences in the numerical simulations. For example, using this "raw" base excitation resulted in an unrealistic pattern of excess pore water pressure built-up, which started much earlier than expected and at a significantly different phase than the base excitation. Consequently, the UBC team decided to process the motions by means of fourth-order highpass digital Butterworth-type filters with bounding frequencies of 0.4–0.8 Hz to 25 Hz. Figure 14.1 shows the filtered base excitations and the corresponding Fourier spectra and velocity and displacement

Table 14.2 Summary of filter used in base excitations

Class	Centrifuge test	Filter range (Hz)	PGA before filter (*g*)	PGA after filter (*g*)
Model A	KyU_A1	0.5–25	0.304	0.205
	KyU_A2	0.5–25	0.134	0.140
	RPI_A1	0.4–25	0.150	0.155
	UCD_A1	0.6–25	0.213	0.168
	UCD_A2	0.6–25	0.150	0.143
Model B	KyU_B1	0.8–25	0.312	0.270
	KyU_B2	0.8–25	0.163	0.154
	RPI_B1	0.4–25	0.164	0.143

time histories. As can be observed, the filters eliminated the low-frequency waves and the deviations in the velocity and displacement time histories but caused some differences in the phase and peak of acceleration records. Changes in the peak acceleration are summarized in Table 14.2. The filtered motions were used as base input in the Type-C simulations of this study.

14.3 Constitutive Model

This section presents a brief description of the constitutive model used throughout this study along with its calibration against the hollow cylinder cyclic torsional shear tests on Ottawa sand conducted for LEAP-ASIA-2019.

14.3.1 SANISAND-Sf Model

The material constitutive model used by the UBC team in simulating both the element and centrifuge tests for LEAP-ASIA-2019 is a recently developed extension of the SANISAND model class. SANISAND stands for Simple ANIsotropic SAND constitutive model, a generic name that was introduced in Taiebat and Dafalias (2008) and follows the basic premises of the original two-surface plasticity model developed by Manzari and Dafalias (1997) and its sequel by Dafalias and Manzari (2004). Its constitutive framework is based on bounding surface plasticity with kinematic hardening of the yield surface and critical state soil mechanics concepts, allowing for a unified description of any pressure and density by the same set of model constants. The former studies represent the core of the constitutive model, and a number of subsequent works include different extensions and constitutive features that can be added to the original framework. This study considers a recent extension developed by Barrero et al. (2020), which addresses the progressive development of large post-liquefaction shear strains. By introducing a new state internal variable named Strain Liquefaction Factor, the extended SANISAND

Table 14.3 SANISAND-Sf model parameters for Ottawa F65

Parameter category	Symbol	Value	Parameter category	Symbol	Value
Elasticity	G_0	125	Dilatancy	n^d	2.5
	ν	0.05		A_0	0.5
Critical state line	M	1.26	Fabric dilatancy	z_{max}	25
	C	0.8		c_z	2000
	e_0	0.780	Overshooting correction	$\bar{e}^p_{eq}$	0.01%
	λ	0.0287		n	1
	ξ	0.8	Semifluidized state	x	3
Yield surface	m	0.02		c_l	80
Kinematic hardening	n^b	2.3		p_{inr}	18 kPa
	h_0	6.0		a	8
	c_h	0.968			

model is able to progressively degrade the plastic modulus and dilatancy, when the model enters the so-called semifluidized state. The simultaneous reduction of plastic modulus and dilatancy allows for increasing the plastic deviatoric strain rate while maintaining the same plastic volumetric strain rate. During undrained cyclic loading, the semifluidized state is defined as the state when sand experiences a sudden but temporary loss of stiffness, typically leading to a progressive accumulation of shear strains in each loading cycle. Such a state essentially happens at very low effective stresses. Extending the SANISAND framework with the semifluidized state formulation overcomes the apparent early lock-up of stress-strain loops in the post-liquefaction of the original model.

The SANISAND version of Dafalias and Manzari (2004), together with an overshooting correction scheme as described in Dafalias and Taiebat (2016) and the novel semifluidized state formulation introduced by Barrero et al. (2020), has been considered as the soil constitutive model in this work, and is referred to as SANISAND-Sf hereafter. Table 14.3 summarizes the model constants. An extensive description of the model formulation and role of the parameters can be found in the related foregoing reference and is not repeated here. Model implementation and testing in FLAC^{3D} v5 (Itasca, 2013) was completed by Barrero (2019). This implementation has already been employed and compared against another one in a different numerical platform in the comprehensive study by Ramirez et al. (2018) and was subsequently used in Reyes et al. (2019). The implementation has then been updated for the extended SANISAND and used for this project.

14.3.2 Model Calibration

As part of Phase I of LEAP-ASIA-2019, the UBC team calibrated SANISAND-Sf against a series of hollow cylinder cyclic torsional shear tests conducted at KyU (Vargas et al., 2023b). The tests selected for this study consisted of saturated samples of Ottawa F65 sand reconstituted to target relative densities (D_r) of 50% and

60% and isotopically compressed to an effective confining pressure of approximately 100 kPa. The samples were then cyclically sheared at cyclic stress ratios (CSR) ranging from 0.10 to 0.20.

Calibration was completed in a single-element configuration in FLAC^{3D}, in which the volume change was prevented during shearing to simulate the undrained conditions of the laboratory test. The elasticity and critical state parameters (see Table 14.3) were inherited from the calibration of the UBC team in LEAP-UCD-2017 (Yang et al., 2022). The parameters controlling the plastic modulus, dilatancy, and fabric dilatancy were updated in light of the new experimental evidence and to accommodate the extended formulation of the model. Details on the recommended calibration procedure for SANISAND-Sf are presented in Barrero et al. (2020). For this study, the calibration aimed first to capture the pre- and post-liquefaction response of the cyclic tests with CSR around 0.15. The pre-liquefaction response, that is, before attaining a mean effective stress close to zero for the first time, was reasonably well captured by tuning the kinematic hardening constants n^b and c_h, and the dilatancy parameters n^d and A_0. For the post-liquefaction response, parameters x, c_l, and p_{inr} from the semifluidized state formulation were selected so as to simulate the extent and pace of development of shear strains in post-liquefaction. For the remaining tests with different CSR, parameter a was selected in order to capture the CSR resistance curve. With this approach, the obtained liquefaction resistance is controlled by a balance between the pre- and post-liquefaction response of the model. Figure 14.2 summarizes the model performance by comparing the

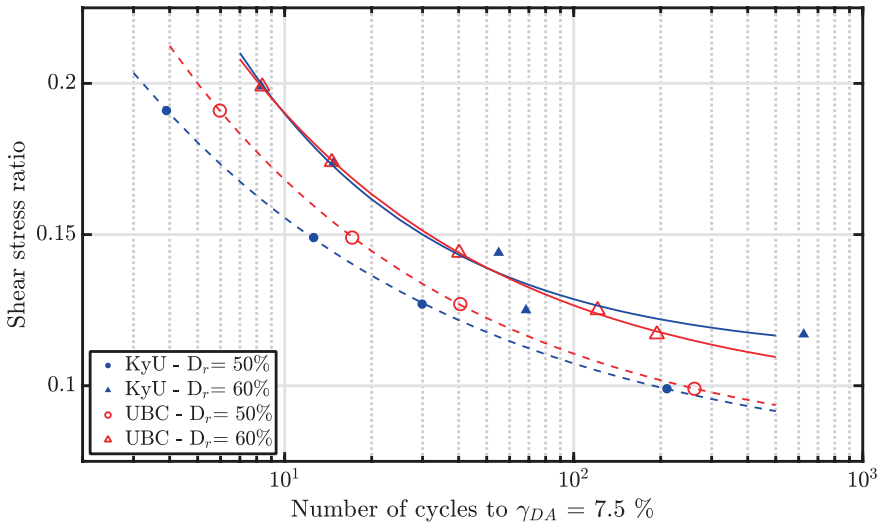

Fig. 14.2 Summary of experiments (blue, solid symbols, Vargas et al., 2023b) and simulations (red, hollow symbols) in terms of shear stress ratios and the corresponding number of cycles to reach a double amplitude shear strain of 7.5%. The lines represent the interpolated liquefaction resistance curves for D_r of 50% (dashed) and 60% (continuous)

liquefaction resistance from experiments and simulations based on the number of cycles to reach a double amplitude shear strain of 7.5%, showcasing a good match between them. Table 14.3 presents the constitutive model constants, which were used in the Type-C simulations.

14.4 Numerical Model Specifications

14.4.1 Numerical Platform

The simulations of the centrifuge tests were conducted in the finite difference program FLAC^{3D}, which uses an explicit time-integration scheme to model the dynamic response of 3D continuous media. In this program, the continuous media is replaced by a discrete-equivalent domain in which forces and displacements involved in the analysis are concentrated at the nodes of the 3D mesh used in representing the domain. Each zone or element of the mesh is comprised by a number of constant strain-rate subzones of tetrahedral shape whose vertices coincide with the ones of the zone. Solid-pore fluid interaction in this platform is based on the well-established coupled formulations of poromechanics originated by Biot (1941) and extended by Detournay and Cheng (1993). The numerical scheme for the coupled formulation in fully saturated media relies on a fluid continuity equation, which relates fluid flow to changes in pore pressure and volumetric strain. Solving this equation requires a series of steps involving fluid flow loops followed by mechanical loops to maintain equilibrium state. The fluid flow loops calculate changes in pore pressure while the mechanical loops address the changes in volumetric strain due to the adjustment of effective stress induced by the fluid flow loops. A built-in isotropic fluid model is used in this study for simulation of the mechanical response of the pore fluid.

14.4.2 Numerical Model Configuration

The numerical models of the centrifuge tests were completed for the prototype scale model, as the main objective of this study was to verify the performance and limitations of SANISAND-Sf. Validation of the generalized scaling law, which was another purpose of the LEAP-ASIA-2019, would have required complementary simulations at the model scale, and was not included in this chapter.

The numerical models consisted of a 3D finite difference mesh built with 40 zones in the slope dip direction, 8 zones in the height direction, and 1 zone in the slope strike direction, for a total of 320 zones. The zone sizes were 0.5 m in the slope dip direction and 0.39–0.61 m in the height direction. The grid points on the

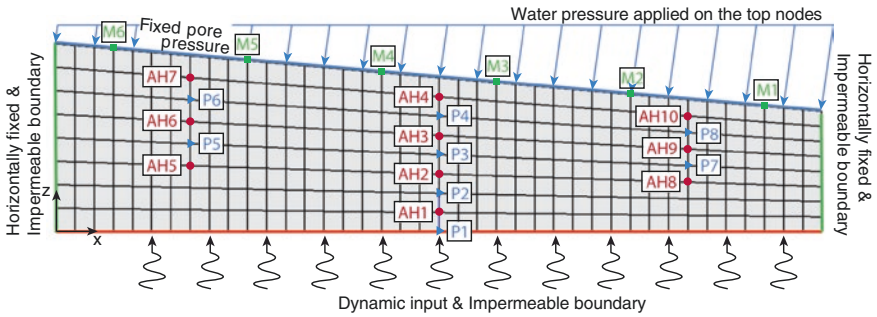

Fig. 14.3 Cross-section of the FLAC^{3D} mesh and boundary conditions adopted in the prototype scale numerical model used. Recording locations are also shown for horizontal accelerations (AH), excess pore water pressures (P), and surface displacement markers (M). Note that the centrifuge facility at RPI adopted a different arrangement of surface markers not shown here

model base were fully constrained along all three directions during the static part of the analysis, while the grid points of the side walls were laterally constrained. This prevented deformation in the slope strike direction, hence working in a similar way as a plain strain condition. During the dynamic stage, the degree of freedom at the model's base corresponding to the shaking direction, i.e., slope dip direction, was freed. The grid points on the top surface of the slope were allowed full drainage with fixed values of pore pressure in order to model the real submerged conditions of the experiments. Furthermore, during the dynamic stage, Rayleigh damping with a small damping target value of 1% was used to prevent high-frequency artificial noise. The mesh density, boundary conditions, and the location of the instrumentation and displacement markers are presented in Fig. 14.3.

14.4.3 Soil Properties

The SANISAND-Sf model parameters determined in Sect. 14.3.2 were used in the centrifuge simulations and they were not updated upon examination of the centrifuge experiment results. Taking advantage of the critical state framework of SANISAND, only the initial void ratio was changed in each centrifuge simulation according to the values in Table 14.1.

For the solid-fluid interaction, the isotropic fluid model implemented in FLAC^{3D} was used, with a water bulk modulus of 2.2×10^6 kPa. Soil hydraulic conductivity was first estimated based on the average initial void ratio of the centrifuge tests and the constant head permeability tests conducted by El Ghoraiby et al. (2020) as $k = 1.15 \times 10^{-4}$ m/s. Note that variation of the hydraulic conductivity with the initial void ratio was negligible.

14.4.4 Simulation Procedure

In order to establish a reasonable initial stress state of the model in the prototype scale, the numerical simulations started with a staged construction of the slope, where the dry soil deposit was constructed in layers and was allowed to establish its stress state under the gravity of 1g. In this process, the mechanical boundary conditions were configured as shown in Fig. 14.3, except for the stress boundary condition on the top surface of the slope. This stage used a simple Mohr-Coulomb material model assigned to the sand layers with a bulk modulus of 6.22×10^5 kPa, shear modulus of 2.38×10^6 kPa, and a friction angle of 33 degrees. After achieving mechanical equilibrium for all layers of the soil deposit, the fluid-mechanical interaction module was activated, and a normal stress gradient representing the target submerged pressures of water was applied on the top surface of the slope, as shown in Fig. 14.3. The pore water pressures at the top surface were fixed to the submerged pressures. Upon reaching mechanical and fluid equilibrium, the constitutive model for the sand was switched to the SANISAND-Sf.

Once the changes of stresses and pore water pressures induced by the change of constitutive model were stabilized, the dynamic analysis feature embedded in the numerical platform was activated. The resulting ratio of effective initial horizontal to vertical stresses (K_0) ranged from 0.44 to 0.6 along the model, with an average of 0.49. Furthermore, the initial ratio of static bias, that is, the ratio of shear stress to effective vertical stress (α), ranged from 0.01 to 0.06 for an overall average of 0.04. For the dynamic analysis, the boundary conditions were updated in two stages: first, Rayleigh damping was added to the entire model, followed by mechanical-fluid-dynamic steps to further stabilize the model. Second, the degree of freedom in the x direction at the model's base was freed to accommodate the base excitation. Also, during the dynamic stage of the analyses, the hydraulic conductivity was doubled to account for the increase of permeability during the liquefaction stage, which has been recognized to occur in different studies (e.g., Manzari & Arulanandan, 1993; Taiebat et al., 2007; Shahir et al., 2012; Yang et al., 2020). The amount of increase was determined following sensitivity analyses which mainly took into consideration the dissipation pattern of pore water pressure. The increased value of hydraulic conductivity, $k^* = 2.29 \times 10^{-4}$ m/s, was kept constant throughout the dynamic stage and for all centrifuge models.

Finally, the filtered accelerations records were applied at the base grid points; the duration of the analyses went beyond the significant duration of the base excitation, allowing for the dissipation of excess pore water pressure and displacement stabilization. The total length of the shearing and dissipation process was determined by the duration of the experimental recordings of accelerations and excess pore water pressure.

14.5 Type-C Simulation Results

The results of the Type-C numerical simulations are presented and compared with the experimental data for the eight centrifuge tests evaluated. The comparison is depicted in terms of acceleration time histories, acceleration response spectra, excess pore water pressure time histories, and displacement time histories at control points and markers at the center of the centrifuge model (see Fig. 14.3). It is important to highlight that although the recorded base accelerations were filtered before their application in the simulations, the experimental recordings of accelerations and others in the soil deposit body were not filtered in the displayed comparison.

14.5.1 Typical Results

Here, the typical results of the simulations are described with respect to the centrifuge model UCD_A2. Figure 14.4 shows the experimental and simulated acceleration response at the center of the model in terms of time histories and response spectra. It can be observed that the simulations are generally successful in capturing

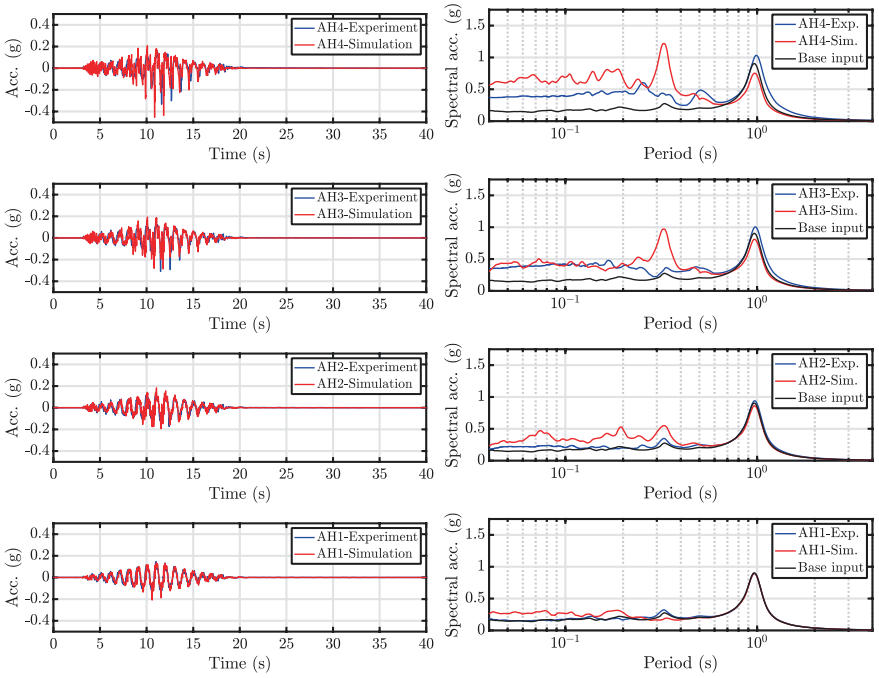

Fig. 14.4 Comparison of experimental and simulated acceleration response in centrifuge test UCD_A2 in terms of time histories and response spectra at the middle of the model

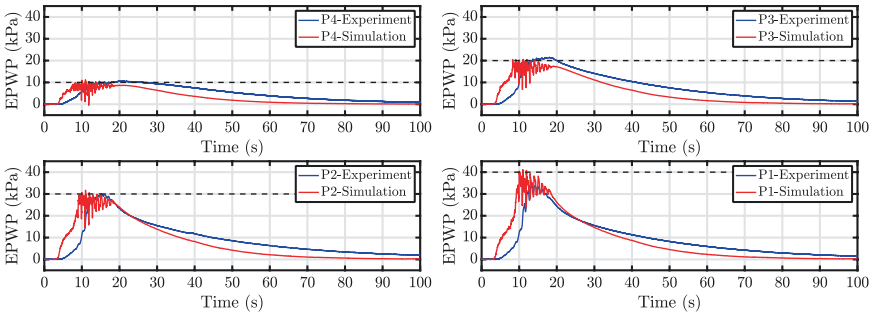

Fig. 14.5 Comparison of experimental and simulated excess pore water pressure response in centrifuge test UCD_A2 in terms of time histories at the middle of the model

the acceleration response in the time domain: in sensors AH1 and AH2, located at the bottom of the centrifuge and where no signs of severe liquefaction are apparent, the accelerations are closely captured. Similarly, in sensors AH3 and AH4, located at shallower depths and where liquefaction occurrence is evident due to the presence of sharp dilations spikes, the simulations were also able to closely capture the acceleration response in the time domain. The comparison in terms of response spectra further indicates that the simulations captured the acceleration response to a reasonable degree. However, it also shows that the simulated spectral accelerations for the fundamental period of the deposit, approximately 1 s, tend to be progressively underestimated at shallower depths, likely due to the occurrence of liquefaction.

Figure 14.5 presents the comparison of experimental and simulated excess pore water pressure generation and dissipation. The initial effective overburden pressures, approximately 40, 30, 20, and 10 kPa for piezometers P1, P2, P3, and P4, respectively, are also shown. The time histories show that the numerical results can reasonably capture the peak values of excess pore water pressure, although they also present relatively large spikes absent in the experimental recordings. Moreover, the rate of generation of excess pore water pressure is overestimated in the simulations. This simulated response has been found to be mostly associated with the SANISAND-Sf underestimation of the pre-liquefaction cyclic resistance at low values of CSR. On the other hand, the simulated dissipation rate is relatively close to the experimental evidence. Sensitivity analyses for this particular centrifuge model showed that around a 50% reduction in the constant and already increased hydraulic conductivity used in the simulations can significantly improve the match in the dissipation rate.

The lateral displacements at the center of the model, both recorded in the experiments and in the simulations, are shown in Fig. 14.6. It can be observed that the simulations tend to overestimate the displacements, in this case, by over 5 cm. This overestimation is thought to be associated, as is the generation of excess pore water pressure, with (a) the stiffness of SANISAND-Sf model for low values of CSR, (b) the presence of initial static shear stresses in the sloped model, and (c) the hydraulic conductivity and its likely variation during and after soil liquefaction.

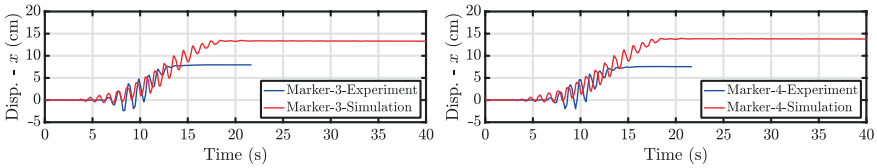

Fig. 14.6 Comparison of experimental and simulated lateral displacement in centrifuge test UCD_A2 in terms of time histories at the middle of the model

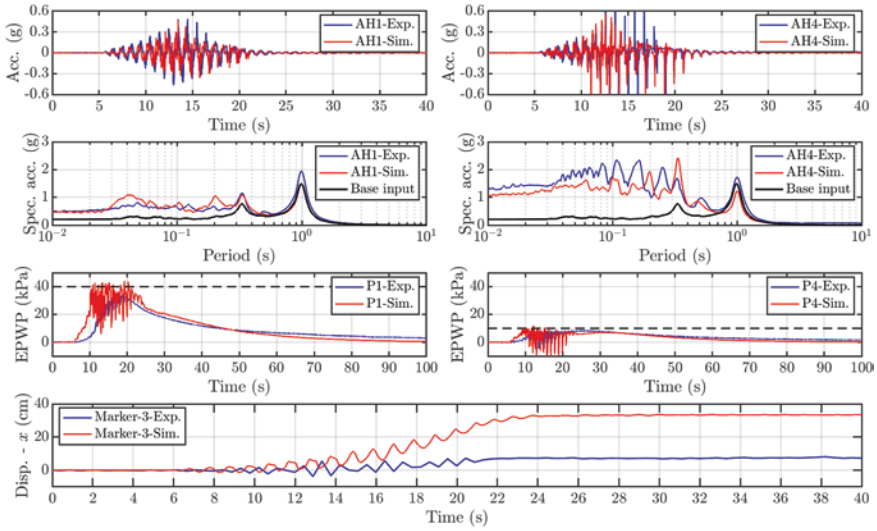

Fig. 14.7 Summary of acceleration, excess pore water pressure, and lateral displacement experimental and simulated response for centrifuge test KyU_A1

14.5.2 Summary of Numerical Simulations

To expand the assessment of the constitutive model performance, the comparison presented in the earlier section is extended to the other seven centrifuge tests. For brevity, the experimental and simulated results are illustrated for accelerometers AH1 and AH4, piezometers P1 and P4, and displacement marker M3, all of which are representative of the response of the center of the centrifuge models. In order to maintain consistency in the comparisons, Figs. 14.7, 14.8, 14.9, 14.10, 14.11, 14.12, 14.13 and 14.14 detail the results using the same scales.

The overall comparison reveals that in the six centrifuge tests where liquefaction occurred (KyU_A1, RPI_A1, UCD_A1, UCD_A2, KyU_B1, RPI_B1), evidenced by the significant dilation spikes in the acceleration records and high values of excess pore water pressure, the simulations were generally successful in capturing the experimental results. However, in most cases, the lateral displacements were overestimated, with the exception of model RPI_B1 where the simulation yielded

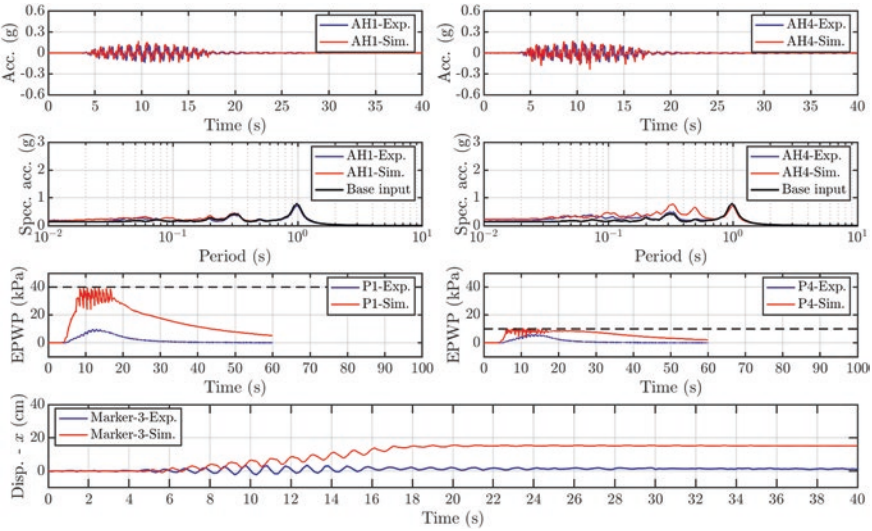

Fig. 14.8 Summary of acceleration, excess pore water pressure, and lateral displacement experimental and simulated response for centrifuge test KyU_A2

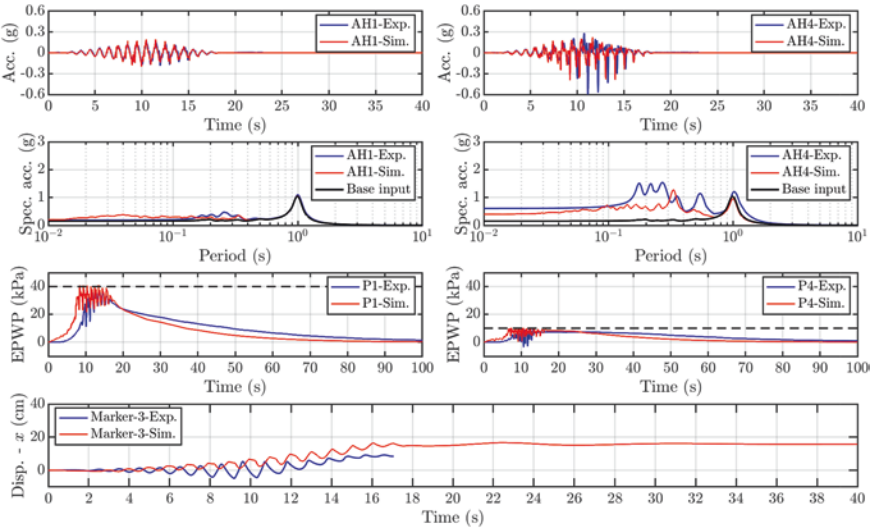

Fig. 14.9 Summary of acceleration, excess pore water pressure, and lateral displacement experimental and simulated response for centrifuge test RPI_A1

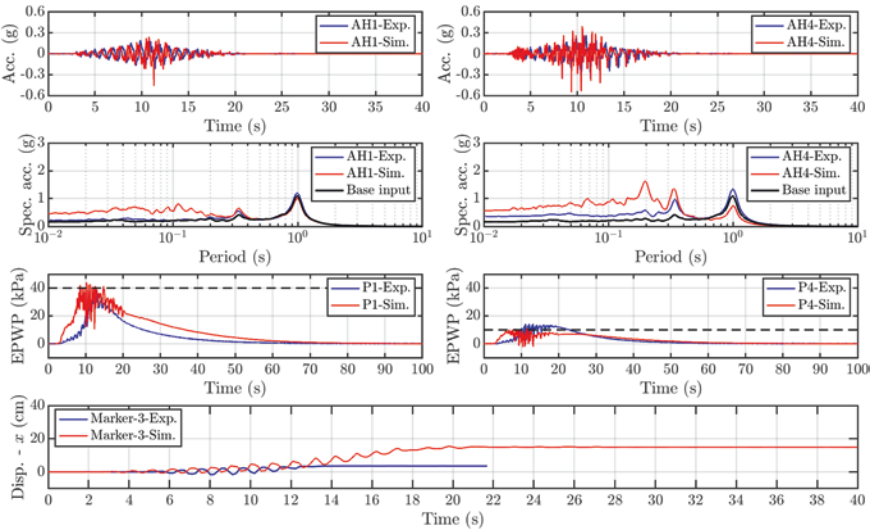

Fig. 14.10 Summary of acceleration, excess pore water pressure, and lateral displacement experimental and simulated response for centrifuge test UCD_A1

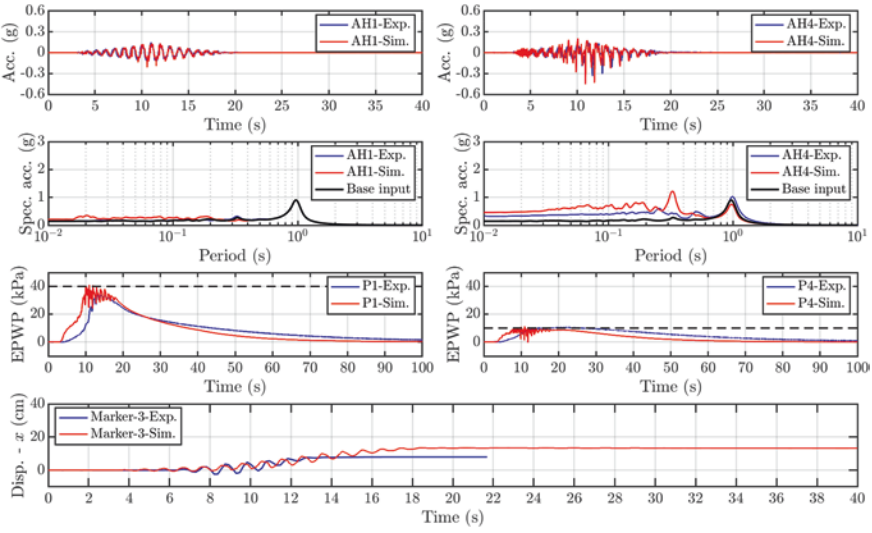

Fig. 14.11 Summary of acceleration, excess pore water pressure, and lateral displacement experimental and simulated response for centrifuge test UCD_A2

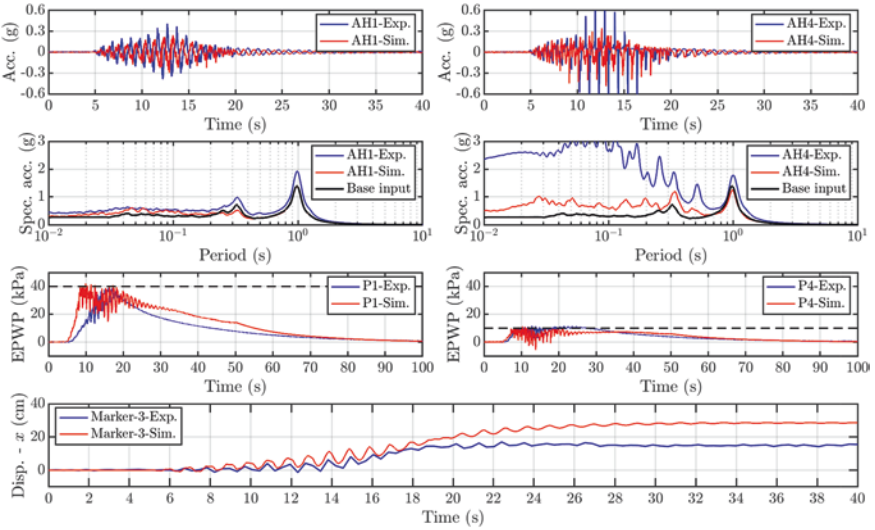

Fig. 14.12 Summary of acceleration, excess pore water pressure, and lateral displacement experimental and simulated response for centrifuge test KyU_B1

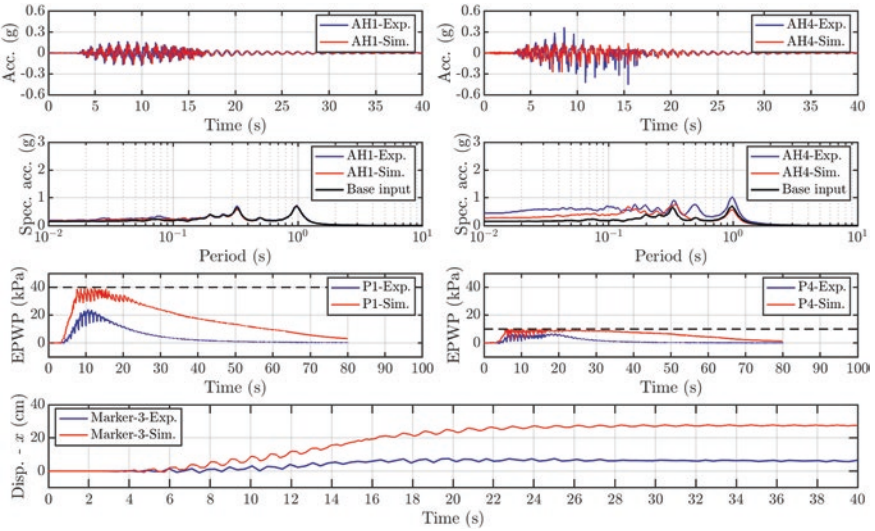

Fig. 14.13 Summary of acceleration, excess pore water pressure, and lateral displacement experimental and simulated response for centrifuge test KyU_B2

lower values than the experimental evidence. As detailed earlier, the overestimation of lateral displacements is likely caused by the underestimation of pre-liquefaction resistance for low values of CSR of the constitutive model, the presence of initial

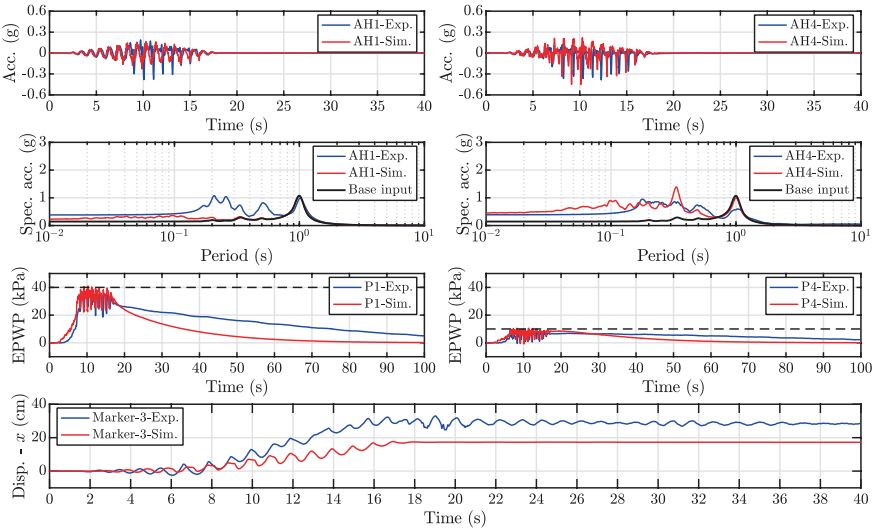

Fig. 14.14 Summary of acceleration, excess pore water pressure, and lateral displacement experimental and simulated response for centrifuge test RPI_B1

static shear stresses in the model, which was not accounted for in Phase I, and the selected value of hydraulic conductivity.

While filtering of base excitations was conducted for all models, an inspection of the acceleration time histories reveals some changes of phase in only a few of the models, particularly UCD_A1 and KyU_B1, which are among the ones with stronger "noise" of the base motion. Additional filtering of the recordings in the deposit body would have probably reduced the changes of phase observed here. Further commentaries on the nature and consequences of this apparent noise are presented in Perez et al. (2023). On the acceleration response spectra, as explained earlier, the simulations tend to underestimate the spectral acceleration for a period of 1 s for the shallower sensor, where evidence of liquefaction was observed in most cases.

As in Sect. 14.5.1, the simulations successfully capture the peak excess pore water pressures recorded in all of the centrifuge tests where liquefaction was triggered. However, the comparisons also reveal that the model overestimated the rate of excess pore water pressure generation, a response largely controlled by the pre-liquefaction stiffness of the extended SANISAND model. Nevertheless, the dissipation rate was surprisingly well captured by the simulations, albeit the use of the same constant value of hydraulic conductivity, k^*, doubled from the laboratory results, for all the numerical models. Yet, it is important to mention that even better results could be obtained by using different values of k* for each model, ranging from 0.5 to 3 times to the value of k. In tests KyU_A2 and KyU_B2, where liquefaction did not occur below sensor P4, the excess pore water overestimation caused further differences in the acceleration response and, most importantly, in the lateral displacements.

14.6 Summary and Outlook

This chapter presents the Type-C numerical simulations conducted at the University of British Columbia for the centrifuge tests of gently sloped liquefiable soil deposits in LEAP-ASIA-2019. For this purpose, the UBC team made use of an extended version of the SANISAND constitutive model, named SANISAND-Sf, which introduces a novel and elegant feature to reduce soil stiffness during undrained cyclic shearing and low values of confining pressure, to allow for the development and accumulation of large post-liquefaction shear deformations.

Phase I of this study consisted of calibrating the new model based on data from undrained hollow cylinder cyclic torsional shear tests. The resulting calibration succeeded in capturing the number of cycles to reach a double amplitude shear strain of 7.5% for different values of cyclic stress ratios. Phase II used such calibration to simulate eight centrifuge models in a finite difference computer program. The simulations revealed that the constitutive model and the adopted numerical modeling approach are reasonably successful in capturing the acceleration and pore water pressure response of the centrifuge tests where liquefaction was evidenced by dilation spikes and high values of excess pore pressure. However, the lateral displacements were overestimated by around 5–15 cm in most of the models.

The results presented here suggest that the performance of the numerical simulations with respect to capturing the experimental results can be improved by increasing the constitutive model stiffness, i.e., its pre-liquefaction resistance, for relatively low values of cyclic shear stress ratios. This can be effectively achieved by considering a new constitutive ingredient in the SANISAND class of models, as was done by Yang et al. (2022). Their latest extension provides the necessary flexibility to capture both pre- and post-liquefaction responses with accuracy. An improved prediction can also be accomplished by evaluating the model predictive capabilities of sand undrained response in the presence of static shear stresses and accounting for their effect. This has been shown to be of major relevance in the recent works of Reyes et al. (2021) and Perez et al. (2023). For this purpose, K_0-consolidated cyclic shear tests with initial static shear stress, representative of the initial stress state of the soil in the centrifuge tests, would be excellent data for model validation. The recent experimental works of El Ghoraiby and Manzari (2021) and Lbibb and Manzari (2023) represent major efforts in producing this type of evidence in which more realistic initial stress states, i.e., $K_0 \neq 1$ with static shear stresses, and cyclic shearing patterns are employed. Furthermore, it was shown that filtering and baseline correction of experimental recordings are important and can cause significant differences in numerical predictions. Ideally, the experimental team should process all records, and the filtering process should be communicated to the numerical simulation team. Finally, hydraulic conductivity and its likely change during and after shaking played a major role in the numerical predictions. Further research is required to determine an efficient procedure to properly model it.

References

Arulanandan, K. (1994). Verification of numerical procedures for the analysis of soil liquefaction problems. In *Conference proceedings* (Vol. 2). Balkema.

Barrero, A. R. (2019). *Multi-scale modeling of the response of granular soils under cyclic shearing.* Doctoral dissertation, PhD thesis. Department of Civil Engineering, University of British Columbia.

Barrero, A. R., Taiebat, M., & Dafalias, Y. F. (2020). Modeling cyclic shearing of sands in the semi-fluidized state. *International Journal for Numerical and Analytical Methods in Geomechanics, 44*(3), 371–388.

Biot, M. A. (1941). General theory of three-dimensional consolidation. *Journal of Applied Physics, 12*(2), 155–164.

Dafalias, Y. F., & Manzari, M. T. (2004). Simple plasticity sand model accounting for fabric change effects. *Journal of Engineering Mechanics, 130*(6), 622–634.

Dafalias, Y. F., & Taiebat, M. (2016). SANISAND-Z: zero elastic range sand plasticity model. *Géotechnique, 66*(12), 999–1013.

Detournay, E., & Cheng, A. H. D. (1993). Fundamentals of poroelasticity. In *Analysis and design methods* (pp. 113–171). Pergamon.

El Ghoraiby, M., & Manzari, M. T. (2021). Cyclic behavior of sand under non-uniform shear stress waves. *Soil Dynamics and Earthquake Engineering, 143*, 106590.

El Ghoraiby, M., Park, H., & Manzari, M. T. (2020). Physical and mechanical properties of Ottawa F65 sand. In *Model tests and numerical simulations of liquefaction and lateral spreading: LEAP-UCD-2017* (pp. 45–67). Springer.

Iai, S., Tobita, T., & Nakahara, T. (2005). Generalised scaling relations for dynamic centrifuge tests. *Geotechnique, 55*(5), 355–362.

Itasca, F. (2013). *Fast Lagrangian analysis of continua in 3 dimensions, Version 5.01*. Itasca Consulting Group.

Korre, E., Abdoun, T., & Zeghal, M. (2023). Experimental evaluation of lateral spreading of a liquefiable sloping deposit using centrifuge and generalized scaling law tests. In *Model tests and numerical simulations of liquefaction and lateral spreading 2: LEAP-ASIA-2019*. Springer.

Kutter, B. L., Carey, T. J., Hashimoto, T., Zeghal, M., Abdoun, T., Kokkali, P., et al. (2018). LEAP-GWU-2015 experiment specifications, results, and comparisons. *Soil Dynamics and Earthquake Engineering, 113*, 616–628.

Kutter, B. L., Carey, T. J., Stone, N., Bonab, M. H., Manzari, M. T., Zeghal, M., et al. (2020). LEAP-UCD-2017 v. 1.01 model specifications. In *Model tests and numerical simulations of liquefaction and lateral spreading: LEAP-UCD-2017* (pp. 3–29). Springer.

Lbibb, S., & Manzari, M. T. (2023). Stress-strain behavior of Ottawa sand in cyclic direct simple shear and modeling of cyclic strength using Artificial Neural Networks. *Soil Dynamics and Earthquake Engineering, 164*, 107585.

Manzari, M. T., & Arulanandan, K. (1993). Numerical predictions for model No. 1. In *Verification of numerical procedures for the analysis of soil liquefaction problems* (pp. 179–185). A.A. Balkema.

Manzari, M., & Dafalias, Y. F. (1997). A critical state two-surface plasticity model for sand. *Geotechnique, 47*(2), 255–272.

Perez, K., Reyes, A., & Taiebat, M. (2023). Roles of pre- and post-liquefaction stages in dynamic system response of liquefiable sand retained by a sheet-pile wall. *Soil Dynamics and Earthquake Engineering, 171*, 107937.

Ramirez, J., Barrero, A. R., Chen, L., Dashti, S., Ghofrani, A., Taiebat, M., & Arduino, P. (2018). Site response in a layered liquefiable deposit: Evaluation of different numerical tools and methodologies with centrifuge experimental results. *Journal of Geotechnical and Geoenvironmental Engineering, 144*(10), 04018073.

Reyes, A., Adinata, J., & Taiebat, M. (2019). Impact of bidirectional seismic shearing on the volumetric response of sand deposits. *Soil Dynamics and Earthquake Engineering, 125*, 105665.

Reyes, A., Yang, M., Barrero, A. R., & Taiebat, M. (2021). Numerical modeling of soil liquefaction and lateral spreading using the SANISAND-Sf model in the LEAP experiments. *Soil Dynamics and Earthquake Engineering, 143*, 106613.

Shahir, H., Pak, A., Taiebat, M., & Jeremić, B. (2012). Evaluation of variation of permeability in liquefiable soil under earthquake loading. *Computers and Geotechnics, 40*, 74–88.

Stone, N. S., Carey, T. J., Santana, A., & Kutter, B. L. (2023). LEAP-ASIA-2019 centrifuge test at University of California, Davis. In *Model tests and numerical simulations of liquefaction and lateral spreading 2: LEAP-ASIA-2019*. Springer.

Taiebat, M., & Dafalias, Y. F. (2008). SANISAND: Simple anisotropic sand plasticity model. *International Journal for Numerical and Analytical Methods in Geomechanics, 32*(8), 915–948.

Taiebat, M., Shahir, H., & Pak, A. (2007). Study of pore pressure variation during liquefaction using two constitutive models for sand. *Soil Dynamics and Earthquake Engineering, 27*(1), 60–72.

Tobita, T., Ichii, K., Ueda, K., Uzuoka, R., Vargas, R., Okamura, M., Sjafruddin, A. N., Takemura, J., Hang, L., Iai, S., Boksmati, J., Fusco, A., Torres-Garcia, S., Haigh, S., Madabhushi, G., Manzari, M., Escoffier, S., Li, Z., Kim, D. S., Manandhar, S., Hung, W. Y., Huang, J. X., Pham, T. N. P., Zeghal, M., Abdoun, T., Korre, E., Kutter, B. L., Carey, T. J., Stone, N., Zhuo, Y. G., Liu, K., & Ma, Q. (2023). LEAP-ASIA-2019: Summary of centrifuge experiments on liquefaction-induced lateral spreading: Validation and applicability of the generalized scaling law. In *Model tests and numerical simulations of liquefaction and lateral spreading 2: LEAP-ASIA-2019*. Springer.

Vargas, R. R., Ueda, K., & Tobita, T. (2023a). LEAP-ASIA-2019 centrifuge test at Kyoto University. In *Model tests and numerical simulations of liquefaction and lateral spreading 2: LEAP-ASIA-2019*. Springer.

Vargas, R. R., Ueda, K., & Uemura, K. (2023b). Dynamic torsional shear tests of Ottawa F-65 sand for LEAP-ASIA-2019. In *Model tests and numerical simulations of liquefaction and lateral spreading 2: LEAP-ASIA-2019*. Springer.

Yang, M., Barrero, A. R., & Taiebat, M. (2020). Application of a SANISAND model for numerical simulations of the LEAP 2017 experiments. In *Model tests and numerical simulations of liquefaction and lateral spreading: LEAP-UCD-2017* (pp. 595–610). Springer.

Yang, M., Taiebat, M., & Dafalias, Y. F. (2022) SANISAND-MSf: a sand plasticity model with memory surface and semifluidised state. *Géotechnique, 72*(3) 227–246.

Chapter 15
LEAP-ASIA-2019 Numerical Simulations Using a Strain Space Multiple Mechanism Model for a Liquefiable Sloping Ground

Yoshikazu Tanaka, Anurag Sahare, Kyohei Ueda, Waka Yuyama, and Susumu Iai

Abstract This chapter presents the numerical simulations using a strain space multiple mechanism model on a liquefiable sloping ground during earthquake excitation which are compared with the results obtained from the centrifuge tests conducted at different centrifuge facilities as a part of LEAP-ASIA-2019 with an effort to validate the generalized scaling laws. The constitutive model parameters were determined based on the results of cyclic torsional shear tests. One of the key objectives of this chapter is to assess the differences arising in the soil system responses depending on the three different predictors when using the same constitutive model. For this purpose, the soil constitutive model parameters were calibrated differently, and all the predictors were able to capture the important features of saturated sand during undrained cyclic shearing. This was followed by the numerical simulations of the centrifuge data, which showed no predominant differences in the simulated results due to the different soil constitutive model parameters. However, the amount of shear-induced dilatancy experienced by the sand during cyclic shearing was found out to be different among predictors. It is also highlighted that predictors may achieve the ideal measured results either by performing numerical simulations in model scale or in prototype scale.

Keywords Liquefaction Experiments and Analysis Project (LEAP-ASIA-2019) · Numerical modelling · FLIP

Y. Tanaka · A. Sahare · K. Ueda (✉)
Disaster Prevention Research Institute, Kyoto University, Kyoto, Japan
e-mail: ueda.kyohei.2v@kyoto-u.ac.jp

W. Yuyama · S. Iai
FLIP Consortium, Kyoto, Japan

T. Tobita et al. (eds.), *Model Tests and Numerical Simulations of Liquefaction and Lateral Spreading II*, https://doi.org/10.1007/978-3-031-48821-4_15

15.1 Introduction

The Liquefaction Experiments and Analysis Project (LEAP) is an international research collaborative venture for validating and assessing the suitability of various soil constitutive models based on the extensive validation exercise with centrifuge testing conducted at different geotechnical centrifuge facilities around the world. The main objective of the LEAP-ASIA-2019 project was to validate the generalized scaling laws proposed by Iai et al. (2005). To this end, this chapter presents the numerical simulation exercise to assess the capability of the strain space multiple mechanism model in capturing the response of a saturated sloping ground during earthquake-induced liquefaction and lateral spreading. It is thought that numerical simulation results might be governed significantly depending on the numerical predictors, for which the numerical simulations were conducted by three different numerical predictors and a particular focus has been given to the problem of (a) constitutive model calibration (b) the effects arising due to a different scale, i.e., model and prototype scale, and (c) effect of mesh size in the simulation.

15.2 Brief Summary of the Centrifuge Experiments

Figure 15.1 shows the adopted schematic model for LEAP-ASIA-2019 centrifuge tests. Some of the centrifuge facilities were excited with an earthquake waveform parallel to the axis of centrifuge, whereas some of the facilities were shaken in the circumferential direction of the centrifuge arm. It is to be noted that in the latter case, the ground surface was curved to consider the influences arising due to a radial gravity field during spin up in a short arm centrifuge (see Tobita et al., 2018 and Sahare et al., 2020 for further details). The model is a liquefiable sloping ground and is composed of Ottawa F-65 sand, with a 5-degree inclination. Figure 15.1 also shows the location of various instrumentations used during the centrifuge testing, where "AH" indicates an accelerometer and "P" portrays a pore pressure transducer. The centrifuge tests were performed at different facilities to capture the soil system response under different physical conditions with a different achieved soil relative density and with different earthquake characteristics having an altered imparted input acceleration amplitude. As mentioned previously, the major objective of LEAP-ASIA-2019 project was to validate the generalized scaling laws, for which two different models were developed: Model A (tested as per the conventional scaling laws) and Model B (tested as per the generalized scaling laws). Tables 15.1 and 15.2 indicate the centrifuge experiments which were used to validate the developed numerical models reported in this chapter.

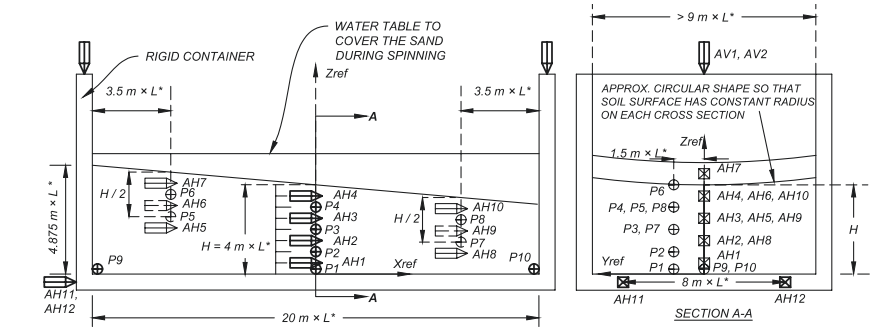

Fig. 15.1 Schematic representation of LEAP-ASIA-2019 centrifuge model tests: (**a**) Sectional view for shaking parallel to the axis of the centrifuge; (**b**) Sectional view for shaking in the plane of spinning of the centrifuge

Table 15.1 Summary of centrifuge experiments, Model A in LEAP-ASIA-2019

Test case	Density (kg/m^3)	Dr (%)	Virtual 1G, μ	Centrifuge, η	PGAeff (g)	Avg. disp. (mm)	Shaking direction
KyU_A_A2_1	1628	56	1	44.4	0.118	11.10	Tangential
RPI_A_A1_1	1651	64	1	23	0.143	99.56	Axial
UCD_A_A2_1	1658.1	67	1	43.75	0.134	77.50	Tangential

Table 15.2 Summary of centrifuge experiments, Model B in LEAP-ASIA-2019

Test case	Density (kg/m^3)	D_r (%)	Virtual 1G, μ	Centrifuge, η	PGAeff (g)	Avg. disp. (mm)	Shaking direction
KyU_A_B2_1	1633	58	2	22.2	0.126	34.54	Tangential
RPI_A_B1_1	1644	62	0.5	46	0.151	303.27	Axial

15.3 Strain Space Multiple Mechanism Model

The numerical analysis was conducted using a strain space multiple mechanism model incorporating a new stress-dilatancy relationship (Iai et al., 2011). The strain space multiple mechanism model was originally proposed by Iai et al. (1992). The model has been implemented into a finite element program, called "FLIP ROSE (Finite Element Analysis Program of Liquefaction Process/Response of Soil-structure Systems during Earthquakes)" (Iai et al., 1995, 1998; Ozutsumi et al., 2002) and has been extended based on the finite strain theory (see Ueda, 2009; Iai et al., 2013) and is widely used to examine the cyclic response of granular materials in Japan as an effective stress model. In this model, the behavior of granular materials is idealized on the basis of a multitude of virtual simple shear mechanisms oriented in arbitrary directions (see Ueda & Iai, 2018).

15.3.1 Determination of Model Parameters

Parameters of the strain space multiple mechanism model are broadly classified into three types according to the volumetric mechanism, shear mechanism, and dilatancy. The calibrated constitutive model parameters are illustrated in Tables 15.3 and 15.4, which were determined from cyclic torsional shear test results performed at a relative density of 60% (see Vargas et al., 2020 for further details about the element tests). As discussed previously, the numerical calibration and simulations were conducted by three predictors hereafter referred to as FLIP1, FLIP2, and FLIP3 as shown in Tables 15.3 and 15.4. The constitutive model parameters were quite different among the three modelers. The liquefaction resistance curves obtained from the cyclic torsional shear test and simulated by the three predictors at a double amplitude shear strain of 7.5% and at different values of the cyclic stress ratio (CSR) are shown in Fig. 15.2. From Fig. 15.2, one can observe all the three numerical models to capture the necessary features of the measured cyclic soil response. At a smaller

Table 15.3 Model parameters for deformation characteristics

Symbol	Parameter designation	FLIP1	FLIP2	FLIP3
ρt	Mass density of a composite of soil and water	2.092	2.092	2.092
pa	Reference confining pressure	75	73.5	75
$K_{L/Ua}$	Bulk modulus	298,302	178,245	329,380
rk	Reduction factor of bulk modulus for liquefaction analysis	0.1	0.69	0.1
lk	Power index of bulk modulus for liquefaction analysis	2	2	2
G_{ma}	Shear modulus	114,386	68,350	126,304
Φ_f^{PS}	Internal friction angle for plane strain	41.6	48	42.83
h_{max}	Maximum damping constant	0.24	0.24	0.24

Table 15.4 Model parameters for dilatancy

Symbol	Parameter designation	FLIP1	FLIP2	FLIP3
Φ_p	Phase transformation angle	28	28	28
ε_d^{cm}	Limit of contractive component	0.2	0.72	0.2
$r\varepsilon_d^c$	Parameter controlling contractive component	7	1.5	7
$r\varepsilon_d$	Parameter controlling dilative and contractive components	1	0.36	0.8
$q1$	Parameter controlling initial phase of contractive component	2	10	2
$q2$	Parameter controlling final phase of contractive component	2	1	2
s_1	Small positive number to avoid zero confining pressure	0.005	0.005	0.005
c_1	Parameter controlling elastic range for contractive component	1.58	1.4	1.80
q_{us}	Undrained shear strength (for steady state analysis)	–	–	–

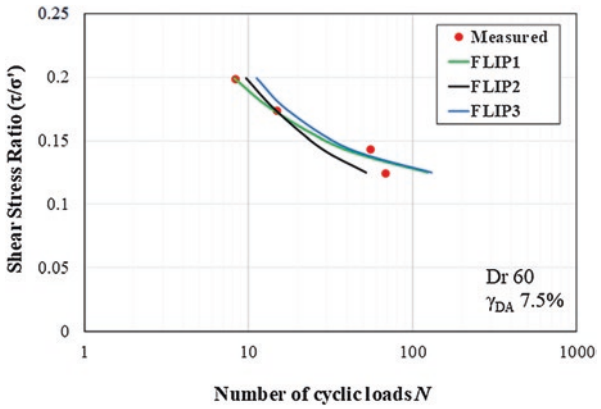

Fig. 15.2 Liquefaction resistance curves obtained from numerical simulation for FLIP 1, FLIP 2 and FLIP 3 (Dr =60%; γ_{DA} 7.5%)

cyclic stress ratio, FLIP1 and FLIP3 slightly overpredicted the number of cycles to achieve the desired strain level. On the other hand, FLIP2 slightly underestimated the number of cycles at the least CSR value.

The typical soil response obtained by the three predictors at a cyclic stress ratio of 0.18 is shown in Fig. 15.3 in terms of stress path and stress-strain relationship at a relative density of 60%. Overall, all the three models with different constitutive model parameters captured the important undrained cyclic soil response as observed in the torsional test including the butterfly-shaped undrained stress path. However, a very similar strain as recorded in the element test was estimated by FLIP3, however at the expense of slightly larger vertical effective stress value. FLIP2 on the other hand predicted the undrained stress-path to approach close to the origin similar to the experiment but at the expense of significantly larger estimated shear strain as shown in Fig. 15.3.

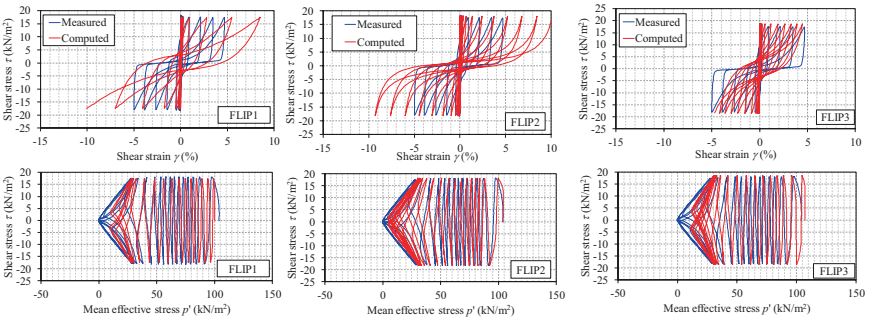

Fig. 15.3 Typical numerically simulated element test results obtained by FLIP 1, FLIP 2, and FLIP 3 (D_r = 60%, shear stress ratio = 0.18)

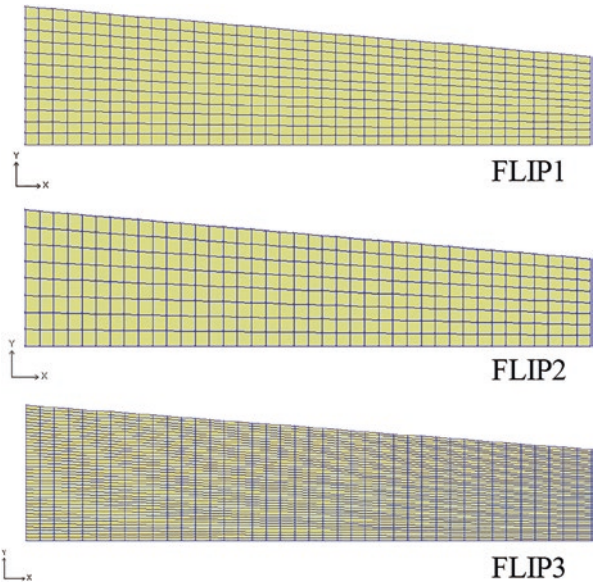

Fig. 15.4 Mesh for the numerical models developed by the three predictors, FLIP1, FLIP2, and FLIP3

15.3.2 Initial Boundary Conditions

The finite element (FE) analysis was carried out considering a two-dimensional plane strain condition. Figure 15.4 represents the mesh developed by each of the numerical predictors. The numerical analysis was carried out considering the four-node quadrilateral elements, which is based on the reduced integration (SRI) technique (Hughes, 1980). The mesh size in FLIP1 numerical model was determined to be less than 1/2 of the input wavelength. The mesh size for FLIP2 was determined to be 1/8 over a quarter wavelength of 4 m to account for reasonable deformation

Table 15.5 Coefficient of permeability (m/s)

	FLIP1		FLIP2	FLIP3	
	Prototype scale	Model scale	Prototype scale	Prototype scale	Model scale
KyU_A_A2_1	5.00E-04	1.13E-05	5.00E-04	3.84E-03	8.64E-05
RPI_A_A2_1	1.00E-04	4.35E-06	1.00E-04	3.77E-05	1.64E-06
UCD_A_A2_1	1.00E-04	2.29E-06	1.00E-04	1.64E-04	3.75E-06
KyU_A_B2_1	5.00E-04	1.34E-05	5.00E-04	3.23E-03	8.64E-05
RPI_A_B1_1	1.00E-04	3.66E-06	1.00E-04	1.95E-04	7.13E-06

Table 15.6 Rayleigh damping factor (β)

	FLIP1		FLIP2	FLIP3	
	Prototype scale	Model scale	Prototype scale	Prototype scale	Model scale
KyU_A_A2_1	1.00E-03	2.25E-05	1.00E-03	8.88E-03	2.00E-04
RPI_A_A2_1	1.00E-03	4.35E-05	1.00E-03	1.84E-02	8.00E-04
UCD_A_A2_1	1.00E-03	2.29E-05	1.00E-03	8.75E-03	2.00E-04
KyU_A_B2_1	1.00E-03	4.50E-05	1.00E-03	4.44E-03	2.00E-04
RPI_A_B1_1	1.00E-03	2.17E-05	1.00E-03	3.68E-02	8.00E-04

mode of the sloping ground, whereas for FLIP3, the mesh size was very fine to consider the effect of high-frequency components.

The degrees of freedom for displacement at the base of the models were fixed both horizontally and vertically, while only horizontal displacement is fixed at the side boundaries. The side and bottom boundaries were set to be impermeable, and pore water pressure at the ground surface was specified to represent a hydrostatic condition.

A self-weight analysis was carried out prior to the dynamic response analysis for evaluating initial stress distribution throughout the numerical model. Numerical time integration was carried out by the SSpj method (Zienkiewicz et al., 2000). The standard parameters for SSpj method are used as per Ueda & Iai (2018).

Table 15.5 shows the coefficients of permeability used by the three predictors during the numerical analysis. The coefficient of permeability of Ottawa F-65 sand was taken from the permeability tests carried out by Kutter et al. (2018) and was adjusted depending on the dissipation process of excess pore water by all the predictors if applicable. For all the facilities, the permeability of soil was adjusted based on the scaling laws adopted by the corresponding centrifuge facility. Because analysis by FLIP1 and FLIP3 was performed in model scale and that by FLIP2 was performed in the prototype scale, FLIP1 and FLIP3 considered the coefficient of permeability of soil in model scale whereas FLIP2 carried out the numerical simulations considering the coefficient of permeability in the prototype scale.

Table 15.6 shows the Rayleigh damping factor (β) adopted by each predictor. For FLIP 1 and FLIP2, the values were determined based on the parametric study after

performing the one-dimensional ground response analysis for a non-liquefiable ground surface and were estimated so that the maximum displacement was no longer affected. However, for FLIP3, the damping factor was directly adjusted based on the results obtained from the centrifuge tests so as to replicate the test results more accurately.

15.4 Results and Discussions for the Type-B Simulations

This section presents the results of Type-B simulations for centrifuge Models A (tested as per the conventional scaling laws) at the geotechnical centrifuge facilities located in Kyoto University, Rensselaer Polytechnic Institute and University of California Davis (indicated as KyU_A_A2_1, RPI_A_A1_1, and UCD_A_A2_1; shown in Table 15.1) and Models B (tested as per the generalized scaling laws) at the geotechnical centrifuge facilities located in Kyoto University and the Rensselaer Polytechnic Institute (indicated as KyU_A_B2_1 and RPI_A_B1_1; shown in Table 15.2).

15.4.1 Observed Soil-System Response During Liquefaction Induced Lateral Spreading

Figures 15.5, 15.6, 15.7, 15.8 and 15.9 show the results obtained from the numerical simulations for the soil-system response in terms of acceleration (AH4), excess pore pressure (P4), and lateral soil displacement for Model A and Model B with considered instrumentations located towards the ground surface in the center array of the model (see Fig. 15.1). FLIP3 adjusted the coefficient of the permeability and the Rayleigh damping factor (β) to match the centrifuge test results and hence FLIP3 results can be said to represent Type-C simulations.

The numerical simulation results seem to be well-matched with the centrifuge test results despite of the fact that the constitutive model parameters were calibrated differently by the three predictors. Overall, the accelerations response in FLIP1, FLIP2, and FLIP3 are found to be well-matched with the test results. However, negative spikes often appeared more prominently as compared to the centrifuge test results in the case of predictors FLIP1 and FLIP2 which indicates large prevailing soil dilatancy. For some of the cases, the dissipation period was estimated to be longer than the centrifuge test results, depending on the coefficient of permeability used by the predictors. The displacements obtained from the numerical simulations are also found to be very close to the centrifuge test results.

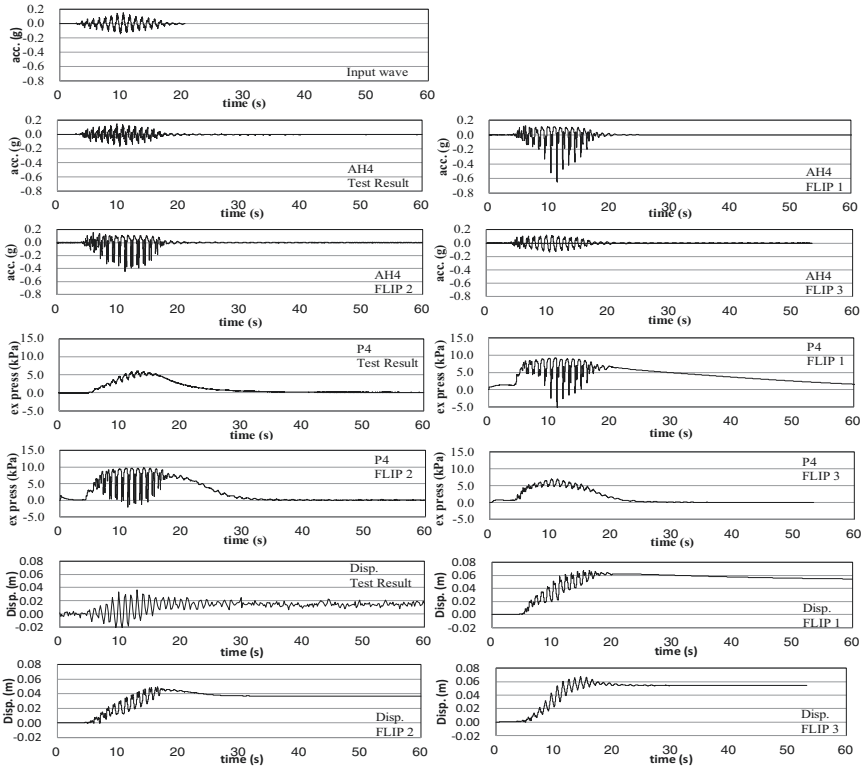

Fig. 15.5 Simulated results by the predictors FLIP1, FLIP2, and FLIP3 for the test KyU_A_A2_1 (Model A) in terms of acceleration response (AH4), excess pore pressure (P4), and soil displacement (see Fig. 15.1 for the location of sensors)

15.4.2 Numerical Analyses in the Model Scale and the Prototype Scale

As described earlier, numerical analyses by predictors FLIP1 and FLIP3 were carried out on a model scale, whereas the predictor FLIP2 conducted the simulations in the prototype scale.

For the simulation results for KyU_A_A2_1, the peak acceleration at sensor AH4 is obtained at 10 s by all the predictors, which was consistent with the timing of peak acceleration measured in the centrifuge model test (Fig. 15.5). FLIP1 obtained maximum horizontal acceleration of 0.65g, whereas FLIP2 obtained a value of 0.44g, and FLIP3 estimated it as 0.14g, as compared to 0.16g obtained from centrifuge test. The excess pore pressure generation for sensor P4 is nearly identical for all the predictors with slight differences observed in the dissipation period. However, larger negative spikes were obtained in the case of FLIP1 and FLIP2. The dissipation period is found to be slightly different for FLIP1 depending

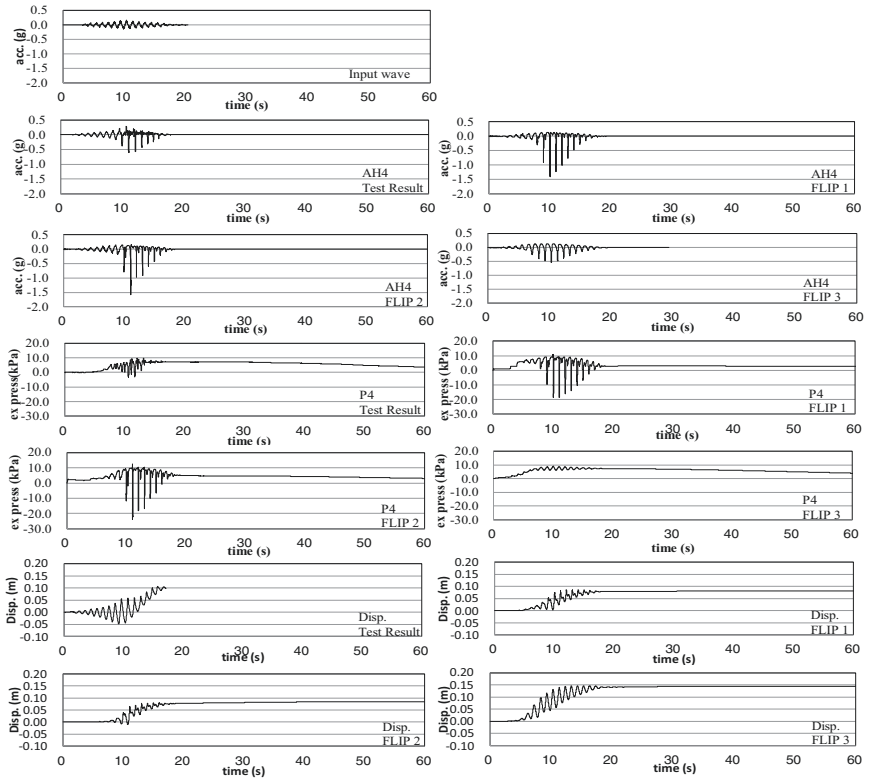

Fig. 15.6 Simulated results by the predictors FLIP1, FLIP2, and FLIP3 for the test RPI_A_A1_1 (Model A) in terms of acceleration response (AH4), excess pore pressure (P4) and soil displacement (see Fig. 15.1 for the location of sensors)

on the lower permeability value used by the corresponding predictor. The peak lateral displacement at the location of marker 2–3 is estimated to be 0.068 m by FLIP1, 0.049 m by FLIP2, and 0.067 m by FLIP 3, respectively. The maximum lateral displacement achieved from the centrifuge test result was 0.0365 m. Hence, it can be seen that the results obtained were nearly similar among all the predictors, which were close to centrifuge results.

For the simulation result of KyU_A_B2_1, the peak acceleration values at sensor AH4 were obtained at 10 s by all the predictors, as it was observed in the centrifuge acceleration response (Fig. 15.8). The maximum estimated horizontal acceleration is 0.40*g* by FLIP1, 0.70*g* by FLIP 2, and 0.40*g* by FLIP 3, respectively, whereas 0.45*g* was obtained from the centrifuge test as is reported in Fig. 15.8. Hence, it can be said that the response is nearly similar with slightly different amplitudes of acceleration depending on the soil dilatancy. The pore pressure variation is also found to

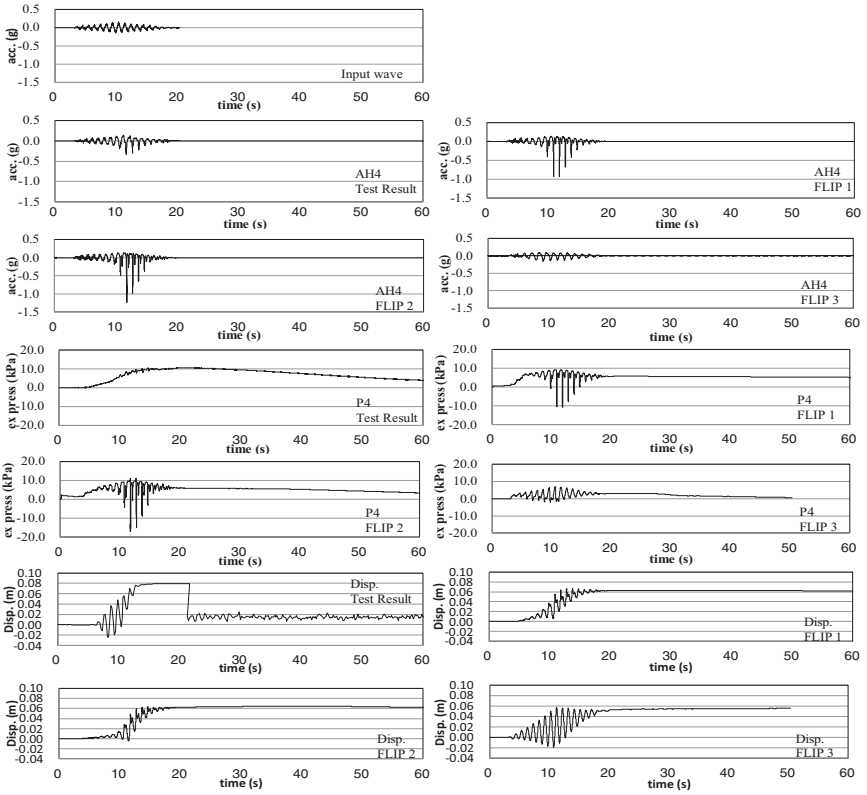

Fig. 15.7 Simulated results by the predictors FLIP1, FLIP2, and FLIP3 for the test UCD_A_A2_1 (Model A) in terms of acceleration response (AH4), excess pore pressure (P4), and soil displacement (see Fig. 15.1 for the location of sensors)

be similar among all the predictors with slight differences observed in the dissipation period. The peak lateral displacement at the location of marker 2–3 is estimated to be 0.065 m, 0.067 m, and 0.126 m for FLIP1, FLIP2, and FLIP3, respectively. The maximum lateral displacement achieved from the centrifuge test is 0.10 m. Hence, the maximum lateral displacement was nearly similar among all the predictors with a slight variation at the period of occurrence.

15.5 Conclusions

This chapter summarizes the differences obtained in the soil system response conducted by the three different numerical predictors using the same soil constitutive model. The following conclusions are derived based on the study.

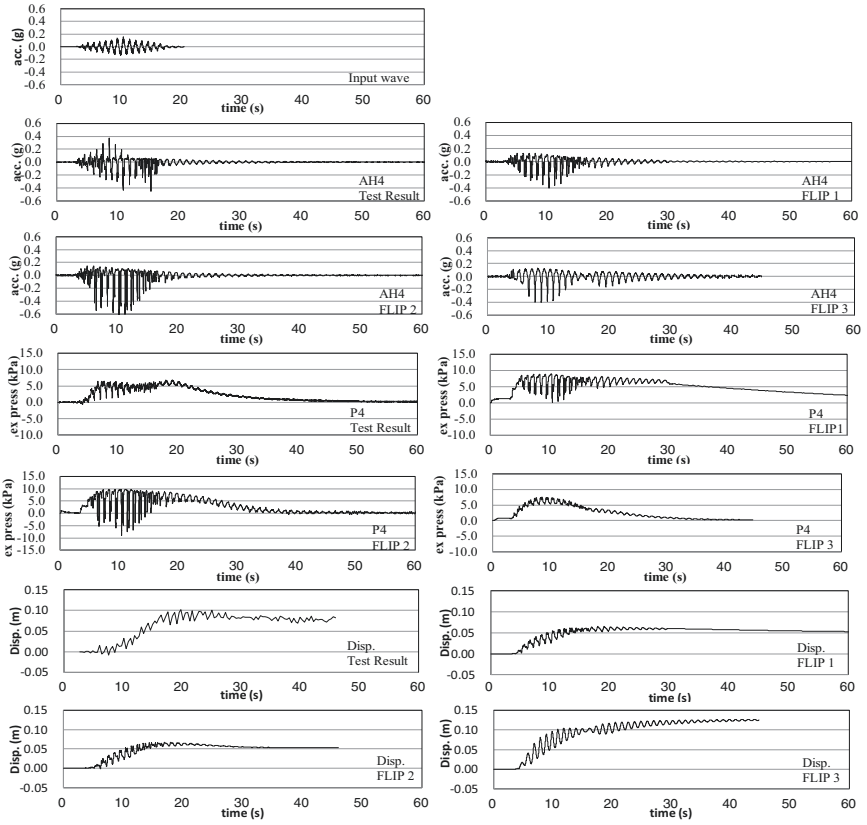

Fig. 15.8 Simulated results by the predictors FLIP1, FLIP2, and FLIP3 for the test KyU_A_B2_1 (Model B) in terms of acceleration response (AH4), excess pore pressure (P4), and soil displacement (see Fig. 15.1 for the location of sensors)

1. *Type-B prediction*

   - It was found that for Type-B prediction, simulated results could predict the centrifuge test results with sufficient accuracy through the strain space multiple mechanism model.
   - From the numerical simulation results conducted by all the three predictors, a dilative pulse was observed in the acceleration response in the downslope direction similar to the centrifuge test results.
   - The rise of excess pore water pressure and its dissipation is found to be well simulated with the centrifuge test results.

2. *Constitutive model parametric variation*

   - FLIP1, FLIP2, and FLIP3 used different soil constitutive model parameters, including the liquefaction and dilatancy parameters. From the simulation results, it is seen that the soil response obtained by all the three predictors in

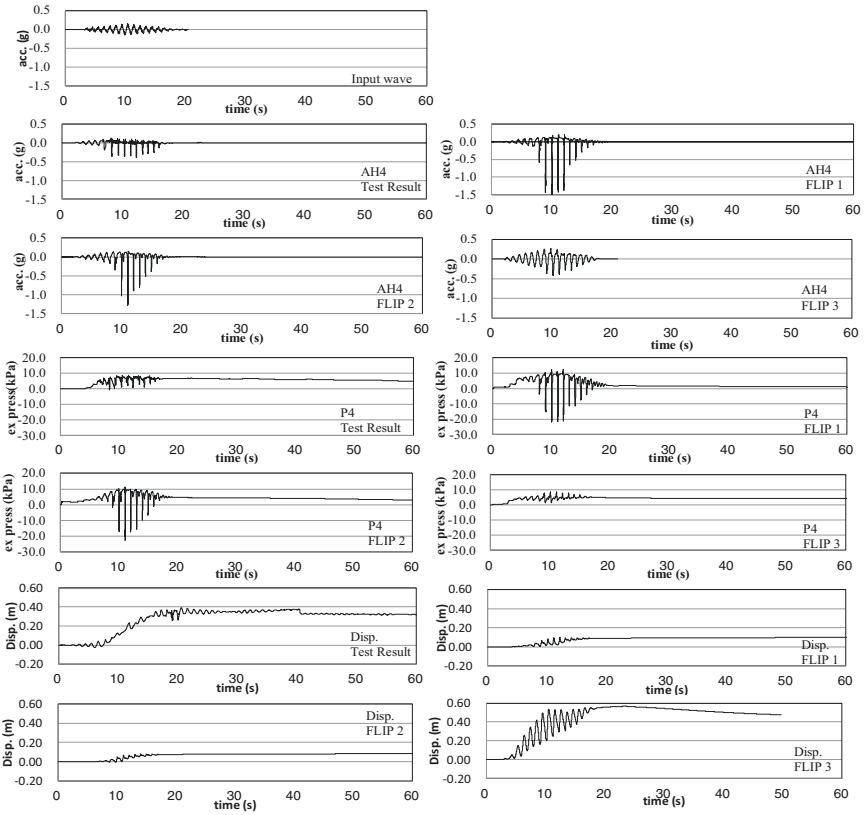

Fig. 15.9 Simulated results by the predictors FLIP1, FLIP2, and FLIP3 for the test RPI_A_B1_1 (Model B) in terms of acceleration response (AH4), excess pore pressure (P4), and soil displacement (see Fig. 15.1 for the location of sensors)

terms of acceleration, pore pressure, and lateral displacement was found to be in good agreement with the centrifuge test results for all the centrifuge facilities reported in this chapter, despite using different constitutive model parameters.

- Hence, it can be said that the soil response to an earthquake loading may not highly depend on the variations in the constitutive model parameters and nearly similar results may be achieved with sufficient accuracy by the different numerical predictors as long as the simulated liquefaction resistance curves and stress-strain behavior during cyclic shear are consistent with each other.

3. *Effect of the different simulation scales*

- The influence of the simulation scale was also studied in the present paper depending on the different scales used by the numerical predictors FLIP1,

FLIP3 (model scale), and FLIP2 (prototype scale) while developing the numerical model. From the numerical analysis, it was found that the simulation results are almost similar for the model scale and the prototype scale. It was also concluded that the strain space multiple mechanism model used for this study is consistent with the generalized scaling law adopted for centrifuge model tests performed in the LEAP project.

Acknowledgments The authors are grateful to all the centrifuge facility groups, who took part in the LEAP Project and allowed their data to be used for numerical simulation exercises.

References

Hughes, T. J. (1980). Generalization of selective integration procedures to anisotropic and nonlinear media. *International Journal for Numerical Methods in Engineering, 15*(9), 1413–1418.

Iai, S., Matsunaga, Y., & Kameoka, T. (1992). Strain space plasticity model for cyclic mobility. *Soils and Foundations, 32*(2), 1–15.

Iai, S., Morita, T., Kameoka, T., Matsunaga, Y., & Abiko, K. (1995). Response of a dense sand deposit during 1993 KUSHIRO-OKI earthquake. *Soils and Foundations, 35*(1), 115–131.

Iai, S., Ichii, K., Liu, H., & Morita, T. (1998). Effective stress analyses of port structures. *Soils and Foundations, 38*(Special), 97–114.

Iai, S., Tobita, T., & Nakahara, T. (2005). Generalised scaling relations for dynamic centrifuge tests. *Geotechnique, 55*(5), 355–362.

Iai, S., Ueda, K., Tobita, T., & Ozutsumi, O. (2013). Finite strain formulation of a strain space multiple mechanism model for granular materials. *International Journal for Numerical and Analytical Methods in Geomechanics, 37*(9), 1189–1212.

Iai, S., Tobita, T., Ozutsumi, O., & Ueda, K. (2011). Dilatancy of granular materials in a strain space multiple mechanism model. *International Journal for Numerical and Analytical Methods in Geomechanics, 35*(3), 360–392.

Kutter, B. L., Carey, T. J., Hashimoto, T., Zeghal, M., Abdoun, T., Kokkali, P., et al. (2018). LEAP-GWU-2015 experiment specifications, results, and comparisons. *Soil Dynamics and Earthquake Engineering, 113*, 616–628.

Ozutsumi, O., Sawada, S., Iai, S., Takeshima, Y., Sugiyama, W., & Shimazu, T. (2002). Effective stress analyses of liquefaction-induced deformation in river dikes. *Soil Dynamics and Earthquake Engineering, 22*(9–12), 1075–1082.

Sahare, A., Tanaka, Y., & Ueda, K. (2020). Numerical study on the effect of rotation radius of geotechnical centrifuge on the dynamic behavior of liquefiable sloping ground. *Soil Dynamics and Earthquake Engineering, 138*, 106339.

Tobita, T., Ashino, T., Ren, J., & Iai, S. (2018). Kyoto University LEAP-GWU-2015 tests and the importance of curving the ground surface in centrifuge modelling. *Soil Dynamics and Earthquake Engineering, 113*, 650–662.

Ueda, K. (2009). *Finite strain formulation of a strain space multiple mechanism model for granular materials and its application*. Doctoral dissertation, PhD thesis. Graduate School of Engineering, Kyoto University [in Japanese].

Ueda, K., & Iai, S. (2018). Numerical predictions for centrifuge model tests of a liquefiable sloping ground using a strain space multiple mechanism model based on the finite strain theory. *Soil Dynamics and Earthquake Engineering, 113*, 771–792.

Vargas, R. R., Ueda, K., & Uemura, K. (2020). Influence of the relative density and K0 effects in the cyclic response of Ottawa F-65 sand-cyclic torsional hollow-cylinder shear tests for LEAP-ASIA-2019. *Soil Dynamics and Earthquake Engineering, 133*, 106111.

Zienkiewicz, O. C., Taylor, R. L., & Zhu, J. Z. (2000). The finite element method: Its basis and fundamentals (6th edition). Elsevier.

Chapter 16
LEAP-ASIA-2019 Centrifuge Test Simulation at UNINA

Gianluca Fasano, Anna Chiaradonna, and Emilio Bilotta

Abstract This chapter describes the numerical simulations carried out at the University of Napoli Federico II in the framework of the LEAP-ASIA-2019 Simulation Exercise. An advanced critical state compatible, bounding surface plasticity model for sand has been adopted and calibrated on the available cyclic laboratory test data. The calibration has been finalized to catch the cyclic strength of the investigated sand. Centrifuge test simulations have been performed by means of the finite element code PLAXIS, which is a commercial code well widespread in the community of geotechnical practitioners. Type-C simulations highlighted the capability of the numerical model to reasonably predict the time histories of acceleration and excess pore water pressure measured during the experimental tests.

Keywords Liquefaction Experiments and Analysis Project (LEAP-ASIA-2019) · Numerical modelling · PM4Sand

16.1 Introduction

LEAP (Liquefaction Experiments and Analysis Projects) is an effort to formalize the process and provide data needed for validation of numerical models designed to predict liquefaction phenomena (Kutter et al., 2018).

After several LEAP projects (Zeghal et al., 2015; Kutter et al., 2018; Manzari et al., 2019), LEAP-ASIA-2018 simulation exercise aimed to validate the generalized scaling law proposed by Iai et al. (2005). To this end, this numerical simulation

G. Fasano · A. Chiaradonna
Department of Civil, Architectural and Environmental Engineering, University of Napoli Federico II, Naples, Italy

E. Bilotta (✉)
Department of Civil, Construction-Architectural and Environmental Engineering, University of L'Aquila, L'Aquila, Italy
e-mail: gianluca.fasano@unina.it

T. Tobita et al. (eds.), *Model Tests and Numerical Simulations of Liquefaction and Lateral Spreading II*, https://doi.org/10.1007/978-3-031-48821-4_16

exercise was designed to assess the capability of constitutive models and the numerical modeling techniques in:

1. Capturing the response of saturated liquefiable soils (such as Ottawa F-65 sand) to cyclic shearing at different levels of confining stress, and
2. Simulating potential effects of confining stresses on the lateral spreading of liquefiable soils caused by earthquakes.

After a brief summary of the centrifuge tests (Sect. 16.2), this chapter describes the process followed in the calibration of the selected constitutive model (Sect. 16.3), covering the essential features of the constitutive model and showing the model parameters.

Section 16.4 describes the finite element analyses carried out and it is divided into three sub-sections. Section 16.4.1. defines the types of predictions, while Sect. 16.4.2 reports the calibration philosophy and the assumptions used in the calibration process. A comparison between the predicted and experimental cyclic laboratory tests and liquefaction resistance curves allowed verifying the accuracy of the calibration process. The adopted constitutive model has been calibrated on the results of the provided cyclic torsional shear tests for a relative density, D_r, equal to 50% and 60% under an initial effective confining stress of 100 kPa.

Section 16.4.3 details the numerical model of the centrifuge experiments, describing the main features of the numerical analysis platform used in the simulation, the model geometry and discretization, the applied boundary conditions, the solution algorithm employed, and some assumptions used in the analyses. Finally, Sect. 16.5 reports the results of the type-C simulations showing the comparisons between predicted and simulated time histories of acceleration and excess pore water pressure. Conclusions are provided in Sect. 16.6 about the lessons learned from the experienced simulation exercise.

16.2 Brief Summary of Centrifuge Experiments

The models were set up in a rigid box by dry pluviation. After saturation the models were positioned on the shaking table in the centrifuge to apply an input motion on the bottom of the box.

Centrifuge model tests were executed with reference to two different models:

- Model A: models identical to LEAP-UCD-2017 simulation exercise (Manzari et al., 2019) whose response was used to confirm the trends obtained in the previous project (Table 16.1).
- Model B: a model similar to Model A to validate the generalized scaling law proposed by Iai et al. (2005). Upon constructing the model to be tested, only the viscosity of pore fluid and the input acceleration were scaled (Table 16.2).

Table 16.1 Summary of centrifuge experiments, Model A in LEAP-ASIA-2018

Test case	Density (kg/m^3)	D_r (%)	Virtual 1G, μ	Centrifuge, η	PGA_{eff} (g)	Avg. disp. (mm)	Shaking direction
IFSTTAR_A_A1_1	1645	62	1	50	0.348	550.00	Axial
KAIST_A_A1_1	1716.55	87	1	40	0.287	33.93	Axial
KyU_A_A1_1	1677	73	1	44.4	0.248	71.04	Tangential
KyU_A_A2_1	**1628**	**56**	**1**	**44.4**	**0.118**	**11.10**	**Tangential**
NCU_A_A1_1	1643	61	1	26	0.144	181.51	Axial
RPI_A_A1_1	**1651**	**64**	**1**	**23**	**0.143**	**99.56**	**Axial**
UCD_A_A1_1	1713.3	86	1	43.75	0.178	30.56	Tangential
UCD_A_A2_1	**1658.1**	**67**	**1**	**43.75**	**0.134**	**77.50**	**Tangential**
ZJU_A_A1_1	1624.6	54	1	30	0.272	390.00	Axial

Table 16.2 Summary of centrifuge experiments, Model B in LEAP-ASIA-2018

Test case	Density (kg/m^3)	D_r (%)	Virtual 1G, μ	Centrifuge, η	PGA_{eff} (g)	Avg. disp. (mm)	Shaking direction
CU_A_B1_1	1606	47	0.5	80	–		Tangential
Ehime_A_B1_1	1650.8	64	2	20	0.158	56.57	Axial
IFSTTAR_A_B1_1	1645	62	2	25	0.405	777.82	Axial
KAIST_A_B1_1	1720.6	88	1.5	26.7	0.317	30.58	Axial
KyU_A_B1_1	1673	72	2	22.2	0.252	153.84	Tangential
KyU_A_B1_2	1669	71	4	11.1	0.248	115.44	Tangential
KyU_A_B2_1	**1633**	**58**	**2**	**22.2**	**0.126**	**34.54**	**Tangential**
NCU_A_B1_1	1626	55	2	13	0.131	87.18	Axial
RPI_A_B1_1	**1644**	**62**	**0.5**	**46**	**0.151**	**303.27**	**Axial**
UCD_A_B1_1	1711.7	85	2	21.9	0.140	−2.23	Tangential
ZJU_A_B1_1	1632.7	57	2	15	0.271	678.82	Axial

The orientation of the shaking table in the geotechnical centrifuge leads to two different models: the shaking direction of can be parallel to the rotation axis of the centrifuge beam or orthogonal to the rotation axis (see shaking direction in Tables 16.1 and 16.2).

The consequence of the two different model orientations is a different shape of the ground surface and water table (Fig. 16.1), due to the distribution of radial acceleration.

The experimental tests reported in bold in Table 16.1 and 16.2 were simulated at the University of Napoli Federico II and, for sake of brevity, only the simulations of Model B types will be discussed in this chapter.

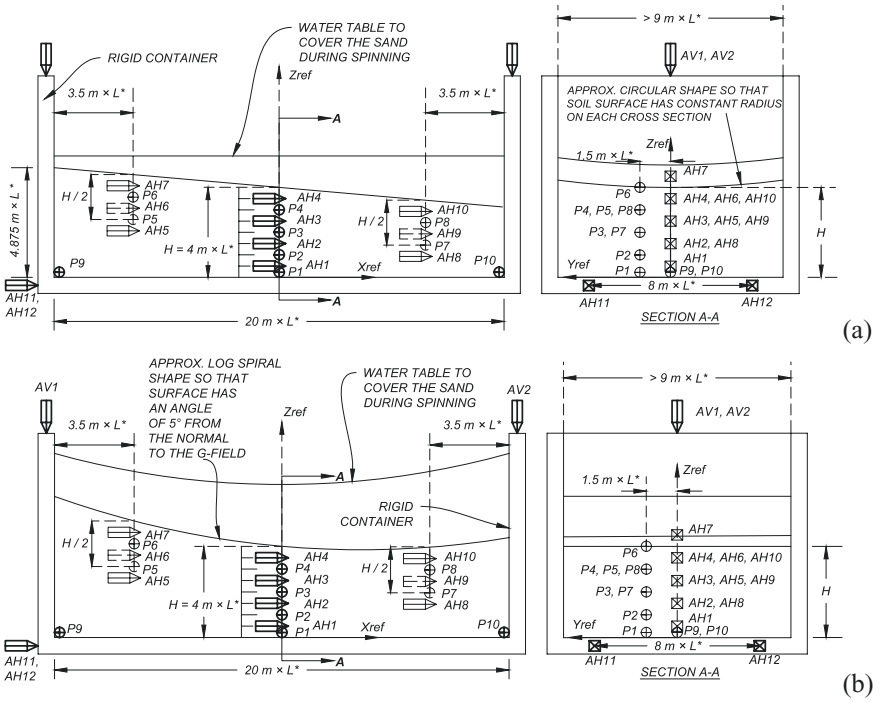

Fig. 16.1 Schematic for LEAP-ASIA-2018 centrifuge model tests: (**a**) Sectional drawing for shaking parallel to the axis of the centrifuge; (**b**) Sectional drawing for shaking in the plane of spinning of the centrifuge

16.3 Constitutive Model of Soils

The constitutive model used in the simulation exercise is the PM4Sand model (Boulanger & Ziotopoulou, 2015). The PM4Sand (version 3.1) model follows the basic framework of the stress-ratio controlled, critical state compatible, bounding surface plasticity model for sands presented by Dafalias and Manzari (2004), who extended the previous work by Manzari and Dafalias (1997) by adding a fabric-dilatancy related tensor quantity to account for the effect of fabric changes during loading. The fabric-dilatancy related tensor was used to macroscopically model the effect that microscopically observed changes in sand fabric during plastic dilation have on the contractive response upon reversal of loading direction. The modifications were developed and implemented to improve the ability of the model to match existing engineering design relationships currently used to estimate liquefaction-induced ground deformations during earthquakes. These modifications are described in the manuals (version 1 in Boulanger, 2010, version 2 in Boulanger & Ziotopoulou, 2012, and version 3 in Boulanger & Ziotopoulou, 2015) and in the associated publications, as listed in the mentioned manuals.

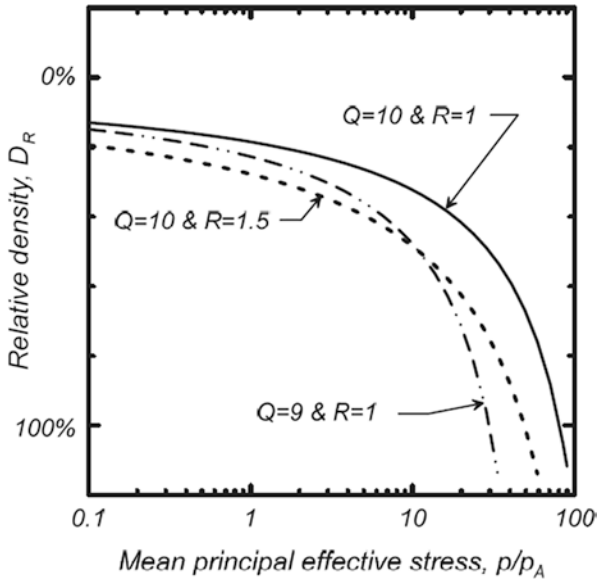

Fig. 16.2 Relative state parameter index and critical state line in the plane D_R: p/p_A

The model is written in terms of effective stresses, with the conventional prime symbol dropped from the stress terms for convenience because all stresses are effective for the model. The stresses are represented by the tensor σ, the principal effective stresses are σ_1, σ_2, and σ_3, the mean effective stress is p, the deviatoric stress tensor is s, and the deviatoric stress ratio tensor is r. The current implementation was further simplified by casting the various equations and relationships in terms of the in-plane stresses only. This limits the implementation to plane-strain (2D) applications, having the further advantage in its simplified implementation to improve the computational speed.

This constitutive model follows the critical state theory and uses the relative state parameter index (ξ_R) as defined by Boulanger (2010) and shown in Fig. 16.2. This relative parameter is defined by an empirical relationship for the critical state line:

$$\xi_R = D_{R,cs} - D_R \tag{16.1}$$

$$D_{R,cs} = \frac{R}{Q - \ln\left(100\dfrac{p}{p_A}\right)} \tag{16.2}$$

where $D_{R,cs}$ is the relative density at critical state for the current mean effective stress, instead, Q and R are two parameters that define the shape of critical curve.

Bounding, dilatancy, and critical surfaces are incorporated in PM4Sand following the form of Dafalias and Manzari (2004), respectively:

$$M^{b} = M \cdot \exp\left(-n^{b}\xi_{R}\right) \tag{16.3}$$

$$M^{d} = M \cdot \exp\left(n^{d}\xi_{R}\right) \tag{16.4}$$

$$M = 2 \cdot \sin\left(\phi_{cv}\right) \tag{16.5}$$

where n^{b} and n^{d} are model parameters and ϕ_{cv} is critical state friction angle.

As the soil is sheared toward critical state ($\xi_R = 0$), the values of M_b and M_d will both approach the value of M. Thus, the bounding and dilatancy surfaces move together during shearing until they coincide with the critical state surface when the soil has reached critical state.

A large portion of the post-liquefaction reconsolidation strains are due to the sedimentation effects which are not easily incorporated into either the elastic or plastic components of behavior. For this reason, in the PM4Sand, a post-shaking function was implemented. In a strongly pragmatic way, this function reduces volumetric and shear moduli, thus increasing reconsolidation strains to somehow simulate the sedimentation ones (not included in the model).

The post-shaking elastic moduli are determined by multiplying the conventional elastic moduli by a reduction factor F_{sed} as,

$$G_{\text{post shaking}} = F_{sed} \cdot G \tag{16.6}$$

$$K_{\text{post shaking}} = F_{sed} \cdot K \tag{16.7}$$

For more information on the F_{sed}, it is possible refer to Boulanger and Ziotopoulou (2015).

The model requires 27 input parameters, 3 of these are considered primary parameters while all the other parameters are suggested to be left with their default values. Table 16.3 reports the most important input parameters of the PM4Sand model, which were defined in the calibration process.

Table 16.3 Input parameters of the PM4Sand model

D_r	Initial relative density
G_0	Shear modulus coefficient
h_{p0}	Contraction rate parameter
p_A	Atmospheric pressure
e_{max}	Maximum void ratio
e_{min}	Minimum void ratio
n_b	Bounding surface parameter
n_d	Dilatancy surface parameter
ϕ_{cv}	Critical state friction angle
ν	Poisson's ratio
Q	Critical state line parameter
R	Critical state line parameter
Post-shake	Post-shaking stiffness parameter

16.4 Finite Element Analyses

Numerical analyses carried out with the abovementioned constitutive model are presented in this section, starting from the description of the calibration process, geometry definition, and boundary conditions of the model.

16.4.1 Definition of Type A, B, and C Predictions

Numerical predictions could be of different classes: "Class A" are true predictions of an event made prior to the event, "Class B" are predictions made during the event, and "Class C" are predictions made after the event (Lambe, 1973).

In this chapter, only Class C predictions are reported with reference to both simulations of cyclic laboratory tests and centrifuge experiments.

16.4.2 Determination of Model Parameters

The model parameters obtained from the calibration process are listed in Table 16.4, which also include some parameters kept at their default value.

The model parameters are obtained by using the results of the provided cyclic torsional shear tests, as described in the following about the calibration procedure. The simulated liquefaction resistance curves for γ_{DA} = 7.5% (i.e., the number of

Table 16.4 Parameters of the PM4Sand model based on the cyclic torsional test data

	Initial relative density	
Model parameters	D_r = 50%	D_r = 60%
D_r	0.5	0.6
G_0	630	730
h_{p0}	0.08	0.05
p_A	101.3	
e_{max}	0.78	
e_{min}	0.51	
n_b	0.5	
n_d	0.3	0.1
ϕ_{cv}	32	
ν	0.3	
Q	10	
R	1	
Post-shake	0	

cycles required to reach a 7.5% double amplitude shear strain) are compared with the laboratory test results in Fig. 16.10a, b for $D_r = 50\%$ and 60%, respectively. The following trends are observed from the curves:

The approach used in the calibration of the constitutive model parameters is hereafter explained.

The PM4Sand constitutive model is calibrated on the results of laboratory element tests. PM4Sand has 27 input parameters (6 primary and 21 secondary) but only 3 of them are required as independent inputs: the initial relative density (D_r), the shear modulus coefficient used to define the small strain shear modulus (G_0), and the contraction rate parameter used for the calibration of the undrained shear strength (h_{p0}). Basically, these three parameters were calibrated against the experimental data. The initial relative density has been set equal the value of relative density used in the cyclic torsional tests, $D_r = 0.5$ and 0.6.

The value of the shear modulus coefficient G_0 was determined as a function of the relative density using the follow relationship:

$$G_0 = 167 \cdot \sqrt{46 \cdot D_r^2 + 2.5} \tag{16.8}$$

The parameter h_{p0} scales the plastic contraction rate and is the primary parameter for the calibration of undrained cyclic strength. It is calibrated using an iterative process, in which undrained single-element simulations are conducted to match with the experimental liquefaction triggering curve by keeping the other parameters fixed.

With reference to the secondary parameters of the model, some with a clear physical meaning have been defined on the available experimental data, while the others have been left with their default values.

Shear strength parameters are computed from the monotonic triaxial test data, available on the NEES Hub (https://www.re3data.org/repository/r3d100010105).

Drained triaxial compression tests, carried out by Vasko (2015) on loose and dense specimens, were used to define the critical state line in the plane q: p' and the constant volume friction angle, ϕ_c'. As well known, the evaluation of critical state conditions in triaxial tests is a very complex issue, being such a test intrinsically affected by a number of experimental limitations (localization, bulging, shear stresses on the rough porous stones, difference between local and external displacements, etc.). One of the best ways to evaluate the final state is therefore the one that analyses dilatancy trend at the end of the tests. Based on all the elaborations of the available experimental data, the best fit of this parameter is the following:

$$\phi_c = 32° \tag{16.9}$$

Minimum and maximum void ratios, e_{max} and e_{min}, have been defined as mean values of the experimental measurements carried out in the LEAP-UCD-2017 Simulation Exercise (Manzari et al., 2019).

To sum up, the model parameters for static loading conditions were defined on the physical properties and tests results provided for the considered sand.

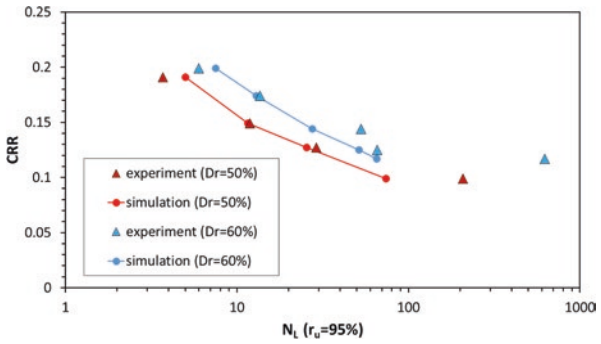

Fig. 16.3 Liquefaction strength curves obtained from experimental and simulated cyclic torsional tests on Ottawa F65 Sand

Table 16.5 Predicted liquefaction strength curves from cyclic torsional test

D_r (%)	CSR	No. of cycles to 95% r_u
50	0.099	74
50	0.127	25.5
50	0.149	11.6
50	0.191	5
60	0.117	65.5
60	0.125	51.5
60	0.144	27.5
60	0.174	13
60	0.199	7.5

Conversely, the model parameters for cyclic loading conditions were defined using experimental data of cyclic torsional tests (D_r = 50% and 60%).

The material parameters used to perform the simulations of the laboratory tests are those reported in Table 16.4 for each relative density. Every cyclic test is simulated imposing the prescribed *CSR* and computing the number of cycles, N_L, to induce liquefaction. Liquefaction condition has been defined according to the stress-based approach, i.e., r_u = 95%, where r_u is the excess pore pressure ratio ($r_u = \Delta u / \sigma'_{m0}$ ratio between the excess pore water pressure increment induced by cyclic loading and the initial effective confining pressure applied during the test, σ'_{m0}).

The liquefaction strength curves, obtained from the simulated cyclic torsional tests, are hereafter plotted and compared with the experimental results (Fig. 16.3). Table 16.3 reports the numerical values of the simulation results, i.e., the cyclic stress ratio, *CSR*, versus the number of cycles until excess pore pressure ratio, $r_u = \Delta u / \sigma'_{m0}$, achieved 95% for each simulated test.

It can be observed how the adopted calibration provides a good prediction of the experimental cyclic resistance curve for high/medium values of the cyclic resistance ratio (*CRR*), while underestimation of the experimental cyclic strength is observed for low values of *CRR* (Table 16.5).

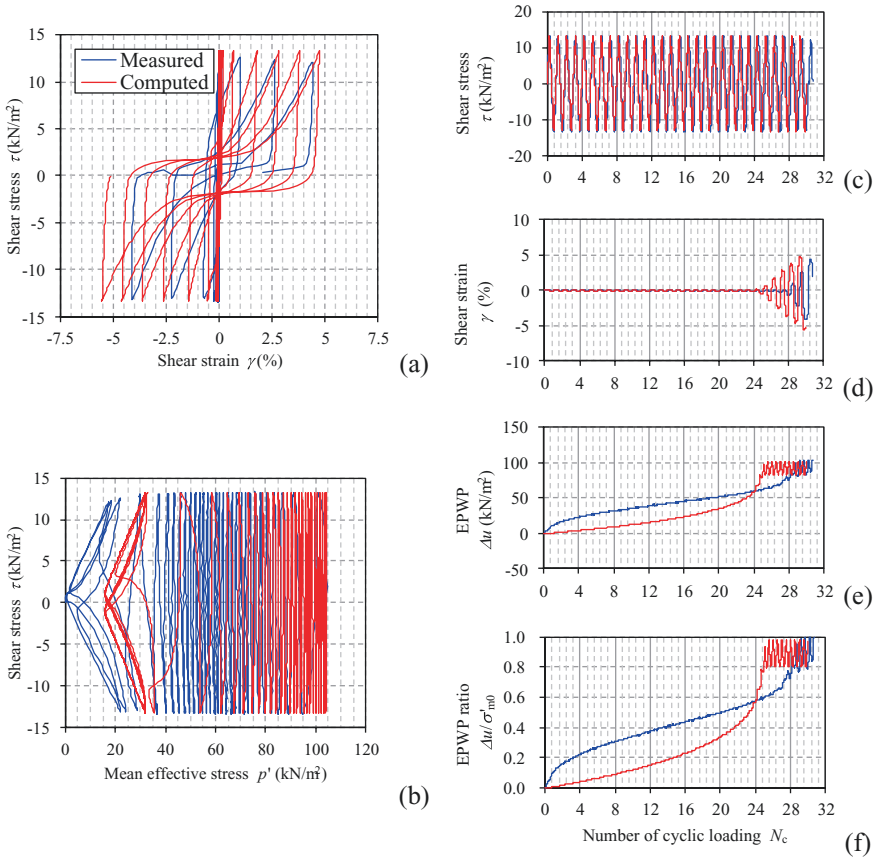

Fig. 16.4 Torsional tests D_r = 50%. CSR = 0.127; Number of cycles until r_u = 95% is achieved =25.5. (**a**) Shear stress-strain cycles, (**b**) stress path, (**c**) shear stress, (**d**) shear strain, (**e**) excess pore water pressure, and (**f**) excess pore pressure ratio as function of the number of cycles

Figures 16.4 and 16.5 compare the model performance on the prediction of the soil volume element response as obtained by cyclic torsional shear tests, for two different values of CSR and relative density. In both cases, the calibrated constitutive model is able to correctly simulate the shear stress-strain cycles and also the time histories of shear stress, strain, and excess pore water pressure.

16.4.3 Initial and Boundary Conditions and Input Motions

The simulations are carried out by using PLAXIS (Brinkgreve et al., 2016) as the analysis platform. PLAXIS is a 2D commercial Finite Element Method (FEM) code that includes several constitutive models. Among them, the PM4Sand model

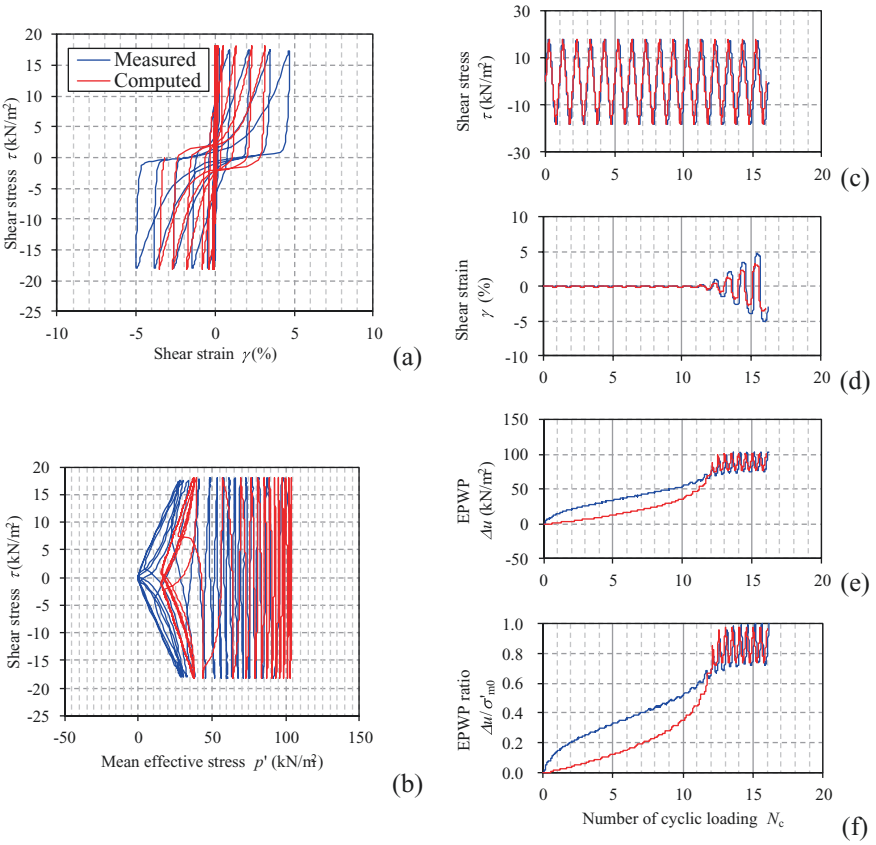

Fig. 16.5 Torsional tests D_r = 60%. CSR = 0.174; Number of cycles until r_u = 95% is achieved =13. (**a**) Shear stress-strain cycles, (**b**) stress path, (**c**) shear stress, (**d**) shear strain, (**e**) excess pore water pressure, and (**f**) excess pore pressure ratio as function of the number of cycles

(Boulanger & Ziotopoulou, 2015) has been adopted as constitutive model in the simulation exercise.

The main reason to use PLAXIS rather than other platforms where such a constitutive model is implemented is that this numerical code, although not specifically oriented to solve boundary value problems in earthquake geotechnical engineering, is quite well widespread in the community of geotechnical practitioners (Fasano et al., 2019b). Hence, it was for this team interesting to check the possible benefit of a rigorous validation of numerical simulation procedures implemented in PLAXIS through experimental data, in order to apply those procedures to a boundary value problem involving soil liquefaction.

Figure 16.6 shows the mesh density and the boundary conditions. The mesh consists of 443 15-noded triangular elements. The nodes located at the base are constrained in y direction while an acceleration time history in direction x is applied on the base and lateral boundaries. The nodes on the ground surface allow full drainage from the base to the top of the scheme.

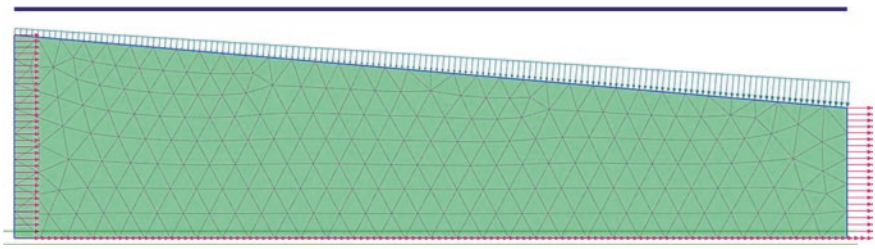

Fig. 16.6 Finite element model with applied boundary conditions

Table 16.6 Parameters of the constitutive model

	Parameters												
Test model	D_r	G_0	hp_0	p_A	e_{max}	e_{min}	n_b	n_d	φ_{cv}	n	Q	R	PostShake
UCD A_A2_1	0.6	730	0.05	101.30	0.78	0.51	0.50	0.10	32.00	0.30	10.00	1.00	0.00
RPI A_A1_1	0.61	740											
KyU A_A2_1	0.56	690											
KyU A_B2_1	0.58	708											
RPI A_B1_1	0.62	750											

The Newmark time integration scheme is used in the simulations where the time step is constant and equal to the critical time step during the whole analysis. The proper critical time step for dynamic analyses is estimated in order to accurately model wave propagation and reduce error due to integration of time history functions.

A full Rayleigh damping formulation has been considered in the simulation and the coefficient α_{RAY} and β_{RAY} are equal to 0.02513 and 6.366* 10^{-3}, respectively.

The soil properties are not changed during the simulations.

Table 16.6 shows the list of model parameters used in the five simulations (A and B models). The model parameters are the same obtained from the calibration, some of them are just updated to take into account for the different relative density used in the experiments.

16.5 Results of Type-C Simulations

Numerical analyses carried out with the abovementioned constitutive model are presented in this section, starting from the description of the calibration process, geometry definition, and boundary conditions of the model.

The results of the Type-C simulations for model B are here reported (RPI_A_B1_1 and KyU_A_B2_1), while all simulation results can be found in Fasano et al. (2019a).

Figures 16.7 and 16.8 report the comparison between recorded and simulated time histories of acceleration and excess pore water pressure for the centrifuge test RPI_A_B1_1.

The comparison shows that the amplitude of the simulated time histories is quite similar to the experimental one in centrifuge test, except for some spikes recorded by the sensors located in the center of the box (Fig. 16.7).

A reasonable prediction of pore water pressure is also provided by the numerical simulation, even though some underestimation is related to the deepest sensors from the surface of the box (Fig. 16.8).

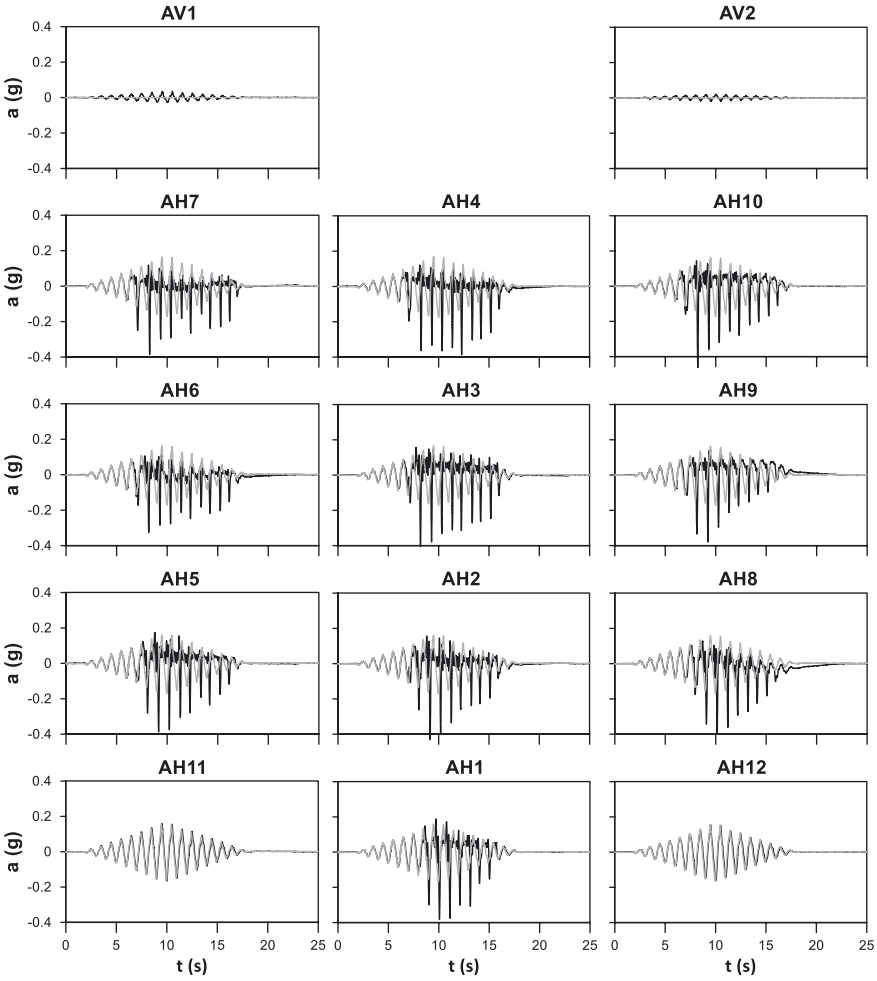

Fig. 16.7 Acceleration time histories for RPI_A_B1_1 (centrifuge results in black lines and numerical results in grey lines)

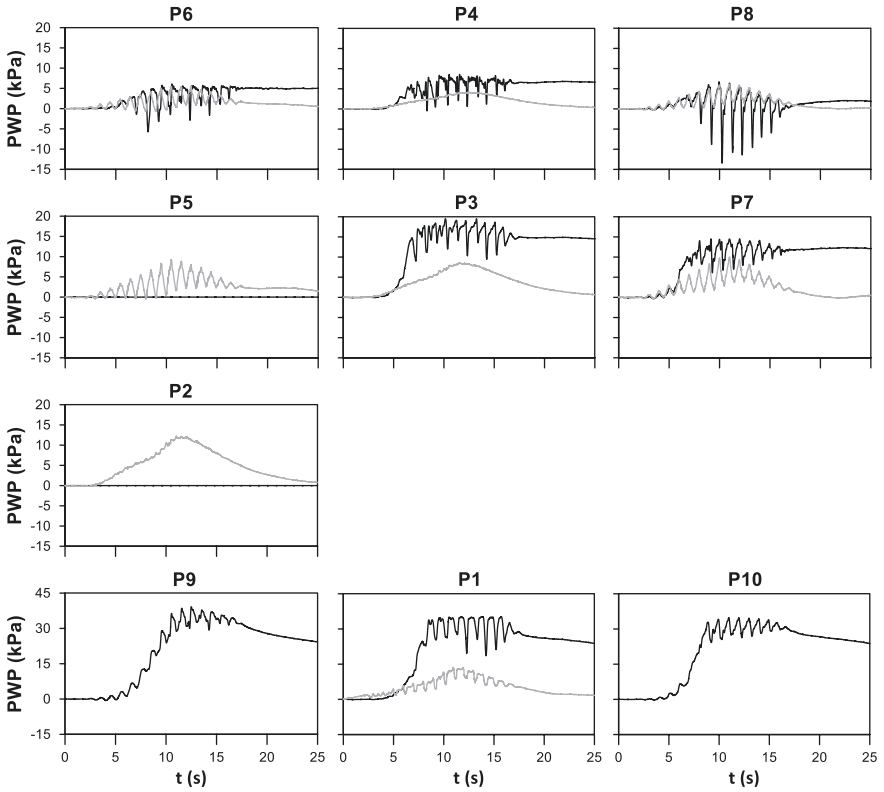

Fig. 16.8 Excess pore pressure time histories for RPI_A_B1_1 (centrifuge results in black lines and numerical results in grey lines)

Figures 16.9 and 16.10 report the comparison between recorded and simulated time histories of acceleration and excess pore water pressure for the centrifuge test KYU_A_B2_1.

The amplitude of the simulated time histories catches the experimental one better than the previous test, even though a probable inversion of the sign of the measured accelerations (Fig. 16.9).

With reference to the pore water pressure, an underestimation of the maximum values is provided by the numerical simulation, while the general trend is adequately reproduced (Fig. 16.10).

16.6 Conclusions

The numerical simulations carried out at the University of Napoli Federico II in the framework of the LEAP-ASIA-2018 Simulation Exercise were described in the paper. A bounding surface plasticity model for sand was calibrated on the results of

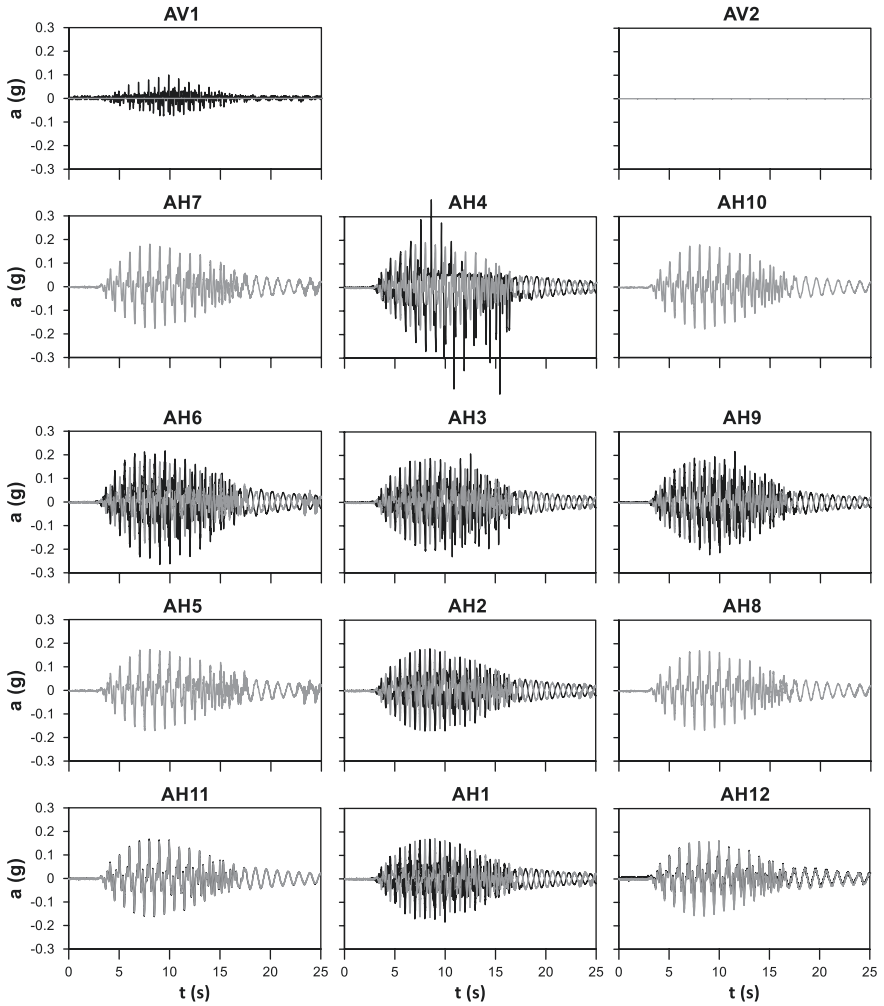

Fig. 16.9 Acceleration time histories for KYU_A_B2_1 (centrifuge results in black lines and numerical results in grey lines)

cyclic torsional shear tests. The calibration correctly reproduced the cyclic strength of the tested sand and the pre-failure behavior observed in terms of shear stress-strain cycles, even though the limitations related to the adoption of plane-strain conditions in the numerical model. Centrifuge test simulations have been performed by means of a finite element code, PLAXIS, largely adopted in the community of geotechnical practitioners. Type-C simulations highlighted the capability of the numerical model to reasonably predict the time histories of acceleration and excess pore water pressure measured during the experimental tests.

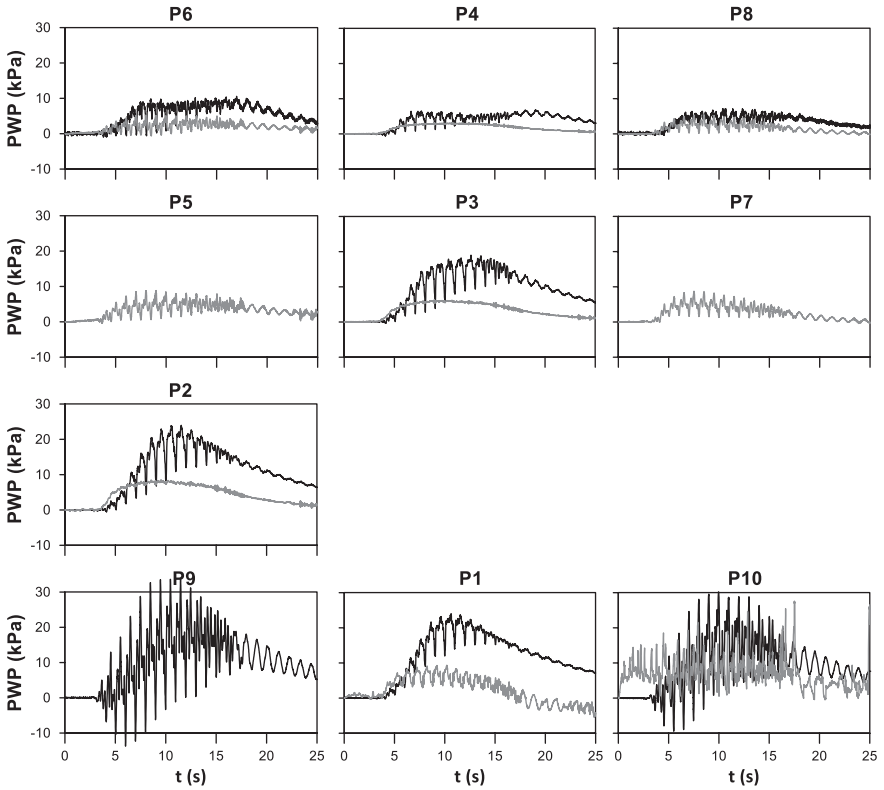

Fig. 16.10 Excess pore pressure time histories for KYU_A_B2_1 (centrifuge results in black lines and numerical results in grey lines)

References

Boulanger, R. W. (2010). *A sand plasticity model for earthquake engineering applications* (Report No. UCD/CGM-10-01. Technical report). Center for Geotechnical Modeling, Department of Civil and Environmental Engineering, University of California.

Boulanger, R. W., & Ziotopoulou, K. (2012). *PM4Sand (Version 2): A sand plasticity model for earthquake engineering applications* (Report No. UCD/CGM-12/01. Technical report). Center for Geotechnical Modeling, Department of Civil and Environmental Engineering College of Engineering, University of California at Davis.

Boulanger, R. W., & Ziotopoulou, K. (2015). *PM4Sand (Version 3): A sand plasticity model for earthquake engineering applications* (Report No. UCD/CGM-15/01. Technical report). Center for Geotechnical Modeling, Department of Civil and Environmental Engineering College of Engineering, University of California at Davis.

Brinkgreve, R. B. J., Kumaeswamy, S., & Swolfs, W. M. (2016). *PLAXIS 2016 User's manual*. Retrieved from PLAXIS. Website: https://www.plaxis.com/kb-tag/manuals/

Dafalias, Y. F., & Manzari, M. T. (2004). Simple plasticity sand model accounting for fabric change effects. *Journal of Geotechnical Engineering Division, 130*(6), 622–634. ASCE.

Fasano, G., Chiaradonna, A., & Bilotta, E. (2019a). *LEAP-Asia-2018 numerical simulation exercise – Phase II*. Type-C simulation report.

Fasano, G., Chiaradonna, A., & Bilotta, E. (2019b). LEAP-UCD-2017 centrifuge test simulation at UNINA. In B. Kutter, M. Manzari, & M. Zeghal (Eds.), *Model tests and numerical simulations of liquefaction and lateral spreading. LEAP-UCD-2017*. https://doi.org/10.1007/978-3-030-22818-7_9

Iai, S., Tobita, T., & Nakahara, T. (2005). Generalized scaling relations for dynamic centrifuge tests. *Geotechnique, 55*(5), 355–362.

Kutter, B. L., Carey, T. J., Hashimoto, T., Zeghal, M., Abdoun, T., Kokkali, P., Madabhushi, G., Haigh, S., d'Arezzo, F. B., Madabhushi, S., Hung, W. Y., Lee, C. J., Cheng, H. C., Iai, S., Tobita, T., Ashino, T., Ren, J., Zhou, Y. G., Chen, Y., Sun, Z. B., & Manzari, M. T. (2018). LEAP-GWU-2015 experiment specifications, results, and comparisons. *Soil Dynamics and Earthquake Engineering, 113*, 616–628.

Lambe, T. W. (1973). Predictions in geotechnical engineering. *Géotechnique, 23*(2), 151–202. https://doi.org/10.1680/geot.1973.23.2.151

Manzari, M. T., & Dafalias, Y. F. (1997). A critical state two-surface plasticity model for sands. *Géotechnique, 47*(2), 255–272.

Manzari, M. T., El Ghoraiby, M., Zeghal, M., Kutter, B. L., Arduino, P., Barrero, A. R., Bilotta, E., Chen, L., Chen, R., Chiaradonna, A., Elgamal, A., Fasano, G., Fukutake, K., Fuentes, W., Ghofrani, A., Haigh, S., Hung, W., Ichii, K., Kim, D. S., Kiriyama, T., Lascarro, C., MSP, G. M., Mercado, V., Montgomery, J., Okamura, M., Ozutsumi, O., Qiu, Z., Taiebat, M., Travasarou, T., Tsiaousi, D., Ueda, K., Ugalde, J., Wada, T., Wang, R., Yang, M., Zhang, J., Zhou, Y., & Ziotopoulou, K. (2019). LEAP-2017: Comparison of the Type-B numerical simulations with centrifuge test results. In B. Kutter, M. Manzari, & M. Zeghal (Eds.), *Model tests and numerical simulations of liquefaction and lateral spreading. LEAP-UCD-2017*. https://doi.org/10.1007/978-3-030-22818-7_9

Vasko, A. (2015). *An investigation into the behavior of Ottawa sand through monotonic and cyclic shear tests*. Master thesis. The George Washington University.

Zeghal, M., Manzari, M. T., Kutter, B. L., & Abdoun, T. (2015). LEAP: Data, calibration and validation of soil liquefaction models. *Proceedings of the 6th international conference on earthquake geotechnical engineering* (in Christchurch, New Zealand); Paper No. 432.

Chapter 17
LEAP-ASIA-2019 Centrifuge Test Simulations of Liquefiable Sloping Ground

Zhijian Qiu and Ahmed Elgamal

Abstract Numerical simulations of a liquefiable sloping ground for LEAP-ASIA-2019 centrifuge tests are presented. The simulations are performed using a pressure-dependent constitutive model implemented with the characteristics of dilatancy, cyclic mobility, and associated shear deformation. The soil model parameters are determined based on a series of stress-controlled cyclic torsional shear tests of Ottawa F-65 sand with relative density D_r = 60% during calibration phase. Computational framework for the seismic response analysis is discussed and the computed results are presented for all selected centrifuge experiments during Type-C phase. Measured time histories of these experiments are reasonably captured. It is demonstrated that the pressure-dependent constitutive model as well as the overall employed computational framework has the potential to predict the response of the liquefiable sloping ground, and subsequently realistically evaluates the performance of an equivalent soil system subjected to seismically induced liquefaction.

Keywords Liquefaction Experiments and Analysis Project (LEAP-ASIA-2019) · Numerical modelling · PressureDependMultiYield03

Z. Qiu
School of Architecture and Civil Engineering, Xiamen University, Xiamen, Fujian, China

A. Elgamal (✉)
Department of Structural Engineering, University of California San Diego, La Jolla, CA, USA
e-mail: elgamal@ucsd.edu

T. Tobita et al. (eds.), *Model Tests and Numerical Simulations of Liquefaction and Lateral Spreading II*, https://doi.org/10.1007/978-3-031-48821-4_17

17.1 Introduction

LEAP (Liquefaction Experiments and Analysis Projects) is an effort to facilitate validation and verification of numerical procedures for liquefaction-induced lateral spreading analysis of a liquefiable sloping ground (Kutter et al., 2015, 2018, 2020). As part of the ongoing LEAP, a new set of centrifuge tests have been performed in LEAP-ASIA-2019 (Ueda, 2018) to simulate the liquefaction induced lateral spreading phenomenon in a fully saturated sloping ground.

On this basis, the numerical simulation results of these new data during Type-C phase are presented. All the finite element (FE) simulations are performed using a pressure-dependent constitutive model (Parra, 1996; Yang, 2000; Yang & Elgamal, 2002; Elgamal et al., 2003; Yang et al., 2003; Khosravifar et al., 2018; Qiu & Elgamal, 2020a, b) implemented with the characteristics of dilatancy, cyclic mobility, and associated shear deformation. The soil parameters are determined based on a series of stress-controlled cyclic torsional shear tests provided in the calibration phase for matching the liquefaction strength curve of Ottawa F-65 sand with relative density $D_r = 60\%$. To better capture the overall dynamic response of each selected centrifuge test during Type-C phase, two contraction parameters c_4 and c_5 controlling the rate of pore pressure build-up were adjusted based on observations from selected centrifuge test results.

The following sections of this chapter outline (1) computational framework, (2) specifics and calibration processes, (3) details of the employed FE modeling techniques, and (4) computed results of the selected centrifuge tests. Finally, a number of conclusions are presented and discussed.

17.2 Brief Summary of the Centrifuge Tests

A schematic representation of the centrifuge tests (El Ghoraiby et al., 2020) is shown in Fig. 17.1. The soil specimen is a sloping layer of Ottawa F-65 sand with 5° slope (target relative density $D_r = 60\%$). The soil layer has a length of 20 m (in prototype scale) and a height of 4 m (in prototype scale) at the center. The specimen is built in a container with rigid walls. All centrifuge models were subjected to a target motion of ramped, 1 Hz sine wave base motion with amplitude $0.15g$. Figure 17.2 shows the achieved base input motions for all selected centrifuge experiments with various relative densities in LEAP-ASIA-2019 (Ueda, 2018).

17.3 Constitutive Model of Soils

A two-dimensional FE mesh (Fig. 17.3) is created to represent the centrifuge test model, comprising 4961 nodes and 4800 quadrilateral elements (maximum size = 0.2 m). All numerical simulations for the selected centrifuge tests during Type-C phase are performed using the computational platform OpenSees. The Open

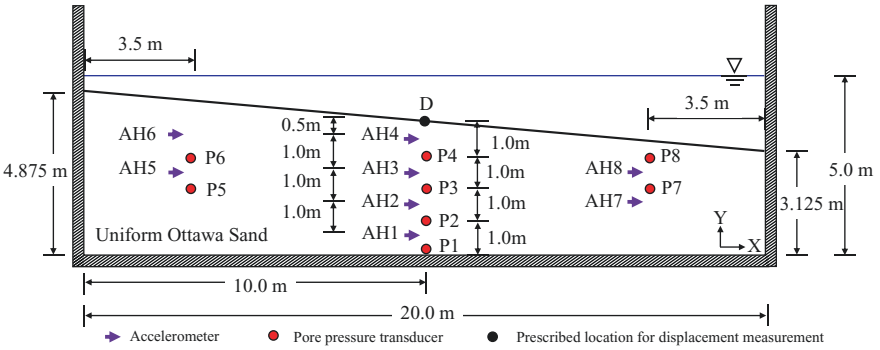

Fig. 17.1 Schematic representation of the LEAP-ASIA-2019 centrifuge test layout

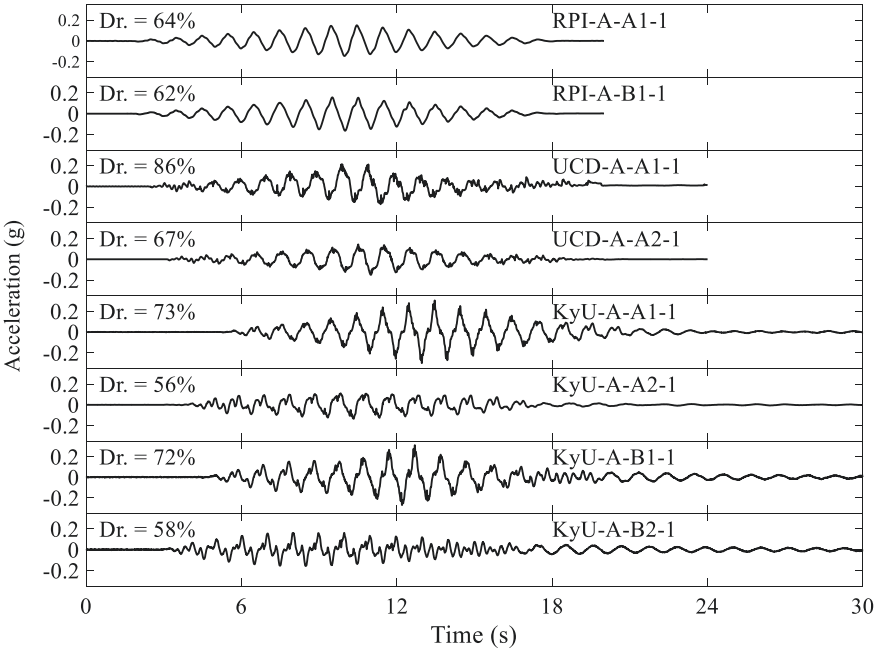

Fig. 17.2 Selected base input motions

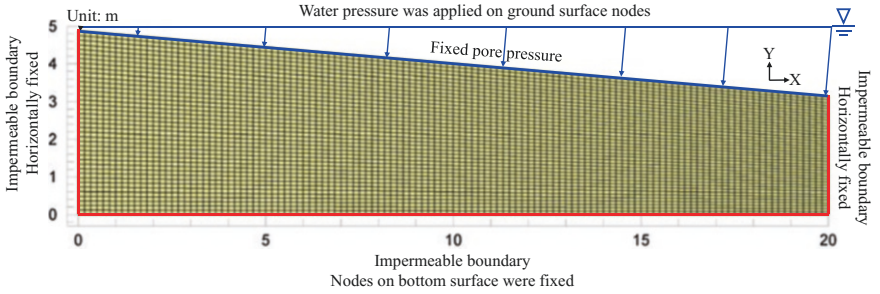

Fig. 17.3 Finite element mesh (maximum size = 0.2 m)

System for Earthquake Engineering Simulation (OpenSees, McKenna et al., 2010, http://opensees.berkeley.edu) developed by the Pacific Earthquake Engineering Research (PEER) Center is an open source, object-oriented finite element platform. Currently, OpenSees is widely used for simulation of structural and geotechnical systems (Yang, 2000; Yang & Elgamal, 2002) under static and seismic loading.

Quadrilateral Four-node plane-strain elements with two-phase material following the *u-p* (Chan, 1988) formulation were employed for simulating saturated soil response, where *u* is the displacement of the soil skeleton and *p* is the pore water pressure. Implementation of the *u-p* element is based on the following assumptions: (1) small deformation and rotation; (2) solid and fluid density remain constant in time and space; (3) porosity is locally homogeneous and constant with time; (4) soil grains are incompressible; (5) solid and fluid phases are accelerated equally. Hence, the soil layers represented by effective stress fully coupled u-p elements (quadUP in OpenSees) are capable of accounting for soil deformations and the associated changes in pore water pressure.

17.3.1 Soil Constitutive Model

The soil is simulated by the implemented OpenSees material PressureDependMultiYield03 (Parra, 1996; Yang, 2000; Yang & Elgamal, 2002; Elgamal et al., 2003; Yang et al., 2003; Khosravifar et al., 2018); In this employed soil constitutive model (Fig. 17.4), the shear-strain backbone curve was represented by

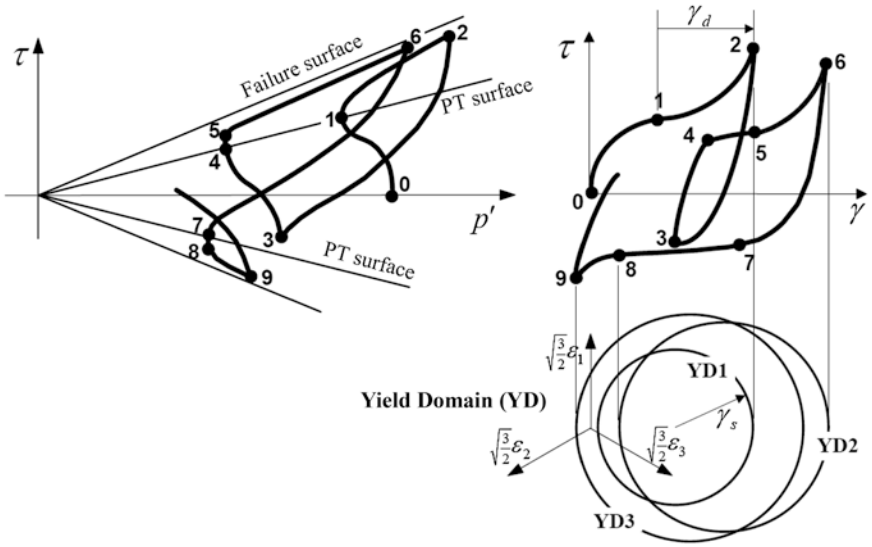

Fig. 17.4 PressureDependMultiYield03 model response and configuration of yield domain in deviatoric strain space. (After Yang & Elgamal, 2002; Elgamal et al., 2003; Yang et al., 2003)

the hyperbolic relationship with the shear strength based on simple shear (reached at an octahedral shear strain of 10%). The low-strain shear modulus under a reference effective confining pressure p_r' is computed using the equation $G = G_0\left(p'/p_r'\right)^n$, where p' is effective confining pressure and G_0 is shear modulus at pressure p_r'. The dependency of shear modulus on confining pressure is taken as $n = 0.5$. The critical state frictional constant M_f (at failure surface) is related to the friction angle ϕ (Chen & Mizuno, 1990) and defined as $M_f = 6\sin\phi/(3\text{-}\sin\phi)$. As such, brief descriptions of this soil constitutive model are included below.

17.3.1.1 Yield Function

The yield function is defined as a conical surface in principal stress space:

$$f = \frac{3}{2}\left(s - \left(p' + p_0'\right)a\right) : \left(s - \left(p' + p_0'\right)a\right) - M^2\left(p' + p_0'\right)^2 = 0 \tag{17.1}$$

where, $\boldsymbol{s} = \boldsymbol{\sigma}' - p'\boldsymbol{\delta}$, is the deviatoric stress tensor, $\boldsymbol{\sigma}'$ is the effective Cauchy stress tensor, $\boldsymbol{\delta}$ is the second-order identity tensor, p' is mean effective stress, p_0' is a small positive constant (0.3 kPa in this chapter) such that the yield surface size remains finite at $p' = 0$ for numerical convenience and to avoid ambiguity in defining the yield surface normal to the yield surface apex, $\boldsymbol{a}$ is a second-order deviatoric tensor defining the yield surface center in deviatoric stress subspace, M defines the yield surface size, and ":" denotes doubly contracted tensor product.

17.3.1.2 Contractive Phase

Shear-induced contraction occurs inside the phase transformation (PT) surface ($\eta < \eta_{PT}$), as well as outside ($\eta > \eta_{PT}$) when $\dot{\eta} < 0$, where, η is the deviatoric stress ratio defined as $\sqrt{\frac{3}{2}s:s}/\left(p' + p_0'\right)$ and η_{PT} is the deviatoric stress ratio at phase transformation surface (Fig. 17.4). The contraction flow rule is defined as:

$$\begin{aligned} P'' &= \left(1 - \frac{\dot{n}:\dot{s}}{\|\dot{s}\|}\frac{\eta}{\eta_{PT}}\right)^2 \left(c_1 + c_2\gamma_c\right)\left(\frac{p'}{p_a}\right)^{c_3}\left(c_4\eta_{rv}\right)^{c_5} \\ \eta_{rv} &= \frac{\sqrt{\left[\left(\sigma_{11} - \sigma_{22}\right)^2 + \left(\sigma_{22} - \sigma_{33}\right)^2 + \left(\sigma_{11} - \sigma_{33}\right)^2\right]/2 + \tau_{12}^2 + \tau_{23}^2 + \tau_{13}^2}}{\left(p' + p_0'\right)} \end{aligned} \tag{17.2}$$

where c_1, c_2, c_3, c_4, and c_5 are non-negative calibration constants, γ_c is octahedral shear strain accumulated during previous dilation phases, p_a is atmospheric pressure for normalization purpose, and $\dot{s}$ is the deviatoric stress rate. In Eq. 17.2, η_{rv} is the

shear stress ratio on load reversal point during cyclic loading, essentially representing the effect of previous shear stress on the subsequent contractive behavior. The $\dot{n}$ and $\dot{s}$ tensors are used to account for general 3D loading scenarios, where, $\dot{n}$ is the outer normal to a surface. The parameter c_3 is used to represent the dependence of pore pressure buildup on initial confinement (i.e., $k\sigma$ effect).

17.3.1.3 Dilative Phase

Dilation appears only due to shear loading outside the PT surface ($\eta > \eta_{PT}$ with $\dot{\eta} > 0$), and is defined as:

$$P'' = \left(1 - \frac{\dot{n} : \dot{s}}{\|\dot{s}\|} \frac{\eta}{\eta_{PT}}\right)^2 \left(d_1 + \gamma_d^{d_2}\right) \left(\frac{p'}{p_a}\right)^{-d_3} \tag{17.3}$$

where d_1, d_2, and d_3 are non-negative calibration constants, and γ_d is the octahedral shear strain accumulated from the beginning of a particular dilation cycle (such as, stage 1–2 or 5–6 in Fig. 17.4) as long as there is no significant load reversal. Subsequently, dilation rate increases as the shear strain accumulates in a particular cycle. Furthermore, a significant unloading (such as stage 6–8 in Fig. 17.4) will reset γ_d to zero. Parameter d_3 in Eq. 17.3 reflects the dependence of pore pressure buildup on initial confinement (i.e., $k\sigma$ effect).

17.3.1.4 Neutral Phase

When the stress state approaches the PT surface ($\eta = \eta_{PT}$) from below, a significant amount of permanent shear strain may accumulate prior to dilation, with minimal changes in shear stress and confinement (implying $P'' = 0$). For simplicity, $P'' = 0$ is maintained during this highly yielded phase until a boundary defined in deviatoric strain space is reached, and then dilation begins. This yield domain will enlarge or translate depending on load history. In deviatoric strain space, the yield domain (Fig. 17.4) is a circle with the radius γ defined as (Yang et al., 2003):

$$\begin{aligned} \gamma &= \frac{\gamma_s + \gamma_{rv}}{2} \\ \gamma_s &= y_1 \frac{p'_{max} - p'_n}{p'_{max}}^{0.25} \int_t^0 d\gamma_c \\ \gamma_{rv} &= y_2 \frac{p'_{max} - p'}{p'_{max}}^{0.25} \operatorname{oct}\left(e - e_p\right) \end{aligned} \tag{17.4}$$

where, y_1 (non-negative) is used to define the accumulated permanent shear strain γ_s as a function of dilation history $\int_0^t d\gamma_c$ and allow for continuing enlargement of the domain, p'_{max} is maximum mean effective confinement experienced during cyclic loading, p'_n is mean effective confinement at the beginning of current neutral phase, and $\langle\ \rangle$ denotes MacCauley's brackets (i.e., $\langle a \rangle = \max(a, 0)$). The y_2 (non-negative) parameter is mainly used to define the biased accumulation of permanent shear strain γ_{rv} as a function of load reversal history and allows for translation of the yield domain during cyclic loading. In Eq. 17.4, oct($\boldsymbol{e} - \boldsymbol{e}_p$) denotes the octahedral shear strain of tensor $\boldsymbol{e} - \boldsymbol{e}_p$, where $\boldsymbol{e}$ is current deviatoric shear strain, and $\boldsymbol{e}_p$ is pivot strain obtained from previous dilation on load reversal point.

17.3.2 Boundary and Loading Conditions

The boundary and loading conditions for dynamic analysis of the liquefiable sloping ground (Fig. 17.3) under a base input motion are implemented in a staged fashion as follows:

1. Gravity was applied to activate the initial static state with the following: (i) linear elastic properties (Poisson's ratio of 0.47 to lower the initial locked shear stress), (ii) nodes on both side boundaries (vertical faces) of the FE model were fixed against longitudinal translation for complicity, (iii) nodes were fixed along the base against vertical translation only to avoid superfluous unrealistic initial locked shear stress at the model base, (iv) water table was specified with related water pressure and nodal forces specified along ground surface nodes, and flow of water was restricted to across the container boundaries.
2. Nodes were fixed along the base against longitudinal translation.
3. Soil properties were switched from elastic to plastic and the internal variables of the constitutive model were adjusted to this stress state (Fig. 17.5 before shaking).
4. Dynamic analysis is conducted by applying an acceleration time history to the base of the FE model.

The FE matrix equation is integrated in time using a single-step predictor multicorrector scheme of the Newmark type with integration parameters $\gamma = 0.6$ and $\beta = 0.3025$ presented in early studies (Chan, 1988; Parra, 1996). The equation is solved using the modified Newton-Raphson method, i.e., Krylov subspace acceleration (Carlson & Miller, 1998) for each time step. For the convergence criterion, a test of energy increment is used with 10^{-6} and maximum number of iterations of 50. Furthermore, the constraints are imposed using Transformation method in OpenSees. Finally, a relatively low-level of initial stiffness proportional damping (coefficient = 0.003 leading to 1% damping ratio at frequency = 1 Hz) with the main damping emanating from the soil nonlinear shear stress-strain hysteresis response (Parra, 1996) was used to enhance numerical stability of the liquefiable sloping system.

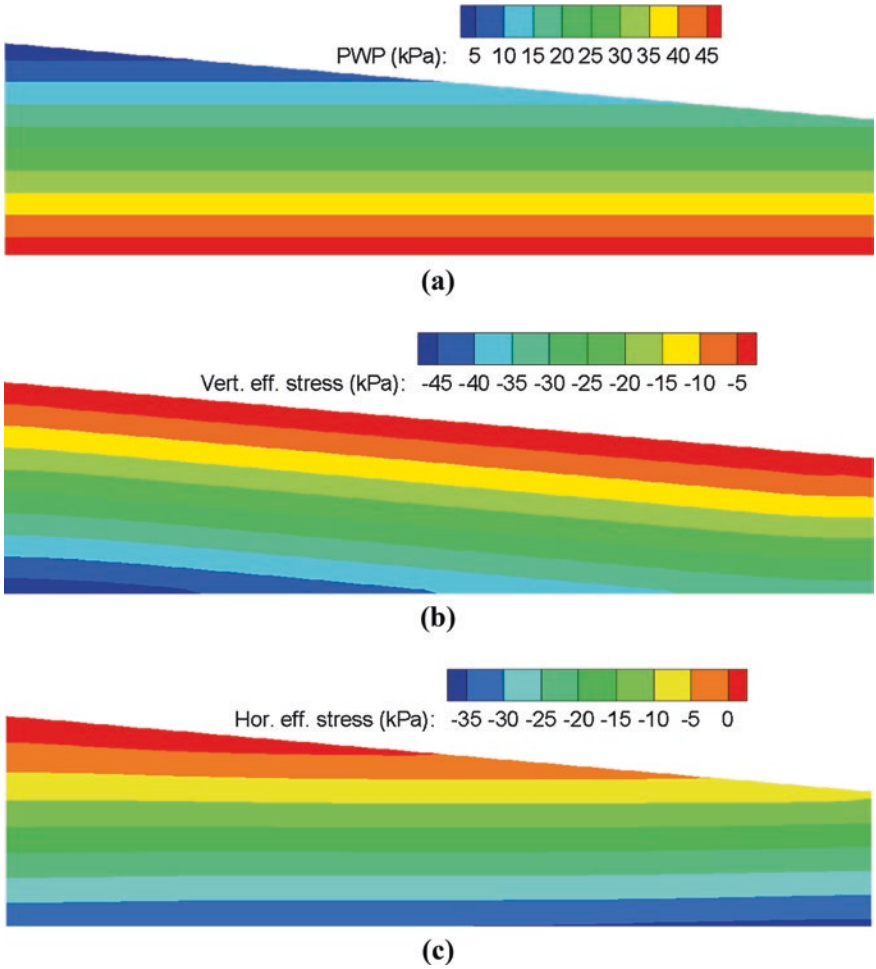

Fig. 17.5 Initial state of soil due to gravity (before shaking): (**a**) Pore water pressure; (**b**) Vertical effective stress σ'_{yy} ; (**c**) Horizontal effective stress σ'_{xx}

17.4 Determination of Soil Model Parameters

To predict dynamic response of centrifuge tests in LEAP-ASIA-2019, the employed soil constitutive model parameters are calibrated for matching the liquefaction strength curve of the Ottawa F-65 sand with relative density D_r = 60%, which will be further used in Type-C simulations. For that purpose, a total of four undrained stress-controlled cyclic torsional shear tests for Ottawa F-65 sand are performed and the laboratory results are provided in calibration phase (Ueda, 2018). The

Table 17.1 Sand model parameters in calibration phase and Type-C simulations

Model parameters	LEAP-ASIA-2019
Relative density	60%
Reference mean effective pressure, p'_r (kPa)	101
Mass density ρ (t/m^3)	2.0
Maximum shear strain at reference pressure, $\gamma_{max,r}$	0.1
Shear modulus at reference pressure, *Go* (MPa)	23
Stiffness dependence coefficient *d*, $G = Go\left(\frac{P'}{P'_r}\right)^d$	0.5
Poisson's ratio *v* (for dynamics)	0.4
Shear strength at zero confinement, *c* (kPa)	0.3
Friction angle, ϕ	30°
Phase transformation angle, ϕ_{PT}	20°
Contraction coefficient, c_1	0.015
Contraction coefficient, c_2	3.0
Contraction coefficient, c_3	0.15
Contraction coefficient, c_4	7.0/0.6[a]/0.2[b]
Contraction coefficient, c_5	4.0/1.0[a]/0.1[b]
Dilation coefficient, d_1	0.06
Dilation coefficient, d_2	3.0
Dilation coefficient, d_3	0.2
Damage parameter, y_1	0.6
Damage parameter, y_2	0.0
Permeability (m/s)	1.1×10^{-4}
Number of yield surfaces	20

[a]Adjusted for RPI-A-A1-1, RPI-A-B1-1, UCD-A-A1-1 and UCD-A-A2-1 centrifuge tests
[b]Adjusted for KyU-A-A1-1, KyU-A-A2-1, KyU-A-B1-1 and KyU-A-B2-1 centrifuge tests

permeability of the Ottawa F-65 sand is about 1.1×10^{-4} m/s determined from El Ghoraiby et al., 2020. On this basis, the calibrated soil model parameters are listed in Table 17.1.

Figure 17.6 shows the comparison results of computed and experimental liquefaction strength curves. The data plotted in Fig. 17.6 is composed of the number of cycles until a 7.5% double amplitude (i.e., 3.75% single amplitude) of strain is achieved versus the applied cyclic stress ratio. It can be seen that the computed results are in good agreement with the laboratory data. An example of undrained stress-controlled torsional shear test with CSR = 0.2 is illustrated in Fig. 17.6b–e. The computed results reasonably match the stress path and shear stress-strain response of laboratory test results (Ueda, 2018).

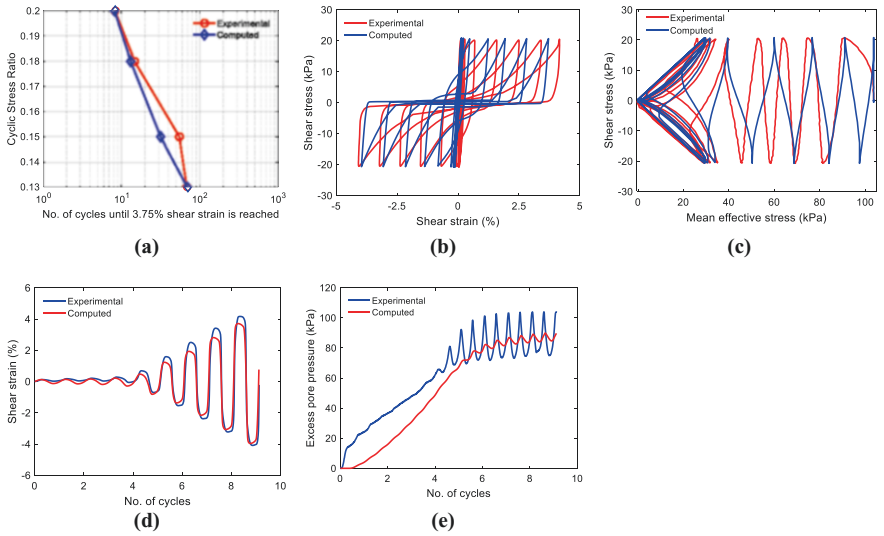

Fig. 17.6 Torsional shear tests: (**a**) Liquefaction strength curve; (**b**)-(**e**) Undrained stress-controlled cyclic soil response with CSR = 0.2. (Qiu & Elgamal, 2020a, b)

17.5 Computed Results of Type-C Simulations

This section presents the simulation results of selected eight centrifuge tests during Type-C phase. The achieved base input motions of selected centrifuge tests with different relative densities at various facilities are displayed in Fig. 17.2. The material parameters (Table 17.1) are calibrated primarily for matching the liquefaction strength curve of Ottawa F-65 sand with D_r = 60% in calibration phase. To better capture the overall dynamic response of centrifuge tests of RPI-A-A1-1, RPI-A-B1-1, UCD-A-A1-1 and UCD-A-A2-1, the contraction parameters c_4 = 7.0 and c_5 = 4.0 in Table 17.1 are adjusted to 0.6 and 0.1, respectively. The experimental results of RPI-A-A1–1 (D_r = 64%) are selected as the calibration basis for adjusting the material parameters c_4 and c_5. As such, the numerical simulations of RPI-A-B1-1, UCD-A-A1-1 and UCD-A-A2-1 are performed based on the material properties from calibration phase (Table 17.1) with the adjusted parameters c_4 and c_5 obtained from the calibration of RPI-A-A1-1.

As observed from the four centrifuge test results of KyU, the pore pressure transducers are not providing consistent results with those from RPI and UCD. As such, contraction parameters c_4 and c_5 are further adjusted to 0.2 and 0.1, respectively, to better capture the much slower pore pressure build-up rate in these centrifuge tests of KyU. In the following results, numerical simulations of four KyU centrifuge tests are performed based on the material properties from calibration phase (Table 17.1) with the newly adjusted parameters c_4 and c_5.

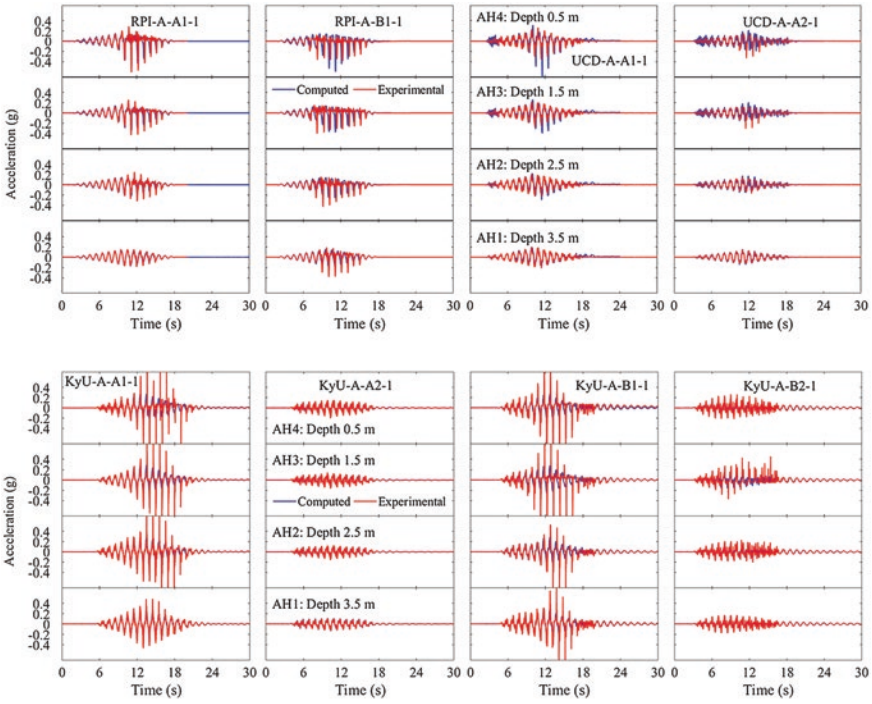

Fig. 17.7 Measured and computed acceleration time histories

17.5.1 Acceleration

Figure 17.7 depicts the computed and experimental acceleration time histories at locations AH1-AH4 (Fig. 17.1). It can be seen that the computed accelerations reasonably match those from the measurements in RPI-A-A1-1, UCD-A-A2-1, KyU-A-A21, and KyU-A-B2-1 (Fig. 17.7). Both the computed results and measurements showed a consistent trend of acceleration spikes due to dilation. However, there are significant differences in the rest of simulations compared to the experimental data. As seen in this Fig. 17.7, the accelerations spikes are overpredicted by RPI-A-B1–1, UCD-A-A1-1, and are underpredicted by KyU-A-A1-1, KyU-A-B1-1, mainly due to the different relative densities at various facilities.

17.5.2 Excess Pore Pressure Ratio

Figure 17.8 illustrates the time histories of excess pore pressure ratio r_u. It can be seen that the computed excess pore pressure r_u reasonably matches with those from the centrifuge tests of RPI-A-A1-1, RPI-A-B1-1, and UCD-A-A2-1. However, in

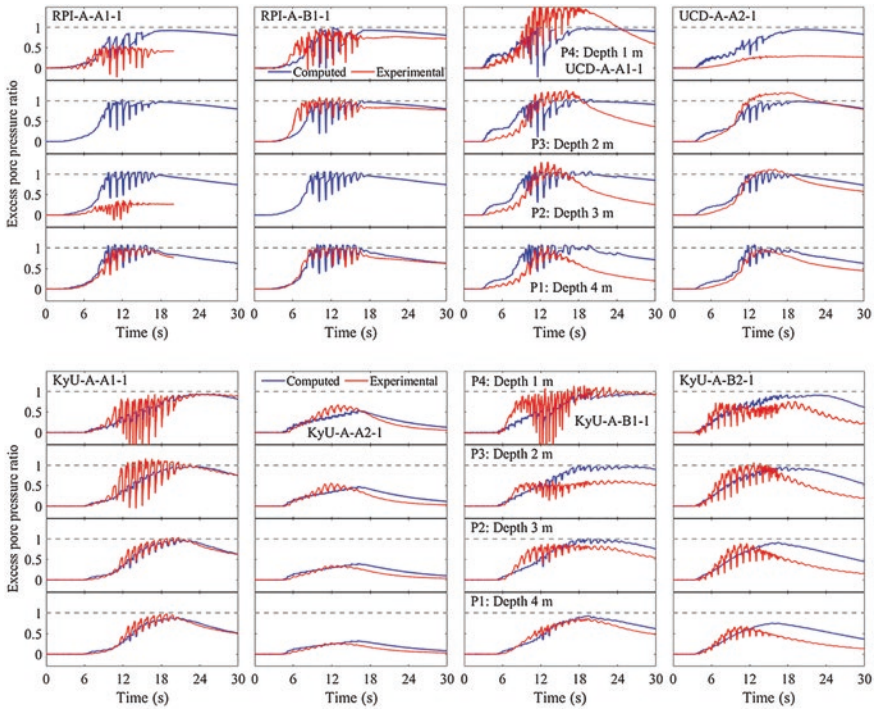

Fig. 17.8 Measured and computed time histories of excess pore pressure ratio

calibration of UCD-A-A1-1, the computed results showed a relatively faster pore pressure build-up compared to the measurements.

In four tests of KyU, the much slower pore pressure build-up rate exhibited in measurements is well captured by further adjusting contraction parameters c_4 and c_5 (as discussed above) in numerical simulations. As such, both the computed results and measurements (Fig. 17.8) showed a consistent trend of negative spikes due to dilation. In addition, the dissipation of computed pore pressure generally following the trend of measurements after shaking.

17.5.3 Displacement

Figure 17.9 displays the computed horizontal displacement time histories and measurements at the midpoint of the ground surface. It can be seen that the computed results of RPI-A-A1-1, UCD-A-A2-1, and the four tests of KyU are in good agreement with those from measurements. However, some discrepancies are seen between the simulation results and experimental measurements in tests of RPI-A-B1-1 and UCD-A-A1-1. This higher amount of experimental permanent displacement of

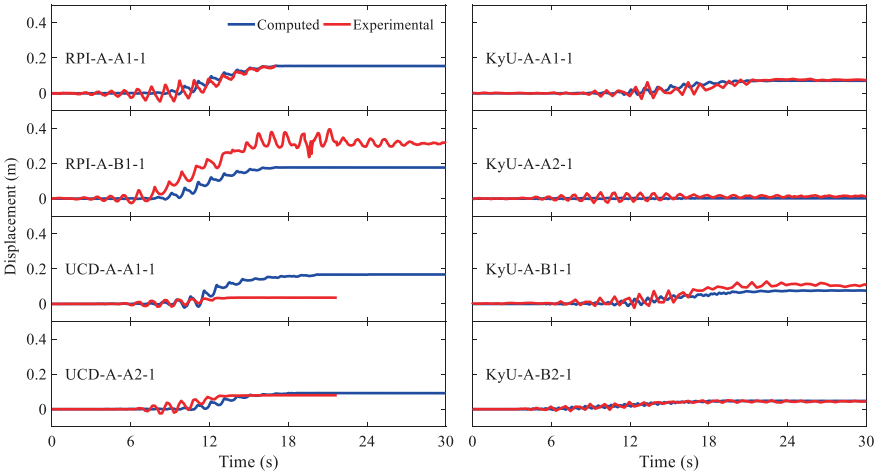

Fig. 17.9 Measured and computed displacement time histories

RPI-A-B1-1 can be better captured by further adjusting the parameter y_2 in numerical simulation (as discussed below).

17.5.4 Computed Response of RPI-A-B1-1

An additional numerical simulation is performed to better capture the horizontal permanent displacement of RPI-A-B1-1. In this scenario, parameter $y_2 = 0$ (Table 17.1) is adjusted to 1.0, in order to reproduce a higher accumulation of shear deformation during earthquake loading. For comparison purposes, the computed results with material parameters $y_2 = 0$ and 1.0 are displayed in one figure (Figs. 17.10 and 17.11). As seen in Fig. 17.10, the computed permanent displacement ($y_2 = 1$) is accumulating faster than that of scenario $y_2 = 0$ after 11 s, and eventually matches the experimental result (about 0.3 m) at end of shaking.

Figure 17.10b shows the horizontal displacement contour with arrows displaying the direction of ground movement. It can be seen that the horizontal displacements of soil ground at deeper depths are also high due to the liquefaction of underlying soil layers (Fig. 17.8). Vertical displacement contour at end of shaking is illustrated in Fig. 17.10c. As seen in this figure, the upslope soil settled about 0.2 m and ground heave in downslope reached about 0.08 m. In accordance with the deformation contour, Fig. 17.10c shows the shear strain γ_{xy} contour with a peak value of about 12% at deeper depth of the liquefiable sloping ground.

Figure 17.11 depicts the computed shear stress versus mean effective stress, and shear stress versus shear strain for integration points near the locations of pore pressure transducers (P1–P4). It can be seen that the computed results with adjusted parameter $y_2 = 1.0$ reproduce a larger cycle-by-cycle accumulation of shear deformation in downslope direction than that of scenario $y_2 = 0$.

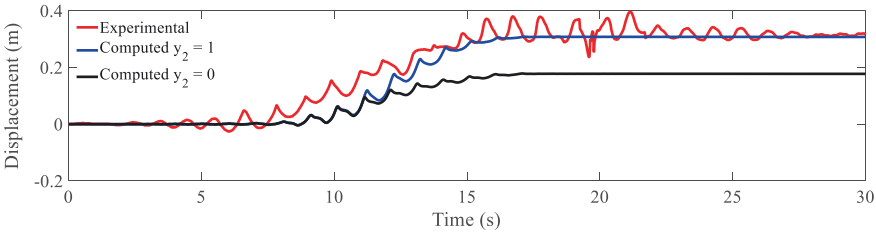

(a)

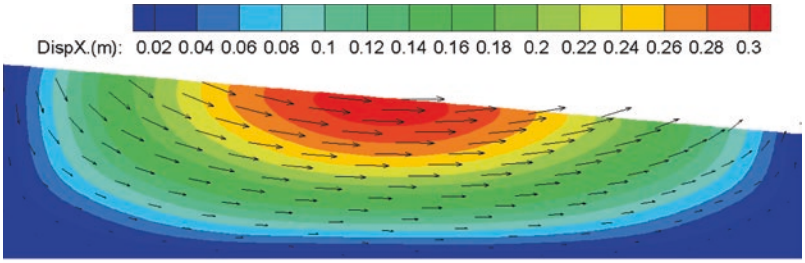

(b)

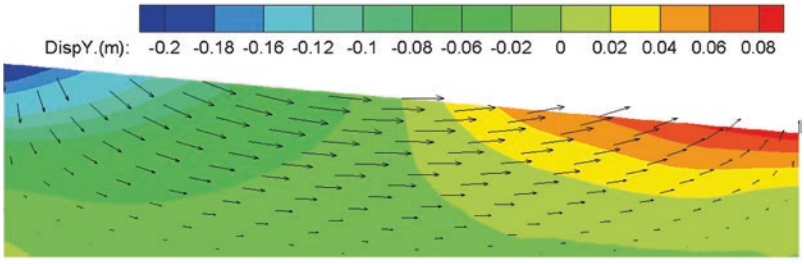

(c)

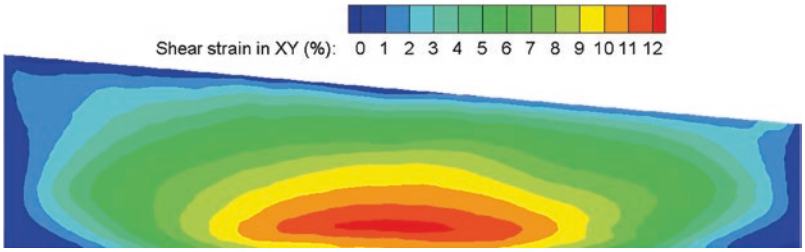

(d)

Fig. 17.10 Adjusted parameter y_2 = 1.0 to capture horizontal permanent deformation of RPI-A-B1–1: (**a**) Displacement time history; (**b**) Horizontal displacement contour; (**c**) Vertical displacement contour; (**d**) Shear strain contour. (Qiu & Elgamal, 2020a, b)

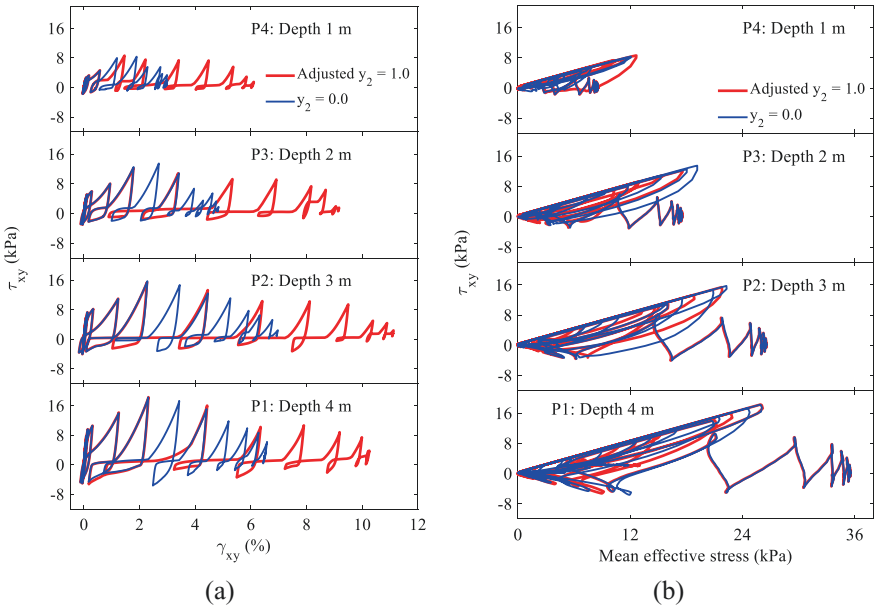

Fig. 17.11 Adjusted parameter $y_2 = 1.0$ to capture horizontal permanent deformation of RPI-A-B1–1: (**a**) Shear stress-strain; (**b**) Mean effective stress-shear stress

17.6 Conclusions

The numerical simulation results of centrifuge model tests (Type-C phase) conducted by various facilities in LEAP-ASIA-2019 for a liquefiable sloping ground are presented. All the numerical simulations are performed using a calibrated pressure-dependent constitutive model (PressureDependMultiYield03) implemented with the characteristics of dilatancy, cyclic mobility, and associated shear deformation. The soil parameters are determined based on a series of stress-controlled cyclic torsional shear tests (provided in the calibration phase) for matching the liquefaction strength curves of Ottawa F-65 sand with relative density $D_r = 60\%$ in LEAP-ASIA-2019. The computational framework and staged analysis procedure are presented as well. The primary conclusions can be drawn as follows:

1. The unintended inconsistencies of centrifuge test results in Type-C phase may indeed hinder the comparisons between numerical simulations and measurements. To better capture the overall dynamic response of selected centrifuge tests, contraction parameters c_4 and c_5 (controlling the pore pressure build-up rate) are suggested to be adjusted to simulate the inconsistent contractive behavior exhibited by Ottawa F-65 sand of various relative densities.
2. Although the centrifuge tests conducted by various institutions are not providing completely consistent results, measured time histories are reasonably captured by the numerical simulations in LEAP-ASIA-2019, using the same soil constitu-

tive model parameters. The good agreement between computed and measured results for each centrifuge test demonstrated that the PressureDependMultiYield03 soil model as well as the overall employed computational methodology have the potential to predict the response of liquefiable sloping ground, and subsequently realistically evaluate the performance of analogous soil systems subjected to seismically induced liquefaction.

3. Permanent deformations of the liquefiable sloping ground are captured to a reasonable level. However, further adjustment of damage parameters y_1 and y_2 is much helpful to quantify the permanent displacement. As such, additional experimental data sets are needed related to large post-liquefaction shear deformation accumulation. As such new data sets become available, parameters y_1 and y_2 of the PressureDependMultiYield03 material can be better calibrated and applied in the prediction of liquefaction-induced lateral spreading.

Acknowledgments The authors are grateful for the kind invitation by Professors Tetsuo Tobita and Kyoheito Ueda to participate in LEAP-ASIA-2019. Partial funding of this effort was provided by Caltrans through a project in which Ottawa sand is being used for experimentation.

References

Carlson, N. N., & Miller, K. (1998). Design and application of a gradient-weighted moving finite element code II: In two dimensions. *SIAM Journal on Scientific Computing, 19*(3), 766–798.

Chan, A. H. C. (1988). *A unified finite element solution to static and dynamic problems in geomechanics*. PhD thesis. University College of Swansea.

Chen, W. F., & Mizuno, E. (1990). *Nonlinear analysis in soil mechanics, theory and implementation*. Elsevier.

El Ghoraiby, M., Park, H., & Manzari, M. T. (2020). Physical and mechanical properties of Ottawa F65 sand. In *Model tests and numerical simulations of liquefaction and lateral spreading* (pp. 45–67). Springer.

Elgamal, A., Yang, Z., & Parra, E. (2003). Modeling of cyclic mobility in saturated cohesionless soils. *International Journal of Plasticity, 19*(6), 883–905.

Khosravifar, A., Elgamal, A., Lu, J., & Li, J. (2018). A 3D model for earthquake-induced liquefaction triggering and post-liquefaction response. *Soil Dynamics and Earthquake Engineering, 110*, 43–52.

Kutter, B. L., Carey, T. J., Hashimoto, T., Manzari, M. T., Vasko, A., Zeghal, M., & Armstrong, R. J. (2015). LEAP databases for verification, validation, and calibration of codes for simulation of liquefaction. In *Sixth international conference on earthquake geotechnical engineering, Christchurch, New Zealand*.

Kutter, B. L., Carey, T. J., Hashimoto, T., Zeghal, M., Abdoun, T., Kokkali, P., Madabhushi, G., Haigh, S. K., d'Arezzo, F. B., Madabhushi, S., & Hung, W. Y. (2018). LEAP-GWU-2015 experiment specifications, results, and comparisons. *Soil Dynamics and Earthquake Engineering, 113*, 616–628.

Kutter, B. L., Manzari, M. T., & Zeghal, M. (2020). Model tests and numerical simulations of liquefaction and lateral spreading. In *LEAP-UCD-2017 proceedings*. Springer.

McKenna, F., Scott, M. H., & Fenves, G. L. (2010). Nonlinear finite-element analysis software architecture using object composition. *Journal of Computing in Civil Engineering, 24*(1), 95–107.

Parra, E. (1996). *Numerical modeling of liquefaction and lateral ground deformation including cyclic mobility and dilation response in soil systems*. PhD thesis. Rensselaer Polytechnic Institute.

Qiu, Z., & Elgamal, A. (2020a). Numerical simulations of LEAP dynamic centrifuge model tests for response of liquefiable sloping ground. In *Model tests and numerical simulations of liquefaction and lateral spreading* (pp. 521–544). Springer.

Qiu, Z., & Elgamal, A. (2020b). Numerical simulations of LEAP centrifuge tests for seismic response of liquefiable sloping ground. *Soil Dynamics and Earthquake Engineering, 139*(2020), 106378. https://doi.org/10.1016/j.soildyn.2020.106378

Ueda, K. (2018). *LEAP-Asia-2018: Stress-strain response of Ottawa sand in cyclic torsional shear tests*. DesignSafe-CI., Dataset. https://doi.org/10.17603/DS2D40H

Yang, Z. (2000). *Numerical modeling of earthquake site response including dilation and liquefaction*. PhD thesis. Columbia University.

Yang, Z., & Elgamal, A. (2002). Influence of permeability on liquefaction-induced shear deformation. *Journal of Engineering Mechanics, 128*(7), 720–729.

Yang, Z., Elgamal, A., & Parra, E. (2003). Computational model for cyclic mobility and associated shear deformation. *Journal of Geotechnical and Geoenvironmental Engineering, 129*(12), 1119–1127.

Chapter 18
LEAP-ASIA-2019 Type-B Simulations Through FLIP

Junichi Hyodo and Koji Ichii

Abstract This chapter presents numerical simulation by using FLIP ROSE (Iai et al, Soils Found 32(2):1–15, 1992). FLIP ROSE is one of effective stress analysis used widely in Japan. It is commonly used to verify the seismic performance in practical design of port structures such as caisson-type quay walls and sheet pile quay walls. By using this program, we conducted the numerical simulation exercise for some cases.

Keywords Liquefaction Experiments and Analysis Project (LEAP-ASIA-2019) · Numerical modelling · FLIP

18.1 Introduction

LEAP (Liquefaction Experiments and Analysis Project) is an international joint research project to discuss the modeling of the centrifuge test and numerical modeling of liquefaction.

Summary of centrifuge experiments is listed in Tables 18.1 and 18.2. In this chapter, numerical simulation of phase II was performed for "KyU_A_2_1", "RPI_A_A1_1," "UCD_A_A2_1," "KyU_A_B2_1," and "RPI_A_B1_1" (Fig. 18.1).

J. Hyodo (✉)
Tokyo Electric Power Services Co., Tokyo, Japan
e-mail: hyoudou@tepsco.co.jp

K. Ichii
Faculty of Societal Safety Science, Kansai University, Osaka, Japan
e-mail: ichiik@kansai-u.ac.jp

T. Tobita et al. (eds.), *Model Tests and Numerical Simulations of Liquefaction and Lateral Spreading II*, https://doi.org/10.1007/978-3-031-48821-4_18

Table 18.1 Summary of centrifuge experiments, Model A in LEAP-ASIA-2018

Test case	Density (kg/m^3)	D_r (%)	Virtual 1G, μ	Centrifuge, η	PGAeff (g)	Avg. disp. (mm)	Shaking direction
IFSTTAR_A_A1_1	1645	62	1	50	0.348	550.00	Axial
KAIST_A_A1_1	1716.55	87	1	40	0.287	33.93	Axial
KyU_A_A1_1[a]	1677	73	1	44.4	0.248	71.04	Tangential
KyU_A_A2_1[b]	1628	56	1	44.4	0.118	11.10	Tangential
NCU_A_A1_1	1643	61	1	26	0.144	181.51	Axial
RPI_A_A1_1[b]	1651	64	1	23	0.143	99.56	Axial
UCD_A_A1_1[a]	1713.3	86	1	43.75	0.178	30.56	Tangential
UCD_A_A2_1[b]	1658.1	67	1	43.75	0.134	77.50	Tangential
ZJU_A_A1_1[a]	1624.6	54	1	30	0.272	390.00	Axial

[a]Test cases optional but highly recommended
[b]Test cases selected as required cases for Type-C simulations

Table 18.2 Summary of centrifuge experiments, Model B in LEAP-ASIA-2018

Test case	Density (kg/m^3)	D_r (%)	Virtual 1G, μ	Centrifuge, η	PGAeff (g)	Avg. disp. (mm)	Shaking direction
CU_A_B1_1	1606	47	0.5	80	––		Tangential
Ehime_A_B1_1	1650.8	64	2	20	0.158	56.57	Axial
IFSTTAR_A_B1_1	1645	62	2	25	0.405	777.82	Axial
KAIST_A_B1_1	1720.6	88	1.5	26.7	0.317	30.58	Axial
KyU_A_B1_1[a]	1673	72	2	22.2	0.252	153.84	Tangential
KyU_A_B1_2	1669	71	4	11.1	0.248	115.44	Tangential
KyU_A_B2_1[b]	1633	58	2	22.2	0.126	34.54	Tangential
NCU_A_B1_1	1626	55	2	13	0.131	87.18	Axial
RPI_A_B1_1[b]	1644	62	0.5	46	0.151	303.27	Axial
UCD_A_B1_1	1711.7	85	2	21.9	0.140	−2.23	Tangential
ZJU_A_B1_1	1632.7	57	2	15	0.271	678.82	Axial

[a]Test cases optional but highly recommended
[b]Test cases selected as required cases for Type-C simulations

18.2 Constitutive Model of Soils

We conducted element test simulation and 2D analysis for the numerical simulation exercises. The 2D analysis was performed by using FLIP ROSE Ver7.4.2. In this program, a strain space multiple mechanism model (Iai et al., 1992, 2011) is used.

The model in FLIP ROSE is based on the multiple mechanism model (Towhata & Ishihara, 1985). In this model, the stress-strain relationship in each arbitrary shear direction was modeled as a hyperbolic relationship. The cocktail glass model is the

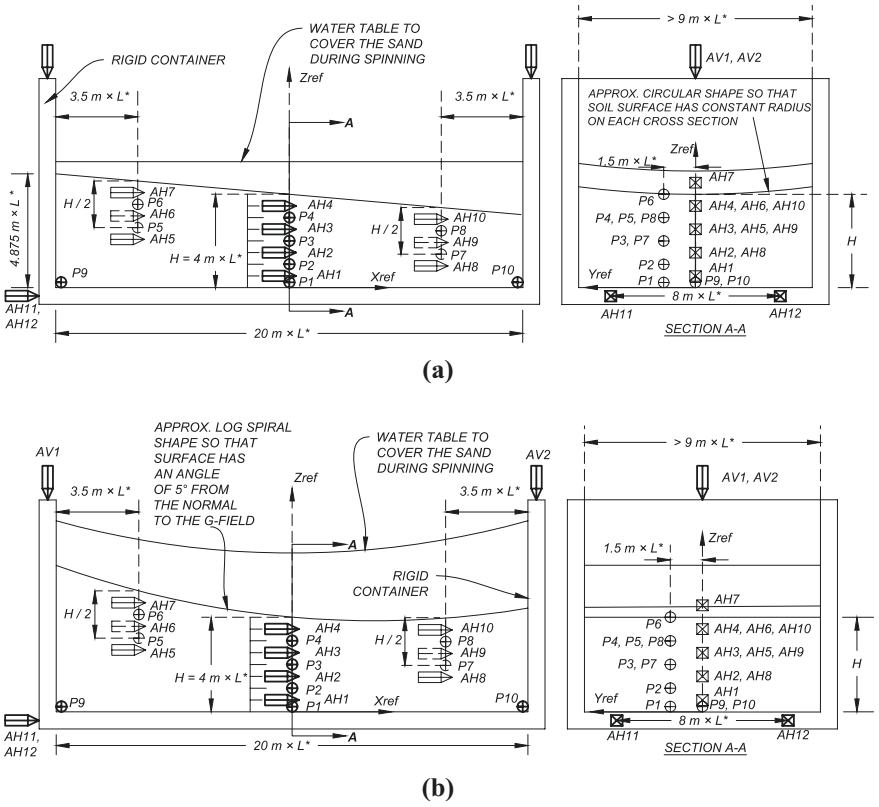

Fig. 18.1 Schematic for LEAP-ASIA-2018 centrifuge model tests: (**a**) Sectional drawing for shaking parallel to the axis of the centrifuge; (**b**) Sectional drawing for shaking in the plane of spinning of the centrifuge

most advanced model for liquefaction in FLIP ROSE. In this model, the dilatancy model is given as the sum of contractive part and dilative part.

18.3 Detailed Specification of Numerical Simulation (FE Analysis)

18.3.1 Phase I of Numerical Simulation

We conducted the simulation exercise to calibrate constitutive models using the results of torsional shear tests (for D_r = 50% and 60% under 100 kPa) Tables 18.3 and 18.4 list the parameters of the strain space multiple mechanism model. The most of parameters were set by various tests. The parameters for dilatancy were decided by trial-and-error. Figure 18.2, 18.3, 18.4, 18.5, 18.6 and 18.7 show the results of the simulation of torsional shear tests.

Table 18.3 Parameters for soil

Parameters			LEAP	Memo
Mass density	ρ	(g/cm^3)	2.04	
Porosity	n		0.370	Computed shear modulus in "LEAP – 2018 – Stress – Strain Response of Ottawa F65.pdf"
Initial shear modulus	G_{ma}	(kN/m^2)	67,900	Computed shear modulus in "LEAP – 2018 – Stress – Strain Response of Ottawa F65.pdf"
Bulk modulus	K_{ma}	(kN/m^2)	177,000	
Mean effective confining pressure	σ'_{ma}	(kN/m^2)	100.0	
Parameter	m_G, m_K		0.50	
Poisson ration	ν		0.330	
Damping constant	h_{max}		0.240	
Cohesion	c'	(kN/m^2)	0.0	
Internal friction angle	φ'	(degrees)	48.0	

Table 18.4 Parameters for dilatancy

Parameters		D_r = 50%	D_r = 60%
Maximum damping constant	H_{maxL}	0.24	0.24
Phase transformation angle	f_p	28.0	28.0
Ultimate value of volumetric strain due to contractive dilatancy	$-\varepsilon_d^{cm}$	0.20	0.20
Specify parameter that controls contractive dilatancy	r_{edc}	3.00	2.00
Truction error for convergence calculation	STOL	1.0×10^{-6}	1.0×10^{-6}
Specify parameter that control both contractive and dilative dilatancy	r_{ed}	0.60	0.60
Specify parameter that control the shape of upstroke parts in the process of buildup or excess pore water pressure	q_1	1.0	1.0
Specify parameter that control the shape of later parts in the process of buildup or excess pore water pressure	q_2	1.0	1.0
Specify reduction factor of bulk modulus	r_K''	0.5	0.5
Specify parameter that represents the confining pressure dependence of bulk modulus in the process from buildup to dissipation of excess pore water pressure	l_K	2.0	2.0
Specify reduction factor of bulk modulus	r_K	0.5	0.5
Specify lower limit of variable S_0	S_1	0.005	0.005
Specify parameter that controls lower limit of liquefaction resistance curve	c_1	1.36	1.45
Specify undrained shear strength at steady state	q_{us}	0.0	0.0
Specify parameter that controls how much influence S0 has on calculating reference strain when considering liquefaction	q_4	1.0	1.0
Reduction factor in tmp methods such as tmp7 method	r_g	0.1	0.1
Specify parameter that controls the area in which the reduction factor described above is set to 0.0 in tmp methods	r_{mtmp}	0.5	0.5
Specify how to calculate the reduction factor r^{tmp} described above in tmp methods	I865SW	0	0

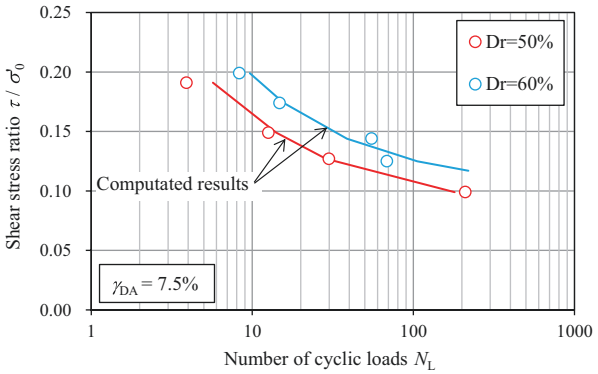

Fig. 18.2 Results of the simulation of torsional shear tests (for D_r = 50% and 60%)

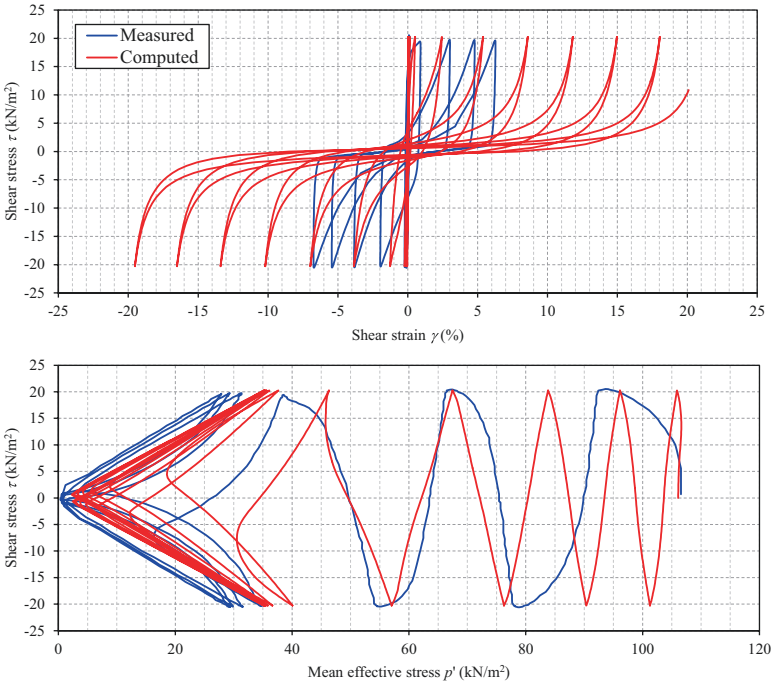

(a) Shear stress ration r=0.19

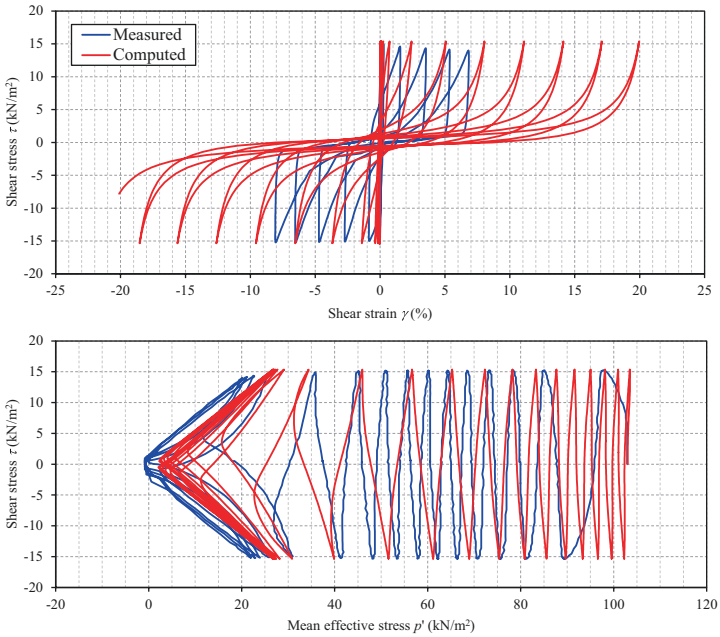

(b) Shear stress ration r=0.15

Fig. 18.3 Results of the simulation of torsional shear tests (for D_r = 50%). (**a**) Shear stress ration r = 0.19; (**b**) Shear stress ration r = 0.15

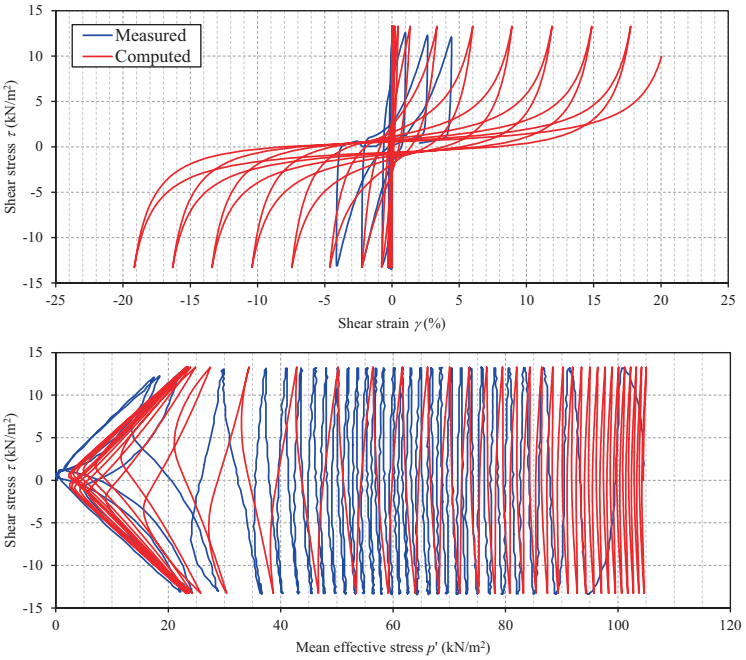

(a) Shear stress ration r=0.13

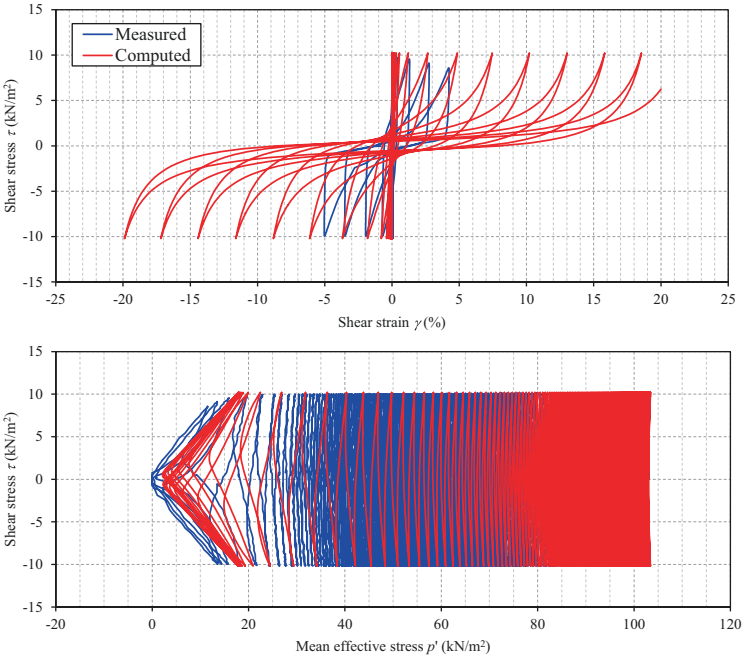

(b) Shear stress ration r=0.10

Fig. 18.4 Results of the simulation of torsional shear tests (for D_r = 50%). (**a**) Shear stress ration r = 0.13; (**b**) Shear stress ration r = 0.10

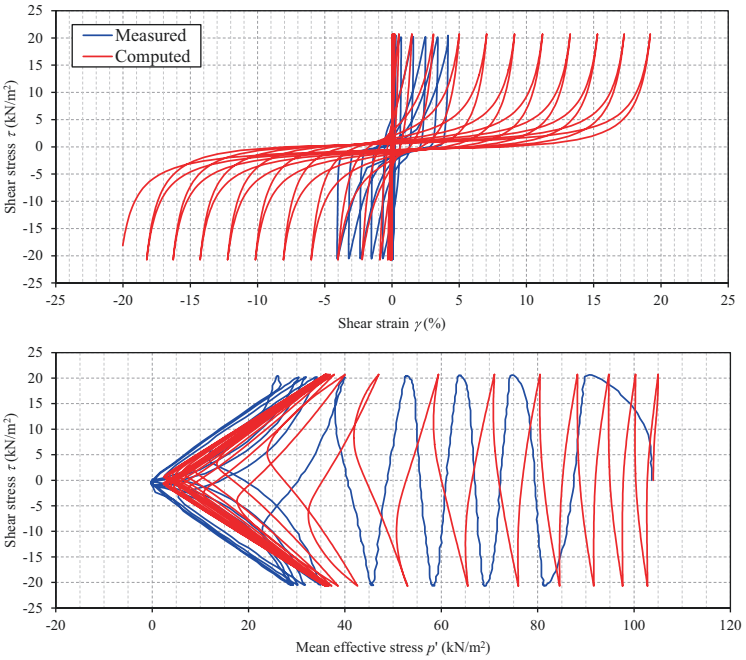

(a) Shear stress ration r=0.20

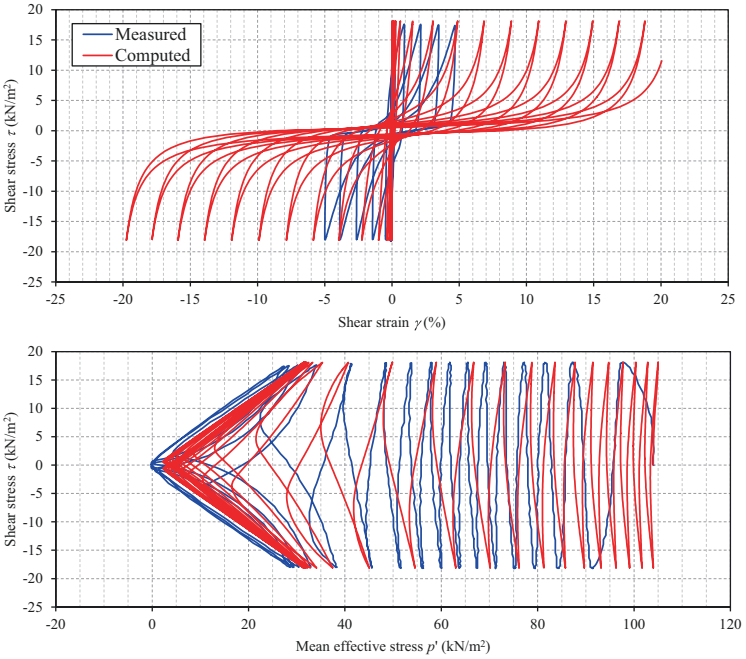

(b) Shear stress ration r=0.18

Fig. 18.5 Results of the simulation of torsional shear tests (for $D_r = 60\%$). (**a**) Shear stress ration $r = 0.20$; (**b**) Shear stress ration $r = 0.18$

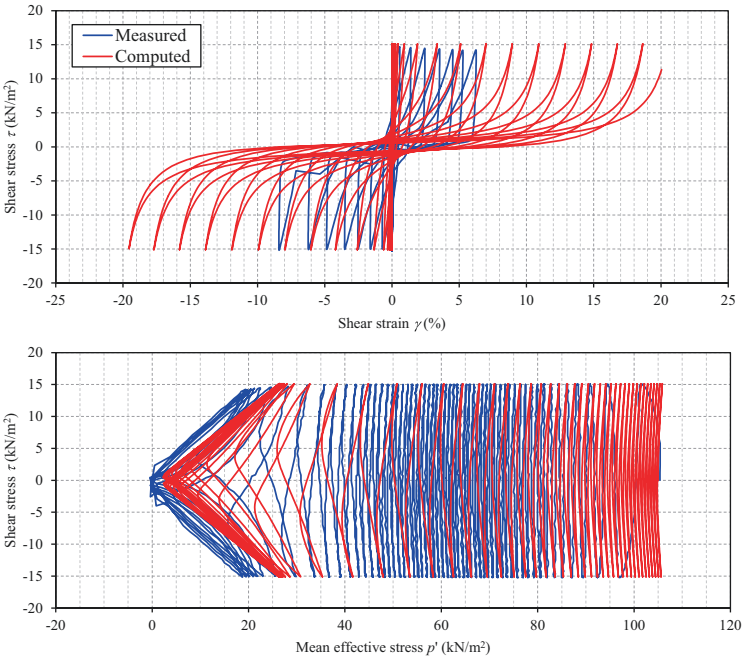

(a) Shear stress ration r=0.15

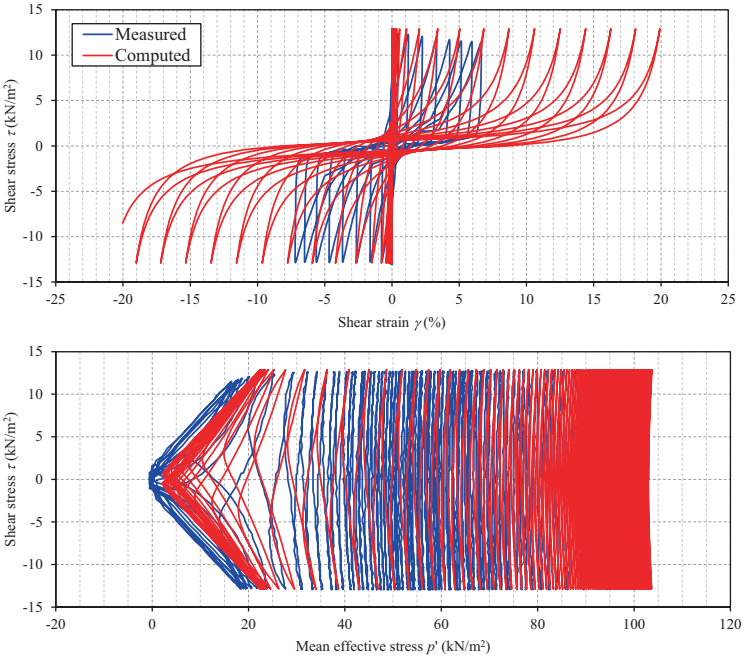

(b) Shear stress ration r=0.13

Fig. 18.6 Results of the simulation of torsional shear tests (for $D_r = 60\%$). (**a**) Shear stress ration $r = 0.15$; (**b**) Shear stress ration $r = 0.13$

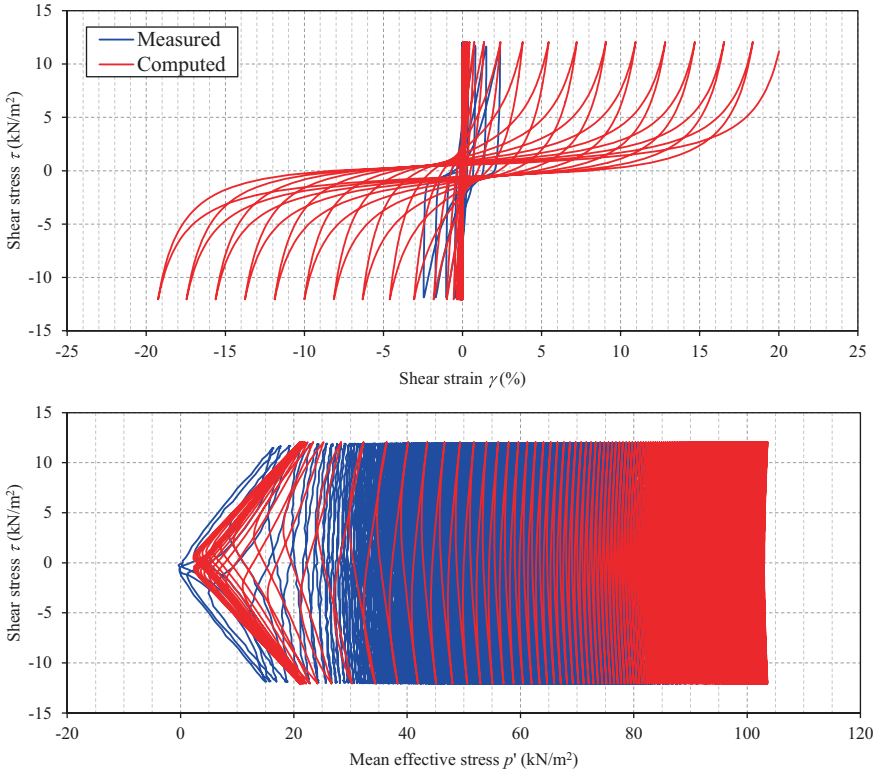

(a) Shear stress ration r=0.12

Fig. 18.7 Results of the simulation of torsional shear tests (for $D_r = 60\%$). (**a**) Shear stress ration $r = 0.12$

18.4 Conclusions

This chapter presents LEAP-ASIA-2018 Type-B Simulations. In this chapter, we conducted effective stress analysis by using FLIP ROSE.

Acknowledgments This report was prepared with volunteer works of the WG members of FLIP consortium.

References

Iai, S., Matsunaga, Y., & Kameoka, T. (1992). Strain space plasticity model for cyclic mobility. *Soils and Foundations, 32*(2), 1–15.

Iai, S., Tobita, T., Ozutsumi, O., & Ueda, K. (2011). Dilatancy of granular materials in a strain space multiple mechanism model. *International Journal for Numerical and Analytical Methods in Geomechanics, 35*(3), 360–392.

Towhata, I., & Ishihara, K., (1985) Modelling soil behavior under principal stress axes rotation. *Proceedings of the 5th international conference on numerical methods in geomechanics*, Vol. 1, pp. 523–530.

Chapter 19
LEAP-ASIA-2019 Simulations at Tsinghua University

Rui Wang, Tong Zhu, Chuang Zhou, and Jian-Min Zhang

Abstract This chapter presents the constitutive model calibration and numerical simulations of centrifuge shaking table tests for LEAP-ASIA-2019, at Tsinghua University. A plasticity model that can provide unified description for the behavior sand at different states under both monotonic and cyclic loading, with focus on the large post-liquefaction shear deformation, is calibrated and used in this study. New undrained cyclic torsional shear test results for Ottawa F65 sand provided in the most recent phase of the LEAP project are used in the calibration process. Typical results for acceleration, excess pore pressure, and displacement for one of the tests are presented in detail, showing that the numerical simulation is able to capture the liquefaction related behavior in the tests well. Comparisons between the simulation and test residual displacement results for the five different tests show conflicting results. The simulations for the two RPI tests under different centrifuge acceleration levels with different stress states and input motion frequencies generally show adequate agreement with test results, exhibiting the constitutive model and numerical simulation method's wide applicability range. However, the simulation results for the KyU tests are significantly different to the test results.

Keywords Liquefaction Experiments and Analysis Project (LEAP-ASIA-2019) · Numerical modelling · Unified plasticity model

19.1 Introduction

LEAP (Liquefaction Experiments and Analysis Projects, Manzari et al., 2014) is an international collaborative effort to verify and validate numerical liquefaction models. It serves to evaluate the state of the art for liquefaction model testing using centrifuge shaking tables and numerical prediction and simulation capabilities using

R. Wang (✉) · T. Zhu · C. Zhou · J.-M. Zhang
Department of Hydraulic Engineering, State Key Laboratory of Hydroscience and Engineering, Tsinghua University, Beijing, China
e-mail: wangrui_05@mail.tsinghua.edu.cn

T. Tobita et al. (eds.), *Model Tests and Numerical Simulations of Liquefaction and Lateral Spreading II*, https://doi.org/10.1007/978-3-031-48821-4_19

advanced constitutive models that have been developed over the past two decades. The Tsinghua University numerical simulation team joined the project during LEAP-UCD-2017 (Wang et al., 2019), using a unified plasticity model for large post-liquefaction shear deformation of sand proposed by Wang et al. (2014). The model was shown to provide a good account of the cyclic mobility, and especially the post-liquefaction shear deformation of sand observed in element tests.

This chapter presents the calibration of the constitutive model and subsequent simulations of centrifuge shaking table tests under the LEAP-ASIA-2019 framework. During LEAP-ASIA-2019, high quality undrained cyclic torsional shear test data was provided to the simulation teams for model calibration. Type-C simulations of centrifuge tests were then conducted. The tests were categorized into Model A tests and Model B tests, which were initially designed to validate the "generalized scaling law" (Iai et al., 2005) for the "model of model" scenario. However, from the simulators' point of view, rather than focusing on the "generalized scaling law," which would be difficult to be proved either right or wrong by numerical simulations, the tests at different centrifugal acceleration g levels provide precious data to examine the performance of the constitutive models and numerical simulation methods under drastically different stress states.

19.2 Constitutive Model for Liquefiable Sand

19.2.1 Basic Features of the Constitutive Model

The unified plasticity model for large post-liquefaction shear deformation of sand proposed by Wang et al. (2014) is used in the simulations at Tsinghua University for LEAP-ASIA-2019, which is consistent with that for LEAP-UCD-2017. The model has been used to provide a unified description of sand of different conditions from pre- to post-liquefaction under both monotonic and cyclic loading on both element test and boundary value problem levels (e.g., Wang, 2016; Wang et al., 2016, 2017; Chen et al., 2018).

The model functions within the framework of elasto-plasticity, with the basic elastic and plastic constitutive equations following:

$$d\varepsilon_{\mathrm{v}}^{\mathrm{e}} = \frac{dp}{K}; \quad d\mathbf{e}^{\mathrm{e}} = \frac{d\mathbf{s}}{2G} \tag{19.1}$$

$$d\mathbf{e}^{\mathrm{p}} = L\mathbf{m}; \quad d\varepsilon_{\mathrm{v}}^{\mathrm{p}} = LD \tag{19.2}$$

Here, $\boldsymbol{\varepsilon}$ is the strain tensor, the volumetric strain is denoted by $\varepsilon_{\mathrm{v}} = \mathrm{tr}(\boldsymbol{\varepsilon})$, the deviatoric strain tensor is $\mathbf{e} = \boldsymbol{\varepsilon} - \varepsilon_{\mathrm{v}}/3\mathbf{I}$. Superscripts e and p represent elastic and plastic, respectively. $\boldsymbol{\sigma}$ is the effective stress tensor, $p = \mathrm{tr}(\boldsymbol{\sigma})/3$ is the mean effective stress, $\mathbf{s} = \boldsymbol{\sigma} - p\mathbf{I}$ is the deviatoric stress. K and G are the elastic bulk and shear

moduli, respectively, L is the loading index, $\mathbf{m}$ is the deviatoric strain flow direction, and D is the dilatancy ratio. $\langle\ \rangle$ are the Macaulay brackets with $\langle x\rangle = x$ for $x > 0$ and $\langle x\rangle = 0$ for $x \leq 0$.

The basic features of the model include the following: (a) dilatancy D is decomposed into a reversible part and an irreversible part following the findings of Shamoto and Zhang (1997) and Zhang (1997), providing explicit control for the dilatancy of sand under cyclic loading; (b) at the liquefaction state, no elastic strains are assumed to be generated while the dilatancy equations are still assumed functional, resulting in the generation of large yet bounded shear strain at the state of zero effective stress; (c) bounding surface plasticity is used to define the plastic modulus, where a maximum stress ratio surface serves as the bounding surface of the model; (d) critical state theory compliance and state dependency is achieved through incorporation of the state parameter (Been & Jefferies, 1985). This chapter only presents the very basic features of the model without explicitly going into its specific formulation, readers should refer to Wang et al. (2014) for the complete formulation of the model.

19.2.2 Calibration of Model Parameters

The calibration method for the model parameters has been documented by Wang et al. (2014). The four critical state parameters based on Vasko (2015) for Ottawa F65 sand were adopted. The model parameters are based on the results of the previous LEAP-UCD-2017 calibration results. However, adjustments were made to the parameters based on the undrained cyclic torsional shear test results provided in LEAP-ASIA-2019. As cyclic torsional shear tests can generally provide higher quality data related to liquefaction behavior, we placed more emphasize on simulating their results during this phase of LEAP. The model parameters are listed in Table 19.1. Note the parameter $\gamma_{d,r}$ is kept at a default value of 0.05.

Figure 19.1 compares the simulation results using the constitutive model directly with the corresponding cyclic torsional shear test results for Ottawa F65 sand at relative densities (D_r) of 50% and 60%, under cyclic stress ratio (CSR) of 0.19 and 0.18, respectively. Based on the results presented in Fig. 19.1, the model is able to capture the shear strain that is generated at liquefaction state very well, the decrease in effective stress under undrained cyclic loading and the eventual "butterfly orbit" of the shear stress-mean effective stress plot is also well represented. Generally, the model is able to simulate the liquefaction resistance. However, it is observed that the cyclic resistance ratio (CRR) curve for the constitutive model tends to be steeper than the measured results, especially at very low CSR.

Table 19.1 Model parameters for the simulations

Sand	G_o	κ	h	M	$d_{re,1}$	$d_{re,2}$	d_{ir}	α	$\gamma_{d,r}$	n^p	n^d	λ_c	e_0	ξ
Ottawa F65	210	0.015	1.2	1.17	0.7	30	0.8	10	0.05	2.25	5.95	0.01	0.7	0.7

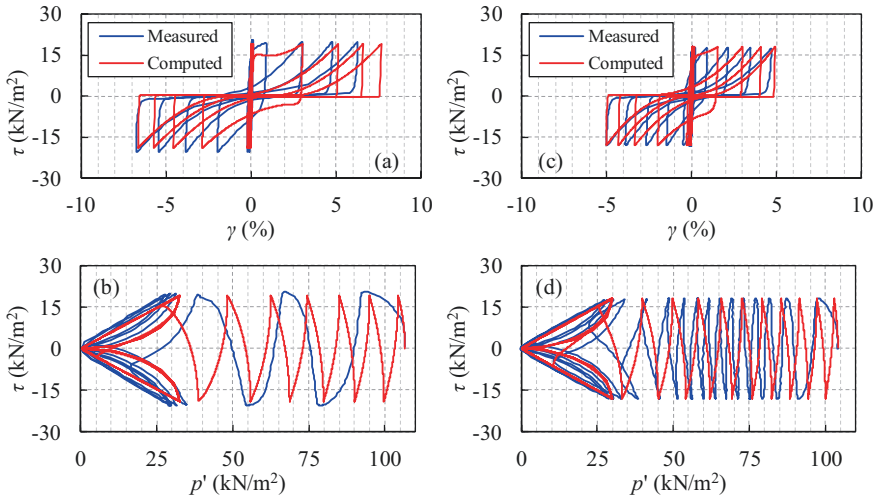

Fig. 19.1 Undrained cyclic torsional shear test results compared with corresponding simulation results: (**a**) $\tau - \gamma$ for Ottawa F65 sand at $D_r = 50\%$ with CSR = 0.19; (**b**) $\tau - p'$ for Ottawa F65 sand at $D_r = 50\%$ with CSR = 0.19; (**c**) $\tau - \gamma$ for Ottawa F65 sand at $D_r = 60\%$ with CSR = 0.18; (**d**) $\tau - p'$ for Ottawa F65 sand at $D_r = 60\%$ with CS R = 0.18

19.3 Detailed Specification of Numerical Simulation

OpenSees (McKenna & Fenves, 2001) was used to conduct the numerical simulations of this study, within which the constitutive model was implemented through a sub-stepping cutting plane algorithm (Wang et al., 2014). As the simulations were 2D plane strain and effective stress based, solid-fluid coupled quadUP elements were used (e.g., Yang et al., 2008). The element is a four-noded quadrilateral plane strain element that has two displacement degrees of freedom and one pore pressure degree of freedom at each node, and follows the u-p formulation proposed by Zienkiewicz and Shiomi (1984).

The mesh used in this study is illustrated in Fig. 19.2, with the same configurations as that of the LEAP-UCD-2017 study (Wang et al., 2019), which consists of 1280 elements and 1377 nodes. The few nodes that are not perfectly aligned with the rest in their respective rows were adjusted so that their coordinates matched those of the measurement sensors in the tests. Five centrifuge tests are simulated in this study, including two from KyU, two from RPI, and one from UCD, as listed in Table 19.2. For the current LEAP project, both Model A and Model B tests were conducted, with Model B being "model of models," where the Model B tests should first be scaled to a "virtual 1G" model with the scaling laws for centrifuge tests, and then further scaled to its prototype through the so called generalized scaling law (Iai et al., 2005). In this study, the simulations are conducted in the 1G scale, which is the prototype for Model A and "virtual 1G" for Model B. The results are then all presented in the prototype scale, with the simulation results for Model B scaled with

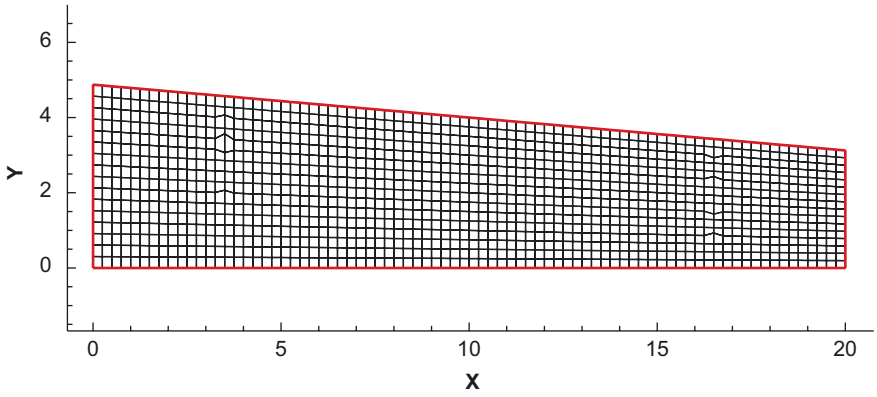

Fig. 19.2 Mesh configuration for the numerical simulations

Table 19.2 Initial relative densities, centrifuge acceleration, and input motion PGA for tests simulated

Test	D_r (%)	Centrifuge acceleration (g)	PGAeff (g)
KyU_A_A2_1	56	44.4	0.118
RPI_A_A1_1	64	23	0.143
UCD_A_A2_1	67	43.75	0.134
KyU_A_B2_1	58	22.2	0.126
RPI_A_B1_1	62	46	0.151

the "generalized scaling law." Therefore, the test and simulation results for the prototype scale are compared. Note this scaling scheme does not provide validation for the generalized scaling law, as the transformation for both test and simulation from "virtual 1G" to prototype are exactly the same, and pure mathematical. However, the comparisons between Model A and Model B do provide validation for the ability of the numerical simulation method in providing unified representation of the liquefaction behavior under different stress states and different input motion frequency. For example, the RPI Model A and B tests were conducted at 23 g and 46 g, respectively, and the dominant input motion frequency were 1 and 0.6 Hz, respectively, at 1G (or "virtual 1G").

Krylov Newton solution algorithm along with a ProfileSPD approach is used to solve the system of equations (OpenSees manual). Newmark time integration scheme is adopted in the simulations. The boundary conditions are enforced using the penalty method with the penalty number of 10^{12}. For the test of convergence, a norm of the displacement increment test is used with a 10^{-3} tolerance and maximum number of iterations of 50. Rayleigh damping with very mall values for α and β (both 0.002) are used. The same permeability corresponding to the density of the sand in each test, based on the test results provided in LEAP-UCD-2017. It is assumed that the permeability remains constant during the entire process, which is a simplification.

The input motions for the simulations follow the exact motions provided to us from the centrifuge tests. Prior to the seismic event simulations, each model is subjected to a gravity step to obtain the initial state of the model. The initial pore pressure and the vertical effective stress after spin-up and before shaking in the simulations are mostly similar to that reported by Wang et al. (2019) for LEAP-UCD-2017, and are not repeated here for brevity.

19.4 Simulation Results

19.4.1 Typical Simulation Results

Typical simulation results for acceleration, excess pore water pressure, and lateral displacement are presented in this section. Test RPI_A_B1_1 is chosen as a representative case for presenting the results.

Figure 19.3 plots the horizontal acceleration time histories at various depths in test RPI_A_B1_1. The input motion is presented in Fig. 19.3a. At AH1, with depth of 3.5 m, the simulated and test acceleration time histories match perfectly until about 8 s. After 8 s, strong spikes in the negative direction are observed in the test, while numerical simulation does not reflect this feature. The spikes in acceleration are often assumed to be related to the dilatancy and subsequent increase in effective stress of the soil during shaking. However, it is surprising that at 3.5 m depth for AH1, the dilatancy spikes would be so significant in the test, as the shear strain in sand is usually not expected to be so strong at large depths. At shallower depths for AH3 (1.5 m) and AH4 (0.5 m), strong dilatancy spikes in the negative direction are

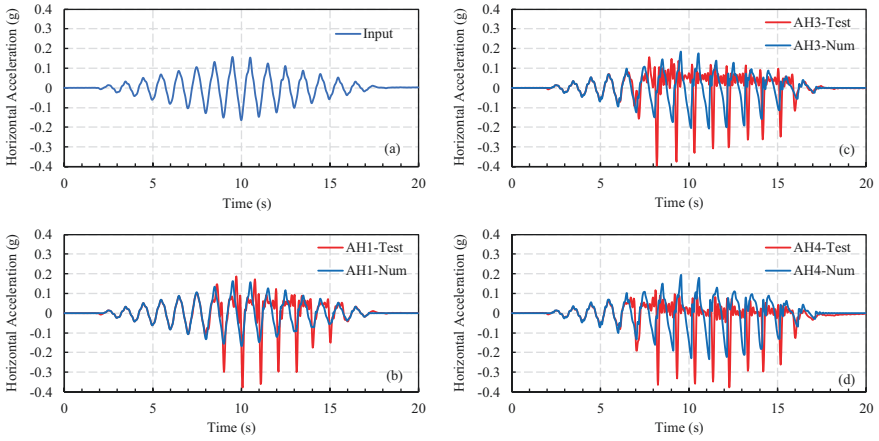

Fig. 19.3 Comparison between test and simulation results for horizontal acceleration at various depths in RPI_A_B1_1: (**a**) input motion; (**b**) at AH1 with 3.5 m depth; (**c**) at AH3 with 1.5 m depth; (**d**) at AH4 with 0.5 m depth

also observed in the tests, at earlier stages of shaking, after about 7 s. The acceleration time history becomes distinctly lopsided, with larger acceleration in the negative direction and smaller acceleration in the positive direction, whereas the input motion is mostly symmetric with respect to zero. The simulation results also captures this behavior. For the results in Fig. 19.3d for AH4, the simulated acceleration time history also shows significant spiking in the negative direction, while the peak acceleration in the positive direction becomes more fuzzy compared to that of the input motion. It should be noted that the measures spikes are generally stronger than those in the simulations.

Figure 19.4 plots the excess pore water pressure at three different depths. At the base of the model (AH4), the sand does not reach initial liquefaction in both test and simulation, as zero effective stress is not achieved. However, the test results show greater fluctuations in pore pressure, which could be related to the dilatancy spikes observed at large depths in Fig. 19.3 At 2 m depth and above, the excess pore water pressure is able to reach the initial effective stress, suggesting that the sand within this depth reaches liquefaction during shaking. Strong fluctuations in the excess pore pressure are observed at P3 and P4 for both test and simulation. The dissipation process is also well simulated.

The lateral soil surface displacement time history at the center of the model in RPI_A_B1_1 is plotted in Fig. 19.5. It can be seen that general good agreement between simulation and test is achieved for the lateral deformation of the model. Again, stronger fluctuations are observed in the test compared with those in the simulations, especially after shaking terminates. The lateral displacement time histories at other locations also show good agreement between simulation and test, and are not presented for conciseness.

19.4.2 Overall Comparison of Lateral Displacement Results

The residual lateral displacement in both simulation and test at each of the reported soil surface locations for all five tests are listed in Table 19.3. Based on the results from the RPI Model A and Model B, it can be seen that the simulation results for lateral displacements generally agreed with the test results, indicating that the constitutive model and numerical simulation method is able to provide a unified description of the seismic response of liquefiable sand under drastically different stress states and different input motion frequencies. The simulation results for the UCD test are also comparable with measurement.

In contrast, for the KyU tests, the simulation and test results are incomparable. Simulation results for KyU_A_A2 and KyU_A_B2_1 exhibit relatively large displacement, in comparison with the extremely small measured displacement. The small measured displacement is surprising, especially in comparison to UCD-A-A2–1, as although the input PGA is slightly smaller compared to that in UCD-A-A2-1, the soil is also much looser (Table 19.2).

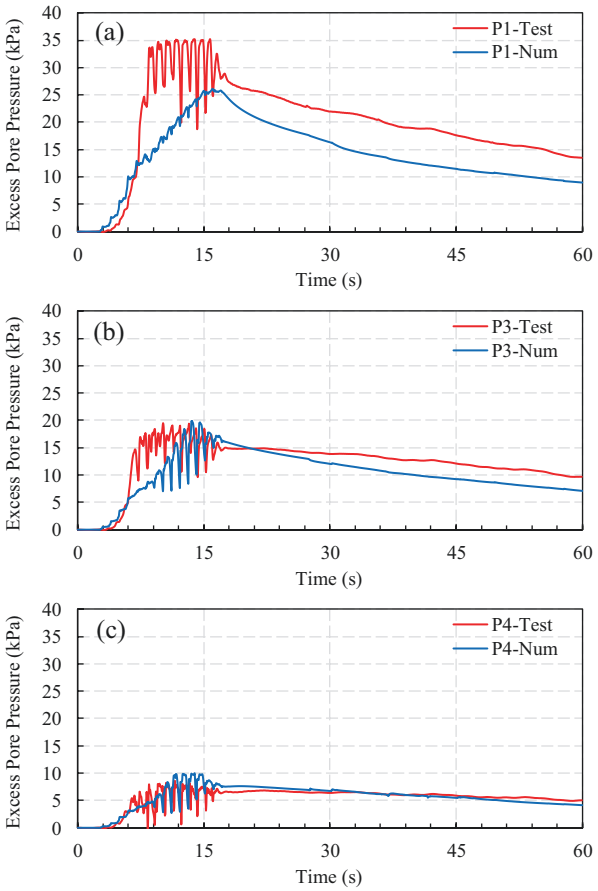

Fig. 19.4 Excess pore water pressure histories at different depths in RPI_A_B1_1: (**a**) P1 with 4 m depth; (**b**) P3 with 2 m depth; (**c**) P4 with 1 m depth

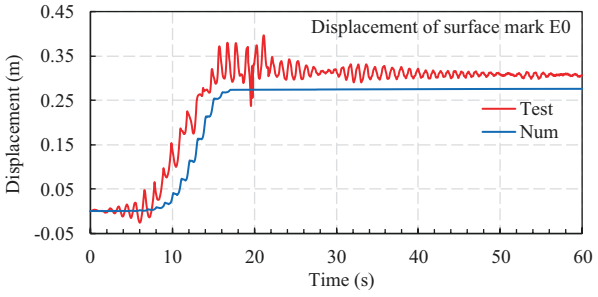

Fig. 19.5 Lateral soil surface displacement at the center of the model in RPI_A_B1_1

Table 19.3 Initial relative densities and centrifuge acceleration for tests simulated

Test case	KyU_A_A2_1				KyU_A_B2_1		
Surface mark	1–2	1–3	3–3	3–5	1–3	3–3	1–4
Simulation (m)	0.365	0.413		0.320	0.422		0.423
Test (m)	0.018	0.015	0.013	0.018	0.078	0.047	0.044
Test case	RPI-A-A1-1						
Surface mark	B	C	D	E0	F	G	H
Simulation (m)	0.102	0.127	0.127	0.123	0.117	0.103	0.076
Test (m)	0.084	0.087	0.098	0.075	0.106	0.089	0.079
Test case	RPI_A_B1_1						
Surface mark	B0	C0	D0	E0	F0	G0	H0
Simulation (m)	0.166	0.248	0.273	0.276	0.252	0.200	0.116
Test (m)	0.256	0.301	0.319	0.304	0.335	0.319	0.299
Test case	UCD-A-A2-1						
Surface mark	2–1	2–2	2–3	2–4	2–5	2–6	
Simulation (m)	0.045	0.073	0.072	0.061	0.042	0.021	
Test (m)	0.018	0.070	0.079	0.076	0.063	0.047	

19.5 Conclusions

This chapter presents the details and results for the simulations at Tsinghua University for the LEAP-ASIA-2019 project. Type-C simulations of five different centrifuge shaking table tests on mildly sloping liquefiable ground.

A unified plasticity model for the large post-liquefaction shear deformation of sand is used in this study. The model is calibrated based on the element test results provided to the simulators in the LEAP-UCD-2017 and LEAP-ASIA-2019 projects. Special emphasis was given to the calibrations against the undrained cyclic torsional shear test results provided in the most recent phase of the LEAP project. We find that cyclic torsional shear tests can provide a better basis for seismic liquefaction related model calibration compared with cyclic triaxial tests.

The details of the numerical simulations were presented in the chapter. Typical results for acceleration, excess pore pressure, and displacement for one of the tests were presented in detail, showing that the numerical simulation is able to capture the liquefaction related behavior in the tests well. Comparisons between the simulation and test residual displacement results for the five different tests showed complicated results, under the same model setup, especially constitutive model parameters. Although the simulations for the two RPI tests under different centrifuge acceleration levels with different stress states and input motion frequencies generally showed adequate agreement with test results, the simulation and test results for the KyU tests were incomparable.

Acknowledgments The authors would like to thank the Tsinghua University Initiative Scientific Research Program (2019Z08QCX01) and the National Natural Science Foundation of China (No. 51678346 and No. 51708332) for funding the work presented in this chapter.

References

Been, K., & Jefferies, M. G. (1985). A state parameter for sands. *Geotechnique, 35*(2), 99–112.

Chen, R. R., Taiebat, M., Wang, R., & Zhang, J. M. (2018). Effects of layered liquefiable deposits on the seismic response of an underground structure. *Soil Dynamics and Earthquake Engineering, 113*, 124–135.

Iai, S., Tobita, T., & Nakahara, T. (2005). Generalized scaling relations for dynamic centrifuge tests. *Geotechnique, 55*(5), 355–362.

Manzari, M.T., Kutter, B.L., Zeghal, M., Iai, S., Tobita, T., Madabhushi, S.P.G., Haigh, S.K., Mejia, L., Gutierrez, D.A., Armstrong, R.J. and Sharp, M.K., (2014). LEAP projects: Concept and challenges. In n Proceedings, 4th International Conference on Geotechnical Engineering for Disaster Mitigation and Rehabilitation (pp. 109–116).

McKenna, F., & Fenves, G. L. (2001). *OpenSees manual*. PEER Center. http://OpenSees.berkeley.edu

Shamoto, Y., & Zhang, J. M. (1997). Mechanism of large post-liquefaction deformation in saturated sands. *Soils and Foundations, 2*(37), 71–80.

Vasko, A. (2015). *An investigation into the behavior of Ottawa sand through monotonic and cyclic shear tests*. Masters thesis. The George Washington University.

Wang, R. (2016). *Single piles in liquefiable ground: Seismic response and numerical analysis methods*. Springer.

Wang, R., Zhang, J. M., & Wang, G. (2014). A unified plasticity model for large post-liquefaction shear deformation of sand. *Computers and Geotechnics, 59*, 54–66.

Wang, R., Fu, P., & Zhang, J. M. (2016). Finite element model for piles in liquefiable ground. *Computers and Geotechnics, 72*, 1–14.

Wang, R., Liu, X., & Zhang, J. M. (2017). Numerical analysis of the seismic inertial and kinematic effects on pile bending moment in liquefiable soils. *Acta Geotechnica, 12*(4), 773–791.

Wang, R., Chen, R. R., & Zhang, J. M. (2019). LEAP-UCD-2017 simulations at Tsinghua University. In B. L. Kutter, M. T. Manzari, & M. Zeghal (Eds.), *Model tests and numerical simulations of liquefaction and lateral spreading-LEAP-UCD-2017* (pp. 549–562). Springer.

Yang, Z., Lu, J., & Elgamal, A. (2008). *OpenSees soil models and solid-fluid fully coupled elements user manual*. UCSD. http://cyclic.ucsd.edu/opensees/OSManual_UCSD_soil_models_2008.pdf

Zhang, J. M. (1997). *Cyclic critical stress state theory of sand with its application to geotechnical problems*. PhD thesis. Tokyo Institute of Technology.

Zienkiewicz, O. C., & Shiomi, T. (1984). Dynamic behaviour of saturated porous media; the generalized Biot formulation and its numerical solution. *International Journal for Numerical and Analytical Methods in Geomechanics, 8*(1), 71–96.

Chapter 20
Class-C Simulations of LEAP-ASIA-2019 via OpenSees Platform by Using a Pressure Dependent Multi-yield Surface Model

Mohamed A. Elbadawy and Yan-Guo Zhou

Abstract In this chapter, Class-C numerical simulations were performed for LEAP-ASIA-2019 centrifuge experiments that took place at different universities testing facilities. A comparative study was conducted among the simulated and experimental seismic responses of a mildly sloping ground of medium-dense to dense Ottawa-F65 sand under ramped sinusoidal acceleration input motions. A pressure dependent multi-yield surface model that can simulate the liquefaction potential of sand soils under earthquake loading was chosen for the numerical simulations through the OpenSees finite element modeling software. An initial calibration of the soil constitutive model, namely "Phase I," was performed against different cyclic torsional shear tests for Ottawa-F65 sand under various Cyclic Stress Ratios (CSRs). Numerical modeling of centrifuge experiments "Phase II" was carried out after a few adjustments to the estimated model parameter values for the sake of providing proper computed output responses. The adopted soil model and simulation technique provide adequate numerical predictions of the liquefaction potential for the mildly sloping ground problem and accurately simulate the time histories of excess pore water pressure, accelerations, and surface deformations, regardless of experiencing a few undesirable responses for simulated Kyoto University centrifuge tests. The capabilities and limitations of the selected constitutive soil model and computational technique are analyzed and discussed through the context.

Keywords Liquefaction Experiments and Analysis Projects (LEAP-ASIA-2019) · Numerical simulation · PDMY02 model

M. A. Elbadawy · Y.-G. Zhou (✉)
MOE Key Laboratory of Soft Soils and Geoenvironmental Engineering, Institute of Geotechnical Engineering, Center for Hypergravity Experiment and Interdisciplinary Research, Zhejiang University, Hangzhou, P. R. China
e-mail: qzking@zju.edu.cn

T. Tobita et al. (eds.), *Model Tests and Numerical Simulations of Liquefaction and Lateral Spreading II*, https://doi.org/10.1007/978-3-031-48821-4_20

20.1 Introduction

Thanks to the new high-end computer processing units and the robust computational capabilities available, performing sophisticated geotechnical numerical simulations is possible for academic researchers and geotechnical professionals. Therefore, it is possible to model different soil types with complex constitutive stress-strain and stress-dilatancy relationships, which is considered to be the most important issue in studying the soil liquefaction phenomenon.

A verification and calibration process must be done towards the employed constitutive soil model to determine model parameters and check its capability of capturing the soil mechanical behavior in different loading conditions. The soil model parameters should first be estimated and calibrated against soil element tests through laboratory testing devices such as direct simple shear, triaxial, and hollow cylindrical torsional shear. The most common way to calibrate a soil model in any Finite Element Modeling (FEM) software is to model a single one element considering appropriate constraints and loading conditions to simulate a specific laboratory soil element test. Then, compare the computed and measured responses. This comparison checks the model's ability to evaluate soil mechanical behavior and capture essential soil characteristics in simple loading conditions.

Eventually, this calibrated soil model should be validated against large-scale experiments that represent real geotechnical field problems. When simulating large-scale models, many other aspects are affecting the output simulation results rather than the main model parameters and their constitutive relations. The main target of this simulation type is to predict appropriate deformations, accelerations, and excess pore water pressure time histories in boundary value problems, which cannot be evaluated through the small-scale/element laboratory testing simulations. So that simulating real boundary value problems provide the final judgment on the soil model and the numerical technique adequacy in being used for earthquake geotechnical engineering practice or not. For physical modeling of real field geotechnical cases, centrifuge model testing is selected for fulfilling this purpose since they are confirmed to produce a reliable and accurate representation of geotechnical engineering systems (Madabhushi & Schofield, 1993; Schofield, 1998). Centrifuge model tests can provide high-quality readings and plenty of measurements that can be employed in validating the FEM tools.

The LEAP "Liquefaction and Analysis Projects" (Manzari et al., 2014; Kutter et al., 2015, 2018, 2020; Zhou et al., 2018) is a collaboration between different universities around the world that aims to study different liquefaction scenarios for various soil structures to evaluate and validate numerical simulation techniques. The project comprises experimental model tests that took place at different centrifuge facilities at the participating universities, as well as computational simulations that performed using various numerical methods and a wide range of constitutive models. The main target of this effort is to assess the available numerical simulation tools and constitutive soil models against practical geotechnical field applications in order to accurately predict soil liquefaction potential and associated hazardous effects.

Through the context, a calibration of the employed constitutive soil model through the OpenSees platform (McKenna, 1997, 2011; OpenSees, 2000) is deeply discussed. After that, Class-C simulations are performed after tuning the parameters' selection of the employed soil model for the sake of getting better simulation results. The computed soil responses are assessed through detailed comparisons with the measured responses, besides highlighting the possibilities and drawbacks of the adopted numerical simulation technique.

20.2 Demonstration of the Selected Centrifuge Experiments for the FE Analysis and Simulation Types

20.2.1 Centrifuge Test Experiments

Seven centrifuge experiments were selected for this finite element simulation work from dozens of tests done at Rensselaer Polytechnic Institute (RPI), the University of California at Davis (UCD), Kyoto University (KyU), and Zhejiang University (ZJU). Two types of physical models are considered in these centrifuge experiments through a one-stage downscaling, namely Model A, and a two-stage downscaling, namely Model B, according to the Generalized Scaling Law (GSL) developed by Tobita et al. (2011). In Model A, 1G filed scaling law with a scaling factor μ is used in downscaling the prototype to a virtual model, whereas in Model B, a scaling factor η is applied to the virtual 1G model for downscaling to a new physical model by employing the conventional scaling law. Table 20.1 summarizes the centrifuge experiments with all related scaling factors, soils' relative densities, and effective Peak Ground Acceleration (PGA_{eff}) of the employed input motions.

A ramped sinusoidal input motion with a predominant period of 1 sec. is employed in all centrifuge experiments with different Peak Ground Accelerations (PGAs) ranging from 0.12 to 0.28 g. Figure 20.1 demonstrates the variations of input motions and the maximum spectral accelerations through the recorded response spectra for each input motion at each centrifuge facility.

The achieved base motions at RPI and UCD centrifuge facilities have the lowest wave oscillations at high frequencies, in comparison with other centrifuge facilities,

Table 20.1 The selected LEAP-ASIA-2019 centrifuge experiments for numerical simulations

Test case	Density (kg/m^3)	D_r (%)	Model type	Virtual 1G, μ	Centrifuge, η	PGA_{eff} (g)
RPI_A_A1_1	1651	64	Model A	1	23	0.143
UCD_A_A2_1	1658.1	67	Model A	1	43.75	0.134
ZJU_A_A1_1	1624.6	54	Model A	1	30	0.272
KyU_A_A2_1	1628	56	Model A	1	44.4	0.118
RPI_A_B1_1	1644	62	Model B	0.5	46	0.151
ZJU_A_B1_1	1632.7	57	Model B	2	15	0.271
KyU_A_B2_1	1633	57	Model B	2	22.2	0.126

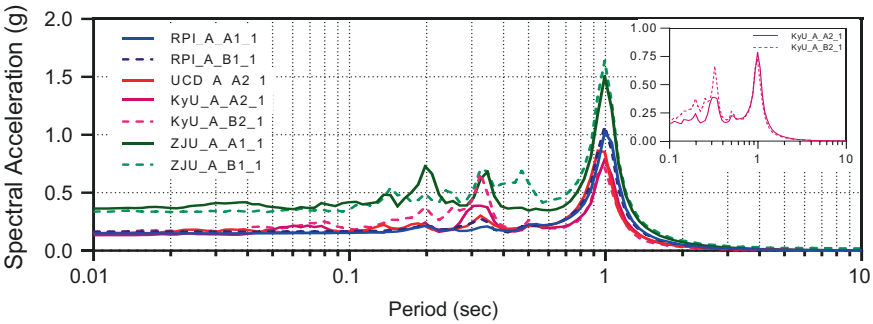

Fig. 20.1 Response spectrum of the recorded input motions at different centrifuge facilities for the selected seven experiments with a magnified plot for the KyU recorded base motions

which have no effects on the computed output results and do not cause any resonant with the soil's natural frequency. In the ZJU centrifuge facility, slightly higher wave oscillations were noticed at frequencies ranging from 3.3 to 5 Hz; however, high wave oscillations arose in conducted centrifuge tests at KyU for the same frequency range, especially with Model B centrifuge experiments. These high wave oscillations can affect the simulation results negatively as well as may biasedly result in overestimating the simulated responses.

20.2.2 Brief Explanation of Numerical Predictions Classes Adopted in LEAP

The LEAP demands that the simulation teams provide the numerical simulations for the centrifuge experiments according to a specific criteria. The numerical simulation process should follow one of these classes according to the requirements of each LEAP event computational modeling task. Class A, B, and C are the standardized LEAP approaches for computational modeling and numerical predictions.

In Class A predictions, blind numerical simulation predictions are performed before commencing any centrifuge tests. In this type of simulations, the numerical predictors only know the soil's main characteristics, the schematic of the centrifuge problem, and the target dynamic input motion for each centrifuge test. Calibration of the constitutive model parameters can be done towards previous/ongoing provided soil element tests. After that, these estimated model parameters are used in numerical simulations of centrifuge experiments.

Class B and C predictions are performed after finishing all centrifuge experiments. The recorded base motions form centrifuge experiments are the only information that is provided to the numerical modeler in Class B predictions. In contrast, all centrifuge measured responses are given to numerical modeler in Class C predictions. Class C simulations are meant to tune the utilized constitutive soil models through the centrifuge experiments to produce better and appropriate numerical predictions.

In LEAP-ASIA 2019 event, class-C simulations are required for being performed for a set of centrifuge model tests in order to address different possibilities and limitations of the available numerical tools and constitutive soil models. The following sections provide a comprehensive demonstration of the utilized soil model, numerical tool, FE model configurations and loading conditions. Thereafter, the computed output results are discussed and compared with measurements in order to highlight the main advantages and disadvantages of the employed numerical simulation technique.

20.3 The Employed Soil Constitutive Model

A multi-yield surface model with pressure dependency, namely PDMY02, was employed in the numerical simulations. The PDMY02 model (Elgamal et al., 2003; Yang et al., 2003) is based on the classical multi-surface plasticity work done by Prevost (1978, 1985) and is further extended to account for complex dilatancy characteristics. The model can capture the soil's cyclic mobility and post liquefaction behaviors under different stress levels. The PDMY02 model employs a kinematic hardening rule to simulate the soil cyclic hysteretic response (Mróz, 1967; Yang et al., 2003). A concise demonstration of the main characteristics of the soil model is reviewed in the following sections.

20.3.1 Yield Surface Definition

The failure surface in the PDMY02 model is a Drucker–Prager conical surface in the principal stress space with a pressure dependency (Lacy, 1986; Elgamal et al., 2003; Yang et al., 2003). The inner nested yield surfaces defines the hardening zone and the outermost yield surface represents the failure zone (Prevost, 1978, 1985; Yang et al., 2003). The yield function is formulated based on the multi-yield-surface J2 plasticity model that is proposed by Prevost (1985) and further modified by Elgamal et al. (2003) and Yang et al. (2003) as follows:

$$f = \frac{3}{2}\left(\tilde{s} - \left(p' + p'_{\text{res}}\right)\right) : \left(\tilde{s} - \left(p' + p'_{\text{res}}\right)\right) - M^2\left(p' + p'_{\text{res}}\right)^2 = 0 \qquad (20.1)$$

where $\tilde{s}$ is the deviatoric stress tensor, p' is the mean effective pressure, and p'_{res} is a small residual pressure value assigned automatically by the model to move the yield surface towards the negative confining stress by p'_{res} when confining pressure equals zero. M is the shear stress ratio that defines the size of the yield surface. The M_{f} that represents the stress ratio of the outermost yield surface at failure is calculated through the soil friction angle that is obtained from the triaxial test (TX) and defined as $M_{\text{f}} = \dfrac{6\sin\left(\phi_{\text{TX}}\right)}{3 - \sin\left(\phi_{\text{TX}}\right)}$ (Chen & Mizuno, 1990).

20.3.2 Stress-Strain Relationships

The stress-strain "$\tau - \gamma$" backbone curve is defined by a hyperbolic relationship at a constant confinement pressure $p_r^{'}$ as follows:

$$\tau_{oct} = \frac{G_{oct,r}\,\gamma_{oct}}{1 + \dfrac{\gamma_{oct}}{\gamma_r}} \tag{20.2}$$

where $G_{oct,\,r}$ is the small strain shear modulus at reference effective confining stress $p_r^{'}$ and γ_r is a calculated shear strain, which is computed internally and satisfies the following equation at failure for a given reference pressure $p_r^{'}$:

$$\tau_{oct_f} = \frac{2\sqrt{2}\sin(\phi)}{3-\sin(\phi)}\,p_r^{'} = \frac{G_{oct,r}\gamma_{oct,max}}{1+\gamma_{oct,max}/\gamma_r} \tag{20.3}$$

where $\gamma_{oct,\,max}$ is the maximin reached shear strain (a user-defined value) that corresponds to the failure octahedral shear stress τ_{oct_f}. In the multi-yield surface plasticity principle, the hyperbolic presentation of the backbone curve is substituted by multi-linear segments that represent the domain of the evolved yield surfaces. Each segment represents a yield surface domain which is characterized by a tangent shear modulus ($G_m = \dfrac{2\left(\tau_{m+1}-\tau_m\right)}{\gamma_{m+1}-\gamma_m}$) and size ($M_m = \dfrac{3\tau_m}{\sqrt{2}\left(p_r^{'}+p_{res}^{'}\right)}$) at each m surface(s), as shown in Fig. 20.2.

The shear G_{oct} and bulk B moduli are pressure dependent and being updated during the simulation with regards to the soil effective confinement stress p' according to Prevost (1985) and Elgamal et al. (2003) as follows:

$$G_{oct} = G_{oct,r}\left(\frac{p'+p_{res}^{'}}{p_r^{'}+p_{res}^{'}}\right)^d \text{ and } B = B_r\left(\frac{p'+p_{res}^{'}}{p_r^{'}+p_{res}^{'}}\right)^d \tag{20.4}$$

where d is a material parameter and equals 0.5 for sandy soils (Kramer, 1996).

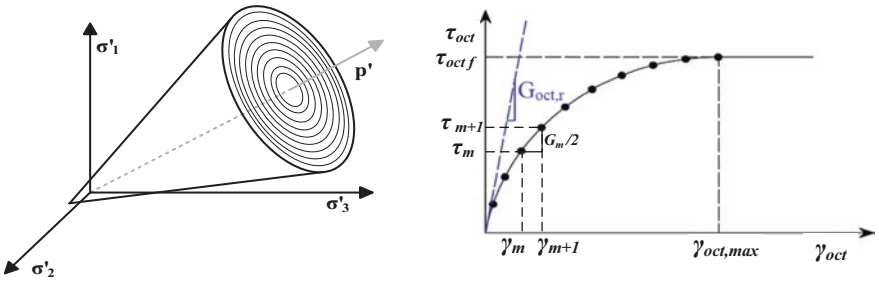

Fig. 20.2 Demonstration of the multi-yield conical surfaces in principal stress space and the octahedral shear stress-strain backbone curve with 10 yield surfaces

20.3.3 The Model Flow Rule

Computation of the plastic shear strain increment is divided into a deviatoric component that follows an associative flow rule and a volumetric component that follows a non-associative flow rule. Based on Prevost and Elgamal considerations (Prevost, 1985; Elgamal et al., 2003), Q and P tensors are normal to the yield surface and the plastic potential surface, respectively. These tensors can be decomposed into two deviatoric and volumetric components, giving $Q = Q + Q'' I$ and $P = P + P'' I$. Q and P are the deviatoric parts that are following associative flow rule, whereas Q'' and P'' are the volumetric components that follow a non-associative flow rule.

The PDMY02 model considers a phase transformation surface (PT), which is first proposed by Ishihara (Ishihara et al., 1975). The contractive soil tendency is occurring if stress state is inside the PT surface when soil subjected to undrained shearing, whereas dilation happens when stress state is outside the PT surface. Volumetric plastic strains are computed during contraction and dilation phases according to Yang and Elgamal (2008, 2009) through the following formulae:

Contractive phase: ($\eta < \eta_{PT}$) or ($\eta > \eta_{PT}$ and $\dot{\eta} < 0$)

$$P'' = -\left(1 - \frac{\tilde{n} : \tilde{s}}{\dot{s}} \frac{\eta}{\eta_{PT}}\right)^2 \left(c_1 + \xi_c c_2\right) \left(\frac{p' + p'_{res}}{p_{atm}}\right)^{c_3} \tag{20.5}$$

Dilative phase: ($\eta > \eta_{PT}$ and $\dot{\eta} > 0$)

$$P'' = \left(\frac{\eta}{\eta_{PT}} - 1\right)^2 \left(d_1 + \gamma_d^{d_2}\right) \left(\frac{p' + p'_{res}}{p_{atm}}\right)^{-d_3} \tag{20.6}$$

where n is a unit outer normal to an imaginary surface in the deviatoric stress space passing by the stress point s. η and η_{PT} are the current shear stress ratio and the shear stress ratio at the PT surface, respectively. c_1 parameter mainly controls the plastic volumetric strain accumulation rate. d_1 controls the accumulated volumetric shear strain per each dilation cycle. d_2 and c_2 account for fabric damage through ξ_c and γ^d which represent the total accumulative volumetric strain and the cumulative octahedral shear strain per each dilation cycle, respectively. c_3 and d_3 parameters account for overburden stress variation effects on contraction and dilation rates "K_σ effect". When η equals η_{PT}, i.e., the neutral phase, the model starts to accumulate shear strains before starting the dilation phase at almost no changing either on shear stresses or soil confinement p'. For the sake of simplification, zero plastic potential component ($P'' = 0$) is maintained during this high yielding phase till reaching a boundary that defined in deviatoric space and dilation starts afterward. An initial isotropic domain is defined through this boundary as a circle in the deviatoric strain space, which will either enlarge or translate based on the loading history as demonstrated in Elgamal et al. (2003) and Yang et al. (2003).

20.4 Model Parameters Estimation and Calibration "Simulation Phase I"

20.4.1 The Initial Determination of the Model Parameters

The PDMY02 model parameters can be separated into four main groups. The first group is concerned with the stress-strain relationships in elastoplasticity, which comprises small strain shear and bulk moduli measured at a referenced confinement pressure "$G_{\text{oct, r}}$, B_{r}," friction angle "ϕ," and phase transformation angle "ϕ_{PT}."

The second group is the flow rule user-input parameters (c_1, c_2, c_3, d_1, d_2 and d_3), described in section 20.3.3, that define the soil contractive-dilative behavior during undrained shearing. The third group is the liquefaction damage parameters (liq_1 and liq_2) that control the development of the liquefaction-induced perfectly plastic shear strain as a function of dilation history and load reversal history.

The last group is a miscellaneous collection of parameters that are estimated according to Yang and Elgamal (2009) recommendations. These parameters are pressure dependent coefficient, number of yield surfaces, and the maximin reached shear strain. A fixed value for soil permeability coefficient of "3×10^5 m/s" is selected for the calibration and centrifuge simulations. The permeability coefficient value has been selected as an average value from previous LEAP simulation work done (Ghofrani & Arduino, 2018; Ziotopoulou, 2018).

The parameters initially estimated through different correlations from a wide range of empirical formulae, previously done soil element testing for Ottawa-F65 sand by Bastidas (2016) and the PDMY02 online model documentation (Yang & Elgamal, 2009). Then, the model parameters values are tuned through a calibration process with the cyclic torsional shear tests conducted by Kyoto University (Ueda, 2018). Unfortunately, the number of drained monotonic triaxial or drained simple shear tests through previous LEAP events is minimal and not providing full data for calibration of the model basic elastoplastic parameters "$G_{\text{oct, r}}$, B_{r}, ϕ, ϕ_{PT}" (Beaty, 2018).

Regarding Ueda conducted tests (Ueda, 2018), the soil samples have slightly different relative densities for each relative density (D_{r}) group. (D_{r} 50%) and (D_{r} 60%) groups comprise samples' relative densities ranges of 50.5–53.0% and 60.5–63.5%, respectively. Therefore, two data sets of model parameters are estimated herein for Ottawa-F65 sand, considering different relative density ranges of (50–55%) and (60–65%).

The soil shear and bulk moduli values are explicitly calculated for each soil relative density of each centrifuge test and are not fixed for each (D_{r}) group. This way contributes to adjusting the issue of using constant contraction and dilation model parameters for each relative density range and overcoming the small variances between relative densities for each (D_{r}) group, i.e., the variance in D_{r} from 54% to 57%. Table 20.2 represents the adopted model parameters of the Ottawa-F65 sand soils for different relative density ranges.

Table 20.2 The PDMY02 estimated model parameters

Parameter	Estimated values		Description and reference
"D_r" range	50%–55%	60%–65%	Relative Density range for each (D_r) group of the Ottawa-F65 sand soil samples
"ϕ_{cv}"	29	29	Constant-volume friction angle (Carraro et al., 2009; (Bastidas, 2016)
"e"	0.65–0.63	0.61–0.60	Void ratio (Bastidas, 2016)
"GS"	2.648		Specific Gravity (Bastidas, 2016)
"ρ" ton/m^3	$\rho = \rho_w \frac{GS+e}{1+e}$		Soil density for a fully saturated sample
"p_r'" kPa	100		Reference effective confining pressure at which other model input parameters were calibrated
"V_s" m/s^2	$85\left[46D_r^2+2.5\right]^{0.25}$		Shear wave velocity at P_r = 1 atm adopted from Andrus and Stokoe (2000) and Ziotopoulou and Boulanger (2012)
"$G_{oct,r}$" kPa	$\frac{3}{\sqrt{6}}\rho V_s^2$		Octahedral shear modulus at small strain = $\frac{3}{\sqrt{6}}\rho V_s^2$ (Khosravifar, 2012)
"ν"	0.33		Poisson's ratio, $\nu = \frac{K_0}{1+K_0}$ where $K_0 = 0.5$
"B_r" kPa	$B_r = \frac{2(1+\nu)}{3(1-2\nu)}G_{oct,r}$		Bulk modulus, $B_r = \frac{2(1+\nu)}{3(1-2\nu)}G_{oct,r}$
"ϕ"	34	35.5	Soil friction angle. Adopted from Bolton (1986) $\phi = \phi_{cv} + 3I_R$ where $I_R = D_r(10 - \ln P') - 1$
"ϕ_{PT}"	25	26	Phase transformation angle adopted from Bastidas (2016) and (Ueda (2018)
"$\gamma_{oct,\,max}$"	0.1	0.1	Peak Shear Strain at "p_r" (Yang & Elgamal, 2009)
"d"	0.5	0.5	Pressure dependent Coefficient (Kramer, 1996)
"c_1"	0.065	0.035	Contraction parameter calibrated against soil element tests by (Ueda, 2018)
"c_2"	5	5	Contraction parameter coefficient (Yang & Elgamal, 2009)
"c_3"	0.19	0.06	Overburden stress effect on contraction rate
"d_1"	0.04	0.08	Dilation rate parameter calibrated against soil element tests by (Ueda, 2018)
"d_2"	3	3	Dilation parameter coefficient (Yang & Elgamal, 2009)
"d_3"	0.2	0.06	Overburden stress effect on dilation rate
liq_1	1	1	Post-liquefaction damage parameter to define permanent shear strain accumulations as a function of dilation history (Yang & Elgamal, 2009)
liq_2	0	0	Post-liquefaction damage parameter to define permanent shear strain accumulations as a function of load reversal history (Yang & Elgamal, 2009)
k (m/s)	3×10^5 m/s		Soil permeability

20.4.2 Cyclic Torsional Shear Test Simulation (Simulation Phase I)

A single four-node element with mixed u-p formulation (QuadUP), which was implemented in OpenSees by Yang et al. (2008), is employed to simulate the undrained cyclic torsional shear test considering the appropriate boundary conditions and loading stages. The output computed results are compared with the measured responses from the soil element testing conducted by Ueda (2018) to calibrate the soil model and adjust selected parameters, as shown in Figs. 20.3 and 20.4.

The output curves show the model capability in simulating the cyclic torsional shear test in terms of $\tau - \gamma$ relationship and stress path curves for all engaged tests with a fair determination of the number of loading cycles required to reach initial liquefaction for medium CSR levels, i.e., 0.15–0.18. However, the model cannot appropriately determine the number of loading cycles to reach initial liquefaction for lower and higher CSR levels.

Figure 20.5 summarizes the whole tests' simulations to highlight the issue of estimating the proper number of loading cycles for triggering liquefaction. This issue is partially solved later in a new model version developed by Khosravifar et al. (2018) that has not been available in OpenSees till the time of commencing this simulation work.

20.5 Specifications of the Finite Element Model for Centrifuge Experiments Simulations

A 2D plane strain analysis was conducted through the OpenSees platform for modeling the soil slope in a rigid container. With Model A simulations, the soil model parameters and the slope geometrical dimensions are in prototype scale. On the other hand, the Model B simulations are performed after downscaling the FE model components to the model scale according to the Generalized Scaling Law (GSL). The figure below represents a schematic view of the modeled centrifuge test with markers and sensor locations for measuring different soil response components (Fig. 20.6).

20.5.1 FE Model Description

A 2D finite element mesh comprised 1377 nodes and 1280 QuadUP elements for Model A and Model B simulations with elements spatial size ranging from (0.2*L to 0.3*L) m, where L equals "1" when modeling in prototype scale and equals $\mu\eta$ when modeling in virtual model scale.

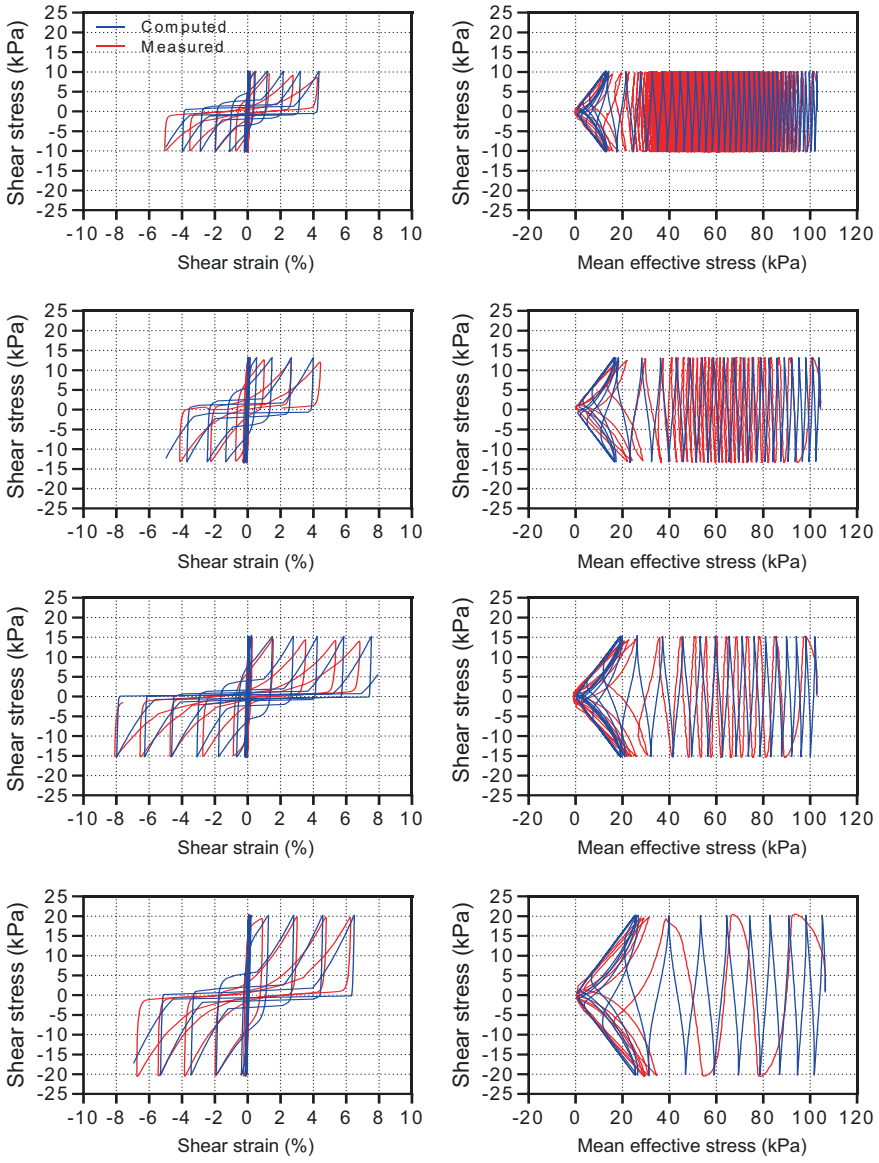

Fig. 20.3 Computed vs. measured output results of undrained cyclic torsional shear test simulations for (D_r 50%) group under CSR values of 0.10, 0.13, 0.15 and 0.19; $\tau - \gamma$ relationship on the left and stress path on the right

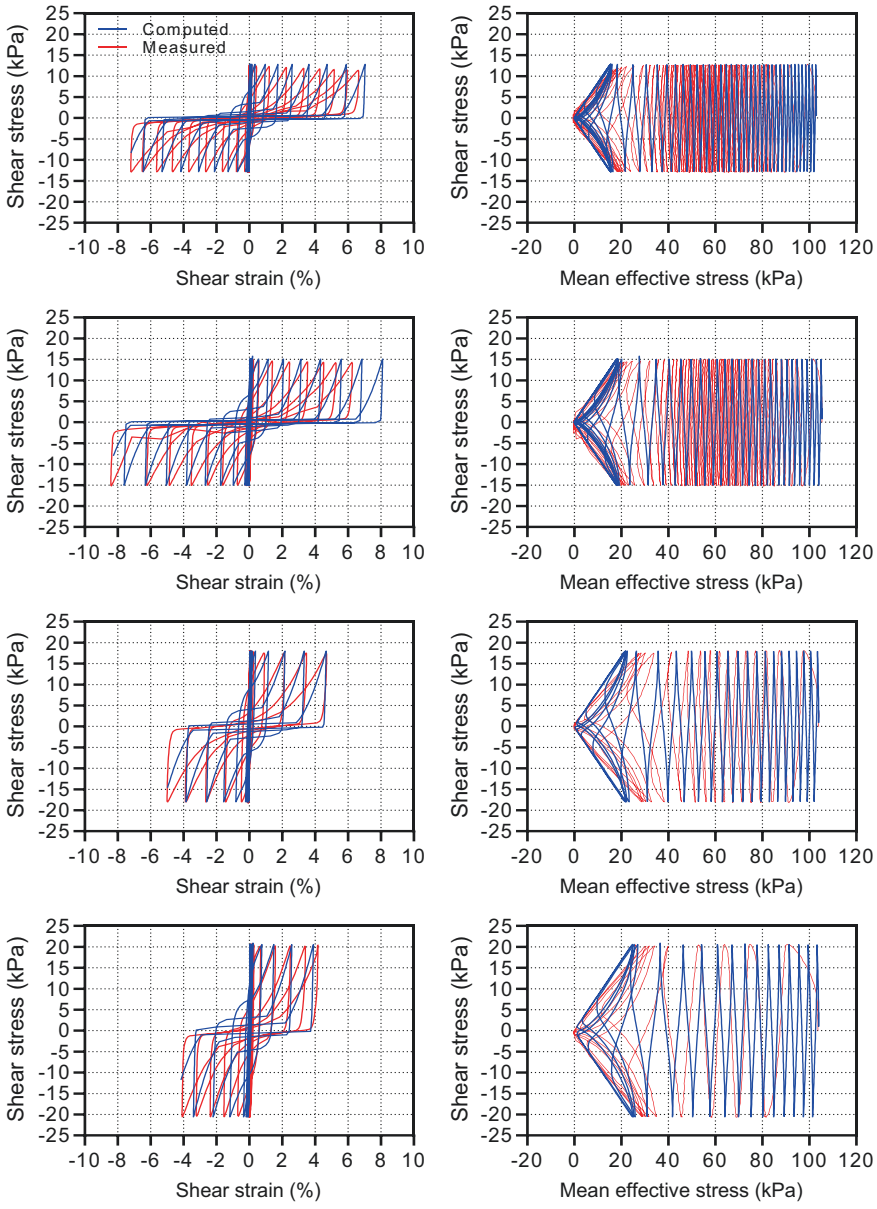

Fig. 20.4 Computed vs. measured output results of undrained cyclic torsional shear test simulations for (D_r 60%) group under CSR values of 0.13, 0.15, 0.18, and 0.20; $\tau - \gamma$ relationship on the left and stress path on the right

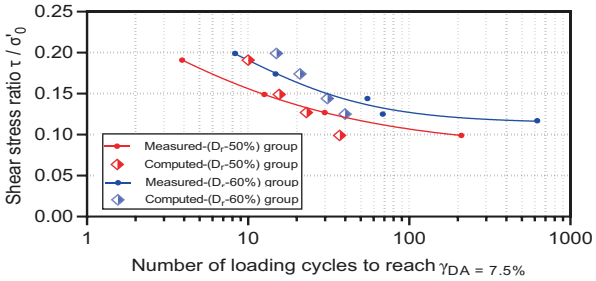

Fig. 20.5 Computed vs. measured number of loading cycles to reach a double amplitude shear strain (γ_{DA}) of 7.5% in cyclic torsional shear tests

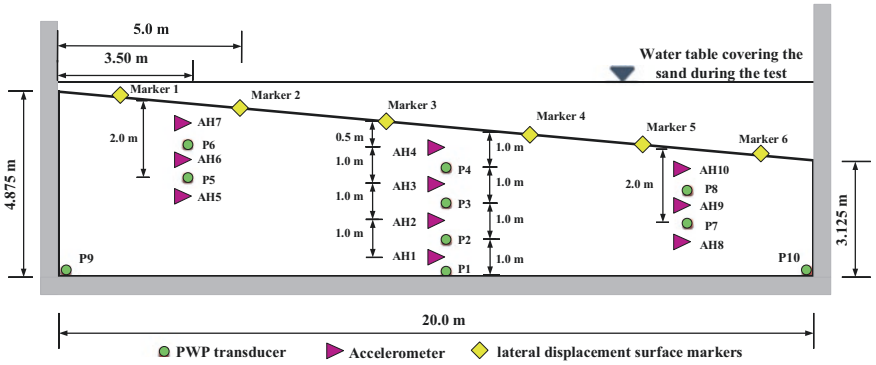

Fig. 20.6 Schematic view of the centrifuge test in prototype scale showing the different sensor locations. (Elbadawy et al., 2022)

The element size range is selected according to Kuhlemeyer and Lysmer (1973) suggestion to consider an element size less than or equal to one-eighth of the wavelength associated with the maximum frequency component of the input wave. The chosen element size range ensures that the mesh can resolve waves up to a frequency of 50 Hz. This way is also adopted by previous researchers in their computational simulations of dynamic analysis of previous LEAP events (Ghofrani & Arduino, 2018).

The quadUP element is used in this simulation to model the cyclic response of soil in partially drained and undrained conditions. The right and left vertical model sides are fixed in the horizontal direction, and the model base is fully fixed in vertical and horizontal directions. Water pressure is applied on the slope surface nodes with prescribed PWP values and appropriate nodal loads during the simulation. Top mesh nodes are fixed for pore water pressure to allow flow across the model surface, whereas model bottom and side boundaries are not allowed for water drainage. Figure 20.7 shows the FE mesh discretization and the model boundary conditions.

The FE analysis is initiated by considering a linear elastic material behavior when applying gravity loads and self-weights. After that, the model is turned to the

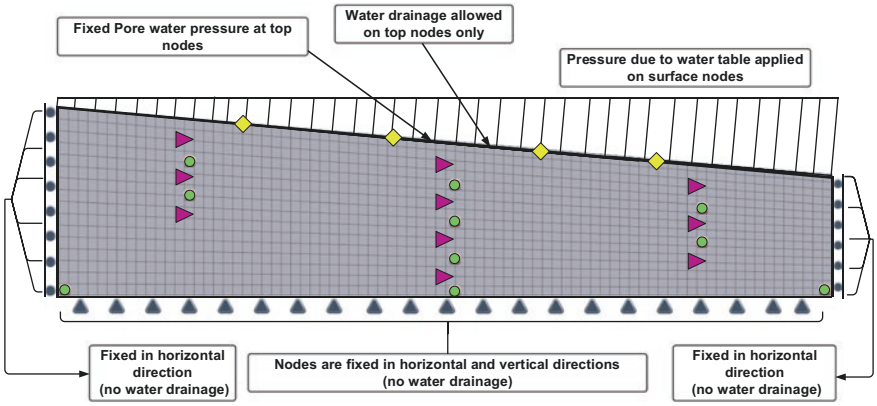

Fig. 20.7 The FE mesh discretization layout is showing the boundary conditions and the different sensor locations. (Elbadawy et al., 2022)

nonlinear elastoplastic stage that considers all material nonlinearity and plastic behaviors. In order to achieve a successful transition, few analysis steps should be run to ensure that the soil's internal variables are adjusted to the new stress-state and to avoid numerical errors for the subsequent simulations. The initial state of stress output results from gravitational loading is presented in Fig. 20.8. The postprocessing contour plots were generated using the Scientific Tool Kit for OpenSees "STKO" (ASDEA-Software, 2019).

After that, dynamic loading is subjected to the FE model base by application of the recorded acceleration time history for each centrifuge test. The numerical simulation is performed according to the Newmark-Beta step by step integration method in the time domain with $\gamma = 0.5$ and $\beta = 0.25$ (Newmark, 1959, 1972). A modified Newton-Raphson solution algorithm is selected for the numerical computations with a Krylov subspace accelerator to accelerate the convergence process (Scott & Fenves, 2010).

The material damping emerging from the soil nonlinear hysteresis behavior is accompanied by a small initial stiffness proportional damping coefficient equals 0.003 as prescribed by Parra (1996) and Yang and Elgamal (2009) in order to ensure stable numerical simulations during high shearing phases. The following section will discuss the output results from the simulation of the centrifuge experiments, besides spotlighting the main findings.

20.6 Result and Discussion

Class C simulation output results are presented in this section comprising time histories of excess PWP, acceleration, and surface horizontal displacement at different sensor locations. For achieving computed model responses as similar to centrifuge

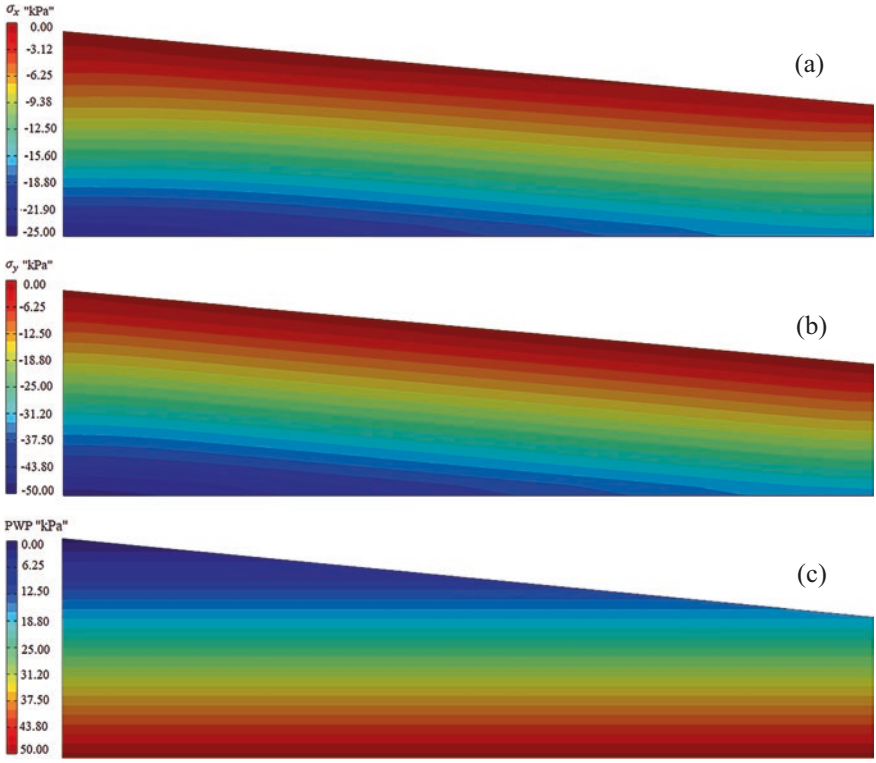

Fig. 20.8 Output contour plots of the initial stress analysis. (**a**) horizontal stress distribution, (**b**) vertical stress distribution, and (**c**) pore water pressure distribution

experiments, a slight change was made to the initially calibrated model parameters. These modifications were done towards c_1 and liq_2 parameters, as presented in Table 20.3.

Increasing the c_1 model parameter results in generating significantly higher excess pore water pressure and magnifying the horizontal surface deformations. Increasing liq_2 model parameter enhances the model predictions of shear strain accumulations, especially in case of the model subjected to initial static shear stresses, which provides proper estimations of the permanent horizontal surface displacements.

The selection of these values for c_1 and liq_2 parameters aims to employ a unified set of model parameters for each relative density group in centrifuge simulations. The PDMY02 estimated model parameters for (D_r 50%) group are used in simulating centrifuge tests done by ZJU and KyU, whereas PDMY02 estimated model parameters for (D_r 60%) group are selected for RPI and UCD centrifuge simulations.

Table 20.3 The modified values of PDMY02 model parameters for class-C simulations

Parameter	Estimated values		Description
(D_r) range	50–55%	60–65%	The relative density ranges of the Ottawa-F65 sand samples
c_1	0.095	0.075	The contraction parameter was changed to capture better output soil response towards excess PWP and horizontal displacement estimations
liq_2	3	3	liq_2 parameter was changed to adjust the model predictions of post-liquefaction accumulated permanent shear deformations

The output responses of middle array sensors "P1, P2, P3, P4, AH1, AH2, AH3, and AH4" and two top surface displacement recorders are selected for the comparisons between computed and measured output results for the selected Model A and Model B centrifuge tests. The figures below show the time histories of excess pore water pressure (PWP), horizontal acceleration, and horizontal surface displacements.

20.6.1 Model A Output Results

From Figs. 20.9 and 20.10, excess PWP and horizontal surface displacements are in good agreement with the experiment output responses despite little overestimation in the displacement output time histories with the UCD_A_A2_1 output result. The acceleration time histories reveal some dilation spikes that cannot be captured by the employed soil model. These spikes are very high in case of modeling the ZJU_A_A1_1 centrifuge test, as shown in Fig. 20.11.

Much higher negative PWP spikes were monitored in all sensor locations in the ZJU_A_A1_1 centrifuge test. The simulated excess PWP generation and dissipation rates in the ZJU_A_A1_1 test matched perfectly with the measured output responses, regardless of the absence of the negative excess PWP spikes in the simulated responses. These intensive negative PWP spikes have resulted from the damage that occurred in the soil fabric when reaching the liquefaction stage, which is why large surface horizontal deformation values are generated in measured and computed time histories.

Despite the accurately computed output results in the previous simulations, KyU_A_A2_1 computed response has deviated from the centrifuge experiment measurements, as presented in Fig. 20.12. This issue is very noticeable in the excess PWP and surface horizontal displacement time histories. On the contrary, the computed and measured acceleration time histories entirely coincide throughout the test duration.

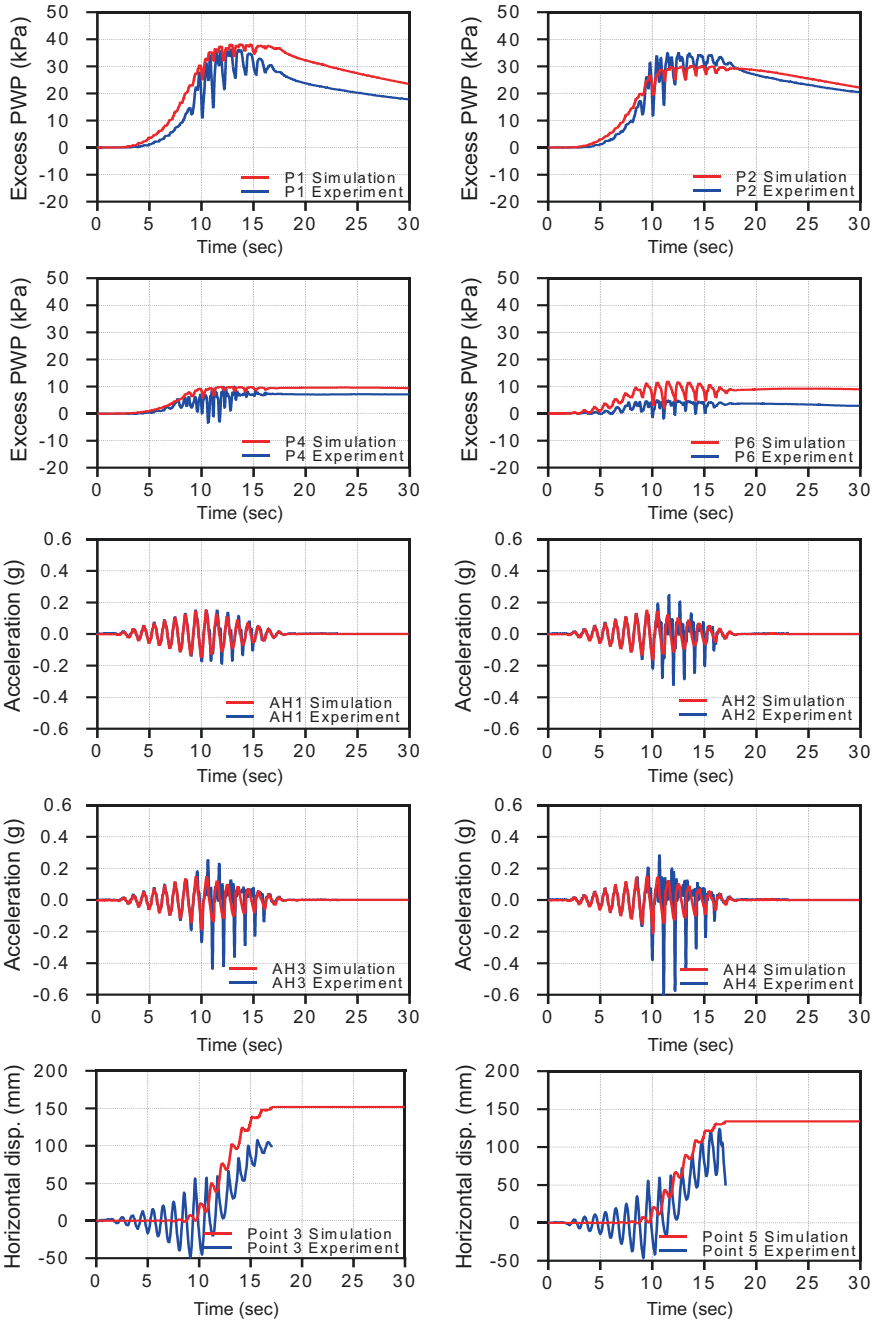

Fig. 20.9 Simulation vs. experiment output results of RPI-A-A1-1; time histories of excess pore water pressure, horizontal acceleration, and horizontal surface displacement (measured PWP data of sensor P3 is not available and exchanged with P6 output results)

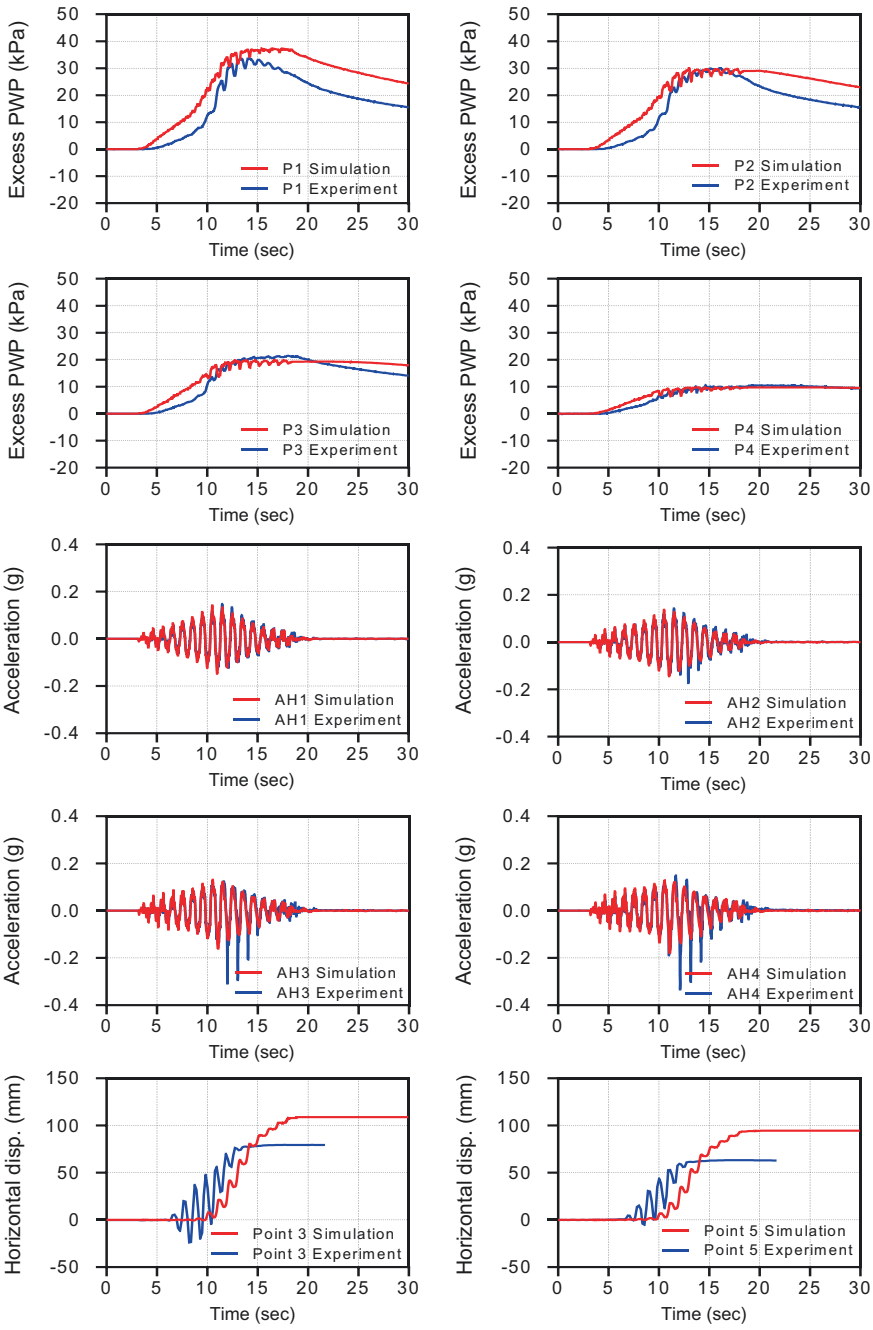

Fig. 20.10 Simulation vs. experiment output results of UCD_A_A2_1; time histories of excess pore water pressure, horizontal acceleration, and horizontal surface displacement

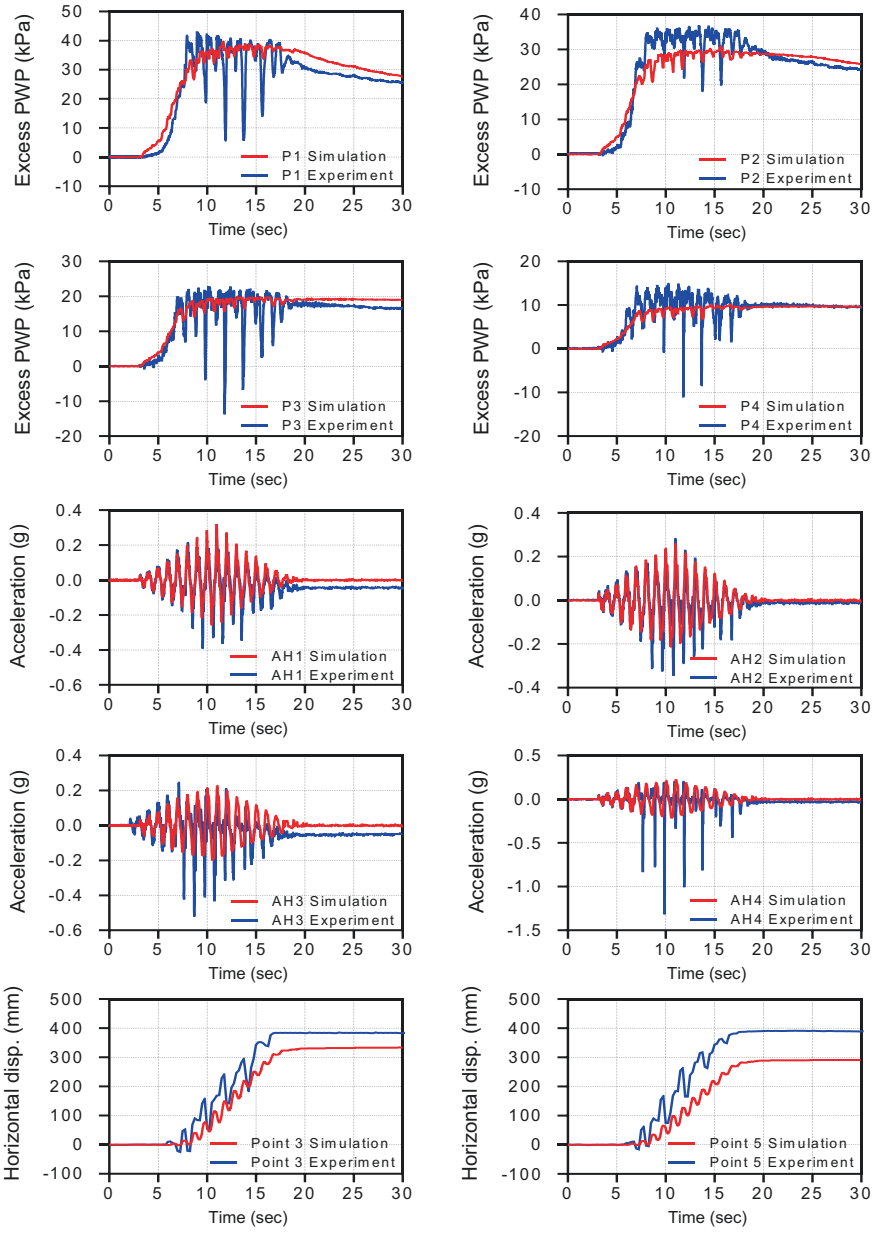

Fig. 20.11 Simulation vs. experiment output results of ZJU_A_A1_1; time histories of excess pore water pressure, horizontal acceleration, and horizontal surface displacement

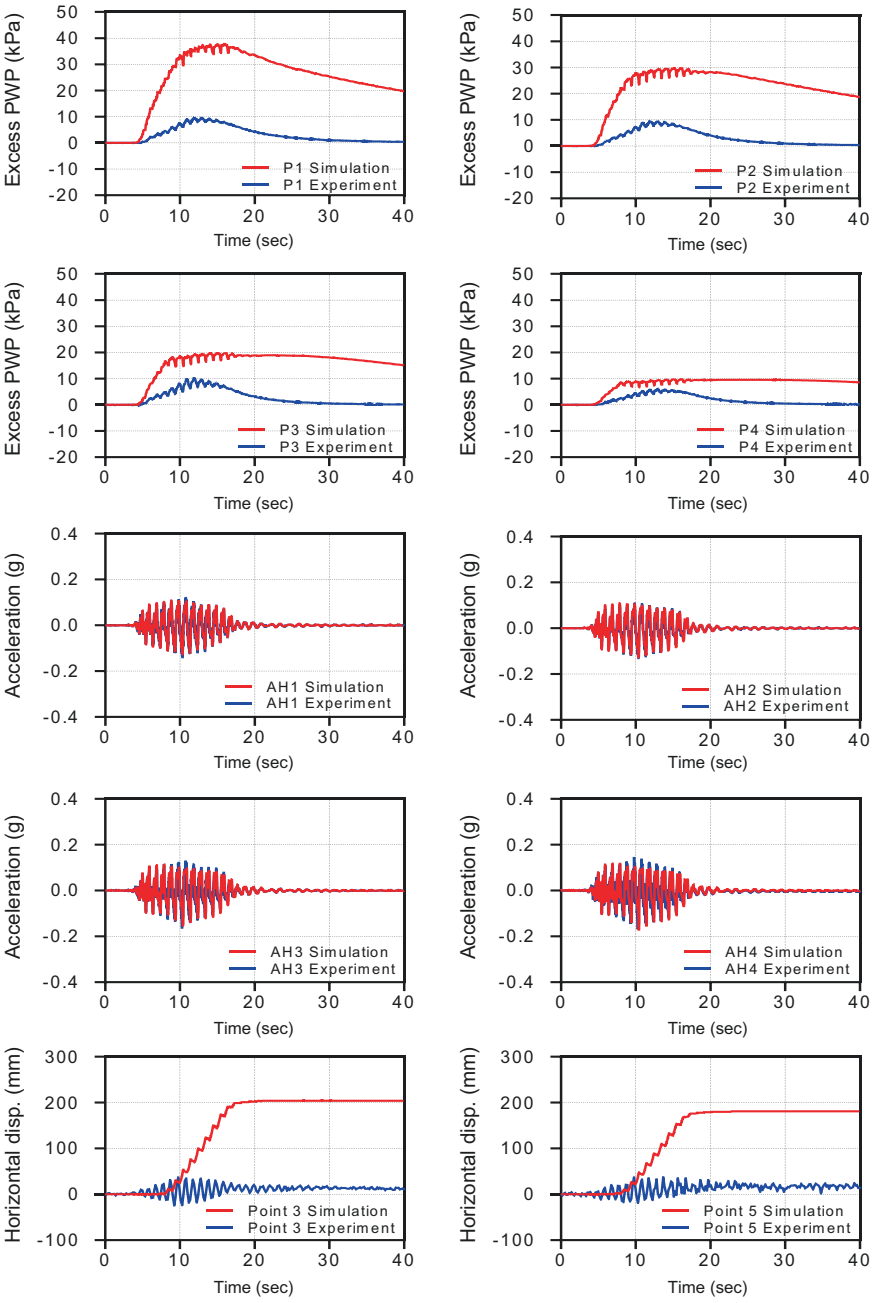

Fig. 20.12 Simulation vs. experiment output results of KyU_A_A2_1; time histories of excess pore water pressure, horizontal acceleration, and horizontal surface displacement

20.6.2 Model B Output Results

The Model B centrifuge experiments were simulated in the model scale. With RPI_A_B1_1 test, Fig. 20.13 shows computed output responses similar to experimental recorded results for the excess PWP and acceleration time histories despite slight disparities regarding the dissipation rate of the excess PWP. The simulated horizontal surface displacements are a bit lower than the experiment outputs, although they are still following similar centrifuge measured trends.

Through Fig. 20.14, there is a good agreement between the computed output results and the centrifuge measured responses, which can be depicted through the time histories of excess PWP and horizontal displacements. Soil dilative behavior appears again in the ZJU_A_B1_1 experiment through negative spikes in excess PWP and acceleration time histories (Fig. 20.15).

With KyU_A_B2_1 centrifuge simulation, the output computed PWP results are slightly better than the results obtained in Model A simulations; however, the displacement time histories are still highly deviated from the measured centrifuge responses. One of the expected reasons for getting overestimated horizontal surface displacements is the high wave oscillations that generated at frequencies near the natural soil frequency, which may cause resonance effects on the simulated model (see Sect. 20.2.1). Moreover, the model's flow rule may generate over estimated responses at low to medium CSR levels, as described in Sect. 20.4.2, which might increase the PWP and horizontal displacement output results.

20.7 Conclusion

Extensive class-C numerical simulations were performed by means of the Finite Element Analysis method to model seven centrifuge tests of mildly sloping ground composed of Ottawa-F65 sand in a rigid container under ramped sinusoidal input motions with different PGAs. Numerical simulations were performed in prototype scale and model scale for simulating Model A and Model B centrifuge experiments, respectively. An elastoplastic multi-yield surface model with pressure dependency, namely PDMY02, was engaged in this simulation work through the OpenSees platform.

The PDMY02 model calibration process, "Simulation Phase I", was carried out by simulating the cyclic torsional shear tests for soil samples with different relative densities composed of Ottawa-F65 sand under different CSR values. The model parameters were first estimated through geotechnical correlations and previous soil laboratory tests and then calibrated with the provided cyclic torsional shear laboratory tests.

The PDMY02 model provides fair computed responses for all cyclic torsional shear test simulations despite estimating inaccurate counts of loading cycles to reach initial liquefaction for very low and very high CSR levels. Prior to

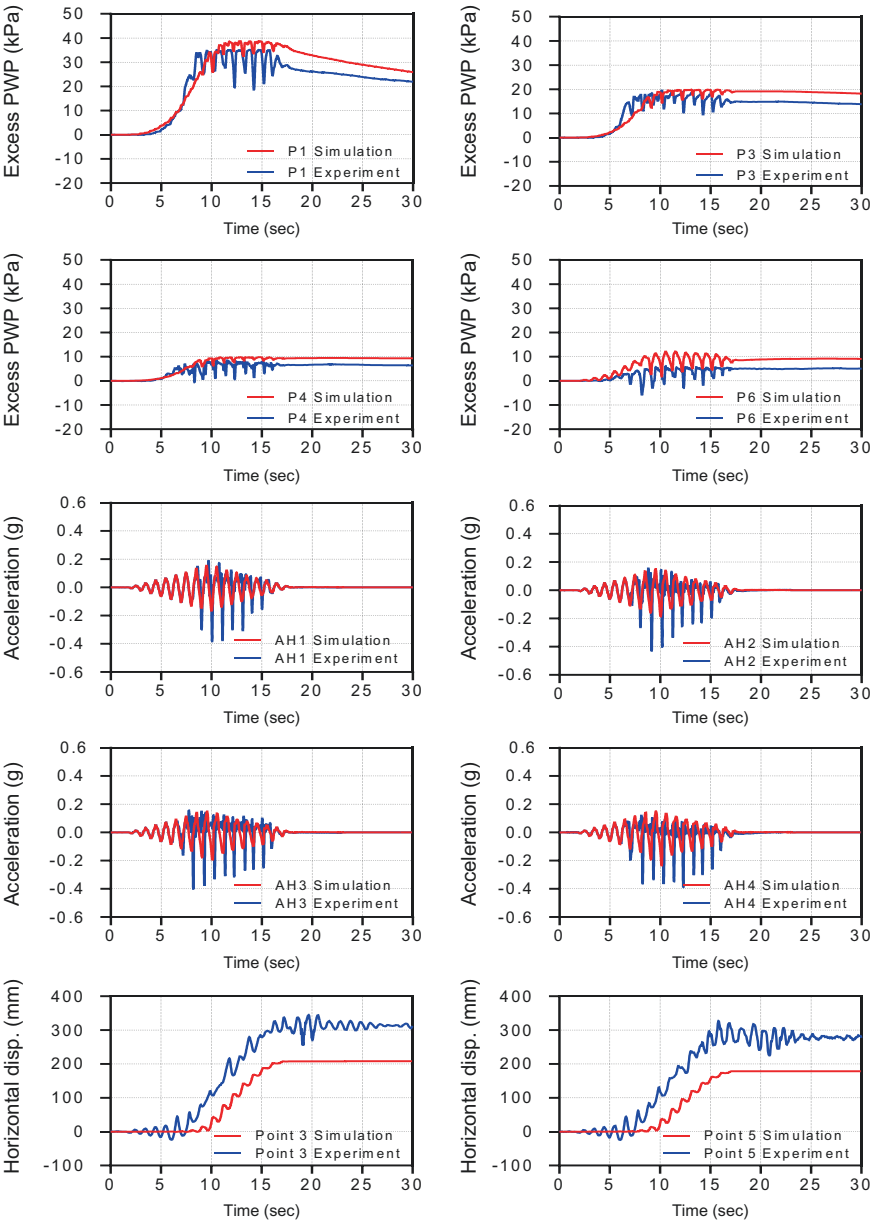

Fig. 20.13 Simulation vs. experiment output results of RPI_A_B1_1; time histories of excess pore water pressure, horizontal acceleration, and horizontal surface displacement (measured PWP data of sensor P2 is not available and exchanged with P6 output results)

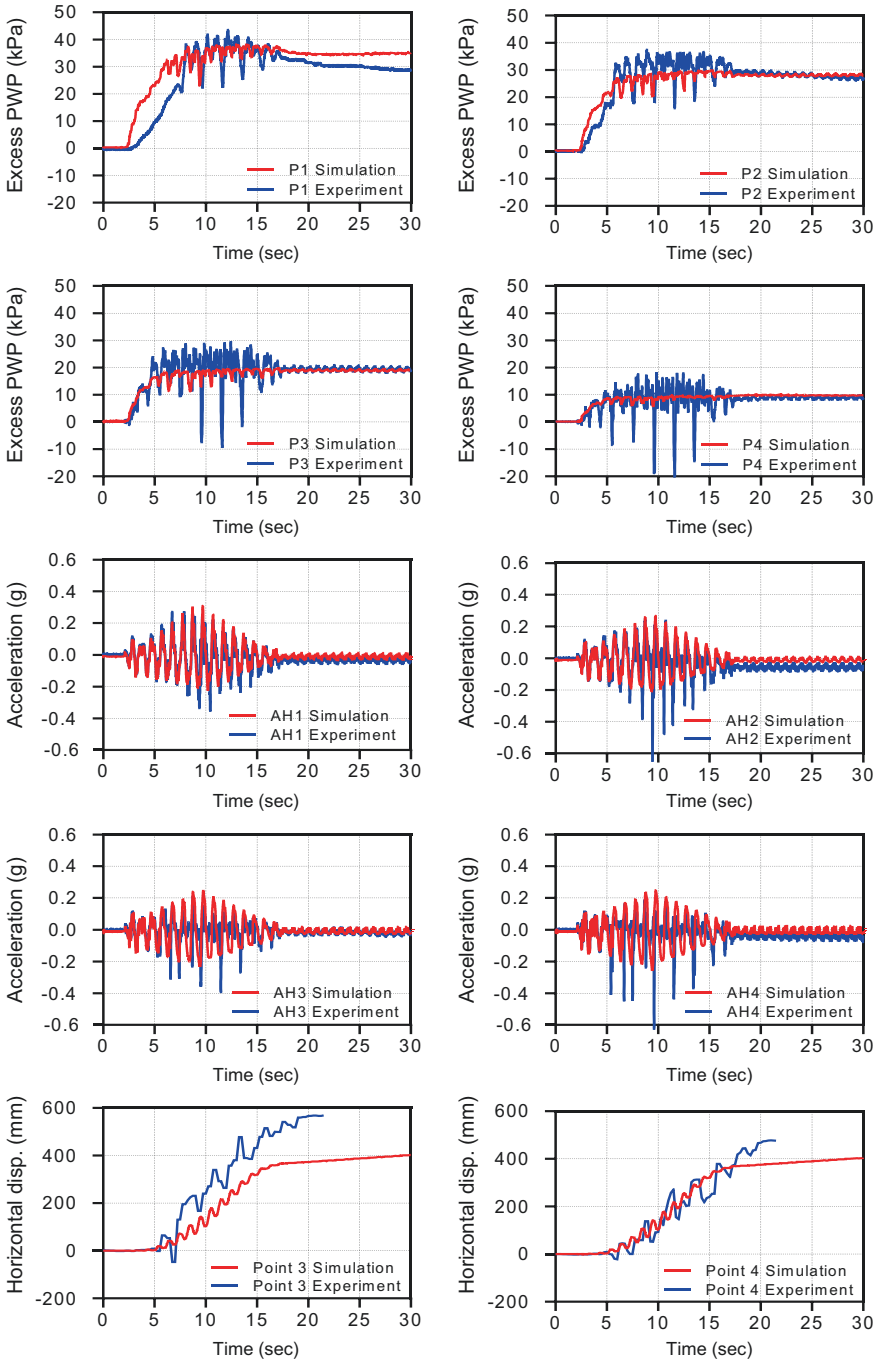

Fig. 20.14 Simulation vs. experiment output results of ZJU_A_B1_1; time histories of excess pore water pressure, horizontal acceleration, and horizontal surface displacement

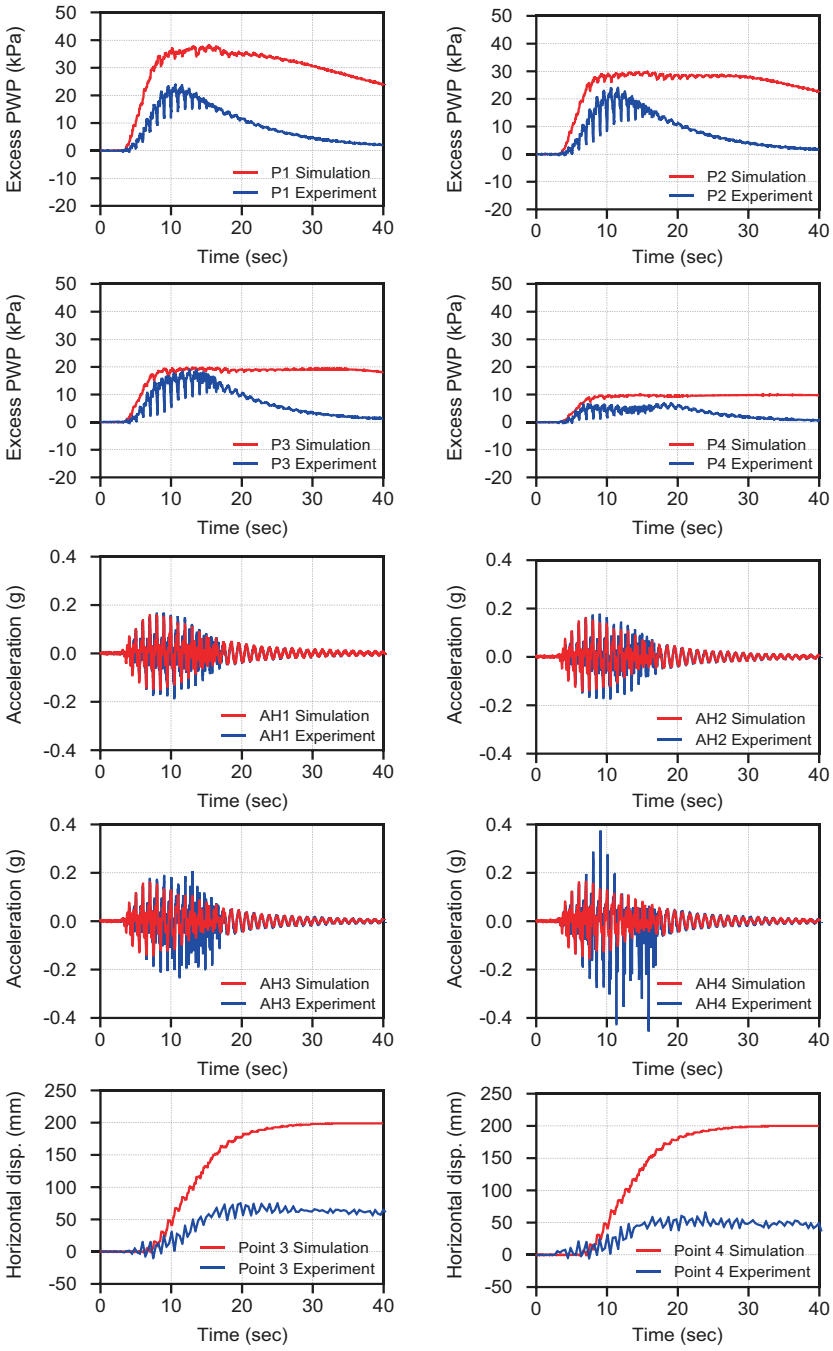

Fig. 20.15 Simulation vs. experiment output results of KyU_A_B2_1; time histories of excess pore water pressure, horizontal acceleration, and horizontal surface displacement

commencing Class C simulations, minor changes were made to model parameter values to deliver proper numerical predictions of the simulated centrifuge experiments. The computed results revealed that the PDMY02 model is capable of predicting the liquefaction potential and lateral spreading of the mildly sloping ground problem. The computed time histories of excess PWP, accelerations, and displacements are in good agreement with the measured responses in all centrifuge tests despite getting disparate simulated responses with experiments that took place at the Kyoto University centrifuge facility.

A prominent drawback when using the PDMY02 model appeared when calibrating the model parameters to predict the appropriate number of loading cycles to trigger liquefaction under a wide range of CSR values. The model's flow rule should be adjusted to accurately predict the number of loading cycles to reach initial liquefaction under different stress levels in order to achieve successful model calibrations and obtain better numerical simulation predictions. Generally, the PDMY02 model was found to be adequate for investigating the liquefaction potential of mildly sloping grounds and providing proper seismic predictions under different dynamic motion intensities.

Acknowledgments This study is supported by the National Natural Science Foundation of China (Nos. 51988101, 51978613, 52278374), the Chinese Program of Introducing Talents of Discipline to University (the 111 Project, No. B18047). The authors would thank Dr. Rui Wang of Tsinghua University as well as Mr. Qiang Ma and Mr. Kai Liu of Zhejiang University for their great help during the numerical simulations.

References

Andrus, R. D., & Stokoe, K. H. (2000). Liquefaction resistance of soils from shear-wave velocity. *Journal of Geotechnical and Geoenvironmental Engineering*. Clemson Univ, Dept Civil Engn, Clemson, SC 29634 USA Natl Inst Stand & Technol, Gaithersburg, MD 20899 USA Univ Texas, Dept Civil Engn, Jennie C & Milton T Graves Chair, Austin, TX 78712 USA, *126*(11), 1015–1025. https://doi.org/10.1061/(ASCE)1090-0241(2000)126:11(1015)

ASDEA-Software .(2019). STKO (*Scientific ToolKit for OpenSEES*). Pescara, Italy. Available at: https://www.asdeasoft.net/

Bastidas, P. (2016). *Ottawa F-65 sand characterization*. PhD thesis. University of California, Davis. Available at: https://datacenterhub.org/app/site/resources/2017/06/14288/FINAL_Ana_Maria_Parra_Bastidas_PhD_Dissertation.pdf

Beaty, M. H. (2018). Application of UBCSAND to the LEAP centrifuge experiments. In *Soil dynamics and earthquake engineering* (pp. 143–153). Beaty Engn LLC. https://doi.org/10.1016/j.soildyn.2017.10.006

Bolton, M. D. (1986). The strength and dilatancy of sands. *Geotechnique, 36*(1), 65–78. https://doi.org/10.1680/geot.1986.36.1.65

Carraro, J. A. H., Prezzi, M., & Salgado, R. (2009). Shear strength and stiffness of sands containing plastic or nonplastic fines. *Journal of Geotechnical and Geoenvironmental Engineering*. Colorado State Univ, Ft Collins, CO 80523 USA Purdue Univ, W Lafayette, IN 47907 USA, *135*(9), 1167–1178. https://doi.org/10.1061/(ASCE)1090-0241(2009)135:9(1167)

Chen, W.-F., & Mizuno, E. (1990). *Nonlinear analysis in soil mechanics: Theory and implementation*. Elsevier.

Elbadawy, M. A., Zhou, Y.-Z., & Liu, K. (2022). A modified pressure dependent multi-yield surface model for simulation of LEAP-Asia-2019 centrifuge experiments'. *Soil Dynamics and Earthquake Engineering, 154*, 107135. https://doi.org/10.1016/j.soildyn.2021.107135

Elgamal, A., et al. (2003). Modeling of cyclic mobility in saturated cohesionless soils. *International Journal of Plasticity*. Univ Calif San Diego, Dept Struct Engn, La Jolla, CA 92093 USA INTEVEP SA, Caracas, Venezuela Arab Acad Sci & Technol, Construct & Bldg Engn Dept, Alexandria, Egypt*, 19*(6), 883–905. https://doi.org/10.1016/S0749-6419(02)00010-4

Ghofrani, A., & Arduino, P. (2018). Prediction of LEAP centrifuge test results using a pressure-dependent bounding surface constitutive model. *Soil Dynamics and Earthquake Engineering*. Univ Washington, Dept Civil & Environm Engn, box 352700, Seattle, WA 98195 USA*, 113*, 758–770. https://doi.org/10.1016/j.soildyn.2016.12.001

Ishihara, K., Tatsuoka, F., & Yasuda, S. (1975). Undrained deformation and liquefaction of sand under cyclic stresses. *Soils and Foundations, 15*(1), 29–44. https://doi.org/10.3208/sandf1972.15.29

Khosravifar, A. (2012). *Analysis and design for inelastic structural response of extended piles shaft foundations in laterally spreading ground during earthquakes*. PhD thesis. University of California, Davis.

Khosravifar, A., et al. (2018). A 3D model for earthquake-induced liquefaction triggering and post-liquefaction response. *Soil Dynamics and Earthquake Engineering, 110*, 43–52. https://doi.org/10.1016/j.soildyn.2018.04.008

Kramer, S. L. (1996). *Geotechnical earthquake engineering 1st Edition*. Prentice Hall.

Kuhlemeyer, R. L., & Lysmer, J. (1973). Finite element method accuracy for wave propagation problems. *Journal of Soil Mechanics & Foundations Div, 99*, 421–427. (Tech Rpt).

Kutter, B. L., et al. (2015). LEAP databases for verification, validation, and calibration of codes for simulation of liquefaction. In *6th international conference on earthquake geotechnical engineering*. Christchurch, New Zealand. Available at: https://secure.tcc.co.nz/ei/images/ICEGE15Papers/Kutter_557.00.pdf

Kutter, B. L., et al. (2018). LEAP-GWU-2015 experiment specifications, results, and comparisons. *Soil Dynamics Earthquake Engineering, 113*, 616–628. Research Institute, Oakland, CA.

Kutter, B. L., et al. (2020). LEAP-UCD-2017 comparison of centrifuge test results. In *Model tests and numerical simulations of liquefaction and lateral spreading* (pp. 69–103). Springer. https://doi.org/10.1007/978-3-030-22818-7_4

Lacy, S. (1986). *Numerical procedures for nonlinear transient analysis of two-phase soil system*. Princeton University.

Madabhushi, S. P. G., & Schofield, A. N. (1993). Centrifuge modelling of tower structures on saturated sands subjected to earthquake perturbations. *Geotechnique, 43*(4), 555–565. Thomas Telford Ltd.

Manzari, M. T., et al. (2014). LEAP projects: Concept and challenges. In *Geotechnics for catastrophic flooding events* (pp. 109–116). Taylor & Francis Group.

McKenna, F. T. (1997). *Object-oriented finite element programming: Frameworks for analysis, algorithms and parallel computing.* PhD thesis, ProQuest dissertations and theses. University of California, Berkeley.

McKenna, F. (2011). OpenSees: A framework for earthquake engineering simulation. *Computing in Science & Engineering, 13*(4), 58–66. IEEE.

Mróz, Z. (1967). On the description of anisotropic workhardening. *Journal of the Mechanics and Physics of Solids, 15*(3), 163–175. https://doi.org/10.1016/0022-5096(67)90030-0

Newmark, N. M. (1959). A method of computation for structural dynamics. *Journal of the Engineering Mechanics Division, 85*(3), 67–94. ASCE.

Newmark, N. M. (1972). Method of computation for structural dynamics. *Pressure Vessels Piping Design Anal, 2*, 1235–1264.

OpenSees. (2000). *The open system for earthquake engineering simulation*. University of California, Berkeley. Available at: http://opensees.berkeley.edu

Parra, E. (1996). *Numerical modeling of liquefaction and lateral ground deformation including cyclic mobility and dilatation response in soil systems*. PhD thesis. Rensselaer Polytechnic Institute.

Prevost, J. H. (1978). Plasticity theory for soil stress-strain behavior. *Journal of the Engineering Mechanics Division, 104*(5), 1177–1194. ASCE.

Prevost, J. H. (1985). A simple plasticity theory for frictional cohesionless soils. *International Journal of Soil Dynamics and Earthquake Engineering, 4*(1), 9–17. https://doi.org/10.1016/0261-7277(85)90030-0

Schofield, A. N. (1998). *Geotechnical centrifuge development can correct a soil mechanics error*. University of Cambridge, Department of Engineering.

Scott, M. H., & Fenves, G. L. (2010). Krylov subspace accelerated Newton algorithm: Application to dynamic progressive collapse simulation of frames. *Journal of Structural Engineering, 136*(5), 473–480. https://doi.org/10.1061/(ASCE)ST.1943-541X.0000143

Tobita, T., et al. (2011). Application of the generalised scaling law to saturated ground. *International Journal of Physical Modelling in Geotechnics, 11*(4), 138–155. https://doi.org/10.1680/ijpmg.2011.11.4.138

Ueda, K. (2018). *LEAP-Asia-2018: Stress-strain response of Ottawa sand in cyclic torsional shear tests*. DesignSafe-CI. https://doi.org/10.17603/DS2D40H

Yang, Z., & Elgamal, A. (2008). Multi-surface cyclic plasticity sand model with lode angle effect. *Geotechnical and Geological Engineering, 26*(3), 335–348. https://doi.org/10.1007/s10706-007-9170-3

Yang, Z., & Elgamal, A. (2009). *Pressure depend MultiYield02 material*. OpenSeesWiki. Available at: http://opensees.berkeley.edu/wiki/index.php/PressureDependMultiYield02_Material

Yang, Z., Elgamal, A., & Parra, E. (2003). Computational model for cyclic mobility and associated shear deformation. *Journal of Geotechnical and Geoenvironmental Engineering*. Univ Calif San Diego, Dept Struct Engn, La Jolla, CA 92093 USA Intevep SA, PDVSA, Caracas 1070A, Venezuela, *129*(12), 1119–1127. https://doi.org/10.1061/(ASCE)1090-0241(2003)129:12(1119)

Yang, Z., Lu, J., & Elgamal, A. (2008). *OpenSees soil models and solid-fluid fully coupled elements: user's manual, version 1*. University of California. Available at: https://opensees.berkeley.edu/OpenSees/manuals/usermanual/1501.htm

Zhou, Y. G., Sun, Z. B., & Chen, Y. M. (2018). Zhejiang University benchmark centrifuge test for LEAP-GWU-2015 and liquefaction responses of a sloping ground. *Soil Dynamics and Earthquake Engineering, 113*, 698–713. https://doi.org/10.1016/j.soildyn.2017.03.010

Ziotopoulou, K. (2018). Seismic response of liquefiable sloping ground: Class A and C numerical predictions of centrifuge model responses. *Soil Dynamics and Earthquake Engineering*. Elsevier, *113*, 744–757.

Ziotopoulou, K., & Boulanger, R. W. (2012, May). Constitutive modeling of duration and overburden effects in liquefaction evaluations. In *Proceedings of second international conference on performance-based design in earthquake geotechnical engineering. Taormina, Italy* (pp. 28–30). Earthquake Engineering Research Institute.

Index

T. Tobita et al. (eds.), *Model Tests and Numerical Simulations of Liquefaction and Lateral Spreading II*, https://doi.org/10.1007/978-3-031-48821-4